DEP Agreement No.: **MN016**
Grantee Name: Florida Atlantic University
Grantee Address: 5600 US-1 N, Ft. Pierce, FL 34946
Grantee's Grant Manager: Dr. Jordon Beckler **Telephone No.:** 772-242-2421
(cell) 404-594-0293

Reporting Period: Final Report (Tasks 1-7 only)
Period of Performance 7/1/21 – 4/15/21

Project Number and Title: FDEP MN016:
Harmful Algal Bloom Innovative Technology: the Harmful Algal Bloom Assessment of Lake Okeechobee System (HALO)

Authored by:

Florida Atlantic University:
Jordon Beckler (PI)
Veronica Ruiz-Xomchuk (postdoc)
Mingshun Jiang (Co-PI)
Yufei Tang (Co-PI)
Malcolm McFarland (Co-PI)
Aditya Nayak (Co-PI)
Tim Moore (Co-PI)
Dennis Hanisak (Co-PI)

Florida Gulf Coast University:
Mike Parsons (Co-PI)

Navocean Inc:
Scott Duncan (Co-PI)

Gulf of Mexico Coastal Ocean Observation System:
Barbara Kirkpatrick (Co-PI)

This report is submitted in accordance with the reporting requirements of DEP Agreement No. MN016 and accurately reflects the activities associated with the project.

4/15/22

TABLE OF CONTENTS

1A: PROJECT OVERVIEW

PROJECT TITLE

Harmful Algal Bloom Innovative Technology: The Harmful Algal Bloom Assessment of Lake Okeechobee System (HALO)

GRANT AND REPORT STRUCTURE

Because of the nature and timing of the project, this Final Report only details results from Tasks 1 thru 7 of the grant agreement, with a separate future report for Tasks 8 thru 13 which are part of a new amendment (#3). This present chapter, **1A: Project Overview,** contains general information applicable all Project Tasks, including an

- **Project Overall Tasks Performed**
- **Project Major Results and Accomplishments**
- **Project Background**
- **Project Location and Activities Conducted** (essentially a task overview)
- **Project Conclusions and Recommended Future Work**.

This chapter is followed by individual appendices that provide comprehensive information on individual Project Tasks or Sub-Tasks (e.g. **Task 3A**, **3B**, and **3C** are complex and are therefore separated as individual appendices, while **Tasks 5A** and **5B** are more logically combined into a single **Task 5** appendix) which each contain a:

- **Task Introduction**
- **Task Methods**
- **Task Activities Scheduled vs. Completed**
- **Task Results and Discussion**
- **Task Conclusions and Future Work**

PROJECT OVERALL TASKS PERFORMED

This report relates specifically to Tasks 1 thru 7 of the Harmful Algal Bloom Assessment of Lake Okeechobee (HALO) observation system specifically conducted from 7/1/20 to 6/30/22, with active monitoring and modeling activities primarily performed during calendar year 2021. The HALO system augments conventional harmful algal bloom (HAB)-related monitoring (e.g. by the South Florida Water Management District; SFWMD) with autonomous HAB detection technologies and advanced environmental measurements of the water, sediment, and air to provide a context for the ecological observations. Additionally, modeling activities aimed to synthesize and abstract results to develop a predictive capacity for Lake Okeechobee HABs, in particular *Microcystis aeruginosa*. In turn, HALO seeks to provide improved HAB-related decision-making and resource planning capabilities for relevant agency and stakeholder management. Activities provide information needed to understand the seasonal progression of blooms, especially regarding the geographical patterns of nutrient sources, utilization, and limitation, as well as the role of environmental factors such as the light and hydrodynamic environment.

Information in regards to where, when, and which species are blooming – but also why –is critical for cost efficient decision making, e.g. for nutrient reduction programs, e.g. fertilizer management, dredging, or interception technologies. Moreover, the means to pinpoint problem areas early enables a much more rapid and efficient mitigation response. But while early detection and/or forecast are critical for deployment of mitigation efforts, the additional benefit of establishing baseline information of environmental characteristics is also imperative for designing of pre-and post- mitigation monitoring strategies. This data additionally develops a comparative reference to evaluate overall efficacy and safety of any of HAB mitigation efforts, as well as any secondary impacts. From inception, the project strived to produce concrete outputs evidenced by the public web portal, several issues of a bulletin during the bloom season of 2021, and two predictive and operational models under continuous improvement. A portion of the data generated is acquired remotely and thus paves the way for a future fully autonomous monitoring system.

Project Task numbers and associated measurements included:

1. The "Harmful Algal Bloom Assessment of Lake Okeechobee" (HALO) web-portal system was implemented as a publicly available database and data portal. The HALO system integrates data collected in other tasks and from other monitoring programs to provide data visualization. Biogeochemical and machine learning models were included within HALO to forecast bloom conditions through data aggregation.
2. Conventional HAB sampling monitoring techniques complemented advanced analytical methods to detect and monitor HABs. This task focused on environmental monitoring; biological sampling and analysis; and water column toxin analysis. Data collection included discrete sampling and the deployment of autonomous in-situ monitoring via innovative optical and acoustic measurement technology.
3. Conventional and innovative sediment sample measurements were utilized to determine the role and controls of sediment nutrient loading to the water column in the context of HABs. Parameters studied included the spatial and temporal variability of sediment legacy nutrient loads; associated nutrient microbial respiration and redox-dependent nutrient transformation processes; benthic fluxes of carbon, nutrients, and toxins; and the analysis of sediment *M. aeruginosa* cysts and toxins.
4. An Autonomous Surface Vehicle (ASV) was employed to provide continuous environmental, meteorological, biogeochemical, and physical monitoring of surface waters with real-time communication. The ASV was programmed to survey the northern lake.
5. Optical measurements of the lake-leaving remote sensing reflectance were monitored in situ in the northern lake at a high temporal frequency to monitor *M. aeruginosa* surface scums, provide "ground truthing" of conventional satellite remote sensing algorithms to establish relative errors, and determine if algorithm refinement is required. Additionally, satellite remotely sensing-based HAB monitoring was conducted to generate routine maps of surface HAB scums.
6. Near real time water quality monitoring was conducted at in surface and bottom waters of Lake Okeechobee. The systems provided an intensive array of continuous water quality monitoring parameters beyond those typically generated by water quality sondes, not limited to Chlorophyll-A, nitrate, and orthophosphate.
7. Microcystin toxins were monitored in aerosols over several discrete survey events, and time-integrated water column toxins were measured at several sites via multi-week deployment of adsorptive resins.

PROJECT MAJOR RESULTS AND ACCOMPLISHMENTS

This section is formatted to list the specific activity and then the major results or accomplishments resulting from that activity:

1. **Biweekly/monthly environmental surveys expanded the temporal and scientific resolution of the ongoing SFWMD sampling regiment. HALO targeted alternate weeks to the extent logistically possible while also obtaining bottom water samples and measurements in addition to the typical surface measurements obtained by SFWMD. Measurements included HAB speciation (flow cytometry and epifluorescence), cell health (live/dead counts), metabolic rates, pigments, variable fluorescence, and toxins.**

- *M. aeruginosa* was the dominant bloom forming cyanobacteria although other toxic taxa were also observed including *Dolichospermum* sp., and *Cylindrospermopsis* sp. (**Task 2B**)
- *M. aeruginosa* blooms appear more vertically stratified in the turbid sites relative to the more optically transparent sites, with cell counts elevated in the surface layer. However, this apparent pattern may be influenced by the hourly timing of the site visit, as vertical cell distributions exhibit a diel dependency (see #2 below). (**Tasks 2B, 2D**)
- Unhealthy or dead cells also often comprised a significant bloom fraction in surface and bottom waters. Dead cells were most abundant during peak bloom periods suggesting patchy and rapidly oscillating cycles of growth and death possibly due to local nutrient limitation. (**Task 2B**)
- Microcystin concentrations were highly variable among sites and over time but were frequently highest in surface waters. (**Tasks 2B, 7C**)
- *M. aeruginosa* photophysiology (Fv/Fm) showed different temporal trends among sites, but was more variable in surface waters suggesting that local, short term light exposure history is important to the health and photosynthetic capacity of populations. (**Task 2B**)
- *M. aeruginosa* metabolic rates were generally highest towards the end of the bloom season in August or September, suggesting a possible switch from autotrophy to chemotrophy. (**Task 2C**)

2. **Innovative in situ HAB detection technologies were tested for sustained monitoring suitability in this optically complex system. These included an in situ holographic microscope deployed during a discrete survey: the AUTOHOLO; and an acoustics-based system deployed for a 2-week period: the Acoustic Zooplankton Fish Profiler).**

- The AUTOHOLO is theoretically capable of detecting *M. aeruginosa* at lower cell concentrations than other state-of-the-art in situ techniques. This new in situ HAB detection technology was demonstrated to work effectively in imaging *M. aeruginosa* colonies, copepods and detrital matter under a variety of particle loads. (**Task 2D**)
- The AZFP, while unable at least at this testing stage to resolve particle identities, was able to detect the apparent diurnal transport of particulates (presumably cells) during a *M. aeruginosa* bloom, with concentration near the surface during daylight hours and more uniform distributions or aggregation near the bottom at night. (**Task 2D**)

3. **Lake optical properties (in-water) and hyperspectral surface reflectance were measured during discrete biweekly/monthly surveys to inform remote sensing-based detection and bio-optical environmental characterization.**

- Discrete remote sensing reflectance data (from hand-held instrumentation) revealed that adjustments to the chlorophyll and *M. aeruginosa* retrieval algorithms that are currently operationally employed via satellites can be modified for more accurate quantification. (**Tasks 2B, 5B**)
- Optical backscatter was extremely high and Secchi depths were very low suggesting standard algorithms for interpretation of remote sensing imagery may be inappropriate for Lake Okeechobee. (**Tasks 2A, 5B**)

4. **Historical remote sensing data syntheses, and the continuous fixed-location SeaPRISM measurements, when combined with these measurements (from #3) allowed validation ("ground-truthing") of satellite algorithms in this specific lake for the first time (e.g., measurements of Cyanobacterial Index, Chlorophyll, and turbidity).**

- HALO data demonstrates that the NOAA remote sensing HAB product (CI) is drastically underestimating cyanobacterial concentrations and a Lake Okeechobee-specific algorithm is needed. (**Tasks 2B, 5B**)
- Over the last 5 years, peak bloom activity is during June through August, but certain parts of the lake also show high bloom activity outside these months. Historical data shows changes with respect to current bloom geographical patterns, and blooms were less frequent from 2004 through 2011 relative to the 2016 to 2021 time period. (**Task 5B**)
- Satellite imagery combined with microscopic analysis revealed at least two different types of cyanobacteria bloom phenomena: *M. aeruginosa* dominated in the central and northern parts of the lake during the spring and summer, while other cyanobacteria (e.g. *Dolichospermum* sp.) was dominant in the western part of the lake in summer and into fall. (**Tasks 2B, 5B**)

5. ***M. aeruginosa* cysts and toxin inventories were measured seasonally in lake sediments.**

- Sediment cores appeared contained visible *M. aeruginosa* colonies that appeared to have settled from the water column onto the surface of the sediment, but viable cysts were rarely detected within the sediments themselves, suggesting remineralization is rapid. (**Task 3D**)
- Microcystin toxins were only present in sediments in significant concentrations when coinciding with current or recent blooms. There does not appear significant carry-over of toxins, e.g. from previous years. Even during blooms at the most turbid mud bottom sites, toxins are not present in surface sediments, suggesting that frequent resuspension/reoxygenation catalyzes degradation. (**Task 3E**)

6. **Sediment nutrient inventories and diffusive fluxes were measured routinely in collected sediment cores, along with relevant environmental parameters. Unique, high depth-resolution vertical electrochemical profiling provided information regarding the relevant microbial respiration pathways and status of mineralogic buffers potentially involved in N and P dynamics.**

- Muddy sediments were completely anaerobic below 2 mm depth, with very low nitrate/nitrite concentrations. Instead, dissimilatory iron(III) reduction is the most dominant respiratory pathway due to the extremely high concentrations of iron hydroxides. (**Tasks 3A-C**)

- In contrast to previous studies, both pore water ammonium and phosphate demonstrated strong site-dependent seasonal patterns that had apparent dependencies on the intensity of Fe(III) respiration and Fe(II) oxidation processes. There is some evidence that storm-induced resuspension may release P in the short term (hourly/daily), but could limit P release over longer timelines (weeks) by causing the reoxidation of Fe minerals and the subsequent scavenging of phosphate. (**Tasks 3A, 6**)
- Phosphate release to pore waters was most intense over late summer and fall, whereas dissolved ammonium in pore waters peaked in the spring at 2 of 3 study sites and declined gradually over the summer and fall. We suspect this process is related to a newly identified form of ammonium removal coupled to iron hydroxide reduction, feammox. These combined patterns lead to drastic changes in the inorganic N:P ratio of the sediment pore waters, with an order of magnitude change between the springtime maximum and late summer minimum. Considering *M. aeruginosa* growth is favored under elevated ammonium conditions, this finding could explain why *M. aeruginosa* blooms were most intense in 2021 in the spring. (**Tasks 2B, 3A**)
- Sulfate reduction co-occurs in sediments during the spring, when warming temperatures may allow a pulse of intense organic respiration. (**Task 3A**)
- Sediment diffusive fluxes of ammonium were more persistent than of phosphate, which may instead require resuspension for delivery. (**Tasks 3A-B**)
- Pahokee Marina was a hotspot for sediment nutrient inventories and fluxes, explaining the intense blooms in this area relative to other lake areas. However, the nearby reference site also contained high nutrient inventories, suggesting dredging may not be a worthwhile mitigation technique. (**Task 3A**)

7. In situ benthic incubations were conducted to determine benthic photosynthesis/respiration rates and nutrient and microcystin toxin fluxes.

- Because biological processes are intense in this lake system relative to ocean systems from which this technique is developed, we are unable to discriminate between effects due to benthic respiration vs. sediment fluxes. Several findings can still be deduced. (**Task 3B**)
- Benthic uptake of ammonium when *M. aeruginosa* is present is extremely rapid and can prevent this nutrient from accumulating. Nitrification can also occur rapidly, within a few hours of commencing the incubation. This can explain why Lake Okeechobee water column is dominated by nitrate in lieu of ammonium, except for under confined conditions with intense fluxes (e.g. Pahokee Marina). (**Tasks 3A- B**)
- Dissolved oxygen consumption covaried with ammonium fluxes, although we cannot distinguish between benthic remineralization vs. sediment fluxes. (**Tasks 3A- B**)
- Ammonium fluxes could explain the water column DIN inventory with a residence time of only 2 days. (**Tasks 3A- B**)
- Phosphate does not flux from sediments into benthic flux chambers until a dissolved oxygen threshold is reached (<50%) suggesting that the dissolution of the iron hydroxide mineral barrier is required. Because water column O_2 concentrations rarely reach this level, diffusive fluxes of phosphate are probably low and resuspension fluxes are probably more important. (**Task 3B**)
- Microcystin toxins accumulated in the benthic incubation chambers, especially when *M. aeruginosa* was present. It is not possible to distinguish between sediment toxin fluxes vs. in situ biological production. (**Task 3B**)

8. **An innovative in situ electrochemical analyzer was deployed to monitor in situ sediment respiration and potential nutrient release processes in real time (i.e. aerobic vs. anaerobic respiration processes). This was to our knowledge, the first in situ autonomous sediment sensor ever deployed for applied HAB-related monitoring.**

- We did not experience a high level of success in deploying this sensor long term for in situ monitoring, with only a few days of useable data collected; however, we did refine the approach in the laboratory and plan to continue testing as part of future HALO work. (**Task 3C**)
- The data shows that microbial iron reduction is the dominant respiratory process. A complex, dynamic biologically-mediated process is evidenced by four tentative iron/sulfur containing molecules consistently detected. Combined with conventional pore water results that demonstrates the coaccumulation of dissolved iron and nutrients, these electrochemically detectable analytes can potentially be used as either direct nutrient proxies or as indicators of conditions conducive to a sediment nutrient flux. (**Task 3C**)

9. **Continuous hourly environmental monitoring of surface and bottom waters in the northern lake was accomplished over a period of 7 months, including water quality and nutrient measurements, using advanced comprehensive sensors transmitting data in near-real time (extension of the Indian River Lagoon Observing Network; IRLON).**

- Significant sensor infrastructure was installed at the north SFWMD tower. The infrastructure remains to easily reinstall these sensors if funded. (**Task 6**)
- Water column phosphate and nitrate concentrations vary over short time scales and demonstrate that conventional biweekly measurements are not sufficient at capturing the required dynamics. Several nearly complete nutrient regeneration/depletion cycles can occur within these two-week windows. (**Task 6**)
- Phosphate is critically linked to turbidity as a function of time, suggesting that sediment resuspension is a major control on the delivery of this nutrient. (**Tasks 3A, 6**)

10. **Surface water environmental, biological, and hydrodynamic monitoring was conducted for one full year using an autonomous sail-powered vehicle in the northern areas of the lake. Measurements included fluorometric measurements of chl. a, phyocyanin, and dissolved organic matter; temperature and conductivity, dissolved oxygen, RGB backscatter for particulates, and depth-resolved current velocities via an ADCP.**

- Triangular loop transects in the northern lake were repeated over 78 times in 2021 that show surface patterns in blooms and water quality parameters, even on cloudy days when satellite remote sensing measurements are not possible. (**Task 4**)
- There is great value in the horizontal and temporal analytical and current velocity gradients captured via the in-water sensors and this data will be mined for years to come. (**Task 4**)
- Different bloom species and stages appear to exhibit variable patterns of chl. a vs. phycyanin, relative to backscatter, as well as dissolved oxygen consumption patterns. These patterns may be characteristic of blooms and thus useful in remote identification, e.g. from fixed location water quality platforms. (**Tasks 2B, 4**)
- Measured chlorophyll or phycocyanin fluorescence intensities, however, may be suppressed by the excess particulates (i.e. backscatter measurements), so a new lake-specific algorithm must be developed to accurately use this fluorometric in situ data going forward. (**Task 4**)

11. **Spatially integrated concentrations of microcystin toxin aerosols, specifically fractionated by size according to human lung penetration/bioavailability, were monitored on half-day surveys during transit and related to in-water toxin concentrations.**

- Airborne microcystin concentrations were generally low, most samples below the limit of quantification (LOQ; ~0.03 ng m^{-3}). In fact, airborne microcystin concentrations were far below levels thought to cause exposure symptoms (4.58 ng m^{-3}; Wood and Dietrich 2011). Air-borne microcystin concentrations were not correlated with water-borne microcystin or Microcystis concentrations, possibly due to the low (non-bloom) concentrations observed during this portion of the study. (**Task 7B**)

12. **A 3-D hydrodynamic and biogeochemical model (ROMS-NZPD) was implemented for the lake environment, forced by river run-off, and nutrient fluxes, atmospheric forcing, and sediment inputs via parameterizations.**

- The model was operationalized on the HALO web portal and provided 4-D forecasts and hindcasts of chl. and nutrient concentrations +/- 7 days from present. (**Task 1E**)
- The model accurately reproduces the hydrology, including the complex water management influences and evaporation, as well as water mass transport. (**Task 1E**)
- Model validation is currently underway and the model is continuously being improved, including the accurate parameterization of sediment nutrients and vertical migration behavior. (**Tasks 2A-B, 3A, 6, 1E**)

13. **An AI Machine Learning model was developed and implemented to provide spatial bloom prediction as “learned” from historical trends.**

- The model based on a deep learning technique called ConvLSTM was operationalized on the HALO web portal and provided spatially resolved forecasts of chl. a. 14 days from present based on a learning dataset that consists of previous days’ information. (**Task 1F**)
- The model was offline trained using year-long multiple and updated in an online manner through incremental learning. (**Tasks 1E, 1F, 5**)
- Data aggregation and preparation (i.e., data cleaning and preprocessing) for model training was a huge undertaking; now efforts are focused on integrating wind as a separate input channel to improve model skill. Validation is underway. (**Task 1F**)

14. **Project results were made publicly available, are archived for future use, and several publications are in preparation.**

- A measurement database was created on a high performance computing server at FAU that serves to host data that is easily accessible via internal collaborators. (**Task 1C**)
- A data portal was created on the Gulf Coast Ocean Observing System (GCOOS) website (halo.gcoos.org) to allow public viewing of certain data types and near-real time tracking of bloom conditions. (**Task 1D**)
- A voluntary HALO bulletin was created and disseminated midway through the project to share results and insights and provide bloom condition updates, with a total of 7 issues released.
- Publications in preparation include:

- Efficient anaerobic sediment processing via a novel sediment core extruder (recently published, Quinan et al., *MethodsX Journal*, Volume 9, 2022) (Task 3)
- The Harmful Algal Bloom Assessment of Lake Okeechobee (HALO): Data synthesis and availability (Tasks 1-7)
- Comparing conventional and innovative HAB detection technologies in Lake Okeechobee (Tasks 2, 4, 5, 6)
- A biogeochemical model for Lake Okeechobee HAB prediction (Task 1E)
- Physics-informed machine learning-based Lake Okeechobee HAB prediction modeling (Task 1F)
- Ecological phytoplankton bloom metabolism, physiology and light regulation, and toxicity in Lake Okeechobee during the 2021 bloom season (Tasks 2, 4, 5, 6, 7)
- A novel benthic lander for lake and estuarine sediment nutrient flux measurements (Task 3B)
- Iron cycling drives seasonal nutrient patterns in a shallow lake environment (Task 3A-C)
- Lake HAB & water quality monitoring via a novel autonomous wind and solar-powered Autonomous Surface Vehicle (Task 4)
- Long term Lake Okeechobee historical harmful algal bloom climatology from satellite remote sensing patterns (Task 5)
- A novel *M. aeruginosa* quantification algorithm for Lake Okeechobee (Task 5)
- High frequency water quality monitoring provide novel insights into Lake Okeechobee HAB dynamics (Tasks 2, 3, 6)

PROJECT BACKGROUND

Over the past decade or two in Lake Okeechobee, recurrent Harmful Algae Blooms (HAB) issues have revolved around extreme blooms of the cyanobacteria *Microcystis aeruginosa*. This common freshwater species is quickly becoming a global health threat, with reported increases in both the frequency and intensity of blooms around the world (e.g., Carey et al., 2012; Lehman et al., 2013; Miller et al., 2010). *M. aeruginosa* is a colonial cyanobacteria that can aggregate into large colonies and use gas vacuole buoyancy regulation to form dense surface blooms that out-compete other phytoplankton. In general, the growth of M. aeruginosa blooms are greatly enhanced by warm temperatures (25 - 30 ◦C), high irradiance, and high nutrients (particularly high phosphorous and/or low N:P ratios) (Fujimoto et al. 1997; Xie et al. 2003; Homma et al. 2008; Davis et al. 2009; liu et al. 2011; Lapointe et al. 2012), environmental conditions which are common to Lake Okeechobee waters year round. In more temperate climates, *M. aeruginos*a blooms are seasonal (summertime - warm water) events, where the cells “over-winter” in the sediments until conditions are more favorable for its growth (Brunberg & Blomqvist 2002). While Lake Okeechobee *M. aeruginosa* blooms are also seasonal, virtually no information is known as to whether the cysts overwinter in the sediments. In addition to creating dense surface mats that clog waterways, give off noxious odors and potentially cause hypoxia/anoxia events, *M. aeruginosa* blooms produce microcystins – potent hepatotoxins that have been linked to skin disease, respiratory distress, liver damage and liver cancer in both animals and humans (e.g. Dawson 1998; Carmichael 2001). Population assemblages of *M. aeruginosa* can be comprised of different strains that may be toxic or non-toxic (e.g. Baker et al. 2001; Davis et al. 2009). In addition, different strains can also have altered toxicity expression and regulation when exposed to different environmental conditions (Kaebernick & Neilan 2001; Ross et al. 2006; Davis et al 2009). Furthermore, *M. aeruginosa* and other cyanobacteria have been reported to produce the neurotoxin, β-N- methylamino-L-alanine (BMAA), which has been linked to amyotrophic lateral sclerosis and symptoms resembling Alzheimer’s (Cox et al. 2003; 2005). These toxins create serious concerns for human health and have led to local warnings regarding exposure, closure of beaches and waterways, and state of emergency declarations within the region. The expected effects of climate change and further eutrophication in coastal environments may only increase this problem worldwide (Paerl 1988; Houghton et al. 2001; Hudnell & Dortch 2008; Paerl & Huisman 2009; Carey et al. 2012).

Blooms of this species now appear to be expanding into and persisting in more saline estuarine environments, including Florida's St. Lucie Estuary (SLE) and the Indian River Lagoon (IRL). When Lake Okeechobee water levels become high due to large rain events, the Army Corps of Engineers discharge Lake Okeechobee water into two main canals, one that feeds water west through the Caloosahatchee River to the coastal waters of Ft. Meyers and Gulf of Mexico beaches, and one that feeds water east to the SLE, IRL and Atlantic beaches. Since large HABs of *M. aeruginosa* are now annual occurrences in Lake Okeechobee, these HABs are now regularly transported into the SLE and the IRL (and west coast regions), where they have resulted in significant ecological and economic damage (http://news.nationalgeographic.com/2016/07/ toxic-algae-florida-beaches-climate-swamp-environment/). For example, as a result of the on-going SLE/IRL *M. aeruginosa* bloom, several Florida counties are or have been under states of emergencies based on negative impacts to the economy, public health and ecosystem viability and submitted a request for a federal disaster declaration. A critical concern for local water managers is that the acute and/or chronic exposure risks of *M. aeruginos*a toxins to marine life and humans in and around the SLE/IRL region have yet to be documented or scientifically understood. Thus, an improved understanding of the ecology and persistence of *M. aeruginosa* blooms and the distribution, release, and bioaccumulation of their toxins represent the key challenges for local scientists and water managers. Despite year-round temperatures potentially within the habitable range for *M. aeruginosa*, the blooms do not typically persist year-round, suggesting other cofactors are involved, such as seasonal nutrient dynamics.

Because of the shallow nature of the lake and thus a high sediment surface area to water column volume ratio, sediments play a large role in nutrient and HAB dynamics relative to other deeper systems. Decades of unchecked nutrient-laden discharges has resulted in the accumulation of "legacy" anthropogenic nutrients in Lake Okeechobee sediments (Brezonik & Engstrom, 1998). Nutrient-rich mud has accumulated in the deepest eastern portion of the lake, and this mud is easily resuspended, affecting both water clarity (and thus light availability) and nutrient loading (Missimer et al. 2021). Nutrient fluxes of both N and P from sediments can flux from sediments due to both passive diffusion of pore water inventories or turbulent wind-driven resuspension. However, this sediment/water column coupling has yet to be evaluated at a high frequency. Further, very little is known regarding the specific biogeochemical processes within sediments that govern the nutrient release of N and P from solid phase organics or minerals to pore waters, which sets the stage for a potential for a subsequent flux. In lab studies, hypoxia, e.g. caused by to excess organic loading, has been demonstrated to further enhance nutrient sediment P release (Fisher et al. 2005). However, the lake is shallow and hypoxia is likely relatively rare, suggesting physical resuspension may be more important. However, very little is known regarding the seasonal controls of sediment nutrient inventories or dynamics. While warm water and organic-rich, chemically reducing conditions tend to contribute to greater accumulation of nutrient dissolved phosphorous in pore waters, the periodic reoxygenation of surface sediments due to mixing may allow the resequestration of these nutrients due to reprecipiration and thus readsorption of P onto iron hydroxides. Nitrogen on the other hand, can be removed by denitrification or coupled denitrification; but high frequency insights into these processes in Lake Okeechobee are not available.

In 2019, the Blue Green Algae Task Force (BGATF) conducted meetings and generated a consensus document with recommendations for combating *M. aeruginosa* HABs. While active mitigation of blooms is a possibility, the triggers and controls of HABs are necessary before wide scale active mitigation efforts can be undertaken. Determining both-short term efficacy and long-term impacts on the underlying triggers of HABs will require ongoing detailed evaluation of the lake water, sediments and trends in algae bloom growth and remission. To this end, this Project originated in response to a State of Florida initiative to seek "innovative technologies" to combat freshwater HABs. Select clauses from the Blue Green Algae Task Force Consensus Document that are specifically addressed in this Project include:

- "Legacy nutrients, as indicated previously, are a concern in the South Florida landscape, and the task force recommends that their contribution to loading figure prominently in the Lake Okeechobee, Caloosahatchee and St. Lucie River and Estuary's Basin Management Action Plans (BMAPs). The Task Force further recommends that projects with the demonstrated potential to expedite legacy nutrient removal merit special attention and be designated as priority projects." (**Task 3** focused on mapping sediment nutrient hotspots and characterize flux dynamics)

- "Integrated monitoring and modeling of implemented BMAP projects should be conducted to ensure that projects are working as expected. Such efforts are, in fact, key to the assessment process and allow for adjustments to be made if necessary." (**Task 1** integrated numerous data sources from **Tasks 2-6** to generate predictive models that can simulate environmental conditions, e.g. nutrient reduction)
- "The task force recommended also investments in technologies with the potential to detect, monitor and forecast harmful algal blooms to enable more proactive response." (**Tasks 2-6** activities all either detected HABs or the associated environment, and generated predictive capabilities in **Task 1**)
- "Department of Environmental Protection's science-based decision-making process. Accordingly, the task force recommends that monitoring programs be designed to address status and trends for key water quality parameters. Monitoring efforts should also be employed to answer specific questions, address unknowns, allow for improved design and adaptive management of agricultural and urban "Best Management Practices" (BMPs), edge of field and regional projects and BMAPs. Greater investments in research will be required to inform monitoring efforts. " (**Tasks 2-6** activities were geared towards answering specific scientific questions regarding, for example, nutrient utilization and toxin generation)
- "The task force recommends that additional environmental parameters, e.g., multiple nitrogen species and algal toxins be incorporated where appropriate into monitoring programs to aid our collective understanding of the factors that lead to the development, maintenance and senescence of harmful algal blooms and toxin production." (**Tasks 2, 3, 6, and 7** resulted in either nitrogen speciation or algal toxin measurements)
- "Of importance and urgent need are studies that address acute and chronic health effects of exposure of humans, wildlife and domesticated animals to algal toxins. An essential component of such studies is ready access to quantitative data on algal toxins in water, sediments and air." **(Task 7** focused on determining the human bioavailability of aerosolized toxins**)**.

Additional Task-specific background information is contained within the respective Task appendices.

PROJECT LOCATION AND ACTIVITIES CONDUCTED

The Project location is Lake Okeechobee in Okeechobee, Martin, Glades, Hendry, and Palm Beach Counties, Florida. Lake Okeechobee is a large, shallow lake located in south-central Florida. With a surface area of 730 square miles, it is the second largest lake within the contiguous United States and has an average depth of 9 feet centered at approximately 26° 96' 00" N, 80° 79' 00" W. All Project monitoring and sampling activities occurred on Lake Okeechobee, waterbody IDs (WBIDs) 3212A through 3212I. Seven primary monitoring sites (Figure 1A-1 and Table 1A-1) were selected at points representing the north (L001), south (L006), east (L004), west (L005), and center (LZ40) of the lake (all corresponding to ongoing South Florida Water Management District sites; SFWMD), as well as two sites along the eastern shore within the Pahokee Marina (PHKM) and just outside the marina as a reference site (PHKO). While we initially designated site "tiers", this notation was phased out soon after project commencement due to changes in project goals, at least with respect to the sediment-related activities. In consultation with FDEP sediment sampling activities were to include more sampling from L001, L004, and LZ40 instead of L005 and L006, the latter two not being mud-dominated and thus not sediments of most concern for eutrophication. Activities conducted at each respective site are described in Table 1A-2. Generally, the most comprehensive discrete monitoring and all sustained in situ monitoring activities occurred at site L001, with other sites subject instead only to discrete sampling activities, except for the continuous Autonomous Surface Vehicle (**Task 4**) which typically conducted a repeated triangular loop of sites L001, L005, and L004, with occasional HAB-response excursions in the Taylor Creek inflow area (extreme north of the lake) and Clewiston (southwestern lake).

The nature of this project required continued regional presence by local scientists, with a handful of visits occurring each month. FAU Harbor Branch is the lead institute developing innovative HAB and biogeochemical technologies and is regionally well-suited for recurring or rapid-response surveys for rapid data collection (approximately 70 minutes away). Logistics were still relatively challenging, with long field days routinely required e.g. for mobilization and deploying benthic instrumentation for 7 hours, followed by demobilization and sample processing; however, much of this work would not have been possible without the relative proximity between Lake Okeechobee and FAU Harbor Branch. Between 20 and 30 staff members representing seven FAU Harbor Branch laboratory groups routinely contributed to the project, with several staff members primarily devoted to this effort. The interdisciplinary FAU Harbor Branch team was complemented with expertise from other collaborators, including colleagues from the Florida Gulf Coast University, the Gulf of Mexico Coastal Ocean Observing System located at Texas A&M (GCOOS; date management and web portal design and maintenance), Navocean Inc. (Autonomous Surface Vehicle design and operation), Analytical Instrument Systems, Inc. (electrochemistry and benthic lander component design).

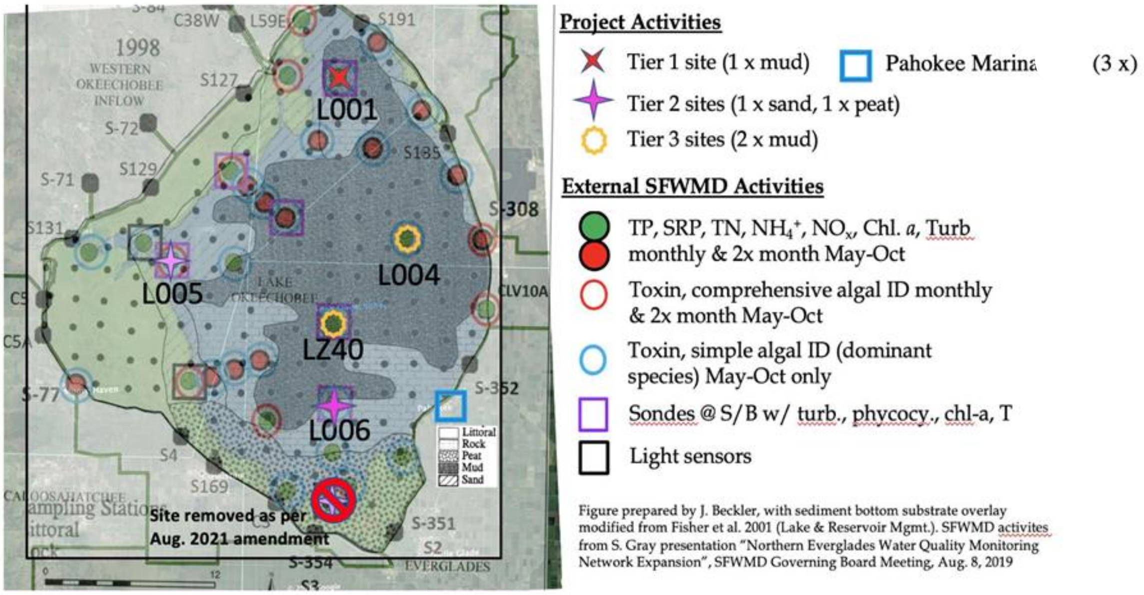

Figure prepared by J. Beckler, with sediment bottom substrate overlay modified from Fisher et al. 2001 (Lake & Reservoir Mgmt.). SFWMD activites from S. Gray presentation "Northern Everglades Water Quality Monitoring Network Expansion", SFWMD Governing Board Meeting, Aug. 8, 2019

Figure 1A-1: Project site map, including bottom type information (see bottom type key visible to the southeast of Lake), as well routine State of Florida monitoring activities. The Project site locations have been selected with colocation with existing South Florida Water Management District sampling sites. The two Pahokee sites (PHKM and PHKO) are bounded by the blue box.

Table 1A-1: Primary site locations and activities.

Site name / bottom type	Lat (ddmmss.sss)	Long (ddmmss.sss)	Activities
North/L001 – mud/sand	270820.01	804736.23	Water column sampling & profiling, high frequency sediment sampling, continuous in situ sensing, Autonomous Surface Vehicle (ASV) track vertex point and location of routine ASV sensor validation
West/L005 - sand	265724.22	805820.58	Water column sampling & profiling, two sediment sampling events (prior to scope changes early in project), vertex point of routine ASV track
South/L006 – mud overlying clay	264921.21	804658.21	Water column sampling & profiling, two sediment sampling events (prior to scope changes early in project)
Central/LZ40 – mud	265406.53	804720.40	Water column sampling & profiling, moderate frequency sediment sampling
East/L004 – mud	265839.66	804234.49	Water column sampling & profiling, moderate frequency sediment sampling, vertex point of routine ASV track.
Pahokee Marina (inside seawall)	264932.46	804042.54	Sediment sampling between Jun. and Oct. 2021 (per Amendment #3)
Pahokee Marina (outside seawall)	264944.40	803947.94	Sediment sampling between Jun. and Oct. 2021 (per Amendment #3)

Table 1A-2: Project timeline. Purple months indicate the deliverable due dates and invoicing activities. Colors represent the status of the sub-task (White = not active; Green = active; Yellow = preparative; Blue = laboratory or data processing). The numbers in some green boxes correspond to the site Tiers that will be sampled, and "P" designates the Pahokee sites. For example, Tiers 1, 2, and 3 will be surveyed in Task 2a in the first two weeks of Feb. 2021 (a total of five sites). For new Tasks added via Amendment #3, symbols designate the following activities: "M" is sediment legacy load mapping; "V" is vertically integrated sediment cores; and "I" indicates sediment incubations. The new Tasks for Amendment #3 are included because they are periodically referenced throughout the Task 1-7 Appendices regarding future work.

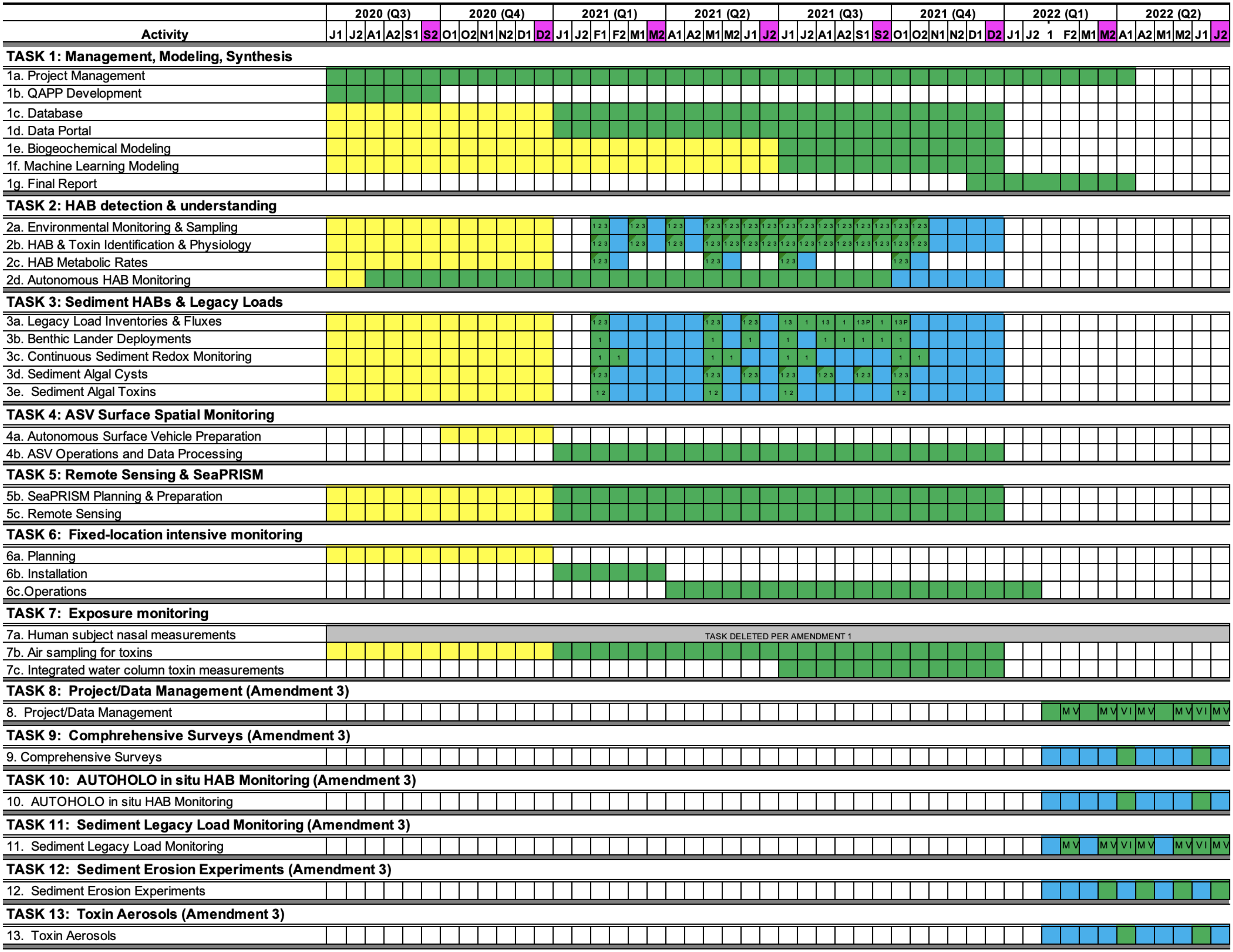

	2020 (Q3)						2020 (Q4)						2021 (Q1)						2021 (Q2)						2021 (Q3)						2021 (Q4)						2022 (Q1)						2022 (Q2)					
Activity	J1	J2	A1	A2	S1	S2	O1	O2	N1	N2	D1	D2	J1	J2	F1	F2	M1	M2	A1	A2	M1	M2	J1	J2	J1	J2	A1	A2	S1	S2	O1	O2	N1	N2	D1	D2	J1	J2	1	F2	M1	M2	A1	A2	M1	M2	J1	J2
TASK 1: Management, Modeling, Synthesis																																																
1a. Project Management	🟩	🟩	🟩	🟩	🟩	🟩	🟩	🟩	🟩	🟩	🟩	🟩	🟩	🟩	🟩	🟩	🟩	🟩	🟩	🟩	🟩	🟩	🟩	🟩	🟩	🟩	🟩	🟩	🟩	🟩	🟩	🟩	🟩	🟩	🟩	🟩	🟩	🟩	🟩	🟩	🟩	🟩	🟩					
1b. QAPP Development	🟩	🟩	🟩	🟩	🟩	🟩																																										
1c. Database	🟨	🟨	🟨	🟨	🟨	🟨	🟨	🟨	🟨	🟨	🟨	🟨	🟩	🟩	🟩	🟩	🟩	🟩	🟩	🟩	🟩	🟩	🟩	🟩	🟩	🟩	🟩	🟩	🟩	🟩	🟩	🟩	🟩	🟩	🟩	🟩												
1d. Data Portal	🟨	🟨	🟨	🟨	🟨	🟨	🟨	🟨	🟨	🟨	🟨	🟨	🟩	🟩	🟩	🟩	🟩	🟩	🟩	🟩	🟩	🟩	🟩	🟩	🟩	🟩	🟩	🟩	🟩	🟩	🟩	🟩	🟩	🟩	🟩	🟩												
1e. Biogeochemical Modeling	🟨	🟨	🟨	🟨	🟨	🟨	🟨	🟨	🟨	🟨	🟨	🟨	🟨	🟨	🟨	🟨	🟨	🟨	🟨	🟨	🟨	🟨	🟨	🟨	🟩	🟩	🟩	🟩	🟩	🟩	🟩	🟩	🟩	🟩	🟩	🟩												
1f. Machine Learning Modeling	🟨	🟨	🟨	🟨	🟨	🟨	🟨	🟨	🟨	🟨	🟨	🟨	🟨	🟨	🟨	🟨	🟨	🟨	🟨	🟨	🟨	🟨	🟨	🟨	🟩	🟩	🟩	🟩	🟩	🟩	🟩	🟩	🟩	🟩	🟩	🟩												
1g. Final Report																																			🟩	🟩	🟩	🟩	🟩	🟩	🟩	🟩	🟩					
TASK 2: HAB detection & understanding																																																
2a. Environmental Monitoring & Sampling	🟨	🟨	🟨	🟨	🟨	🟨	🟨	🟨	🟨	🟨	🟨	🟨			🟩 1 2 3	🟦	🟩 1 2 3	🟦	🟩 1 2 3	🟦	🟩 1 2 3	🟩 1 2 3	🟩 1 2 3	🟩 1 2 3	🟩 1 2 3	🟩 1 2 3	🟩 1 2 3	🟩 1 2 3	🟩 1 2 3	🟩 1 2 3	🟩 1 2 3	🟩 1 2 3	🟦	🟦	🟦	🟦												
2b. HAB & Toxin Identification & Physiology	🟨	🟨	🟨	🟨	🟨	🟨	🟨	🟨	🟨	🟨	🟨	🟨			🟩 1 2 3	🟦	🟩 1 2 3	🟦	🟩 1 2 3	🟦	🟩 1 2 3	🟩 1 2 3	🟩 1 2 3	🟩 1 2 3	🟩 1 2 3	🟩 1 2 3	🟩 1 2 3	🟩 1 2 3	🟩 1 2 3	🟩 1 2 3	🟩 1 2 3	🟩 1 2 3	🟦	🟦	🟦	🟦												
2c. HAB Metabolic Rates	🟨	🟨	🟨	🟨	🟨	🟨	🟨	🟨	🟨	🟨	🟨	🟨			🟩 1 2 3	🟦					🟩 1 2 3	🟦			🟩 1 2 3	🟦					🟩 1 2 3	🟦																
2d. Autonomous HAB Monitoring	🟨	🟨	🟩	🟩	🟩	🟩	🟩	🟩	🟩	🟩	🟩	🟩	🟩	🟩	🟩	🟩	🟩	🟩	🟩	🟩	🟩	🟩	🟩	🟩	🟩	🟩	🟩	🟩	🟩	🟩	🟦	🟦	🟦	🟦	🟦	🟦												
TASK 3: Sediment HABs & Legacy Loads																																																
3a. Legacy Load Inventories & Fluxes	🟨	🟨	🟨	🟨	🟨	🟨	🟨	🟨	🟨	🟨	🟨	🟨			🟩 1 2 3	🟦	🟦	🟦	🟦	🟦	🟩 1 2 3	🟦	🟩 1 2 3	🟦	🟩 1 3	🟩 1	🟩 1 3	🟩 1	🟩 1 3 P	🟩 1	🟩 1 3 P	🟦	🟦	🟦	🟦	🟦												
3b. Benthic Lander Deployments	🟨	🟨	🟨	🟨	🟨	🟨	🟨	🟨	🟨	🟨	🟨	🟨			🟩 1	🟦	🟦	🟦	🟦	🟦	🟩 1	🟦	🟩 1	🟦	🟩 1	🟦	🟩 1	🟩 1	🟩 1	🟩 1	🟩 1	🟦	🟦	🟦	🟦	🟦												
3c. Continuous Sediment Redox Monitoring	🟨	🟨	🟨	🟨	🟨	🟨	🟨	🟨	🟨	🟨	🟨	🟨			🟩 1	🟩 1	🟦	🟦	🟦	🟦	🟩 1	🟩 1	🟦	🟦	🟩 1	🟩 1	🟦	🟦	🟦	🟦	🟩 1	🟩 1	🟦	🟦	🟦	🟦												
3d. Sediment Algal Cysts	🟨	🟨	🟨	🟨	🟨	🟨	🟨	🟨	🟨	🟨	🟨	🟨			🟩 1 2 3	🟦	🟦	🟦	🟦	🟦	🟩 1 2 3	🟦	🟩 1 2 3	🟦	🟩 1 2 3	🟦	🟩 1 2 3	🟦	🟩 1 2 3	🟦	🟩 1 2 3	🟦	🟦	🟦	🟦	🟦												
3e. Sediment Algal Toxins	🟨	🟨	🟨	🟨	🟨	🟨	🟨	🟨	🟨	🟨	🟨	🟨			🟩 1 2	🟦	🟦	🟦	🟦	🟦	🟩 1 2	🟦	🟦	🟦	🟩 1 2	🟦	🟦	🟦	🟦	🟦	🟩 1 2	🟦	🟦	🟦	🟦	🟦												
TASK 4: ASV Surface Spatial Monitoring																																																
4a. Autonomous Surface Vehicle Preparation							🟨	🟨	🟨	🟨	🟨	🟨																																				
4b. ASV Operations and Data Processing													🟩	🟩	🟩	🟩	🟩	🟩	🟩	🟩	🟩	🟩	🟩	🟩	🟩	🟩	🟩	🟩	🟩	🟩	🟩	🟩	🟩	🟩	🟩	🟩												
TASK 5: Remote Sensing & SeaPRISM																																																
5b. SeaPRISM Planning & Preparation	🟨	🟨	🟨	🟨	🟨	🟨	🟨	🟨	🟨	🟨	🟨	🟨	🟩	🟩	🟩	🟩	🟩	🟩	🟩	🟩	🟩	🟩	🟩	🟩	🟩	🟩	🟩	🟩	🟩	🟩	🟩	🟩	🟩	🟩	🟩	🟩												
5c. Remote Sensing	🟨	🟨	🟨	🟨	🟨	🟨	🟨	🟨	🟨	🟨	🟨	🟨	🟩	🟩	🟩	🟩	🟩	🟩	🟩	🟩	🟩	🟩	🟩	🟩	🟩	🟩	🟩	🟩	🟩	🟩	🟩	🟩	🟩	🟩	🟩	🟩												
TASK 6: Fixed-location intensive monitoring																																																
6a. Planning	🟨	🟨	🟨	🟨	🟨	🟨	🟨	🟨	🟨	🟨	🟨	🟨																																				
6b. Installation													🟩	🟩	🟩	🟩	🟩	🟩																														
6c.Operations																			🟩	🟩	🟩	🟩	🟩	🟩	🟩	🟩	🟩	🟩	🟩	🟩	🟩	🟩	🟩	🟩	🟩	🟩	🟩	🟩										
TASK 7: Exposure monitoring																																																
7a. Human subject nasal measurements	TASK DELETED PER AMENDMENT 1																																															
7b. Air sampling for toxins	🟨	🟨	🟨	🟨	🟨	🟨	🟨	🟨	🟨	🟨	🟨	🟨	🟩	🟩	🟩	🟩	🟩	🟩	🟩	🟩	🟩	🟩	🟩	🟩	🟩	🟩	🟩	🟩	🟩	🟩	🟩	🟩	🟩	🟩	🟩	🟩												
7c. Integrated water column toxin measurements																									🟩	🟩	🟩	🟩	🟩	🟩	🟩	🟩	🟩	🟩	🟩	🟩												
TASK 8: Project/Data Management (Amendment 3)																																																
8. Project/Data Management																																							🟩	🟩 M V	🟩	🟩 M V	🟩 V I	🟩 M V	🟩	🟩 M V	🟩 V I	🟩 M V
TASK 9: Comphrehensive Surveys (Amendment 3)																																																
9. Comprehensive Surveys																																							🟦	🟦	🟦	🟦	🟩	🟦	🟦	🟦	🟩	🟦
TASK 10: AUTOHOLO in situ HAB Monitoring (Amendment 3)																																																
10. AUTOHOLO in situ HAB Monitoring																																							🟦	🟦	🟦	🟦	🟩	🟦	🟦	🟦	🟩	🟦
TASK 11: Sediment Legacy Load Monitoring (Amendment 3)																																																
11. Sediment Legacy Load Monitoring																																							🟦	🟩 M V	🟦	🟩 M V	🟩 V I	🟩 M V	🟦	🟩 M V	🟩 V I	🟩 M V
TASK 12: Sediment Erosion Experiments (Amendment 3)																																																
12. Sediment Erosion Experiments																																							🟦	🟦	🟦	🟩	🟦	🟩	🟦	🟩	🟦	🟩
TASK 13: Toxin Aerosols (Amendment 3)																																																
13. Toxin Aerosols																																							🟦	🟦	🟦	🟦	🟩	🟦	🟦	🟦	🟩	🟦

PROJECT CONCLUSIONS AND RECOMMENDED FUTURE WORK

The HALO Project is ultimately focused on providing value for the State of Florida with respect to the economy and human and ecosystem health (Figure 1A-2). As recognized by the Blue Green Algal Task Force, the HAB efforts to date have not been sufficient to solving Florida's HAB crisis, with the problem becoming significantly worse, arguably even over the past decade. A low intensity monitoring program maintains low levels of monitoring, so blooms are large by the time they are detected, resulting in the greatest costs to the economy and health, as well as intractable costs associated with any mitigation efforts. An alternative approach would be to scale existing State of Florida efforts to a level to where blooms could be detected at least at moderate concentrations so that mitigation would be more feasible, although the total and long-term costs for both monitoring and mitigation are still likely prohibitive. Instead, HALO's approach is to conduct targeted monitoring efforts, especially early on, to develop the necessary information to develop predictive models and ensure optimal site selection for more permanent monitoring installations. By combining these carefully selected, critical monitoring data to both inform science to ultimately develop and feed simulative predictive models, the upfront cost is relatively high, but the cost can come down in the long term as the model requirements are optimized, i.e. the number of sites providing continuous monitoring data are refined to only those critical for prediction. More importantly, however, the ultimate economic and health damage is minimized, and active mitigation becomes a tractable problem if blooms can be identified prior to or early on in their emergence.

HALO's efforts in this first year of the project have primarily focused on collecting baseline data to understand the temporal and seasonal controls and patterns in blooms and their causes. The work revealed major new insights, but also raises many new questions regarding remaining knowledge gaps related to light requirements and vertical migration, especially in the context of frequent turbidity-inducing storm events, the relative roles of resuspension and diffusive sediment nutrient fluxes, and the controls on pore water nutrient inventories. These major outstanding questions were rationalized not only from observations, but were also guided by identified modeling needs going forward, i.e. those items that are most likely to help with model predictive accuracy going forward.

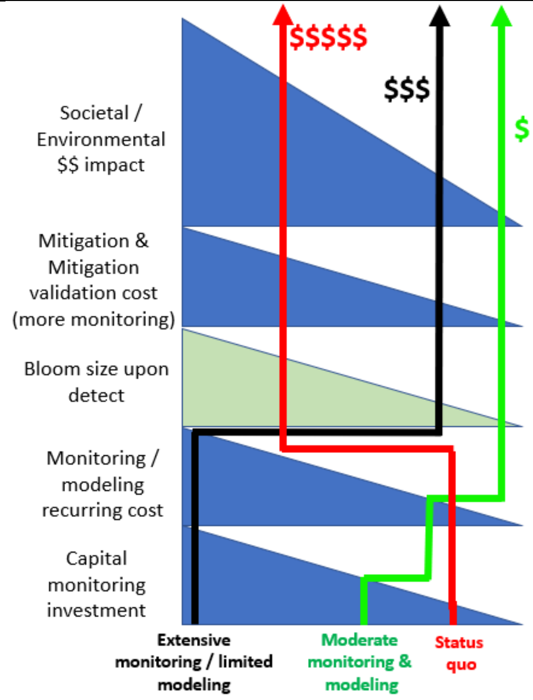

Figure 1A-2: Framework of HALO strategy within the context of solving Florida's HAB crisis – HALO's strategy of moderate monitoring to inform modeling is arguably the most cost-effective long-term strategy for mitigating HABs, with the least effect to human and ecosystem health.

Although there are clear lake-wide seasonal trends in environmental parameters such as temperature, conductivity, oxygen, and backscatter, efforts to monitor HAB abundance and physiology showed that these characteristics vary rapidly in both space and time (**Tasks 2, 4, 6**). HAB distributions throughout the lake are extremely patchy and these local aggregations appear to have unique physiological characteristics. Efforts to assess bloom status and/or model growth trajectories (e.g. **Tasks 1E-F**), therefore, must employ high resolution and high frequency observations to obtain accurate results. Over wide areas and long-term scales, on the other hand, HALO efforts for the first time established the relative errors associated with operational satellite remote sensing techniques, and long term climatological patterns demonstrate that while HAB frequency is increasing, the geographical and seasonal patterns are also changing (**Task 5**).

The **Task 7** data demonstrates that *M. aeruginosa*-derived toxins are indeed aerosolized and monitoring staff are potentially exposed to breathing these toxins, although toxin concentrations were far below the hypothetical concentrations thought to elicit exposure symptoms (~0.03 versus 4.58 ng m^{-3}, respectively; Wood and Dietrich 2011). Airborne microcystin concentrations were below limits of quantification (LOQ) when concurrent water-borne microcystin concentrations were elevated (April and June sampling), demonstrating a general disconnect between water-borne and airborne microcystin concentrations, albeit this phenomenon could be due to the low (non-bloom) concentrations observed during this portion of the study. Regardles, going forward autonomous monitoring techniques are important for limiting occupational exposure. Sediment *M. aeruginosa* cysts and toxins were also both relatively low (**Tasks 3D-E**) except during the maximum bloom periods, as were sediment-to-water column toxin fluxes (**Task 3B**) suggesting that human or ecotoxicological exposure is likely also limited limited to intense bloom periods.

We now know from **Task 3A** data that sediment inventories of dissolved phosphorous and nitrogen change seasonally, and that the N:P ratio of the sediment pore waters – the phase most available for fluxing to the water column – is most elevated in the spring when HABs were most intense and is at a lowest when blooms declined in late summer. Assuming that the monitoring efforts are continued, the baseline data allows us to examine the severity and timing of HABs in subsequent years in the context of these sediment nutrients to provide potential explanations. The baseline data also allows parameterization of the predictive models with real sediment flux data, given that the sediments are such important nutrient sources for HABs in this lake. However, there exists disparate production/consumption patterns with respect to N and P sediment cycling, although both may be tied to iron cycling. Indeed, **Task 3A-C** data demonstrated that microbial iron reduction is the dominant respiratory pathway in the sediments. **Task 3B** in situ data also reinforces previous research that shows enhanced phosphate sediment fluxes under induced hypoxia. HALO results on the other hand demonstrate that phosphate fluxes are virtually non-existent under normal oxic conditions (**Task 3B**) due to "capture" by surface sediment mineral layers, despite high pore water inventories and vertical gradients suggestive of fluxes (**Task 3A**). While these pore water P inventories and "apparent" (i.e. based on vertical gradients) sediment-to-water column fluxes covary with sediment oxygen demand (i.e. diffusive oxygen uptake), the fluxes of N as revealed by vertical pore water gradients are instead temporally disconnected (**Task 3A**). Combined with **Task 6** continuous real time monitoring data, we instead see that resuspension on the other hand can be a significant phosphate and/or nitrate source to the water column. New **Task 11 and 12** efforts will aim to directly monitor these processes in situ and attempt to make quantitative links between hydrodynamic conditions and the amount of sediment nutrients that are delivered to the water column.

Our work also has implications for conventional monitoring activities. The continuous nutrient sensor data revealed that dissolved phosphate inventories in the water column can be entirely depleted and then regenerated within the 2-week interval between typical SFWMD districts. Additionally, the observation of diurnal presumed migration has important implications for spatial comparison efforts relating to HAB patterns. For example, we do not see vertical *M. aeruginosa* stratification at L001 and L005, the first two sites that we routinely visited, typically by 10 am (**Task 2B**). However, the **Task 2D** data did not typically show aggregation of cells to the surface until the early afternoon, i.e. when we typically sampled other sites (i.e. L004, LZ40, and L006) that do indeed show a greater density of cells near the surface at this time. However, the L001 and L005 sites are also shallower and less turbid, providing an environmental explanation for not seeing vertical stratification. Therefore, we ultimately do not know if the cause of these spatial disparities is the timing of the site visits or the environmental characteristics of the specific sites. These same uncertainties would apply to the SFWMD conventional monitoring efforts (which do not routinely sample bottom waters). Perhaps the order of site visits should be randomized, or a vertically integrated sample should be collected. Alternatively, continuous monitoring technologies could be employed. New **Task 9 and 10** activities are focused on resolving these remaining questions by repeatedly sampling, or continuously monitoring for full day/night cycles.

HALO efforts did indeed focus on developing and testing new technologies to provide the required information needed to identify blooms autonomously and inform models. The AUTOHOLO was demonstrated to function properly in this optically complex environment, outputting *M. aeruginosa* colony information; we were not certain that it would yield valuable data but the risk was warranted considering the potential utility of the outputted information. The sensor detected an active zooplankton population, suggesting that it is important to simulate grazing in the predictive model. Going forward, we will use the AUTOHOLO for round-the-clock monitoring (**Task 9**) to examine these dynamics over an approximately week-long time period. Also, HALO efforts demonstrated for the first time, to our knowledge, that acoustics-based techniques can detect *M. aeruginosa* – potentially paving the way for both local and global efforts to utilize this relatively low-cost technique.

The ASV data (**Task 4**) provided a full year of spatial chlorophyll and phycocyanin data, in addition to environmental data. We observed spatial and seasonal patterns with regards to the production of chlorophyll and Phycocyanin, as well as complex relationships with CDOM and turbidity. Not only early bloom formation, but also displacement patterns where detected. While the implications are not yet fully realized as we are only beginning to mine this data for patterns and trends, we are excited about the prospect of comparing the spatial gradients of the sensor data within the context of the validation samples that provide species-level information. Relative sensor readings, e.g. " the phycocyanin to chl-a ratios, relative to backscatter intensity", have been used to identify *M. aeruginosa* previously using relatively simple and commercially available sensors. While these relationships are not readily apparent in the combined dataset (more that 2 million points), we could identify conditional relationship during specific events that should be explored separately. Additionally, this data provides round-the-clock environmental information and diel cycles are evident. Using this ASV-collected environmental data across these spatial gradients – gradients that may transition between different spatial regimes dominated by certain species of phytoplankton – we can also potentially add other measurements to these criteria for species-level detection, e.g. "a level of daytime O_2 depletion that corresponds with the suspected cell concentrations (as indicated by the chl/backscatter relationship)". These potential new cell count indicators can be applied not only to the ASV, but to other monitoring installations containing this same common sensor suites.

Overall, HALO project work to date has provided numerous critical insights into Lake Okeechobee HABs. However, many important gaps remain with respect to our knowledge base – gaps which must be filled in order to most efficiently develop a predictive capacity to identify blooms while mitigation is still a tractable problem. Based on results from **Tasks 1 thru 7**, HALO activities were refined to continue to address questions old and new. This work will continue on into the 2022 bloom season as per Amendment #3.

TASK 1C: DATABASE (TASK LEAD: RUIZ-XOMCHUK)

INTRODUCTION AND METHODS

Given the high volume of data generated during this project, the data management approach was critical for organizing and sharing data amongst tasks. FAU designed and maintained the primary HALO database and developed most data ingestion pipelines. For much of the data, the Gulf of Mexico Coastal Ocean Observing System (GCOOS) retrieved data stored in the FAU HALO database. Sources of HALO data were highly variable as were the diverse operational flows. In many cases the use of novel technologies and combined assessments created complex data storage and organization requirements. Here we distinguish two groups of data generation: sensor or computationally generated data (**Tasks 1E, 1F, 2D, 4, 5 & 6**), and data that required human input and calibration (**Tasks 2, 3 & 7**). This material division in the database organization is made due to constraints of timing and automatization. While automatic routines can be developed for ingesting, processing, and quality controlling the first tier of datasets once established, in the second case data, on the other hand, availability is dependent on laboratory results and human handling, which can impact the completeness of individual datasets. Following this constraint and the readiness of data due to experimentation phase (e.g., findings brought by new technologies were not meant to be immediately publicly shared), the implementation and storage of all generated datasets was approached in two ways: either for public release or for internal use. The data generation and flow paths are shown in Figure 1C-1, where computational and sensor data are identified in blue, and human handling dependent data are identified in yellow. In all cases data flow was channeled through a local centralized storage High Performance Research Computing Center (i.e. the FAU DMZ) that allowed 24/7 availability of data once uploaded. Datasets designed for public release were stored in an environment that allowed automatized queries from GCOOS for subsequent data portal visualization (**Task 1D**). Other datasets were accessible from external portals for internal (**Task 4**) and public (**Task 5B**, **Task 6**) access.

Data outputs from different tasks required routines for data conversions to create data formats suitable for public sharing (e.g., ERDAPP or netCDF via GCOOS) or long-term storage, or for upload. These routines were created in Python programing language, and are detailed in the corresponding sections when relevant:

- **Task 1E**: routines for periodic upload of model data and download for model ingestion
- **Task 1F**: routines to create a file formatting including metadata assimilable via ERDAPP.
- **Task 2**: routines for integration of excel spreadsheets in netcdf files with metadata assimilable via ERDAPP for public sharing, and routines for cleanup and integration of a final dataset in tabular format (.csv)
- **Task 3**: routines for cleanup and integration of a final dataset in tabular format (.csv)
- **Task 4**: routines for remote access via query on Navocean ASV servers (model use), and routines for merging and quality control of logger datasets after mission uploads.
- **Task 5**: automatization routines for periodic upload, and routines for querying Aeronet servers (for model use)
- **Task 6**: routines for querying IRLON servers (for model use)

ACTIVITIES SCHEDULED vs. COMPLETED

Overall, the database required substantial unanticipated effort from the FAU Data Science postdoctoral researcher, effort that was originally budgeted for data analyses of various tasks. Typically, the standardization of data formats, e.g. via the provision of NetCDF templates to data providers (i.e.

researchers) is the role of the data management organization and not of the researchers. Still, the database was completed by the time of report submission with all data archived as appropriate. Routine meetings with project partners and collaborators were conducted according to schedule and reported quarterly, to:

- Establish an internal centralized data storage system for cloud availability (the FAU HPRC system).
- Implement the necessary pipelines to transfer data from the original source to internal or public sharing, and train personnel in using those pipelines.
- Understand individual data structures and implement data file formats (and conversion routines) agreeable with requirements for ingestion in the GCOOS-ERDAPP system for the HALO web portal, or for long term storage.
- Implement automatization routines for different kinds of tasks including producing, uploading and requesting data and products for internal use.
- Establish requirements for visualization products showcased in Task 1D.

Information regarding HALO database structure plans was assembled, based on the GCOOS Data Management Plan (DMAC), with HALO- specific fields and data pipelines indicated, e.g. block diagrams of data flow from the source to the database. The database structure underwent frequent changes according to data availability and was adapted as different file formats and data cleaning protocols were established. A schematic of the data flow from each task source to public or internal sharing is shown in Figure 1C-1.

The FAU HPRC DMZ storage has been operational over the project duration for data fetching to GCOOS HALO portal, and data sharing among FAU researchers for model development. Details on datasets are presented in the results section.

Regarding public accessibility of data (visualizations are described in **Task 1D**), the **Task 2** data access is publicly available via ERDDAP through the HALO web portal. The **Task 4** data is available only through visualization or direct request of HALO staff, but is also available via the Navocean ASV portal. **Task 5A** data is available via ERDDAP through HALO portal. **Task 5B** data is available through NASA Aeronet site. Finally, **Task 6** data is publicly available through IRLON network. **Task 7** was research-oriented and while archived, is not publicly available.

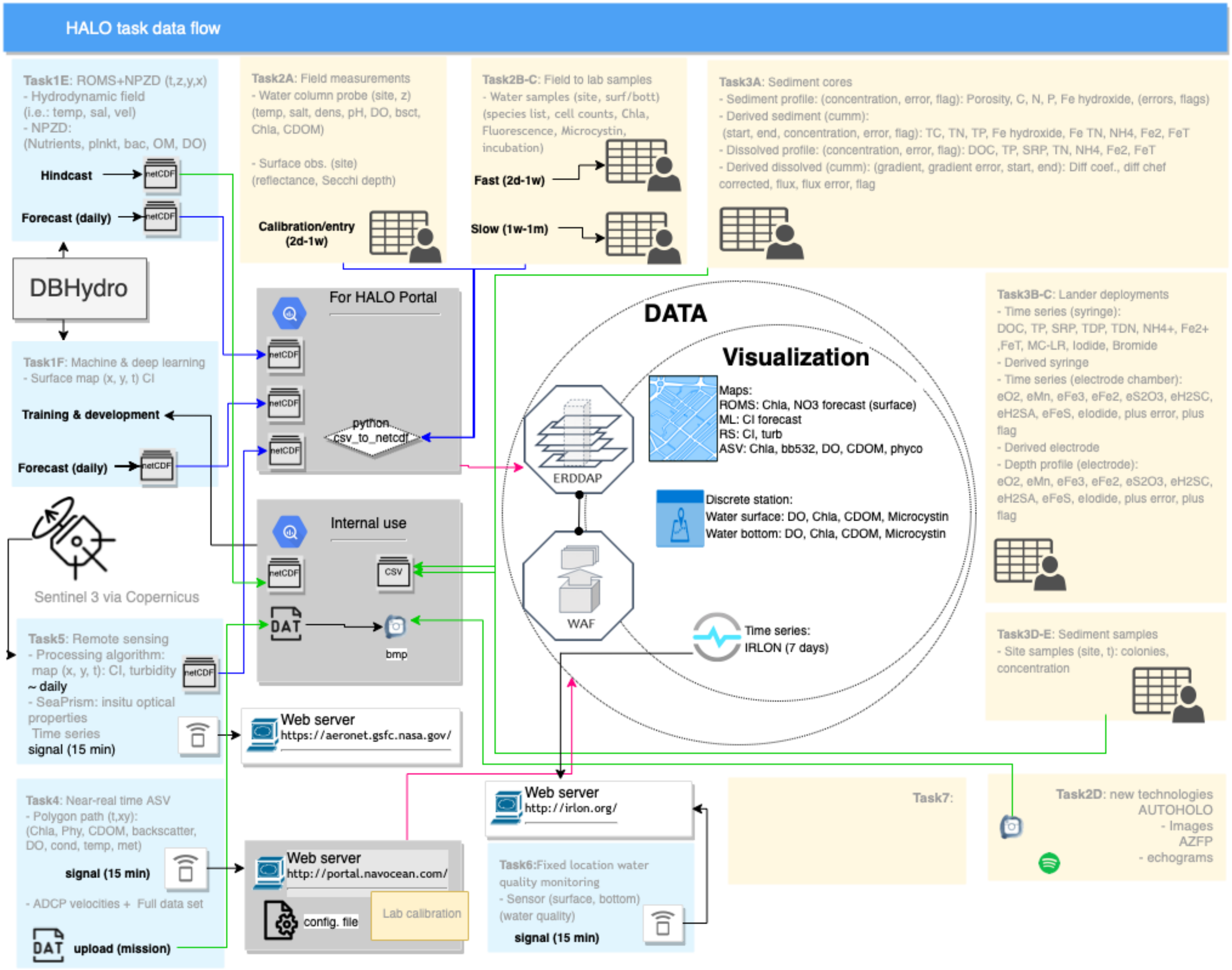

Figure 1C-1: Data flow structure for individual tasks into permanent internal (grey) and public (white) storage. Internal storage was separated in flow for public (blue arrows) or internal (green arrows) use. Connection to the HALO portal (magenta) was thus achieved from internal servers.

RESULTS AND DISCUSSION

Datasets generated during the execution of the project are detailed in Table 1C-1. An indication is made on the individual dataset coverage, the data status, variables contained, data storage location, file organization and format, and whether currently publicly available.

Model data (**Tasks 1E, 1F**) were generated and stored in .nc format. NetCDF (Network Common Data Form) files are machine-independent data formats that support the creation, access, and sharing of array-oriented scientific data, and is often a community standard for sharing gridded scientific data (UCAR Community Programs, 2022.). **Task 1E** generates the files natively via the Regional Ocean Modeling System Routines, and the default output and contained metadata is suitable for public sharing and ERDAPP servers. **Task 1F** dataset were generated through Machine Learning computation, and a section was added to the routine to store data in the .nc format following IOOS conventions ACDD 1.3 and CF 1.7 (Integrated Ocean Observing system, n.d.).

Task 2 data had an unconventional mixed format, which included de combination of 1) point observations (lon, lat, time): secchi depth, etc; 2) Spectral data (lon, lat, time, wave lenght): surface reflectance; 3) Depth profiles (lon, lat, time, depth): probe data including temperature, conductivity, pH; and 4) Surface/bottom (lon, lat, time, layer): water grab samples.
To integrate this data in a .nc format as was required by GCOOS for public display in the server, IOOS conventions were followed, and 1) Lat Lon dimensions were assigned for each site; 2) Time dimensions were assigned for each sampling occasion; 3) Profile depth dimension for probe data, Surface/bottom layer dimension for water grabs; and 5) Wavelength dimension was assigned for spectral data.

While exhaustive attempts were made to provide **Task 3** data in .nc format following IOOS conventions as above, a consensus with our partners at GCOOS was not achieved (See **Task 1D**) and they deemed the data structure to be unacceptable. Nevertheless, the data was instead stored for internal use (e.g. for ongoing **Task 1E** model parameterization) in a standard protocol for comma delimited files (.csv) as a full dataset with quality-controlled variables in which each row corresponded to a sample with: Site, Lon, Lat, time, depth (sediment), variable, unit, and variable QC.

Task 4 ASV datalogger sensor data was compiled in mission combined comma delimited files (.csv), where the rows were identified by the variable TIMESTAMP. Every ID row had a full set of optical and environmental surface variable collocated with geolocation latitude/longitude variables. Weather variables were stored separately with the corresponding lat/lon and TIMESTAMP variables. ADCP variables were treated separately: each depth band (3) velocity vector component was treated as a separate variable such as 3 values to each component were registered. QA/QC corrections of data are described in the **Task 4** section.

Task 5A data was generated using NASA software (NASA, n.d.), and processed via python routines to which a section was added to store data in the .nc format following IOOS conventions. **Task 5B** is released as tabular text data through Aeronet Portal.

Task 6 data was stored and distributed directly via IRLON network and portal and is already available via an API.

Task 7 data was made available by the end of the project and saved in a standard protocol for comma delimited files (.csv) as a full dataset for long term storage.

Table 1C-1: Description of all datasets generated during HALO and stored in the database.

Task	Product	Description	Period	Status	Variables	File storage	File organization format	Public?
Task 1E	LakeO-NPZD	A simple nutrient-phytoplankton-zooplankton (NPZ) model with 8 groups which include chlorophyll, NO3, NH4, phytoplankton, zooplankton, dissolved and particulate organic nitrogen (DON and PON), and dissolved oxygen (DO) (Fennel et al. 1986)	2018-2019 hindcast	calibrated		FAU HPC	monthly .nc	no
	LakeO-HAB	A multiple nutrients (nitrogen-N, phosphorus-P), multiple plankton (diatoms, cyanobacteria, microzooplankton, and mesozooplankton), and dissolved and particulate organic groups model	2021	uncalibrated		FAU HPC	monthly .nc	no
	LakeO-ROMS-NPZD	Operational prototype: rolling forecast system run automatically once a week producing a 13-day simulation (6 day hindcast and 7 day forecast) of the lake hydrodynamics and biogeochemistry	07-01-2021 to 12-31-2021	operational		FAU HPC HALO portal	7day forecast .nc	yes
Task 1F	Linear Autoencoder Satelite CI derived ML	Preliminary deep learning model: a Linear Autoencoder ML model was trained over preprocessed historical Sentinel-3 remote sensing Cyanobacterial Index (CI)	07-07-2021 to 03-31-2022	Experimental (backup model, using remote sensing data only)	CI	FAU HPC HALO portal	14 day forecast .nc	yes

		data (3-year period from 2016–2019). The trained model was used to generate 14-day rolling predictions.						
	Conv-LSTM	Operational prototype: a Convolutional Long-short Term Memory ML model was trained over hybrid datasets that include remote sensing data and physical model outputs (3-year period from 2018-2020). A rolling forecast system based on the trained ConvLSTM runs automatically once per day producing a 14-day forecasting of the lake Chl-A.	01-01-2021 to 08-31-2021	Operational (full model, using both remote sensing data and physical model data)	Chla	FAU HPC	14 day forecast .mat	no
Task 2A	In-water environmental and optical data.	A total of 15 field surveys, five sites on each survey day.	2/1/2021 - 10/31/2021	quality controled	Profiles: conductivity, temperature, pH, dissolved oxygen, backscatter, Chlorophyll a, phycocyanin, and fluorescent dissolved organic matter (DOM). Above water measurements of hyperspectral remote sensing	FAU HPC HALO portal	full dataset (sampling event) .csv per station/ date .nc	yes

					reflectance (Rrs, 400 – 850 nm) Secchi depth			
Task 2B	Biology and toxins	Laboratory based analyses was conducted on samples collected during Task 2a to identify algal presence and physiology	2/1/2021 - 10/31/2021	quality controled	Surface, bottom: algal taxa present, chlorophyll a, concentrations of microcystins, flow cytometry cell concentrations for several groups of algae and Microcystis aeruginosa, ratios of dead to live cells of M. aeruginosa, variable fluorescence of algae			
Task 2C	Metabolic rates	Live M. aeruginosa cells were analyzed to assess their relative metabolic rate immediately after sample collection.	2/1/2021 - 10/31/2021	quality controled	Surface, bottom: fluorescein diacetate (FDA) fluorescence			

Task 2D	AUTOHOLO	In situ holographic images from three different stations (200 holograms/station)	8/24/21	experimental	images	FAU HPC	dir per deployment (3) .bmp	no
	Acoustic Zooplankton Fish Profiler (AZFP)	Echosounder backscatter deployed at the bottom in the vicinity of the L001 tower.	07/17/2021 - 07/27/2021	experimental	echo			no
Task 3A		Data from sediment cores were collected at sites over a range of lake locations and bottom types, with sampling conducted semi-monthly to biweekly, depending on the site and the time of year.	12/17/20 - 10/27/21	quality controlled		FAU HPC	full dataset (sampling event) .csv	no
Task 3B	Benthic lander deployments						full dataset (sampling event) .csv	no
Task 3C	Continuous in situ redox monitoring						full dataset (sampling event) .csv	no
Task 3D	Sediment HAB cyst measurements	Sediment samples from monthly sampling events from sites L001, LZ40, L004, or L006 plus additional samples from the Pahokee marina	02/26/2021 - 09/29/2021				full dataset (sampling event) .csv	no
Task 3E	Sediment toxin						full dataset (sampling event) .csv	no

Task 4	Autonomus surface vehicle	Sustained in-situ environmental, biogeochemical, and physical measurements on Lake Okeechobee 24 hrs/day via saliboat deployments, surveying a polygonal area in NW Lake Okeechobee (L001, NES135, NCENTER, KBARSE, POLESOUT, POLESOUT1, POLESOUT2, POLESOUT3, L008, L005)	12/31/2020 - 01/01/2022		Surface water: fluorometric (Chl-a, CDOM, phycocyanin), optical backscatter (red, green, blue), and dissolved O2, conductivity, temperature Meteorology: wind speed and direction, air temperature, barometric pressure ADCP 3D current at 3 depth bins full lake depth	FAU HPC HALO portal Navocean server	sensor/mission (5 min) .dat mission deploiments (5 min) .csv web query (15 min)	yes
Task 5A	Remote sensing	Sentinel3 products for Lake Okeechobee: Turbidity derived from Dogliotti et al. 2015; Cyanobacteria Index derived from Wynn et al. 2010	10/27/2016 - 03/31/2022		Turbidity CI	FAU HPC HALO portal	daily .nc	yes
Task 5B	SeaPrism	In situ optical properties at L001				Aeronet portal	full dataset (15 min) .txt	yes
Task 6	Fixed location water quality monitoring	Biogeochemical and meteorological sensors that provide real-time, high-	07/01/2021 – 01/31/2022			IRLON portal	web query (15 min)	yes

		accuracy and high-resolution water quality/weather data							
Task 7							FAU HPC		no

TASK 1D: DATA PORTAL PROJECT SUMMARY (TASK LEAD: KIRKPATRICK)

INTRODUCTION

Rapid data visualization is particularly important for this project given its purpose of informing HAB mitigation activities. A publicly accessible information portal also raises awareness of State of Florida-funded activities that provide a service to public health. Additionally, the data portal is central to data aggregation and visualization, providing project partners and stakeholders with an ability to get a "big picture" view of HAB and environmental conditions on the lake at any given time. To this end, the HALO Data Portal (hereafter referred to as "HALO Portal"; halo.gcoos.org) was developed in collaboration with the Gulf of Mexico Coastal Observing System (GCOOS) to display project data. Data from several tasks was ingested directly into the web portal system for display, while others were first transmitted internally to the FAU High Performance Computing database (see **Task 1C**) for subsequent display on the GCOOS HALO web portal. These observations, encompassing a wide suite of environmental/chemical/optical properties, also provide important information on the ecological drivers of algal bloom initiation, as well as other phases (e.g., bloom decay). The HALO Portal is modeled after a highly regarded data portal developed for oceanographic monitoring, the GCOOS Gulf AUV Network and Data Archiving Long-term Storage Facility (GANDALF; https://gandalf.gcoos.org/). GANDALF is used for piloting Autonomous Underwater Vehicles (AUVs) and Autonomous Surface Vehicles (ASVs) and examining data for applied purposes (e.g. marine HAB monitoring). Features provided included:

1) The primary HALO Portal page is a spatial map of Lake Okeechobee, with the main landing page overlay displaying the most up-to-date Chlorophyll-A concentrations as measured and/or interpolated by any number of reliably collected measurements.
2) Various selectable layers corresponding to data streams, either real time or discrete, and model outputs. Most layers have its own series of options; for example, opacity (for overlays), date range sliders, and any other relevant factors that can be captured in changes of symbology. These include surface or bottom water data sources.
3) The ASV track (**Task 4**), satellite imagery (**Task 5B**), and models (**Task 1E&F**) are visible for configurable date ranges.
3) For temporal measurements (e.g. **Task 5&6** fixed-location data), users can link spatially distributed icons to link to time series charts corresponding to sensor data.

METHODS

Technical details regarding the web portal construction and are available in the projects QAPP (Data Management Plan). Briefly, the HALO Portal design was developed through multiple meetings with Task Leads and Project Partners. The HALO Portal was programmed in Python using the Flask micro-templating framework. Additional tools and libraries were used where appropriate.

Data for the web and mobile applications are stored and served using a Digital Ocean droplet. The droplet is configured as an Ubuntu 16.10 instance with 8GB of RAM, 4 virtual CPUs, an 80GB solid state disk drive and a data transfer allowance of 5 TB/month. The droplet is located in Digital Ocean's NYZ Zone 3. Digital Ocean uses only premier datacenter facilities for co-locating their equipment including Equinix, Telex and Telecity. Each site is staffed 24/7/365 with onsite security to protect against unauthorized entry. Each site has security cameras that monitor both the facility premises as well as each area of the datacenter internally. There are biometric readers for access as well as at least two-factor authentication to gain access to the building. Each facility is unmarked so as not to draw any additional attention from the outside and adheres to strict local and federal government standards. The master datasets were stored and served using four rack-mounted Unix-based servers housed in the environmentally controlled data center at TAMU in College Station, TX. The machine room provides backup storage, uninterruptable power supplies, back-up generators and dual 10Gb Internet connections. The TAMU System also provides a comprehensive enterprise-grade infrastructure and support system to handle network availability and security, firewalls, software maintenance and scanning for malware.

The GCOOS Data Management system adheres to the IOOS standards and best practices documented in “Guidance for Implementation of the Integrated Ocean Observing System (IOOS) Data Management and Communications (DMAC) subsystem”. The system employs: a Service Oriented Architecture requiring registry and external monitoring, standards-based data access services including OPeNDAP and Open Geospatial Consortium (OGC) Sensor Observation Service, common data formats (NetCDF, text/CSV/TSV, XML: both OGC GML and OGC SWECommon with WMS/WFS/WCS; KML and JSON are under consideration as data formats), metadata standards (ISO 19115), common vocabularies, QARTOD QA/QC, storage and archiving, planning and coordination and long-term operations.

ACTIVITIES SCHEDULED VS COMPLETED

The web portal was publicly accessible during the entire scheduled period (Figure 1D-1).

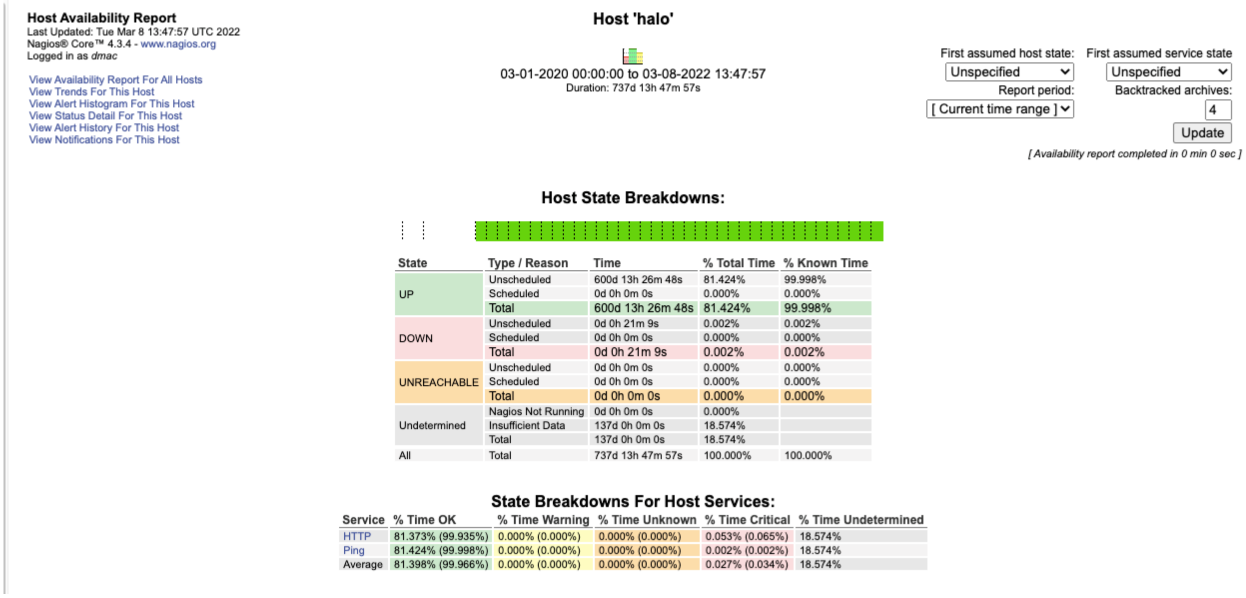

Host Availability Report
Last Updated: Tue Mar 8 13:47:57 UTC 2022
Nagios® Core™ 4.3.4 - www.nagios.org
Logged in as *dmac*

Host 'halo'

03-01-2020 00:00:00 to 03-08-2022 13:47:57
Duration: 737d 13h 47m 57s

First assumed host state: Unspecified
First assumed service state: Unspecified
Report period: [Current time range]
Backtracked archives: 4

[Availability report completed in 0 min 0 sec]

Host State Breakdowns:

State	Type / Reason	Time	% Total Time	% Known Time
UP	Unscheduled	600d 13h 26m 48s	81.424%	99.998%
	Scheduled	0d 0h 0m 0s	0.000%	0.000%
	Total	600d 13h 26m 48s	81.424%	99.998%
DOWN	Unscheduled	0d 0h 21m 9s	0.002%	0.002%
	Scheduled	0d 0h 0m 0s	0.000%	0.000%
	Total	0d 0h 21m 9s	0.002%	0.002%
UNREACHABLE	Unscheduled	0d 0h 0m 0s	0.000%	0.000%
	Scheduled	0d 0h 0m 0s	0.000%	0.000%
	Total	0d 0h 0m 0s	0.000%	0.000%
Undetermined	Nagios Not Running	0d 0h 0m 0s	0.000%	
	Insufficient Data	137d 0h 0m 0s	18.574%	
	Total	137d 0h 0m 0s	18.574%	
All	Total	737d 13h 47m 57s	100.000%	100.000%

State Breakdowns For Host Services:

Service	% Time OK	% Time Warning	% Time Unknown	% Time Critical	% Time Undetermined
HTTP	81.373% (99.935%)	0.000% (0.000%)	0.000% (0.000%)	0.053% (0.065%)	18.574%
Ping	81.424% (99.998%)	0.000% (0.000%)	0.000% (0.000%)	0.002% (0.002%)	18.574%
Average	81.398% (99.966%)	0.000% (0.000%)	0.000% (0.000%)	0.027% (0.034%)	18.574%

Figure 1D-1 The HALO Data Portal achieved a 99.998% uptime record.

Results from the most recent water column analyses (**Task 2**) were available in tabular format as a popup dialogue when clicking on a site location (Figure 1D-2).

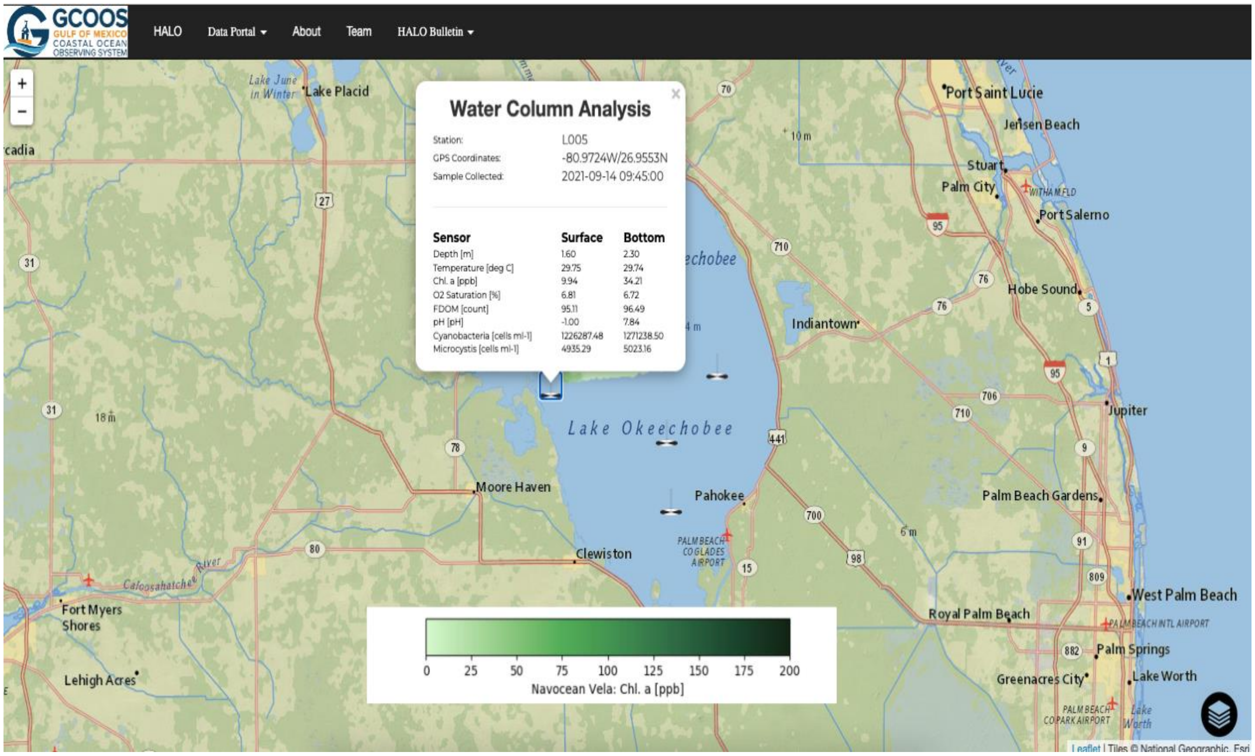

Water Column Analysis

Station: L005
GPS Coordinates: -80.9724W/26.9553N
Sample Collected: 2021-09-14 09:45:00

Sensor	Surface	Bottom
Depth [m]	1.60	2.30
Temperature [deg C]	29.75	29.74
Chl. a [ppb]	9.94	34.21
O2 Saturation [%]	6.81	6.72
FDOM [count]	95.11	96.49
pH [pH]	-1.00	7.84
Cyanobacteria [cells ml-1]	1226287.48	1271238.50
Microcystis [cells ml-1]	4935.29	5023.16

Figure 1D-2 – Results from the most recent water column analyses (i.e. Task 2 data)

The ASV track (**Task 4**) was displayed on the data portal, with a server-side configurable date range, which was typically set for 7 days. The vessel track was color-coordinated by a user-selectable parameter, e.g. for chl-a or phycocyanin (Figure 1D-3), and tabular data is available by clicking a single point.

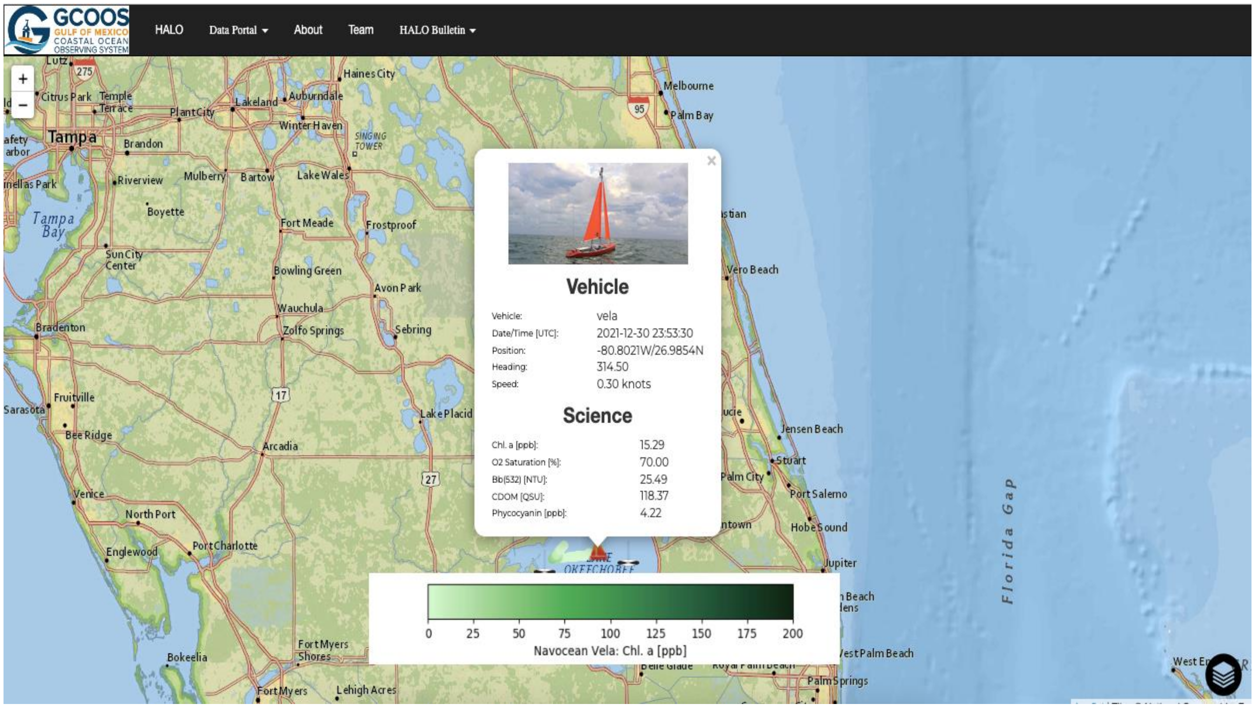

Vehicle

Vehicle: vela
Date/Time [UTC]: 2021-12-30 23:53:30
Position: -80.8021W/26.9854N
Heading: 314.50
Speed: 0.30 knots

Science

Chl. a [ppb]:	15.29
O2 Saturation [%]:	70.00
Bb(532) [NTU]:	25.49
CDOM [QSU]:	118.37
Phycocyanin [ppb]:	4.22

Figure 1D-3 The Nav2 ASV track and data display for onboard Chl-a sensors.

Remote sensing imagery for turbidity and the Cyanobacterial Index (CI) (**Task 5B**) is selectable for a specific date range via a slider bar at the bottom of the portal display (Figures 1D-4&5).

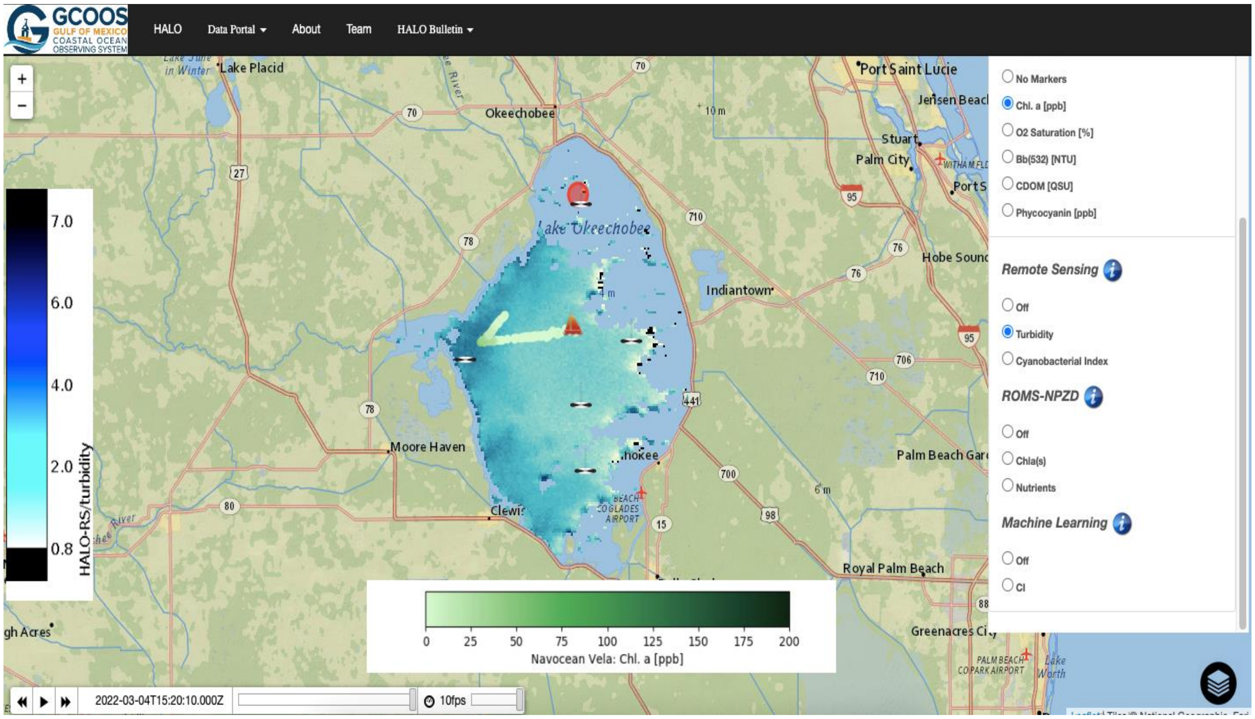

Figure 1D-4: Example satellite remote sensing turbidity imagery on HALO Data Portal

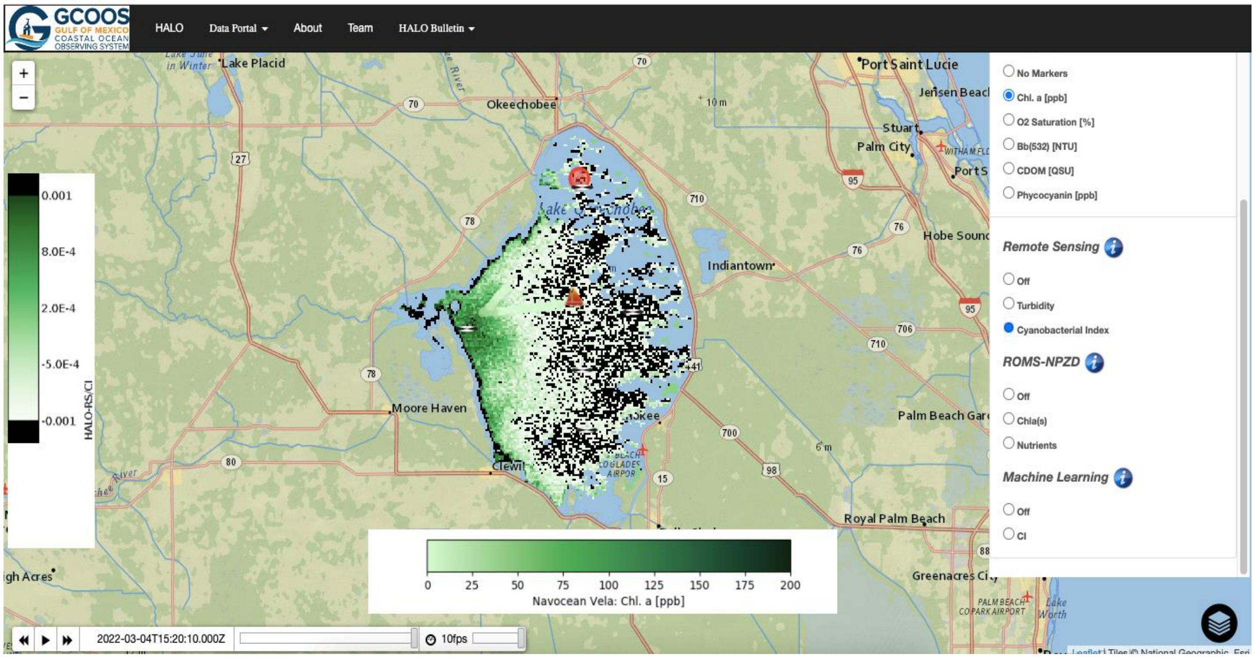

Figure 1D-5: Example satellite remote sensing cyanobacterial index imagery on HALO Data Portal

The physical/biogeochemical model data (chl-a and nitrate; **Task 1E**) is available as a time-selectable layer that is also capable of “playing” through a sequence (Figures 1D-6&7).

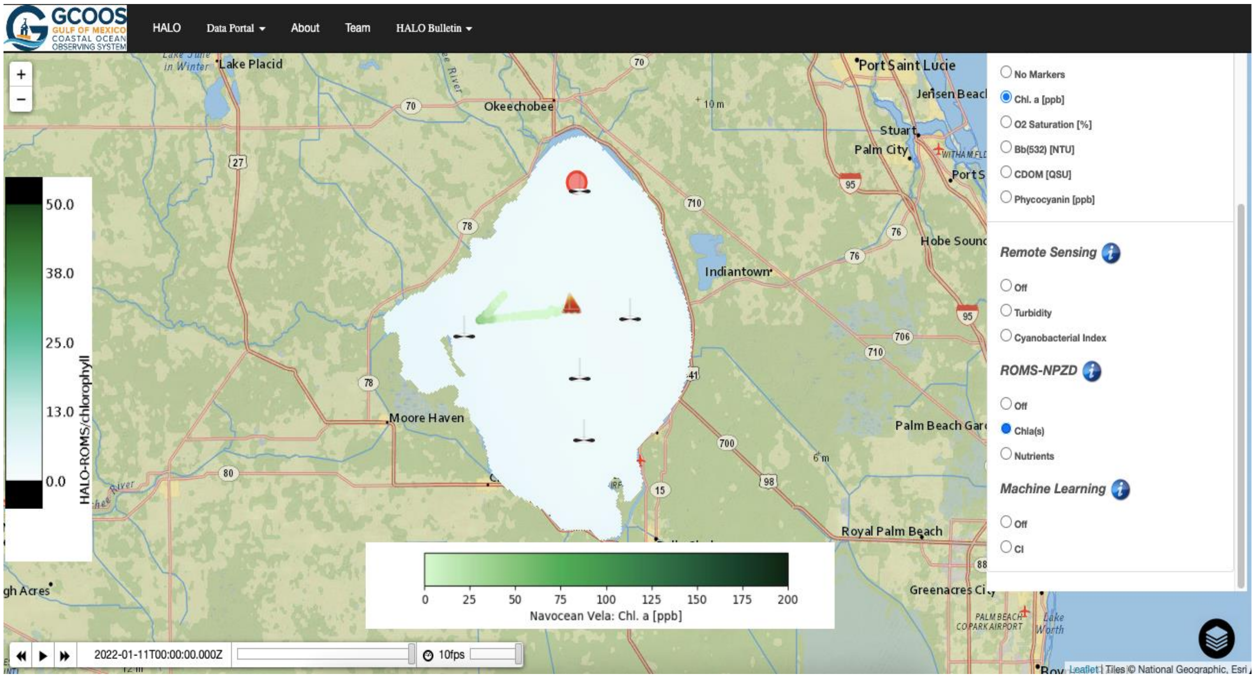

Figure 1D-6: Example physical/biogeochemical model output on HALO Data Portal (low chl-a variability is shown here).

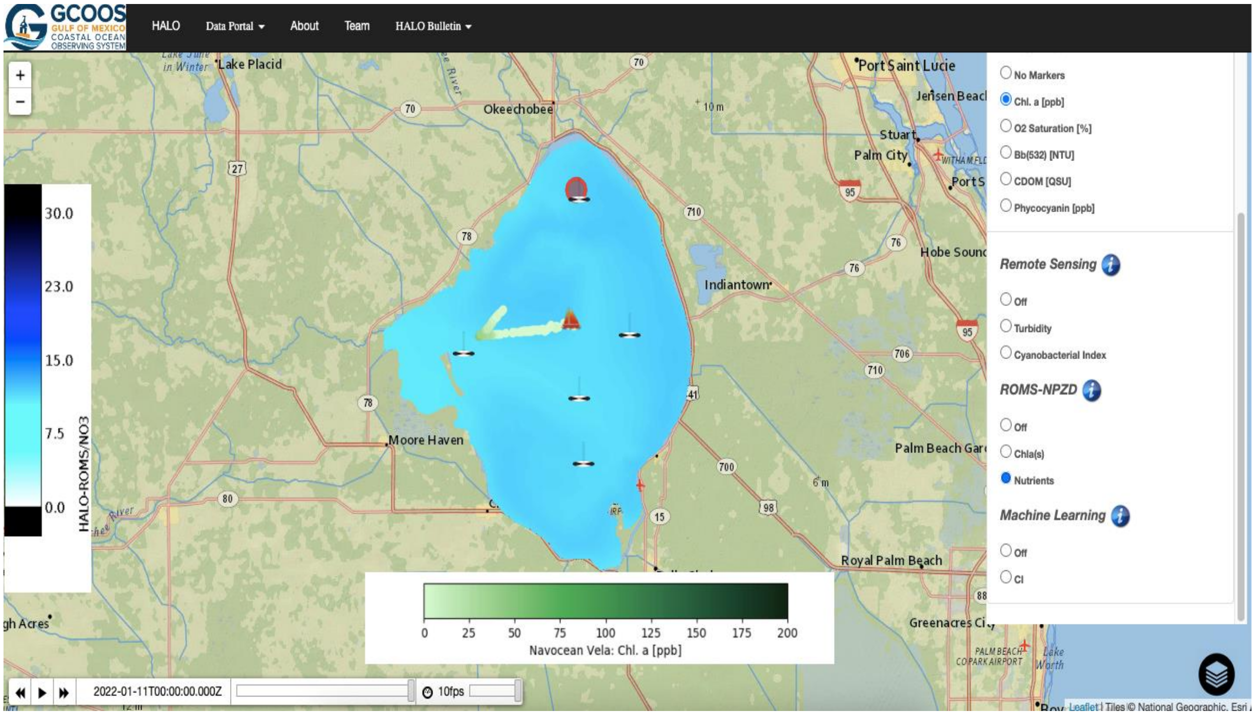

Figure 1D-7: Example physical/biogeochemical model output on HALO Data Portal, for nitrate concentration output.

The machine learning model data (predicted cyanobacterial index; **Task 1F**) is available as a time-selectable layer that is also capable of "playing" through a sequence (Figures 1D-8).

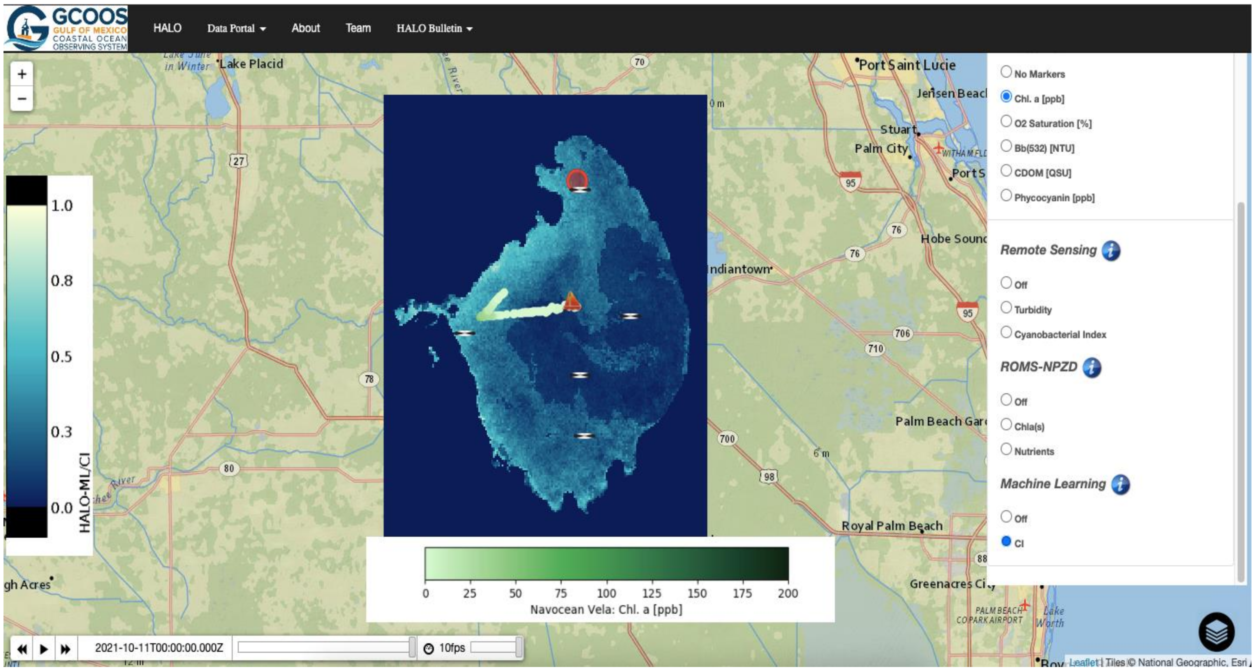

○ No Markers
● Chl. a [ppb]
○ O2 Saturation [%]
○ Bb(532) [NTU]
○ CDOM [QSU]
○ Phycocyanin [ppb]

Remote Sensing
○ Off
○ Turbidity
○ Cyanobacterial Index

ROMS-NPZD
○ Off
○ Chla(s)
○ Nutrients

Machine Learning
○ Off
● CI

Figure 1D-8: Example machine learning model output on HALO Data Portal for the Cyanobacterial Index (CI).

The user is additionally provided with sensor-specific details to inform interpretation (Figures 1D-9).

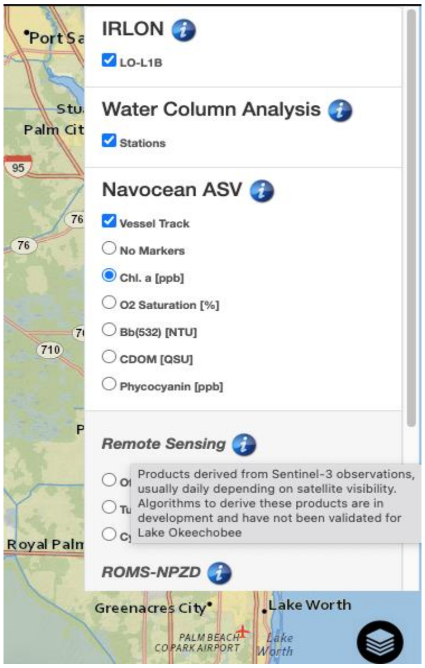

IRLON
☑ LO-L1B

Water Column Analysis
☑ Stations

Navocean ASV
☑ Vessel Track
○ No Markers
● Chl. a [ppb]
○ O2 Saturation [%]
○ Bb(532) [NTU]
○ CDOM [QSU]
○ Phycocyanin [ppb]

Remote Sensing

Products derived from Sentinel-3 observations, usually daily depending on satellite visibility. Algorithms to derive these products are in development and have not been validated for Lake Okeechobee

ROMS-NPZD

Figure 1D-9: Context-sensitive information is available to provide disclaimers and info to the user.

Task 6 data is not directly available on the HALO portal; instead, a link is provided by clicking the Task 6 icon which then links to the IRLON site (Figure 1D-10).

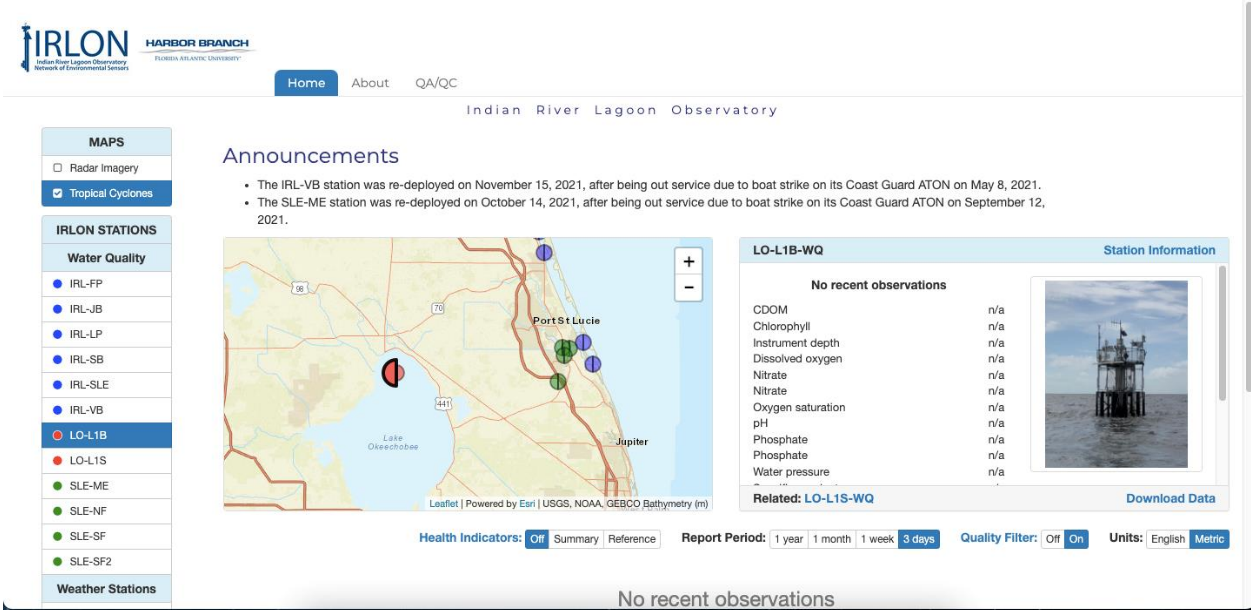

Announcements

- The IRL-VB station was re-deployed on November 15, 2021, after being out service due to boat strike on its Coast Guard ATON on May 8, 2021.
- The SLE-ME station was re-deployed on October 14, 2021, after being out service due to boat strike on its Coast Guard ATON on September 12, 2021.

LO-L1B-WQ

No recent observations

CDOM	n/a
Chlorophyll	n/a
Instrument depth	n/a
Dissolved oxygen	n/a
Nitrate	n/a
Nitrate	n/a
Oxygen saturation	n/a
pH	n/a
Phosphate	n/a
Phosphate	n/a
Water pressure	n/a

Related: LO-L1S-WQ

Health Indicators: Off Summary Reference

Report Period: 1 year 1 month 1 week 3 days

Quality Filter: Off On

Units: English Metric

No recent observations

Figure 1D-10: The IRLON Lake Okeechobee display linked to from the HALO web portal.

Ancillary project information about the project, including task descriptions, team members (Figure 1D-11), and links to the HALO Bulletin (Figure 1D-12) is provided via the web portal top menu bar.

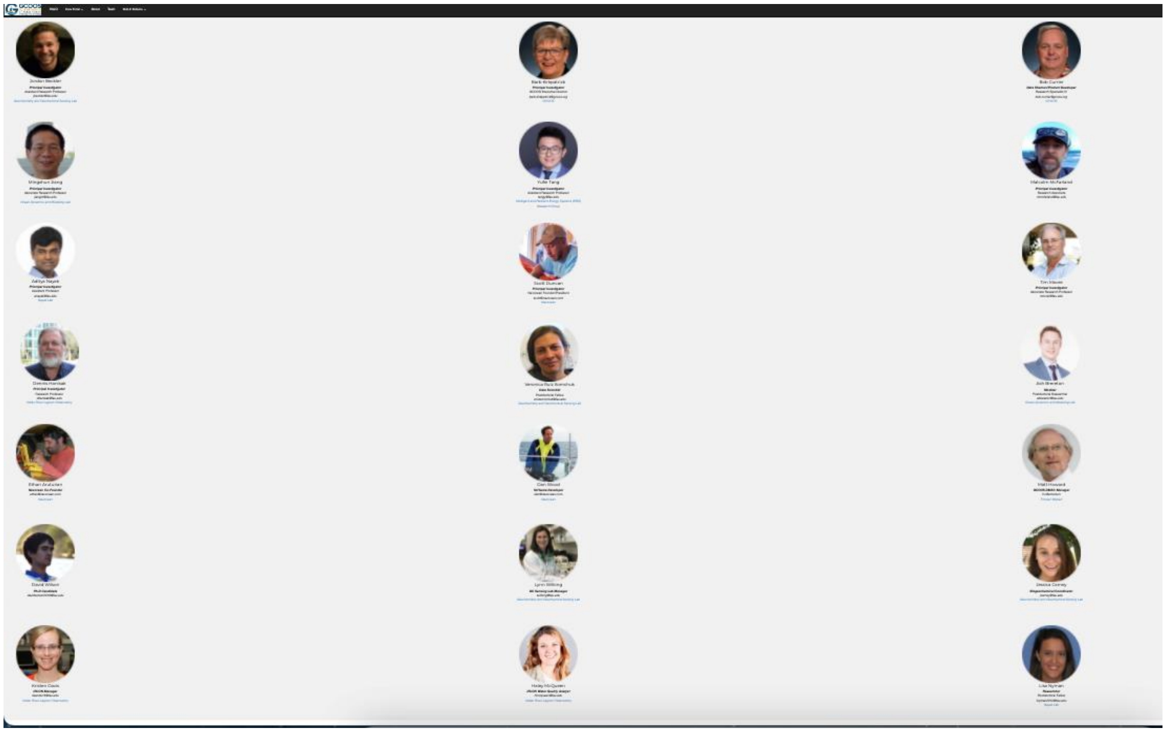

Figure 1D-11: HALO Project team members linked via a navigation menu option.

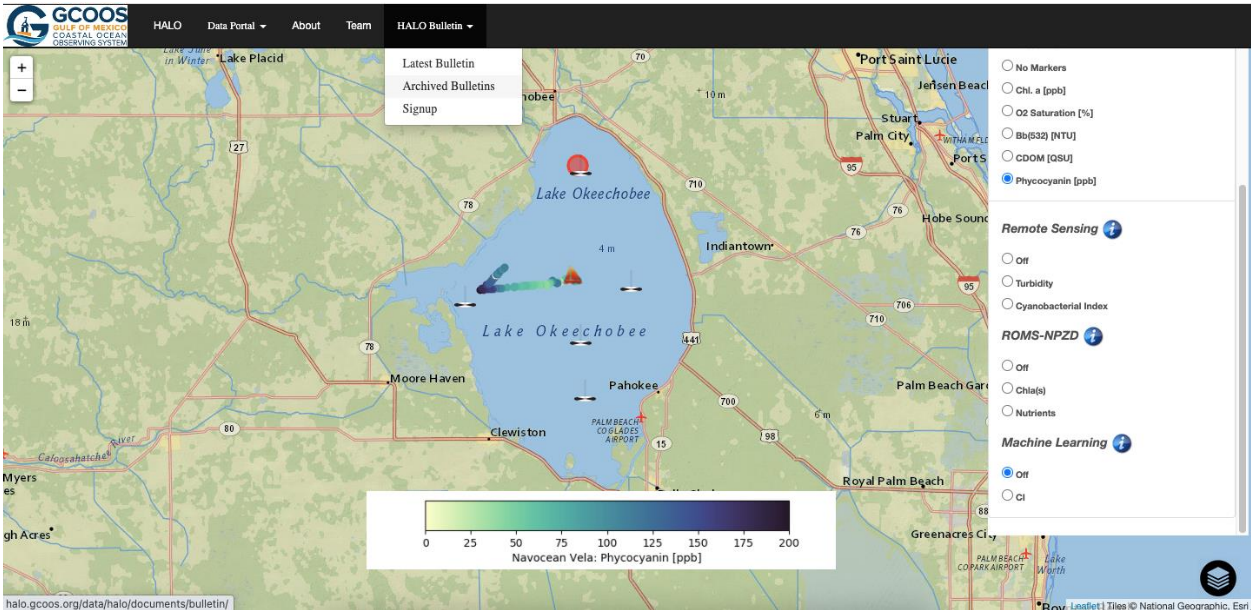

○ No Markers
○ Chl. a [ppb]
○ O2 Saturation [%]
○ Bb(532) [NTU]
○ CDOM [QSU]
● Phycocyanin [ppb]

Remote Sensing

○ Off
○ Turbidity
○ Cyanobacterial Index

ROMS-NPZD

○ Off
○ Chla(s)
○ Nutrients

Machine Learning

● Off
○ CI

Figure 1D-12: Link to the HALO Bulletin

TASK 1E: 3-D PREDICTIVE BIOGEOCHEMICAL MODEL (TASK LEAD: JIANG)

INTRODUCTION

The objectives of this subtask are 1) to develop a coupled three-dimensional (3-D) physical-biogeochemical model that simulates hydrodynamics, nutrient cycling, and phytoplankton blooms (particularly *M. aeruginosa*) in Lake Okeechobee, and 2) to develop and implement an operational forecast model that provides a short-term (weekly or bi-weekly) forecast of these parameters (Fennel et al. 2006; Jiang et al. 2014). Before the implementation of the operational forecast system, the model was first calibrated for 2018-2019 and then validated for 2020, based on available historical data and new data collected in this project. While this modeling effort is primarily designed as an operational tool in assisting HAB mitigation activities, it is also useful in helping to understand HAB dynamics and the roles of key physical-biogeochemical processes. Successful model hindcasts demonstrate a fundamental understanding of the key processes in play.

METHODS

Model descriptions: The hydrodynamic model is based on the Regional Ocean Modeling System (ROMS), which solves equations of water motions driven by meteorological forcing, including heat and wind fluxes, and input/output flows (e.g. Warner et al. 2005). The model domain covers the entire lake with grid size ~150 m. Such a high resolution allows us to simulate water movements and mixing in details (Figure 1E-1). Vertically, there are 10 terrain-following layers with variable thickness.

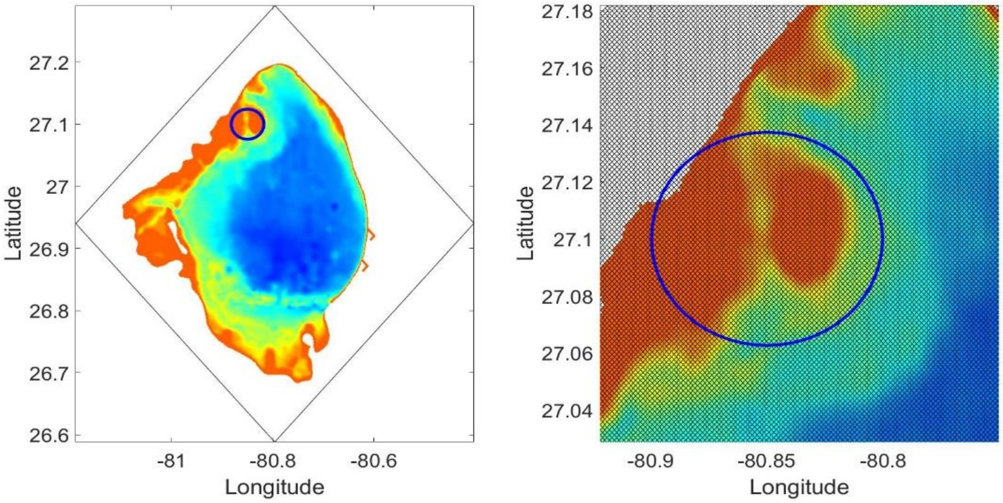

Figure 1E-1: Left: Model domain (bounded by the black thin line) and bathymetry (color). Watershed included in the model domain is shown as blank. Right: Details of the horizontal grid and bathymetry used for the area surrounding Kissimmee River (blue square in left panel).

Two biogeochemical models have been developed, 1) a simple nutrient-phytoplankton-zooplankton (NPZ) model with 8 groups which including chlorophyll, nitrate, ammonium, phytoplankton, zooplankton, dissolved and particulate organic nitrogen (DON and PON), and dissolved oxygen (DO) (Fennel et al. 1986) (LakeO-NPZD hereafter), and 2) a multiple nutrients (nitrogen-N, phosphorus-P), multiple plankton (diatoms, cyanobacteria, microzooplankton, and mesozooplankton), and dissolved and particulate organic groups (LakeO-HAB model hereafter) (Figure 1E-2). Both biogeochemical models simulate nitrogen and dissolved oxygen cycle due to phytoplankton photosynthesis and nutrient uptake, zooplankton grazing, and remineralization of organic nitrogen. Nitrogen loading, including inorganic and organic nitrogen due to river transports from upstream, local watershed runoffs, and sediment inputs via mixing, are also included. However, sediment re-suspension is not directly simulated. Similarly, DO from these sources (or sinks) are included. Surface DO flux is also simulated depending on wind speed and water DO saturation to account for air-lake exchange.

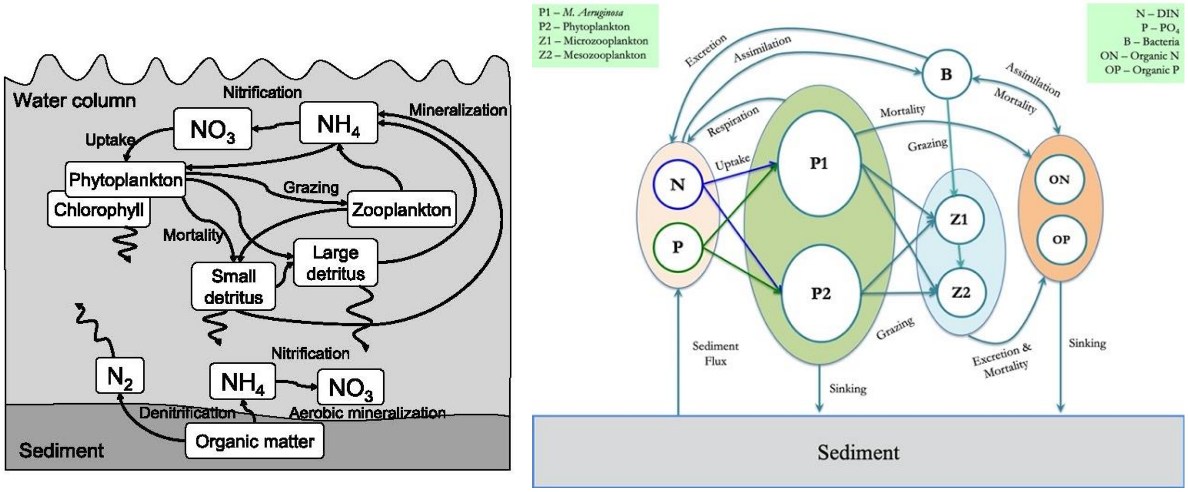

Figure 1E-2: Left: A diagram for the LakeO-NPZD model, which is based on Fennel et al. (2006). Note sediment processes are not directly simulated in this project. Right: A diagram the LakeO-HAB model. The DO cycle is not shown in either case.

In addition to N and DO cycles, the LakeO-HAB model also allows simulation of the P cycle and hence examination of potential P limitation to phytoplankton growth. Phytoplankton is partitioned into two groups, *M. aeruginosa* and all other phytoplankton, and zooplankton is partitioned into microzooplankton and mesozooplankton, including copepods. In addition to DON and PON, organic P is partitioned into dissolved organic P (DOP) and particulate organic P (POP). A bacteria group is explicitly included, which allows us to explicitly simulate the microbial loop. Additionally, the model allows direct simulation of vertical migration of *M. aeruginosa* due to buoyancy regulation via several mechanisms including light, colony formation, and O_2 bubbles.

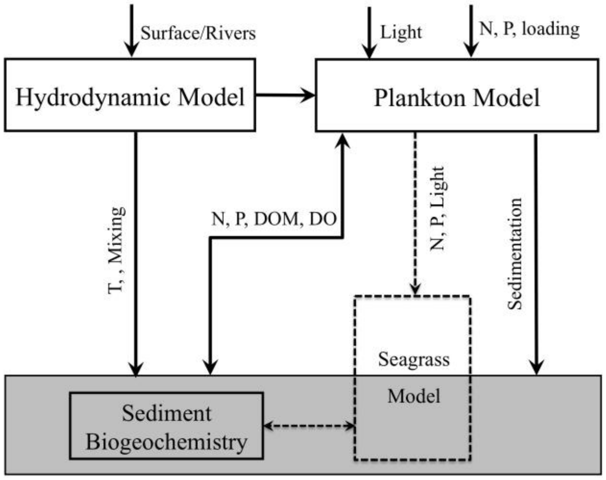

Figure 1E-3: Diagram for the coupled hydrodynamic-biogeochemical model. Neither the sediment biogeochemistry (i.e. explicit sediment diagenesis) nor the seagrass module is implemented.

Both biogeochemical models are coupled with the hydrodynamic model (Figure 1E-3). The model forcing includes river run-off, atmospheric forcing, and sediment inputs. Meteorological forcing is derived from the NOAA North American Regional Re-analysis (NARR) model output. The river inputs are derived from river flows and biogeochemical data collected by SFWMD accessed via DBHYDRO (https://www.sfwmd.gov/science-data/dbhydro). There are total 17 rivers and canals that either supply waters to or receive waters from Lake Okeechobee (Figure 1E-4). River flows and nitrate and DON concentrations are shown in Figure 1E-5 to1E-7. Sediment inputs of N, P (for LakeO-HAB), and DO (sediment demand) are empirically specified as fixed fluxes inversely proportional to water depth, although an analytical parameterization of true sediment fluxes (**Task 3**) is continuing. The coupled models will be referred respectively, as LakeO-ROMS-NPZD, and LakeO-ROMS-HAB hereafter.

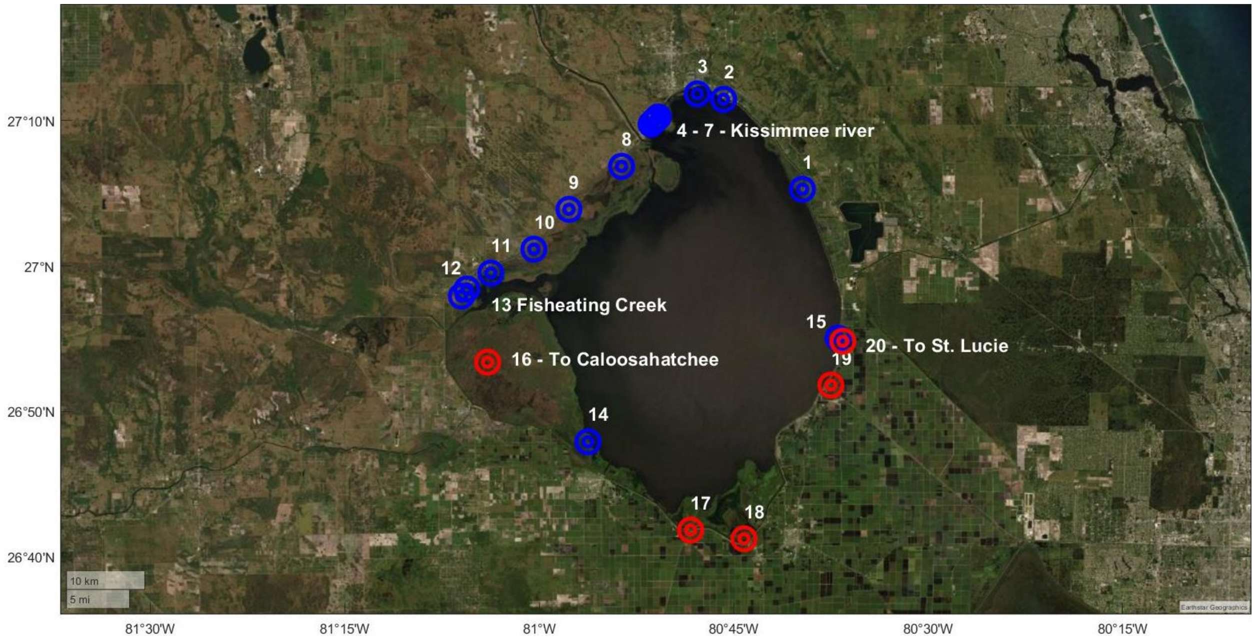

Figure 1E-4: Locations of rivers included in the model. Blue indicates a river that provides inflow to the model and red indicates an outflow. Rivers 4-7 provide flow transport for the Kissimmee river, but equally spread over 4 individual river "mouths" to improve model stability.

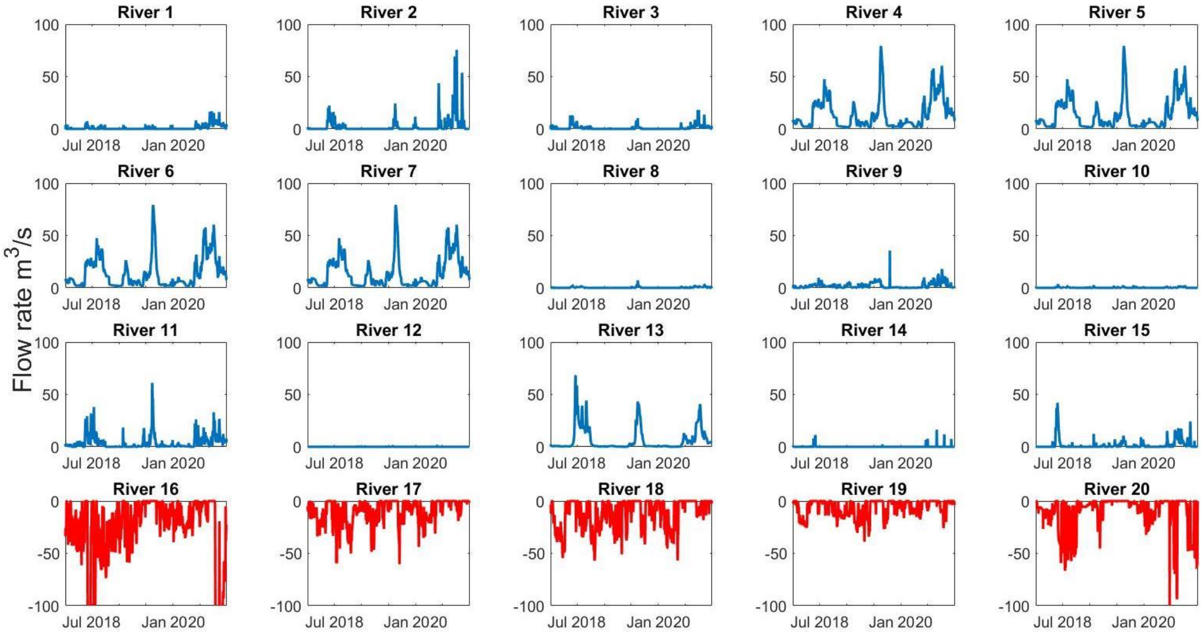

Figure 1E-5: River flow for all of the 20 model rivers (4-7 has equal flow, which combine to be the total flow for Kissimmee River).

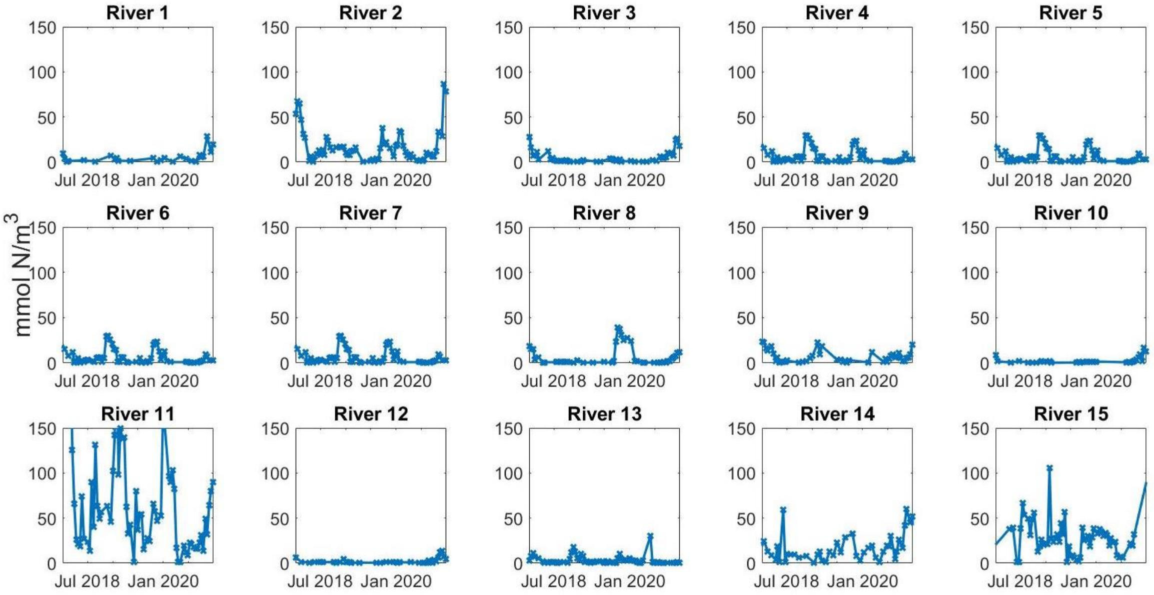

Figure 1E-6: Nitrate concentration for all of the incoming rivers (concentration in 4-7 is the same for Kissimmee River).

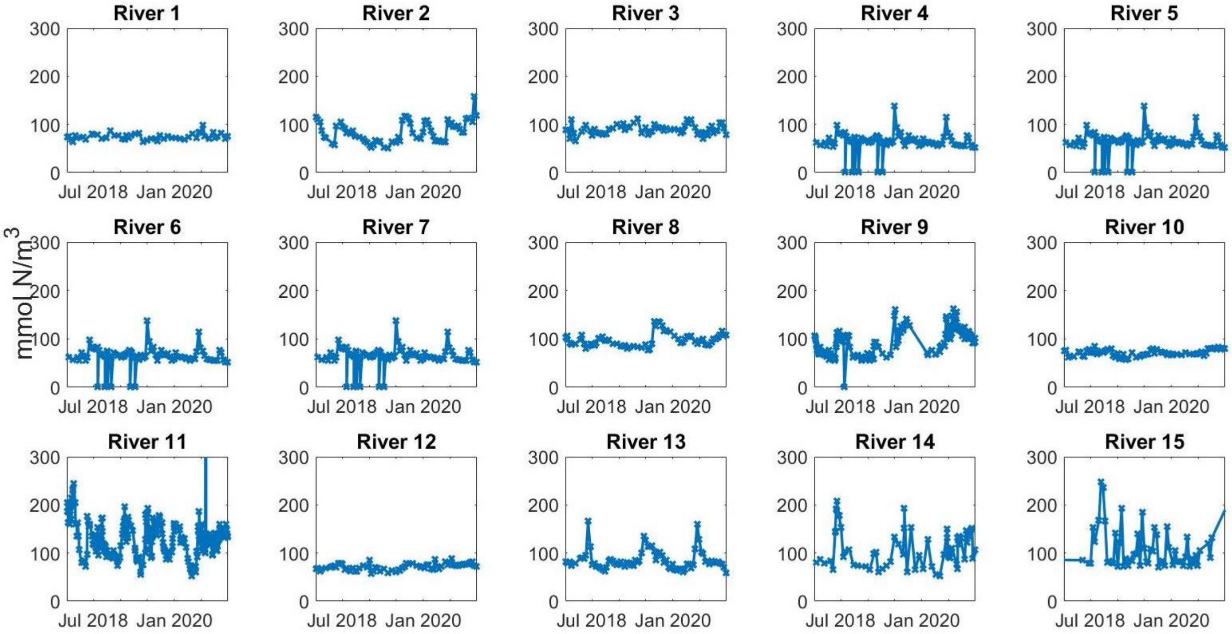

Figure 1E-7: DON concentration for the incoming rivers (concentration in 4-7 is the same for Kissimmee River).

Model implementation, calibration, and validation: Several modifications have been made to ROMS codes to accommodate specific needs for modeling water quality and HABs in a freshwater lake such as Lake Okeechobee. These include, 1) the modification of model configuration to allow outflows of water from the modeling domain for canals such as C-43 and C-44, 2) the revision of model coding to account for the water volume changes due to precipitation or evaporation, and 3) the modification of model coding to ensure correct export fluxes of tracers (e.g. nutrients, phytoplankton). These modifications are needed to ensure the conservation of water volume and materials in the model. All of these have been implemented and tested with satisfactory results.

To ensure reasonable model performance, model parameters and formulations were calibrated using model simulation for 2018-2019 period for comparison to observations for selected parameters. Validation of key physical and biogeochemical variables was planned to be carried out separately for 2020. This plan was deemed impractical later because the HALO field work focused on 2021 and therefore HALO data was not available until mid-way through the project. In the end, the LakeO-ROMS-NPZD model was calibrated for the entire 2018-2020 period using only DBHYDRO data.
As a newly constructed biogeochemical model, extensive testing and revision are needed, including model formulation. Therefore, a one-dimensional (1-D) version of LakeO-ROMS-HAB model was constructed and tested before the implementation of the 3-D version. These tests provide important insight into the blooms dynamics and also allow initial adjustment of model parameters. To date, the 3-D version of LakeO-ROMS-HAB has been implemented for 2021, which was chosen because the HALO data were concentrated in that year. This version is not yet fully calibrated but the work is ongoing.

Operational forecast: A prototype operational forecasting system was developed and implemented based on the LakeO-ROMS-NPZD model (Figure 1E-8). This is a rolling forecast system similar to a meteorological forecast and is run automatically once a week producing a 13-day simulation (6 day hindcast and 7 day forecast) of the lake hydrodynamics and biogeochemistry. The system consists of Unix (shell & Python) and Matlab scripts for download and processing of available data, running the ROMS model, and disseminating results to HALO portals, while providing the means for HALO web portal and online display. There are four main components: 1) downloading data from various sources, 2) parsing and processing these data to produce required model inputs (initial conditions, surface forcing, river inputs) with appropriate format, 3) numerical simulations, and 4) disseminating model output to the HALO web portal for online display.

As a rolling forecast system, model initial conditions for every new run is provided by the results from previous simulation. However, to ensure the model simulation won't veer too far from reality, the initial conditions were modified by assimilating available in situ data and near real-time remote sensing observations. The in situ data include temperature, nutrients and chlorophyll obtained from bottle samples and sailboat sensors. The remote sensing team provided the cyanobacteria index (CI) which was converted to chlorophyll. Algorithms were developed and tested to assimilate this information. However, integration of a disparate information into coherent three-dimensional structures is not straightforward given the spatial-temporal heterogeneity of different data coverage and the uncertainty that comes with different measurements. For example, while remote sensing CI index has good horizontal-spatial coverage when it is available, it only represents cyanobacteria and has no vertical information. Therefore, this method will be further improved when more data are available.
A separate algorithm was developed to provide a forecast of river flow in Kissimmee River, which is needed for the model forecast. The algorithm is based on a significant correlation between precipitation over the upstream areas (greater Orlando metropolitan) and the river flow. There is a time delay of ~1 week between the upstream precipitation and Kissimmee flow near the lake, which is fortuitous from the forecast perspective.

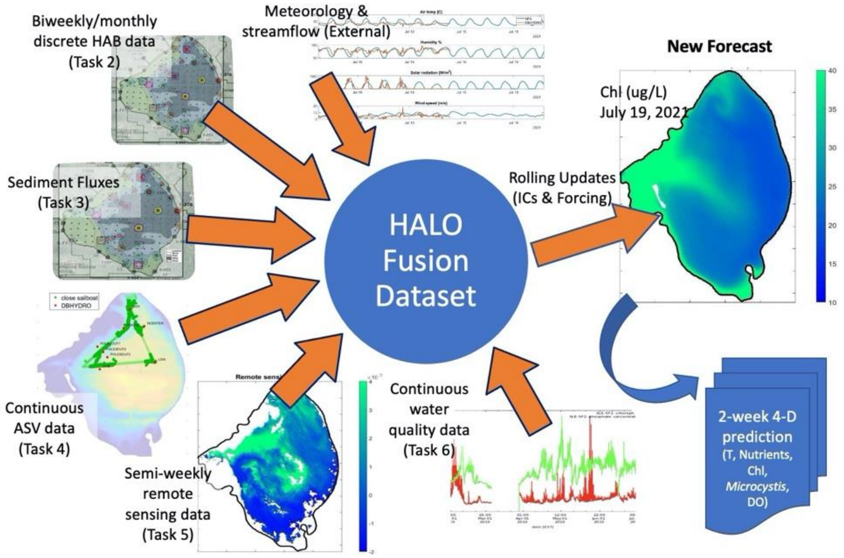

Figure 1E-8: A diagram for the operational forecast.

ACTIVITIES SCHEDULED vs. COMPLETED

Major activities planned for this subtask included: 1) the development of a hydrodynamic model and the development of biogeochemical model. This activity was completed; 2) The numerical simulation, calibration and validation of coupled physical-biogeochemical model. This task is partially completed. The LakeO-ROMS-NPZD model was calibrated and validated, but the LakeO-ROMS-HAB is currently undergoing calibration and validation; 3) The development of a provisional operational forecast model:. This activity is mostly completed. The LakeO-ROMS-NPZD model is fully operational, but the LakeO-ROMS-HAB has not been operationalized because the calibration and validation has not yet been completed. As the project progress, it was decided that we would develop a relatively simple LakeO-ROMS-NPZD and converted it into operational mode, instead of developing a more complicated biogeochemical model, i.e. LakeO-ROMS-HAB. Extensive testing was accomplished for the 1-D version, yet the 3-D version is not yet fully calibrated, primarily due to the departure of a modeling postdoctoral research associated in November 2021. Maintaining operational forecast proved to be time-consuming as any script errors, data source errors (e.g. river flow observations, or DBHYDRO web site maintenance), or High Performance Computing issues (e.g. job queue was too long and such that forecast was not able to complete in time) could cause the forecast failure. Therefore, an individual must be constantly monitoring the forecast in order to find and fix the problems. A second postdoc (hired in Nov. 2021) was new to this project and but also had to spend most of his time on this project to learn and maintain the operational forecast system. Nevertheless, we expect to complete the calibration and validation of this model by June 30, 2022.

RESULTS & DISCUSSION

The model generates 3-D output for the entire model period, which includes spatial patterns and temporal variability. The spatial patterns are highly dynamic. The physical transport and mixing are dominated by winds with additional contribution from surface heat fluxes and freshwater inputs. The spatial patterns of biogeochemical parameters are also dominated by physics but likely are also affected by heterogeneous sediment inputs and river inputs. Unfortunately, we have very limited information to verify these spatial patterns, although HALO activities to date and planned as part of Amendment #3 will increase this resource base (e.g. **Task 4** ASV ADCP current velocities and planned Task 12 Sedimen Erosion experiments). Below, we focus on the temporal variability.

LakeO-ROMS-NPZD model: A water level comparison (Figure 1E-9) demonstrates good agreement with a root-mean-squared (RMS) of 4 cm for the full year, although the model appears to have underestimated the water losses somewhat. It is clear that the water level exhibits strong annual variation with the magnitude ~30 cm in 2018.

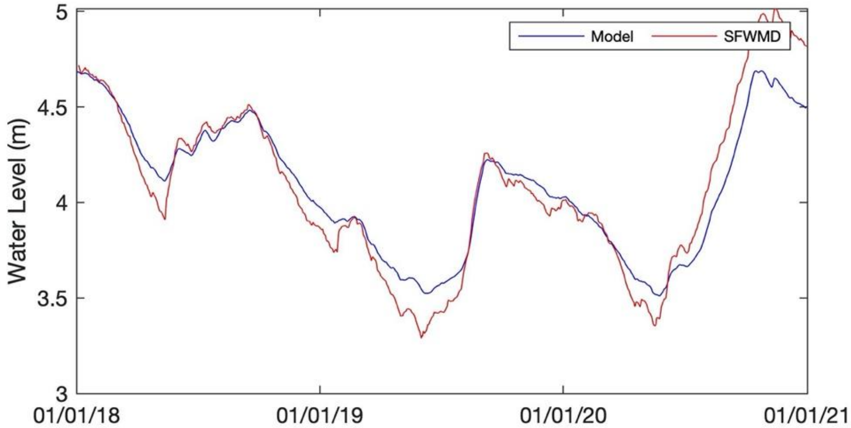

Figure 1E-9: A comparison between observations at L004 and the model prediction.

Figure 1E-10 shows a comparison between modeled and observed surface temperature at station L004 for 2018, indicating a very good agreement on monthly to seasonal time-scales. Overall, the model somewhat overestimates temperature, particularly during the summer period. On average, the RMS bias is 1.2ºC. Both model and observations indicate phytoplankton growth in shallow areas is different compared to deeper areas, likely due to bottom nutrient fluxes and light limitation differences. To better represent the entire lake, therefore, eight observational stations were chosen to represent the entire lake, and both the model output and observations were averaged over the stations (Figure 1E-11). Both model and observations show clear seasonal variations for all variables except organic matter. Model chlorophyll peaks around March-April, which was earlier than observed Chl-a, with blooms usually occurring during the summer months. Both model nitrate and ammonium concentrations show larger maxima and larger oscillations than observed. Ammonium is rarely detected in the lake, suggesting that nitrification is underestimated by the model. Model DON and PON compare well to the observations in terms of magnitude. DO cycles also agree with observations overall, although the model over-estimates the concentration in the summer.

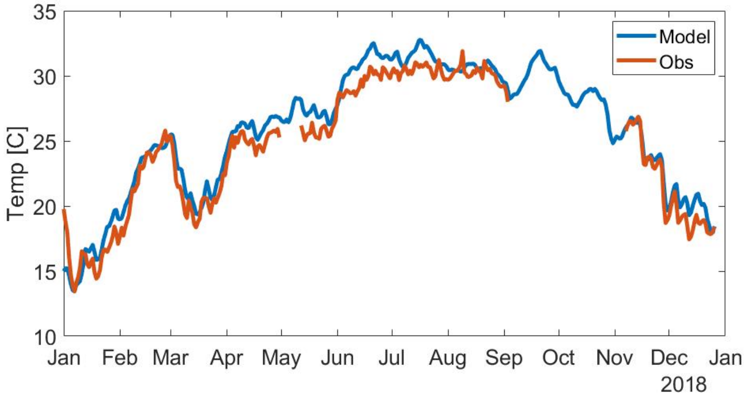

Figure 1E-10: A comparison of surface temperature between observations and the model at L004 in 2018.

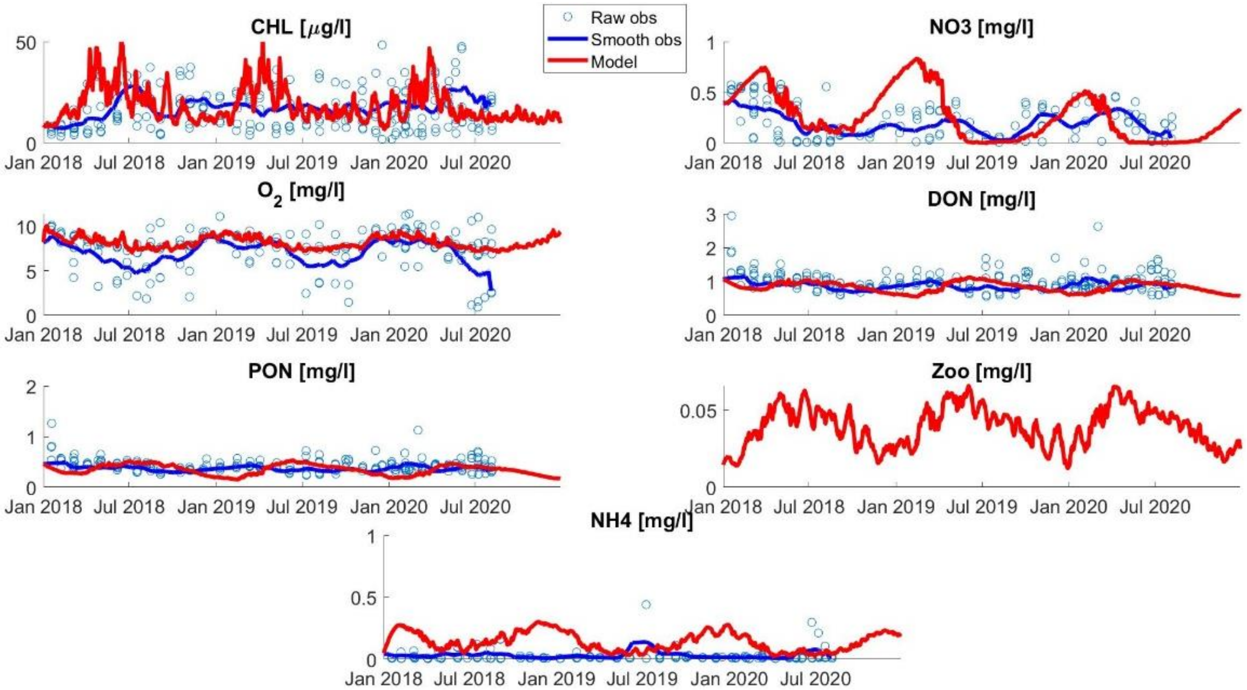

Figure 1E-11: Model vs data comparison for all stations across the lake. Zooplankton data were not available.

Though average comparisons are useful in condensing the overall dynamics, it is also useful to compare model-data site by site. Figure 1E-12 shows a comparison of modeled and observed nitrate and chlorophyll at 4 selected stations. Here L004 is in the deeper part of the lake and both the phase and magnitude of chlorophyll are generally in line with observations, whereas at Polesout site observed nitrate was very low and the observed chlorophyll were off-phase with model in 2019 and 2020. The comparison for L007 and LZ30 appear to show some middle ground where model and observed nitrate agree reasonably in phase and magnitude, yet model chlorophyll was still largely off-phase with data. All of this suggest there were significant spatial variations in term of bloom dynamics, although the causes were not immediately clear.

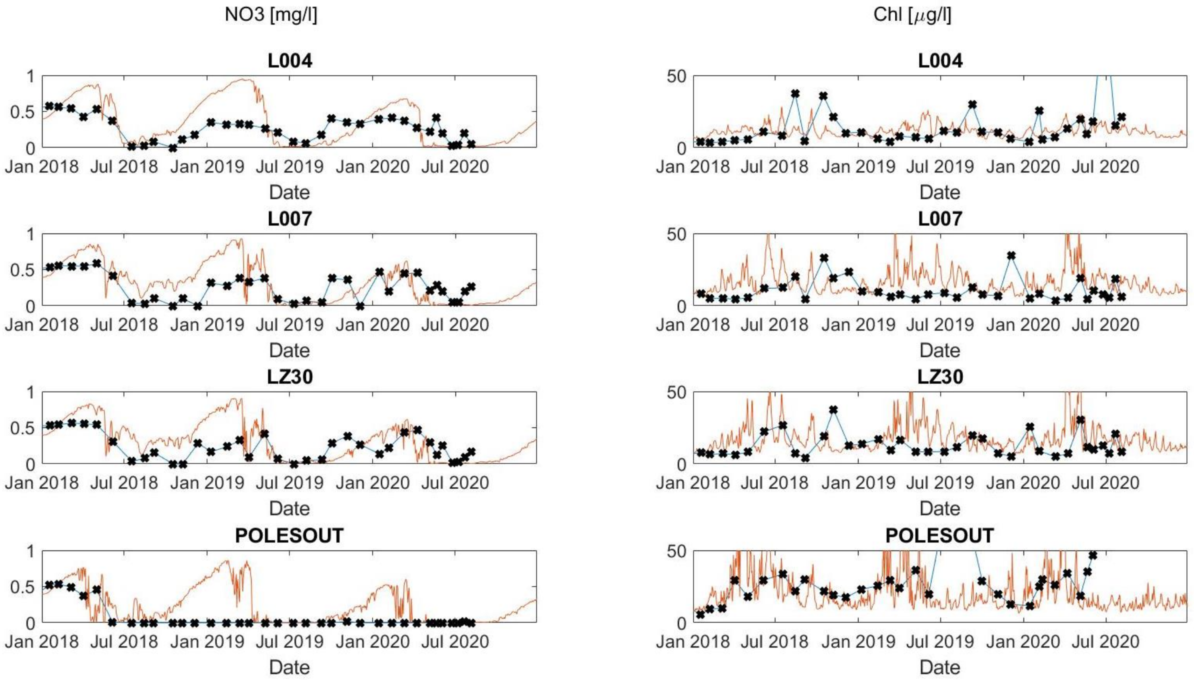

Figure 1E-12: Model-data comparison for nitrate (left panels) and chlorophyll (right panels) at 4 stations. Note L007, LZ30, and Polesout are shallow stations whereas L004 is in the relatively deeper central eastern areas.

<u>LakeO-ROMS-NPZD Operational Forecast</u>: Beginning 7/1/21, the operational forecast system had been implemented and ran successfully once every week, which continued through 12/ 31/21. Figure 1E-13 shows an example of the forecast for 7/14/21. The forecast skills were not fully evaluated because observing data were limited and often weren't available for more than one week after the forecast. Yet a cursory checking with remote sensing Cyanobacterial Index (CI) suggests that sometimes the modeled chlorophyll pattern agrees well with CI (Figure 1E-14), although they are not exactly equivalent (see **Task 5**). Yet in other cases, modeled chlorophyll patterns were quite different from the observed CI pattern.

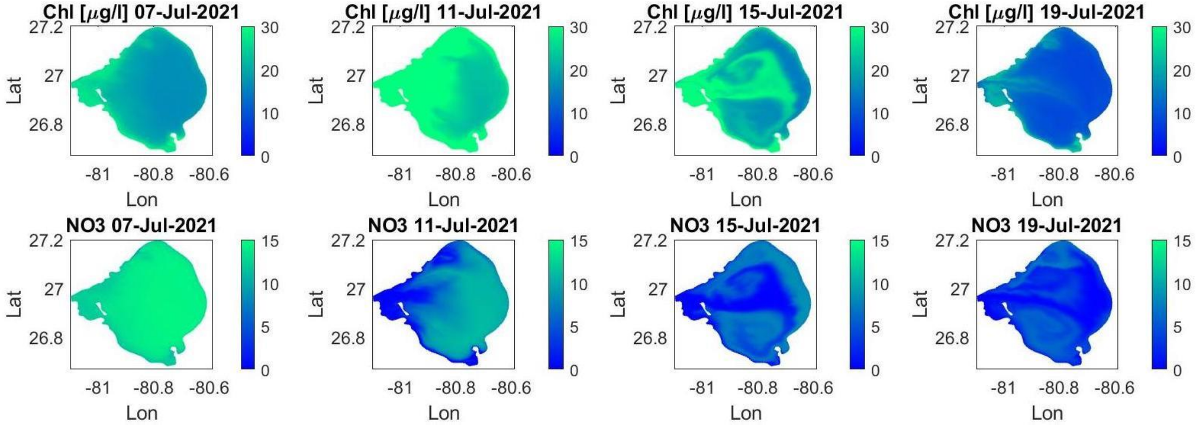

Figure 1E-13: Surface chlorophyll (top panels) and NO$_3$ (bottom panels) on selected dates from forecast on 7/14/21 (7/7/21-7/13/21 were hindcast and 7/14/21-7/19/21 were forecast).

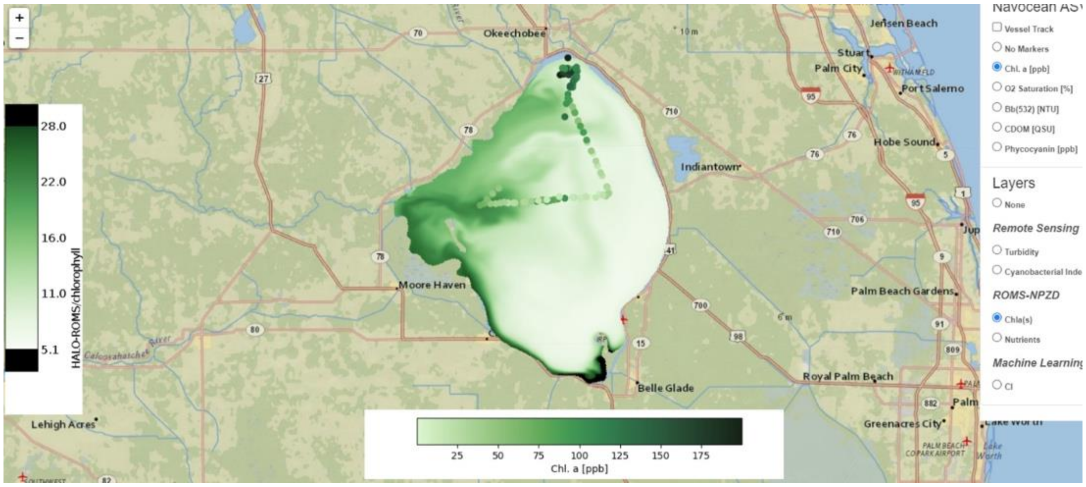

Figure 1E-14: A screen grab of forecast surface chlorophyll (vertical bar) along with observed chlorophyll (horizontal bar) on 7/8/21 from the ASV (Task 4), which indicates consistent patterns. Note the color-scale for the sailboat data is not the same as the modeled chlorophyll.

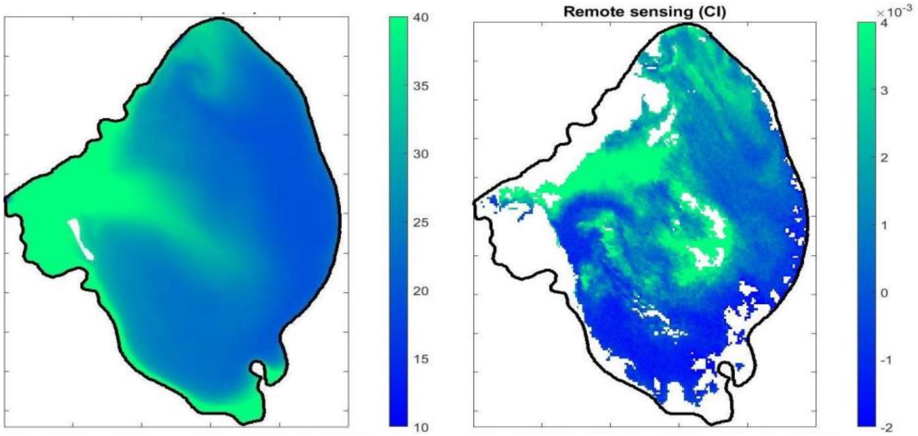

Figure 1E-15: An example of model surface chlorophyll versus CI index on 7/19/21.

<u>LakeO-ROMS-HAB model, 1-D version</u>: The 1-D model allows us to quickly test model parameters and formulations. One important process we had tested was the vertical migration of *M. aeruginosa*, which proved to be important based on **Task 2** data. An example is shown in Figure 1E-16 to compare model results with and without vertical migration. Importantly, vertical migration allows *M. aeruginosa* to bloom for much of the year, although blooms are much more frequent in summer and early fall when the lake was warm and winds weak (favoring phytoplankton cells to stay at surface). One of the net effects is there was rapid drawdown of nutrients during late spring and summer due to these blooms. Moreover, when plotting against temperature, it is clear modeled surface chlorophyll when *M. aeruginosa* is allowed to migrate shows a significant dependence on temperature (Figure 1E-17). Another important aspect about vertical migration is that it would lead to stronger diurnal cycling of chlorophyll during summer time than in the case without vertical migration (Figure 1E-18). The contrast is more pronounced when there is relatively stronger wind mixing during the day.

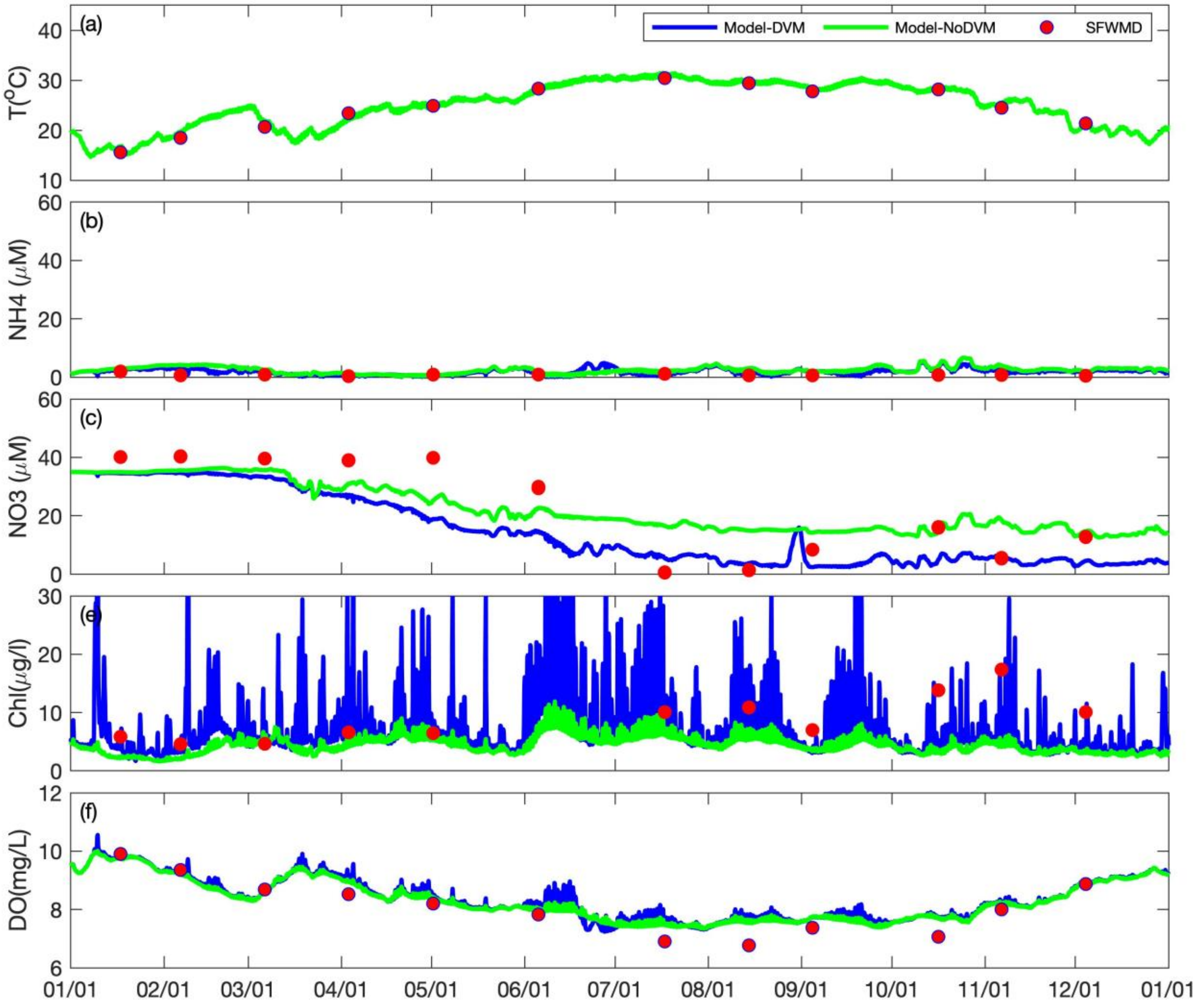

Figure 1E-16: One-year (2018) simulation of LakeO-ROMS-HAB 1-D model with (blue lines) and without (green lines) vertical migration. Red circles are observations.

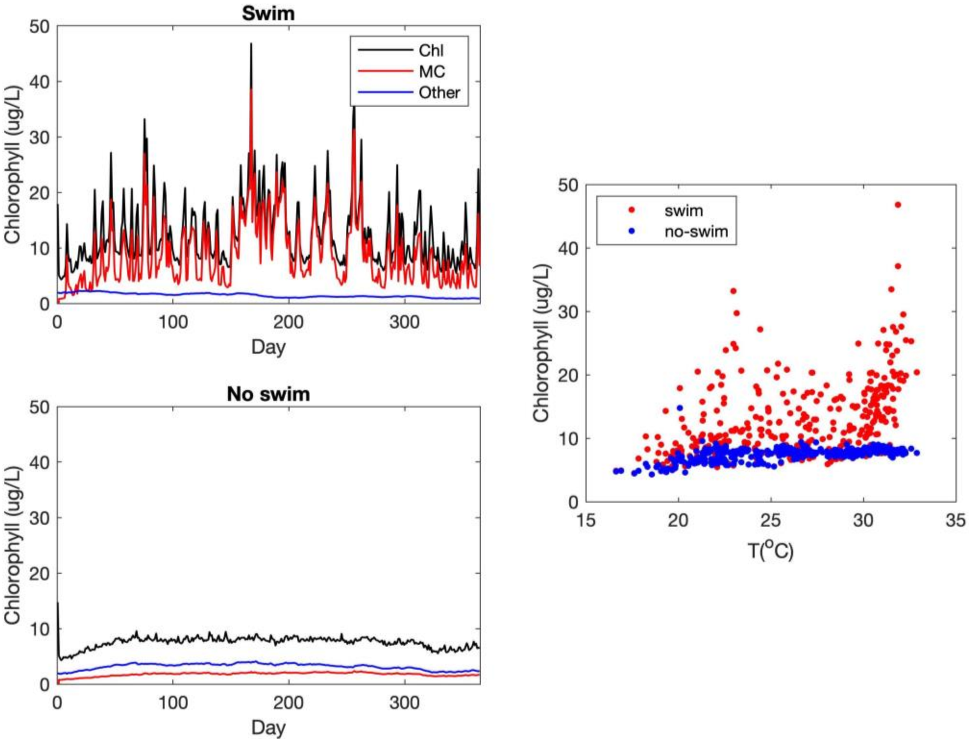

Figure 1E-17: A comparison of model surface chlorophyll with (top left) and without (bottom) vertical migration. The right panel shows the correlations of model chlorophyll versus temperature (blue: no migration, red: migration).

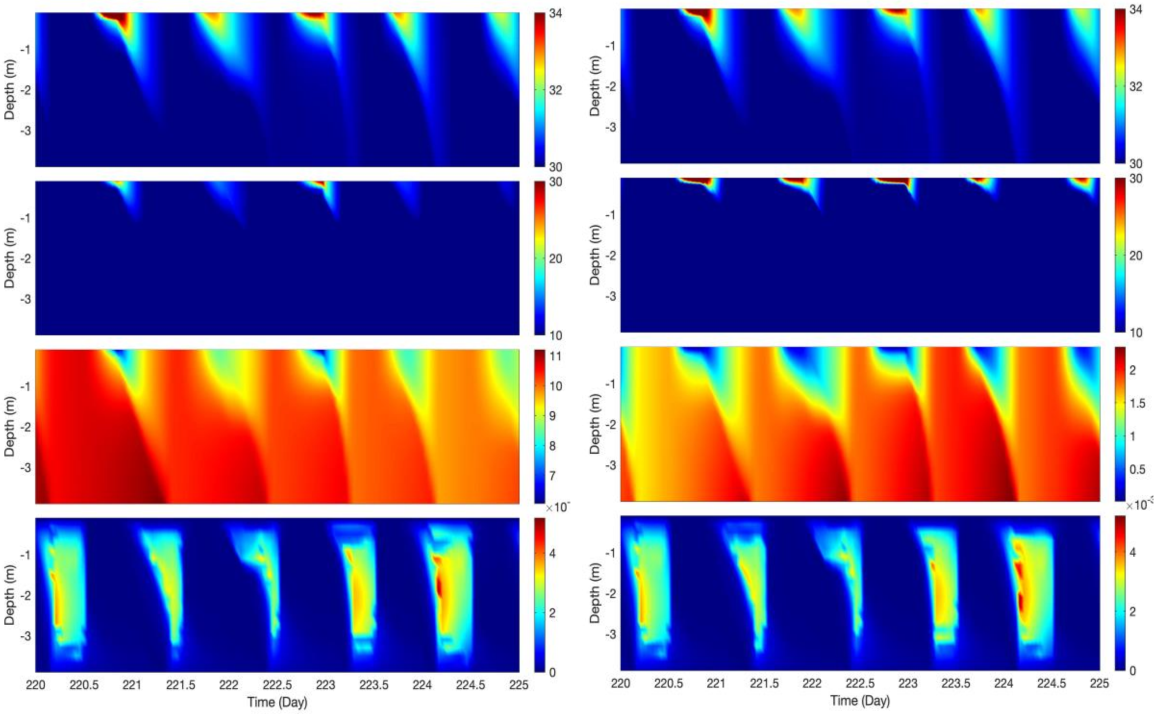

Figure 1E-18: From top to bottom: Diurnal cycling of temperature, chlorophyll, nitrate + ammonium, and mixing coefficient for weak migration (w=1 m/day) (left panel) versus strong migration (w=10 m/day).

LakeO-ROMS-HAB model, 3-D version: A three-year (2018-2020) 3-D simulation has been nearly completed. We are performing final calibration at the moment and the current results are promising. For example, the model shows that vertical migration may play a critical role in the phytoplankton blooms. An example is shown in Figure 1E-19. Diurnal cycles of both *M. aeruginosa* and other phytoplankton are a prominent feature, which are driven by the diurnal cycling of both wind stress and surface heat fluxes (cooling at night and heating during the day). Moreover, *M. aeruginosa* migration (10 m/day in this case) was not strong enough to overcome wind mixing during moderate-to-strong wind events. As a result, major *M. aeruginosa* blooms can and only occur during weak wind periods (e.g. 8/17/21 – 8/22/21). The day-night contrast is most prominent in deeper areas where *M. aeruginosa* concentrations can be quite low at night while major blooms may take place during the day (Figure 1E-20).

The current model results already agree with data collected by SFWMD in general. The agreement is very good in the deeper area of the lake for all most key parameters (Figure 1E-21). It seems, however, that the model underestimates the phytoplankton blooms in the shallower areas especially southwest of the lake (Figure 1E-22). In addition, model appears to overpredict phosphate in the central lake while underpredicting phosphate in shallow areas, suggesting that the parameterization of the bottom phosphate flux may need revision.

A simple analysis suggests wind and temperature play a key role in driving the phytoplankton blooms, mainly *M. aeruginosa* (Figure 1E-23, 24, 25). As noted above, it appears that *M. aeruginosa* migration, while important, are not strong enough to overcome strong wind mixing. As a result, both model and field observations suggest that most of the strongest bloom events occur under low wind conditions. This is particularly true for the central lake where water is deeper and strong winds should disrupt any potential blooms. Temperature is also important in affecting the growth directly. One combined effect of these two factors is that strong blooms mostly occur in the summer and early fall when water is warm and winds are typically weak. Model correlation between temperature and chlorophyll agree with data (Figure 1E-23).

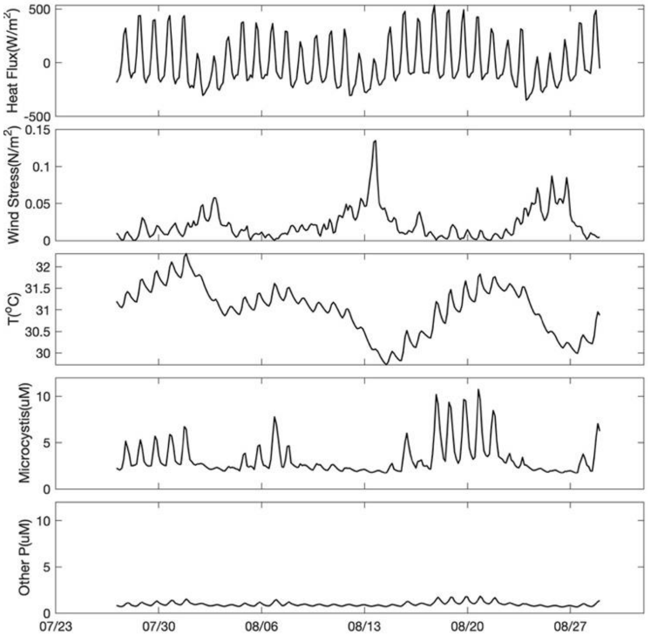

Figure 1E-19: Diurnal cycles of key variables at a station in the central eastern lake. From top to bottom: Net heat flux, wind stress, surface temperature, *M. aeruginosa* , and other phytoplankton in August 2021.

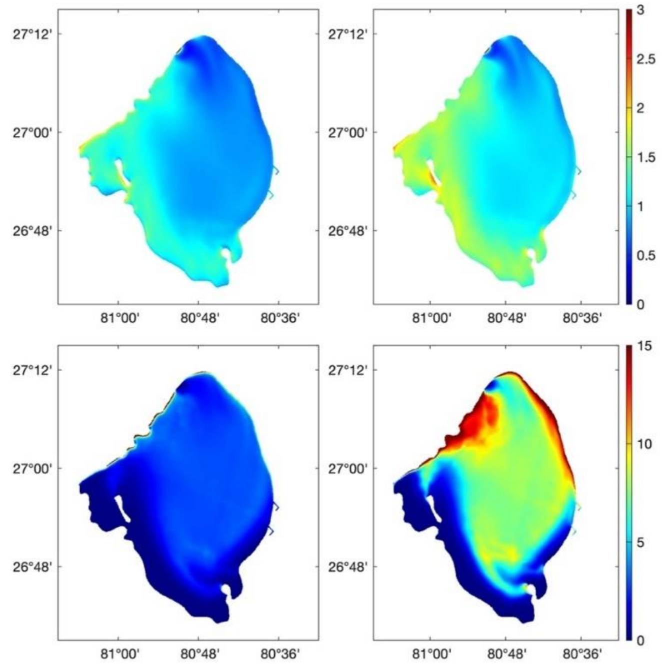

Figure 1E-20: An example of surface phytoplankton concentrations during night (left panels) and day (right panels): Other phytoplankton (top panels) vs *M. aeruginosa* . Note the different color-scales.

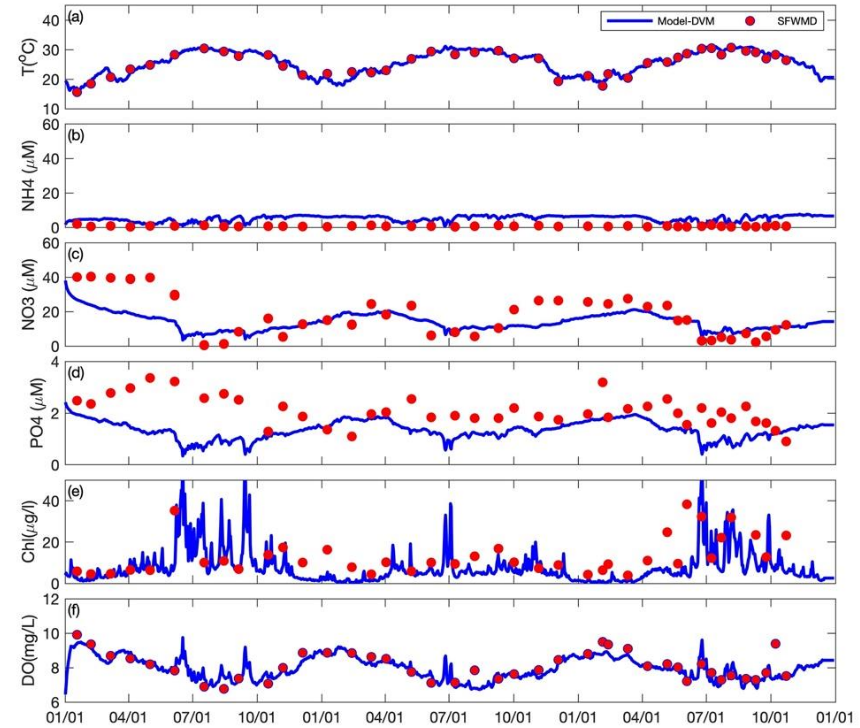

Figure 1E-21: Model-data comparison at a central lake station (LZ40) for a 3-year simulation.

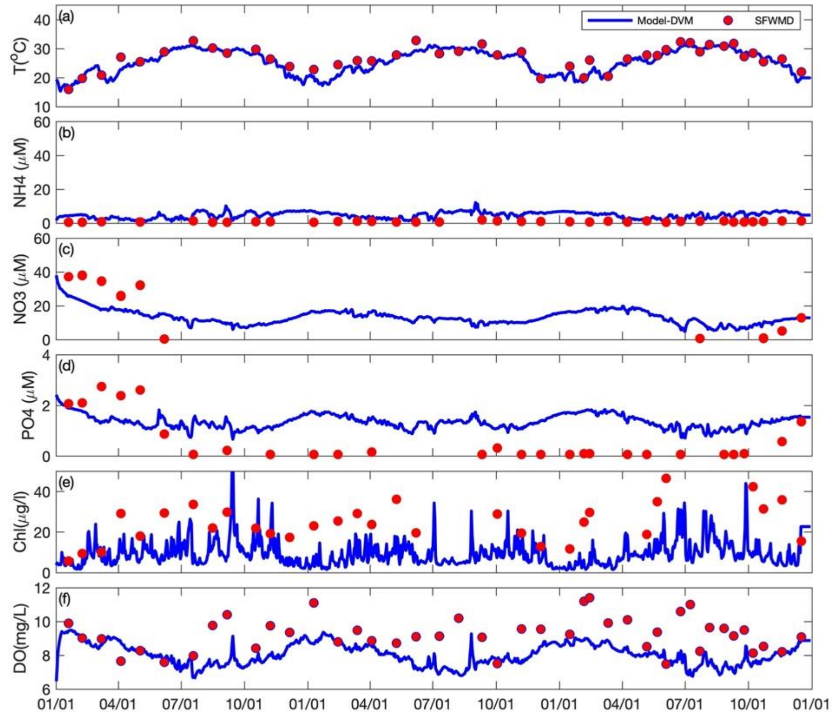

Figure 1E-22: Model-data comparison at a shallow station (Polesout) for a 3-year simulation.

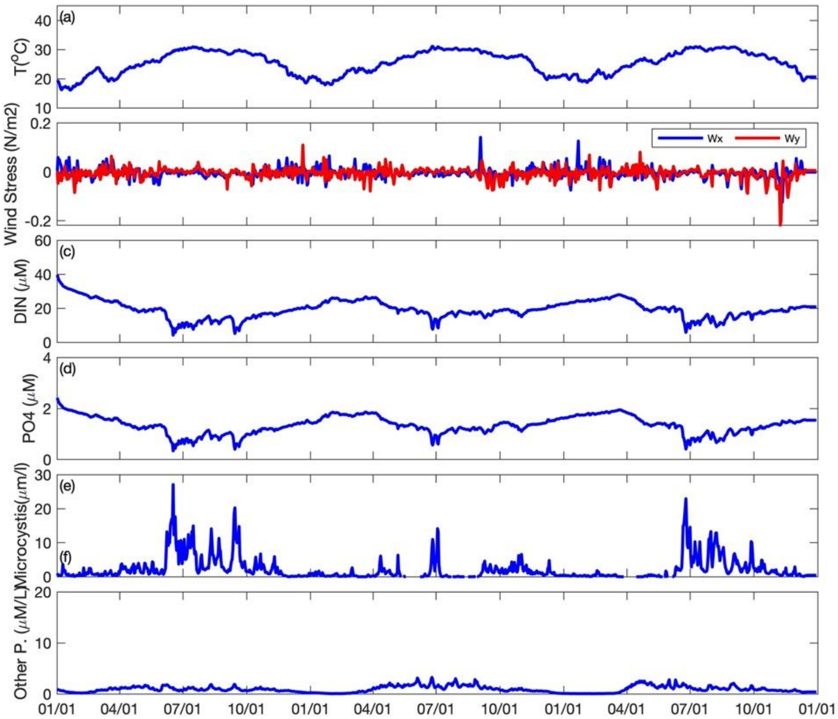

Figure 1E-23: Key parameters (temperature, wind stress, DIN, PO4), ***M. aeruginosa,*** **and all other P forms at a central lake station (LZ40) for a 3-year simulation.**

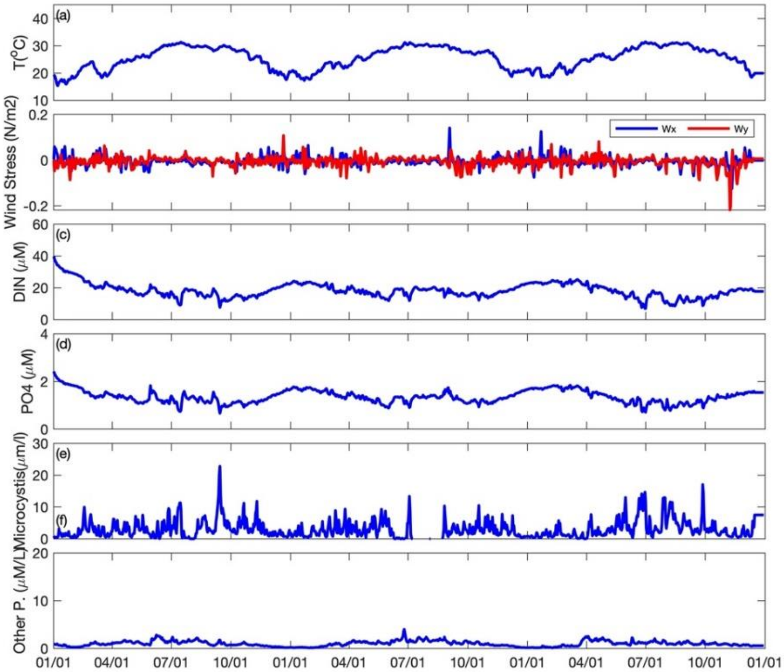

Figure 1E-24: Key parameters (temperature, wind stress, DIN, PO4), ***M. aeruginosa,*** **and all other P forms at a shallow station (Polesout) for a 3-year simulation.**

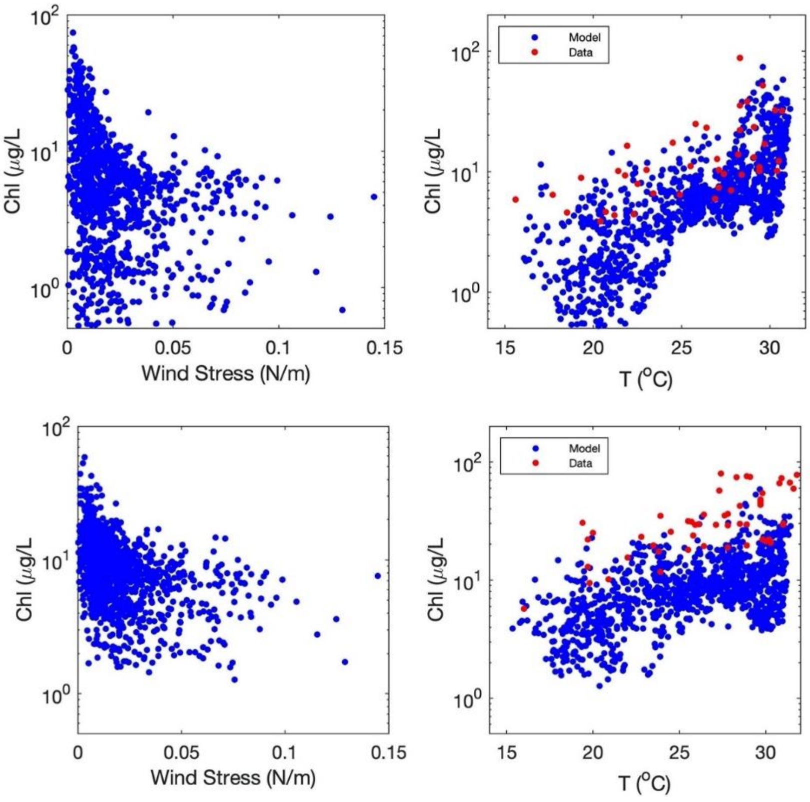

Figure 1E-25: Importance of wind forcing (left panels) and temperature (right panels) in central lake (LZ40, top panels) vs shallow sites (Polesout, bottom panels).

TASK 1F: MACHINE LEARNING MODELING (TASK LEAD: TANG)

INTRODUCTION

In this task, machine learning models were developed to predict *M. aeruginosa* surface blooms based on current and recent environmental conditions. The machine learning approach is unique and relies on high computing power to develop predictions based on artificial intelligence pattern recognition. The machine learning model inputs consist of recent (days to weeks) and current environmental, geochemical, and biological data (including HAB conditions), and the model outputs the likelihood of occurrence and intensity of near-future (days to weeks), spatially resolved, *M. aeruginosa* blooms. The machine learning model was constructed based on deep learning techniques, which have been used with high degrees of success in weather forecasting and other similar domains. Our model builds on the state-of-the-art deep learning algorithm, combined with the best knowledge available and observational data generated from the other project tasks, to provide predictions for future Chl-a concentration. The deep learning model is developed in two phases, where phase 1 focuses on mining statistical relationship knowledge from historical datasets (Figure 1F-1) as well as knowledge transitioning and phase 2 focuses on moving the model into production by automating model runs and outputting results to the HALO portal.

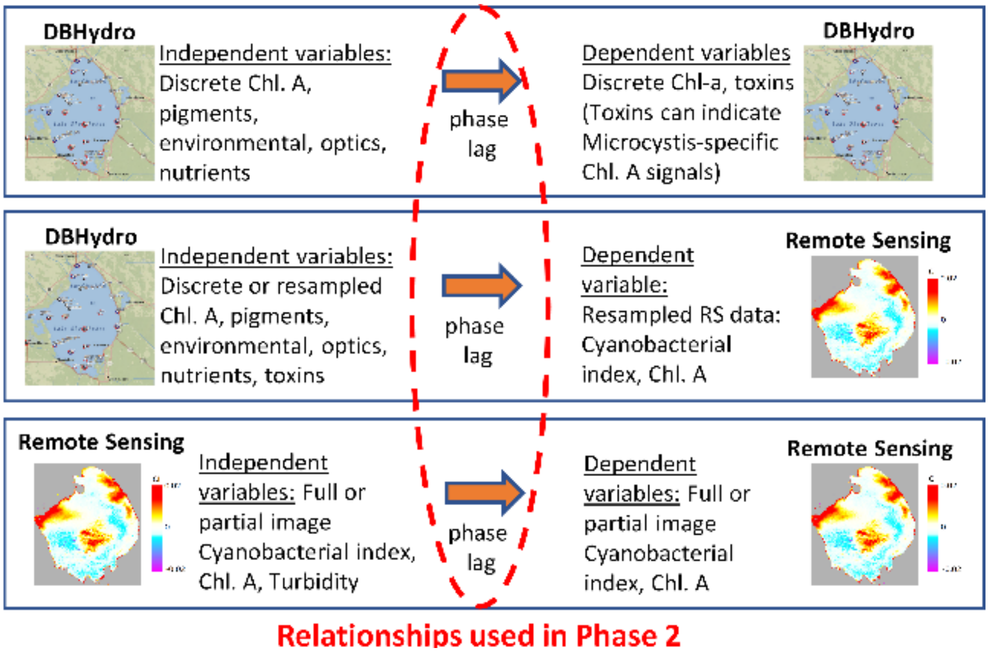

Figure 1F-1: Historical datasets used to develop statistical relationships and train models in phase 1, for employment in the operational Phase 2 model. The left hand side can be envisioned as the set of predictive training variables/conditions/features, with the right hand side being the set of variables to be predicted.

METHODS

Overall methodology: During phase 1 of machine learning model development (Figure 1F-1) historical datasets that are both internal to the project and external (e.g., DBHydro and historical satellite imagery) have been used to discover the statistical relationships between environment condition variables. Various machine learning models were developed and evaluated using these historical data. Specifically, a provisional model is diagrammed, with sources of model feature data indicated (model "inputs"; e.g., field measurements, database, DBHydro, etc.), as well as model outputs, e.g., indicators of HAB measurements. Supervised classification techniques use HALO database measurements, not limited to in situ Chl-a, nutrient data collected from fixed-location moorings, autonomous surface vehicles, and remote sensing. These measurements are "linked" to other physicochemical and biological time-series measurements.

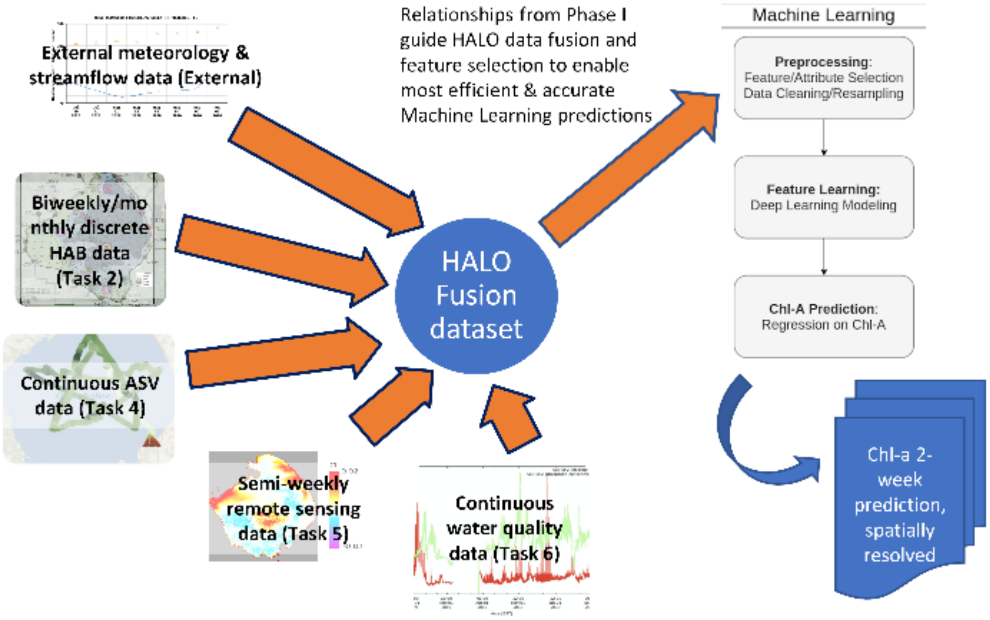

Figure 1F-2: Relationships in phase 1 used with HALO data for rapid prediction.

For the historical datasets, lake-wide surface water quality data from various monitoring sites throughout Lake Okeechobee (i.e., DBHydro data) as well as historical remote sensing data were used for the deep learning model training. All Lake Okeechobee sites (> 25) within the DBHydro database from all date ranges were considered. We first focused on site-independent machine learning, i.e., water quality parameters or other environmental features are the primary training inputs. Additionally, for the model training, historical remote sensing data available for the 2016 to present time period were generated via processed sentinel-3 satellite data (**Task 5**). These data were preprocessed using basic quality control measures (e.g., removing extreme and NaN values, resampling and interpolating missing values in both time and space). The preprocessing pipeline in phase 1 is developed with phase 2 in mind and is capable of direct porting to the new data streams from other project tasks.

During phase 2, data collected from tasks 2–6 (nutrients, cell counts, Chl. a, remote sensing, etc.; Figure 1F-2) were fused to form a dataset that serves as the machine learning input. In the machine learning pipeline, the datasets are automatically preprocessed, i.e., data is cleaned and resampled for feature/attribute (input) selection. These selected features are further processed by deep learning models (i.e., deep neural networks) for feature learning. Finally, these extracted features are used to predict the concentrations of the HAB indicator Chl-a. After the model algorithm was developed and trained, the model was then deployed and operationalized via the HALO database and portal. Specifically, the most up-to-date HALO task data is automatically ingested for a two-week prediction. Model outputs are continuously archived on the HALO database and consist of a time series of 2-dimensional surface data for Chl-a concentrations.

Deep learning model: We specifically used the Convolutional Long-short Term Memory Network (ConvLSTM) to build our deep learning predictor. ConvLSTM is a hybrid model of the LSTM network and CNN network. The basic idea is the same as LSTM, which utilizes the previous layer's output as the input for the following layer. The most significant change is that weight computation of weight value is now a convolution operation. The inner structure of ConvLSTM is shown in Figure 1F-3.

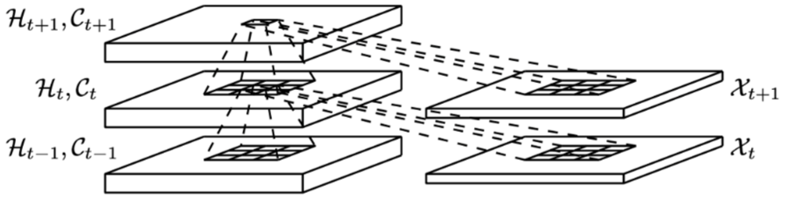

Figure 1F-3: Inner structure of the ConvLSTM deep learning model.

With the addition of the convolution operation, ConvLSTM can not only establish a timing relationship similar to LSTM, but also has a spatial feature extraction capability similar to CNN. Thus, ConvLSTM is able to capture underlying spatial-temporal correlations. The key equations of ConvLSTM are shown below, with the $*$ represents convolution operator and o the Hadamard operator.

$$
\begin{aligned}
i_t &= \sigma(W_{xi} * \mathcal{X}_t + W_{hi} * \mathcal{H}_{t-1} + W_{ci} \circ \mathcal{C}_{t-1} + b_i) \\
f_t &= \sigma(W_{xf} * \mathcal{X}_t + W_{hf} * \mathcal{H}_{t-1} + W_{cf} \circ \mathcal{C}_{t-1} + b_f) \\
\mathcal{C}_t &= f_t \circ \mathcal{C}_{t-1} + i_t \circ \tanh(W_{xc} * \mathcal{X}_t + W_{hc} * \mathcal{H}_{t-1} + b_c) \\
o_t &= \sigma(W_{xo} * \mathcal{X}_t + W_{ho} * \mathcal{H}_{t-1} + W_{co} \circ \mathcal{C}_t + b_o) \\
\mathcal{H}_t &= o_t \circ \tanh(\mathcal{C}_t)
\end{aligned}
$$

We use the encoding-forecasting ConvLSTM structure illustrated in Figure 1F-4 to solve the spatial-temporal prediction issue. It is made up of two networks: an encoding network and a forecasting network. The forecasting network's initial state and cell output are replicated from the encoding network's final state. Both networks are created by stacking several ConvLSTM layers. We connect all the states in the forecasting network and feed them to the convolutional layer to construct the final prediction since the target and input of spatial-temporal prediction generally have the same dimensions.

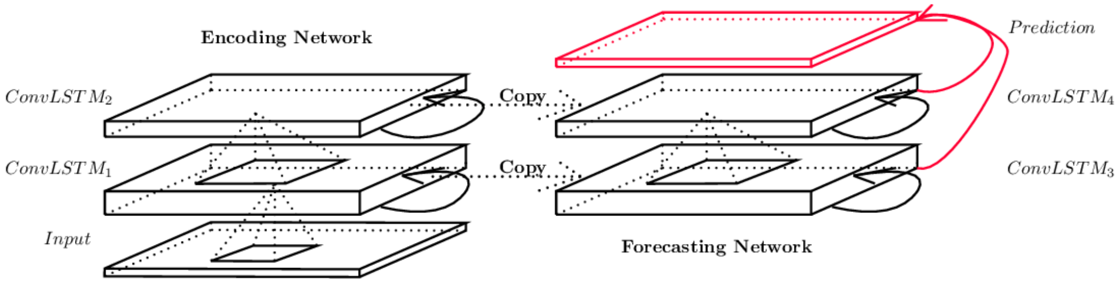

Figure 1F-4: Encoding-forecasting structure in the ConvLSTM.

To build the complete model, we use four ConvLSTM2D layers with batch normalization followed by a Conv3D layer for spatial-temporal outputs. Figures 1F-5 and 1F-6 are the complete model diagram and the summary of the model parameters. The ConvLSTM2D layer only accepts the inputs that have the same shape (batch Size, sequence, width, height, channels). We use 14 days of data as the input to predict a single day (i.e., repeat 14 times for a 14-day prediction), thus we reshape the data in each batch that has a sequence of 14 images. For the model evaluation, we mainly use a set of quantitative metrics, specifically, root mean square of errors (RMSE) and normalized standard deviation (STD).

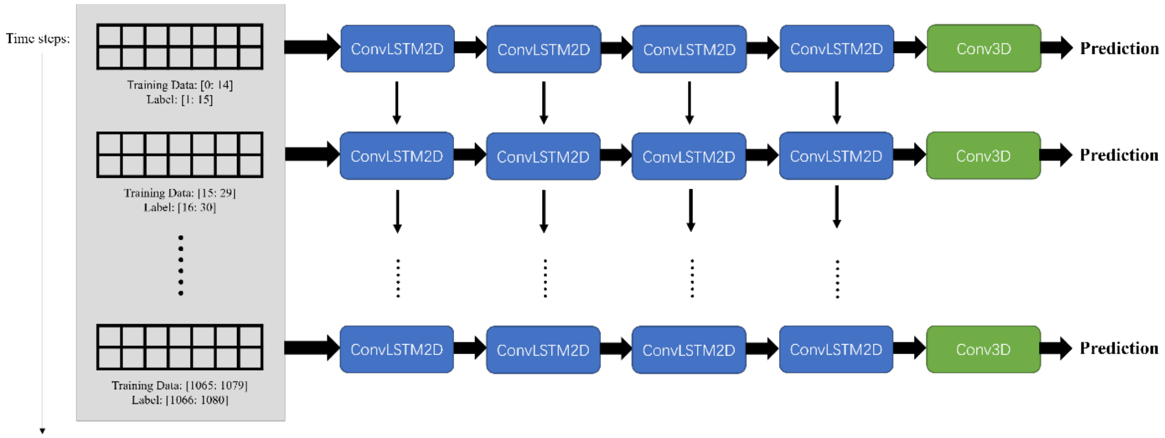

Figure 1F-5: Complete ConvLSTM model that used for training and online prediction.

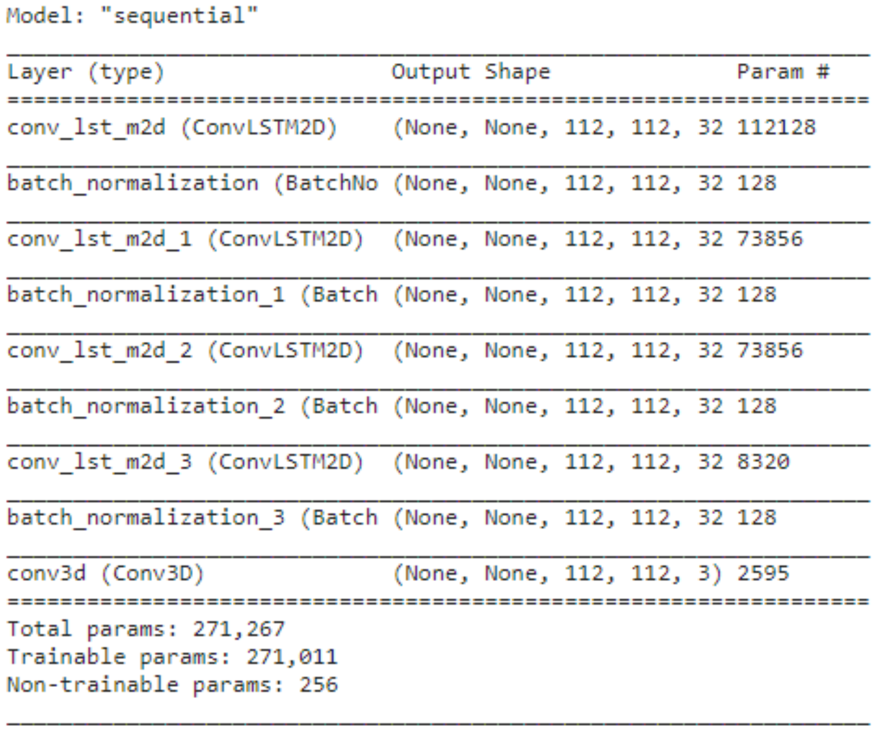

```
Model: "sequential"
_________________________________________________________________
Layer (type)                 Output Shape              Param #
=================================================================
conv_lst_m2d (ConvLSTM2D)    (None, None, 112, 112, 32 112128
_________________________________________________________________
batch_normalization (BatchNo (None, None, 112, 112, 32 128
_________________________________________________________________
conv_lst_m2d_1 (ConvLSTM2D)  (None, None, 112, 112, 32 73856
_________________________________________________________________
batch_normalization_1 (Batch (None, None, 112, 112, 32 128
_________________________________________________________________
conv_lst_m2d_2 (ConvLSTM2D)  (None, None, 112, 112, 32 73856
_________________________________________________________________
batch_normalization_2 (Batch (None, None, 112, 112, 32 128
_________________________________________________________________
conv_lst_m2d_3 (ConvLSTM2D)  (None, None, 112, 112, 32 8320
_________________________________________________________________
batch_normalization_3 (Batch (None, None, 112, 112, 32 128
_________________________________________________________________
conv3d (Conv3D)              (None, None, 112, 112, 3) 2595
=================================================================
Total params: 271,267
Trainable params: 271,011
Non-trainable params: 256
_________________________________________________________________
```

Figure 1F-6: Summary of the ConvLSTM model parameters.

ACTIVITIES SCHEDULED vs. COMPLETED

We first carried out exploratory data analyses using historical datasets including but not limited to DBHydro and Sentinel-3 satellite imagery. Correlations between individual water quality and nutrient measurements were carried out for newly processed data for 26 DBHydro sites at various locations throughout Lake Okeechobee (Table 1F-1).

Table 1F-1: An example correlation vector for the preprocessed features compared against Chlorophyll-A for station L001, a site located in the north region of the lake.

Feature	Corr. Coef.
CHLOROPHYLL-A:	1.000000
CHLOROPHYLL-A, CORRECTED:	0.952709
CAROTENOIDS:	0.647978
TEMP:	0.369804
PH, FIELD:	0.365582
PHEOPHYTIN:	0.311678
KJELDAHL NITROGEN, TOTAL:	0.263776
CHLORIDE:	0.216922
SECCHI DISK DEPTH:	0.166500
ALKALINITY, TOT, CACO3:	0.137846
SP CONDUCTIVITY, FIELD:	0.090744
AMMONIA-N:	0.024777
COLOR:	-0.005360
DISSOLVED OXYGEN:	-0.041304
TOTAL SUSPENDED SOLIDS:	-0.062138
NITRITE-N:	-0.116564
PHOSPHATE, TOTAL AS P	-0.170625
TURBIDITY	-0.200912
NITRATE-N:	-0.394327
NITRATE+NITRITE-N:	-0.436971
PHOSPHATE, ORTHO AS P:	-0.450035

Preliminary deep learning models were implemented and evaluated based on preprocessed historical Sentinel-3 remote sensing data over the 3-year period from 2016–2019. Baseline hindcasts of the Cyanobacterial Index (CI) were conducted with a Linear Autoencoder, a deep learning model that capable of learning the statistical relationships between CI values from a given date and their values on subsequent dates. This preliminary model output has been tabulated and stored in NetCDF format and provided to the HALO development portal (Figure 1F-7). This predicted surface coverage was for a date in the near future but was derived using data from only the previous sampling date based on knowledge extracted via pattern recognition for all dates. The model output is conveniently displayed automatically on the HALO server in an operational manner.

To create a deep learning model with spatial-temporal prediction capabilities, we evaluated several approaches. First, the composite LSTM autoencoder marks the first deep learning model applied on HALO data capable of forecasting sequences of spatially resolved CI. The model is capable of reconstructing future sequences of CI on instances with similar characteristics to data seen during the model training. However, the model suffers from generalization issues with poor reconstruction performance. The major reason is that the current data is of low quality from a machine learning perspective (e.g., incomplete data sequence and non-uniform time steps). Example outputs of training and testing instances are provided in Figure 1F-8.

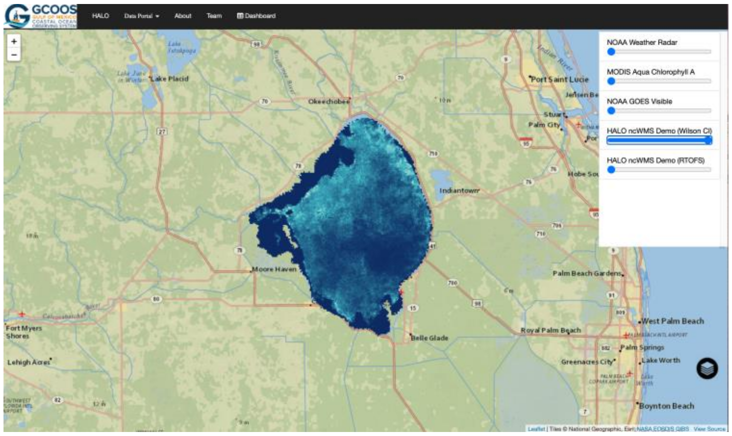

Figure 1F-7: Preliminary model results for cyanobacterial index.

Training:

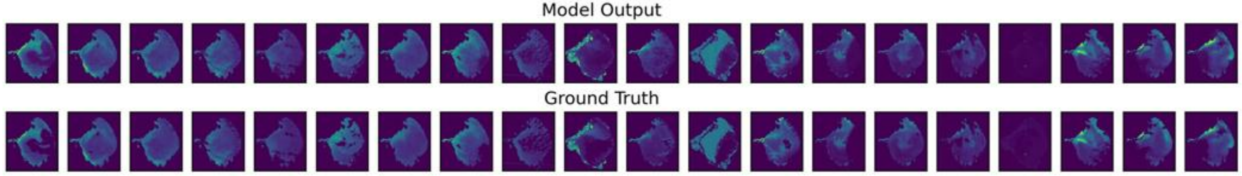

Hindcast:

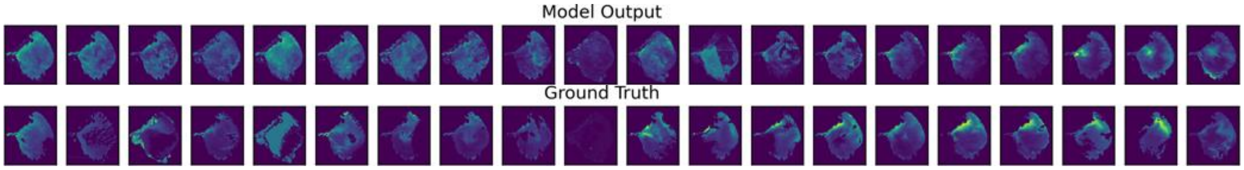

Figure 1F-8: Model training is conducted on filtered and preprocessed sequences of length 20. Each frame corresponds to a normalized non-uniform timestep of CI measured from Sentinel 3 imagery. The training data consists of the first 16 images, while the hindcast testing data corresponds to the last 4 images. During the training phase, the model is only exposed to sequences from the training data, while during the testing phase, the model is evaluated on the unseen testing set.

Next, the convolutional LSTM autoencoder was implemented to incorporate learning abilities from multi-channel input data while also adding the capability of spatial features. The non-convolutional LSTM model is only capable of learning temporal characteristics from a flattened vector of input data, whereas the ConvLSTM is capable of learning both spatial and temporal characteristics to better model geographical and temporal complexity of the Lake Okeechobee system. This model is theoretically capable of automatically learning functional mapping between multidimensional input features and a spatiotemporal sequence corresponding to predicted cyanobacteria index for a 14-day period over the surface of the lake. This comes at the cost of greater computational complexity and difficulty achieving convergence without both higher quality and quantity of data.

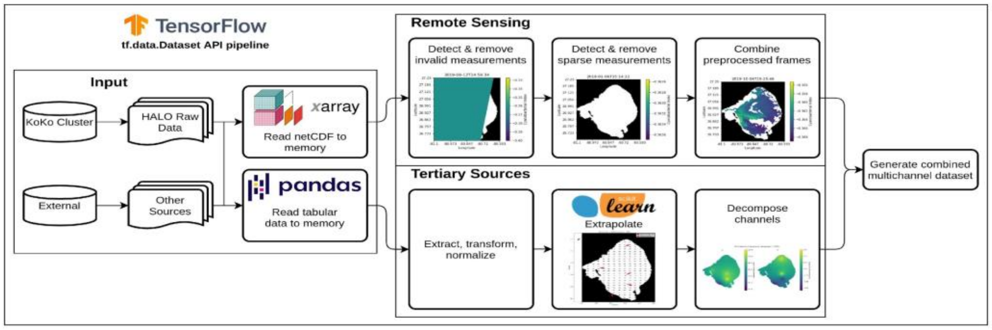

Figure 1F-9: The proposed automated data pipeline for machine learning model deployment.

Further model planning relies on a reliable and valid pipeline before further experiments can be conducted with newly available measurements and before operationalization efforts can commence. Figure 1F-9 illustrates the proposed block diagram for the data pipeline. The data pipeline consists of three main blocks. The input block is designed to automatically fetch both locally available data provided from other HALO tasks stored on the high-performance supercomputing cluster as well as remote data from tertiary sources such as DBHydro. Then a 14-day forecast is generated and saved as a '.nc' file. The deep leaning model predicts the forecast for the next day. It then uses this one-day forecast as further input for predicting the subsequent day.

The HALO portal pulls the machine learning data from the FAU High Performance Computing cluster daily. The script requires the machine learning task lead to use their personal FAU login dual authorization to login each time, which creates non-trivial issues. Two different attempts are being made to fix this issue: 1) remove single sign on from the Duo authorization requirements; and 2) add remote host keys to High Performance Computer cluster without a password. The 14-day forecast can be viewed via the time series using the controls seen in the bottom right boxed in Figure 1F-10. Figure 1F-11 shows a simple 3-day example of the rolling time series.

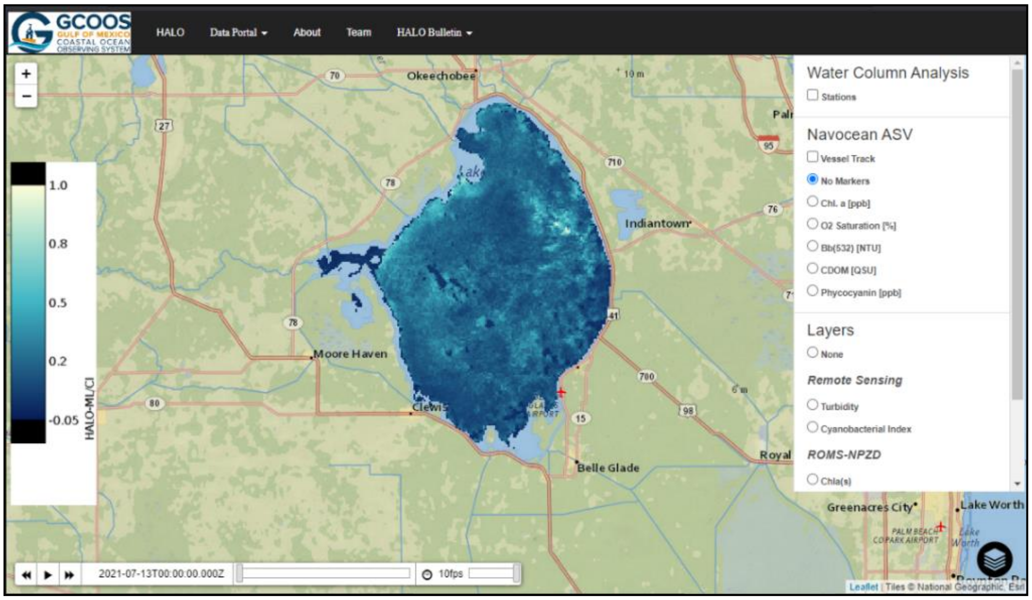

Figure 1F-10: Forecast on HALO portal, where the controls are in the bottom right box.

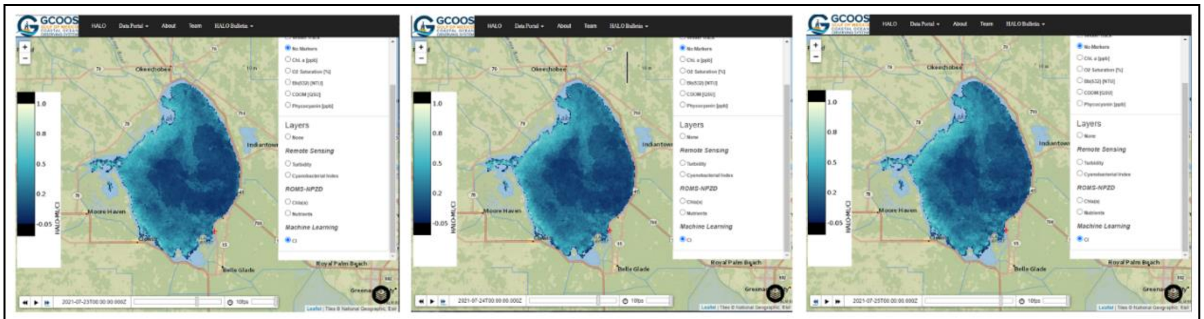

(a) July 23 (b) July 24 (c) July 25

Figure 1F-11: A typical 3-day timeseries 7/23 - 7/25 that was predicted by the Linear Autoencoder.

To improve the spatial-temporal ConvLSTM model performance, a higher quality and quantity of data are required. Thus, the model was expanded by further using hydrodynamic physical conditions from **Task 1E**, generating a “Physics-informed Machine Learning Model” validated on real remote sensing measurements. The image dataset generated by the hydrodynamic model as part of **Task 1E** is comprised of a 3-year simulation split into monthly files which contain daily averaged output. Figure 1F-12 (left) is an example of the original physics model image file that has a size of 386*386, which is excessively large for the machine learning model and causes an “Out of Memory” error. Downsampling of the dataset is required, and the image was cropped and resampled to 112*112. Although the sharpness of the pictures is reduced, it is still acceptable for forecasting. Figure 1F-12 (right) is one of the data images after downsampling. Data normalization is finally applied to the downsampled images, and Figure 1F-13 shows 14 days of data after normalization.

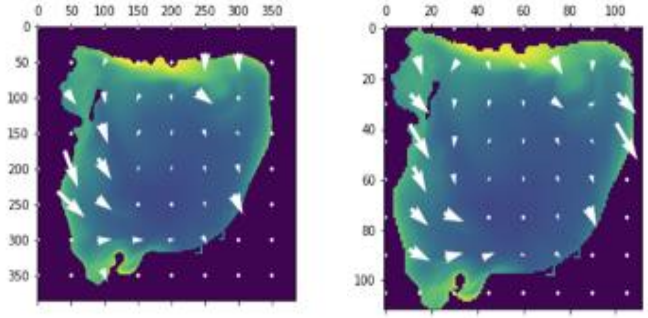

Figure 1F-12. Physics model output. Left: original image that contains Chl-A and lake circulation. Right: data after downsampling.

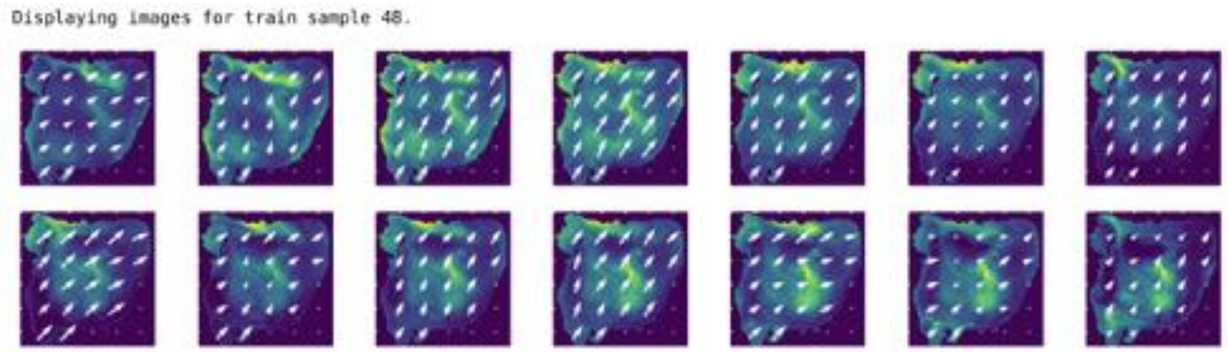

```
Displaying images for train sample 48.
```

Figure 1F-13. Physics model output images with downsampling and normalization (14 days).

RESULTS & DISCUSSION

ConvLSTM results, single day prediction: Figure 1F-14 shows typical predictions on the validation dataset. Compared to the ground truth, the results are promising (Figure 1F-15) where the model converges fast.

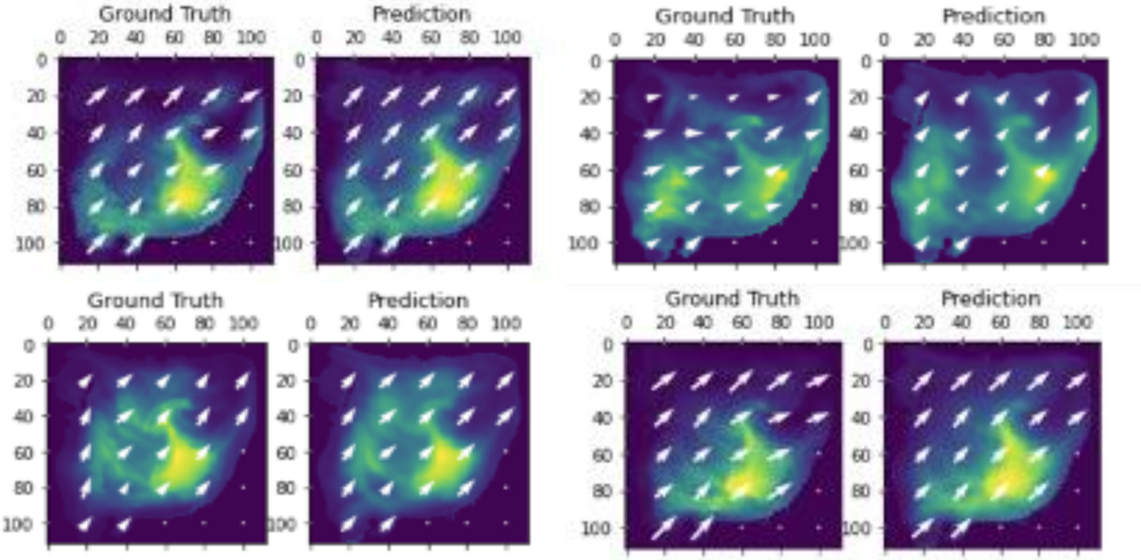

Figure 1F-14: Typical predictions of the ConvLSTM. Ground truth and prediction are presented. Note that "Ground truth" is the reality we want our model to predict. Prediction is the model output after training. The model is trained in a way that the output will be as close to reality ground truth as possible.

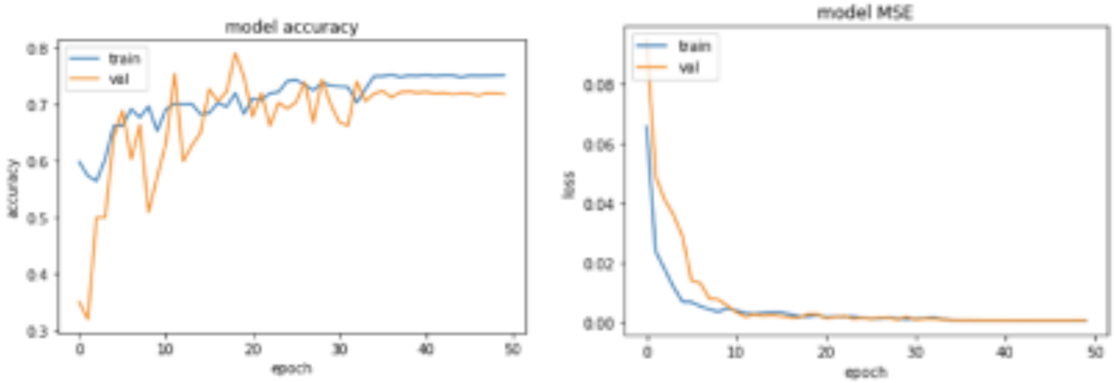

Figure 1F-15: Left: model accuracy. Right: model mean squared error.

ConvLSTM results, 14-day prediction: The goal is to have a 14-day prediction, with the predicted result as an input to predict the next day. Figure 1F-16 shows the 14-day prediction.

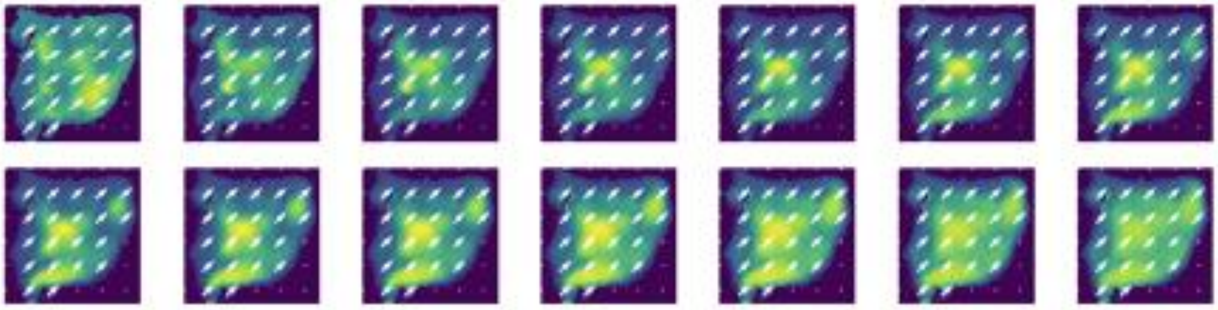

Figure 1F-16: A 14-day prediction using the '14-day to 1-day' setting.

Additionally, 14 days of data were used to predict 2 days (14-day to 2-day). We can see that the results are still accurate, shown in Figure 1F-17. The ultimate goal was to generate a 14-day prediction, with the results are shown in Figure 1F-18.

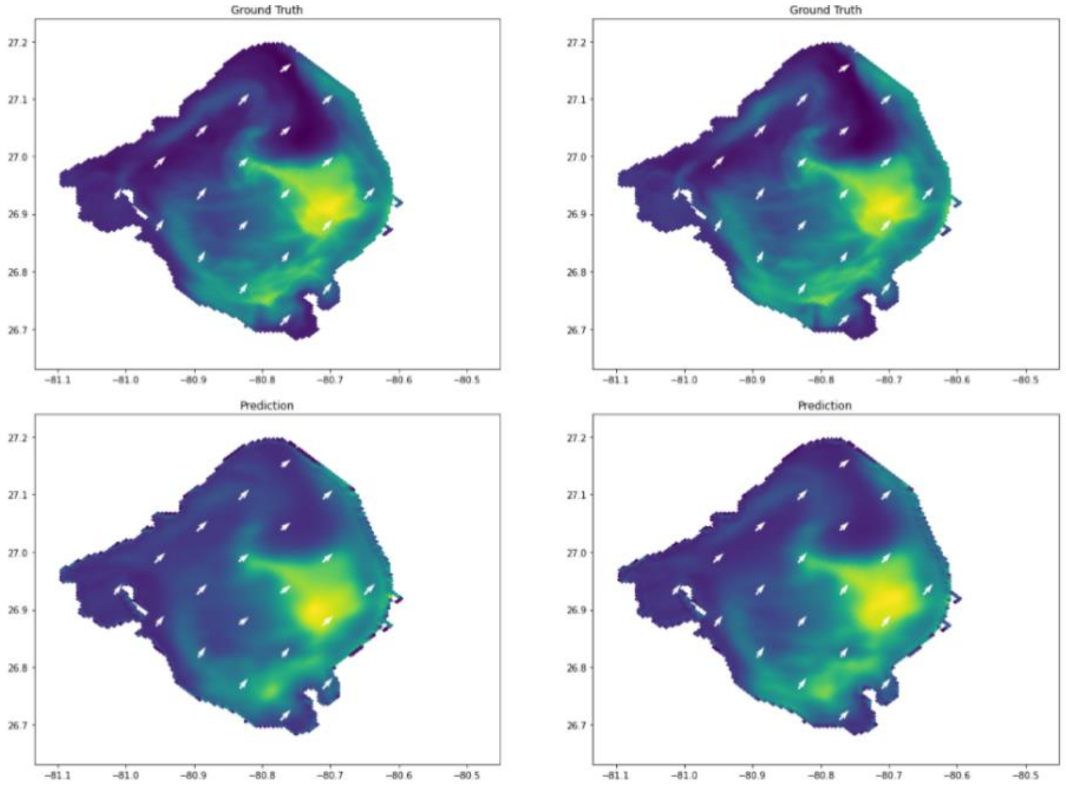

Ground Truth

Ground Truth

Prediction

Prediction

Figure 1F-17: 14-day to 2-day result. Note that the top two are ground truth, and the bottom two are predictions.

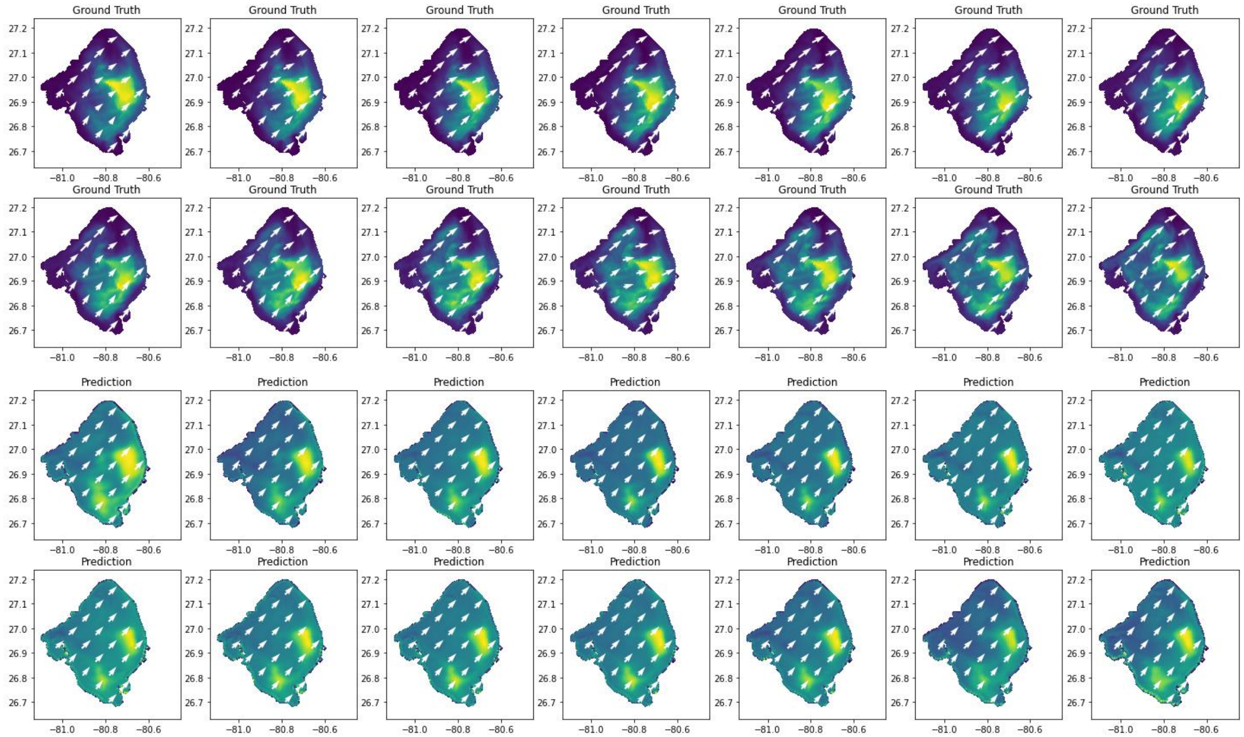

Figure 1F-18: 14-day to 14-day prediction results, where the top row is the 14-day ground truth, and the bot are the 14-day predictions.

CONCLUSIONS & FUTURE WORK

From the single-day prediction result, predictions are very close to the ground truth, demonstrating that the HAB prediction model (i.e., predicting Chl-A over the whole lake) built with ConvLSTM is successful. In rolling prediction, the blur caused by downsampling will be superimposed, and this inaccuracy causes the input picture to become more and more blurry, affecting the prediction of the model. This problem can be solved by restoring the image to a higher resolution after downsampling. Finally, multisource information fusion is a promising method for accurate HAB prediction; however, deep learning methods are sensitive to data which requires that all data sources should be of high quality. Because the algae blooms are seasonal, data should be separated into different seasons and then build disparate models for each season. For the spatial-temporal ConvLSTM machine learning model, a paper is in preparation with plan to submit to the IEEE Journal of Selected Topics in Applied Earth Observations and Remote Sensing in early May 2022.

TASK 2A: ENVIRONMENTAL MONITORING & SAMPLING (TASK LEAD: MCFARLAND)

INTRODUCTION

This task included conventional field measurements for monitoring environmental parameters potentially regulating HABs. Measurements included water column full depth profiles of common water quality parameters, including fluorometric measurements of colored dissolved organic matter (FDOM) by fluorometric proxy), Chlorophyll a, and phycocyanin, with the latter two being common measurements employed to quantify phytoplankton and HABs. Backscatter measurements collected are an improvement over turbidity measurements because they can be directly incorporated into optical algorithms. Direct remote sensing reflectance was determined with a hand-held spectroradiometer to enable ground truthing of satellite remote sensing efforts (**Task 5A-B**) and determine the "true" reflectance signal of lake waters with and without *M. aeruginosa* and other HAB blooms. Water samples were also collected from surface and bottom water for subsequent analyses in **Task 2B-C**. Measurements were scheduled to target off-weeks relative to SFWMD sampling to the greatest extent possible to expand the resolution of the Lake-wide time series.

METHODS

We developed and adhered to a calendar of scheduled monitoring at monthly (between 2/1/2021 and 4/30/2021) and biweekly (between 5/1/2021 and 10/31/2021) intervals to collect environmental data, as well as samples for subsequent analyses as part of other (sub)tasks of the project. Data and samples were collected at Tiers 1, 2, and 3 sites (i.e. L001, L004, LZ40, L005, and L006) for each sampling event, with occasional ad-hoc grabs at other sites of interest. Surface and bottom water samples were collected at each station (10 total samples for each sample event at all 5 stations). Samples were held at ambient temperature in a lake-water filled cooler and returned to the laboratory for same-day algal-related analyses as part of **Task 2B** (note: water samples for water column nutrient measurements reported in **Task 3A**, which were <u>not</u> formally funded by FDEP, were instead kept on ice although not filtered in the field). In-water environmental and optical data at each site was collected and included full profiles of conductivity, temperature, pH, dissolved oxygen, backscatter, Chlorophyll a, phycocyanin, and fluorescent dissolved organic matter (FDOM). Conductivity, temperature, and sensor package depth were measured with a Seabird Scientific SBE 49 FastCAT CTD Sensor calibrated by the manufacturer. pH was measured with an analog Seabird Scientific SBE 27 pH Sensor calibrated regularly using three pH standards (4.01, 7.0, and 10.01 pH) and stored in Orion pH electrode storage solution when not in use (Thermo Fisher Scientific). Dissolved oxygen concentrations were measured with a Seabird Scientific SBE 43 Dissolved Oxygen Sensor calibrated by the manufacturer at the start of the project (as per the QAPP; calibrations drift < 0.5% over 1,000 hours of on-time). Optical backscatter (b_b) at 469 nm was measured with a Seabird Scientific ECO Scattering Sensor calibrated yearly according to Sullivan et al. 2013 (similar manufacturers instructions). Chlorophyll a, phycocyanin, and FDOM concentrations were measured by fluorescence using Seabird Scientific ECO Fluorometers calibrated during the project using a direct corresponding standard, but with quinine sulfate used for FDOM. Above water measurements of hyperspectral remote sensing reflectance (R_{rs}, 400 – 850 nm) were recorded at each survey site with a hand-held field radiometer (Analytical Spectral Devices, Inc.). Measurements were acquired according to NASA standard protocols using a ~10% reflective sprectralon plaque and data was processed according to (Gould et al. 2001). Secchi depth measurements were collected as a measure of water clarity. For all data, processing included translation of archived data to a common format, application of calibrations, correction for environmental characteristics, and averaging of replicates or time series deployment data into appropriate depth bins.

ACTIVITIES SCHEDULED vs. COMPLETED

A total of 15 field surveys were scheduled and conducted as planned, monthly between 2/1/2021 and 4/30/2021 (three total sampling events) and biweekly between 5/1/2021 and 10/31/2021 (12 total sampling events). Five predetermined sites were visited on each survey day. Data for this task was collected in situ and processed within 2 weeks of collection. After review for quality control, erroneous data was removed and data was reprocessed to ensure accuracy of all measured results. Reflectance and pH data were unavailable for some sample events or sites due to instrument malfunction or unsuitable environmental conditions. Backscatter data was outside of quantifiable ranges for some stations due to the extreme turbidity of lake waters.

RESULTS & DISCUSSION

Secchi depths varied somewhat among sites, with site L005 showing substantially greater water clarity during summer months presumably due to the sandy bottom. Water clarity at all sites other than L005 tended to increase in the late summer and fall (Figure 2A-1) with the onset of quiescent conditions. Water temperature did not usually vary substantially with depth but did vary considerably at all sites over time (Figure 2A-2). Temperatures ranged from 22 to 32 °C over the study period. Peak water temperatures were generally recorded in August and early September, after which they began to decline. Conductivity varied seasonally during the study as well (Figure 2A-3). It increased at all sites from February to June, peaking in July and August. Conductivity decreased in the fall, most rapidly at sites L001 and L005. Measured pH profiles were much more variable than other parameters and often varied substantially among sites (Figure 2A-4), with pH most often elevated during documented bloom periods and crashing soon after. Site L001 often had the lowest pH while site L005 was often highest. Some vertical structure was observed in pH but no coherent pattern could be identified. Dissolved oxygen profiles showed high concentrations during the spring and early summer and lower values in late July, August, and September (Figure 2A-5); however, minimal vertical structure was observed, and no truly hypoxic waters were detected (i.e. < 2 mg L^{-1}). Backscatter was highest from February through July (Figure 2A-6), consistent with Secchi-determined water clarity, but decreased at all sites in after September. The lowest backscatter was seen at sites L001 and L005, sites with a mixed mud/sand and sand bottom, respectively. In situ profiles of Chl-a were very noisy during the first part of the study period when turbidity was highest (Figure 2A-7). More accurate assessment of chlorophyll a was possible after July where data show chlorophyll concentrations were generally highest at sites L001 and L005, and lowest at sites LZ40 and L004. We suspect based on Autonomous Surface Vehicle data (**Task 4**) that this variability may be caused by quenching of the fluorescence signal at the elevated turbidities. Interestingly, there was minimal seasonal variation observed in this data. Profiles of FDOM showed little vertical structure and generally decreased in the late summer and fall (potentially a biproduct of the decreased turbidity and thus decreased fluorescence quenching), although concentrations remained high at sites L001 and L005 (Figure 2A-8). Phycocyanin profiles were highest at site L005, especially in one profile from 10/12/21 (Figure 2A-9). There were no clear seasonal trends that could be identified in these data, but ongoing data interpretation will integrate this fluorometric data with **Task 2B** phytoplankton community structure information. Remote sensing reflectance spectra was variable among sites and over time in magnitude and spectral shape (Figure 2A-10) and on its own is not generally useful; it requires additional processing as performed in **Task 5**.

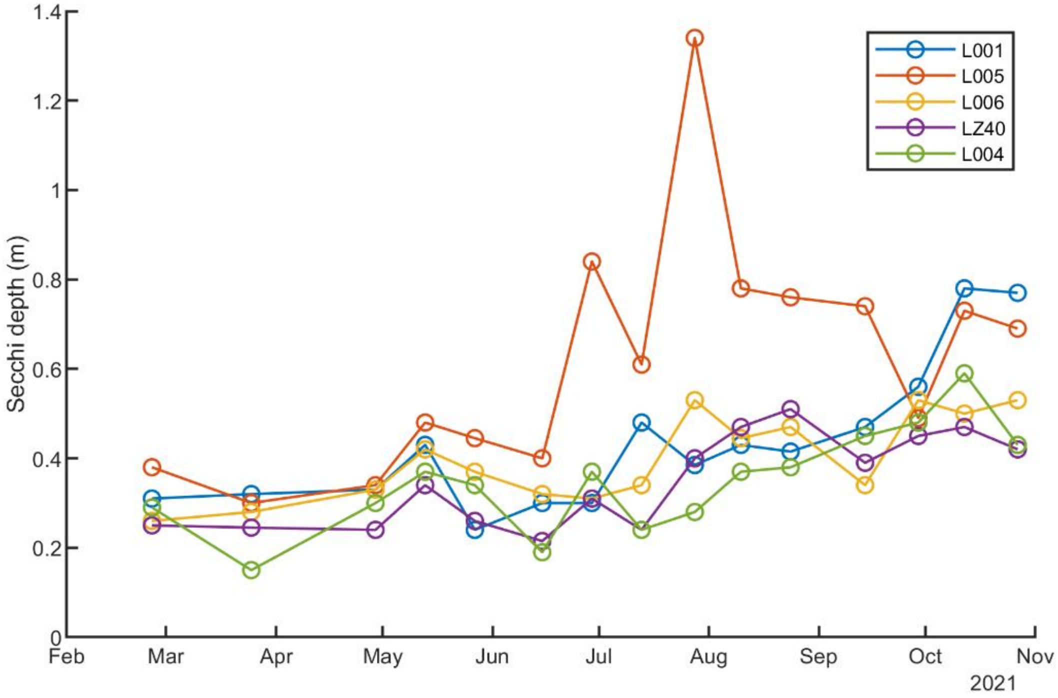

Figure 2A-1: Secchi depth at all stations and dates.

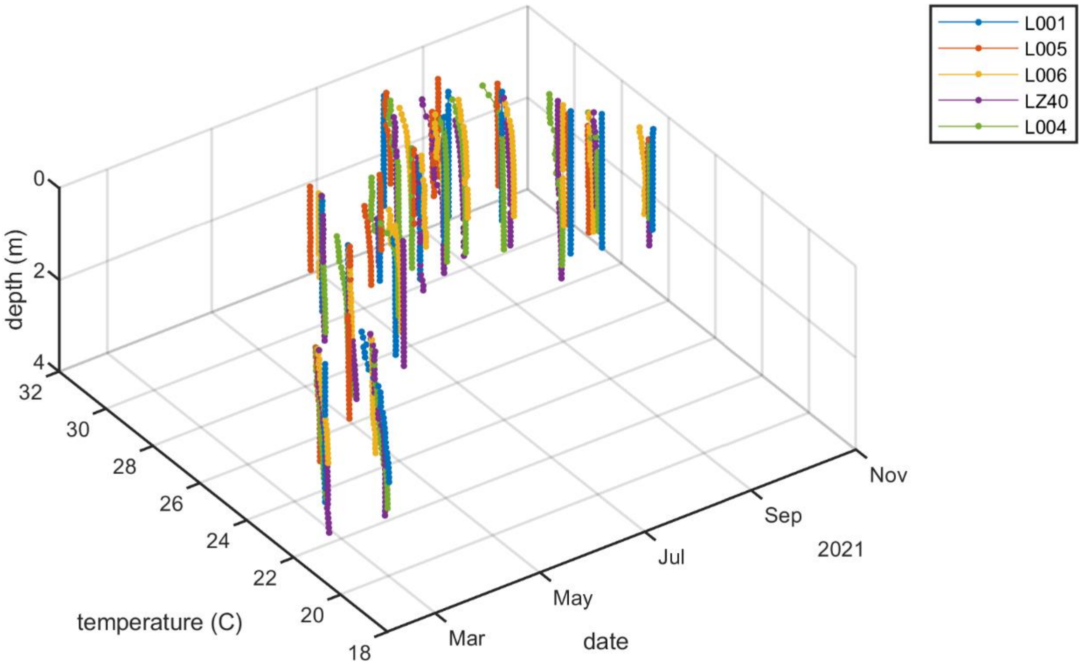

Figure 2A-2: Temperature profiles for all stations on all dates.

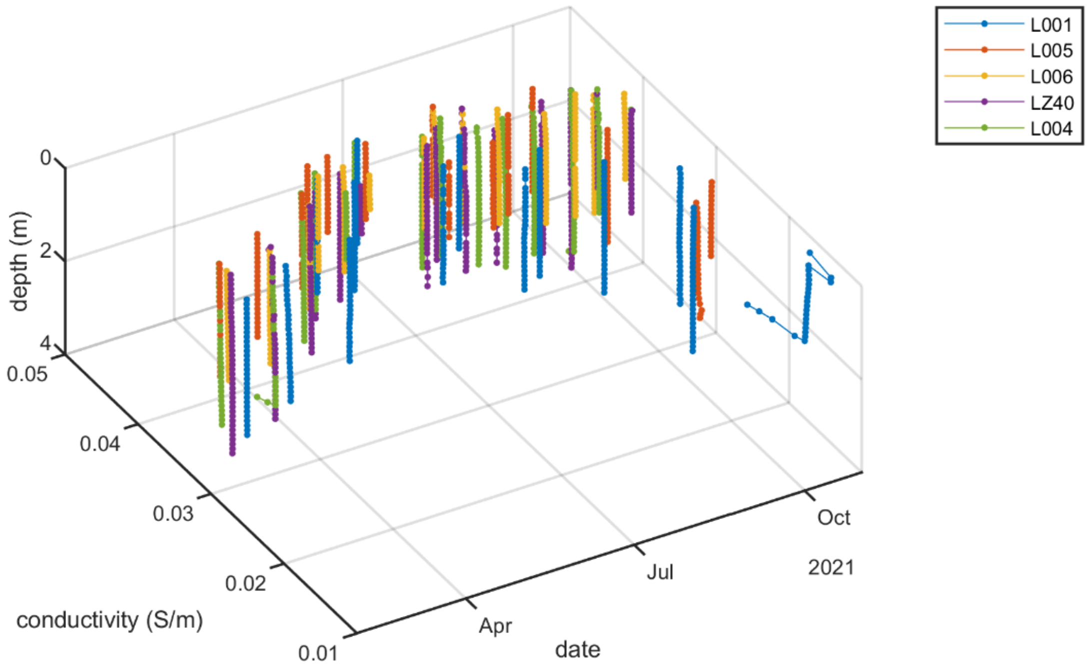

Figure 2A-3: Conductivity profiles for all stations on all dates.

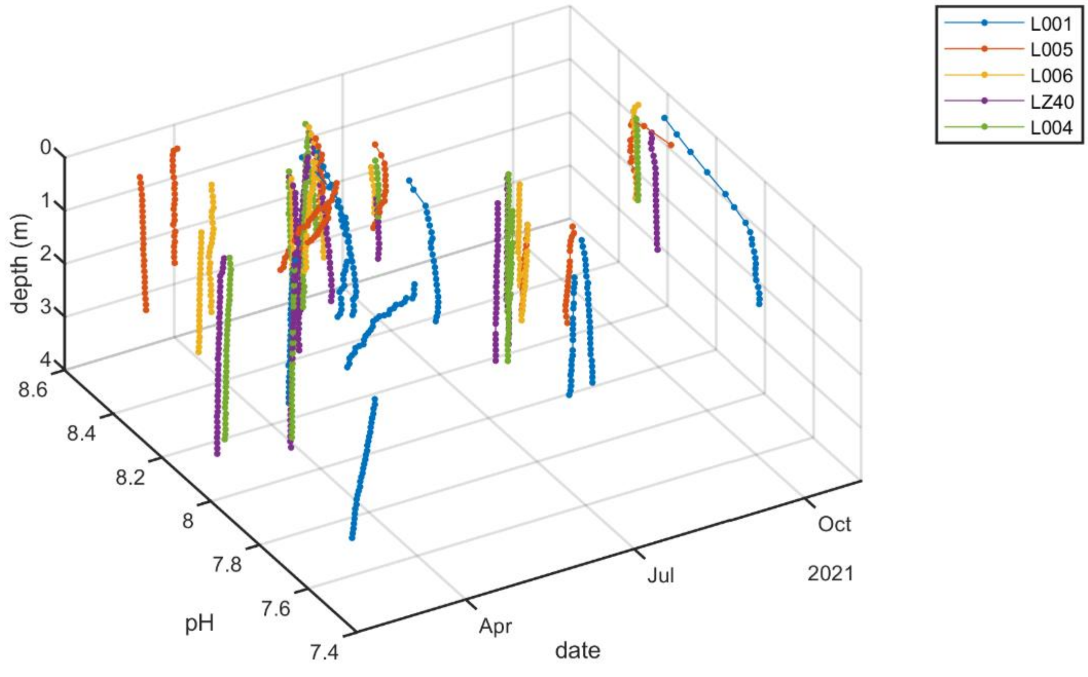

Figure 2A-4: pH profiles for all dates.

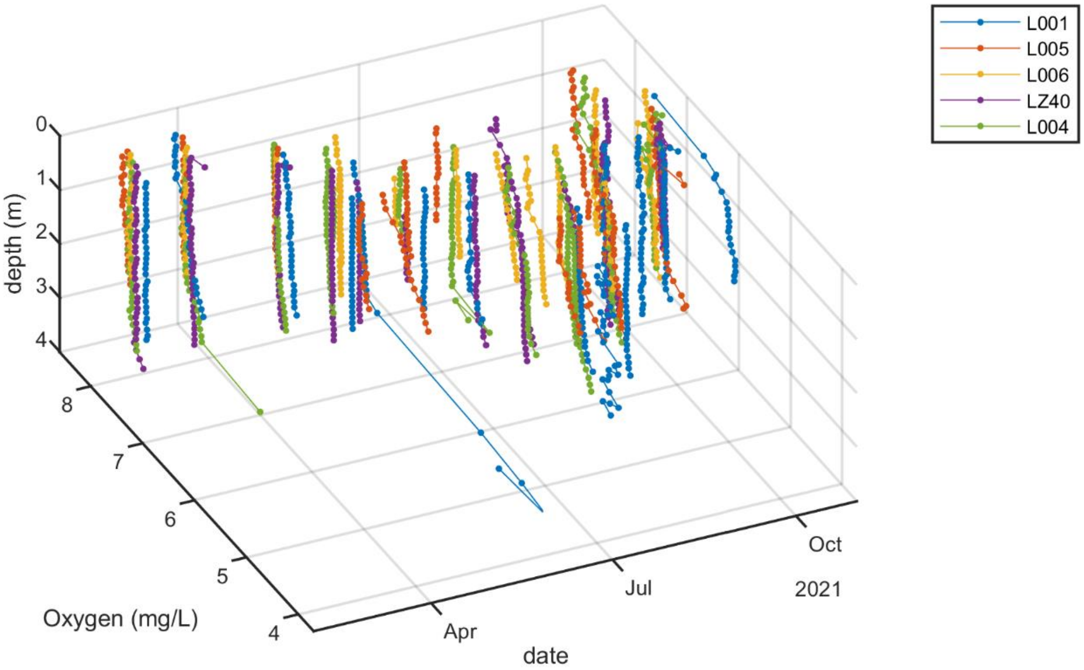

Figure 2A-5: Oxygen profiles for all stations on all dates.

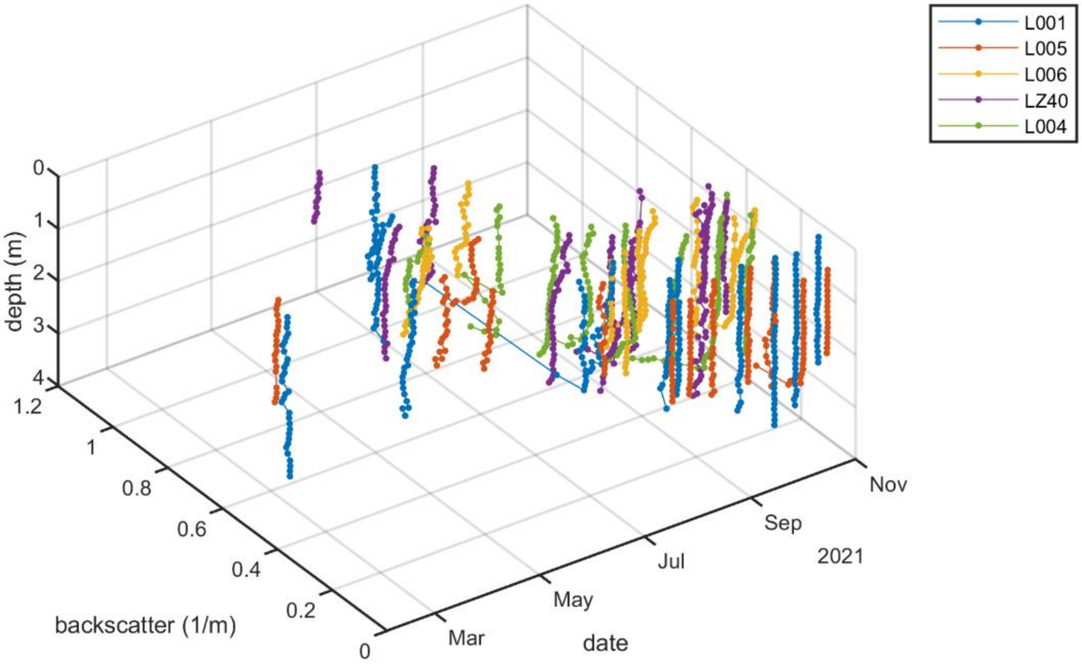

Figure 2A-6: Backscatter (469 nm) profiles for all stations on all dates. Missing data is due to post-processing removal of sensor-saturated data.

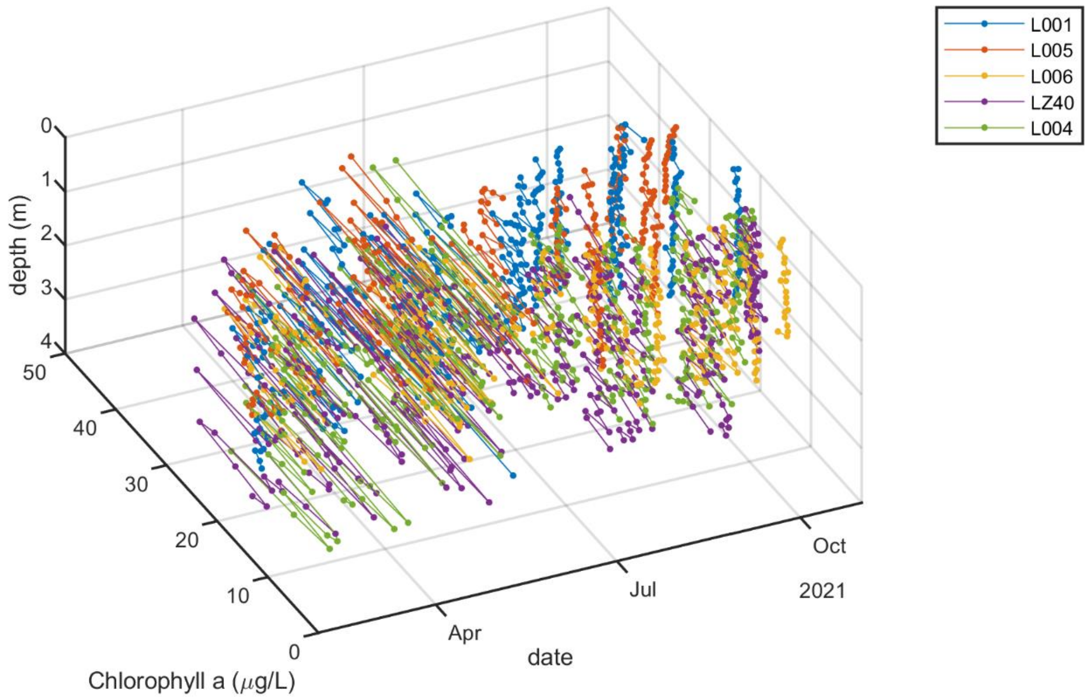

Figure 2A-7: In situ chl-a profiles for all stations on all dates.

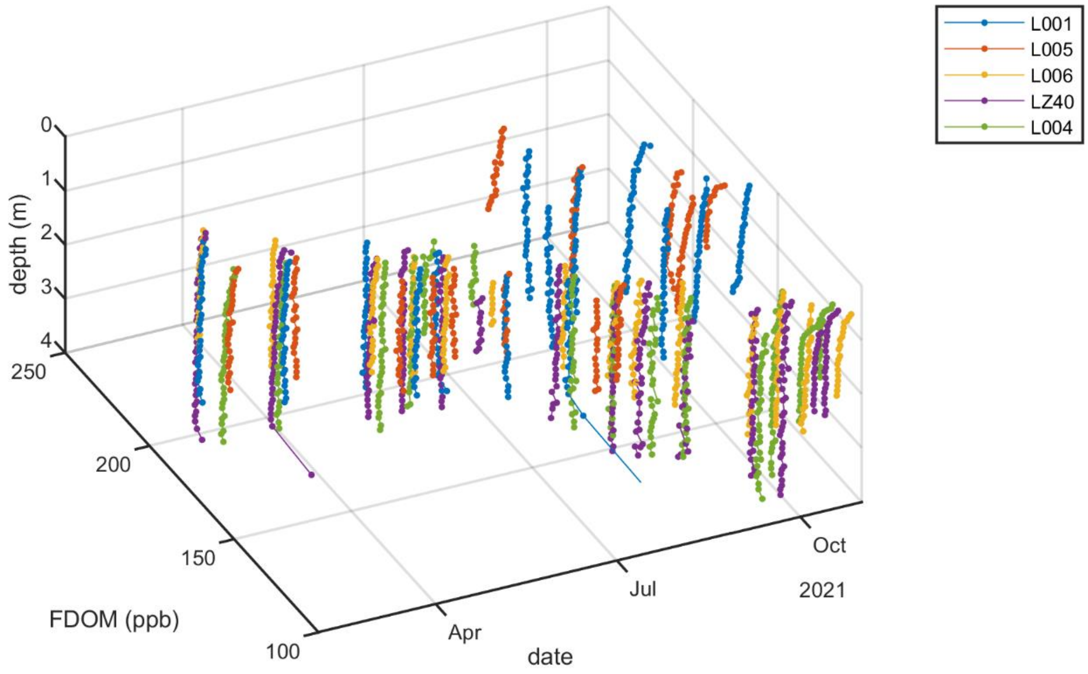

Figure 2A-8: Profiles of fluorescent dissolved organic matter (FDOM) for all stations and dates.

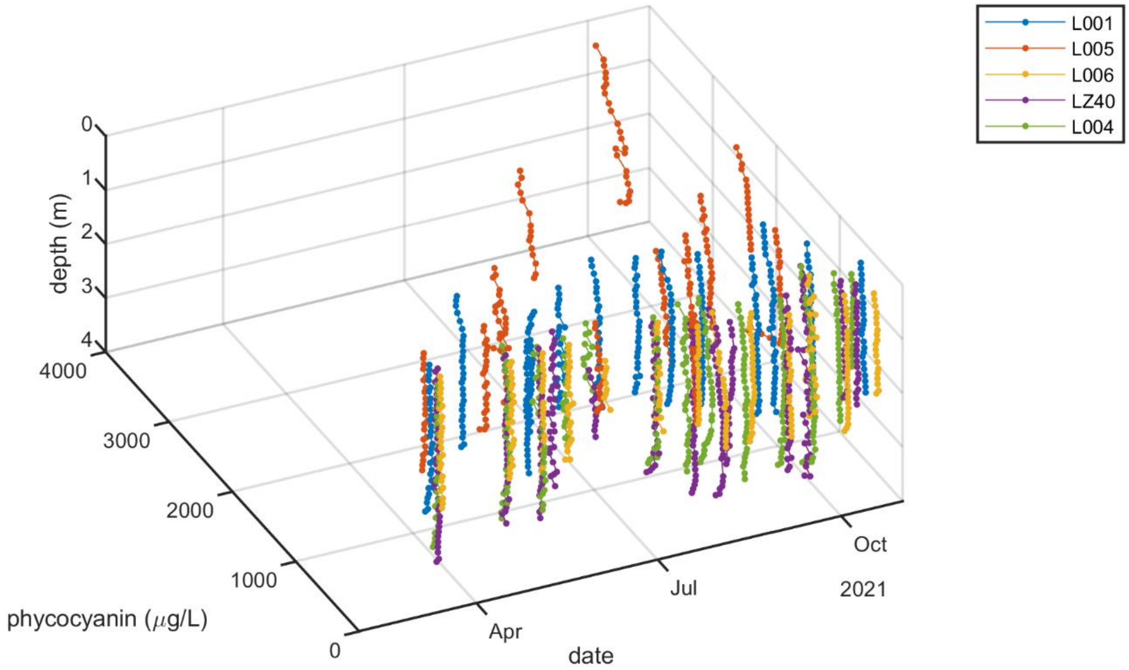

Figure 2A-9: In situ phycocyanin profiles for all stations on all dates.

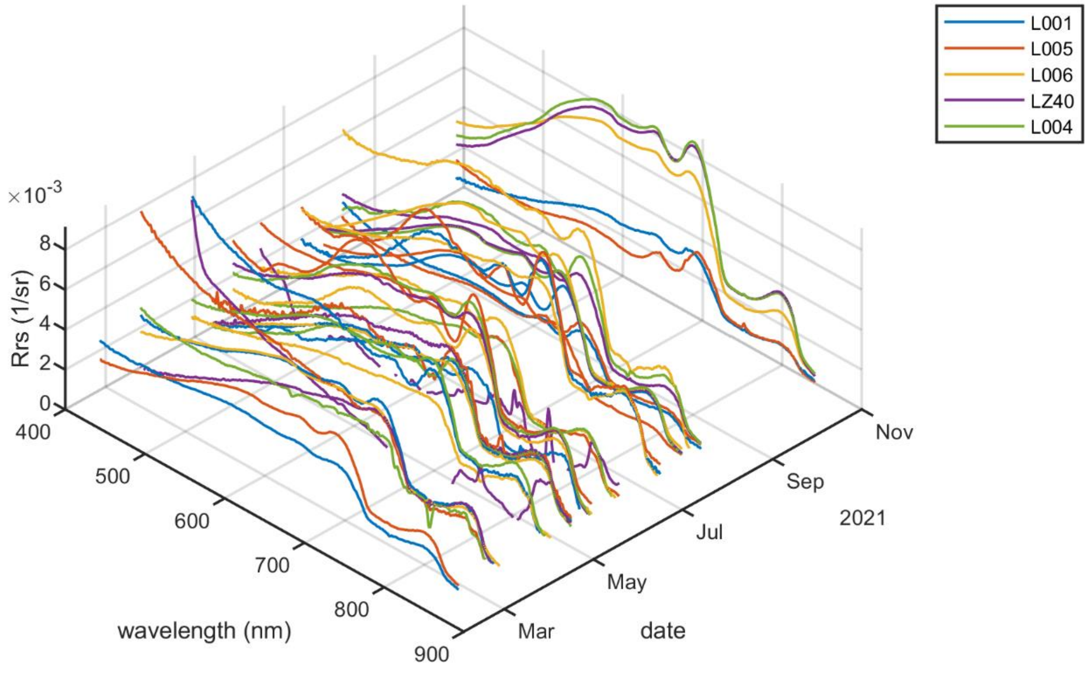

Figure 2A-10: Remote sensing reflectance (Rrs) spectra measured at each site on each date.

CONCLUSIONS & FUTURE WORK

Some variation over horizontal spatial and temporal scales was evident in all data collected. Vertical structure in measured parameters was usually not observed throughout the study period, except for some parameters on some rare occasions. However, the instrument package used for in situ measurements could not sample the top ~0.5 m of the water column. It was in this upper surface layer where toxic algae like *M. aeruginosa* were often most abundant due to the positive buoyancy of their cells and colonies. The abundance and characteristics of these algae, therefore, should be reflected more accurately in the sample analyses of **Tasks 2B-C**. Seasonal variation was substantial in many measured parameters including FDOM, R_{rs}, backscatter, oxygen, conductivity, temperature, and Secchi depth. Consistent spatial variation among sites was also evident for phycocyanin, FDOM, chlorophyll a, backscatter, pH, conductivity, and Secchi depth. These measured parameters show a broad overview of lake characteristics that are associated with harmful algal bloom distributions and abundances, and are critical for ongoing data interpretation of other task efforts. Sites L001 and L005 in the north and west appear to be environmentally distinct from sites LZ40, L004, and L006 in the central, eastern, and southern portions of the lake.

TASK 2B: HAB TOXIN IDENTIFICATION & PHYSIOLOGY (TASK LEAD: MCFARLAND)

INTRODUCTION

A set of laboratory analyses was conducted on samples collected during **Task 2A** to identify algal taxa present, measure total chlorophyll a concentrations, measure concentrations of microcystin toxins, quantify cell concentrations for several groups of algae and *M. aeruginosa* by flow cytometry, determine ratios of dead to live cells of *M. aeruginosa*, and measure the variable fluorescence of alga to determine their photophysiological state. These analyses provided a comprehensive and detailed picture of algal abundance, composition, and health throughout the lake over the full course of the annual bloom cycle.

METHODS

Field collected surface and bottom water samples were maintained in a cooler at ambient water temperature for up to 6 hours until return to the lab for analyses. Phytoplankton were identified to the lowest taxonomic classification possible based on size and morphology using a Nikon Eclipse Ni upright compound microscope. Immediately after collection, one mL subsamples containing live cells were placed into a Sedgewick-Rafter chamber and observed at 100X magnification using phase contrast illumination. Presence or absence was determined by scanning through 500 µL of the sample. Cell concentrations of select phytoplankton groups were determined with a BD Accuri C6 flow cytometer equipped with blue (488 nm) and red (640 nm) excitation lasers and detectors for forward scatter, side scatter, green fluorescence (533nm/30nm bandwith), chlorophyll fluorescence (>670 nm), and phycocyanin fluorescence (675nm/25 nm bandwith) as described in (Marie et al. 2005). For each sample, up to 60,000 cells or 200 µL of sample were analyzed. Prior to analysis, subsamples were briefly sonicated for 5 seconds to disaggregate colonies to allow for accurate enumeration. This procedure was tested with *M. aeruginosa* cultures before analysis of field samples to ensure minimal cell loss and effective disaggregation. Algal cells measured by flow cytometry were classified into 4 identifiable groups including nanoeukaryotes, microeukaryotes, picocyanobacteria, and *Microcystis* spp. Chlorophyll a concentrations were measured by fluorescence using a Turner model 10AU fluorometer according to EPA method 445 (Arar and Collins, 1997). Depending on algal concentrations, 5-15 mL of sample was filtered using GF/F filters (Whatman) and extracted in 90% acetone overnight before analysis. Variable fluorescence of the algal community was measured with a Satlantic FIRe fluorometer (Gorbunov et al. 2020). The instrument provided the ratio of variable to maximum fluorescence (Fv/Fm), a measure of the photosynthetic capacity of cells. The ratio of dead to live *M. aeruginosa* cells was determined for cells analyzed by flow cytometry after staining with SYTOX green. This membrane impermeant nucleic acid probe becomes fluorescent upon binding to the DNA of dead cells with compromised membranes. Cells with enhanced green fluorescence, therefore, were identified as dead and compared to cells without green fluorescence to determine the ratio of dead or dying cells to live cells within the population (Bouchard and Purdie 2011, Mikula et al. 2012, Chapman et al. 2016). Finally, subsamples were stored frozen at -20 °C and later analyzed by Enzyme Linked Immunosorbent Assay (ELISA) to determine concentrations of microcystin toxins. ELISA kits from Eurofins Abraxis in a 96 well plate format (P/N 520011SAES) were used along with a plate reading spectrophotometer according to the manufacturer's instructions. Samples were subjected to 3 freeze/thaw cycles prior to analysis to release intracellular microcystins into solution. Samples that were initially too concentrated for accurate determination of toxin concentrations were diluted and reran until results were within a quantifiable range.

ACTIVITIES SCHEDULED vs. COMPLETED

All scheduled water sample collections and subsequent laboratory analyses have been completed. A total of 150 surface or bottom samples from 5 sites over 15 sampling events were acquired and analyzed. Analysis of dead vs. live *M. aeruginosa* cells could only be performed when sufficient cell concentrations were present in collected samples. This occurred for 59 of the 150 samples collected. One Chl-a measurement from 4/29/2021 at L001 was lost due to equipment malfunction.

RESULTS

The number of taxa observed in collected samples from all sites generally increased from February to October (Figure 2B-1). The full community composition is archived in the HALO database. *M. aeruginosa* was observed in 51 of 75 surface samples and 23 of 75 bottom water samples. In addition, *M. aeruginosa* was observed at one or more sites on all collection dates except for the February sampling event. Other potentially toxic cyanobacteria commonly observed included *Dolichspermum* sp. and *Cylindrospermopsis* sp. Cell concentrations determined by flow cytometry showed seasonal variation in the abundance of nanoeukaryotes and picocyanobacteria, with peak abundances in late June or July (Figure 2B-2). Picocyanobacteria were most abundant but likely not the dominant biomass due to their small cell size. Microeukaryotes and *M. aeruginosa* showed less seasonal variation and were absent or present only at relatively low concentrations before late April. Chl-a concentrations were often higher in surface samples except for site L001 (Figure 2B-3). Concentrations varied substantially over time and among sites with no clear seasonal pattern except for an increase in winter and early spring. The Fv/Fm ratio showed some large and sudden variations in the photosynthetic capacity of cells as well as longer term site specific seasonal trends (Figure 2B-4). Sites L001 and L006 showed peak Fv/Fm in late June and early July while sites LZ40 and L004 showed a possible increase in Fv/Fm over time. Site L005, however, showed a general decrease in Fv/Fm with time and a sudden dip during late July and early August. The ratio of dead to live cells could not be determined for all samples so trends for individual sites were difficult to determine (Figure 2B-5). However, a general decrease in the ratio over time was observed with lower values after July. Microcystin concentrations were highly variable over time especially at sites LZ40 and L004 where the highest concentrations were measured (Figure 2B-6). Concentrations were also generally higher in surface water samples at sites L006, L004, and LZ40. A less drastic difference between surface and bottom samples was seen at sites L001 and L005. Several measured microcystin concentrations were more than 100 ppb and the highest measured concentration was more than 300 ppb at LZ40 in July.

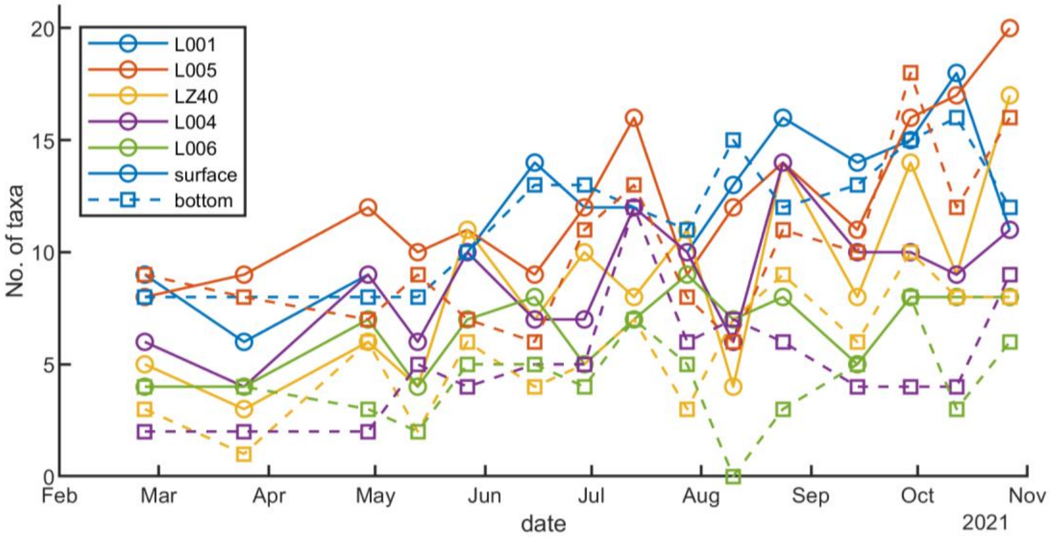

Figure 2B-1: Number of identifiable phytoplankton taxa in all collected samples.

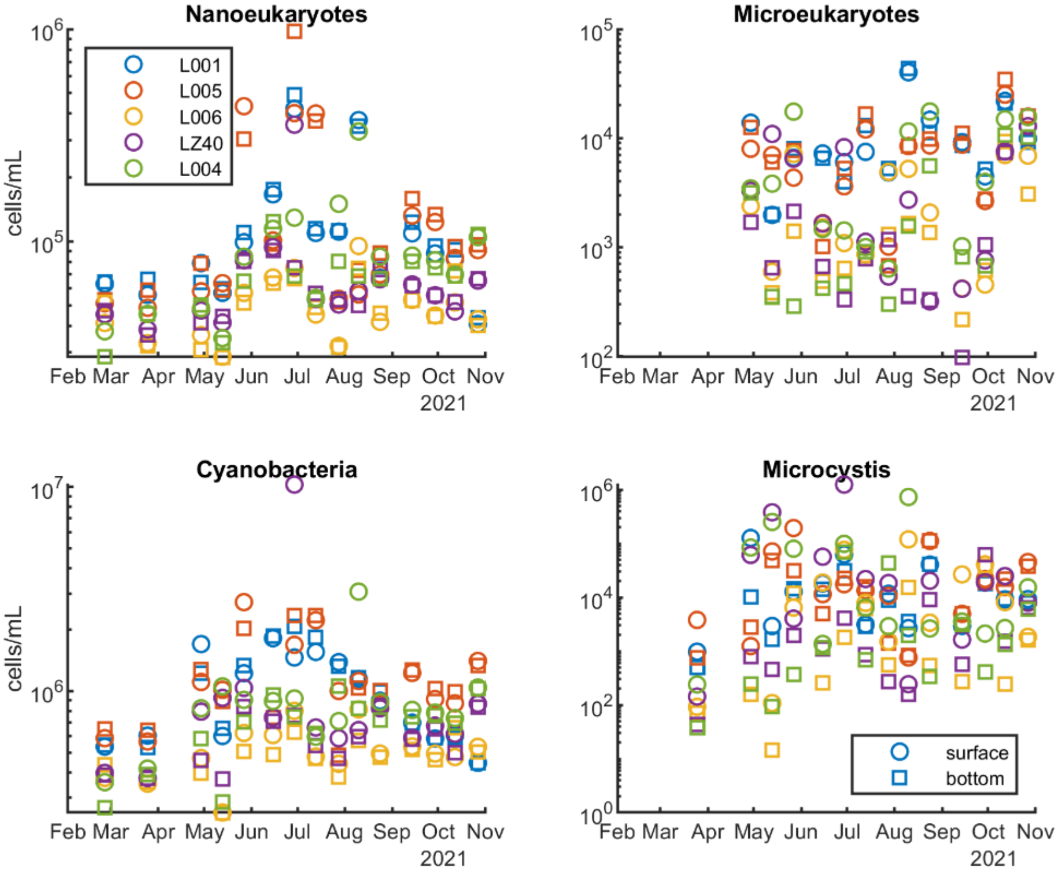

Figure 2B-2: Cell concentrations for 4 different classes of phytoplankton in all samples.

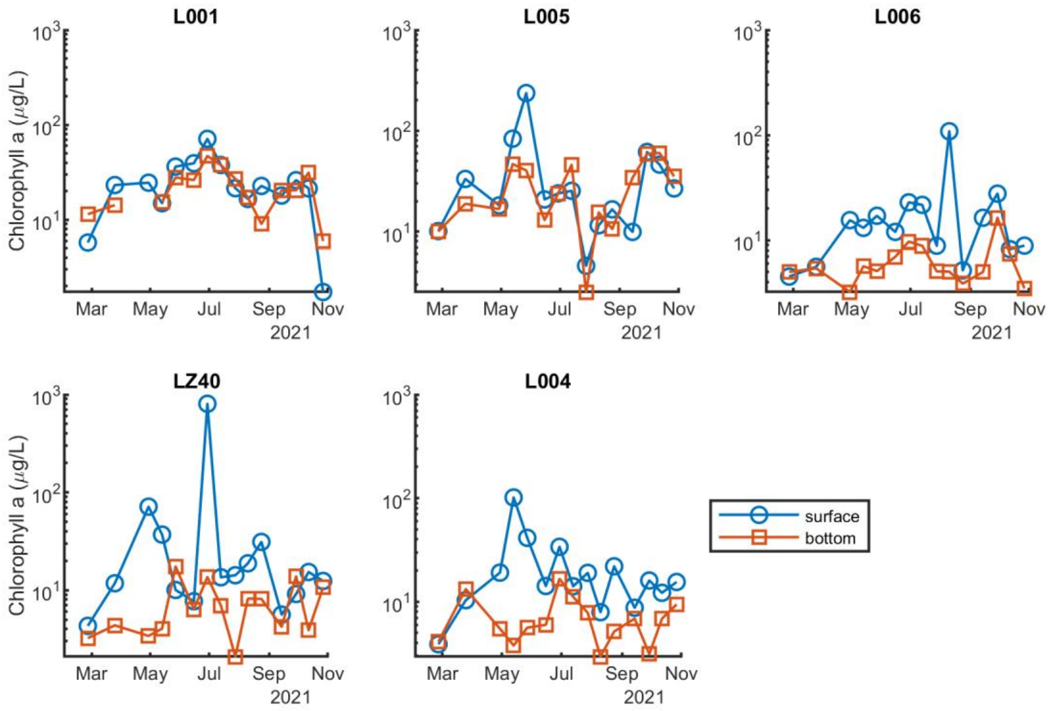

Figure 2B-3: Surface and bottom chl-a a concentrations for all sites and sample dates.

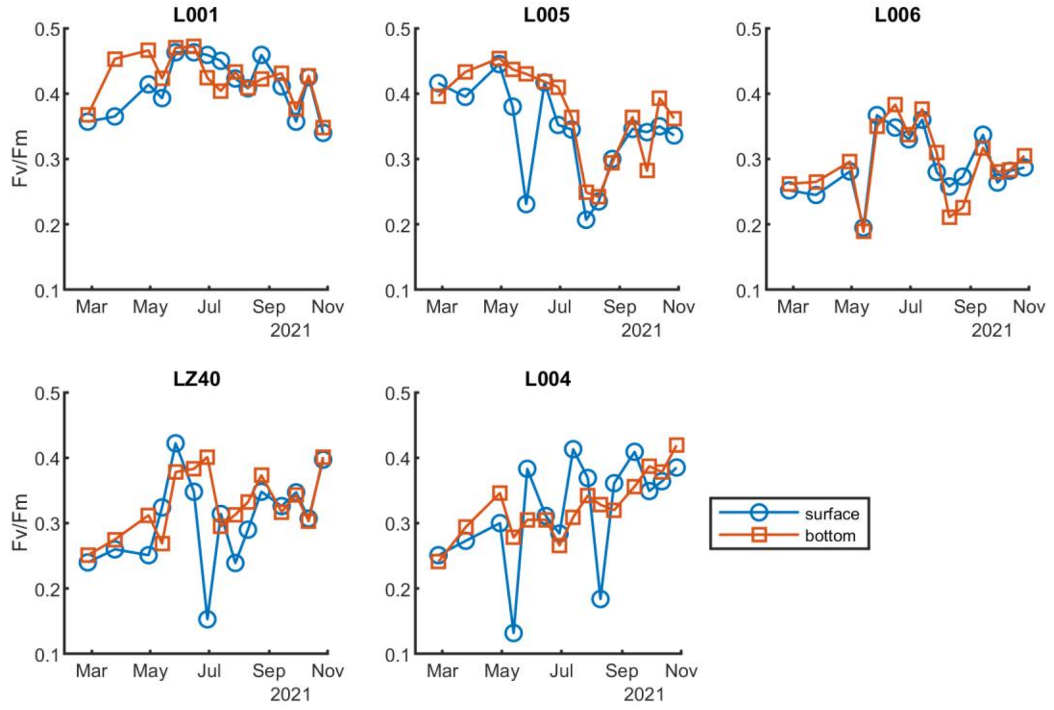

Figure 2B-4: Ratio of variable to maximum fluorescence in all collected samples at each site.

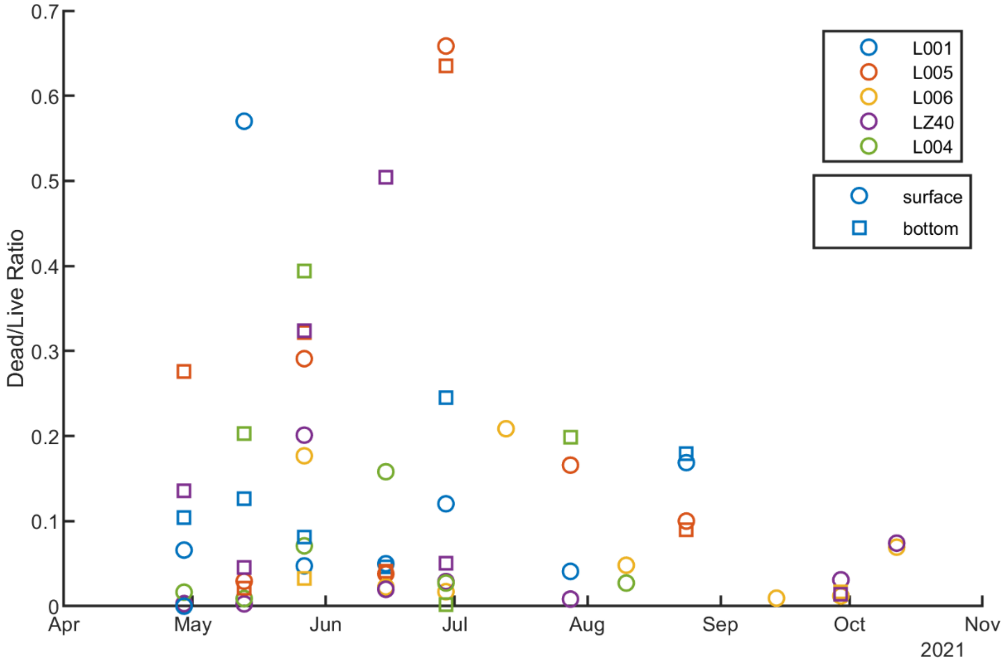

Figure 2B-5: Ratio of dead to live cells determined for all samples with sufficient cell densities.

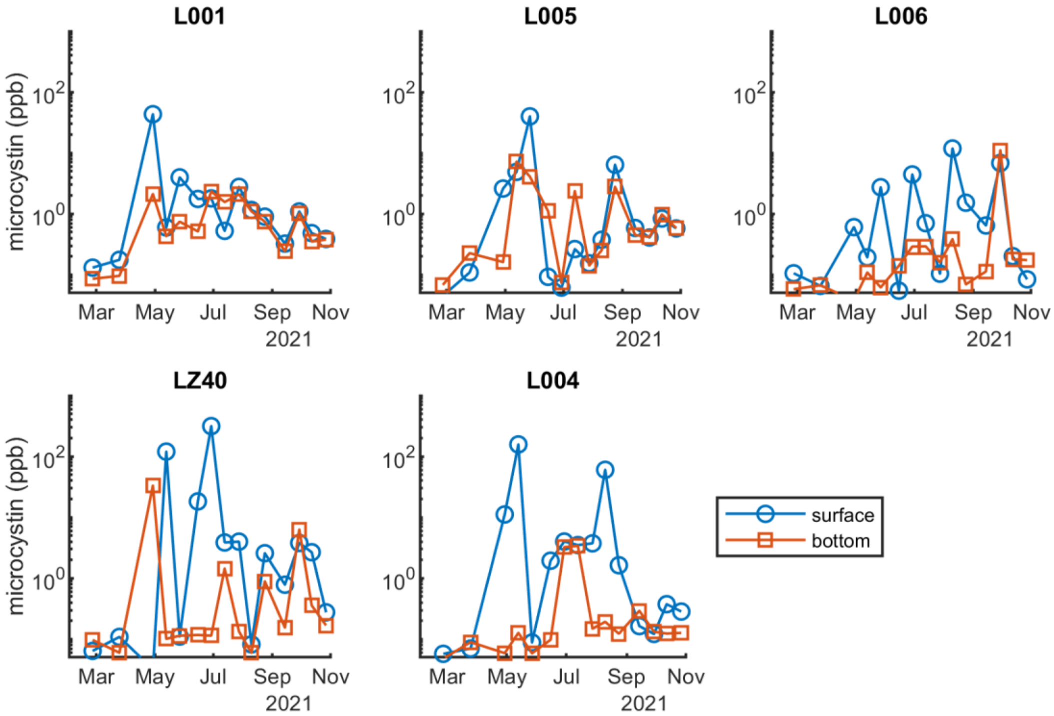

Figure 2B-6: Concentration of microcystins in all samples. Vertical axes begin at the lower limit of quantification (0.05 ppb).

DISCUSSION

Variation in phytoplankton composition during the study showed both expected and unexpected trends. Diversity increased in the fall and cell concentrations for *M. aeruginosa*, nanoeukaryotes, and picocyanobacteria were highest during summer as was expected. However, *M. aeruginosa* concentrations varied substantially among locations and over time, even during peak bloom months suggesting that its abundance and distribution throughout the lake is patchy. Higher spatial and temporal resolution observations would assist in identification of the environmental gradients that determine cell concentrations, as well as ongoing comparison with other task data. Total algal biomass as represented by chl-a concentrations was not always an accurate reflection of *M. aeruginosa* abundance or microcystin concentrations. Microcystin was generally found at low to moderate concentrations with some extremely high concentrations observed at specific stations. This variation is another indication of the extreme patchiness of *M. aeruginosa* blooms in Lake Okeechobee. Unexpectedly, the ratio of dead to live cells decreased in late summer and fall as *M. aeruginosa* cell concentrations declined somewhat. This suggests that although cells were decreasing in number, those that remained were healthy and viable. This information may be key when combined with nutrient and light availability data. Photophysiology (i.e. Fv/Fm) of the phytoplankton showed inconsistent trends over time at the different sites and substantial variability, especially in surface waters. Higher variability of Fv/Fm in surface water samples is likely attributable to a more varied light exposure history with variations in cloud cover, and possible local depletion of nutrients in near surface waters with higher cell concentrations.

TASK 2C: HAB METABOLIC RATES (TASK LEAD: MCFARLAND)

INTRODUCTION

Live *M. aeruginosa* cells were analyzed to assess their relative metabolic rate immediately upon return to the lab after sample collection. We used fluorescein diacetate (FDA) as an indicator of metabolic activity (Geary et al. 1998) and analyzed its fluorescence within cells by flow cytometry (Xiao et al. 2011, Mikula et al. 2012). This allowed for targeting of *M. aeruginosa* populations among the broader phytoplankton community. FDA is taken up by cells and broken down into its chemical constituents, becoming fluorescent in the process. After a fixed incubation period, cells capable of rapidly consuming and digesting the FDA display a brighter green fluorescence relative to those whose metabolic rate is slower.

METHODS

Initial laboratory experiments with uni-algal cultures of *M. aeruginosa* were used to determine the optimal FDA incubation time. We measured FDA fluorescence after incubations of 2 to 48 minutes at several concentrations (Figure 2C-1). Cultures were previously isolated from Lake Okeechobee and maintained in BG11 medium at 25 ˚C with a 12:12 hour light:dark cycle. An optimal incubation time of 18 minutes at an FDA concentration of 30 mg/L was selected and used for analysis of all field samples. Field collected samples were analyzed immediately upon return to the laboratory within 6 hours of collection.

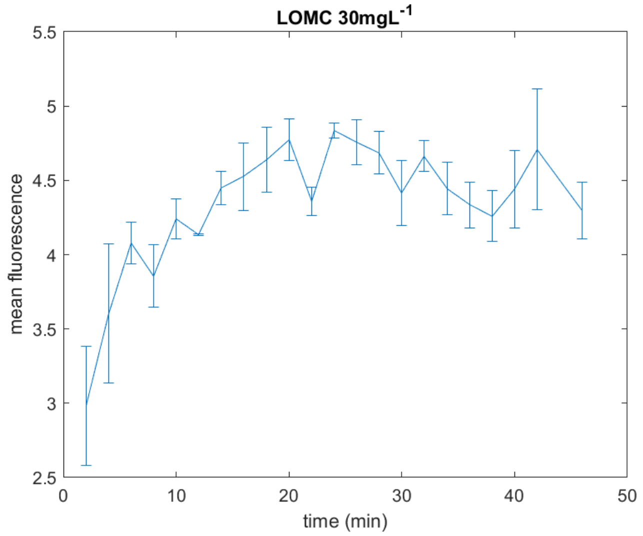

Figure 2C-1: FDA fluorescence of M. aeruginosa culture after various incubation times.

ACTIVITIES SCHEDULED vs. COMPLETED

Metabolic rate analyses were scheduled to be conducted on surface and bottom samples from all five sites a total of 4 times in February, May, July, and October for a total of 40 samples. Analyses were conducted in excess of contractual obligations for a total of 60 samples collected on 6 sample dates in February, May, June, July, August, and September. For most analyses, however, there were insufficient cell concentrations to produce accurate results and the total number of samples “successfully” analyzed was 27.

RESULTS

Metabolic rates in surface samples increased at all sites except L006 from spring to summer (Figure 2C-2). Sites L001, L005, and LZ40 subsequently decreased in late August or September. The range of variation seen over time at each site was similar.

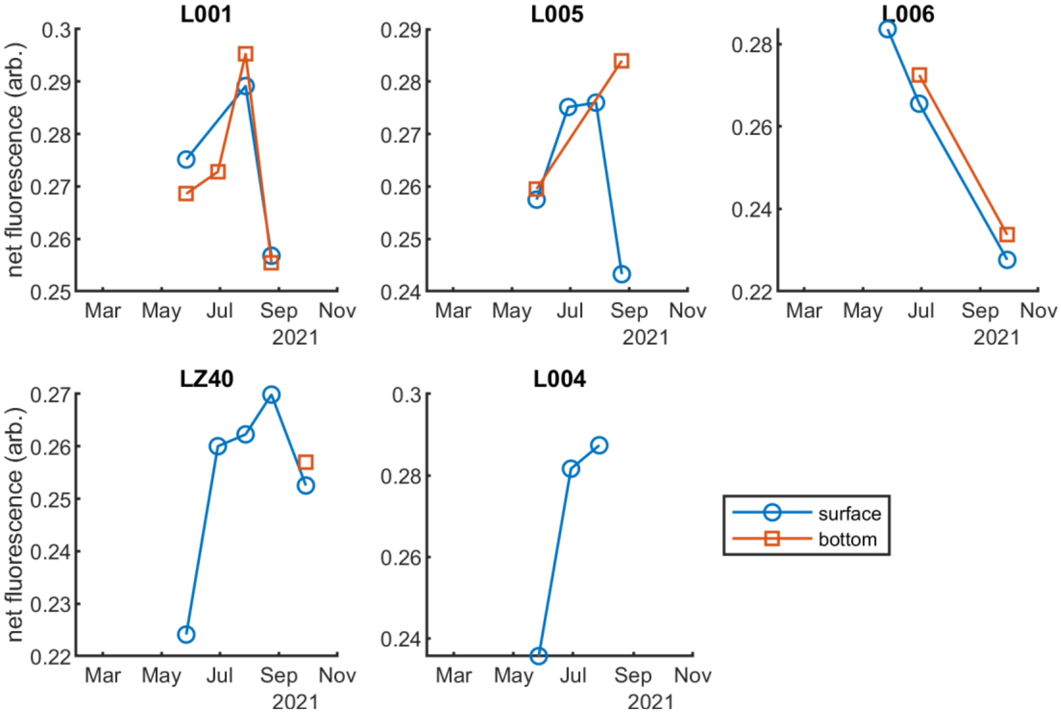

Figure 2C-2: Metabolic rates determined by net FDA fluorescence, normalized to cell density, for all successfully analyzed samples.

CONCLUSIONS & FUTURE WORK

Patterns of metabolic rate in *M. aeruginosa* over time suggest a coherent seasonal variation with peak rates in the late summer followed by a decline in early fall. Surface and bottom samples were often similar except for one date at L005. When compared with the cell concentrations of *M. aeruginosa* (**Task 2B**), these observations suggest seasonal patterns that are independent of total abundance which peaks much earlier in the year. This data may be indicative of shift from autotrophy to chemotrophy as nutrients essential for photosynthesis decline in surface waters; however, no field studies have been conducted to provide a context for this data. This data may become more informative upon integration into the greater dataset that considers nutrients and light availability.

TASK 2D: AUTONOMOUS HAB MONITORING (TASK LEAD: NAYAK)

INTRODUCTION

This task focused on testing two new technologies for the suitability in detecting M. aeruginosa and perhaps other HABs/biological species in the turbid Lake Okeechobee environment. First, the AUTOHOLO is a submersible holographic imaging system, which is designed to image aquatic particles and plankton in situ (Figure 2D-1). The recording medium is a high resolution, 4920 x 3280 (16 MP) Imperx camera, acquiring data at a frame rate of up to 3.2 Hz. Processing of the holograms enable characterization of particles/plankton within the size range 20 µm – 1.5 cm can be imaged using the system, providing a baseline of the local plankton community composition, which can help supplement direct sampling efforts. An added advantage of the system design is the adjustable 12 cm sampling length between the two windows, which corresponds to a sampling volume of 71.4 mL per hologram. This is an order of magnitude higher than the volume sampled per hologram in commercially available holographic imagers. The large sample volume also allows for studying particles, bubbles and droplets in their natural environment, while minimizing breakage/dispersal. Data is stored on-board using 4 TB solid state hard drives and retrieved and processed after each deployment. As part of this work, two main goals were considered. The main point of interest was whether the system would be able to function in the high turbidity environment of Lake Okeechobee. This included laboratory and field testing of the instrument in diverse environments on both coasts of Florida (Indian River Lagoon and coastal Gulf of Mexico) as well as the actual field deployment in Lake Okeechobee.

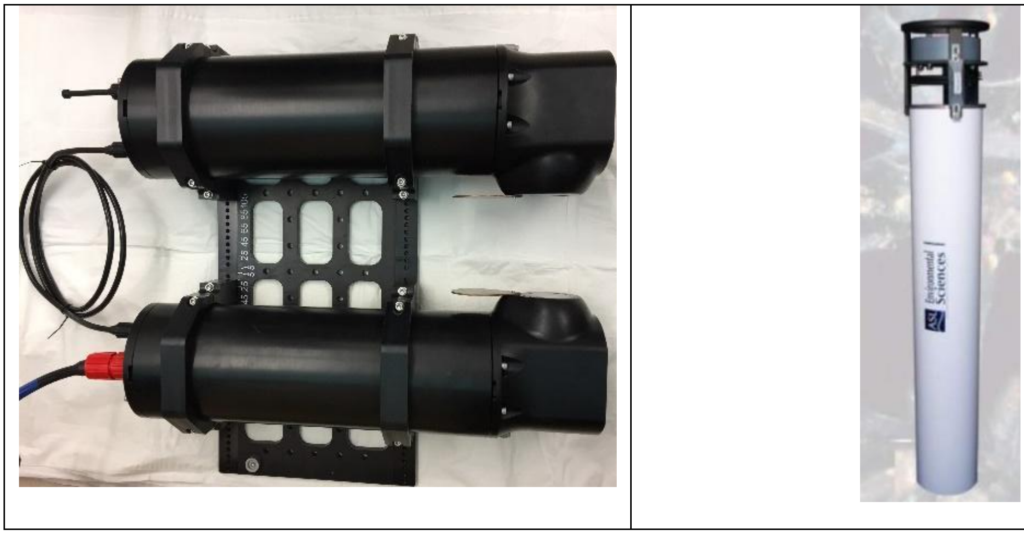

Figure 2D-1: Left: The AUTOHOLO submersible holographic imaging system; Right: the Acoustic Zooplankton Fish Profiler.

Next, the Acoustic Zooplankton Fish Profiler (AZFP; ASL Environmental Sciences; Figure 2D-1) is a monostatic, active, scientific echosounder system. The AZFP transmits a short pulse of high-frequency sound and then records the echoes. Sound is backscattered from targets such as plankton. This backscatter is influenced by many factors, including the size, orientation, and quantity of organisms present within the acoustic beam. It is often possible to discriminate between different species based on the way that the targets scatter sound at different frequencies. The AZFP supports up to four individual channels, and in this case, the instrument had center frequencies at 125 kHz, 200 kHz, 455 kHz, and 769 kHz. Since each AZFP channel is calibrated, the measured backscatter is known on an absolute scale. This facilitates comparison against theoretical backscattering models for the organisms, where such models exist. In the case of *M. aeruginosa*, there is presently a paucity of acoustical data measured from these organisms in their natural environment. The goal is to collect as much data as possible for future purposes as well as analyze some data to get preliminary results on the feasibility of this method for HAB detection. It should be noted that this technology implemented for use in detecting HABs is a very novel application and to our knowledge this is the first of its kind.

AUTOHOLO METHODS, ACTIVITIES CONDUCTED, AND RESULTS

Indian River Lagoon testing: Field testing of the AUTOHOLO was conducted in the Indian River Lagoon (IRL) on 12/8/20. We sampled at three different stations, representative of different optical (turbid) conditions. Three different path lengths corresponding to 2 cm, 4 cm and 6 cm were used at each location and together, a set of nine different batches of holograms were recorded for analysis over these different parameters. Deployment details are provided in Table 2D-1 and photos from the actual deployment are provided in Figure 2D-2. Between different samples, over 1500 good quality holograms were recorded (full processing still ongoing). For this particular deployment, the AUTOHOLO was configured with a 1 cm path length and a 10X objective lens to obtain a resolution of 0.45 µm/pixel. As mentioned previously, this optical configuration is variable and a lens-less configuration was used at Lake Okeechobee.

Figure 2D-2: (a) The AUTOHOLO being deployed at one of the stations during the 12/8/20 field effort. (b) Image showing the qualitative difference in turbidity between two distinct water masses during the sampling event.

Example raw holograms from each of the 9 different samples are shown in Figure 2D-3. The best quality holograms were recorded at station 1, with negligible variations as the path length was increased from 2 cm to 4 cm to 6 cm. At stations 2 and 3, the hologram quality was acceptable at the 2 cm path length, despite the increased turbidity. However, by the time the sampling path length was increased to 6 cm, the quality of the holograms was degraded in either case. Thus, maintaining a 2 cm (or lesser) path length seems to provide acceptable hologram quality in turbidities ranging to at least 5 *1/m*. Lake Okeechobee on the whole exhibits higher turbidity which led us to also perform additional tests in the lab (reported later).

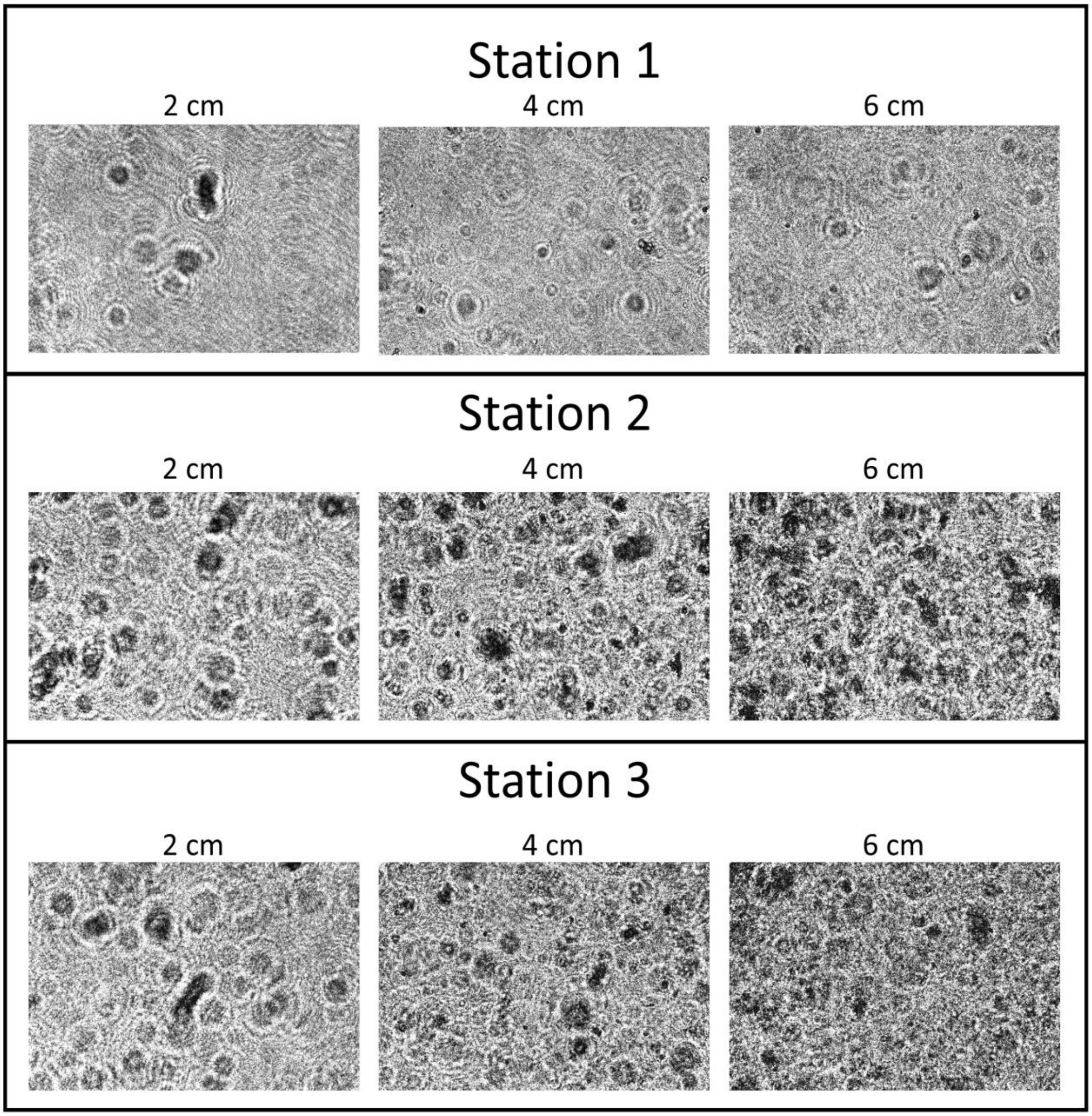

Figure 2D-3: Sample raw holograms recorded during the 12/8/20 sampling event, showing variations at stations based on turbidity and path length. Station 1 recorded the overall lowest attenuation reading (a = 2.4 1/m), while the readings were higher in stations 2 and 3 (4 1/m and 4.9 1/m respectively).

Table 2D-1: Deployment details for the southern IRL field sampling on 12/8/20. At each station, three different path lengths (distance between windows) were used to record data.

Station Name	Latitude	Longitude	Time (EST)	# images		
				2cm	4cm	6cm
Station1	27.51874	-80.33879	10:30	422	408	431
Station2	27.46728	-80.31471	11:48	409	406	401
Station3	27.47250	-80.29040	13:49	541	419	406

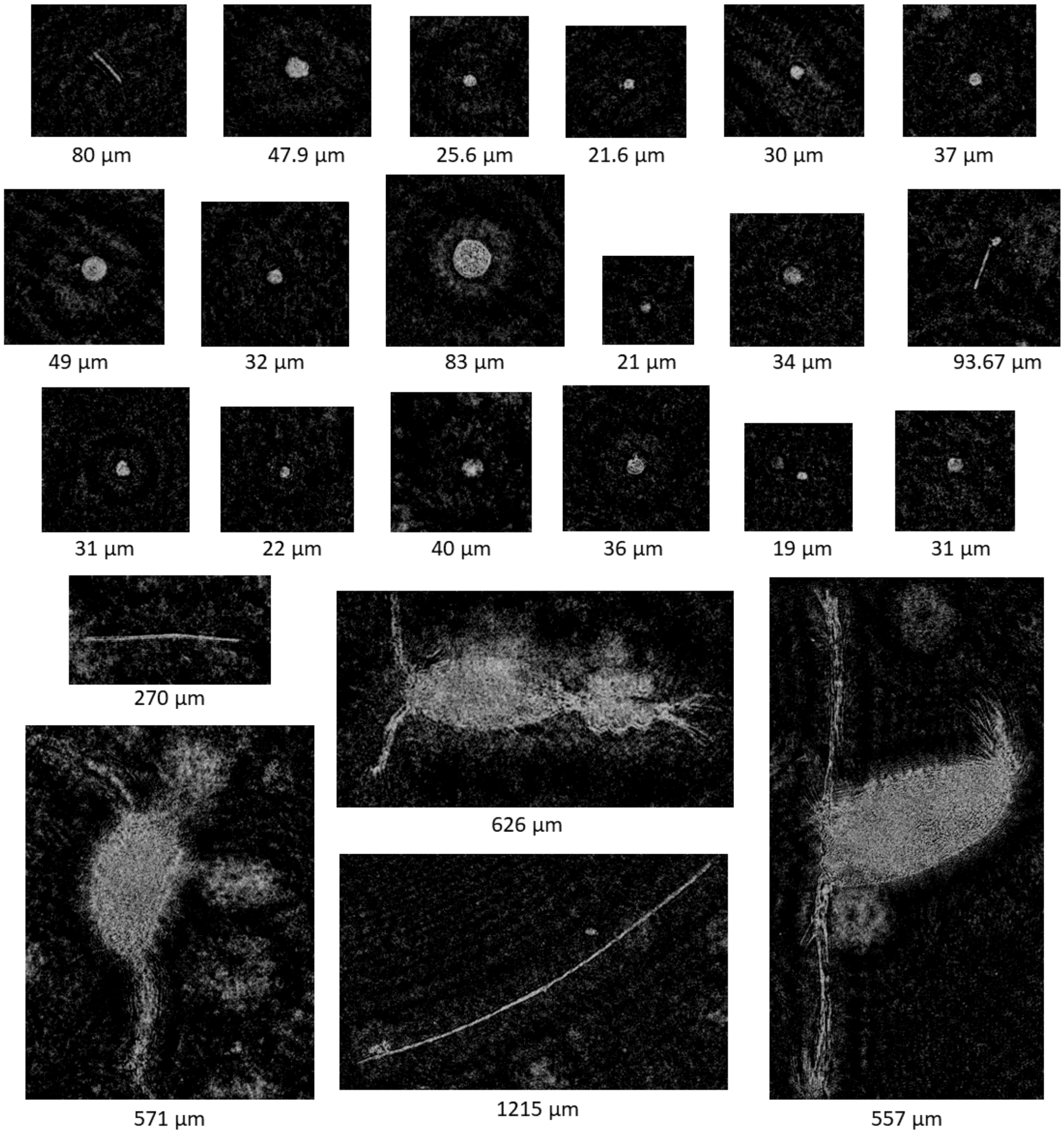

Figure 2D-4: Sample in focus particles and organisms recorded during the 12/8/20 sampling event across a wide size range (including copepods with/without egg sacs and diatom chains), corresponding to expected size range of M. aeruginosa colonies and other plankton.

Gulf of Mexico testing: A second round of field testing, in a different environment, was conducted in the coastal Gulf of Mexico, off the Fort Myers coast. In situ sampling was conducted at four different stations

(Figure 2D-5), representative of different optical (turbid) conditions. Details are provided in Table 2D-2 and a map of the sampling locations is provided in Figure 2D-5. At each sampling station, about 300 holograms were recorded. For this particular deployment, the AUTOHOLO was configured with either a 2, 4 or 6 cm path length at each station based on the turbidity. A 10X objective lens was used to obtain a resolution of 0.45 µm/pixel, as in the previous deployment.

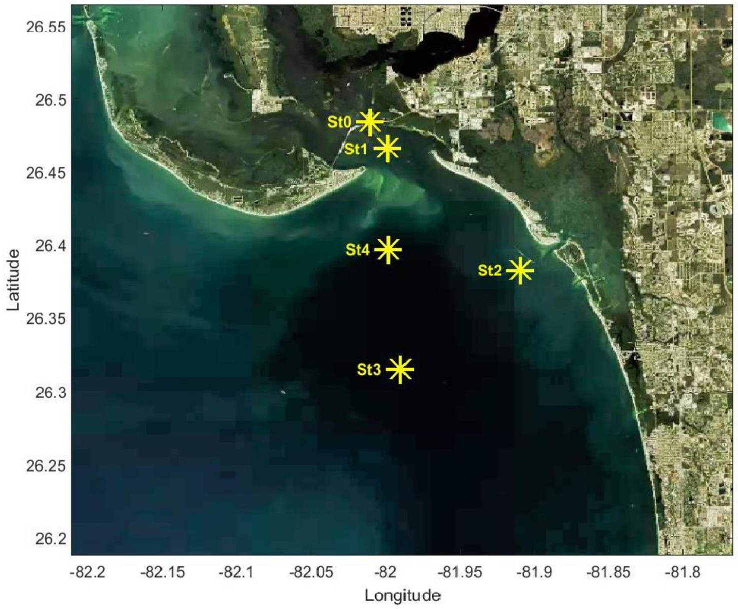

Figure 2D-5: Map showing the stations at which AUTOHOLO was deployed during the 1/7/21 field effort. Holograms collected in situ at Stations 1-4. Physical water samples collected and analyzed in the lab at all five stations.

Table 2D-2: Deployment details for the Gulf of Mexico field sampling on 1/7/21.

Station Name	**Time (EST)**	***K. brevis* Cells/mL (AUTOHOLO)**	***K. brevis* Cells/mL (Flow cytometry)**
Station1	1121	762	970
Station2	1258	835	1045
Station3	1423	5984	5981
Station4	1518	797	435

Water samples were also collected at each station and flow cytometry data was collected upon return to the lab. While the flow cytometer has poor accuracy for *K. brevis* populations at low cell concentrations (<1000 cells/mL), it is still useful to make a comparison with the AUTOHOLO cell counts (which are higher fidelity because of the larger sample size). Except at Station 4, the cell concentrations were comparable (within ~ 25%) between both methods. At high concentrations (~ 6,000 cells/mL, Station 3), the cell counts were nearly the same in both methods (Table 2D-2). These continued field experiments were useful to inform the AUTOHOLO deployment for this project; specifically, giving us a feel for the path lengths that work best for varying turbidities.

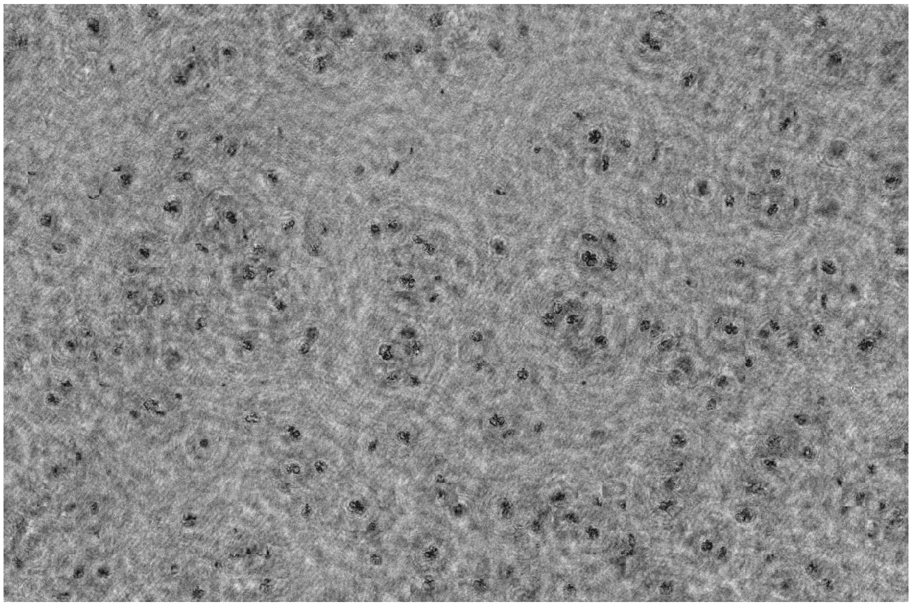

Figure 2D-6: Sample hologram from Station 3, showing very high K. brevis concentrations.

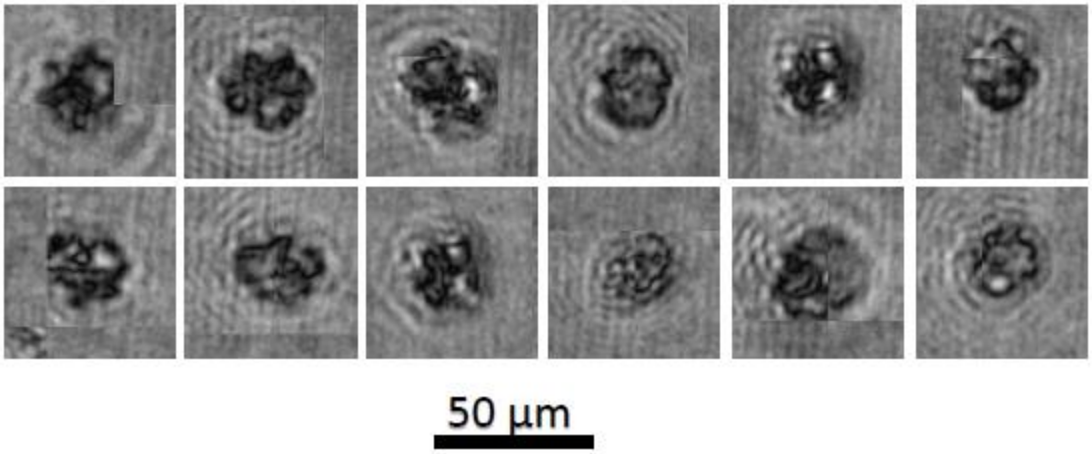

Figure 2D-7: Sample processed holograms showing K. brevis cells at different stations.

<u>Laboratory testing:</u> To supplement the field testing, laboratory experiments were conducted under controlled conditions at even higher particle loads (and consequently, turbidity) than those observed in the field. Diatomaceous earth was used as the particle of choice across the lab measurements. A range of tests were carried out at different attenuation and path length ranges. Keeping a constant path length of 1 cm, holograms were recorded at various path lengths corresponding to attenuation values of 1, 2 and 6 1/m respectively. Sample holograms at each case are shown in Figure 2D-8. At this path length, hologram quality was relatively unaffected even at the highest attenuation value. In Figure 2D-9, sample holograms for the same attenuation values, but an increased constant path length of 20 cm are shown. Clearly, at the highest attenuation, the hologram quality is seriously compromised, especially when it comes to characterizing smaller particles. This controlled experiment shows us that the minimum path length achievable with the AUTOHOLO (1 cm) is sufficient to record good quality data at very high attenuation readings, which provided us confidence for Lake Okeechobee deployments.

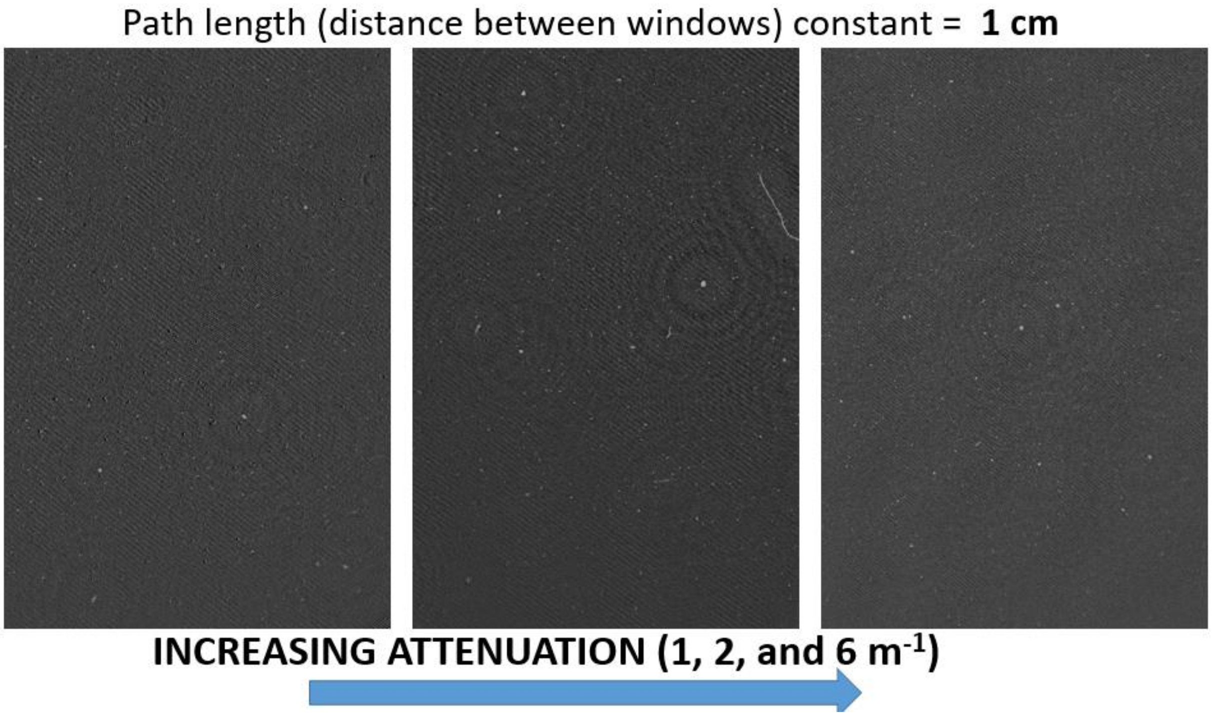

Figure 2D-8: Sample holograms for attenuation values of 1,2 and 6 1/m at constant sampling length of 1 cm. Diatomaceous earth particles were used in this lab experiment.

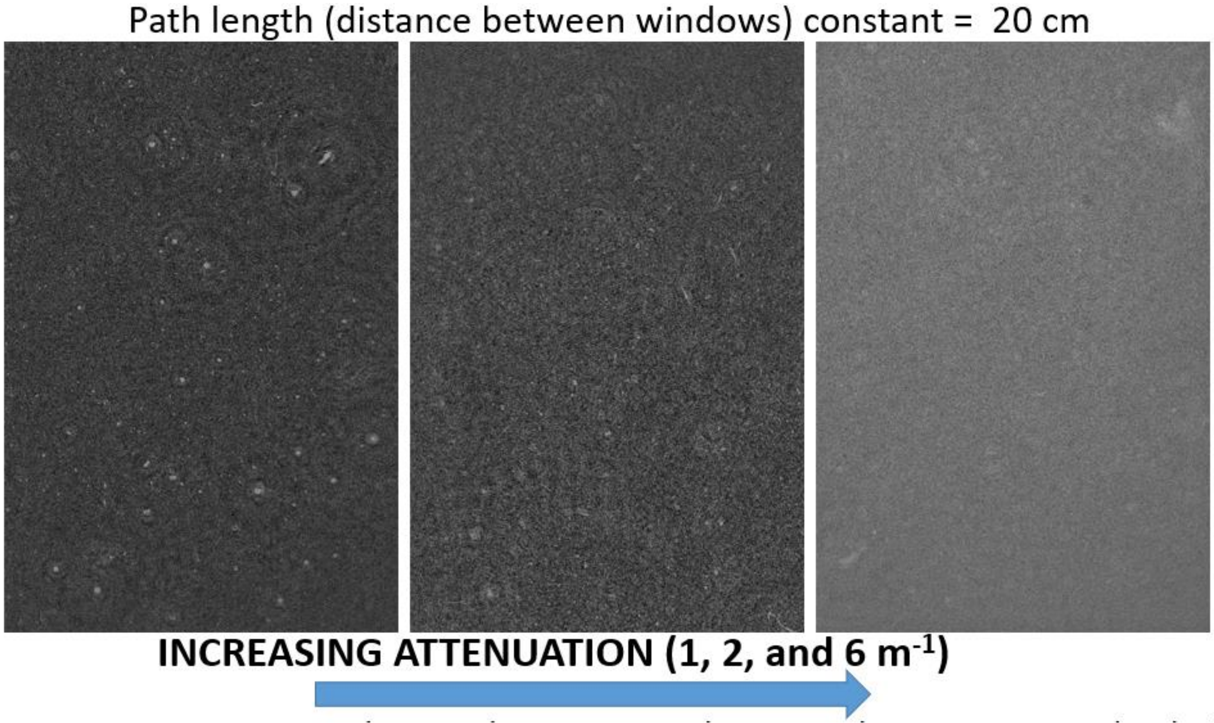

Figure 2D-9: Sample holograms for attenuation values of 1,2 and 6 1/m at constant sampling length of 20 cm. Diatomaceous earth particles were used in this lab experiment.

Lake Okeechobee testing: The AUTOHOLO was deployed during a routine sampling event at Lake Okeechobee on 8/24/21. The instrument was configured with a 1 cm path length due to high turbidity in the water; this was informed by previous testing in different optical environments as reported in earlier quarters. Holograms were recorded in the lensless configuration (to image larger objects such as *M. aeruginosa* colonies and zooplankton) with a resolution of 5.5 µm/pixel and a field of view (FOV) of 18 X 27 mm, corresponding to a sample volume of 4.86 mL per image. *In situ* holographic images were recorded from three different stations – at each station, 200 holograms were recorded. The Secchi depths of stations 1, 2, and 3 are 0.415 m, 0.76 m, and 0.47 m, respectively. Further details are provided in Table 2D-3. At all stations, the AUTOHOLO successfully recorded good quality holograms. Stations 1 and 3, with higher turbidities, had a high number of small particles (possibly detrital matter). In station 2, we observed *M. aeruginosa* colonies, consistent with results obtained from the lab samples (Figure 2D-10). In all datasets, several copepods were also recorded, sparsely distributed in all three stations. A collage of these different particles/organisms is shown in Figure 2D-11.

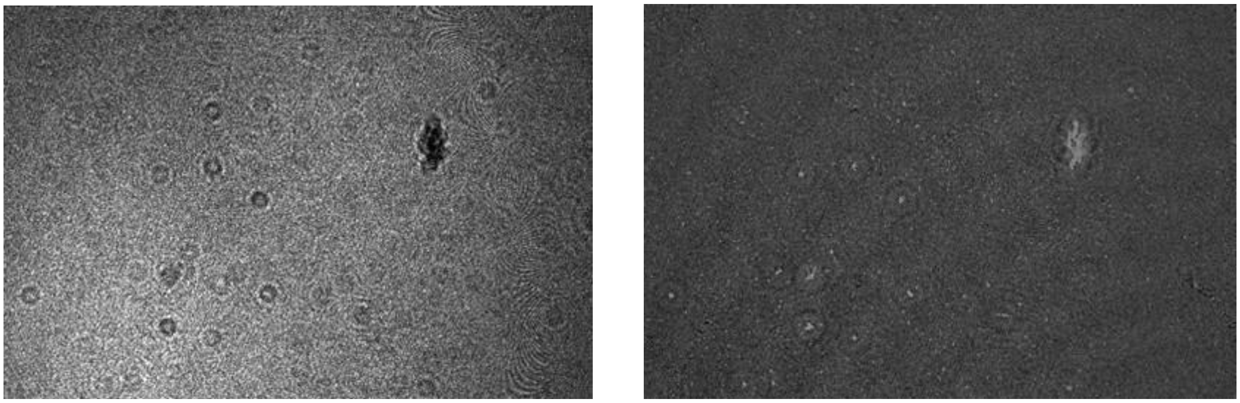

Figure 2D-10: Sample AUTOHOLO image from Station 2. (a) Raw image; and (b) Processed (reconstructed) composite image showing all the in focus particles on the same plane.

Table 2D-3: Deployment details for the Lake Okeechobee field sampling using AUTOHOLO on 8/24/21.

Stations	Geographical Location	No. of Holograms	Secchi depth (m)
Station 1	27.139 N, -80.789 W	200	0.415
Station 2	26.957 N, -80.97 W	200	0.76
Station 3	26.82 N, -80.78 W	200	0.47

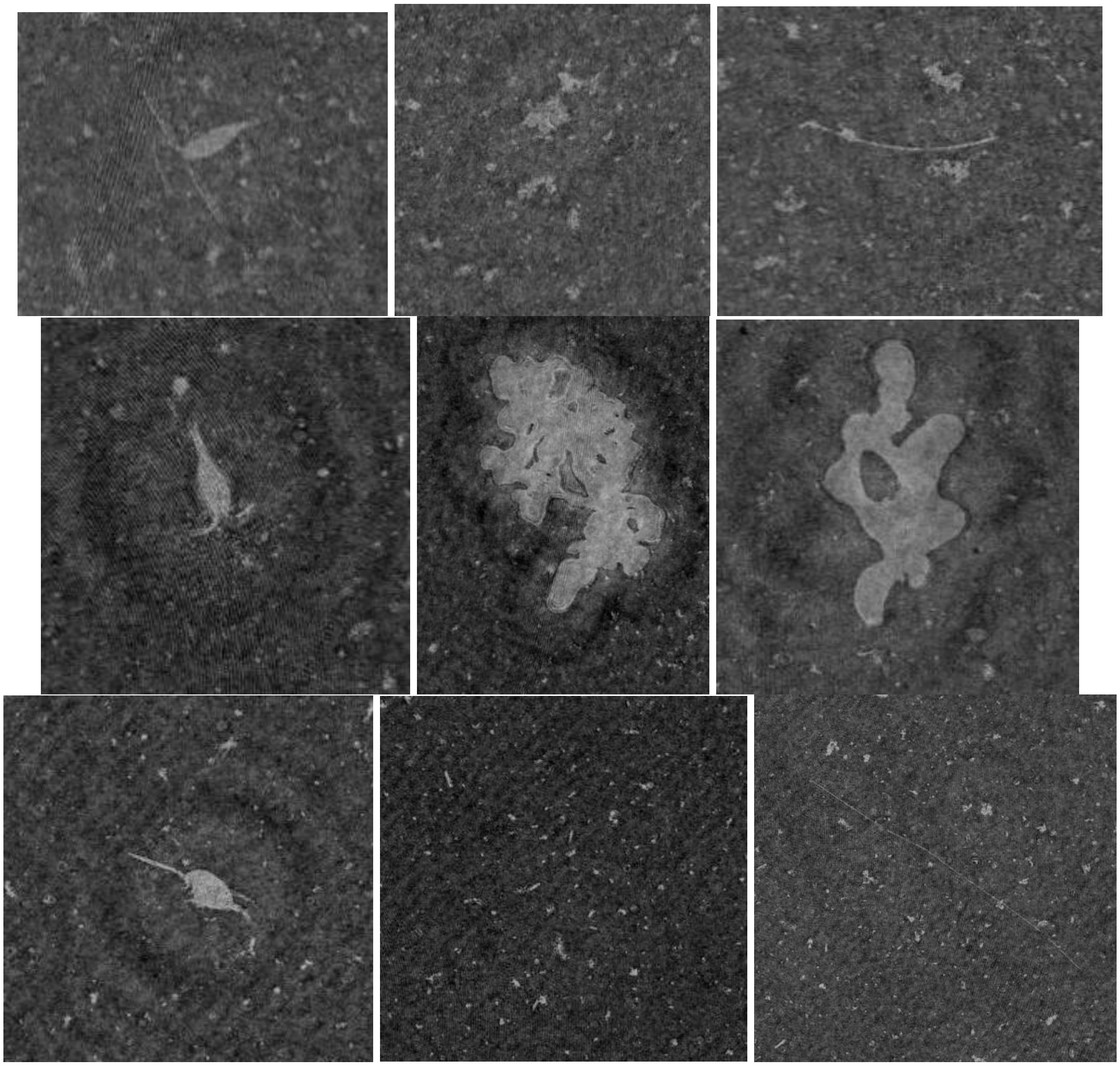

Figure 2D-11: A collage of particle/organism crops from various holograms seen at Station 1 (top row), Station 2 (middle) and Station 3 (bottom row). Left panels in each row show copepods seen at different orientations. Middle and right crops in center row are clearly imaged *M. aeruginosa* colonies. Two unidentified diatom/cyanobacterial colonies (elongate chains) are seen in rightmost panel in the top and bottom rows. Small, detrital particles seen in background in most images.

For each of the three stations, based on the above initial observations, holograms were post-processed to look at the following data: (i) *M. aeruginosa* colony presence and abundance; (ii) copepod abundance; and (iii) general particle characterization in the lake, including size distributions and fitting a slope to the data. Particle size is characterized either by the major axis length (MAL) – defined as the longest dimension of the particle - or the equivalent size diameter (ESD) which is defined as $ESD = \sqrt{4A/\pi}$, where A is area of the particle.

M. aeruginosa colonies were absent at Stations 1 and 3. At Station 2, a total of 25 particles were positively identified as *M. aeruginosa* colonies. The minimum and maximum *M. aeruginosa* colony size (MAL) were 0.93 mm and 4.5 mm respectively, with a mean value of 1.85±0.9 mm. It is important to note here that the AUTOHOLO has the ability to measure how large *M. aeruginosa* colonies get in their natural environment. Typical sampling methods depend on manual collection and are prone to size biases induced due to fragmentation of collected colonies during the collection and transport process. Observing them directly in situ provides an insight into their ecology which might not otherwise be possible. Copepods were also observed at all stations in the imagery. While the sample size is admittedly limited (200 holograms at each site), there are some interesting observations. A total number of 6, 11 and 3 individuals were observed at Stations 1, 2 and 3 respectively. These corresponded to 6.1, 11.3 and 3 copepods/L respectively at each of the stations. From previous oceanic observations, the typical values indicate roughly around 1 individual/L, highlighting that these abundances were above the base normal. While again reiterating that the small sample size might make these observations statistically insignificant, this effort highlights interesting questions that can be addressed with longer deployments. For example, copepod abundance was seemingly higher at the only station where M. aeruginosa was detected. The minimum and maximum sizes (as defined by major axis length) were 396 µm and 1051 µm, with a mean length of 680±200 µm.

Broadly, the AUTOHOLO data also reveals insights into the overall particle distributions at the different stations. Results were compared using both MAL and ESD parameters (the latter is more common in the marine optics/particle characterization community, so results are presented using that format here). Figure 2D-12 shows the particle size distributions for Station 1 on a log-log plot (as is the norm in these cases). The values of the slopes in the PSD (~4.3), are higher than those typically seen in marine environments (~3-4), indicating higher abundance of particles at the smaller end of the size spectrum. The data is also presented as a histogram, with data divided into 20 µm bins. The results show most of the particles are present in the <100 µm range, with a highest particle abundance of ~ 100 particles/mL in the first bin (~20-40 µm). Similar plots for station 2 and 3 (Figures 2D-13 and 2D-14) reveal the same trends; highest abundance occurs at the smallest scales. Station 3 showed the highest particle abundance among all three stations (~ 150 particles/mL in the first bin). These results again highlight the usefulness of the AUTOHOLO in characterizing particle abundance and distributions even in turbid/high particle load environments such as Lake Okeechobee.

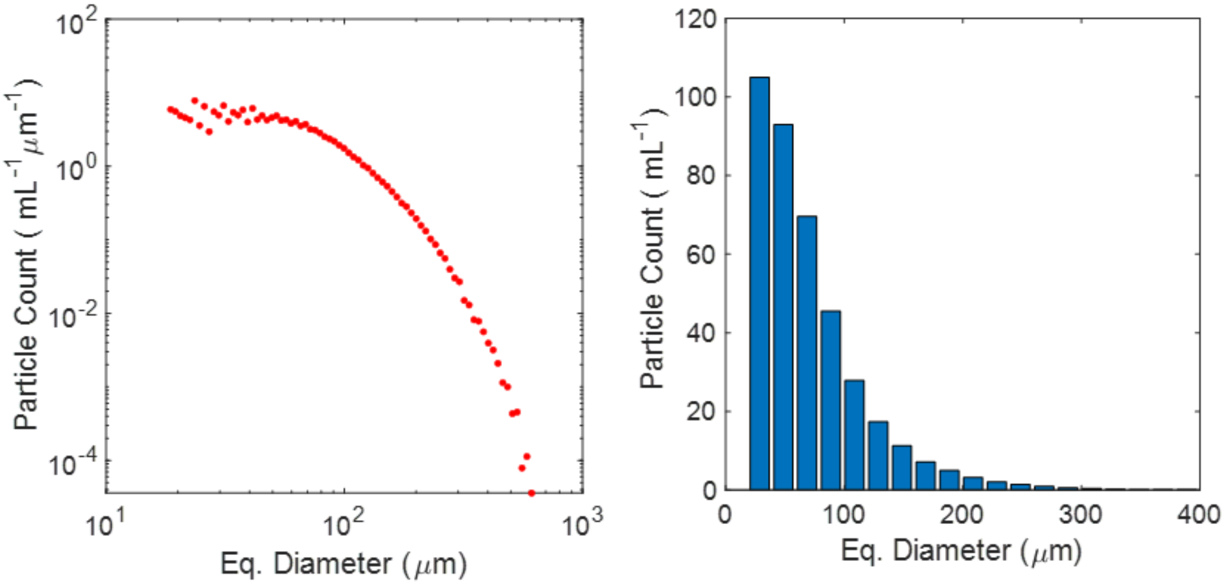

Figure 2D-12: (i) Particle size distribution and (ii) particle abundance obtained from post-processed holograms at Station 1.

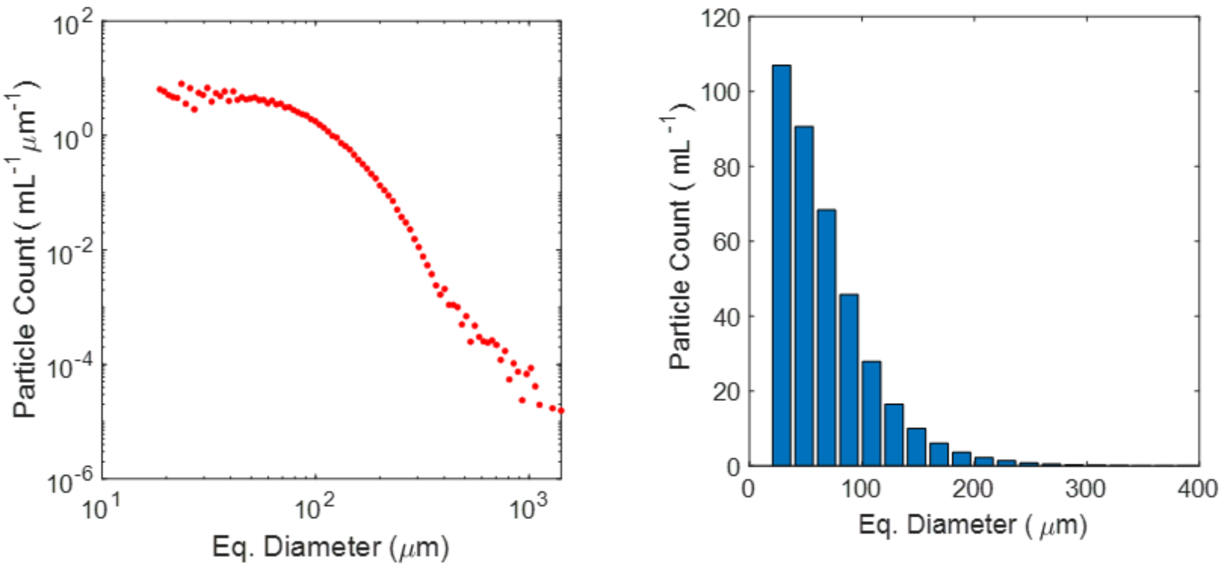

Figure 2D-13: (i) Particle size distribution and (ii) particle abundance obtained from post-processed holograms at Station 2.

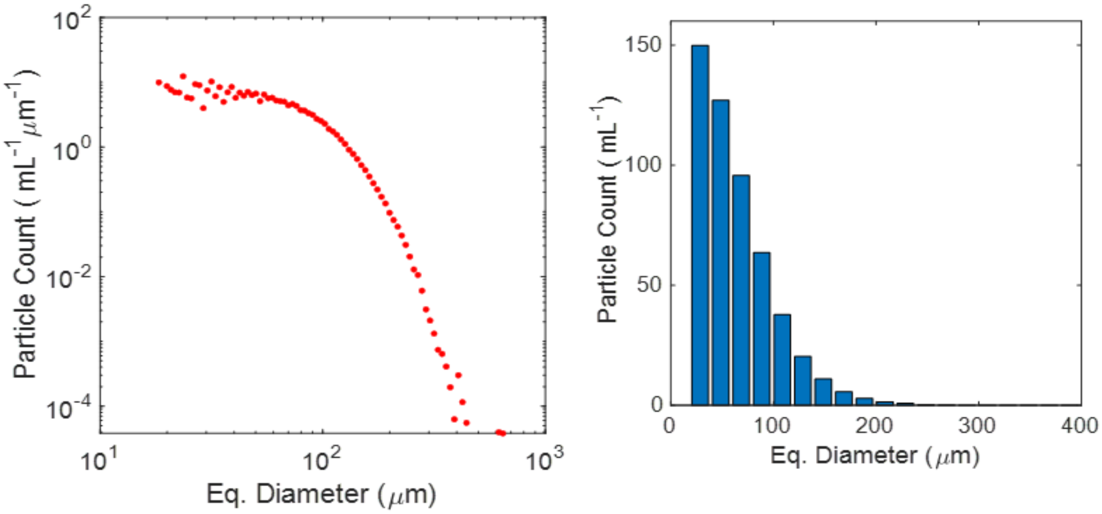

Figure 2D-14: (i) Particle size distribution and (ii) particle abundance obtained from post-processed holograms at Station 3.

AZFP METHODS, ACTIVITIES CONDUCTED, and RESULTS

Based on advice received by previous email discussions with Paul Gray (Audubon Florida) and Zach Welch (SFWMD), the AZFP deployment was scheduled to be deployed in Jun-July 2021. The instrument was received at FAU-HBOI from ASL Environmental Sciences on 6/5/21, after undergoing factory calibrations. It consists of (i) a main cylindrical body which hosts the battery and electronics (Figure 2D-15); and (ii) A multi-frequency transducer that can transmit and record returns at four discrete frequencies: 125, 200, 465 and 700 kHz. A bottom mounting frame to house the instrument was custom-built at HBOI (Figure 2D-15). The instrument was tested in the lab and programmed to match deployment requirements using the vendor software AZFPLink (Figure 2D-16). The instrument was deployed at the bottom in the vicinity of the L001 tower on 6/17/21. Divers were used to: (i) appropriately position the instrument on the bottom; and (ii) ensure no cables or other objects were blocking the instrument's acoustic path. The instrument was recovered on 7/27/21. Due to rough weather and challenging conditions, we were unable to record images or video of the actual instrument deployment. Post-deployment and recovery, the instrument was shipped back to ASL Environmental Sciences Inc., in late August 2021. The deployment was successful and over 20 GB of data was recorded during this period. As part of their contract, ASL Environmental Science, Inc., provided a detailed data analysis.

Figure 2D-15: AZFP main body containing electronics and battery, AZFP multi-frequency transducer, capable of recording responses at 4 transducer frequencies (125, 200, 460 and 760 kHz respectively), and model of the bottom mounting frame designed to place the instrument at the lakebed near L001.

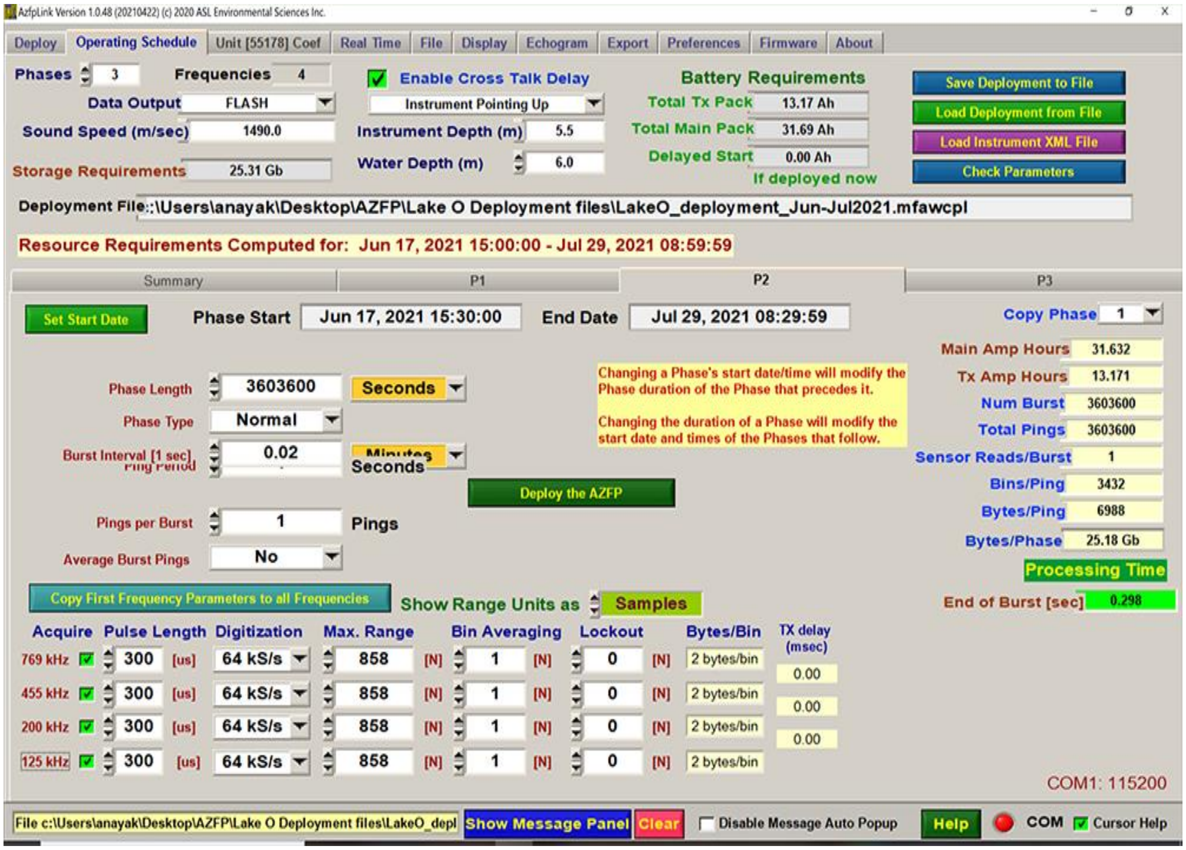

Phases 3
Frequencies 4
Data Output FLASH
Sound Speed (m/sec) 1490.0
Storage Requirements 25.31 Gb
☑ Enable Cross Talk Delay
Instrument Pointing Up
Instrument Depth (m) 5.5
Water Depth (m) 6.0
Battery Requirements
Total Tx Pack 13.17 Ah
Total Main Pack 31.69 Ah
Delayed Start 0.00 Ah
If deployed now
Deployment File::\Users\anayak\Desktop\AZFP\Lake O Deployment files\LakeO_deployment_Jun-Jul2021.mfawcpl
Resource Requirements Computed for: Jun 17, 2021 15:00:00 - Jul 29, 2021 08:59:59

Phase Start Jun 17, 2021 15:30:00
End Date Jul 29, 2021 08:29:59
Copy Phase 1
Phase Length 3603600 Seconds
Phase Type Normal
Burst Interval [1 sec] 0.02 Minutes
Ping Period Seconds
Pings per Burst 1 Pings
Average Burst Pings No

Changing a Phase's start date/time will modify the Phase duration of the Phase that precedes it.

Changing the duration of a Phase will modify the start date and times of the Phases that follow.

Main Amp Hours 31.632
Tx Amp Hours 13.171
Num Burst 3603600
Total Pings 3603600
Sensor Reads/Burst 1
Bins/Ping 3432
Bytes/Ping 6988
Bytes/Phase 25.18 Gb
End of Burst [sec] 0.298
Show Range Units as Samples

	Acquire	Pulse Length		Digitization	Max. Range		Bin Averaging		Lockout		Bytes/Bin	TX delay (msec)
769 kHz	☑	300	[us]	64 kS/s	858	[N]	1	[N]	0	[N]	2 bytes/bin	0.00
455 kHz	☑	300	[us]	64 kS/s	858	[N]	1	[N]	0	[N]	2 bytes/bin	0.00
200 kHz	☑	300	[us]	64 kS/s	858	[N]	1	[N]	0	[N]	2 bytes/bin	0.00
125 kHz	☑	300	[us]	64 kS/s	858	[N]	1	[N]	0	[N]	2 bytes/bin	

COM1: 115200
File c:\Users\anayak\Desktop\AZFP\Lake O Deployment files\LakeO_depl
☐ Disable Message Auto Popup

Figure 2D-16: A snapshot of the AZFPLink software during instrument programming prior to the deployment.

The raw echograms from two time periods (6/20/21 –6/25/21 and 7/19/21 – 7/24/21), at all 4 different frequency returns are shown in Figures 2D-17 and 2D-18. Please note that returns above ~ 3.5 m are to be ignored – the instrument was operated with a max range of 10 m to allow us some flexibility. Although we wind up with 'extra' data, operating with a longer-than-necessary max range ensures that we see all the way to the surface. Strong backscattering signal is represented in red and progressively weaker ones in yellow, light and dark blue respectively. The strong red signature just below 4 m represent the lake surface. A periodic pattern of high and low scatter is also seen in the water column on many days, corresponding roughly to a daily frequency; similar signatures are typically present in representative diel migration patterns in the ocean.

The types of scatterers observed in the echograms can be divided into different functional groups based on morphological characteristics. *M. aeruginosa* cells regulate their buoyancy in response to light levels; thus, it is possible that colonies would exhibit vertical migration. Such vertically migrating targets are visible in the 125 kHz echogram data, appearing as streaks, as shown in Figure 2D-18. Some sample echograms with interesting observations across much smaller time intervals are also discussed. For example, scattering intensely in the 125 kHz channel are orb-like features that are believed to be horizontally moving fish or other suspended biology (Figure 2D-19). Another type of target are strongly scattering 'clusters' that appear within 1 m of the surface, and scatter strongly at all frequencies, often saturating at the upper end of what the instrument is capable of measuring, as shown in Figure 2D-20. This is believed to be bubbles or sediment that have been entrained in the water column. There may also be evidence that these are algae that have collected near the surface during day-light hours, that gradually sink down as large clumps at night.

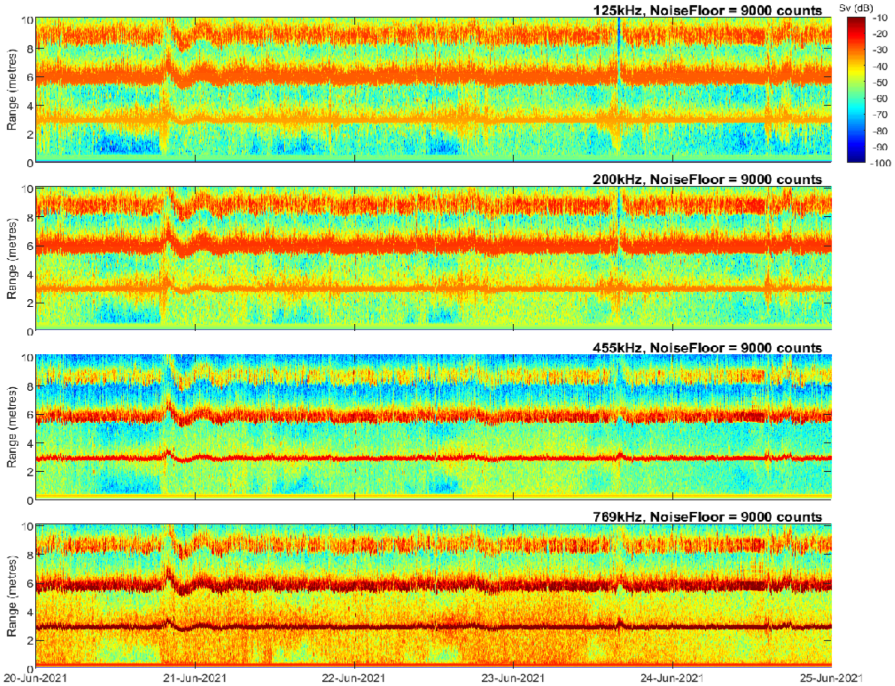

Figure 2D-17: Raw echograms from the AZFP data over the time period 6/20/21 – 6/25/21. Echograms returns are from top to bottom panels: (a) 125kHz; (b) 200 kHz; (c) 460 kHz; and (d) 760 kHz respectively).

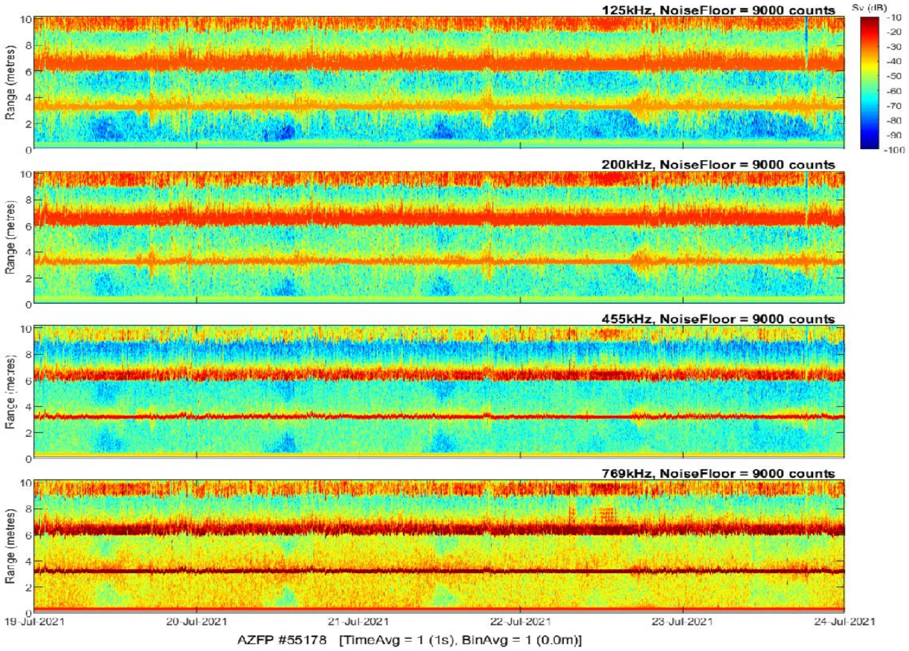

Figure 2D-18: Raw echograms from the AZFP data over the time period 7/19/21 – 7/24/21. Echograms returns are from top to bottom panels: (a) 125kHz; (b) 200 kHz; (c) 460 kHz; and (d) 760 kHz respectively).

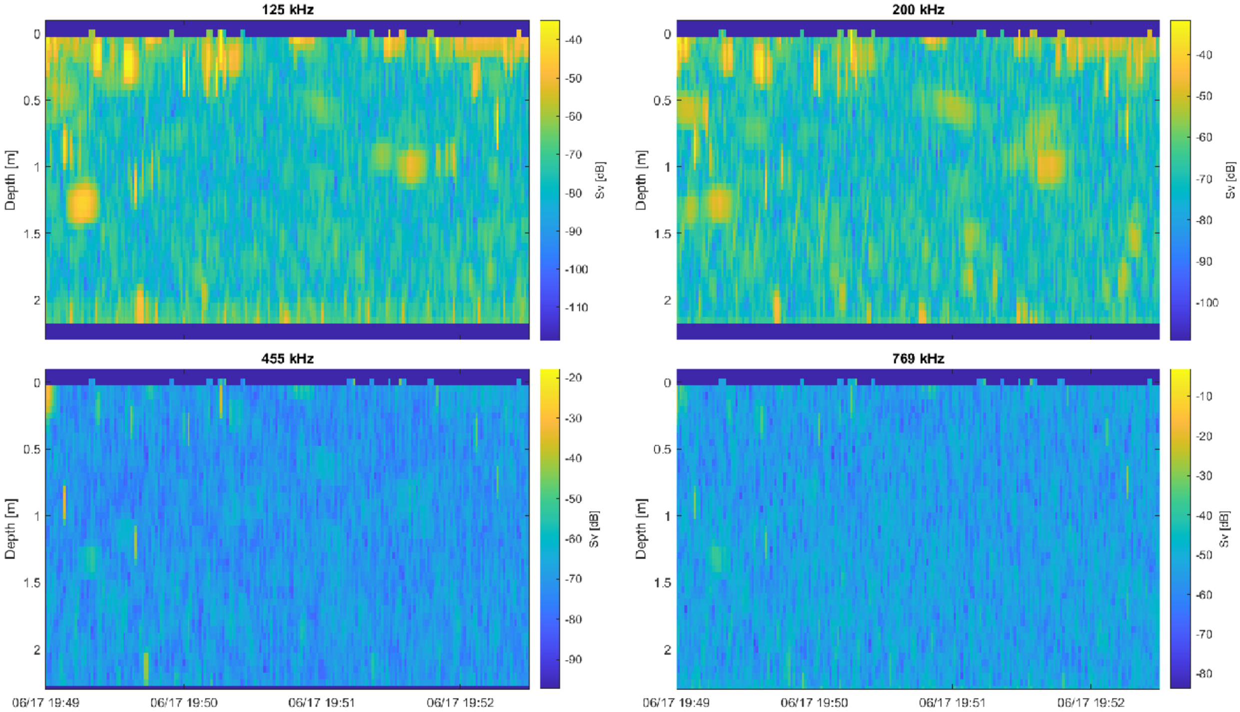

Figure 2D-19: Echograms for a 4 minute time span (19:49-19:53) on 6/17/21. Example illustrates slow and horizontally moving biology (spherical shapes, top) and fast/horizontally moving biology (narrow vertical lines that are present only for one or two seconds, bottom).

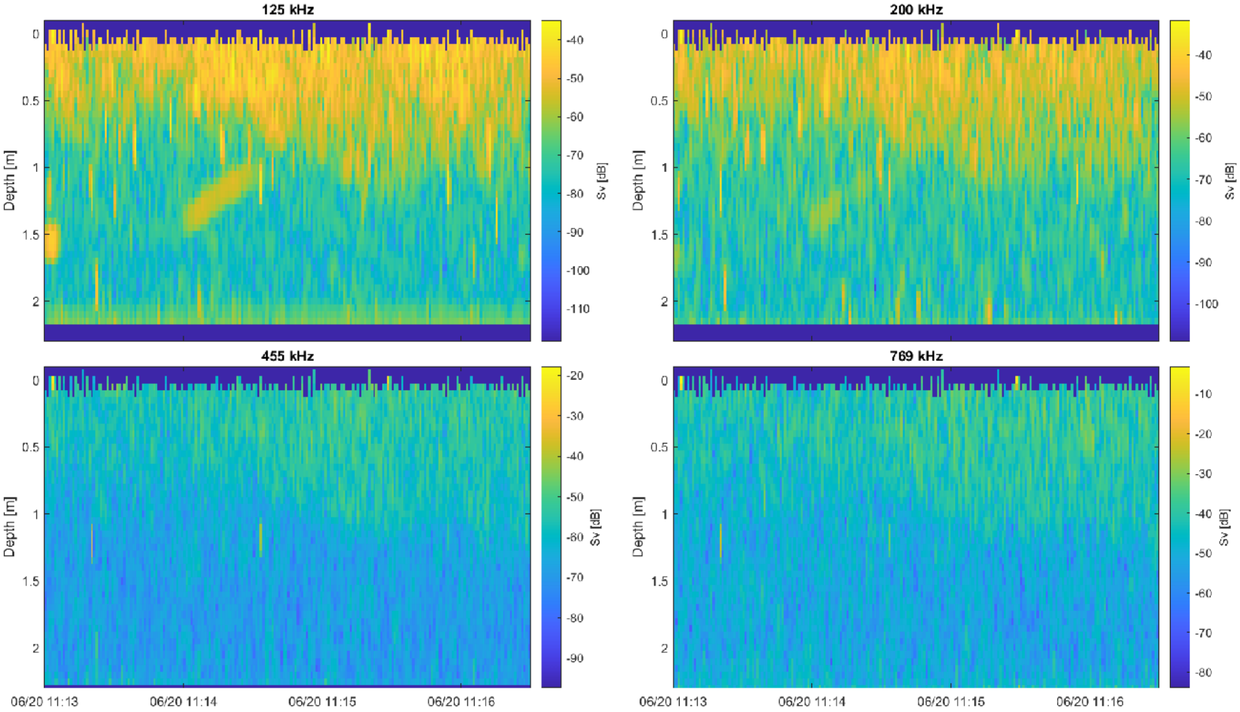

Figure 2D-20: Echograms for a 4 minute time span (11:13-11:17) on 6/20/21. Example illustrates clouds of surface matter that are bubbles entrained by wind mixing or suspended biological matter. Also seen are mid-water column streaks which may be fast-moving fish.

Further, as part of the processing efforts, a time series of the center of mass (CM) and Nautical Area Scattering Coefficient (NASC) were computed as a proxy for organism/particle abundance. NASC is a measure of acoustic signal per surface area and indicates the integrated sum of scattering intensity over the water column. CM is the weighted mean depth (units of m) of scattering intensity integrated through the water column. CM and NASC are calculated for each functional biological scattering group, and for each frequency channel. The data were integrated over the full water column, and also split into upper and lower layers. The upper layer is integrated over 0 to 1.2 m water depth. The lower layer is integrated from 1.2 m to the maximum depth of valid data.

For the NASC, the 769 kHz frequency channel had significant noise and was not used for definition of functional scattering groups. The noise level in the 769 kHz channel was evident in the mean of the full-water column NASC for this channel. The CM for the three frequency channels, not contaminated by noise, were all within the upper 1 m of the water column, with mean CM of 0.72, 0.75, and 0.99 for the 125, 200, and 455 kHz channels, respectively. For these three frequencies, the mean NASC of the upper half of the water column was found to be between 4 times to 8 times the mean NASC of the lower half of the water column. This confirms that the strongest acoustic scatterers were concentrated in the upper half of the water column. Future work may improve our ability to discriminate *M. aeruginosa*, at which time these NASC values may be converted to *M. aeruginosa* biomass.

CONCLUSIONS & FUTURE WORK

Over the course of the reporting period, the AUTOHOLO was tested and proved to be feasible for plankton measurements in Lake Okeechobee. Over the field deployment at Lake Okeechobee, over 600 holograms were recorded at multiple stations. Data processing provided abundances for *M. aeruginosa*, copepods, and more generally, small particle distributions. Copepod abundances ranged from 2-11 individuals/L, albeit with the caveat that the overall actual sampling size was too small to be statistically significant. The highest abundances coincided with locations where *M. aeruginosa* colonies were detected. This pilot study shows the value in future long-term deployments of the AUTOHOLO which might enable us to better characterize *M. aeruginosa* abundances, as well as particle and plankton community composition at Lake Okeechobee. Our efforts especially highlight the importance of in situ high resolution measurements in ensuring measurement of particle/plankton fields in their natural environments in an undisturbed manner, thus enabling a more realistic representation of size distributions, especially of colonial plankton.

This pilot AZFP study yielded encouraging results. *M. aeruginosa*-like targets have been identified, segmented, and analyzed. It is possible that future studies may yield improved results based off lessons learned from the pilot study. Two attempts were made at isolating *M. aeruginosa* distinct from other biological scatterers in the water column. However, it was not possible to separate the different groups (vertically migrating streaks versus horizontal moving spheres versus cloud-like material near the surface) by relying solely upon acoustical scattering models. This work could be performed manually but would be incredibly time consuming and prone to analyst bias and error. It is suspected that this discrimination could be accomplished via alternative methods, potentially utilizing morphological and/or behavioral information to augment the acoustical scattering model approach. One alternative method that could be used is a machine learning based approach for classification. This type of classification method has been performed for the classification of herring schools, aggregations of juvenile salmon, and near surface bubbles, achieving precision and recall exceeding 90% (Alex Slonimer, personal communication). Herring and juvenile salmon have very similar acoustic scattering signatures; they are similar in size, and both have swim-bladder organelles that are filled with air. The result is that classification of these species via acoustic scattering signature alone is not possible. However, the morphological characteristics of the organisms in echograms are distinct. When this information is used in conjunction with acoustical scattering models, classification with a U-Net has been successful. To implement this type of method for classification of *M. aeruginosa* would require the development of a set of approximately 100 hours of annotated echogram data. These annotations would be used to train a neural network to recognize the different classes of data. In implementation, the network would be capable of classifying echogram data at a rate of three seconds per hour of echogram data. This level of classification could enable higher resolution analysis of the rising velocity of *M. aeruginosa* under varying conditions throughout the deployment. Individual *M. aeruginosa* colonies would be identified using a connected component analysis, and the rate of ascent could be found for each colony. In summary, while the methodology and approach employed seems to be robust, it is deemed necessary for further studies with co-located daily sampling events to clearly delineate *M. aeruginosa* colonies from other similar scattering particles/plankton.

The results of these two powerful techniques are being further pursued in continuing **Task 10**. The AUTOHOLO will be deployed seasonally for a period of several days during a hydrodynamic and quiescent period to determine to what extent *M. aeruginosa* may be vertically migrating, e.g. for light during the day and nutrients from sediments at night. Discrete cell counts from **Task 2B** data demonstrate that cell counts were not vertically stratified at the time of its routine sampling (~0930 hrs). However, the AZFP data demonstrated that vertical migration did not apparently occur until after this time. Therefore, discrete sampling cannot rule out vertical stratification/migration, and thus continuous observation is necessary. While the AZFP testing and data processing is not yet capable of revealing the exact nature of the particles, the AUTOHOLO does have this capability. Therefore, the AUTOHOLO was selected to be deployed continuously for **Task 10** to unambiguously determine if vertical migration is occurring. New **Task 9** sampling activities over several 16-hr periods are scheduled to overlap with these deployments to provide validation data. Overall, information about vertical migration, and any light, nutrient, or other environmental drivers of such, will be critical for informing the mechanistic model of **Task 1E**.

TASK 3A: LEGACY LOAD MONITORING (TASK LEAD: BECKLER)

INTRODUCTION

The need to monitor the sediment chemistry is well warranted and recognized in the Blue-Green Algae Task Force (BGATF) consensus document, given disproportionate internal versus overall loading contributions. Inorganic P fluxes demonstrated from core incubations and core diffusive profiles demonstrate that internal loading (i.e. from sediments) is on the same order of external inputs (Fisher et al. 2005). Legacy loading from sediments may continue to provide nutrients to fuel blooms long after direct, obvious inputs are stopped (e.g. from the Kissimmee River, Fisheating Creek, S191 basin or Taylor Creek). Moreover, certain nutrient conditions/dynamics/triggers within the sediments may directly promote the emergence of *M. aeruginosa* cysts and initiate full scale HABs, although this is poorly understood. Project activities within this Task refine information regarding of the importance of internal loading and elucidate the factors responsible for respective spatial and temporal variations - ultimately improving our ability to select, design, and target passive and active mitigation strategies. Specifically, a quantitative, spatial, and temporal understanding of sediment biogeochemical inventories, conditions, and fluxes is desired for understanding the formation and fate of *M. aeruginosa* and other HABs. This task is therefore focused on quantifying these sediment spatial inventories and speciation of carbon and nutrients and their respective benthic fluxes, as well as other analytes such as iron that may be involved in regulating these inventories, transformations, and fluxes. Measurements were mostly conventional in nature, although one innovative technique that was also employed is voltametric redox analyte profiling of sediment cores that provided additional contextual information regarding microbial respiration processes and mineral solubilization (i.e. linked to pore water phosphate release) for observed nutrient cycling (Meiggs & Taillefert 2011).

Overall, Lake Okeechobee water column total phosphorous and soluble reactive phosphorous (SRP; i.e. dissolved phosphate) concentrations have increased over time *despite reductions* in external loading (Figure 3A-1). Long term nitrogen increases (both total dissolved and dissolved inorganic nitrogen) are not as evident. Annual cycles are present with both; wintertime highs are followed by summertime depletion along with the algae bloom emergence over the spring/summer. However, N in the water column is depleted several weeks earlier than P, at least over the last few years (Figure 3A-1) – likely a combination between algal requirements and disparate geochemical processes in sediments. This contrasts with the general paradigm in which phosphate limitation (relative to N limitation) is unlikely in the later stages of the bloom due to enhanced positive feedbacks in which organic carbon deposition leads to more chemically reducing sediment conditions and therefore less phosphate sediment sequestration and greater pore water inventories. There also appears to be close connections between sediment resuspension and water column nutrients, at least as to the extent that can be inferred from water column turbidities (Figure 3A-1). Annual averages of water column turbidities closely match those of SRP and DIN, suggesting resuspension exerts a dominant control on nutrient concentrations.

Nutrient loading to sediment pore waters (and thus possibly to sediment-localized *M. aeruginosa* cysts) is controlled by either anaerobic degradation and the direct release of organic/inorganic P and N during respiration to pore waters followed by diffusive fluxes, the dissolution of sorbent mineral phases (Rozan et al. 2002; Peretyazhko and Sposito, 2005) and similar diffusive fluxes, especially when occurring in the near-surface sediment layer, and/or the physical resuspension of nutrients within sediment pore waters. This task, **Task 3A**, is not directly focused on the resuspension of particulate nutrients to the water column; however, future project phases (e.g. Amendment #3 **Task 12**) will examine both dissolved and particulate nutrient resuspension (Kalnejais et al., 2010, Couceiro et al., 2013). Lake Okeechobee sediments are not homogeneous, and sediment diffusive nutrient flux processes are extremely variable and dependent on the sediment composition (Moore et al. 1998). Sediment nutrient solubilization is stimulated by increases in temperature, respiration, and water column stratification/hypoxia (i.e. benthic oxygen demand). The current body of literature regarding Lake Okeechobee diffusive fluxes demonstrates that muddy sediments are greater than those from sand or peat cores, but fluxes from all increase drastically under anaerobic conditions, probably due to the anaerobic acceleration of iron mineral solubilization. The ability of Lake Okeechobee to retain sediment phosphorous is potentially decreasing as mineralogy is altered and surface sites are saturated (proposed in Fisher et al. 2001), as has been demonstrated in the northern drainage basin soils (Nair & Graetz 2002). Cumulative eutrophication leads to not only nutrient additions, but also enhancements to organic carbon deposition and thus a more cumulative chemically reducing environment, which should lead to a decrease in the iron (oxy)(hydr)oxide mineral phosphate sorption buffers. While this is difficult to establish over only one year of sampling, spatial and seasonally variability could lend insights into this possibility. It is also possible that over short timescales (days to weeks), sediment nutrient fluxes can lead additional eutrophication and positive feedbacks in the sediment chemical reducing "pressure" and therefore additional sediment fluxes.

On the contrary, a long term increases in P-rich mud has occurred, primarily localized over nearly 50% of the lake floor surface in the deeper, pelagic areas. Comparing sediment layers corresponding to prior to the main anthropogenic basin modifications in the early 1900s until near the turn of the century, the sediment TP concentrations have dramatically increased (Brezonik & Engstrom, 1998). Most of this accumulation, however, is in the form of organic and non-apatitic inorganic P (NAI-P). The former is expected to be remineralized to inorganic phosphate (organic-P to phosphate) and to subsequently become associated with iron either as Fe-P or Fe oxide minerals. The latter NAI-P is probably much of this new inorganic phosphorous now bound to iron oxides that is susceptible to redox-mediated release processes over seasonal time scales. We hypothesize that microbial iron reduction is *the* dominant respiratory process in the muddy lake sediments that have been the subject of most concern. Microbial iron reduction results in the dissolution of iron oxides to form reduced Fe(II) (either dissolved in pore waters or re-adsorbed onto other iron oxides), and should thus compete with phosphate for iron oxide adsorption sites. Near the sediment surface or during resuspension events, the Fe(II) can reoxidize and reprecipitate as Fe(III) hydroxides, thus regenerating the overall P retention capabilities. We may expect to see signatures of this process during resuspension, but we should also consider that the form of Fe(II), including organic complexation with chemically reduced organic ligands, could stabilize the Fe(II) and limit the reoxidation and thus reprecipitation.

There does not appear to be drastic increases in sediment solid phase N, at least between the years of 1988 and 1998 (Fisher et al. 2009). This suggests that the nitrogen is efficiently removed by denitrification, or some other transformation, or is flushed out of the lake either in dissolved or particulate form (unlike phosphate which has a high tendency to adsorb onto iron oxides). However, despite not seeing an increase in solid phase TN, pore water ammonium N did increase between 1988 and 1998. More cumulatively reducing conditions may promote N retention by limiting annamox or coupled nitrificiation-denitrification (i.e. less oxidants such as nitrate or O_2), or by promoting the dissimilatory nitrate reduction to ammonium in lieu of canonical denitrification to N_2. However, we also hypothesize a newly discovered N removal process may also be limited by any decreases in iron oxide inventories, specifically the iron-mediated oxidation of ammonium, i.e. Feammox:

$$8Fe(OH)_3 + NH_4^+ + 14H^+ \rightarrow 8Fe^{2+} + 21H_2O + NO_3^- \qquad \text{Eq. 3A-1}$$

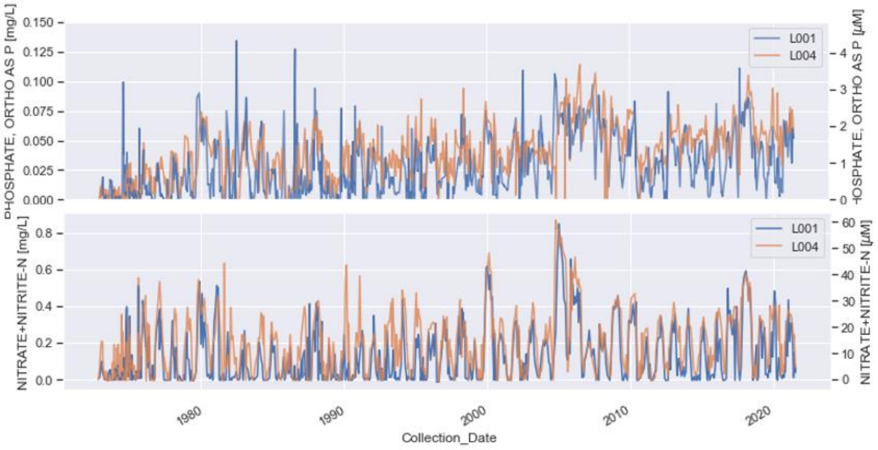

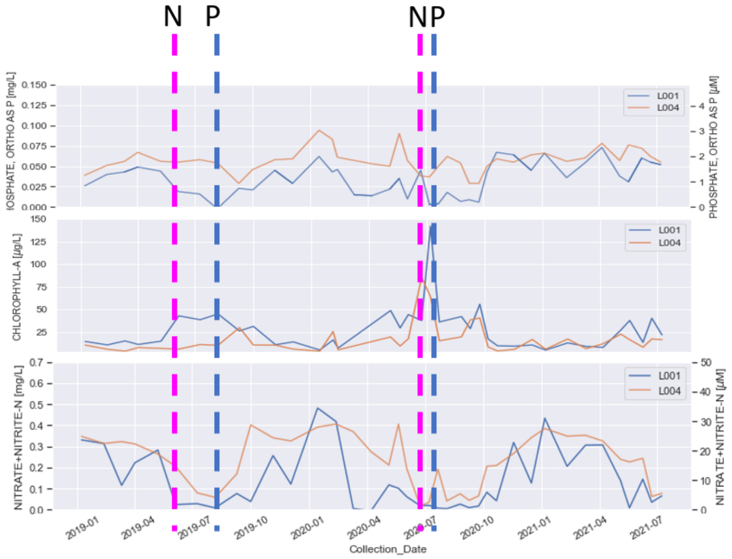

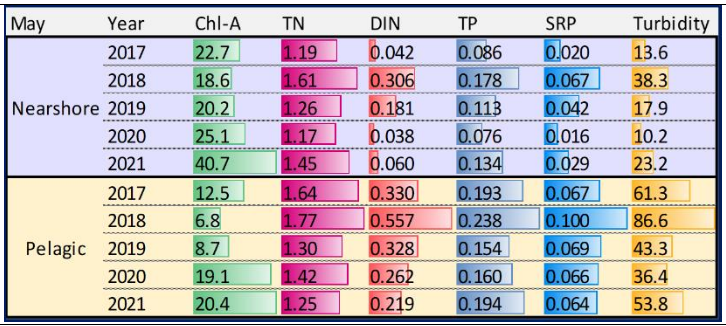

May	Year	Chl-A	TN	DIN	TP	SRP	Turbidity
Nearshore	2017	22.7	1.19	0.042	0.086	0.020	13.6
	2018	18.6	1.61	0.306	0.178	0.067	38.3
	2019	20.2	1.26	0.181	0.113	0.042	17.9
	2020	25.1	1.17	0.038	0.076	0.016	10.2
	2021	40.7	1.45	0.060	0.134	0.029	23.2
Pelagic	2017	12.5	1.64	0.330	0.193	0.067	61.3
	2018	6.8	1.77	0.557	0.238	0.100	86.6
	2019	8.7	1.30	0.328	0.154	0.069	43.3
	2020	19.1	1.42	0.262	0.160	0.066	36.4
	2021	20.4	1.25	0.219	0.194	0.064	53.8

Figure 3A-1: Top: Data from the SFWMD demonstrated the long term trends in SRP and NO_3^- $+NO_2^-$ in the northern lake mud/sand bottom site receiving Kissimmee River inflows (site L001) and the eastern mud-bottom area (site L004); Center: Time series from 3-years demonstrating the seasonal patterns in nutrient depletion, specifically the depletion of NO_3^-+NO_2^- prior to SRP; Bottom: The lake average turbidities vs. dissolved and particulate nutrients suggest that sediment resuspension is a strong control on nutrient inventories. All data is from the SFWMD DBHydro database, while the bottom figure was presented by Sean Sculley at a Blue Green Algal Task Force meeting in 2021.

Feammox accounts for a significant portion of nitrogen removal in Lake Taihu (Yao et al. 2019), a highly eutrophic and HAB-impacted lake in China, and there is no reason to expect it is not important in Lake Okeechobee sediments, which are even more rich in iron oxides. While Task 3A does not specifically evaluate Feammox, we hypothesize that it is ongoing and is the subject of future planned work (i.e. Amendment #3 **Task 11**). Once remobilized from sediments, ammonium is highly bioavailable for *M. aeruginosa* and appears to be short lived, either being uptaken rapidly or nitrified to form NO_3^- which is the dominant form of DIN in the lake, except in confined areas such as the Pahokee Marina which are theoretically less oxygenated. This competition between *M. aeruginosa* and nitrifying microbes is similarly not explicitly evaluated as part of Task 3A, but will also be considered in **Task 11**.

Overall, spatial and temporal measurements of the following components/processes are necessary to improve our fundamental understanding of their relation to HABs, develop quantitative maps and track changes in trends, predict the likelihood of sediment fluxes, and emergence models for HABs (and toxins). This task focused on monitoring the following parameters:

- Sedimentary distributions of solid phase precursors to dissolved nutrients, including a) Organic carbon, nitrogen, and phosphorous particulates, and b) Mineral adsorbent phases and their current phosphorus saturation level, e.g. iron oxides
- Sediment porewater dissolved components and fluxes, including a) Porewater content of dissolved organic and/or inorganic C, N, and P; b) redox parameters such as iron speciation and partitioning; and c) Fluxes of this dissolved material
- Dominant sediment respiration pathways, i.e. aerobic vs. anaerobic respiration processes (while this was originally planned as **Task 3B**, the data is more logically presented as part of this task)

Data is first presented for the most comprehensively monitored site, L001, with a focus on unraveling the dominant biogeochemical processes and controls and showcasing the applied methods, and then other sites are examined to reveal spatial variability and lake-wide correlations.

METHODS

Study sites and overall approach: Sediment cores were collected between 12/17/20 and 10/27/21. Sites were visited by project staff and by divers, depending on the scheduled activities. Sites comprised a range of lake locations and bottom types, with sampling conducted semi-monthly to biweekly, depending on the site and the time of year. The original sites included L005 and L006, but after visiting the sites and reevaluating the ultimately project goals, it was decided to focus only on the mud-bottom sites L001, LZ40, and L004, but at a greater frequency (Figure 3A-2 and Table 3A-1). The Pahokee Marina sites were added via Amendment #1 in concert with SFWMD and FDEP, shortly after the intense 2021 summertime bloom. Cores underwent processing for sediment solid phase and pore water analyses, and electrochemical profiling (Hg/Au voltammetry) was routinely conduct at Sites L001 and once at PHKM (although electrochemical profiling was formally planned to be performed in situ by the benthic lander under **Task 3B**). The inventory of collections and analyses is presented in Table 3A-2.

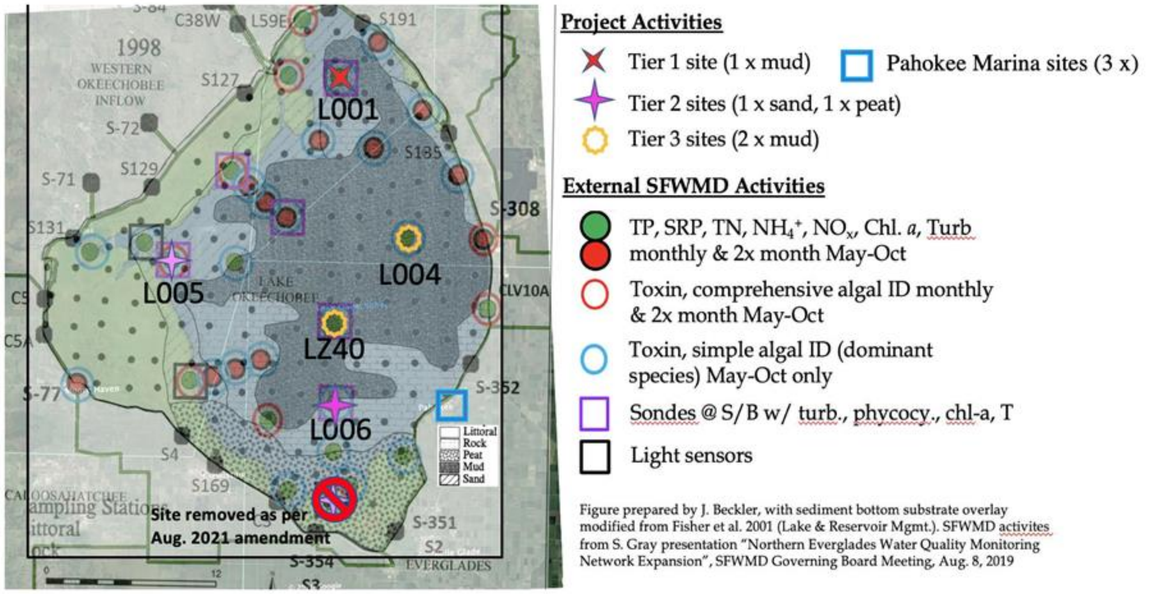

Figure prepared by J. Beckler, with sediment bottom substrate overlay modified from Fisher et al. 2001 (Lake & Reservoir Mgmt.). SFWMD activites from S. Gray presentation "Northern Everglades Water Quality Monitoring Network Expansion", SFWMD Governing Board Meeting, Aug. 8, 2019

Figure 3A-2: Project site map, including bottom type information (see bottom type key visible to the southeast of Lake), as well routine State of Florida monitoring activities. The Project site locations have been selected collocated with existing South Florida Water Management District sampling sites. Site names are directly on the map, except for Pahokee Marina inside (PHKM) and Pahokee Marina outside (PHKO) which are both in the blue box.

Table 3A-1: Coordinates for the sampled sites

SiteSite Name / bottom type	Lat (ddmmss.sss)	Long (ddmmss.sss)
North/L001 – mud/sand	270820.01	804736.23
West/L005 - sand	265724.22	805820.58
South/L006 – mud overlying clay	264921.21	804658.21
Central/LZ40 – mud	265406.53	804720.40
East/L004 – mud	265839.66	804234.49
Pahokee Marina (inside seawall)	264932.46	804042.54
Pahokee Marina (outside seawall)	264944.40	803947.94

Table 3A-2: Inventory of collected sediment cores and respective measurements.

Collection Date	Site	Method	Core diameter	Sectioned?	E-chem profile?	Solid phase	Surface & Bottom water	Pore water
12/17/20	L001	Diver	2"	yes	yes	yes	yes	yes
12/17/20	L005	Diver	2”	yes	no	yes	yes	no
12/17/20	L005	Diver	2"	yes	no	yes	yes	yes
12/17/20	LZ40	Diver	2”	yes	no	yes	yes	yes

2/26/2021	L001	Diver	3" & 2"	yes (2")	yes (Core B)	yes	yes	yes
2/26/2021	L005	Diver	3" & 2"	yes (2")	no	yes	yes	yes
2/26/2021	L006	Diver	3" & 2"	no	no	no	yes	yes
2/26/2021	LZ40	Diver	3" & 2"	yes (2")	no	yes	yes	yes
2/26/2021	L004	Diver	3" & 2"	yes (2")	no	yes	yes	yes
3/25/2021	L001	Mud dart	2"	yes	yes (Core A)	yes	yes	yes
3/25/2021	L006	Mud dart	2"	yes	no	yes	yes	yes
3/25/2021	L004	Mud dart	2"	yes	no	yes	yes	yes
4/29/2021	L001	Mud dart	2"	yes (Core B)	yes (Core A)	yes	yes	yes
4/29/2021	LZ40	Mud dart	2"	yes (Core A)	no	yes	yes	yes
4/29/2021	L004	Mud dart	2"	yes (Core A)	no	yes	yes	yes
5/27/2021	L001	Diver	3" & 2"	yes (Core A & B)	yes (Core B)	yes	yes	yes
5/27/2021	LZ40	Diver	3" & 2"	yes (Core B)	no	yes	yes	yes
5/27/2021	L004	Diver	3" & 2"	yes (Core B)	no	yes	yes	yes
6/17/2021	L001	Diver	3" & 2"	yes (Core B)	no	yes	yes	yes
6/17/2021	LZ40	Diver	3" & 2"	yes (Core B)	no	yes	yes	yes
6/17/2021	L004	Diver	3" & 2"	yes (Core B)	no	yes	yes	yes
6/17/2021	PHKM	Diver	3"	yes	no	yes	yes	yes
7/13/2021	L001	Mud dart	2"	yes (Core A & B)	yes (Core C)	yes	yes	yes
7/28/2021	L001	Diver	3"	yes (Core A)	Yes (Core A & B)	yes	yes	yes
7/28/2021	L004	Diver	3"	yes (Core A)	no	yes	yes	yes
7/28/2021	LZ40	Diver	3"	yes (Core A)	no	yes	yes	yes
7/28/2021	PHKM	Diver	3"	yes	no	yes	no	yes
8/10/2021	L001	Mud dart	2"	yes (Core B)	yes (Core A)	yes	yes	yes
8/10/2021	L004	Mud dart	2"	yes	no	yes	yes	yes
8/10/2021	LZ40	Mud dart	2"	yes	no	yes	yes	yes
8/25/2021	L001	Diver	3"	yes (CORE B)	yes (Core A)	yes	yes	yes
8/25/2021	L004	Diver	3"	yes	no	yes	yes	yes
8/25/2021	LZ40	Diver	3"	yes	no	yes	yes	yes
8/25/2021	PHKM	Diver	3"	yes (Core A)	yes (Core B)	yes	yes	yes
8/25/2021	PHKO	Diver	3"	yes	no	yes	yes	yes
9/15/2021	L001	Diver	3"	yes (Core B)	yes (Core A)	yes	yes	yes
9/15/2021	L004	Diver	3"	yes	no	yes	yes	yes
9/15/2021	LZ40	Diver	3"	yes	no	yes	yes	yes
9/15/2021	PHKM	Diver	3"	yes	no	yes	yes	yes
9/15/2021	PHKO	Diver	3"	yes	no	yes	yes	yes
9/29/2021	L001	Mud dart	2"	yes (Core B)	yes (Core A)	yes	yes	yes
9/29/2021	L004	Mud dart	2"	yes	no	yes	yes	yes
9/29/2021	LZ40	Mud dart	2"	yes	no	yes	yes	yes
10/27/21	L001	Diver	3”	yes	Yes (Core A)	yes	yes	yes
10/27/21	L004	Diver	3”	yes	no	yes	yes	yes
10/27/21	PHKM	Diver	3”	yes	no	yes	yes	yes
10/27/21	PHKO	Diver	3”	yes	no	yes	yes	yes

Sediment core and water column sample processing and analyses: All analyses are detailed in the project QAPP but are briefly described here. Upon return to FAU Harbor Branch or in a mobile processing laboratory, the cores underwent processing in an anoxic (N_2) glove bag. Overlying water was siphoned, and sediments were vertical sectioned into 0.5 to 1.5 cm increments (targeting 9 cm total depth but occasionally collected cores were shorter). A small sample of wet sediments were added to a pre-weighed 1.5 mL falcon tube (PP) for porosity, and a second sample was added to 15 mL falcon tubes that were filled with 10 mL of 0.5M HCl and pre-weighed (for total Fe(II) measurement). The remaining bulk sediments were centrifuged (3,000 RPM) for between 10 and 30 minutes, depending on the amount of pore water extracted, decanted via pouring into the back of a 10 mL syringe, and plunged through a 0.2 µm filter (PES) into 15 mL falcon tubes (PP). Overlying waters were also filtered similarly. Dissolved iron(II) ($Fe(II)_d$) was measured spectrophotometrically using the Ferrozine method (Stookey, 1970) immediately upon filtration in the glove bag. Total dissolved iron (Fe_d) was measured in separate aliquots by reducing pore waters in 100 mM hydroxylamine and 50 mM HCl prior to addition of Ferrozine, and dissolved iron(III) ($Fe(III)_d$) was quantified by the difference of Fe_d and $Fe(II)_d$ (Viollier et al., 2000). This technique should quantify both the truly soluble (<0.02 µm) and colloidal Fe(III) (0.02– 0.2 µm) (Beckler et a. 2015). Water samples were frozen prior to analyses of other nutrients. Immediately upon defrosting, samples were analyzed on a SEAL discrete autoanalyzer for soluble reactive phosphate (SRP) via the molybdate technique and for NO_3^-+NO_2^- via the cadmium reduction method and subsequent sulfanilamide/NEDD azo reaction (Strickland and Parsons 1972). For SRP, a blank sample was analyzed immediately prior to the actual analytical sample, and the results of the blank were subtracted from each analytical sample. Specifically, this blank did not contain ascorbic acid and therefore should not produce a color proportional to the SRP concentration. However, the blank does typically produce a slight color change due to reaction with dissolved silica and is therefore used to correct the measured SRP concentration for background absorbance due to silica. This correction can be a significant in sediments, and sometimes reduces the incorrect SRP concentration by up to 30%. Ammonium (NH_4^+) was measured via the salicylate-indophenol blue method (Bower and Holm-Hansen 1980). Sample aliquots for Dissolved organic carbon (DOC) and total dissolved nitrogen (TDN) analyses were added to 24 mL vials, diluted to 15 mL with deionized water, and analyzed via a Shimadzu TOC-L with autosampler and total nitrogen module. Organic N was determined by subtracting NH_4^+ and NO_3^-+NO_2^- from TDN.

The porosity samples were weighed again and then dried at 60˚C for 72 hours for dry weight determination. The total Fe(II) samples were weighed again and allowed to extract overnight prior to analyses of the supernatant via the Ferrozine Fe(II) analytical technique, and extracted Fe(II) concentrations were normalized to the sediment dry weight (i.e. µmol $gram^{-1}$ dry weight). The centrifuged sediments were frozen for later analyses. Analyses included 24-hr ascorbic acid extractions of iron hydroxides ($Fe(OH)_3$), with measurement of liberated Fe(II) via the ferrozine technique to extract mainly the most amorphous, reducible, and biologically labile iron hydroxide and oxyhydroxide minerals (e.g. ferrihydrite and lepidocrocite) (Kostka and Luther 1994). Liberated soluble reactive phosphorous (SRP) was also analyzed in extracts via the molybdate technique. Both the Fe and P were normalized to dry sediment weight, which itself was determined by a second pre/post sample weight difference after 72 hours of oven drying at 60˚C. Total phosphorous (SedP) was determined via a 500◦C burn followed by acidification with 1 M HCl and subsequent analyses via the molybdate technique. Non-Fe bound P was determined by subtracting the ascorbic acid extractable P from the total SedP. Loss-on-ignition (LOI) was determined via combustion at 550˚C and again at 950˚C to determine the organic weight and carbonate content. Total sediment carbon and nitrogen (SedC and SedN) were determined on dry samples via a Thermo Scientific FlashSmart Elemental analyzer.

Water column nutrient analyses was not specified as a task in the Scope of Work. However, we include this data in certain analyses (e.g. Figure 3A-16) as it provides a context for data interpretation. These measurements were not NELAC compliant are therefore only for research purposes.

Sediment core electrochemical profiling: $O_{2(aq)}$, Mn(II), Fe(II), $\sum H_2S$ (=H_2S + HS^- + S(0) + S_x^{2-})(Brendel and Luther, 1995), soluble organic–Fe(III) complexes, ($Fe(III)_{volt}$, Taillefert et al., 2000), and $FeS_{(aq)}$ (Theberge and Luther, 1997) were measured using solid-state mercury/gold (Hg/Au) voltametric microelectrodes designed for profiling sediment cores. Au/Hg voltammetric microelectrodes were constructed as previously reported (Luther et al., 2008) and used as part of a 3-electrode system (including Ag/AgCl reference and Pt counter electrodes) with a DLK-70 potentiostat (Analytical Instrument Systems, Inc.). Sediment cores were placed under an automated microprofiler, the electrode was inserted into the microprofiler manifold so that the electrode tip extended downwards into the core overlying water, and a 1/16" OD pH electrode (Microelectrodes, Inc) was affixed with electrical tape to the Au/Hg voltametric electrode so that they would both be monitoring the same depth simultaneously. Over the course of a few hours, electrodes were continuously lowered in small increments (0.2 to 4 mm) depending on the observed gradients of analytes of interest; the sediment/water interface was profiled the most carefully. A sequence of scans were operated at each depth with the sequence adjusted depending on observations.

Unlike $Fe(III)_d$ determined using the Ferrozine technique, $Fe(III)_{volt}$ measured voltammetrically should only represent truly soluble Fe(III) (less than a few nm) (Buffle and Horvai, 2000; Taillefert et al., 2000). However, laboratory testing demonstrates that Fe(II) phosphate complexes may also generate an electrode response, although this has not been rigidly evaluated (Beckler, unpublished). $O_{2(aq)}$ was quantified by linear sweep voltammetry (LSV), whereas $Fe(III)_{volt}$, Fe(II), Mn(II), $\sum H_2S$, and $FeS_{(aq)}$ were detected by square-wave voltammetry (SWV), between -0.1 and -1.75 V at a scan rate of 200 mV/s after a conditioning step of 10 s at -0.1 V when $Fe(III)_{volt}$ and $\sum H_2S$ were not detected (Brendel and Luther, 1995). If these compounds were detected, an initial conditioning step of 10 s at -0.9 V was added to this procedure to clean the electrode surface between subsequent analyses (Taillefert et al., 2000). Voltammograms were integrated using the semi-automated VOLTINT software package (Bristow and Taillefert, 2008). Electrodes were calibrated with Mn^{2+}, and concentrations of Fe(II) and $\sum H_2S$ determined with the pilot ion method (Brendel and Luther, 1995; Luther et al., 2008). As their exact chemical composition is unknown, $Fe(III)_{volt}$ and $FeS_{(aq)}$ could not be quantified (Theberge and Luther, 1997; Taillefert et al., 2000). To compare their current intensities in different samples, each electrode's sensitivity to Mn(II) was normalized to a typical value (0.12 nA uM^{-1} Mn(II)), and this ratio was used to adjust their current response.

Flux determination: Diffusive Oxygen Uptake (DOU) was determined from the electrochemical profiles using Fick's First Law for porous media:

$$F_{DOU} = -\Phi D^0 \left(\frac{\delta C}{\delta Z}\right)$$

where F_{DOU} is the flux (mmol m^{-2} day^{-1}), Φ is sediment porosity, and D^0 is the molecular diffusion coefficient of solutes in water (cm^2 s^{-1}), and dC/dZ is the O_2 gradient across the sediment water interface (Boudreau 1997). Fluxes for other pore water analytes were determined similarly but using the near surface concentration gradient, always excluding the overlying water data point, always including the shallowest sediment data point, and then extending downward over the apparent linear range, although never below 2 cm (i.e. typically the 2.5, 7.5, and 1.5 cm datapoints).

ACTIVITIES SCHEDULED vs. COMPLETED

A total of 47 cores were collected for solid phase and pore water analyses over the project period, compared to an expected 33. (Sampling was expected monthly for Feb, Mar, Apr and biweekly for May-Oct). The expected cores to be analyzed were monthly at L001 and L004, and all sampling events for L001. While we did not meet the required sampling frequency of core sampling missing a total of five scheduled cores, we did compensate for this by collecting 13 profiles at other dates or sites not formally scheduled. An additional nine cores from L001 and one additional core from Pahokee Marina were also collected and profiled electrochemically, compared to nine formally scheduled as part of **Task 3B**.

All planned analyses of cores was completed except for total dissolved phosphorous (and thus dissolved organic P), and Total sediment C and N for Pahokee cores only (this data will be finished by 6/30/21). We were unable to derive an efficient method for its measurement after accounting for the pore water volumes of other analytes. Typically, with 3" cores we are limited to 10-20 mL of pore waters for 1 cm tall depth increments, depending on porosity. We have a high degree of confidence in all other data except for total dissolved nitrogen, and thus dissolved organic N, which sometimes returned negative values. Because ammonium concentrations are typically very high relative to the organic fraction, we are subtracting a large number from another large number, and the errors can be significant after accounting for a dilution factor sometimes as high as 20x (required to work with small volumes). We have since learned of a new technique for analyzing pore waters in these cases (Burdige and Zheng 1998), although it requires substantially more time and effort as the sample must be individually basified and sparged prior to TDN analyses to remove the volatile ammonium (at high pH). We plan to implement these changes for future phase of the project. For the results to date, we present the organic-N values as measured but with zero values displayed when a negative concentration was determined by difference, but we caution their use for decision making and these suspect values are flagged in the database (**Task 1C**). Results from water column and benthic chamber analyses of TDN/org-N/NH_4^+ are reasonable in the context of historical lake measurements, suggesting this is only a pore water related problem.

Table 3A-3: Scheduled vs collected cores, with indications of those actually scheduled and sampled (X), scheduled but not sampled (O), or additional cores not formally part of the scope of work (A). Electrochemical profiling activities are also indicated (E).

Month (period)	L001	LZ40	L004	PHKM	PHKO	Other cores or notes
Dec (2020)	A (E)	A				L5, L5
Feb	X	X	X			L5, L6
March	X (E)	O	X			L6
April	X (E)	X	X			
May (1)	O					Water samples only
May (2)	X (E)	X	X			
June (1)	O					Water samples only
June (2)	X (E)	X	X	A		
July (1)	X (E)					
July (2)	X	X	X	A		
Aug (1)	X (E)	A	A			
Aug (2)	X (E)	X	X	X (E)	X	
Sep (1)	X (E)	A	A	X	X	
Sep (2)	X (E)	X	X			
Oct (1)	O					Water samples only
Oct (1)	X (E)	O	X	X	X	

RESULTS & DISCUSSION

Site L001 sediment profile data: The data is first presented as a time series of each individual vertical section (Figure 3A-3). Sediment profiles of solid phase and pore water concentrations resulting from the sectioning are presented in Figure 3A-4. Vertical discrimination is important for understanding geochemical processes and future diagenetic modeling. $Fe(II)_d$ profiles are generally non-uniform as a function of depth, with concentration gradients occasionally rapidly increasing immediately below the sediment-water interface (e.g. 3/25/21), and at other times increasing deeper (e.g. 5/27/21 and 6/15/21), and with one instance (9/15/21) illustrating the entire surface 9 cm sediment column is dominated by its accumulation. These patterns could be caused by periods of intense respiration or low removal in the late spring and fall, or periods of more resuspension and thus reoxidation in the winter/early spring and during summer storms. Surprisingly, $Fe(III)_d$ on the other hand remained very low to the point that it was no longer measured (i.e. measured through 7/13/21) and these measurements were instead substituted for *total* solid phase Fe(II) measurement, which capture a true measure of the overall amount of iron reduction having occurred in the sediments (whereas dissolved $Fe(II)_d$ is only a fraction due to its adsorption onto solid minerals). In previously studies of organic rich environments such as blackwater river estuaries (Beckler et al. 2015) or even in the upper Caloosahatchee Estuary (Beckler, unpublished), $Fe(III)_d$ comprised the majority of the total dissolved iron inventory, suggesting that it is either not generated in significant quantities in the lake or is rapidly consumed. However, this substitution was potentially short sighted due to the unanticipated increase in pore water dissolved $Fe(II)_d$ in late summer, which may have resulted in considerable $Fe(III)_d$ production. Solid phase ascorbic-acid extractable reactive iron (i.e. $Fe(OH)_3$) was typically greatest in surface sediments and was progressively observed in lesser concentrations with depth, suggesting it is either freshly deposited or regenerated via oxidation in near-surface sediments, or cumulatively removed as a function of depth due to microbial iron respiration processes.

SRP in pore waters is low in the winter and increases in the spring, consistent with a pulse in respiration as the environment warms; however, removal is evident over the mid-summer period consistent with resuspension events (see electrochemical profile data below). By late summer, concentrations increased once again probably due to an increase as iron respiration intensifies and it is again released to pore waters. Total sediment phosphorous increases as the temperature warms, although the near-surface concentrations (0 – 3 cm) show more uniformity seasonally. However, the relative fraction bound to Fe hydroxides is much more variable, showing increases over the summer, perhaps reflecting the solubilization of organic-P and the subsequent incorporation into poorly crystalline Fe mineral phases. Pore water DOC exhibits a peak in near surface sediments on several sampling events, although concentrations remain low throughout most cores except for a few exceptions, which typically occurred in the winter and spring (2/26/21 and 4/29/21). DOC concentrations also appear to be low over the summer when iron hydroxides were at their highest levels, potentially due to iron-mineral associations. Total sediment carbon and nitrogen typically covaried and were generally elevated in near-surface sediments in the winter and spring but appeared more uniformly vertically distributed over the summer and early fall, reflecting enhance fresh deposition and vertical redistribution beginning in June. Some of this variability was explained by porosity, with lower porosities also reflecting lower total C and N. Ammonium profiles were more typical with respect to a diagenetic profile, with concentrations low at the surface and progressive increases with depth. Surprisingly, NH_4^+ peaked in the spring probably due to a pulse in respiration, but *decreased* with the progression of summertime, despite presumably stronger respiration. Overall, the patterns when comparing NH_4^+ vs. SRP suggest that the P is much more subject to mineral associations and is more sensitive to redox transformations. Finally nitrate (and nitrite) were extremely low compared to ammonium, reflecting the poor permeability and high respiration rates occurring in these sediments, i.e. oxygen penetration is minimal and any nitrate that would be formed is likely rapidly consumed via denitrification.

Site L001 electrochemical profiles: The sediment core Hg/Au voltametric profiles are plotted with all analytes for a single month presented in a single panel, as the true value in this technique is comparing the fine-scale vertical patterns between the various measured analytes (Figure 3A-4). Dissolved O_2 was never detected below 2mm in sediments, reflecting the impermeability, intense respiration, and considerable oxygen demand of reduced species in these organic rich muds. However, it is difficult to truly "visualize" the sediment water interface in the relatively turbid overlying waters. Regardless, this does not affect the fluxes calculated (see "Diffusive flux determination" section below), which only use the maximum O_2 gradient across the sediment-water interface. Dissolved Fe analytes do appear to dominate most of the depth interval over which the measurements were conducted, providing strong evidence of the importance of microbial iron reduction in Lake Okeechobee mud sediments and highlighting the need to understand the dynamics regarding associated nutrient cycling. Active iron biogeochemical cycling (i.e. evidenced by either dissolved Fe(II) or organic-Fe(III)) does appear to intensify and approach closer to the surface with the onset of the summer, consistent with the pore water profile data (Figure 3A-3).

On the other hand, hydrogen sulfide (or an organic sulfur analyte associated with Fe reduction; see discussion of **Task 3C**) was detected in the spring and early summer, at a time when pulses of "fresh" organic material may stimulate respiration with such an intensity that both iron and sulfate reduction can cooccur; however, sulfate concentrations are obviously limited in the lake environment compare to the marine environment, so concentrations never exceed a few tens of µM. Still, the relative role of these two pathways have implications for nutrient cycling, with sulfate reduction probably causing more enhanced nutrient release due to the subsequent sulfidization of iron oxides and thus a depressed P-sequestration capacity. While no $Fe(III)_d$ was detected in pore water measurements (Figure 3A-3), the detection of significant quantities of organic-Fe(III) in the voltametric profiles suggests either: 1) The dissolved Fe(III) is electrochemically labile but not labile for reaction with the Ferrozine reagent; or 2) The dissolved Fe(III) is essentially an artifact caused by the oxidation of organic-Fe(II) or Fe(II)-phosphate complexes at the electrode surface, the latter a phenomenon that we have preliminary evidence for, but may theoretically be possible. The implications are the same however, in that either electrochemical "peak" indicates dissolved Fe and thus active Fe cycling. However, we must heed caution: the concentrations of dissolved Fe(II) derived from the electrochemical profiles do not appear to be quantitative, as they are up to an order of magnitude greater than those from pore water sectioning. From the opposite perspective, the pore water sectioning and centrifugation may also artifactually remove iron from the system. Therefore, while the pore water sectioning $Fe(II)_d$ is a better candidate for routine mapping/monitoring because it is more quantitative and able to be measured by more research groups, the voltametric data is instead only qualitative (at least for Fe(II)) but is more powerful for resolving the vertical zonation of the various respiration processes.

In all cores, there is a vertical gap of 0.2 to 3.8 cm between the detected O_2 and the next detected analyte, either dissolved Fe(II) or organic-Fe(III); excepting the profile from 8/10/21 in which there was no other analytes detected. This gap probably comprises the zone in which some other anaerobic respiratory process dominates, most likely denitrification, albeit very low nitrite is detected in pore waters (Figure 3A-3; measured as the sum NO_3^-+NO_2^-); however, the Hg/Au voltametric technique is not capable of measuring any N redox analytes. Another possibility is that iron cycling is active but the detection limits of the technique are not low enough to detected any dissolved Fe near the surface. Regardless, we plotted the "Dissolved Fe first detect depth" seasonally (Figure 3A-5). Dissolved Fe is detected only deeper in the winter, but this detection depth approaches the surface through mid-summer. However, in mid-July, the depth move drastically lower until 8/10/21 when no iron was even detected; later in August dissolved iron is once again detected and again approaches the surface. We suspect this is related to resuspension events during the mid to late summer, which result in the reoxidation of the surface sediment layer, the regeneration of iron hydroxides, and thus either the direct removal of dissolved Fe or its removal via adsorption onto newly formed iron hydroxides. Indeed, the decrease in the pH in the surface sediment layers 7/28/21 and 8/25/21 support this hypothesis, as the oxidation of Fe(II) indeed is expected to decrease the pH (Figure 3A-4). Additionally, dissolved O_2 fluxes directed into sediments (Figure 3A-5), i.e. the diffusive oxygen uptake (DOU) calculated from the O_2 flux gradient across the sediment-water interface for the voltametric profiles in Figure 3A-4, increase rapidly during the period. While this could also be caused by overall organic-deposition or temperature enhanced sediment remineralization rates, the stark decline in *benthic water column* SRP that begins on 7/28/21– despite still having significant *sediment* pore water diffusive SRP flux (at least calculated from sediment pore water profiles; see the "Sediment Diffusive Fluxes" section below) – may indicate that the regeneration of a surface iron hydroxide layer is actually preventing this "apparent" SRP flux from leaving the sediments to the water column, potentially demonstrating that the storms serve as a "redox switch" to limit the true P flux. More quiescent conditions after 8/10/21 then allows the gradual reestablishment of iron reducing conditions; accordingly, the pH steadily increases in the surface sediments. Overall, these exciting results may provide insights into the biogeochemical controls of phosphate dynamics that are unattainable from conventional pore water separation techniques due to the inherent homogenization and relatively poor depth resolution, especially near the critical surface layer. These dynamics are critical for informing mitigation activities such as dredging, sediment capping, or aeration. These conventional pore water separation techniques are still important for routine inventory mapping and probably ammonium flux determination as well.

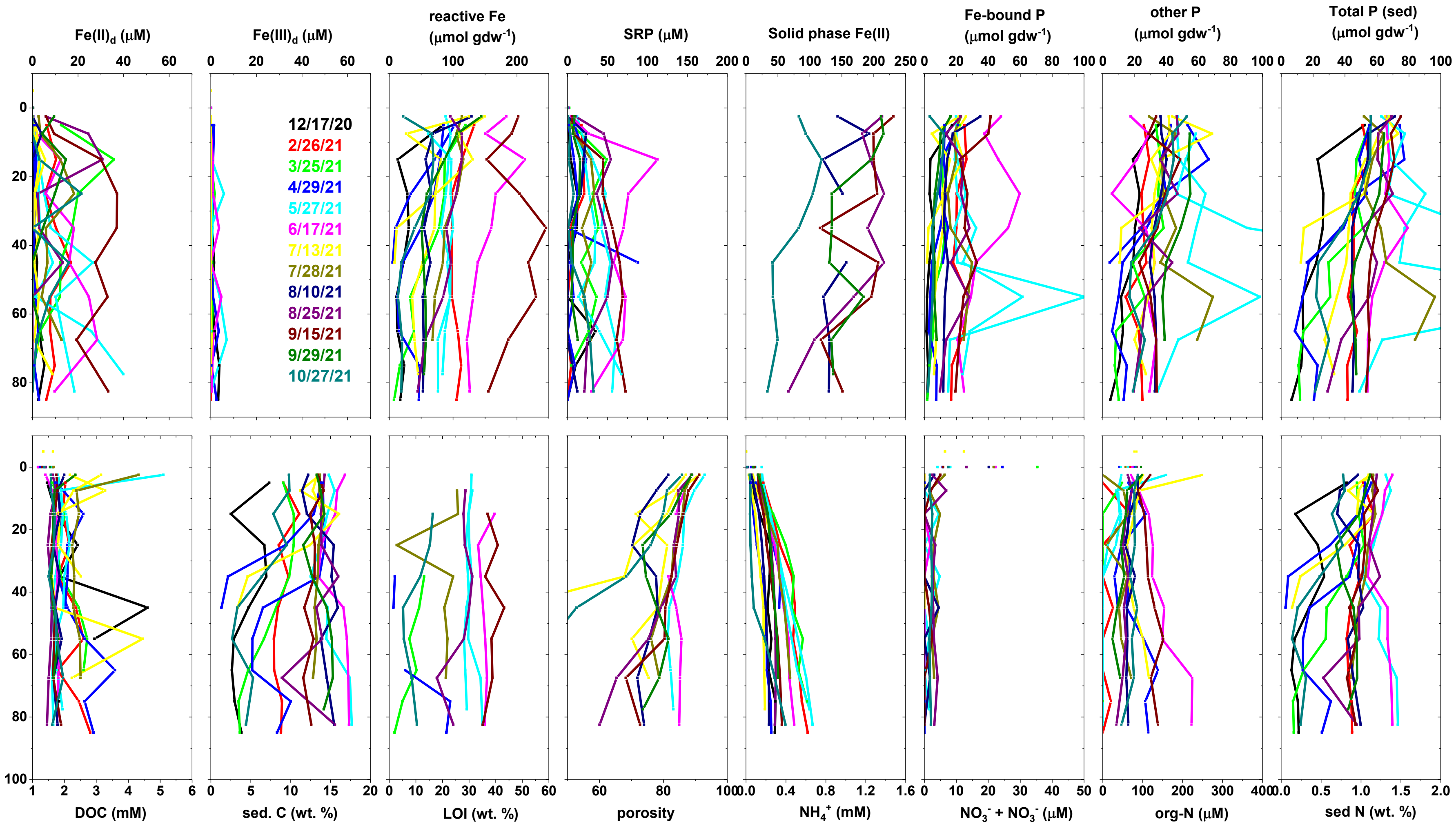

Figure 3A-3: Sediment core profiles from the most comprehensively monitored site, L001.

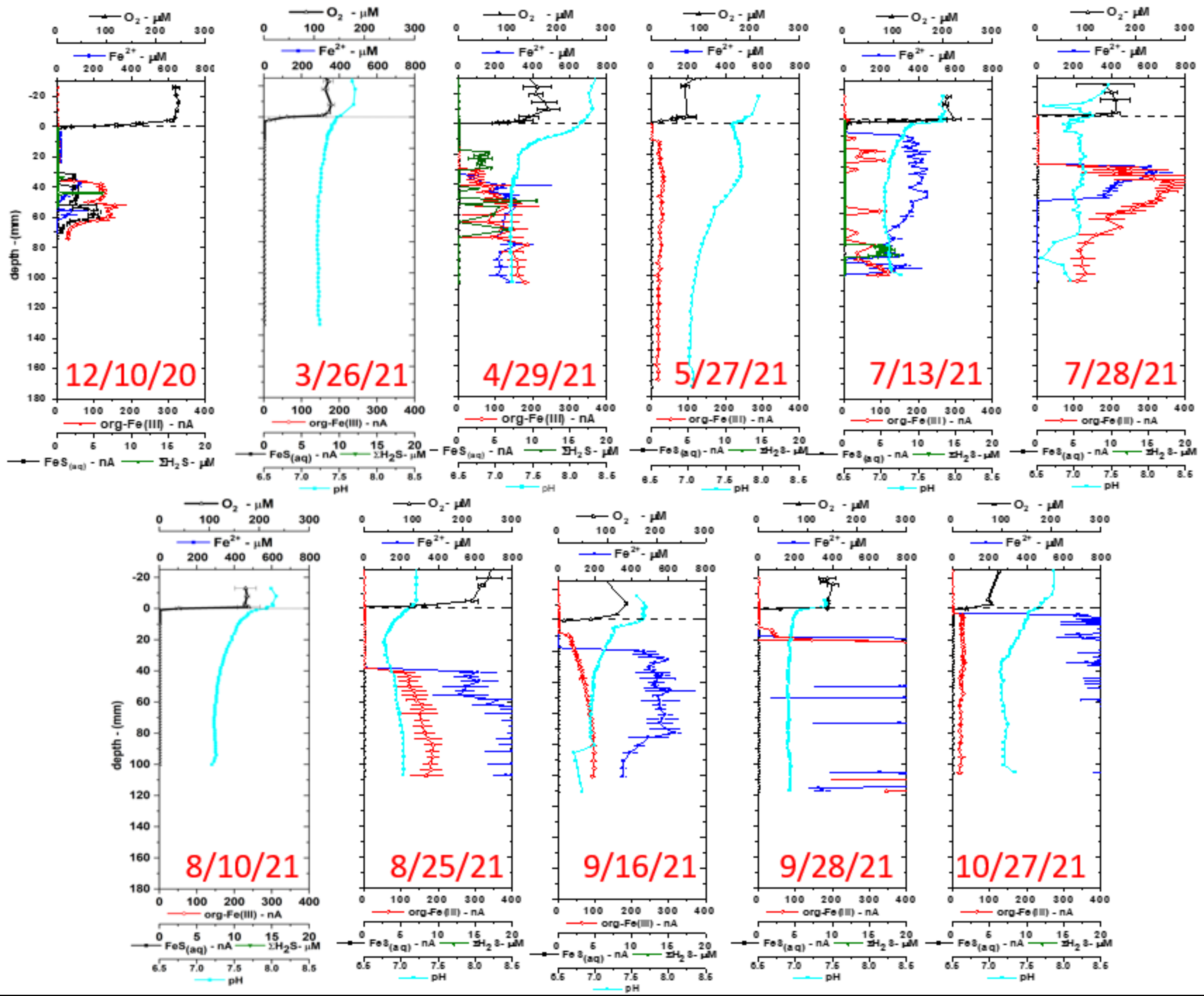

Figure 3A-4: Sediment core electrochemical depth profiles. Dissolved O_2 fluxes across the sediment-water interface were used to calculated Diffusive Oxygen Uptake (DOU). Fe reduction (evidenced by dissolved Fe^{2+} and organic-Fe(III)) demonstrates increasing intensity until 7/28/21, when a storm event potentially causes reoxidation of the surface Fe oxygen layer and removal of the dissolved Fe via oxidation, also evidenced by a low pH in this zone. It gradually returns beginning after 8/10/21 with the onset of highly Fe-reducing conditions.

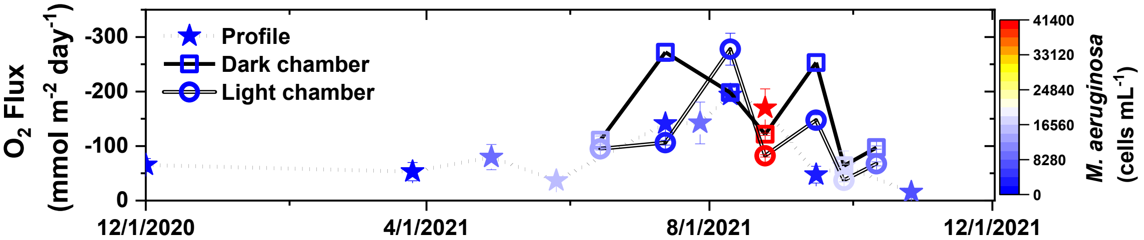

Figure 3A-5: Diffusive Oxygen Uptake (DOU) calculated from voltammetric profiles (stars), as well as the total Benthic Oxygen Demand (BOD) from the Task 3B dark and light benthic chamber incubations. Colors represent the ambient bottom water *M. aeruginosa*. The DOU demonstrated enhanced O_2 consumption is evidenced by at least 7/13/21 but declines by 9/16. We suspect this is caused at least partially by storm-induced sediment reoxidation. The BOD on the other hand, is more often of larger magnitude because it includes bottom water respiration processes. The presence of *M. aeruginosa* limits the BOD- perhaps due to photosynthetic benthic O_2 production, but cell presence has a limited effect on the DOU.

Integrated L001 pore water profile and electrochemical iron onset depths: The full annual time series data in Figure 3A-6 provide tremendous new insights into the seasonal cycling of the sediment geochemical conditions at site L001 for nearly a full year (Dec. 2020 thru Oct. 2021). This time series data can help explain water column nutrients, and thus HAB trends, as observed by more routine conventional monitoring activities. First, SRP generally demonstrates an increase from winter to a maximum in June, but then a sudden decrease by late July (unfortunately an analytical issue prevented SRP determination for the 7/13 sample event) and a relative minimum on the 8/10/21 sampling event, coinciding with the apparent sediment reoxygenation event (i.e. evidenced in Figure 3A-4). Concentrations steadily rebuild until 9/15/21 but then decline again 10/27/21, consistent with more typical winter time conditions observed in December of 2020. While the expected buildup in SRP over the spring/early summer are expected as respiration increases, the precipitous decline after June may be indicative of mineral-mediated P sequestration processes (Figure 3A-7). As discussed in the previous section, the proposed reoxidation of Fe minerals as evidenced by the deepening of the dissolved Fe detection depth, the lower pH, and the enhanced sediment DOU could explain the decrease in pore water SRP inventories due to scavenging in pore waters. Although not formally part of this project, water column SRP were measured and similarly show a stark decline between 7/28/21 and 8/10/21 (referenced below and illustrated in Figures 3A-16 and 6-7), suggesting the termination of sediment diffusive fluxes and/or the scavenging of water column SRP by resuspended iron hydroxides. Ultimately, this event seemed to lead to a stark decline in *M. aeruginosa* at this time (see Figures 4-22 and 6-7). Figure 3A-6 shows a decrease in pore water $Fe(II)_d$ over this late summer time period, providing additional support for this hypothesis. The eventual rebuilding of SRP inventories in the fall can then be attributed to the reestablishment of Fe reducing conditions, until ultimately decreasing as more typical of the wintertime conditions in the late fall. *M. aeruginosa* does not seem to ever reestablish itself at intense levels, suggesting that this event was a primary driver of the 2021 bloom.

This highly complex P cycling is overlaid upon a more conservative *total* sediment P time series. While the total solid phase P similarly increases with warming temperatures, given the decades of eutrophication, these inventories are far less likely to undergo seasonal differences. While some new input can be expected from river/creek inflows, we suspect instead that these changes are instead due to P in deeper sediment layers (i.e. below 9 cm) being remobilized and transported upwards into the sampled profile interval (0 to 9 cm). The iron hydroxide-bound P ($Fe(OH)_3$-P) generally covaried with the concentrations of the iron hydroxides themselves ($Fe(OH)_3$). However, their relative ratio, which should be considered as a measure of the P-saturation capacity, did vary seasonally, with the lowest values evident in September. Interpretation is ongoing, but we suspect this saturation is expected to be related to SRP pore water concentrations, with the greatest SRP pore water concentrations expected when the ratio is most elevated and Fe reduction is most intense (Figure 3A-6). Over interannual and decadal timescales, these mineral inventories and potentially, increasing P saturation, could explain the overall increase of water column SRP inventories.

The trends in pore water NH_4^+ inventories were surprising (Figure 3A-6). Ammonium concentrations increased with the onset of spring and early summer probably due to the intense respiration of labile organic-N, but generally decreased starting in June. Combined with generally greater pore water SRP concentrations beyond mid-summer, the pore water and diffusive flux NH_4^+:PO_4^{3-} ratio (Figures 3A-6 & 3A-17, respectively) exhibited stark difference between the spring and early summer vs. mid-summer to early fall. Considering that *M. aeruginosa* “prefers” elevated N:P ratios, this variability could have contributed to highest bloom concentrations similarly occurring in the earlier half of the year. However, the actual N or P availability to the organism would depend on both the diffusive and resuspension fluxes, given that diffusive fluxes did not seem to be a significant SRP source to the water column, whereas NH_4^+ diffusive fluxes were persistent, intense, and highly bioavailable for biological utilization (described in **Task 3B**). However, resuspension was likely a source of both pore water localized nutrients, although NH_4^+ concentrations arguably would require a stronger resuspension event to remobilize the most elevated pore water concentrations, which were more consistently localized at deeper sediment depths than the SRP. Thus, accurate simulation and modeling of sediment legacy nutrient loading to the water column must consider both the temporal and vertical distributions of N and P, as well as the role that the resuspended depth interval would play regarding the relative concentrations of N:P. We are further evaluating these dynamics by comparing this task’s results to those of Task 6 continuous monitoring of bottom water nutrient concentrations. Additionally, the Amendment #3 in situ resuspension monitoring (**Task 11**) and laboratory sediment erosion experiments (**Task 12**) can also shed light on these processes. The apparent removal of this NH_4^+ from the pore waters requires further examination. Because nitrification or annamox, i.e. the two major removal processes, are expected to be minimal below a few cm given the lack of appropriate oxidants (i.e. O_2 and NO_2^-), some other process is likely responsible. Given the extremely high reactive iron hydroxide concentrations in Lake Okeechobee sediments, we suspect that the newly discovered Feammox process (Figure 3A-8) is a potential explanation, in which the NH_4^+ removal is coupled to the reduction of iron hydroxides. This would also be expected to promote additional dissolved Fe(II) and thus adsorbed SRP release, thereby coupling both the N and P cycles. An inverse relationship between iron hydroxides and pore water NH_4^+ suggests that mineral surface site availability exerts a kinetic control on this process if it is occurring, which could be further complicated by passivation of surface sites by phosphate adsorption.

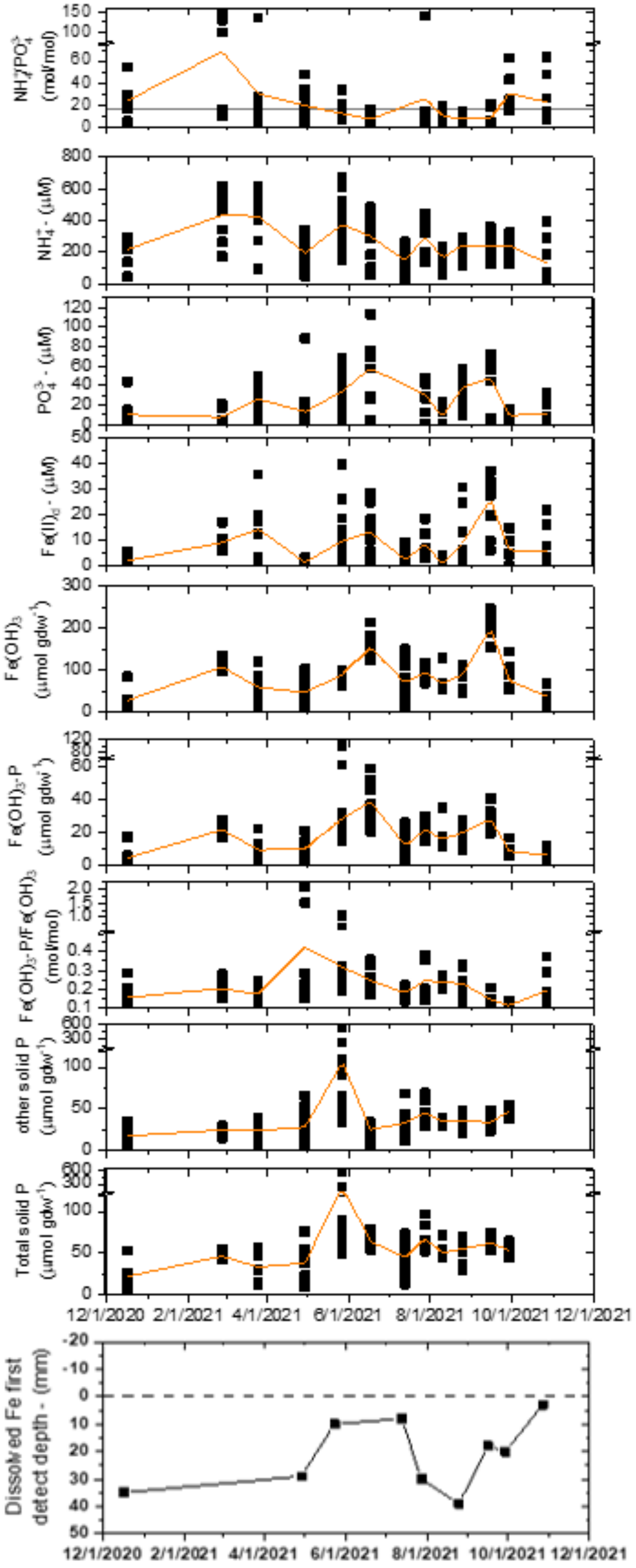

Figure 3A-6: Site L001 pore water inventories plotting each of the individual pore water datapoints from Figure 3A-3. The fitted line corresponds to the mean values. The overlying water data points from the cores are excluded from the graphs and fitted line. The "Dissolved Fe first detect depth" is instead determined from the electrochemical profiles in Figure 3A-4. This is the depth at which either dissolved Fe(II) or organic-Fe(III) is first detected via high resolution electrochemical profiling. Note, the profile from 8/10/21 never detected any iron and is therefore omitted; however, this provides even more evidence for the idea that the iron was removed via oxidation during late summer.

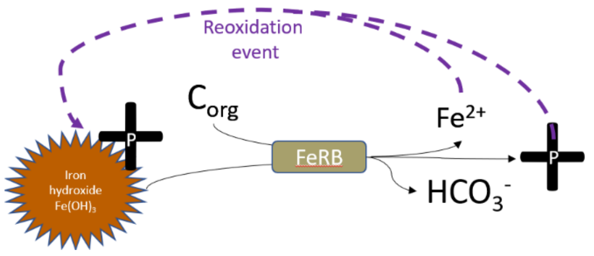

Figure 3A-7: Proposed scheme of Fe-coupled P cycling. P adsorbed onto Fe hydroxides is released due to microbial iron reduction (FeRB) fueled by organic carbon, but reoxidation of the new Fe(II) results in the scavenging of pore water SRP, generating complex cycling on seasonal and shorter timescales associated with wind-induced resuspension.

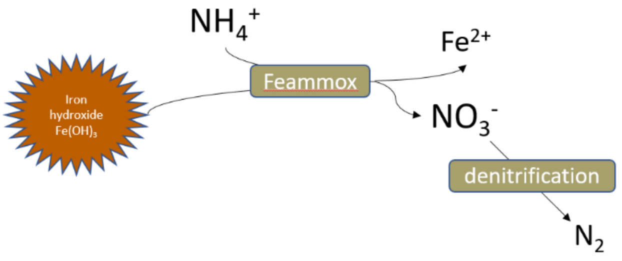

Figure 3A-8: The Feammox process which can be ultimately fueled by organic matter decomposition to form NH_4^+. The process can result in either nitrate or N_2, but ultimately, the NO_3^- is expected to be denitrified and removed from the system.

<u>Spatial comparison to other sites (L004 and LZ40)</u>: As Fisher et al. 2009 demonstrates decadal trends in sediment nutrients, our study is instead focused on explaining seasonal variability, the spatial variability, and any geochemical explanations for the long-term variability, whether it be changes in external inputs, or inherent geochemical properties. Indeed, Fisher et al. 2009 demonstrated that both pore water PO_4^{3-} and NH_4^+ increased in concentration between 1988 and 1998, although the change in PO_4^{3-} was larger. Surprisingly, solid phase total N did not increase. We again restate our overarching hypotheses that if true, could explain both processes: 1) Eutrophication causes enhanced organic carbon and nutrient loading, and thus excessive chemical reducing equivalents in sediments; 2) Fe hydroxides are in turn decreasing in concentration due to this more reducing environment, and Fe hydroxide P saturation states are in turn elevated, retaining less SRP; 3) this decrease in Fe hydroxides, combined with enhanced P "coating" that passivates the overall surface reactivity of these Fe hydroxides, may limit NH_4^+ removal via the Feammox process.

Sites L004 and LZ40 are mud sites from deeper areas of the lake, farther away from river/creek inputs. Overall, pore water NH_4^+ content generally decreased in the order L001>LZ40>L004 (Figure 3A-9), consistent with previous mapping efforts in 1998 (Fisher et al. 2009; Figure 3A-10). Pore water profiles from these sites are presented in Figures 3A-11 & 3A-12. Seasonal differences were not as evident compared to L001, perhaps reflecting variability in these external inputs, a lack of temporal dependency with regards sediment-localized NH_4^+ production, seasonally disparate production and removal processes that serve to moderate annual concentrations, or simply that a decreased sampling frequency limits the inferable information. Seasonal Feammox rate determination planned in Amendment #3 is aimed at resolving this question. In contrast, these two sites do generally show a similar pore water SRP seasonal pattern as L001, with enhanced concentrations in the late summer and fall, with similar implications on the pore water inorganic NH_4^+:PO_4^{3-} ratio. Dissolved Fe(II) similarly peaks in the summer, suggesting the SRP release is linked to iron hydroxide reduction. Surprisingly, iron hydroxides ($Fe(OH)_3$) and associated phosphate ($Fe(OH)_3$-P) are generally enhanced during this period, suggesting that there are high rates of Fe recycling; i.e. the minerals are continuously reduced and reoxidized, with this recycling perhaps critical for maintaining anaerobic microbial iron reduction. This recycling could be enabled via frequent resuspension and reoxidation of the fine grained surface sediment flocculant layer. In contrast, total sediment P only increases slightly during this period, suggesting that the Fe hydroxide fraction is the most critical and active form in regulating nutrient cycling.

Pahokee Marina: Sediments from inside (Figure 3A-13 & 3A-15) and outside (Figure 3A-14) of the Pahokee Marina demonstrate much greater nutrient and dissolved Fe concentrations than the other open lake areas. The grant was initially amended (Amendment #1) to include the Pahokee Marina sites because this is a hotspot of bloom formation, and elevated NH_4^+ was observed in the bottom waters after the intense summertime 2021 blooms. The sediment pore waters are indeed elevated in NH_4^+ relative these other sites, with approximately 3x greater mean concentrations than the next highest site, L001. Pore water SRP inside the marina (PHKM) and outside the marina (PHKO), on the other hand, was approximately 2x and 5x greater, respectively than at the three primary open lake sites (L001, L004, and LZ40) (Table 3A-4). Microbial Fe reduction is more intense at these sites than the open lake sites, providing a potential explanation for these nutrient patterns. The pore water SRP enrichment at PHKO relative to PHKM was surprising, however, considering that the marina was expected to have greater inventories of nutrients given its confinement and potential source pollution. These processes may have to do with mineralogy – one explanation is that the more cumulatively reducing conditions fueled by organic inputs within the marina have led to relatively short residence time of SRP within marina sediments. Analyses of total sediment C and N is pending and will hopefully provide some clues. These measurements were conducted to provide actionable information; specifically, should dredging of the marina proceed given that it is a confined, tractable solution. However, our data shows that nutrients are elevated both inside and outside of the marina, expanding the potential dredging target areas. Overall, results demonstrate that additional mapping efforts should likely be conducted prior to commencing any mitigative actions. We continue to sample these sites (monthly) as part of Amendment #3 **Task 11**.

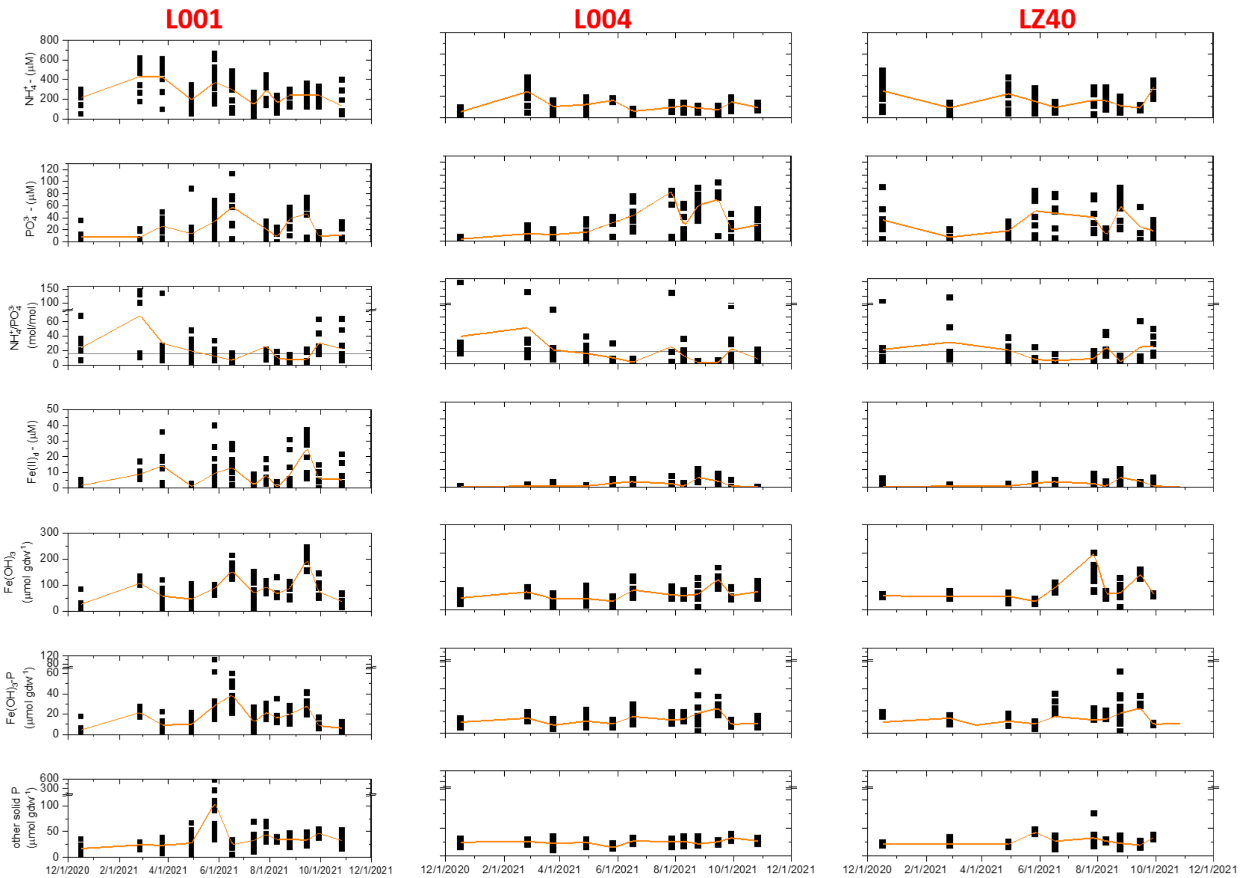

Figure 3A-9: Time series comparison of L001 (reproduced from Figure3A-6 for easy comparison), L004, and LZ40 sites sediment conditions. Each data point corresponds to a single sediment core section, and the line is fitted through the mean.

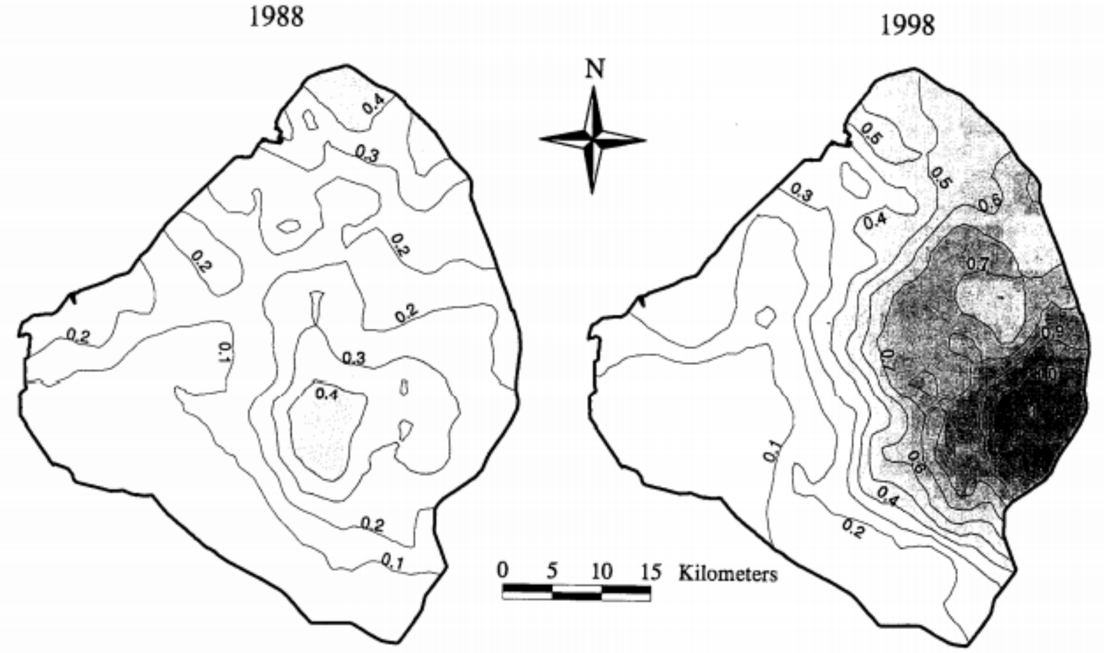

Figure 2. -Maps of dissolved reactive phosphorus content (mg L^{-1}) in the porewater of Lake Okeechobee surface (0-10 cm) sediments in 1988 and 1998.

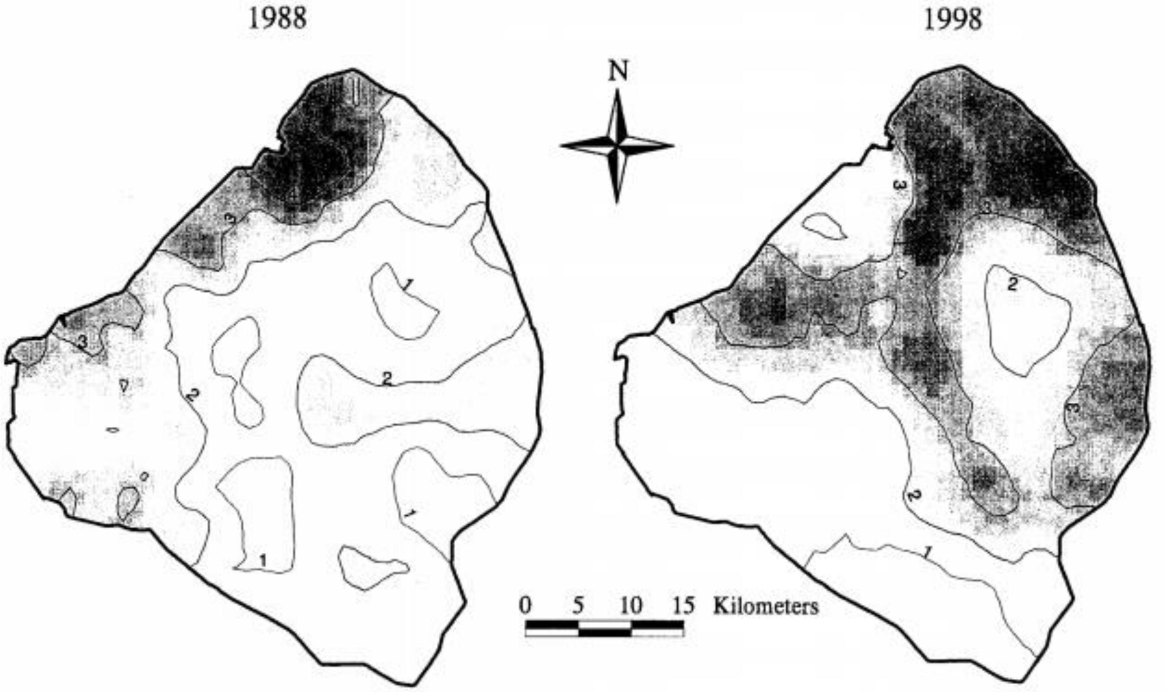

Figure 6.-Maps of the ammonium-N content (mg L^{-1}) in the porewater of Lake Okeechobee surface (0-10 cm) sediments in 1988 and 1998.

Figure 3A-10: Maps of pore water SRP (top) and NH_4^+ reproduced from Fisher et al. 2009. Approximate site locations of are marked in the bottom right map: L001 = green, L004 = blue, LZ40 = red.

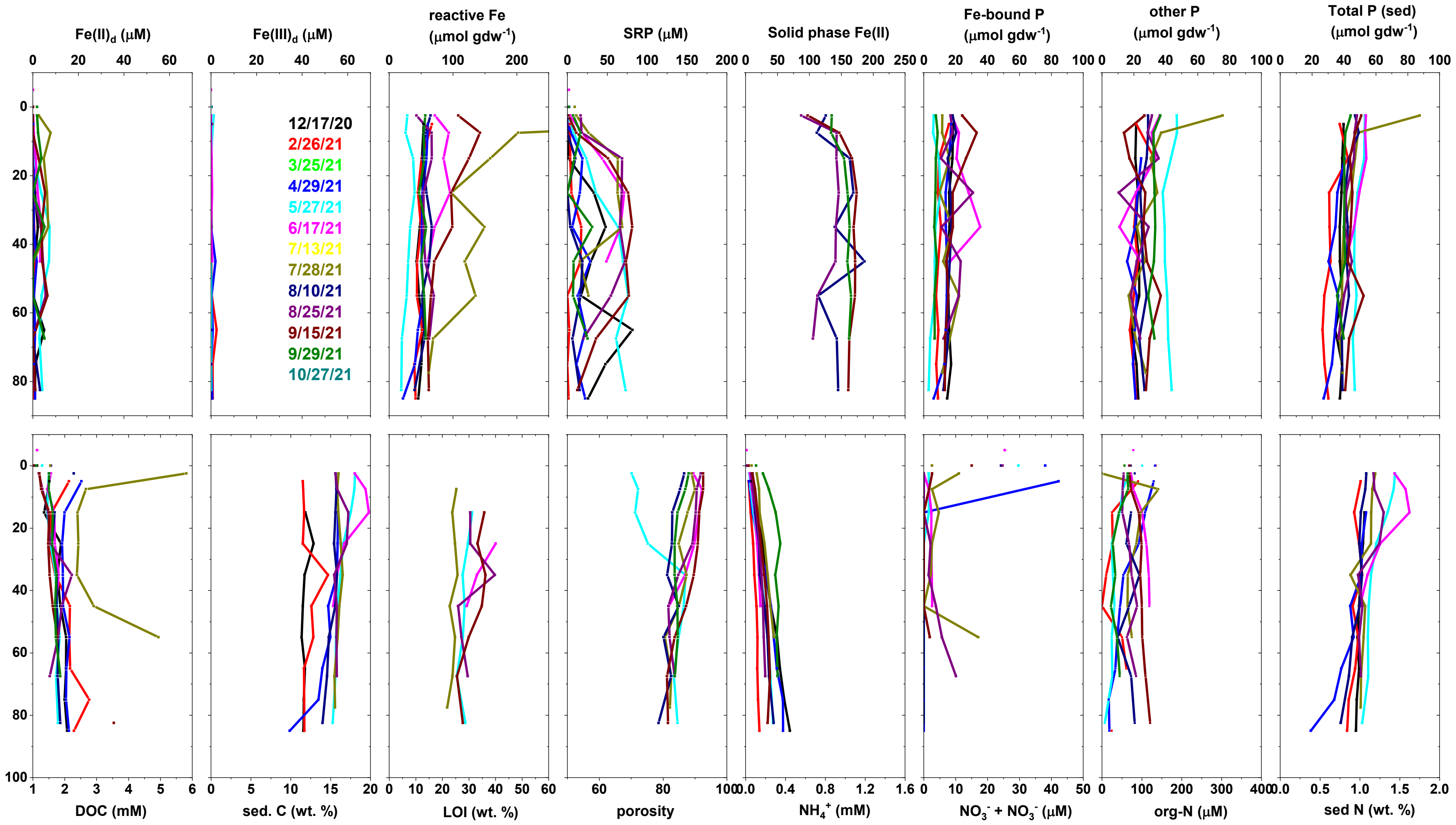

Figure 3A-11: Sediment profiles from site LZ40.

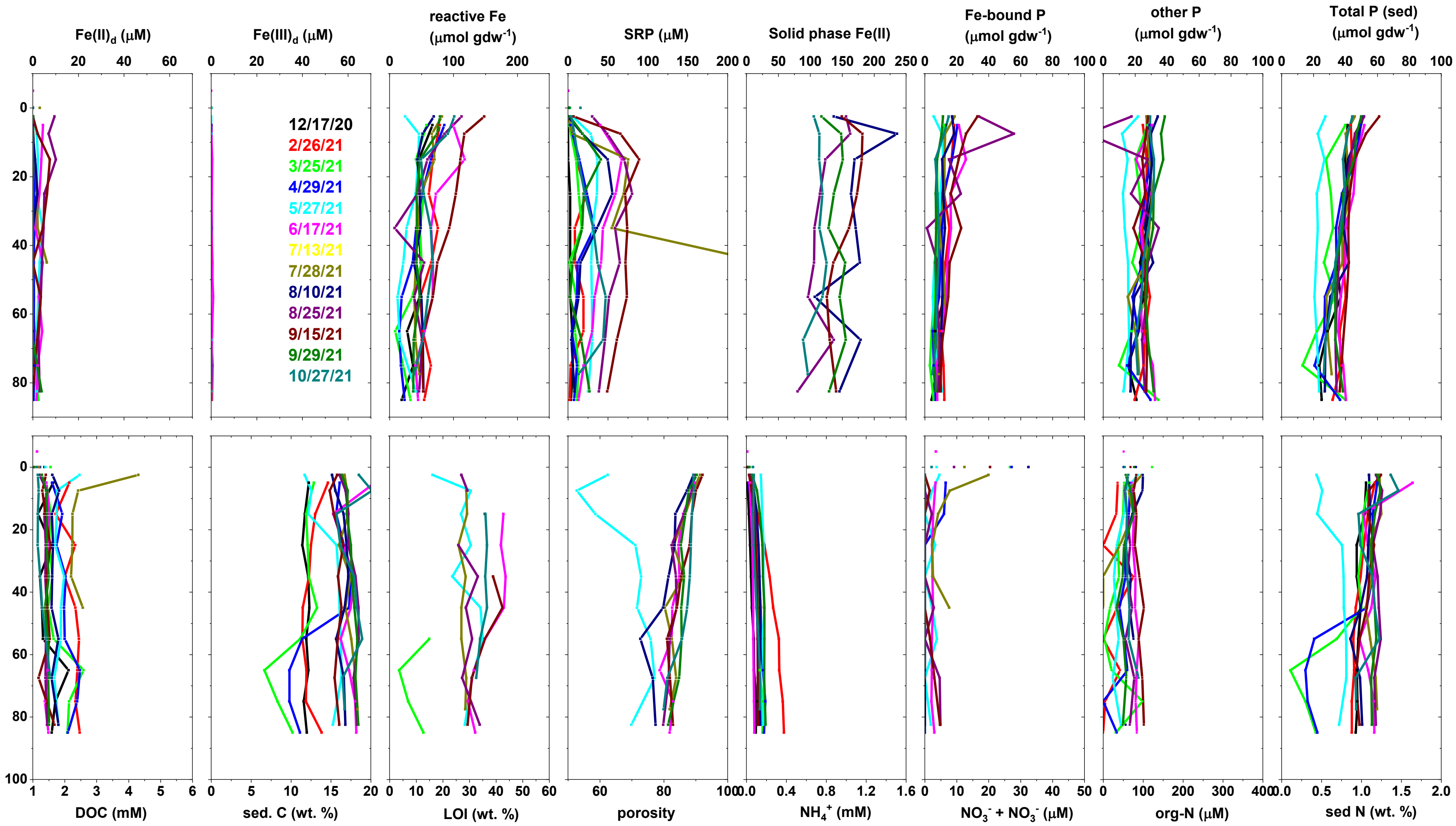

Figure 3A-12: Sediment profiles from site L004.

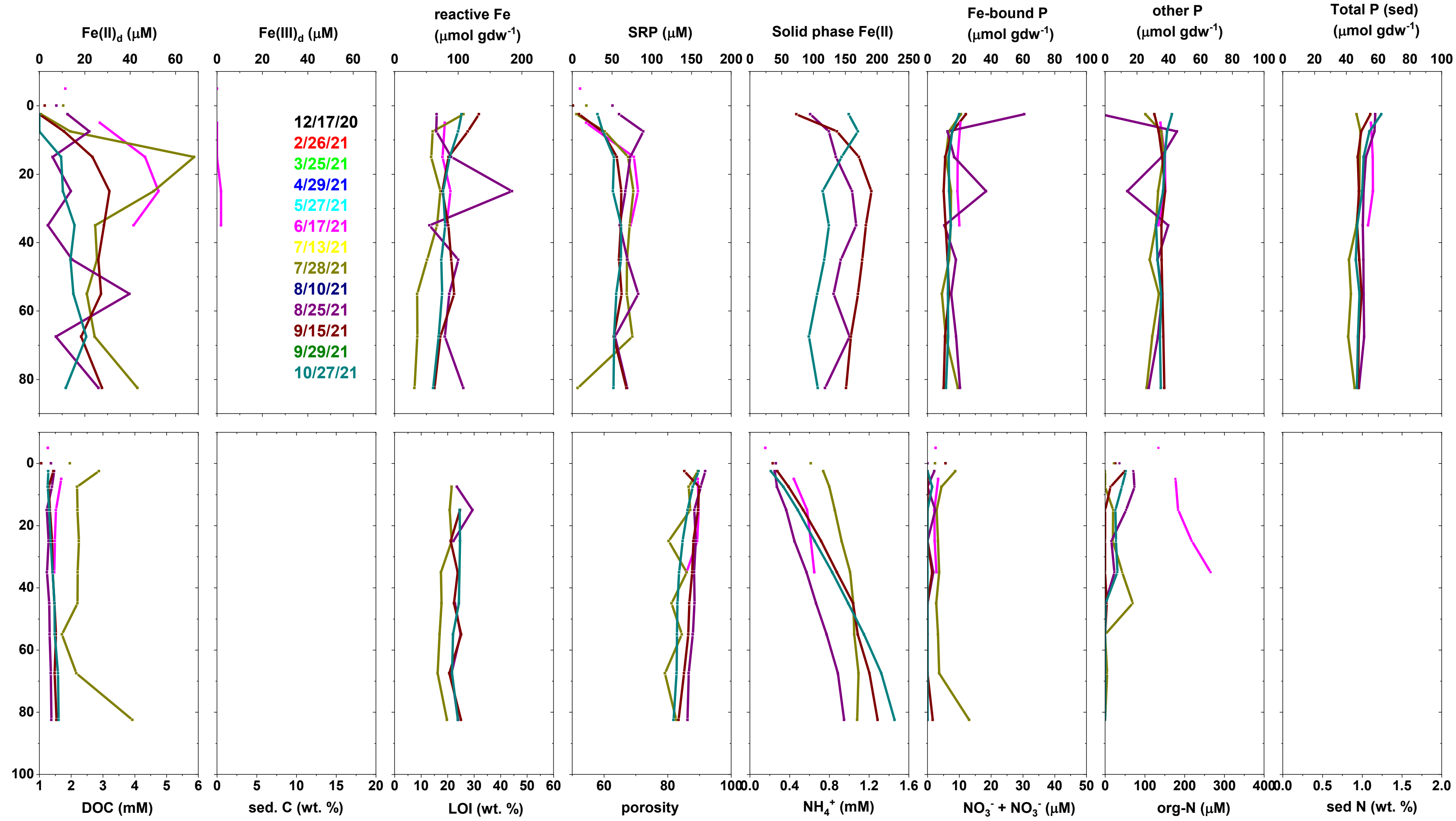

Figure 3A-13: Sediment profiles from Pahokee Marina (inside).

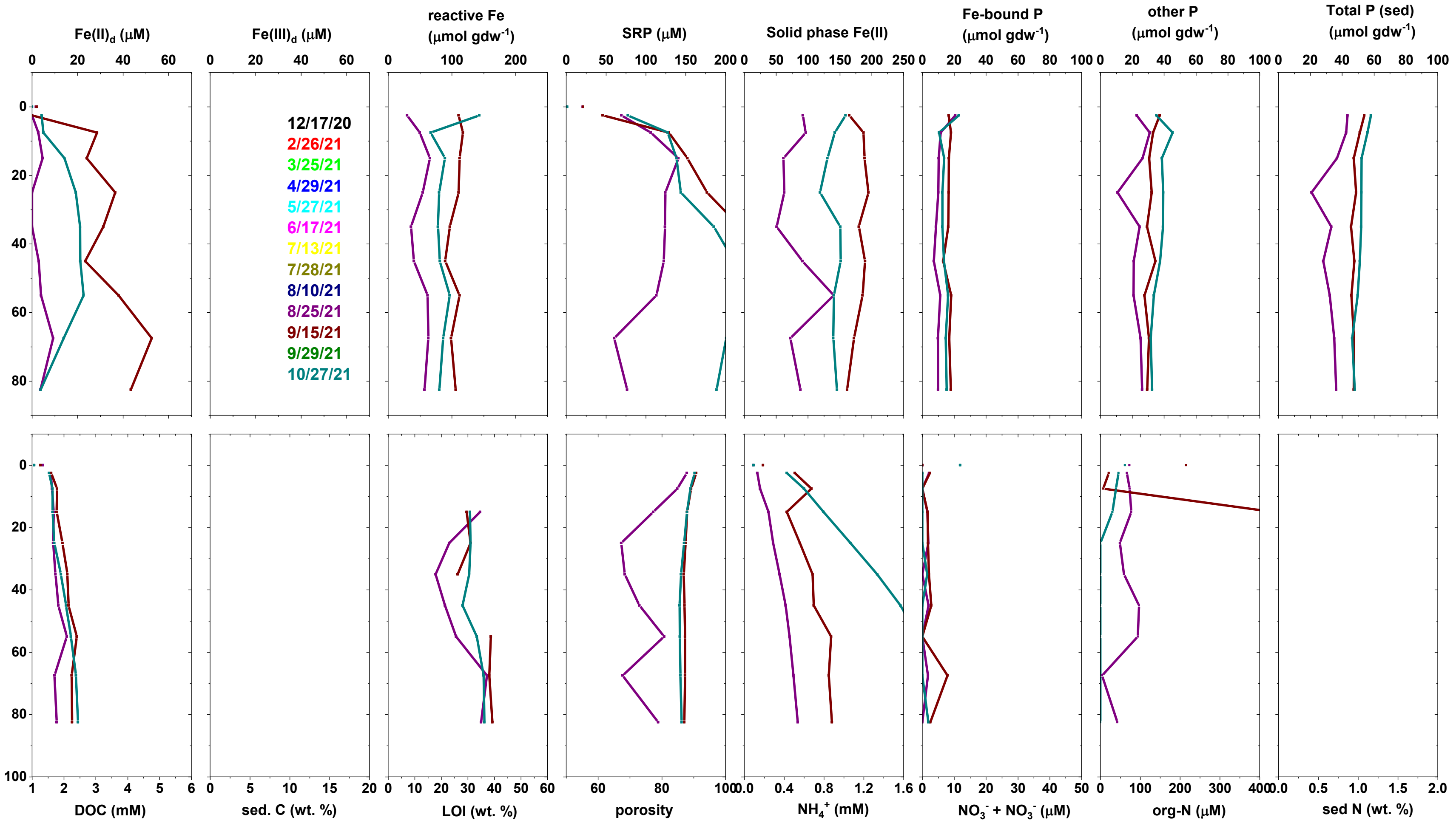

Figure 3A-14: Sediment profiles from Pahokee Marina (outside).

Table 3A-4: Pore water summary statistics by site. S308 refers to a single core collected in the lake, just inside the control structure. It is not included in the Scope of Work but is included here for reference. Units are µM for dissolved analytes and %w/w for Sed P, Sed N, and Sed C.

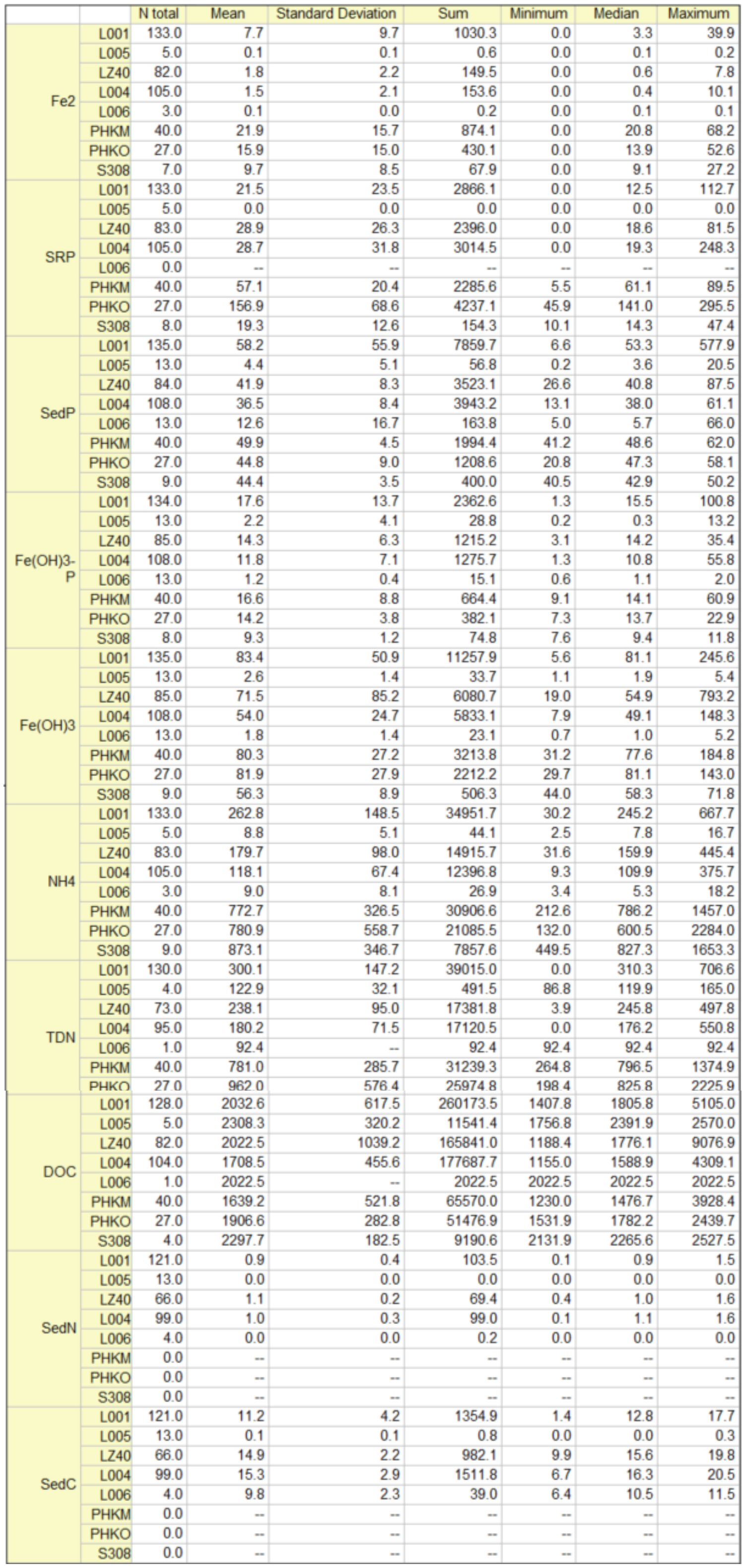

		N total	Mean	Standard Deviation	Sum	Minimum	Median	Maximum
Fe2	L001	133.0	7.7	9.7	1030.3	0.0	3.3	39.9
	L005	5.0	0.1	0.1	0.6	0.0	0.1	0.2
	LZ40	82.0	1.8	2.2	149.5	0.0	0.6	7.8
	L004	105.0	1.5	2.1	153.6	0.0	0.4	10.1
	L006	3.0	0.1	0.0	0.2	0.0	0.1	0.1
	PHKM	40.0	21.9	15.7	874.1	0.0	20.8	68.2
	PHKO	27.0	15.9	15.0	430.1	0.0	13.9	52.6
	S308	7.0	9.7	8.5	67.9	0.0	9.1	27.2
SRP	L001	133.0	21.5	23.5	2866.1	0.0	12.5	112.7
	L005	5.0	0.0	0.0	0.0	0.0	0.0	0.0
	LZ40	83.0	28.9	26.3	2396.0	0.0	18.6	81.5
	L004	105.0	28.7	31.8	3014.5	0.0	19.3	248.3
	L006	0.0	--	--	--	--	--	--
	PHKM	40.0	57.1	20.4	2285.6	5.5	61.1	89.5
	PHKO	27.0	156.9	68.6	4237.1	45.9	141.0	295.5
	S308	8.0	19.3	12.6	154.3	10.1	14.3	47.4
SedP	L001	135.0	58.2	55.9	7859.7	6.6	53.3	577.9
	L005	13.0	4.4	5.1	56.8	0.2	3.6	20.5
	LZ40	84.0	41.9	8.3	3523.1	26.6	40.8	87.5
	L004	108.0	36.5	8.4	3943.2	13.1	38.0	61.1
	L006	13.0	12.6	16.7	163.8	5.0	5.7	66.0
	PHKM	40.0	49.9	4.5	1994.4	41.2	48.6	62.0
	PHKO	27.0	44.8	9.0	1208.6	20.8	47.3	58.1
	S308	9.0	44.4	3.5	400.0	40.5	42.9	50.2
Fe(OH)3-P	L001	134.0	17.6	13.7	2362.6	1.3	15.5	100.8
	L005	13.0	2.2	4.1	28.8	0.2	0.3	13.2
	LZ40	85.0	14.3	6.3	1215.2	3.1	14.2	35.4
	L004	108.0	11.8	7.1	1275.7	1.3	10.8	55.8
	L006	13.0	1.2	0.4	15.1	0.6	1.1	2.0
	PHKM	40.0	16.6	8.8	664.4	9.1	14.1	60.9
	PHKO	27.0	14.2	3.8	382.1	7.3	13.7	22.9
	S308	8.0	9.3	1.2	74.8	7.6	9.4	11.8
Fe(OH)3	L001	135.0	83.4	50.9	11257.9	5.6	81.1	245.6
	L005	13.0	2.6	1.4	33.7	1.1	1.9	5.4
	LZ40	85.0	71.5	85.2	6080.7	19.0	54.9	793.2
	L004	108.0	54.0	24.7	5833.1	7.9	49.1	148.3
	L006	13.0	1.8	1.4	23.1	0.7	1.0	5.2
	PHKM	40.0	80.3	27.2	3213.8	31.2	77.6	184.8
	PHKO	27.0	81.9	27.9	2212.2	29.7	81.1	143.0
	S308	9.0	56.3	8.9	506.3	44.0	58.3	71.8
NH4	L001	133.0	262.8	148.5	34951.7	30.2	245.2	667.7
	L005	5.0	8.8	5.1	44.1	2.5	7.8	16.7
	LZ40	83.0	179.7	98.0	14915.7	31.6	159.9	445.4
	L004	105.0	118.1	67.4	12396.8	9.3	109.9	375.7
	L006	3.0	9.0	8.1	26.9	3.4	5.3	18.2
	PHKM	40.0	772.7	326.5	30906.6	212.6	786.2	1457.0
	PHKO	27.0	780.9	558.7	21085.5	132.0	600.5	2284.0
	S308	9.0	873.1	346.7	7857.6	449.5	827.3	1653.3
TDN	L001	130.0	300.1	147.2	39015.0	0.0	310.3	706.6
	L005	4.0	122.9	32.1	491.5	86.8	119.9	165.0
	LZ40	73.0	238.1	95.0	17381.8	3.9	245.8	497.8
	L004	95.0	180.2	71.5	17120.5	0.0	176.2	550.8
	L006	1.0	92.4	--	92.4	92.4	92.4	92.4
	PHKM	40.0	781.0	285.7	31239.3	264.8	796.5	1374.9
	PHKO	27.0	962.0	576.4	25974.8	198.4	825.8	2225.9
DOC	L001	128.0	2032.6	617.5	260173.5	1407.8	1805.8	5105.0
	L005	5.0	2308.3	320.2	11541.4	1756.8	2391.9	2570.0
	LZ40	82.0	2022.5	1039.2	165841.0	1188.4	1776.1	9076.9
	L004	104.0	1708.5	455.6	177687.7	1155.0	1588.9	4309.1
	L006	1.0	2022.5	--	2022.5	2022.5	2022.5	2022.5
	PHKM	40.0	1639.2	521.8	65570.0	1230.0	1476.7	3928.4
	PHKO	27.0	1906.6	282.8	51476.9	1531.9	1782.2	2439.7
	S308	4.0	2297.7	182.5	9190.6	2131.9	2265.6	2527.5
SedN	L001	121.0	0.9	0.4	103.5	0.1	0.9	1.5
	L005	13.0	0.0	0.0	0.0	0.0	0.0	0.0
	LZ40	66.0	1.1	0.2	69.4	0.4	1.0	1.6
	L004	99.0	1.0	0.3	99.0	0.1	1.1	1.6
	L006	4.0	0.0	0.0	0.2	0.0	0.0	0.0
	PHKM	0.0	--	--	--	--	--	--
	PHKO	0.0	--	--	--	--	--	--
	S308	0.0	--	--	--	--	--	--
SedC	L001	121.0	11.2	4.2	1354.9	1.4	12.8	17.7
	L005	13.0	0.1	0.1	0.8	0.0	0.0	0.3
	LZ40	66.0	14.9	2.2	982.1	9.9	15.6	19.8
	L004	99.0	15.3	2.9	1511.8	6.7	16.3	20.5
	L006	4.0	9.8	2.3	39.0	6.4	10.5	11.5
	PHKM	0.0	--	--	--	--	--	--
	PHKO	0.0	--	--	--	--	--	--
	S308	0.0	--	--	--	--	--	--

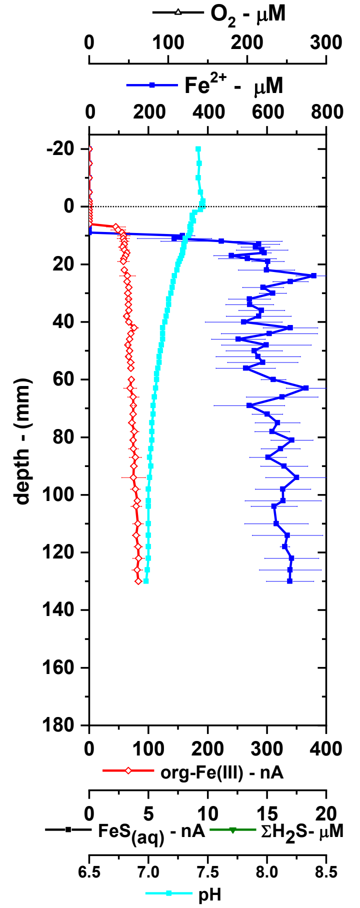

Figure 3A-15: Pahokee Marina electrochemical profile from 8/25/21. Despite minimizing the volume of core overlying water (by pushing up the core piston so that only ~2cm of overlying water is present) in an attempt to ensure O_2 diffusion from the atmosphere, the overlying waters were anoxic, suggesting that extremely high diffusive oxygen uptake is present. Sediments are highly iron-reducing, providing an explanation for high pore water nutrients and fluxes to the overlying water as demonstrated via routine SFWMD sampling (the initial motivation for this Pahokee Marina effort).

<u>Sediment diffusive fluxes and water column coupling</u>: The pore water fluxes of inorganic nutrients from the three primary sites (L001, L004, LZ40) were calculated and placed in the context of water column measurements obtained the same day (Figure 3A-16), although the figure also includes data from the other two sites that were visited routinely (L005, L006). Fluxes were only routinely measured at the former given the relative importance of mud bottom sites as legacy load and remineralization hotspots, compared to the sand (L005) or clay with thin mud veneer (L006). It is also challenging to collect pore waters at fine resolution from these bottom types using sediment coring techniques. Overall, data interpretation is ongoing and there is a wealth of data not plotted that should also be considered in the context of sediment fluxes, e.g. **Task 2A** field data (water column O_2, turbidity, etc.) and **Task 2B** data (phytoplankton community structure, total cyanobacteria, etc.).

SRP pore water diffusive fluxes were relative uniform in intensity across these three primary sites, although seasonal trends were obvious. Fluxes increased in June, but at all sites, temporarily decreased at one or two points over the summer probably due to the surface sediment reoxidation discussed above. Fluxes continued to peak in Aug./Sep. (excepting one anomalously high value at L001 in June). These fluxes generally mirrored water column SRP concentrations in the spring and early summer, although fluxes remained elevated in late summer and fall despite water column concentrations decreasing. We suspect this observation is misleading and is actually an artifact of the pore water gradient technique used to measure fluxes; while pore water gradients remained high, we expect that surface oxidized mineral layers effectively quenched fluxes past the sediment-water interface. Ammonium fluxes, on the other hand, were at times an order of magnitude greater at L001 than at LZ40 or L004. At L001, NH_4^+ fluxes peaked early in the spring, nearly coinciding with the first and strongest *M. aeruginosa* bloom that occurred at this site, perhaps due to warming temperatures and respiration of labile organic nitrogen as discussed above. However, concentrations steadily declined through the year, perhaps to the Feammox process also discussed above. At LZ40 and L004 however, there was much less of a consistent trend except a relatively minor increase in the late summer and fall. It is not clear why L004 and LZ40 exhibit different behavior than L001, although the former two sites are more similar in composition to one another than the Kissimmee River influenced L001 site. Surprisingly, L001 on average contained lesser overall total sediment carbon and nitrogen than these two other sites (Table 3A-4). However, the relative concentrations of C/N/P in sediments at L004 and LZ40 demonstrate greater depletion of N, and especially P, relative to site L001 (Figure 3A-17). Remineralization at L001 is likely intense, suggesting the Kissimmee is inputting more labile solid nutrient forms, whereas L004 and LZ40 may instead be comprised of more refractory solid phase nutrient forms already stripped of labile organics and nutrients due to their age, while being subsequently "spilled over" from the shallower sites. Another set of potential explanations are due to continued resuspension at L004 and LZ40. This could 1) Enable the protection of the organics by association with reprecipitating iron oxides. Indeed, an organic mineral matrix is evident at the turbid sites (Missimer et al. 2020), and dissolved pore water Fe^{2+} is present in low concentrations, or 2) prevent the establishment of a well-defined vertical diagenetic cascade, preventing efficient syntrophic microbial respiration.

Dissolved iron fluxes were similarly more intense at L001 in comparison to LZ40 and L004 (Figure 3A-16). The iron fluxes were more sporadic, probably due to the redox sensitive nature of this analyte, although the discernible seasonal trends can be logically explained: fluxes were elevated in early spring due to the pulse of remineralization (as with NH_4^+ fluxes), were more variable over the summer due to resuspension/reoxidation events, and then reached a seasonal maximum in late summer and fall when microbial Fe reduction was most intense. The Fe fluxes somewhat mirror patterns in DOU; this is logical considering that the more chemically reducing conditions (i.e. a higher DOU) should allow Fe to remain in the reduced dissolved form. Finally, because NO_3^-+NO_2^- was routinely detected in core overlying waters and the first core section, but was almost always remove from below this depth, the fluxes were not determined. While some researchers use core overlying water and the shallowest sediment section gradient, or do the same but by substituting lake bottom water for the core overlying water data point, we prefer to use only pore water gradients (excluding overlying waters) due to the artificial accumulation of these analytes in overlying waters. Because of greater overlying water concentrations than in the underlying sediments, we can at least infer that NO_3^-+NO_2^- fluxes would have nearly always have been negative (indicating a flux into the sediments due to denitrification). Sediment core incubations or denitrification incubations could be used to determine these flux rates, but nitrification in overlying waters complicates this process. Instead, nitrogen isotope tracing techniques offer the best approach and will be explored in new **Task 11**.

The bottom water inorganic N:P ratios were compared as a function of time to those of the sediment fluxes (Figure 3A-18). The sediment NH_4^+:SRP ratio generally mirrors the water column DIN:SRP, suggesting they are closely coupled. Relative to the Redfield ratio (N:P=6.6), the L004 and LZ40 bottom water column theoretically became biologically N-limited in mid-summer, lagging a similar trend by approximately 1 month of the sediment fluxes becoming N-depleted. While this does not necessarily mean that there is not enough N to support the growth of phytoplankton, the growth of *M. aeruginosa* is likely not favorable due to its preferred high-N regime. Indeed, cell counts were most elevated in the late spring and early summer, except for a two individual sampling events at L004 after August (Figure 3A-16). While this could reflect bloom patchiness, sampling artifacts (i.e. the fact that samples are not vertically integrated), or just short term variability, the general long term trend overall suggests that the sediment fluxes and water column nutrients are closely coupled.

CONCLUSIONS & FUTURE WORK

Going forward, we are excited to more closely analyze the sediment inventories and fluxes in the context of water column nutrients and the *M. aeruginosa* bloom. Comprehensive figures of virtually all of the measured parameters will be generated for analyses of these time series. While spatial mapping has been conducted over decade scales via the SFWMD, we have instead for the first time to our knowledge, obtained the high frequency sediment inventories and fluxes. The timing of the nutrient fluxes appears related to the observed bloom intensities, for example why the *M. aeruginosa* bloom of 2021 occurred relatively early in the HAB season, i.e. in April and May (based on **Task 2B** data and SFWMD data). More specifically we provide some preliminary evidence for the controls of both N and P dynamics in the sediments, both being redox controlled and both potentially involving iron. For the data generated to date, one of the most important items that still needs addressing is the phosphorous solid phase speciation, for which we have yet to be able to really unravel and draw conclusions from. While we can look at ratios, a 1-dimensional diagenetic model is perhaps the best way to tackle this problem given the inherent complexity.

This information is critical for **1**) informing model processes and parameterization; **2**) serving as a baseline for future comparison of future annual bloom anomalies, so long as similar parameters are continuously measured; **3**) informing passive mitigation strategies, e.g. nutrient reduction strategies as we now can refine the importance of the sediment nutrient source vs. external loading. Because we are beginning to understand how muddy sediments behave over seasonal time scales, these results can be spatially extrapolated using previous SFWMD mapping data to create more accurate legacy load estimates; and **4**) mitigation targeting, presuming we now know when the nutrients will be most intense from these types of sediments over an annual scale; and **5**) conceiving and testing mitigation strategies either directly related to sediments (e.g. zero valent iron to slow phosphate flux), or predicting how sediment nutrient fluxes may react to active mitigation efforts (e.g. clay or alum additions).

In 2022, a new Florida bill was proposed to further investigate the feasibility of dredging lake sediments. A previous pilot scale dredging study was conducted in the early 2000's that examined the effects of removing various layers of sediments on phosphorous fluxes (Reddy et al. 2002). The major findings were that the removal of surface sediments reduces the total P inventory (~65% in surface 30 cm) and the potential P flux into the water column, but this study was admittedly a "black box" approach which did not look further into the sediment biogeochemical processes; instead, it used core incubation approaches to examine interactions between sediments and overlying water. The study suggested that next steps should examine the biotic and abiotic controls regulating the P flux – in particular the microbially-mediated processes, electron acceptors, and organic matter turnover – to examine why *deep* sediments have a poor P retention capacity and ultimately understand the response of Lake Okeechobee sediments to total or partial dredging. The authors acknowledge that the flux of P is dependent on the status of the surface mineralogy, e.g. retention by iron oxides. Our work nicely adds to these knowledge gaps by determining that the surface sediment layers are relatively enriched in iron hydroxides, which appear to be relatively saturated with iron oxides and thus sensitive to dissolution, that dissimilatory iron reduction appears to be the dominant respiratory process at least at site L001, and that Fe redox coupling affects not only P over short time scales, but also possibly N cycling.

HALO results differ from previous Lake Okeechobee sediment studies in several ways; however, 15-25 years has elapsed since much of this work was performed and the ecosystem status has obviously undergone significant changes just based on HAB increases alone (e.g. see **Task 5** historical HAB climatological results), raising the possibility that these disparities are truly due to changes in the environment. In particular: 1) Biweekly/monthly N and P diffusive flux loading is highly variable, especially at the L001 site, as compared to previous quarterly studies that concluded P fluxes were relatively constant (Fisher et al. 2005; Moore et al. 1998); 2) HALO pore water dissolved phosphate and NH_4^+ (Figure 3A-3) was routinely far more elevated in muddy sediments than detected in June 1999 (i.e. maximum of 1.5 mg L^{-1} or 48 µM phosphate P, and of 0.05 mg L-1 or 214 µM NH_4^+-N; Fisher et al. 2005). HALO calculated fluxes of phosphate-P and ammonium-N (Figure 3A-16) were similarly elevated compared to June 1999 measurements determined from pore water gradients (i.e. ~27 µmol m^{-2} day^{-1} for phosphate-P and 221 µmol m^{-2} day^{-1} for ammonium-N); 3) HALO sediment oxygen demands (as inferred by both DOU (electrochemical profiling) and SOD (benthic chamber incubations; **Task 3B**) were also much higher at site L001 as compared to the greatest value measured at any lake site in 1999, i.e. 27.0 mmol O_2 m^{-2} day^{-1} vs. values nearly an order of magnitude greater determined by both core profiling and chamber incubations (Figure 3A-5); 4) HALO oxygen penetration depth in muddy sediments is minimal: most often < 1 mm and at maximum 6 mm (at least at site L001), compared to the ~1 cm previously reported (Reddy et al. 2002), suggesting that the surface layer regulating P flux is even "shorter" and more difficult to capture with conventional core separation techiques; 5) iron hydroxide-bound P comprised ~23% of total sediment P in the surface 10 cm of the muddy sediments (and more at other sites), an order of magnitude greater than the 2% of total sediment P reported in Reddy et al. (2002). The correlation of P with iron hydroxides demonstrates that this layer is likely highly susceptible to redox-induced mobilization.

Going forward, we aim to better constrain the relationship between sediment phosphate inventories, resuspension fluxes, and the resulting water column concentrations (Amendment #3 **Task 11** and **12**). HALO results alone to date cannot be used to estimate lake-wide internal loading due to the greater temporal resolution acquired at the expense of the loss of spatial resolution; granted, this was not the purpose of this study. However, HALO seasonal differences in fluxes obtained to date can probably be used to adjust fluxes inferred from existing high spatial resolution substrate maps to better constrain both annual and seasonal fluxes, e.g. by scaling the flux estimates from low-temporal but high-spatial resolution literature measurements according to HALO-measured minimum and maximum seasonal values and then integrating over time. The next phase of HALO measurements will focus on ensuring that this procedure can be more easily implemented, by mapping sediment legacy nutrient inventories at greater spatial resolution and at high temporal resolution using multiple depth-integrated bulk single 0-10 cm depth bins (for high horizontal resolution), while still analyzing a few sites as a function of high-depth resolution to continue to improve our understanding of the biogeochemical processes controlling nutrient release (**Task 11**). Finally, we aim to analyze specific nitrogen transformation processes, i.e. why ammonium is removed from pore waters at L001 over time during the season (**Task 11**). We plan to collect further high-resolution depth-resolved redox profiling at site L004 in addition to continuing the profiling at site L001. These efforts were conceived by the results of this current task, and we feel that the newly designed scope is balanced to continue measurements necessary to develop the long term "baseline" understanding required to understand HAB ecology in Lake Okeechobee, while also steadily gaining new knowledge to address those questions that will ultimately be most important for constructing a successful predictive model.

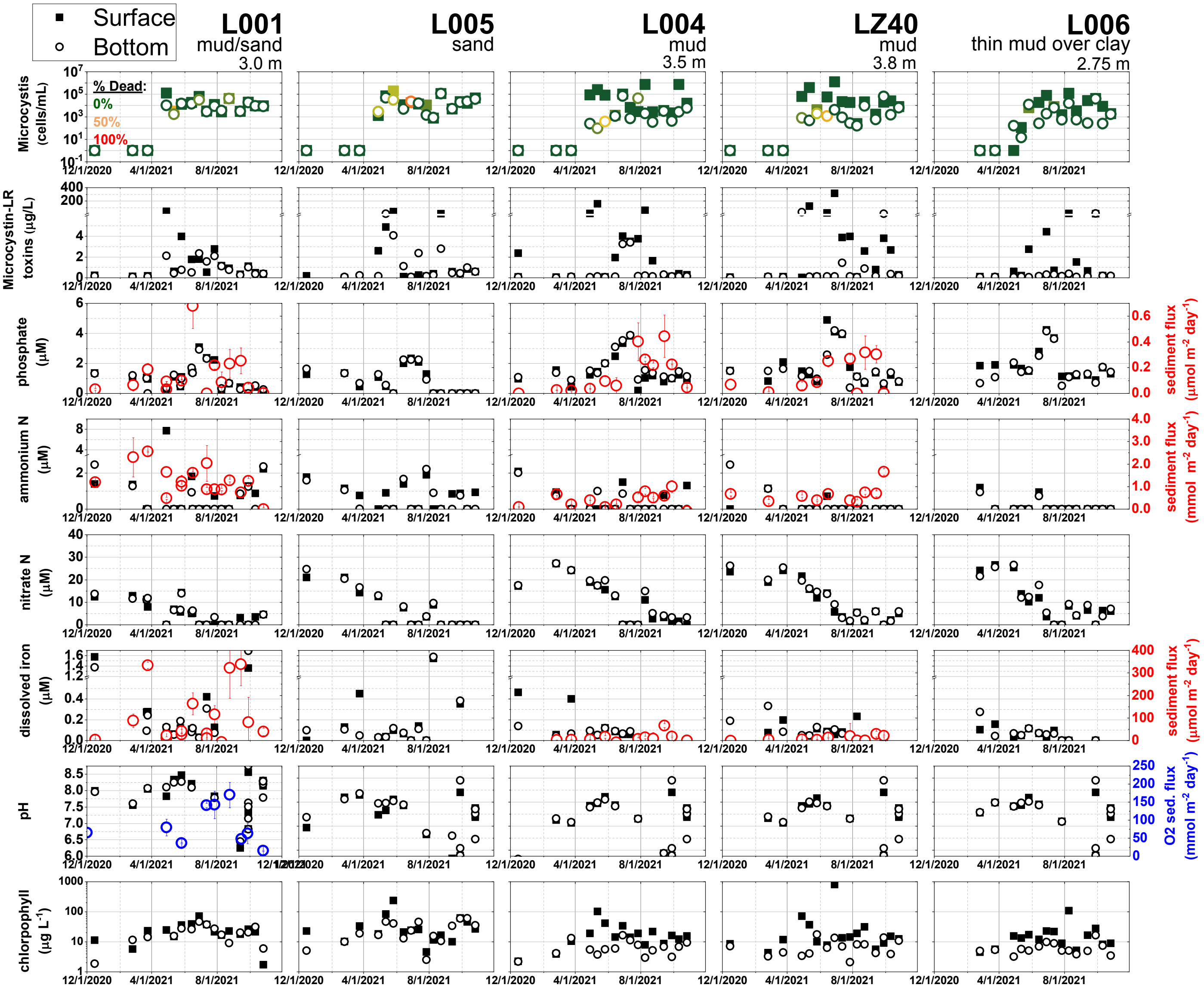

Figure 3A-16: Compiled sediment flux data from the five primary sites in the context of Task 2 data. All data points except those in red and blue are a time series of discrete surface and bottom water column *M. aeruginosa* and cell health, microcystin-LR toxins, SRP, ammonium, dissolved total iron, pH, and chlorophyll (measured in the laboratory via extraction) corresponding to surface (black squares) and bottom water depths (open black circles). *M. aeruginosa* cells are colored according to ratio of percent dead (see color bar scale in the top left). In some cases, this ratio is unable to be determined, especially at lower cell concentrations; these time points are kept as 0% live. Water column nutrient analyses were not specified as a task in the scope of work and are not NELAC compliant, although we have high confidence in the data and it is useful for data interpretation. Sediment diffusive fluxes from pore water near-surface concentration gradients (i.e. Figure 3A-4) are in red and their respective y-axis is on the right hand side of the figure. Finally, diffusive oxygen uptake (DOU) of L001 sediments as determined via electrochemical profiling is in blue, similarly using the right-hand y-axis.

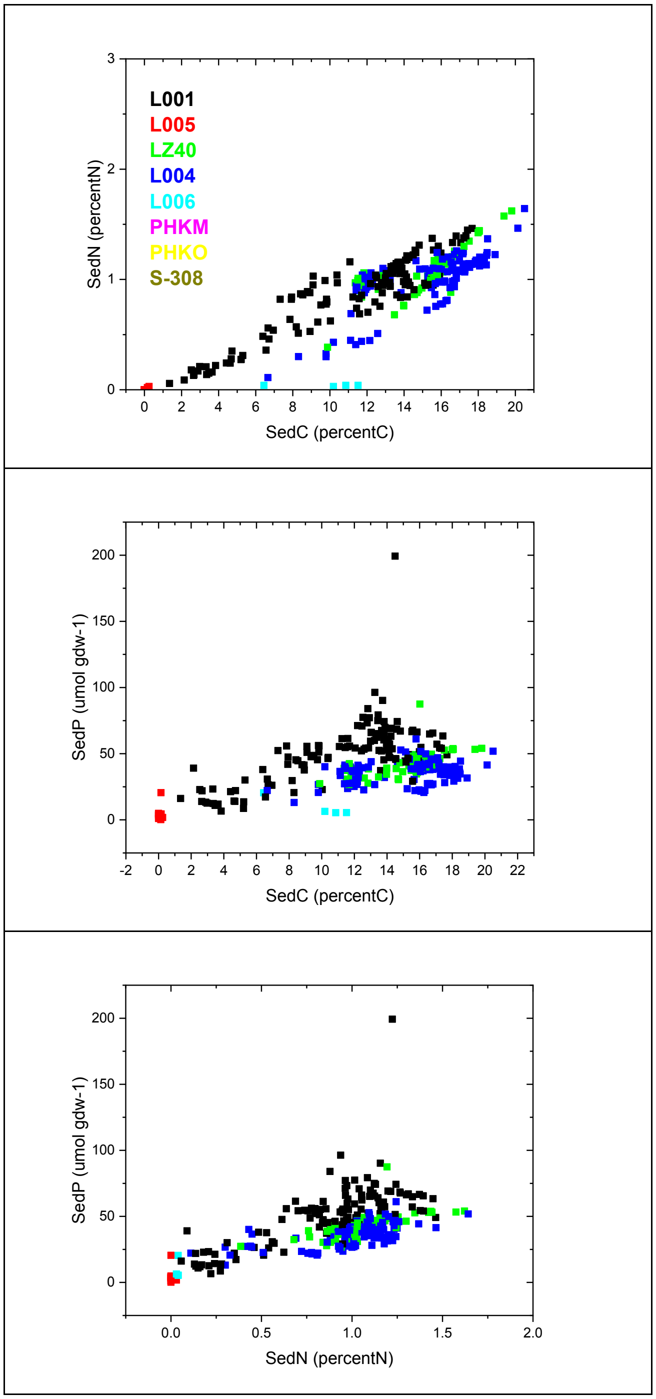

Figure 3A-17: Total sediment solid phase C/N and C/P, and N/P ratios by site (color) for all cores. Pahokee Marina (inside and outside) still require processing.

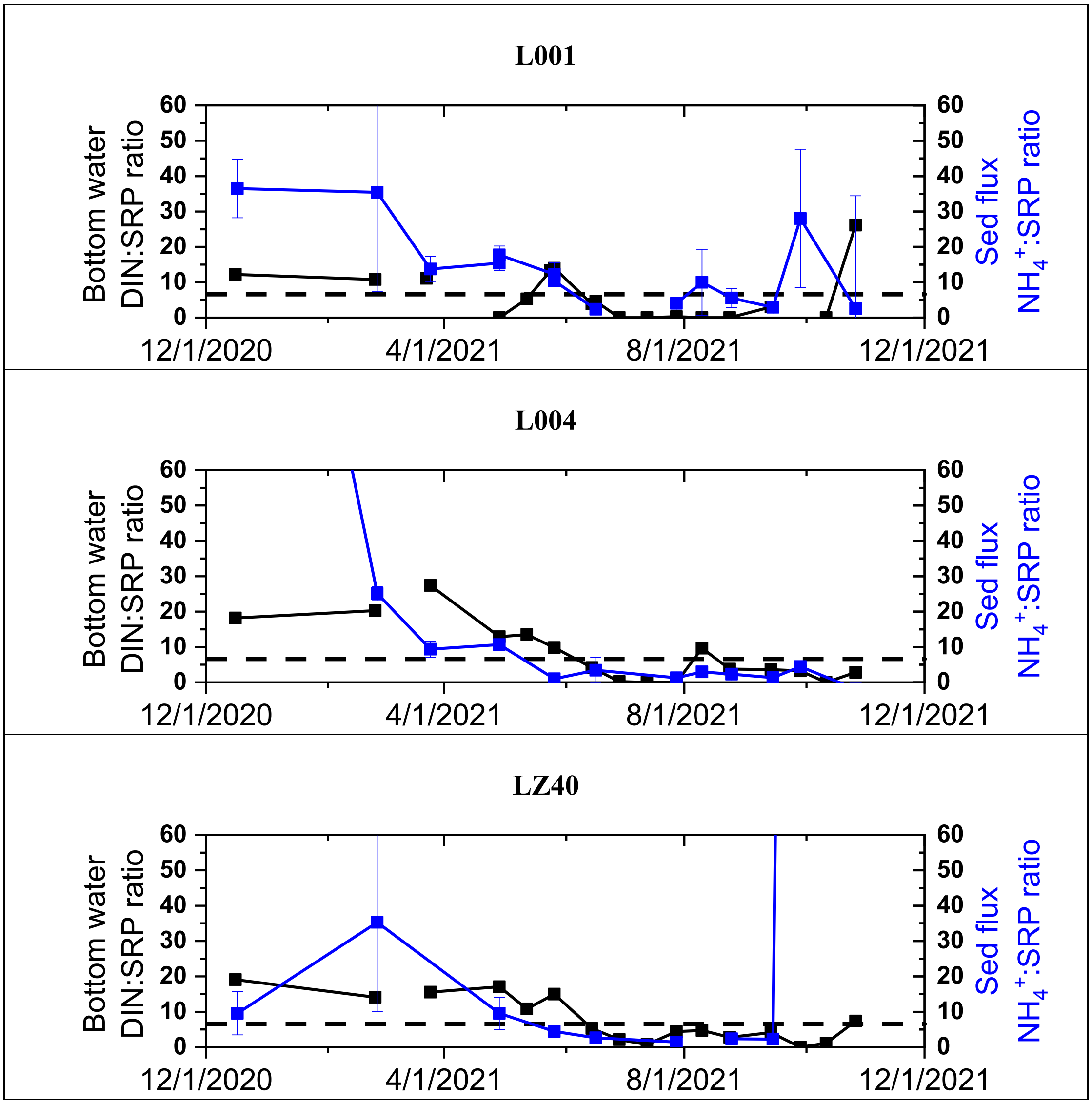

Figure 3A-18: Bottom water DIN:SRP ratios and the NH_4^+:SRP ratio of sediments for the three primary sites. DIN is used in the water column ratio because, while sediment fluxes were dominated by NH_4^+ relative to NO_3^-+NO_2^-, the rapid nitrification limits accumulation of NH_4^+ in the water column. Error bars for flux ratios are propagated from the standard error associated with fitting of the respective near-surface concentration gradients for the Fick's Law calculations. The horizontal line is the Redfield Ratio

TASK 3B: BENTHIC LANDER DEPLOYMENTS (TASK LEAD: BECKLER)

INTRODUCTION

While **Task 3A** provides necessary, conventional, community-accepted sediment biogeochemical measurements and benthic fluxes, measurements collected from sediment cores may display artifacts from extrusion and processing. Diffusive sediment fluxes depend on the concentration gradient between the surface-most sediment layer and the bottom water. Analytes in deeper pore water layers obviously diffuse upwards and affect the concentrations in this surface-most sediment layer; however, there may be processes such as organic nutrient remineralization or mineral adsorption (e.g. by iron hydroxides) that can ultimately enhance or limit the true surface-leaving flux. Sediment core profiling and pore water diffusive calculations, while common practice, rely on the near-surface pore water gradients (**Task 3A**). Unfortunately, this technique is limited by the vertical resolution at which pore waters can be successfully extracted. In our case, 5 mm resolution barely generates enough pore waters to conduct the necessary analyses, and undesirable vertical homogenization and mixing with overlying waters is unavoidable regardless of how meticulously the procedure is performed. Electrochemical profiling (e.g. Figure 3A-4) is one approach to avoid these artifacts, but the analyte selection is limited. Another approach is to collect cores from the field and incubate them for a period in the laboratory as has been performed previously for Lake Okeechobee sediments (Fisher et al. 2005). These experiments provided critical data, demonstrating that muddy sediments were potentially intense sources of phosphate, especially if anoxia was deliberately induced on the cores (presumably due to iron oxide mineral dissolution). While there are advantages to this technique, the removal of sediment cores from their natural environment and equilibration between sediments and the overlying water is also unavoidable, even if surface waters are replaced prior to starting the incubation.

Instead, in-situ benthic flux measurements using benthic incubation chambers provide a more accurate in situ means to quantify sediment inventories and diffusive fluxes, although the technique requires complex instrumentation and long periods of time spent on-site manually collecting samples, unless an automated sample collection system is implemented (Tengberg, De Bovee et al. 1995, Kononets, Tengberg et al. 2021). Benthic flux incubation chambers are perhaps the most intuitive of the approaches for measuring diffusive fluxes. Essentially, a small volume of water is forced to be in contact (incubate) with a known area of sediment by emplacing a confined chamber on top of the sediment, which is open to sediments on the bottom and sealed on the top. The analytes of interest may accumulate (flux from sediments) or deplete (flux into sediments) over time in the chamber. The chambers are affixed to a larger lander which is lowered to the seafloor for a discrete period, although the chamber lids are initially opened for a short period of time to allow equilibration with bottom waters and to prevent the capture of air bubbles. Upon the incubation start (time zero), the chamber lid is mechanically closed at time zero. A pump gently circulates the entrained water (before and after lid closing) to ensure the contents are homogenous. A tracer solution is often injected into the chamber and is subsequently measured both initial and throughout the incubation to allow back-calculation of the chamber volume and thus height, i.e. critical information for ultimate normalization of fluxes to units of sediment surface area. The chamber lids can be opaque or transparent, allowing the discrimination of respiration only, or the combined effect of respiration and photosynthesis, respectively. The lander is deployed for several hours to days, with shorter deployments in areas with more active environments. Too long of deployments can result in the induction of anoxia and thus the artificial enhancement of fluxes linked to redox processes such as the release of phosphate due to the dissolution of iron oxide minerals Analytes of interest are monitored either in situ with equipped sensors, or post-retrieval in samples collected as a function of time from the chamber during the deployment (e.g. using syringes).

Importantly, each chamber incubation only generates a single flux measurement per analyte, and because these techniques were developed in the oceanographic community in environments less dynamic and active than lakes, all changes in the chamber are assumed to be caused by the sediment influence; despite knowing that effects due to respiration in bottom waters or nutrient assimilation is certainly possible, especially in lake environments. Ambient water processes are also often monitored to at least provide some information as to whether these "background" processes are important, e.g. if dissolved O_2 becomes depleted due to natural hypoxia. Most often, dissolved O_2 concentrations will decrease over the course of multiple hours/days in an opaque chamber, providing a measure of Sediment Oxygen Demand (SOD; due to both biological oxygen demand and the oxidation of legacy chemically reduced species). Nutrient concentrations instead usually increase due to an upward benthic flux, although nitrate can decrease if sediment denitrification is in excess of cumulative nitrification caused to ammonium oxidation at the sediment surface of in the chamber. For a cylindrical chamber, if one knows the volume of water entrained by the chamber (*V*), the surface area of sediment available for exchanges (i.e. chamber bottom surface area; *S.A.*), the incubation length of time (*dt*), and finally the analyte concentrations at time zero (C_0) and upon incubation termination (C_f), it is possible to infer the benthic flux in units of moles m^{-2} day^{-1} over time using simple mass-balance:

$$\mathrm{Flux} = \frac{(\mathrm{C_f - C_0})}{\mathrm{dt}}\left(\frac{\mathrm{V}}{\mathrm{S.A.}}\right) = \left(\frac{\mathrm{moles}}{\mathrm{m^3 \times day}}\right) \times \frac{\mathrm{m^3}}{\mathrm{m^2}} = \frac{\mathrm{moles}}{\mathrm{day}} \times \frac{1}{\mathrm{m^2}}$$

The (*V/S.A.*) term can just be replaced with the chamber height for a cylindrical chamber. However, it is far more desirable to obtain a time series of measurements beyond just an initial and final timepoint, as the rate of accumulation is often non-linear and there are many opportunities for errors associated with sample collection, leaks, homogenization, etc. In this case, the rate of change *dC/dt* can be determined as the slope of a fitted a line through the concentration time series, using manual discretion to select those data points up to the time at which any non-linearity is observed. Regardless, the ultimate normalization to sediment surface is convenient for data interpretation and utilization: if the deployment is performed in a representative, homogeneous location with a specific bottom substrate type, flux magnitudes can be easily extrapolated over basin scales, e.g. over the mud area of a lake.

To this end, an innovative benthic lander package equipped with in situ benthic flux incubation chambers and ancillary sensors was constructed, tested, and deployed at Site L001 on multiple events over the project duration, typically coincident with sediment core collection (**Task 3A**). The chamber incubations reveal ***diffusive*** fluxes and no information regarding ***resuspension***-induced fluxes, assuming the sediments were not resuspended within the chamber during the incubations.

METHODS

Deployments ultimately yielded time series concentration measurements of carbon, nutrient, dissolved O_2, and microcystin toxins from 5x collected samples from each benthic chambers as well as bottom water sonde-acquired water quality measurements. The lander was based on previous designs deployed in blackwater river estuaries and adjacent shelves in southeast Georgia (U.S.) (Meiggs and Taillefert, 2011). The benthic lander was partially constructed prior to beginning the project and construction was completed as part of this task. The lander was equipped with dual benthic flux chambers (one transparent, one opaque), a multiparameter sonde, and a microprofiler with Hg/Au voltammetric microelectrodes to provide in situ sediment profiles of redox active metabolites (Figure 3B-1). However, we experienced unforeseen problems with the in situ voltametric sediment profiling we suspect were caused by lower conductivities as compared to oceanographic research that were prohibitive to the long distances between "working" and "counter" electrodes (~ 0.5 meters). We therefore instead always substituted laboratory voltametric profiling of sediment cores for the in situ profiling. This laboratory core profiling technique is otherwise identical to the lander-acquired profiling system; although not in situ, it does allow for improved depth-resolution (< 1 mm increments vs. ~3 mm increments) and analytical adjustments during the profiling not possible with the in situ system. This data is more logically presented as part of **Task 3A**, however, and is described therein.

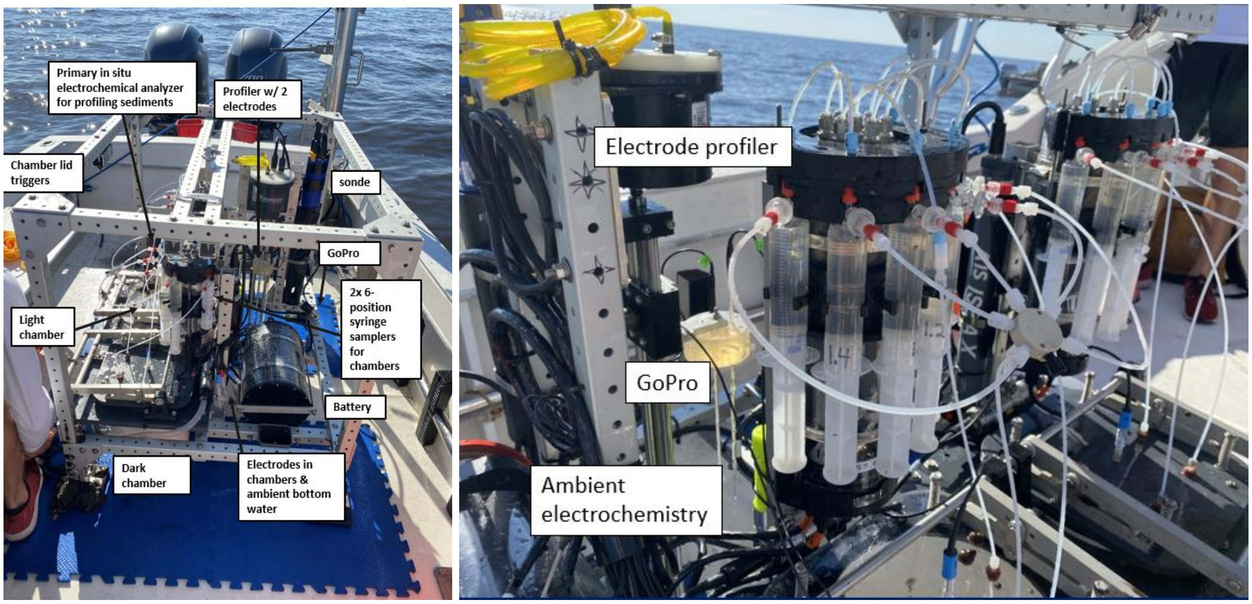

Figure 3B-1: The lander with indicated components and filled syringes post deployment.

The lander was deployed from a 26’ boat with a small davit crane and winch each morning (~9:30 am), allowing single day operations via deployment in the morning, additional on-water operations through the afternoon, and retrieval in the afternoon. Because testing revealed that dissolved O_2 in chambers was depleted more rapidly than expected based on previous oceanographic work, the routine deployments conducted once a reliable procedure was established (i.e. after June 2021) were typically < 8 hours in duration so that oxygen would not be depleted more than half of the initial concentration. Upon lowering to the seafloor, the sealing of the lids and thus the start of incubations is accomplished via a spring-loaded lid that is initially elevated (unsealed) position prior to deployment. After a period of at least 10 minutes on the lake floor to allow equilibration, the lid is sealed via activation of mechanical trigger. The trigger is released by jerking a line tethered to a surface buoy that floats above the lander, thus commencing the incubation.

To ensure that the parcel of water within each benthic chamber is homogenous (e.g. free of density gradients) and so that the syringes obtain a representative sample, two separate Seabird gear pumps (SBE 5T, 1,300 RPM estimated 20 mL/sec) are configured to recirculate water in each chamber. The pump inlet and outlet are pass through the wall of each cylindrical chambers, approximately 180 degrees around the perimeter, via Tygon tubing. The pumps (and the syringe sampling systems described below) are powered on immediately prior to deployment via plugging in to a 12V 50 Ah LiFePO4 battery (Bienno Power BLF-1250A) in an underwater 100 m pressure-proof acrylic housing (Blue Robotics) using a custom underwater connector (DragonFish Mfg.)

The lander employs two independent 6-syringe sampling systems (Syringe-1, AIS Inc.) corresponding to each of the two flux chambers. Under standard operation, both syringe sampling systems have identical timing, because both benthic chambers are initially "sealed" simultaneously, thus commencing the incubation. Each syringe sampling system has a set of six polypropylene (60 mL) syringes that can be programmed to operate bidirectionally enabling both expulsion and aspiration. The syringes are filled using a pump internal to each syringe sampler system, instead of the more traditional reliance on a spring-loaded mechanism that mechanically elongates the syringe plunger. Each of the syringes has a length of Tefzel tubing connected to a common port on either chamber. The first of the six syringes on each system was configured to expel a known volume of an inert sodium bromide tracer (50 mL of 50 mM NaBr) into the chamber. The diluted concentrations were then measured in each of the subsequent 5x collected syringe samples (per chamber) using an Ion-Selective Electrode to 1) calculate the initial chamber volume and 2) ensure no leaks were evident over the deployment duration. These other five syringes are programmed to fully aspirate benthic chamber samples sequentially over the course of the entire deployment. Each of the 5x collected samples (per chamber) were analyzed for: dissolved organic carbon, DOC; Soluble Reactive phosphorus, SRP; Total Dissolved Nitrogen, TDN; ammonium, NH_4^+; nitrate + nitrite, NO_3^-; organic nitrogen, org-N determined by difference of NH_4^+ and NO_3^- from TDN; dissolved iron(II), $Fe(II)_d$; total dissolved iron, Fe_d; dissolved iron(III), $Fe(III)_d$ by difference of Fe_d and $Fe(II)_d$; and microcystin toxins (via ELISA) according to the SOPs referenced in the Project QAPP. Because of the extremely high turbidities of the lake, in situ filtration of the syringes was not possible. As soon as the lander was recovered, the syringes were immediately capped and placed in an ice-filled cooler.

The lander is equipped with an in situ electrochemical analyzer system (ISEA-X; Analytical Instrument Systems, Inc.) that operates 4x Hg/Au voltammetric. One electrode is positioned across the benthic chamber lid with single-piece finger-tight high-pressure PEEK fittings to monitor concentrations of the analytes in the chamber as a function of time (for inferring Sediment Oxygen Demand, for example). These benthic flux chamber measurements are programmed to start prior to the incubation lid closing and obtain data at a much greater frequency than analytes measured post-deployment and captured in the benthic chamber syringes. Two additional electrodes are affixed to the lander frame at a single location to provide ambient bottom water time series measurements. The ISEA-X was programmed to conduct repeated series of voltametric measurements at each electrode, with each electrode being reoperated every ~20 minutes. The Hg/Au poly-ether-ether-ketone (PEEK) voltammetric "working" microelectrodes are typically used as part of a 3-electrode system consisting of Ag/AgCl "reference" and Pt "counter" electrodes (Luther et al. 2008). The reactive surface of the Hg/Au, an elemental mercury surface amalgam on a gold wire, mediates redox reactions and the simultaneous detection of dissolved oxygen, $O_{2(aq)}$; hydrogen peroxide, H_2O_2; soluble organic-Fe(III) complexes, org-Fe(III); dissolved iron(II), $Fe(II)_{volt}$; aqueous iron sulfide clusters, $FeS_{(aq)}$; dissolved manganese(II), Mn^{2+}; thiosulfate, $S_2O_3^{2-}$; and total dissolved reduced sulfur species (i.e. hydrogen sulfide: $\Sigma H_2S=H_2S+HS^-+S^{2-}$, elemental sulfur: $S_8^{(0)}$; and polysulfides: S_x^{2-}) (Meiggs and Taillefert, 2011). While testing in the Indian River Lagoon did detect ΣH_2S in the benthic chamber, no analytes except $O_{2(aq)}$ were detected within the benthic flux incubation chambers during Lake Okeechobee benthic lander deployments. The lander was also equipped with a sonde (YSI EXO2) that monitored the ambient waters ~25 cm above the lake floor during deployments. Every one minute, the sonde monitored salinity, temperature, water depth, fluorometric total chlorophyll, fluorometric phycocyanin, fluorescent dissolved organic matter (FDOM), and dissolved O_2.

ACTIVITIES SCHEDULED vs. COMPLETED

A total of 9x lander deployments at Site L001 were scheduled to occur in Feb., May, Jun., Jul., Aug. (2x), Sep.(2x), and Oct. 2021 (**Table 3B-1**). Beyond extensive laboratory testing of individual components prior to field deployments, we ultimately conducted a total of 11x deployments over the duration of the project, including one deployment in the Indian River Lagoon to test a critical change in early June. The first 3x lake deployments (Feb., Mar., May.) did not generate the expected data, in particular the bromide tracer concentrations measured in the chambers were much less than those expected based on the amount initially injected, but also the dissolved O_2 did not decrease as expected and no consistent nutrient trends were observed. Through additional laboratory testing, it was discovered that the positioning of the recirculating pumps above the chambers was preventing their ideal operation probably due to pressure differentials. The pumps were moved to be below the chamber lids and the system was tested and demonstrated functional at Harbor Branch on 6/9/21; therefore, data is not trustworthy prior to this date. Additionally, one deployment on 810/21 was tampered with and the surface buoy used for retrieving the lander was stolen. We returned to the lake on 8/12/21 and discovered that the lander was flipped on its side. By looking at the bromide, sonde, and dissolved O_2 data, we inferred that the lander was moved approximately 120 minutes after deployment; thus the only useable data from that deployment was the initial rate of dissolved O_2 consumption. Ultimately, a total of 6x deployments from Lake Okeechobee between 6/15/21 are considered most or entirely useable. The lander system is certainly innovative technology and the Scope of Work does have a clause: "Lander deployments are complex and subject to a relatively high failure rate with respect to all systems functioning (~30%), so the Department accepts that Task completion will be demonstrated by deployment occurrence according to the schedule, not necessarily by the complete success of the multiple lander independent systems (e.g. benthic chamber syringe samples, electrode microprofiler, sonde, etc.). However, the Department has an expectation that the GRANTEE will continually refine instrument designs and processes demonstrated by progressive increased frequency of successful data collection." Based on the successes of the more recent deployments, this performance satisfies the deployment requirements of the Scope of Work.

With respect to the analyses, the in situ electrochemical profiling system was used for the first deployments but was eventually omitted in lieu of laboratory electrochemical profiling (discussed in the above Methods section). All planned chemical analytes were conducted on all syringes except for organic phosphorous, as sample requirements (10 mL of a total of ~45 mL total collected) were not feasible after accounting for other monitored analytes. We did attempt method development to decrease these sample requirements using a small volume absorption flow cell but were not successful. To compensate, however, we did conduct analyses in excess of those planned using our more optimized small-volume techniques including NO_3^-, Fe_d (and thus $Fe(III)_d$ by difference), and microcystin toxins on seven total deployments instead of the planned four deployments. These both ended up being critical analyses due to 1) evidence of in situ nitrification in the syringes; and 2) the potential for a wrong inferences regarding iron flux: while $Fe(II)_d$ does appear to increase over time, it does so at the expense of Fe(III)d, essentially negating the true iron flux.

Table 3B-1: Summary of lander deployments conducted over the project duration

Date	Retrieval	Site	Deployment Length	Flux chamber & electrode configuration	Syringe Samplers	Syringes analyzed	Electrode profiling	Sonde time series?	GoPro video?
2/25/2021	2/26/2021	L001	22 hrs.	Lids did not close; lander on side likely; PEEK elecs. in each chamber w/ 1 in WC	All syringes fired completely (20min, 3min, 2hr, 3hr, 4hr, 4hr)	yes; essentially a bottom water time series	2 glass @ 3mm resol.; 210mm sed. penetration	yes; all analytes recorded	yes; did not turn on light so no visibility
3/23/2021	3/25/2021	L001	44 hrs.	positive chamber 1 closed, chamber 2 uncertain?; elecs. in each chamber w/ 1 in WC	All syringes fired completely (20min, 3min, 2hr, 3hr, 4hr, 4hr)	yes; benthic flux time series (at least Chamber 1; Chamber 2 uncertain if closed)	2 glass @ 1mm resol.; 210mm sed. penetration	yes; all analytes recorded	yes; facing bottom of chambers & profiler
5/25/2021	5/27/2021	L001	48 hrs.	Both chambers closed; elecs. In each chamber + 2 in WC; BC flux echem time series	All syringes fired completely (20min, 3min, 2hr, 3hr, 4hr, 4hr)	yes; benthic flux time series	Did not run profiler	yes; all analytes recorded	yes; facing bottom of chambers & profiler
6/09/2021	6/09/2021	Harbor Branch channel	7 hrs.	Both chambers closed; elecs. In each chamber + 2 in WC; BC flux echem time series	All syringes fired completely (20min, 3min, 2hr, 3hr, 4hr, 4hr)	Yes, benthic flux time series	Did not run profiler	yes, all analytes recorded	No
6/15/2021	6/15/2021	L001	8 hrs.	Both chambers closed; elecs. In each chamber + 2 in WC; BC flux echem time series	All syringes fired completely (20min, 3min, 1hr, 1hr, 2hr, 3hr)	yes; benthic flux time series	Did not run profiler	yes; all analytes recorded	yes; facing bottom of chambers & profiler

7/13/2021	7/13/2021	L001	8 hrs.	Both chambers closed; elecs. In each chamber + 2 in WC; BC flux echem time series	All syringes fired completely except for 1.1 & 2.3 (20min, 3min, 1hr, 1hr, 2hr, 3hr)	yes; benthic flux time series	Scheduled to start @ 9:30am; failed to fire for unknown reason	Used LOBO LO-LIB-WQ data	yes; facing bottom of chambers & profiler
8/10/2021	8/12/2021	L001	~48 hrs (sabotaged)	Both chambers closed; elecs. In each chamber + 2 in WC; BC flux echem time series	All syringes fired completely (20min, 3min, 1hr, 1hr, 2hr, 3hr)	yes; benthic flux time series, although data not useable in the context of a true incubation	2 glass @ 5mm resol.; 230mm sed. penetration	yes; all analytes recorded	yes; facing bottom of chambers & profiler
8/24/2021	8/24/2021	L001	7 hrs.	Both chambers closed; elecs. In each chamber + 1 in WC; BC flux echem time series	All syringes fired completely (20min, 3min, 1.5hr, 1.5hr, 1.5hr, 1.5hr)	yes; benthic flux time series	2 glass @ 5mm resol.; 230mm sed. penetration	yes; all analytes recorded	yes; facing bottom of chambers & profiler
9/14/2021	9/14/2021	L001	7 hrs.	Both chambers closed; elecs. In each chamber + 2 in WC; BC flux echem time series	All syringes fired completely (20min, 3min, 1.5hr, 1.5hr, 1.5hr, 1.5hr)	yes; benthic flux time series	2 glass @ 5mm resol.; 230mm sed. penetration	yes; all analytes recorded	yes; facing bottom of chambers & profiler
9/29/2021	9/29/2021	L001	7 hrs.	Both chambers closed; elecs. In each chamber + 2 in WC; BC flux echem time series	All syringes fired completely (20min, 3min, 1.5hr, 1.5hr, 1.5hr, 1.5hr)	yes; benthic flux time series	2 glass @ 5mm resol.; 230mm sed. penetration	yes; all analytes recorded	yes; facing bottom of chambers & profiler
10/12/2021	10/12/2021	L001	7 hrs.	Both chambers closed; elecs. In each chamber + 2 in WC; BC flux echem time series	All syringes fired completely (20min, 3min, 1.5hr, 1.5hr, 1.5hr, 1.5hr)	yes; benthic flux time series	Not used	Used LOBO LO-LIB-WQ data	Not used

RESULTS

Lander time series: Analytes from autonomously collected discrete syringe samples are generally congruent with the ambient bottom water samples collected via Niskin immediately prior to the deployments (Figure 3B-2). The logistics of sealing the chamber lid manually by pulling on a separate line extending to the lake surface prevented the obtainment of the pre-programmed first syringe sample exactly at "time zero" immediately after the lid closed (i.e. the commencement of the incubation). The first sample time was therefore between 13 and 16 minutes after the lid closed. Combined with the possibility for undesirable resuspension induced from the lander touching down on the lake floor, some analytes such as NH_4^+ (and therefore DIN) and org-N do show elevated concentrations above the ambient bottom water. We did not include the ambient bottom water as a data point when calculating the initial flux rates although there are arguments both for and against doing this.

Bromide is an obvious exception, with concentrations typically approximately an order of magnitude greater in the first syringe of each chamber of each deployment than those of the ambient water due to the direct injection of NaBr into each chamber. Note the tracer syringe did not function properly on 7/13/21, so the volume of 14.5 L is estimated from the depth of chamber penetration based on accumulated mud on the lander frame upon lander retrieval (Table 3B-2). Concentrations only decreased slightly, suggesting that the chambers did not leak and the losses are due instead to diffusion into the sediments over the course of the incubation. An exception to this is on 8/10/21 due to the obvious movement of the lander due to vandalism after the third syringe. The chamber volumes were calculated from the initial volume injected and that measured in the first syringe after dilution, with results consistent with the chamber geometry and assuming a penetration of the chambers ~10 to 20 cm into the sediments. It is important to preface these results with a disclaimer that we were unable to filter samples in situ as soon as they were automatically aspirated by the lander due to filter clogging. Therefore, it is possible that biological activity continued within the syringes until and filtration immediately upon return to the laboratory within 2-3 hours (although they were kept on ice during transit). Because the lander was routinely retrieved late in the day (typically ~5 pm), we were not able to filter in the field so as to avoid night operations and trailering of the 26' boat.

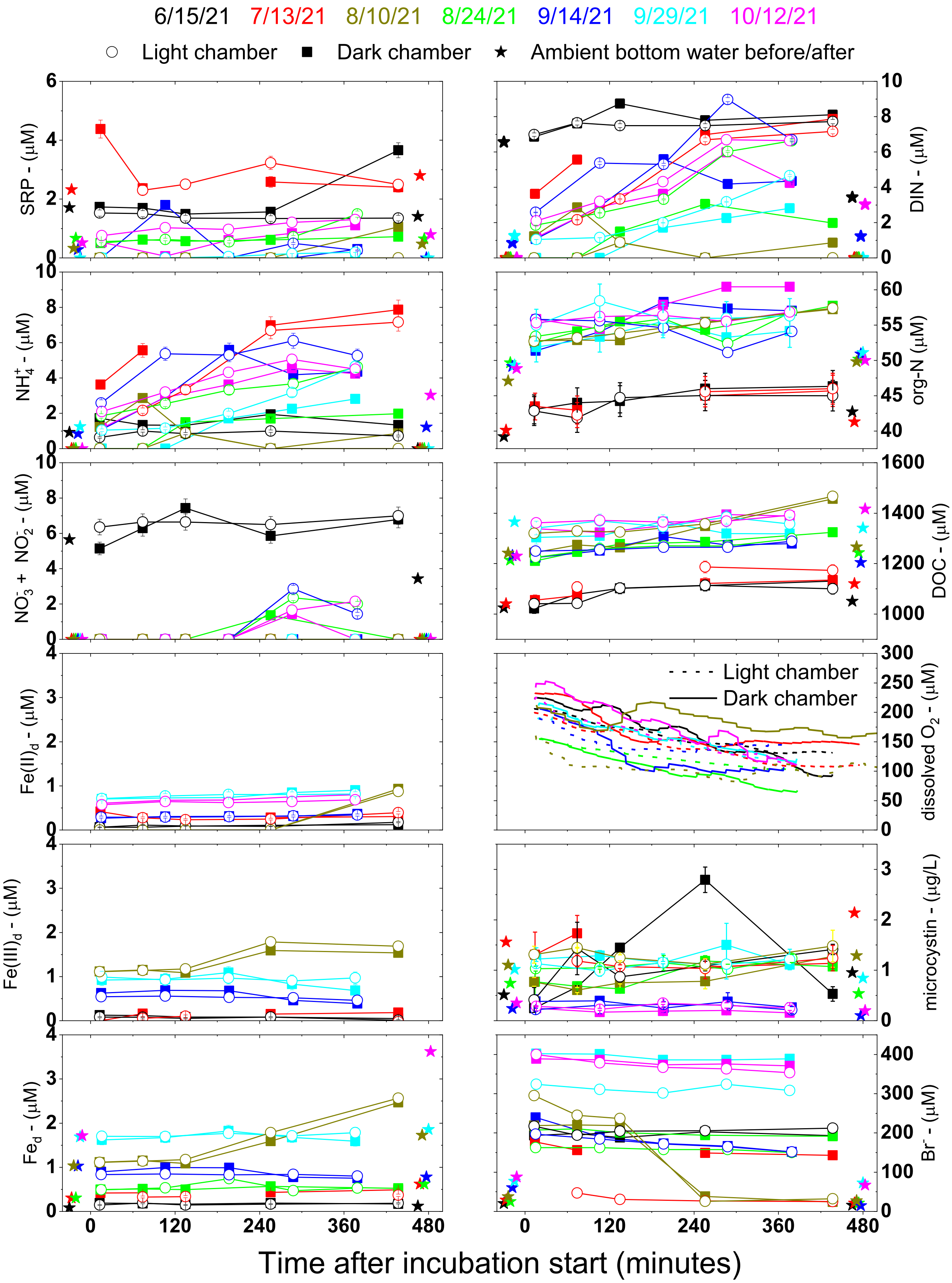

6/15/21
7/13/21
8/10/21
8/24/21
9/14/21
9/29/21
10/12/21
Light chamber
Dark chamber
Ambient bottom water before/after
SRP - (µM)
DIN - (µM)
NH_4^+ - (µM)
org-N (µM)
NO_3^- + NO_2^- - (µM)
DOC - (µM)
$Fe(II)_d$ - (µM)
dissolved O_2 - (µM)
Light chamber
Dark chamber
$Fe(III)_d$ - (µM)
microcystin - (µg/L)
Fe_d - (µM)
Br^- - (µM)
0
120
240
360
480
Time after incubation start (minutes)

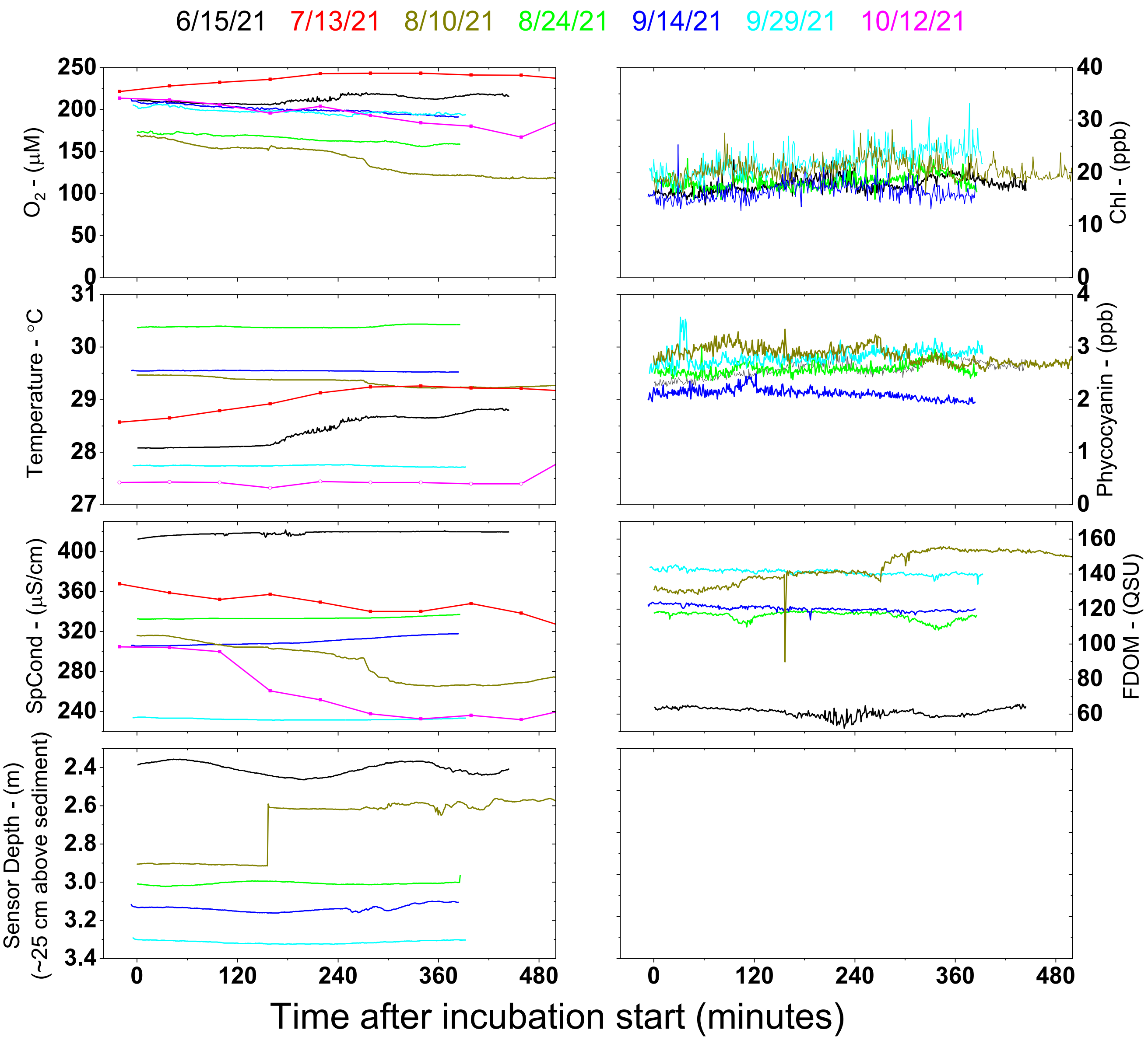

Figure 3B-2: Previous page: Time series data from discrete water samples collected during the lander deployments. Colors indicate the lander deployment date. Symbols indicate autonomously collected syringe samples from the Light (circles) and Dark (squares) incubations, as well as Ambient (stars) bottom water concentrations collected via a hand-held Niskin sampler immediately before and after the deployments (the exact times for the latter are not represented and their x-axis positions are only adjusted so that data points do not obscure others). Current page: Bottom water conditions as measured during the incubation by the sonde affixed to the lander (clean lines) and via the co-located LOBO system (Task 6). Chl, Phycocyanin, and FDOM from the LOBO system are not plotted because these were obtained with a separate model of sensor operating at different wavelengths and are thus not directly comparable. Note the incubation on 8/10/21 was sabotaged after ~120 minutes so data is not trustworthy beyond this point. Also, $Fe(II)_d$ was not measured in ambient water column samples and therefore $Fe(III)_d$ can not be determined by difference. Any other obviously missing data was due to sample loss or suspected sample collection issue and thus discarding, e.g. a leak between the sampling syringe, tubing, and benthic chamber.

Dissolved oxygen concentrations measured with Hg/Au voltametric microelectrodes embedded in chamber lids generally decreased as a function of time in each chamber (Figure 3B-2 and Figure 3B-3), although this decrease is only evident for the first ~120 minutes in the vandalized 8/10/21 deployment. The final O_2 concentration relative to the initial O_2 concentrations were between 53-78% for the light chamber and 43-63% for the dark chamber compared to 86-106% for the ambient water column, suggesting photosynthetic processes were at least at play to some extent despite the highly turbid water column. The dark chamber experienced a greater relative O_2 loss for all deployments except for 7/13/21. Overall, a deployment duration of ~7 hours strikes an appropriate balance of not becoming so hypoxic so as to artificially induce nutrient fluxes, while still allowing enough time for nutrient fluxes to be observable. No other redox active analytes were observed during the course of the incubations, i.e. no dissolved Fe (MDL ~ 20 µM), Mn(II), or hydrogen sulfide.

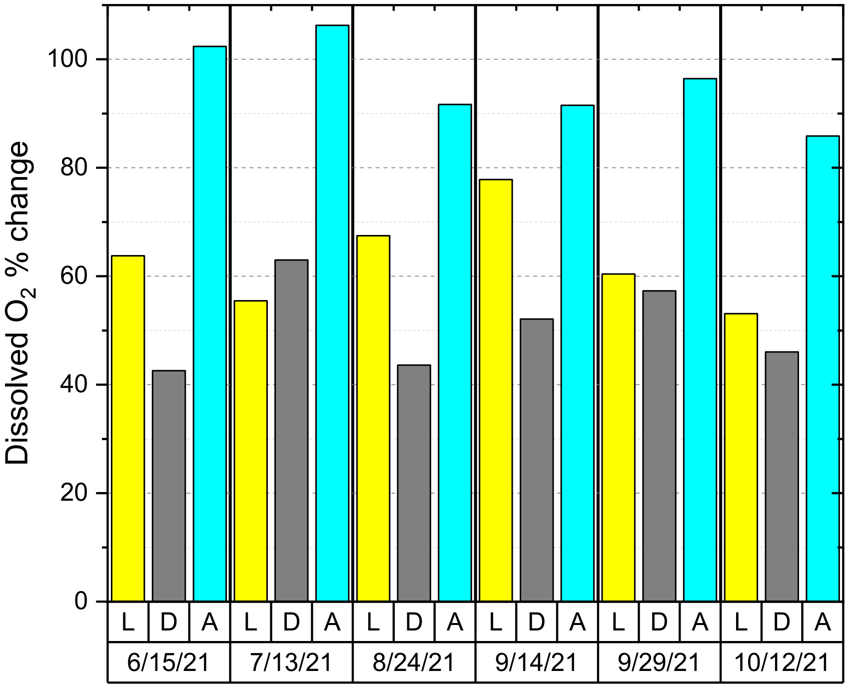

Figure 3B-3: Dissolved O_2 percent change over the duration of each ~6 to 8 hour incubation at Site L001 for transparent light chamber ("L"), opaque dark chamber ("D"), and ambient unincubated bottom waters.

Concentrations of NH_4^+, DIN, org-N, and DOC generally increased in the chambers as a function of time. SRP, NO_3^-+NO_2^-, and Fe_d, on the other hand, did not increase consistently, at least in the beginning of the incubation. A sudden increase in SRP was evident at the last time point of the incubations from 8/24/21 (light chamber) and 6/15/21 (dark chamber), perhaps due to reaching a minimum hypoxia threshold to allow liberation from iron oxide minerals, although this inference is risky due to a lack of replication. NO_3^-+NO_2^- was below the detection limit in most collected samples except for the incubation on 6/15/21, consistent with observed ambient water concentrations. However, NO_3^-+NO_2^- did increase approximately halfway through the incubations on 8/24/21 (light chamber), 9/14/21 (light), 10/12/21 (light and dark), suggesting nitrification of the newly inputted ammonium was occurring, given that sediment pore water NO_3^-+NO_2^- concentrations tended to be very low. In fact, NH_4^+ accumulation appears to somewhat level off as the incubation progresses, additional evidence of this conversion process. Indeed, DIN tends to be more linear throughout the incubations. The iron chemistry is somewhat deceiving: while fluxes of dissolved $Fe(II)_d$ do present in all incubations except 7/13/21 (Fe(II) was not measured on 8/24/21 due to an equipment issue), this is generally at the expense of Fe(III)$_d$. This indicates either 1) there is a flux of reduced Fe(II)$_d$ from the sediments, but it continuously oxidizes and precipitates; 2) the biological uptake of Fe(III)$_d$ prevents the overall accumulation of Fe$_d$; or 3) Fe(II)$_d$ sediment flux is instead formed largely from the dissimilatory reduction of Fe within the chamber. Concentrations of org-N in the first syringe samples were several μM greater than in the ambient water column (although note the y-axis does not extend to zero). Concentrations generally increased over time in both light and dark incubations (although slightly more in the dark incubations) on 6/15/21 and 7/13/21, but only in the dark chamber during later incubations on 8/24/21, 9/14/21, 10/12/2; some incubations show inconsistent trends, such as an initial increase but then decrease (e.g. 9/29/21 light chamber). Org-N does appear to similarly asymptote after approximately halfway through several of the incubations. DOC concentrations to some extent mirrored org-N concentrations, albeit without as dramatic of decreases in those incubations. A similar asymptotic behavior was often observed. Notably, the presence of *M. aeruginosa* appeared to dramatically affect the accumulation of nutrients, with lesser accumulation if cells were present in ambient waters (cell counts are listed in Table 3B-2 and this figure is referenced later in Figure 3B-6). Microcystin toxins only showed significant increased on 6/15/21 and 8/24/21, and slight decreases or no changes on other dates.

Calculated fluxes: Fluxes were determined based on the rates of accumulation of the analytes as measured in syringes or in situ (for dissolved O_2) (Table 3B-2). For most syringe-collected analytes, the rate of accumulation was extracted from the time series ad-hoc based on the initial maximum rate of accumulation, using at least two data points but more often more. If there is an error associated with the rate in Table 3B-2, this indicates that at least three data points were used. This is the typical technique used for data evaluation in the oceanographic discipline; however, processes are typically slower so there are usually more samples collected during this initial period of concentration changes. In this study, there is low confidence of fluxes for two analytes: SRP and NO_3^-+NO_2^-. SRP generally behaved erratically and few consistent trends, likely evidence of mineral associations in sediments as well as the potential for adsorption onto resuspended sediments. As previously discussed, NO_3^-+NO_2^-, on the other hand, typically only accumulated during the mid-point of the incubation, probably due to nitrification. Therefore, the rate of accumulation used for flux calculations did not necessarily include the first time point and instead used the maximum rate of accumulation at whatever time this corresponded to during the incubation.

Calculated flux time series are graphically presented in Figure 3B-4. Data description is challenging due to inconsistencies, although several general trends are evident. Fluxes, especially inorganic and organic nitrogen analytes, DOC, and O_2, tended to be higher in magnitude prior to 9/29/21. NH_4^+ fluxes typically dominated DIN fluxes. SRP and Fe$_d$ fluxes were both positive (fluxes from sediments) and negative (fluxes into sediments), reflecting the adsorption and redox sensitivities of these analytes. Because of the relatively short period of time represented by these measurements (~ 4 months), the data is better visualized using covariate plots described in the discussion section below.

Table 3B-2: Summary of lander deployment results. “L” and “D” for the Chamber column represent light and dark chambers, respectively. “M. aerug.” is the concentration (cells mL^{-1}) of *Microcystis aeruginosa* measured in a water sample prior to the deployment. “Chamb. Vol” corresponds to the that volume (*L*) of that benthic chamber back calculated from the injection of the bromide tracer. All fluxes are in units of µmol m^{-2} day^{-1} except for microcystin toxins which are units of µg m^{-2} day^{-1}. The residence time is indicated by “Tau” and is calculated using the ambient bottom water concentration measured immediately prior to the deployment and using a constant water depth of 3.0 m. The “Err” column immediately after each column indicates associated errors propagated from the line fitted through the time series concentration changes (from Figure 3B-2), with “NA” indicating that no error was calculated because only two data points were used. Values of “NA” for residence times indicate that either no flux data was determined or that the ambient bottom water concentration was below detection limits. Negative residence times indicate that the sediments are a sink for that analyte, instead of a source.

Chamb	Date	M. aerug.	Chamb. Vol	NH4 Flux	Err	NO3 Flux	Err	DIN Flux	Err	Tau DIN	Err	SRP Flux	Err	Tau SRP	Err	Fed Flux	Err	Tau Fed	Err	O2 Flux	Err	Tau O2	Err	DOC Flux	Err	Tau DOC	Err	org-N Flux	Err	Tau org-N	Err	Toxin Flux	Err	Tau Toxin	Err
L	6/15	14055	12.7	-8	204	411	177	3888	NA	5.1	NA	-511	223	-10	4.4	258	NA	0.9	NA	-94826	2279	-6.7	0.2	54512	29897	56.4	30.9	2311	1199	50.9	26.4	542	421	2.8	2.2
L	7/13	2850	14.5	10428	866	0	NA	10428	866	NA	NA	2165	273	3.2	0.4	45.9	2	20	0.9	-106185	4443.7	-6.3	0.3	75320	61337	41.5	33.8	4253	1890	28.3	12.6	95	162	49	84
L	8/10	3576	9.5	NA	NA	NA	NA	NA	NA	NA	NA	NA	NA	NA	NA	NA	NA	NA	NA	-277692	29232.1	NA	NA	NA	NA	NA	NA	NA	NA	NA	NA	NA	NA		
L	8/24	41336	16	3660	100	11766	NA	6637	1719	NA	NA	2348	884	0.9	0.3	639	241	1.4	0.5	-81980	1987.9	-6.4	0.2	79448	16353	45.8	9.4	2314	3035	64.4	84.4	190	126	12	7.8
L	9/14	3034	15.4	13442	NA	13735	NA	9173	2348	0.3	0.1	478	271	1.8	1	-18	46	-171	437	-147268	10193.4	-4.3	0.3	42464	9645	87	19.8	-3822	2456	-38.6	24.8	-6	95	-130	2217
L	9/29	18171	7.9	2916	254	0	NA	2524	254	1.5	0.1	168	21	NA	NA	-18	NA	-284	NA	-36983	2896.7	-16.4	1.3	26339	20041	156	118.4	33.5	1156	4416	2E+05	72	62	42	36
L	10/12	9323	7.4	2319	149	2493	768	3466	513	NA	NA	298	60	5.2	1	53.1	17	97	31	-67363	3613.7	-9.4	0.5	13475	6848	274	139.2	535.7	424	273	216.2	3	39	320	3804
D	6/15	14055	14.4	-76	401	7674	0	6335	718	3.1	0.4	-804	297	-6.4	2.4	-68	19	-3.5	1	-110916	7472.2	-5.7	0.4	87449	30244	35.2	12.2	3201	615	36.7	7.1	561	1409	2.8	6.9
D	7/13	2850	18.7	17233	NA	0	NA	4822	1281	NA	NA	-17823	NA	-0.4	NA	21.7	NA	42	NA	-271914	16703.9	-2.5	0.2	102943	18913	30.3	5.6	3349	828	35.9	8.9	-519	457	-9.0	7.9
D	8/10	3576	13.5	NA	NA	NA	NA	NA	NA	NA	NA	NA	NA	NA	NA	NA	NA	NA	NA	-197965	9701	NA	NA	NA	NA	NA	NA	NA	NA	NA	NA	NA	NA	NA	NA
D	8/24	41336	13.7	630	21	4373	NA	6333	1107	NA	NA	166	50	12.2	3.6	36.3	35	25	24	-121637	2294.7	-4.3	0.1	94281	18785	38.6	7.7	3958	1261	37.6	12	425	220	5.2	2.7
D	9/14	3034	14	9854	1013	0	NA	9854	1013	0.3	NA	-526	1206	-1.6	3.7	436	NA	7.1	NA	-252934	12230.4	-2.5	0.1	57637	36795	64.1	40.9	6381	2660	23.1	9.6	-112	92	-6.5	5.4
D	9/29	18171	6.8	2401	724	0	NA	1914	429	2	0.4	NA	NA	NA	NA	218	63	23	6.7	-63826	3117.8	-9.5	0.5	8095.3	18861	506	1179.3	958.7	878	154	141.4	-3	120	-971	37076
D	10/12	9323	8.3	2848	396	1123	648	3971	547	NA	NA	656	25	2.3	0.1	123	14	42	4.9	-97212	2996.9	-6.5	0.2	44744	14925	82.5	27.5	3956	1174	37	11	-39	25	-27	17

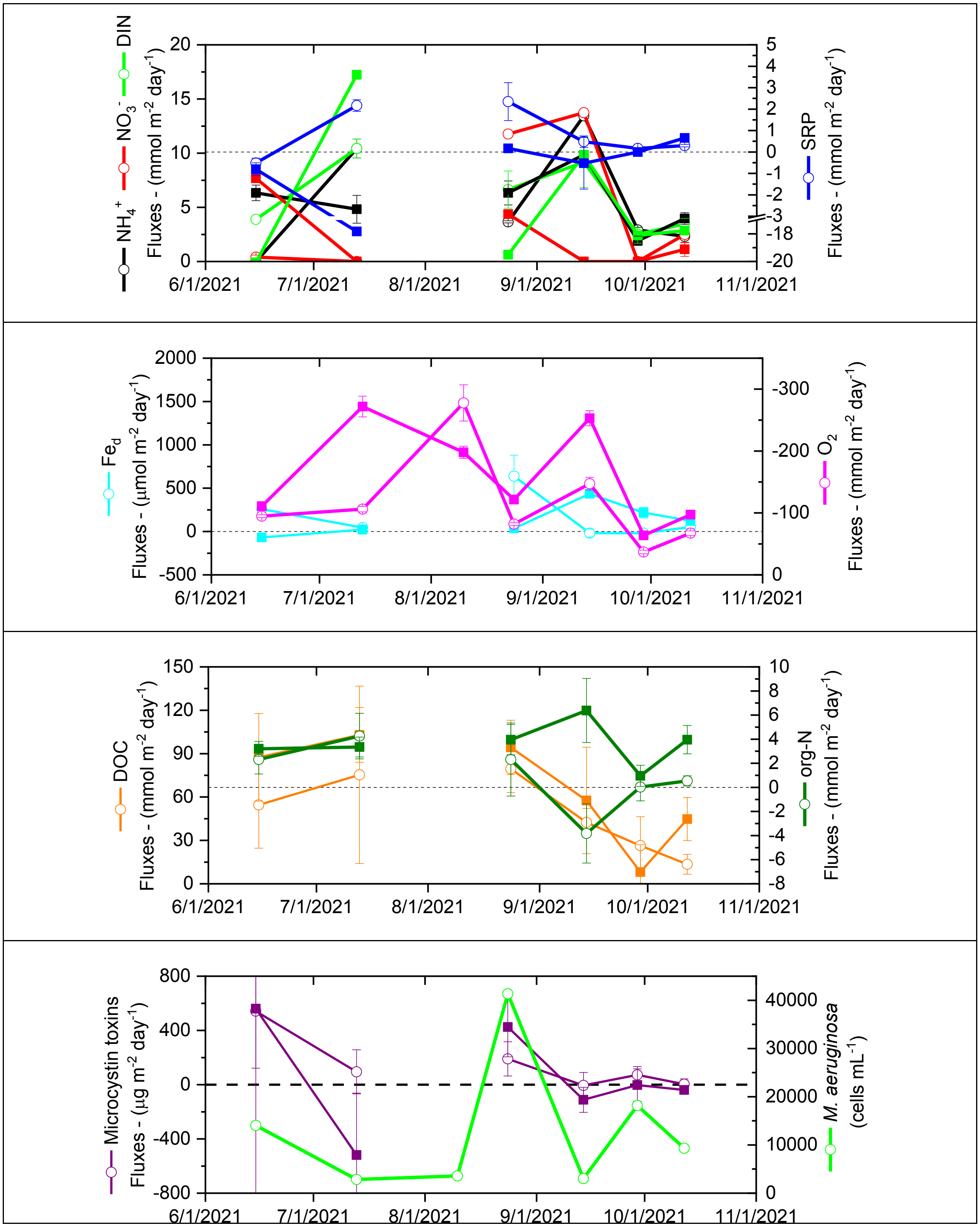

Figure 3B-4: Time series of calculated fluxes for light (open circles) and dark (closed square) incubations. The bottom plot displays ambient bottom water *M. aeruginosa* cells in samples collected just prior to the lander deployment.

Residence times were calculated assuming the fluxes were diluted into a 3 m tall by 1 m^2 footprint water column (an approximation of the depth at Site L001 and much of wider lake; Table 3B-2). The ambient bottom water concentration measured prior to the deployment was multiplied by this water column volume (3,000 L i.e. $3m^3$) to derive the total number of µmol, then dividing by the flux in units of µmol m^{-2} day^{-1} to obtain the residence times in days. The negative sign while not technically meaningful is left to indicate the direction of the flux (negative means the sediments are consuming the analyte). While the residence times associated with individual measurements are variable, the averages (Table 3B-3) are more easily interpretable. Because of the disconnect regarding nitrogen speciation, i.e. the dominance of NH_4^+ as the fluxing component but the dominance of NO_3^-+NO_2^- in the water column, DIN is the most appropriate choice for considering residence times. The residence times of DIN and SRP are on the order of ~2 days and ≤ 1 day, respectively, suggesting a fast turnaround due to biological utilization or mineral interactions. Iron fluxes indicate that the iron is cycled on the order of 1 to 2 months but that the sediments can serve as both a source or a sink, although high associated errors suggest the negative (sediments as a sink) may not actually be the appropriate interpretation of the data. Oxygen fluxes behaved as expected, suggesting that the sediments will consume the entire water column O_2 inventory on the order of a week, with the dark chamber results suggesting that a lack of benthic photosynthesis to some extent buffers this water column inventory. DOC residence times are on the order of a few months; despite large sediment fluxes of DOC, the water column already contains a very large inventory of DOC that is presumably of a low biogeochemical lability. Org-N fluxes were on the order of 2 months to ~2 years, again signifying a large water column inventory. Finally, microcystin toxin residence times were highly variable when all incubations are considered, with residence times between approximately 1.5 months for the light chamber and 6 months for the dark chamber when averaged. However, for the individual incubations in which the toxins were demonstrated to accumulate, results are more reasonable, with residence times on the order of 3-12 days with respect to the entire L001 water column.

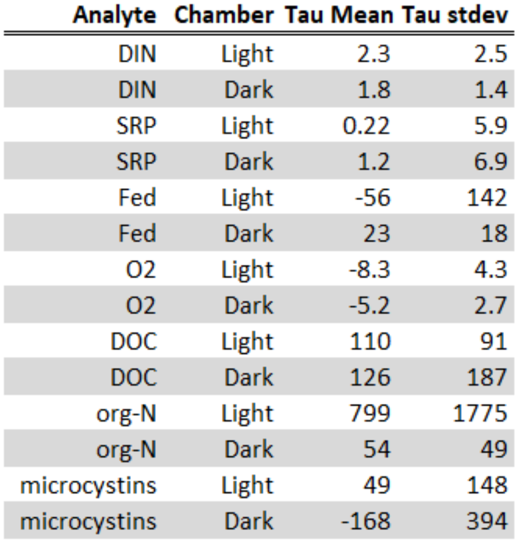

Analyte	Chamber	Tau Mean	Tau stdev
DIN	Light	2.3	2.5
DIN	Dark	1.8	1.4
SRP	Light	0.22	5.9
SRP	Dark	1.2	6.9
Fed	Light	-56	142
Fed	Dark	23	18
O2	Light	-8.3	4.3
O2	Dark	-5.2	2.7
DOC	Light	110	91
DOC	Dark	126	187
org-N	Light	799	1775
org-N	Dark	54	49
microcystins	Light	49	148
microcystins	Dark	-168	394

Table 3B-3: Average residence times for analytes in light and dark chambers. There is significant variability with many analytes, and thus it is recommended that the results for individual incubations be examined in the context of other factors, such as *M. aeruginosa* ambient bottom water cell concentrations.

DISCUSSION

Overall utility of data: The data presented represents work corresponding to one year of activity and only a half-year of deployments. The lander represents innovative technology typically used for the oceanographic environment but now applied to a much more dynamic lake system that presents specific challenges. The task results were successful with respect to the expectations of the scope of work, but the information extractable from individual deployments should be considered in a greater context. Flux measurements, however, were affected by an inability to filter samples prior to the introduction into the syringes. Oceanographic systems do not attempt to filter during sample collection, so this need was not anticipated. One of the main limitations of this, however, is that biological activity does not stop in the syringes once the samples are collected. Additionally, the presence of biological organisms in the bottom waters during the deployments at concentrations greater than in the marine environment also limits the validity of the "fluxes" as serving as a true representation of the actual benthic flux. Instead, we must consider the results in a complicated context in which 1) nutrients fluxing from the sediments may be rapidly assimilated or transformed upon crossing the sediment-water interface, thus limiting their accumulation in the chamber and thus sample syringes; and 2) nutrients, once aspirated in the syringe, may undergo additional transformation until processing via filtration in the lab.

One approach for analyzing the validity of the data is by comparing the fluxes of individual analytes using covariate plots (Figure 3B-5) and statistics (Table 3B-4). The data points are further discriminated (data point colors) according to the ambient bottom water *M. aeruginosa* concentrations to determine if biological processes occurring within the benthic chamber incubations themselves could be affecting results. This approach yields very important information in that 1) the fluxes of various analytes do indeed correspond to one another (i.e. covary), demonstrating the validity of the overall approach; and 2) biological processes do appear to affect nutrient accumulation. For example, NH_4^+ accumulation is limited in the presence of higher *M. aeruginosa* cell counts (Figure 3B-5); in fact, very little NH_4^+ accumulation is evident at the highest cell counts, suggesting that the organisms are indeed consuming this nutrient in the benthic waters as fast as it fluxes.

Data interpretation: Compared to the reference lines for the expected nutrient release assuming the Redfield Ratio (106 org-C&O_2:16 N:1 P), the data demonstrates consistent trends (Figure 3B-5). The observed O_2 fluxes tended to exceed those of inorganic and organic N and DOC. Considering that *M. aeruginosa* grown under non-nutrient limiting conditions is enriched in N relative to the conventional Redfield ratio (78C : 15N : 1P; Tsukada et al. 2006), then we would expect that nitrogen fluxes should instead exceed O_2 fluxes whether the observed nutrient changes in the chamber were caused by their benthic remineralization or due to sediment fluxes. Instead, the relatively higher apparent sediment O_2 demand suggests that some portion of the O_2 is instead reoxidizing chemically reduced analytes in the sediments, or that some of the fluxing NH_4^+ is being assimilated. The high sediment oxygen demands are indicative of high rates of remineralization of a cumulatively reduced sedimentary environment that has been subject to decades of eutrophication. The best correlation observed between all analytes is between NH_4^+ and O_2 (Table 3B-4), suggesting that that benthic remineralization is driving ammonium production and thus a nutrient source to the water column.

The short residence times of DIN suggests that the sediments are an important nutrient source. Normalized to the Redfield ratio, DIN fluxes exceeded those of org-N, especially in the light chamber. However, Normalized DIN fluxes were relatively less than those of DOC. If we consider that DOC is perhaps the most conservative of the measured analytes, i.e. it is the least likely to react, then this suggests that both DIN and org-N are being consumed in the benthic chamber. Overall, these findings highlight the importance of these bottom water processes in governing nutrient dynamics and suggest that *M. aeruginosa* may be assimilating nutrients in the benthos, including org-N. Additionally, the observation of apparent nitrification in the benthic chamber does shed light on the competition for NH_4^+ between nitrifying organisms and *M. aeruginosa* assimilation.

SRP did not consistently accumulate in the incubations, and the sediments were sometimes a sink for SRP. This is consistent with previous findings that demonstrate that SRP fluxes are most evident under anoxic conditions but that resuspended particulates can also scavenge SRP from the water column. In two incubations, an increase in SRP was evident in the last collected syringe, suggesting that a critical O_2 threshold was reached, despite O_2 concentrations not being fully depleted. The onset of SRP fluxes upon O_2 depletion is rapid in both sediment core incubations and observed in site in Lake Erie, another *M. aeruginosa* affected system (Anderson et al. 2021). Similarly, dissolved iron also displayed this inconsistent behavior, probably due to similar mineral-associated processes. However, our results demonstrate the importance of monitoring the *total* concentrations of dissolved iron, not just the reduced form which is often mistakenly assumed to be the only soluble component.

Microcystin toxins did accumulate in some chamber incubations, and more so when *M. aeruginosa* was present in the bottom waters (**Figure 3B-6**). The purpose of supplementing these measurements as part of the project was to determine if the sediments were a potentially long-lasting source of toxins to the water column and thus affecting ecological health. However, we cannot conclusively answer this question due to biological activities within the sediments. We do note, however, that we apparently do not observe a significant microcystin toxin flux in the absence of *M. aeruginosa* in the ambient bottom waters (when cells $mL^{-1} < 14k$). The observed increases in toxins in the presence of *M. aeruginosa* suggests that either 1) the cells are producing toxins directly in the benthic chamber; or 2) the current or recent presence of cells does result in the accumulation of sediment toxins and thus a benthic flux. In some oceanographic studies of contaminants that have a relatively low benthic flux intensity, chamber incubations are extended longer than typical (i.e. several days) with artificial aeration (to limit induced hypoxia). This may be necessary in the case of HAB toxins.

Although not presented here, we also monitored fluxes of colored-dissolved organic matter (CDOM) as part of a coordinated NASA project. Diffusive fluxes are evident, indicating that the sediments may be an important control on regulating water clarity not just via the resuspension of particulates but also via persistent diffusive fluxes. Further, preliminary data suggests that both organic matter and associated complex dissolved iron both contribute to the absorption signal.

CONCLUSIONS AND FUTURE WORK

Overall, more data interpretation is needed to fully interpret these results. The time series fluxes were only derived for the period of Jun.-Oct. 2021, which does not provide for enough data to truly interpret the seasonal dynamics. Perhaps more concerning is that there will always be some element of ambiguity given that the samples could not be filtered in situ. We can still draw several conclusions from the data, especially in regard to the relative accumulation of specific analytes with respect to others monitored during the same incubation, however:

- The sediments are an important sink for dissolved O_2 and are able to consume the entire water column inventory within several days to a week. This highlights the importance of vertical ventilation in maintaining oxygenated conditions.
- Microcystin toxins do accumulate in bottom waters when *M. aeruginosa* cells are present, and existing water column toxins potentially even decrease (via adsorption onto suspended material) at low cell concentrations, although we cannot directly discriminate between new toxin production and sediment inputs with this instrumentation.

- Benthic nutrient uptake is substantial, so much so that several thousand cells mL^{-1} of "trapped" *M. aeruginosa* can consume almost all fluxing DIN over the course of a half-day.
- Phosphate does not consistently accumulate in the bottom waters due to diffusive sediment fluxes, so resuspension is probably the most important process for delivering sediment SRP to the water column.
- Even with very little light reaching the bottom waters at site L001, we do observe differences in the dark and light incubations with respect to O_2, nutrient, and toxin dynamics. There is subtle evidence that nutrient uptake is more substantial in dark incubations (compare the org-N vs. DIN flux plots in Figure 3B-5), suggesting that the cells are "primed" to uptake nutrients under dark conditions at night (consistent with vertical migration signals in **Task 2D**).

Improvements to the lander system are being currently undertaken as part of a separate project, and we hope to employ the modified system for the HALO project in the future. Specifically, the pumps are being replaced with a stronger version that can pump for longer periods of time without "burning out". In laboratory testing with collected Lake Okeechobee water, we did attempt to use 0.7 µm GFF filters in lieu of the 0.2 µm filters to at least provide some level of filtration, although these were still not adequate as only a few mL of sample was successfully filtered. We may also implement a multi-stage filtration system in future lander iterations. One advantage of using GFF filters would be to allow the collection of particulate material in the chamber, thus potentially providing insights into changing nutrient contents of the cells as well as information regarding their metabolic conditions (whether nutrient enriched or depleted at certain times of the year). Additional syringes (i.e. more than 5x per chamber) could help with interpreting data, as even a single "bad" collection caused by a fluidic leak could compromise the entire data set when interpreting results and fitting fluxes. Perhaps most importantly, we are designing a new lander capable of long-term deployment and multiple measurements of sediment fluxes, e.g. several per week for as long as one month. The development of this new system was motivated specifically by the demands of this project, specifically the highly dynamic system. Whereas oceanographic systems can provide sufficient information when deployed in a "one-off" seasonal capacity, it is obvious that a much-improved temporal resolution is required for a system such as Lake Okeechobee. Finally, the new lander will be capable of conducting "ambient" water incubations that are isolated from the sediments. By accounting for these background changes, e.g. by subtracting ambient incubation results from typical incubations conducted in contact with sediments, it may be possible to deconvolute the respective benthic boundary layer biogeochemical vs. sediment flux processes.

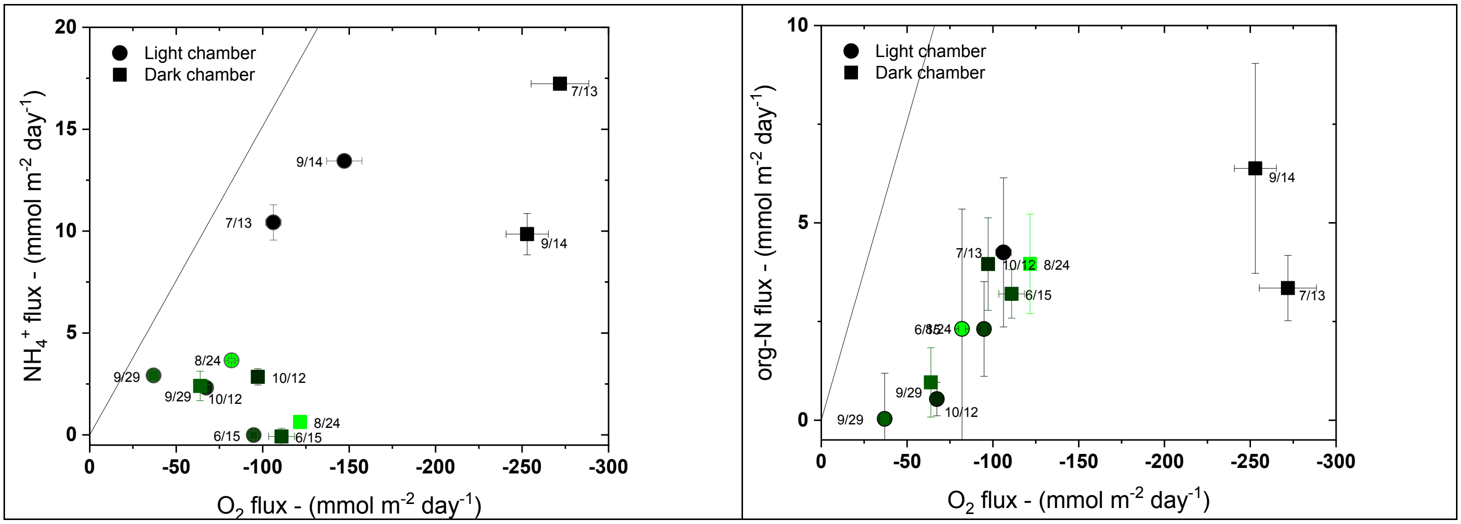

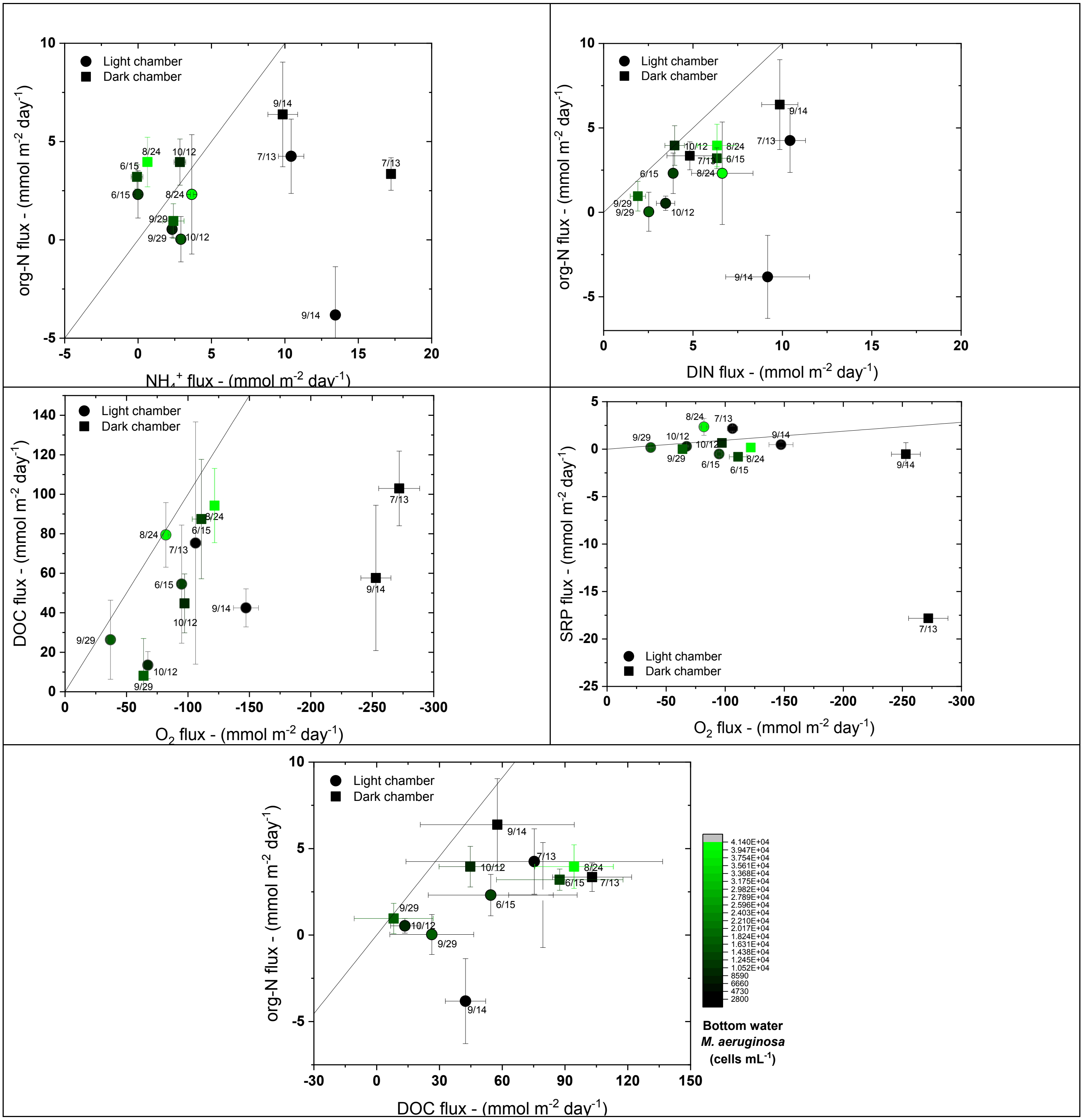

Figure 3B-5: Flux correlations for Light (circles) and Dark (squares) incubations, colored by the corresponding bottom water Microcystin toxins (see colorbar in the bottom-most figure panel). The reference line corresponds to the concentrations expected based on Redfield Ratios, i.e. $O_2/NH_4^+=6.6$; O_2/org-N=6.6; NH_4^+/org-N=1; DIN/org-N=1; O_2/DOC=1; O_2/SRP = 106; and DOC/org-N=6.6.

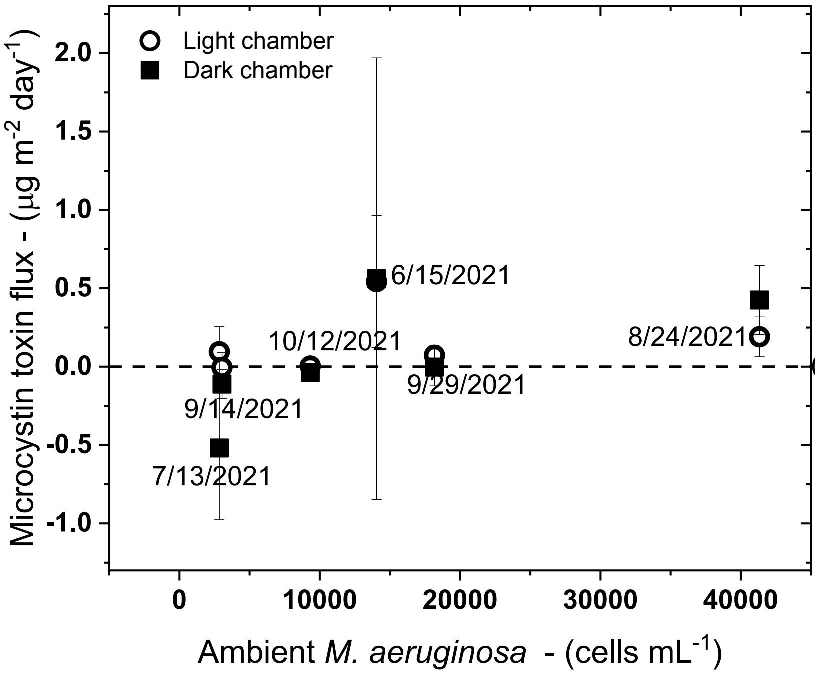

Figure 3B-6: Microcystin toxin fluxes as a function of ambient bottom water *M. aeruginosa* cell concentrations for Light (circles) and Dark (squares) incubations. The y-axis error bars are the standard error of the line fitted through all five of the microcystin toxin concentration data points as measured in the syringe samples.

Table 3B-4: Pearson Correlation Coefficients and p-values for calculated nutrient fluxes.

Combined Light and Dark chamber fluxes

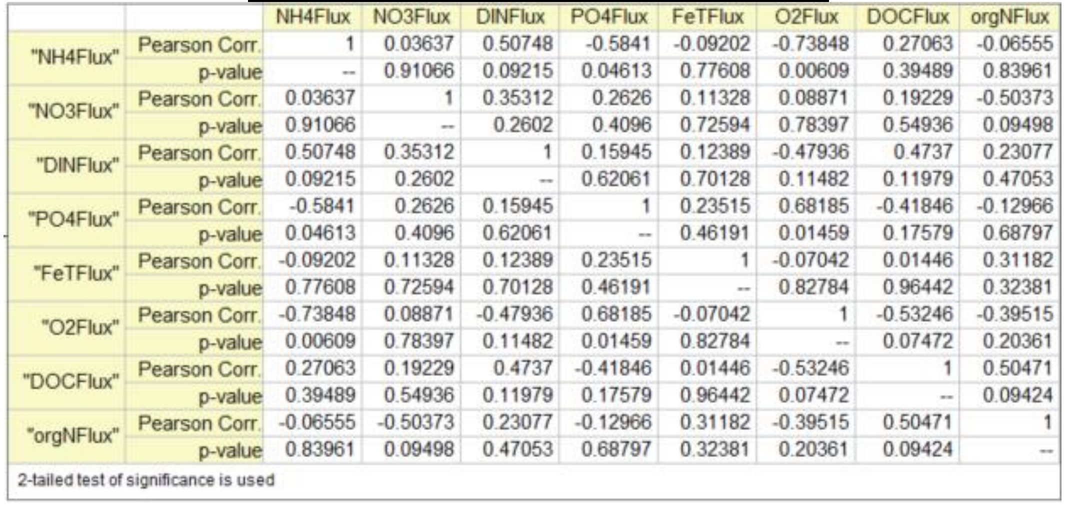

		NH4Flux	NO3Flux	DINFlux	PO4Flux	FeTFlux	O2Flux	DOCFlux	orgNFlux
"NH4Flux"	Pearson Corr.	1	0.03637	0.50748	-0.5841	-0.09202	-0.73848	0.27063	-0.06555
	p-value	--	0.91066	0.09215	0.04613	0.77608	0.00609	0.39489	0.83961
"NO3Flux"	Pearson Corr.	0.03637	1	0.35312	0.2626	0.11328	0.08871	0.19229	-0.50373
	p-value	0.91066	--	0.2602	0.4096	0.72594	0.78397	0.54936	0.09498
"DINFlux"	Pearson Corr.	0.50748	0.35312	1	0.15945	0.12389	-0.47936	0.4737	0.23077
	p-value	0.09215	0.2602	--	0.62061	0.70128	0.11482	0.11979	0.47053
"PO4Flux"	Pearson Corr.	-0.5841	0.2626	0.15945	1	0.23515	0.68185	-0.41846	-0.12966
	p-value	0.04613	0.4096	0.62061	--	0.46191	0.01459	0.17579	0.68797
"FeTFlux"	Pearson Corr.	-0.09202	0.11328	0.12389	0.23515	1	-0.07042	0.01446	0.31182
	p-value	0.77608	0.72594	0.70128	0.46191	--	0.82784	0.96442	0.32381
"O2Flux"	Pearson Corr.	-0.73848	0.08871	-0.47936	0.68185	-0.07042	1	-0.53246	-0.39515
	p-value	0.00609	0.78397	0.11482	0.01459	0.82784	--	0.07472	0.20361
"DOCFlux"	Pearson Corr.	0.27063	0.19229	0.4737	-0.41846	0.01446	-0.53246	1	0.50471
	p-value	0.39489	0.54936	0.11979	0.17579	0.96442	0.07472	--	0.09424
"orgNFlux"	Pearson Corr.	-0.06555	-0.50373	0.23077	-0.12966	0.31182	-0.39515	0.50471	1
	p-value	0.83961	0.09498	0.47053	0.68797	0.32381	0.20361	0.09424	--

2-tailed test of significance is used

Light chamber only

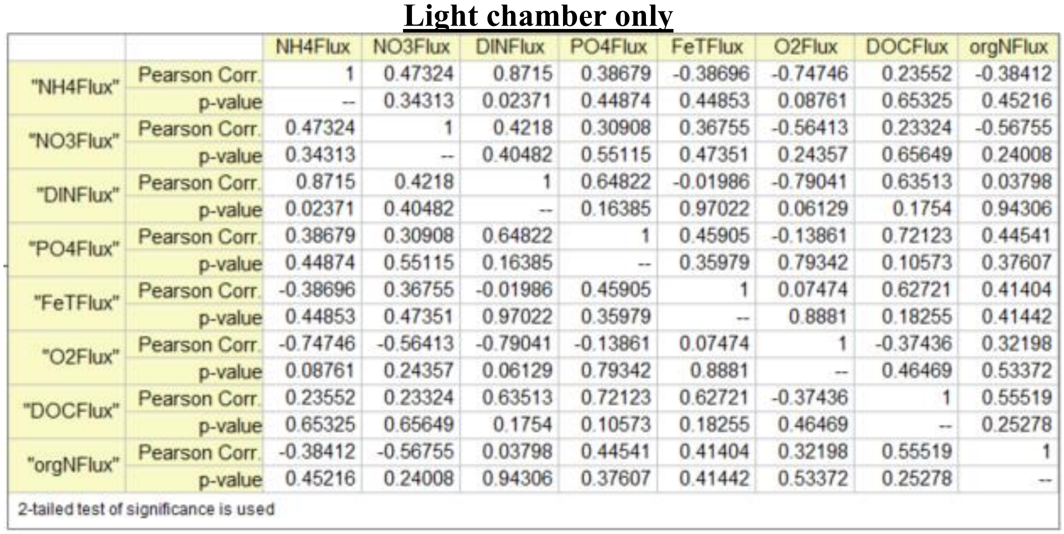

		NH4Flux	NO3Flux	DINFlux	PO4Flux	FeTFlux	O2Flux	DOCFlux	orgNFlux
"NH4Flux"	Pearson Corr.	1	0.47324	0.8715	0.38679	-0.38696	-0.74746	0.23552	-0.38412
	p-value	--	0.34313	0.02371	0.44874	0.44853	0.08761	0.65325	0.45216
"NO3Flux"	Pearson Corr.	0.47324	1	0.4218	0.30908	0.36755	-0.56413	0.23324	-0.56755
	p-value	0.34313	--	0.40482	0.55115	0.47351	0.24357	0.65649	0.24008
"DINFlux"	Pearson Corr.	0.8715	0.4218	1	0.64822	-0.01986	-0.79041	0.63513	0.03798
	p-value	0.02371	0.40482	--	0.16385	0.97022	0.06129	0.1754	0.94306
"PO4Flux"	Pearson Corr.	0.38679	0.30908	0.64822	1	0.45905	-0.13861	0.72123	0.44541
	p-value	0.44874	0.55115	0.16385	--	0.35979	0.79342	0.10573	0.37607
"FeTFlux"	Pearson Corr.	-0.38696	0.36755	-0.01986	0.45905	1	0.07474	0.62721	0.41404
	p-value	0.44853	0.47351	0.97022	0.35979	--	0.8881	0.18255	0.41442
"O2Flux"	Pearson Corr.	-0.74746	-0.56413	-0.79041	-0.13861	0.07474	1	-0.37436	0.32198
	p-value	0.08761	0.24357	0.06129	0.79342	0.8881	--	0.46469	0.53372
"DOCFlux"	Pearson Corr.	0.23552	0.23324	0.63513	0.72123	0.62721	-0.37436	1	0.55519
	p-value	0.65325	0.65649	0.1754	0.10573	0.18255	0.46469	--	0.25278
"orgNFlux"	Pearson Corr.	-0.38412	-0.56755	0.03798	0.44541	0.41404	0.32198	0.55519	1
	p-value	0.45216	0.24008	0.94306	0.37607	0.41442	0.53372	0.25278	--

2-tailed test of significance is used

Dark chamber only

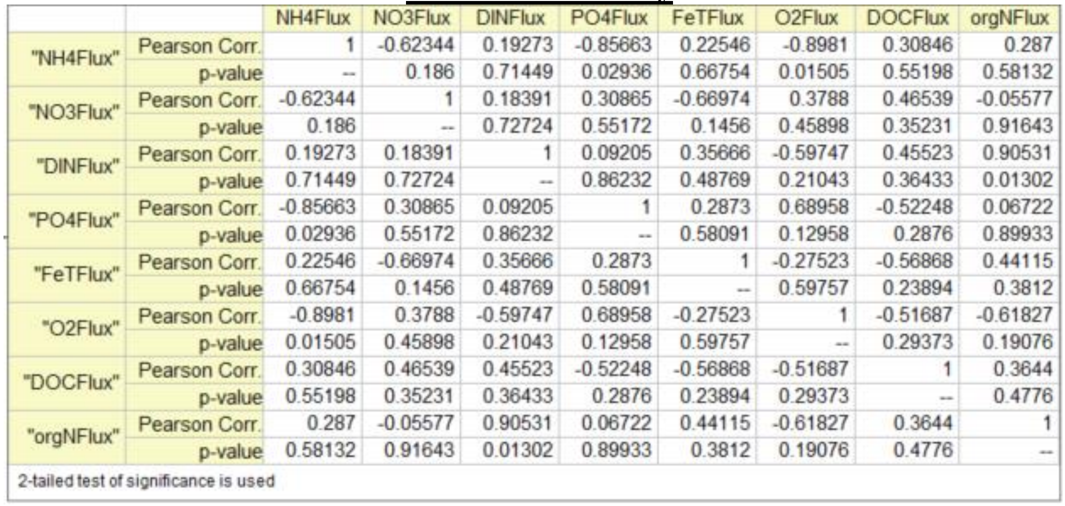

		NH4Flux	NO3Flux	DINFlux	PO4Flux	FeTFlux	O2Flux	DOCFlux	orgNFlux
"NH4Flux"	Pearson Corr.	1	-0.62344	0.19273	-0.85663	0.22546	-0.8981	0.30846	0.287
	p-value	--	0.186	0.71449	0.02936	0.66754	0.01505	0.55198	0.58132
"NO3Flux"	Pearson Corr.	-0.62344	1	0.18391	0.30865	-0.66974	0.3788	0.46539	-0.05577
	p-value	0.186	--	0.72724	0.55172	0.1456	0.45898	0.35231	0.91643
"DINFlux"	Pearson Corr.	0.19273	0.18391	1	0.09205	0.35666	-0.59747	0.45523	0.90531
	p-value	0.71449	0.72724	--	0.86232	0.48769	0.21043	0.36433	0.01302
"PO4Flux"	Pearson Corr.	-0.85663	0.30865	0.09205	1	0.2873	0.68958	-0.52248	0.06722
	p-value	0.02936	0.55172	0.86232	--	0.58091	0.12958	0.2876	0.89933
"FeTFlux"	Pearson Corr.	0.22546	-0.66974	0.35666	0.2873	1	-0.27523	-0.56868	0.44115
	p-value	0.66754	0.1456	0.48769	0.58091	--	0.59757	0.23894	0.3812
"O2Flux"	Pearson Corr.	-0.8981	0.3788	-0.59747	0.68958	-0.27523	1	-0.51687	-0.61827
	p-value	0.01505	0.45898	0.21043	0.12958	0.59757	--	0.29373	0.19076
"DOCFlux"	Pearson Corr.	0.30846	0.46539	0.45523	-0.52248	-0.56868	-0.51687	1	0.3644
	p-value	0.55198	0.35231	0.36433	0.2876	0.23894	0.29373	--	0.4776
"orgNFlux"	Pearson Corr.	0.287	-0.05577	0.90531	0.06722	0.44115	-0.61827	0.3644	1
	p-value	0.58132	0.91643	0.01302	0.89933	0.3812	0.19076	0.4776	--

2-tailed test of significance is used

TASK 3C: CONTINUOUS IN SITU SEDIMENT REDOX MONITORING
(TASK LEAD: BECKLER)

INTRODUCTION

While **Task 3A and 3B** provide discrete single time point measurements of sediment inventories and fluxes, few, if any, geochemical techniques in existence provide long term, sustained measurements of sediment conditions. It is well known, for example, that sediment redox conditions can affect not only the favorability of biogeochemical reactions, but also the release of nutrients to sediment pore waters and thus the potential for subsequent diffusive and resuspension fluxes. We therefore tested and then deployed an innovative, continuous, in-situ sediment electrochemical monitoring package several times at the lake. The electrochemical analyzer continuously operates four electrodes positioned at fixed-depths, originally targeting the benthic boundary layer, 1 cm deep, 4 cm deep, and 8 cm deep. By providing both depth- and time-resolved data, the sensors provide a general indication of the redox environment and could reveal variations in microbial respiration processes as affected over short time scales by diel and hydrodynamic processes, or changes induced by variability in benthic water column dissolved O_2 concentrations. A previous generation system was previously deployed Lake Champlain and demonstrated diel variability, with enhanced chemical reducing conditions at night and during HAB presence (Smith et al. 2011). Typical redox measurements employ a simple platinum electrode and only measure the redox potential and thus the "likelihood" of a certain respiratory regime, whether it be an aerobic, metal-reducing, or sulfidic environment. Instead, using a different electrochemical technique, i.e. voltammetry with a mercury amalgam functionalizing a gold electrode (i.e. the mercury coating mediates the electrochemical reactions), the employed system was capable of conducting a series of scans to collect specific analyte concentration at each electrode on the order of every 20 minutes. This is a similar system that was used in **Task 3B** to monitor redox active metabolites (mainly dissolved O_2) undergoing changes within the benthic flux chambers.

In voltammetry, the current of a redox reactive analyte is recorded at a counter electrode as a function of time as the potential at a working electrode in contact with an electrolyte is varied relative to the potential of a reference electrode. The development of solid-state Au microelectrodes with Hg amalgam (Brendel and Luther, 1995) offers a particularly useful window for environmental chemistry as numerous redox active species undergo electron transfer within the 0 to -2.0 V window. Specifically, the system measures dissolved oxygen, $O_{2(aq)}$; hydrogen peroxide, H_2O_2; soluble organic-Fe(III) complexes, org-Fe(III); dissolved iron(II), $Fe(II)_{volt}$; aqueous iron sulfide clusters, $FeS_{(aq)}$; dissolved manganese(II), Mn^{2+}; thiosulfate, $S_2O_3^{2-}$; and total dissolved reduced sulfur species (i.e. hydrogen sulfide: $\Sigma H_2S=H_2S+HS^-+S^{2-}$, elemental sulfur: $S_8^{(0)}$; and polysulfides: S_x^{2-}) (Meiggs and Taillefert, 2011). At each electrode, a range of potentials is scanned (-0.1 to -1.8V) and measured increases in current correspond at certain pre-established, calibrated potentials correspond to each of the above analytes. This powerful technique is one of the only in situ long-term sediment monitoring system in existence. It is theoretically possible to monitor the progression of the "redox switch" potentially responsible for controlling sediment nutrient fluxes, i.e. the onset of anaerobic conditions (evidenced directly by O_2 depletion in benthic boundary layer), the subsequent dissolution of sediment minerals (evidenced directly by Mn and Fe detection) and the release of oxide mineral-associated phosphate. Ultimately, this system could provide innovative insights into benthic-water column coupling processes, with data that can eventually be used to improve knowledge of biogeochemical processes and initialize models. At the very least, the system should provide information about the dominant respiratory process in sediments.

METHODS

Two low-cost electrochemical analyzer systems were purchased from Analytical Instrument Systems, Inc. (AIS ISEA-X). One unit was equipped with a larger battery pack to allow longer term measurements on the order of 1 month, while the other smaller system had a battery capacity of approximately one week with continued operation. The larger unit was primarily used in the laboratory, while the smaller unit was used for laboratory testing and for **Task 3B** benthic chamber monitoring. A small lander was constructed to allow the deployment of the ISEA-X via hand-lowering into place from the 26' boat, and divers were used to physically then insert an array of the four electrodes into the sediments at a pre-determined depth intervals. Electrode preparation is described below. The electrodes were affixed to the array with zip ties, and the base of the array was physically marked with large zip ties that served as a reference point that the divers would be able to "feel" while inserting into the sediments to ensure the array was inserted to the ideal depth so that each individual electrode would ultimately be operating at the targeted depth during the deployment. Two arrays were used: 1) the first array consisted of a single PVC stake to which electrodes were mounted at various depths; and 2) due to concerns with disruptions to the sediments caused by this larger stake, a freestanding PVC array with four separate locations for mounting electrodes vertically, at different heights, so that no single electrode affects the sediments around the others. On several deployments without divers, the electrodes were instead affixed directly to the lander frame, typically two electrodes on the top of the frame (benthic boundary layer) and two on the side of the lander feet that would instead enter the sediments, although the exact depth could not be determined. We also conducted laboratory testing in which a "bundle" of 4-electrodes was inserted several cm into the sediments to analyze the electrode inter-variability and microheterogeneity of the sediment system.

The ISEA-X was preprogrammed with sequence for all deployments that cycled a series of voltammtric scans at all four electrodes in series. The sequence was pre-programmed to start at a certain time, typically ~10-20 minutes after deployment to be conservative, as operation in the air would destroy the Hg amalgam. At all times during the deployment, any electrode not currently running scans is subject to a holding potential at -0.9 V to prevent memory effects and electrode "poisoning" from hydrogen sulfide. Dissolved O_2(aq) is typically measured by scanning the potential linearly at a constant rate using linear sweep voltammetry (LSV), ideal for non-reversible reactions (Brendel and Luther, 1995). Other redox species are typically detected by square-wave voltammetry (SWV), as good detection limits and high selectivity allow for the measurement of a variety of redox species simultaneously using this technique, particularly those that have some degree of reversibility (e.g. metals) (Luther et al., 2008). Finally, ASWV scans are added but are typically only useful if hydrogen sulfide is expected in high concentrations; which is not the case in the lake although it is periodically detected in sediment cores in **Task 3A**. The electrochemical data was processed directly by the manufacturer AIS, Inc via a proprietary technique. For some deployments, thousands of scans were generated. The scans were smoothed and a curved baseline subtracted from each scan, and the peak potentials, heights, and areas calculated after a fitting routine. Data discrimination is sometimes challenging due to peak convolution, thus this service proved to be invaluable. The manufacturer is working towards a fully automated processing routine for future related work.

The electrodes themselves are manufactured by AIS. Briefly, the working electrodes consist of PEEK plastic encasing a gold wire and filled with marine grade epoxy. In our lab, we first polish the electrode surface using four successively finer grits of diamond paste, so a lower limit of 250 nm. Then, we electrodeposit Hg(II) onto the electrode by applying a potential of -0.1 V (relative to Ag/AgCl reference electrode) for 4 minutes, forming a 100 μm diameter mercury "bead". The electrodes are then polarized by applying -9.0V in a solution of 1 M NaOH. The electrodes are stored in deionized water for up to 1 week prior to use, although calibrations are ideally performed within 48 hours of use. For use in Lake Okeechobee, two-point calibrations were performed for O_2 determination: both nitrogen degassed, and air-saturated filtered lake water, while recording the temperature to allow calculation of the corresponding molarity, which can be compared to the measured current height (the independent variable). For all other analytes, the “pilot ion” technique was used: lake water is amended with five concentrations of Mn^{2+} (as $MnCl_2$) to determine the Mn^{2+} sensitivity (measured nA/μM), which is then multiplied by a suite of literature constants to determine the sensitivities for the other analytes. However, due to the potential for the measured current to be affected by chemical complexation, the technique is only semi-quantitative for Fe^{2+} and organic-Fe(III) in organic rich waters such as Lake Okeechobee, while FeS_{aq} is always semi-quantitative due to the everchanging nature of its stoichiometry and phase (colloidal vs. soluble). Finally, other unknown current signals have been previously observed and are thus also only qualitative until their future identification.

ACTIVITIES SCHEDULED vs. COMPLETED

A total of four deployments were scheduled, each being a week or more in duration and to be conducted seasonally. Overall, the approach yielded extremely insightful results, but the overall goal of continuous in situ monitoring towards a fully “operational” sense was not met. Unfortunately, a significant problem affected the earliest deployments that required substantial troubleshooting. The sensor was tested in several lab and field tests ranging from 24 to 72 hours beginning in Fall 2020, and the tests generated reproducible scans and “logical” data. Because the sensor was a prototype when received, however, a simple fix to overcome a software bug (related to polarity) required manually configuring the sensor (on our end) with a holding potential of *positive* (+) 0.90 V in order to actually apply the desired *negative* (-) 0.90 V, that is required to limit electrode fouling. This situation was known to all parties and was not problematic. However, when beginning deployments in the lake, we received an updated sensor for which this bug was now fixed but weren’t relayed this information. Therefore, the first two field deployments were compromised as we deployed the sensors and were now actually applying +0.9 V, which causes rapid electrode degradation by essentially destroying the mercury amalgam. Because of the previous successes during testing, the difficulty of and many steps involved with preparing “good” electrodes (approximately a half day to prepare and calibrate four electrodes), the potential for contamination or the destruction of the amalgam, and many other potential sources of problems in the field, it is logical to assume the electrodes were just of poor quality. Indeed, this technique, while powerful, is notoriously non-robust and only ~75% of electrodes typically reveal useable post-deployment, and often less with inexperienced operators. After the second deployment (3/25/21 to 4/29/21) also demonstrated rapid electrode degradation, we conducted an informal lab test with a single electrode in early May in a beaker of 0.1 M NaCl water to determine if it was just an issue specific to Lake Okeechobee, e.g. caused by organic loading. Because the electrode again degraded rapidly (within 24 hours), we carefully revisited all system settings, inquired with the manufacturer about the polarity issue, and received the news that the bug had been fixed by the manufacturer, essentially explaining our problems.

Finally, we conducted a laboratory test with four electrodes using Lake Okeechobee water in May and achieved the high-quality data that was expected. The next field deployment (5/27/21-6/15/21) was partially successful, with only two of the four electrodes providing “good” data, although we were unable to determine the cause of the problems. We attempted another deployment two days later beginning 6/17/21. The sensor was relayed to the divers that morning by leaving on the L001 tower unattended for ~90 minutes, rather than a direct hand-off. However, the system was flooded upon retrieval on 7/28/21. We were not able to determine the responsible party, which could have been caused by a manufacturers defect in the housing (Blue Robotics), rough handling during the diver-deployment (there was no reason to suspect this was the case), or possibly warping of the housing or o-rings due to heating during the 90 minute transfer period to the divers. Fortunately, the manufacturer did replace the instrument at no charge, although the new instrument was not received until mid-September. We did conduct a 5-day long laboratory test in August which is probably the most successful data generated from this task to date. We were unable to deploy the system in October as planned due to a staffing problem. Overall, we did technically meet the "number of deployments" requirements for this system and conducted extensive troubleshooting and laboratory testing (Table 3C-1). However, we are not satisfied with the overall level of success to date relative to the overall potential of this sensor system to provide impactful data for the lake. We therefore aim to continue to deploy the system in the lake as part of the new Tasks planned for Amendment #3, particularly the **Task 9** "Comprehensive field weeks", although this is not formally promised in the Scope of Work as we are uncertain about staffing and logistical resources given the otherwise intensive work planned. For brevity, only results for successful and scientifically impactful testing and deployments are presented in the remainder of this task report. Raw or processed data associated with other testing is archived and is available upon request.

Table 3C-1: Deployment and lab testing activities for this Task.

Deployed	Retrieved	Site	Method deployed	Method retrieved	Actual monitoring duration	Quality / Data status	Photos?
9/3/20	9/4/20	Gulf of Mexico blue hole	Strapped to lander of leveraged project	Winch	24 hours	High quality time series.	no
12/16/20	12/16/20	Lake O L001 water column	Strapped to lander	Winch	8 hours	No data, instrument did not start due to programming (operator error)	yes
2/26/2021	3/23/2021	L001	Diver	diver-less	*Approx. 14 days (scans for 2/24/2021 - 3/10/2021 only)	Rapid electrode degradation, 3 of 4 electrodes scans were deemed unusable for deployment period 2/26/2021 - 3/23/2021. Only Cyclic Voltammograms as square waves scans compromised.	yes
3/25/2021	4/29/2021	L001	diver-less electrodes attached to lander frame/legs	diver-less	Approx. 32 days (scans for 3/25/2021 - 4/25/2021 only)	Rapid electrode degradation	yes
5/4/21	5/10/21	Lab test	Electrodes in beaker of NaCl sol'n.	benchtop	5 days	Rapid electrode degradation. Shortly after, realized was	no

						caused by software settings	
5/12/2021	5/17/2021	Lab test	Electrodes in beaker of Lake O water	benchtop	Approx. 5 days (5/12/2021-5/16/2021)	Dissolved O2 data is high quality and is processed.	yes
5/27/2021	6/15/2021	L001	diver	diver-less	Approx. 16 days (scans for 5/27/2021 - 6/11/2021 only)	Electrodes 2 & 4 appear OK for at least 3 days. Other electrodes not great - must investigate.	yes
6/17/2021	7/28/2021	L001	diver	diver-less	Unknown; SD card corrupted	Instrument was flooded upon retrieval - waterproof housing failed.	yes
8/13/2021	8/18/2021	Lab test	Electrodes in sediment core taken same day	benchtop	5 days	Electrode overlays; Data is high quality.	yes

RESULTS & DISCUSSION

The initial deployments were conducted using the small lander frame with the ISEA-X, with the electrode cable connected to electrodes individually mounted at various depths to a single PVC stake that was inserted by diver into the sediments (Figure 3C-1). The electrodes from the deployment conducted on 2/26/21 rapidly degraded due to the programming issues described in the previous section. However, the first few hours of the deployment did generate useable data, but only for the cyclic voltammetry scans and not for the more desirable square wave scans due to a programming error (Figure 3C-2). Specifically, the sensor-monitored current range was mistakenly set to 100 µA instead of 100 nA, thus the range was far too large to discriminate between smaller peaks. The data that was collected was “logical” and did demonstrate dissolved O_2 in the benthic boundary layer electrode, no O_2 but dissolved Mn^{2+} at 2 and 6 cm deep, and no O_2 and no other analytes at 14 cm deep. Surprisingly, there was no dissolved iron detected as was the case in the **Task 3A** voltametric profiles collected in lab cores (albeit in low concentrations); however, the winter was overall a period of relatively low detected Fe, probably due to high resuspension activity and thus iron reoxidation and precipitation processes. Unfortunately, the **Task 3A** sediment core voltametric profile data exists for only dates sandwiching this Feb. 2021 **Task 3C** deployment (i.e. Dec. 2020 and Apr. 2021), so we cannot directly compare the in situ (**Task 3C**) vs. laboratory (**Task 3A**) conditions; however, from a geochemical sense this **Task 3C** data does overall support that this is a period of low iron-solubilization activity and thus also low dissolved phosphate release.

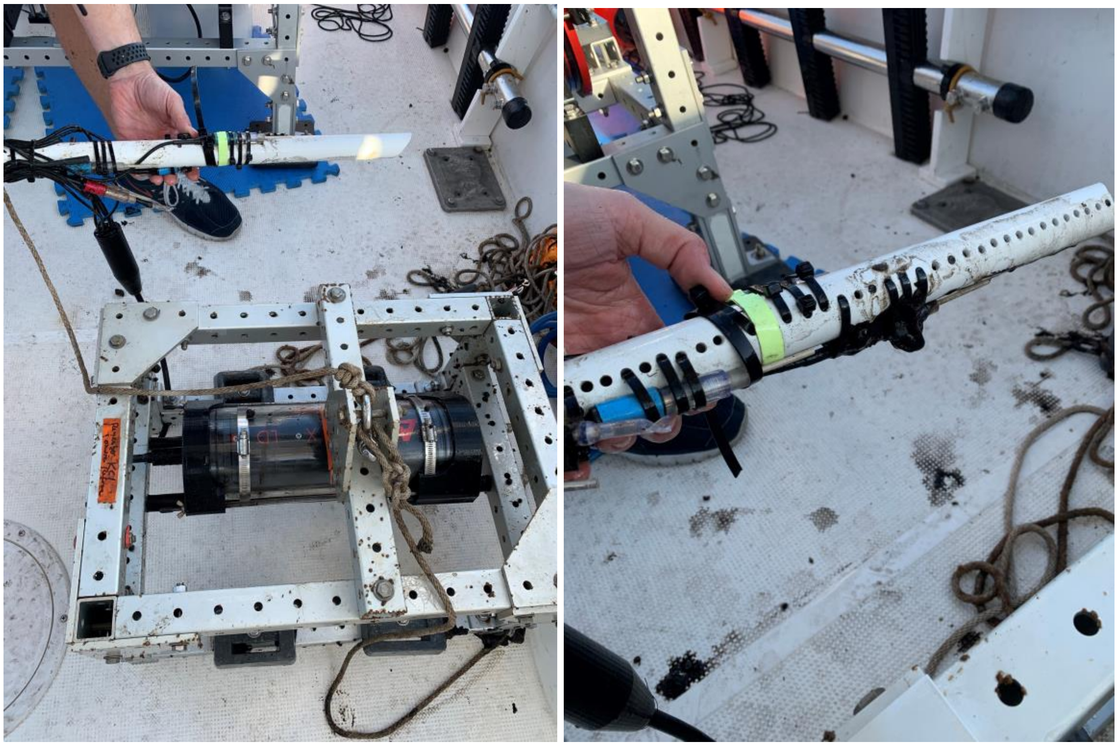

Figure 3C-1: The "mini-lander" used to deploy the ISEA-X and the single electrode array with four electrodes mounted at various depths (PVC stake).

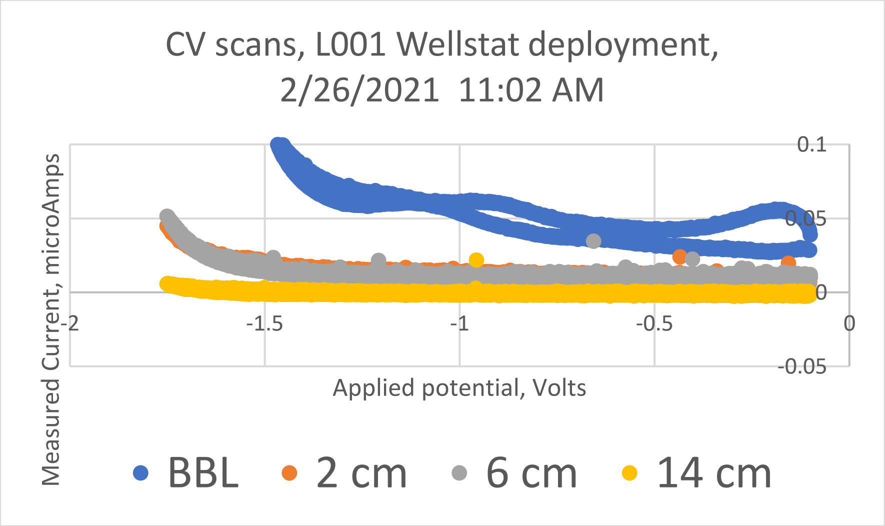

Figure 3C-2: Example cyclic voltammetry scans from each of the electrodes from the beginning of the deployment started Feb. 2021. Evidence of dissolved O_2 presents at -0.9 V (this is actually a peak caused by hydrogen peroxide reduction that serves as a proxy because the peroxide is formed from the reduction of O_2 at the electrode surface), while dissolved Mn^{2+} presents via the small inflection peak at -1.5 V. More negative (left) of -1.6V, the increase in current is due to the reduction of Na^+ ions at the mercury surface and is thus the limit of the "window" for electrode use in this lake system.

Because divers were unavailable to assist with the field deployment activities in March 2021, the electrodes were instead attached directly to the lander frame (Figure 3C-3). The instrumentation was immediately redeployed (i.e. on 3/23/21) with freshly prepared electrodes. Two electrodes should have entered the surface sediments as they are attached to the lander legs, and two should have been in the benthic boundary layer approximately 10 and 20 cm from the sediment-water interface, respectively. The data was of low quality, and thus led to laboratory testing.

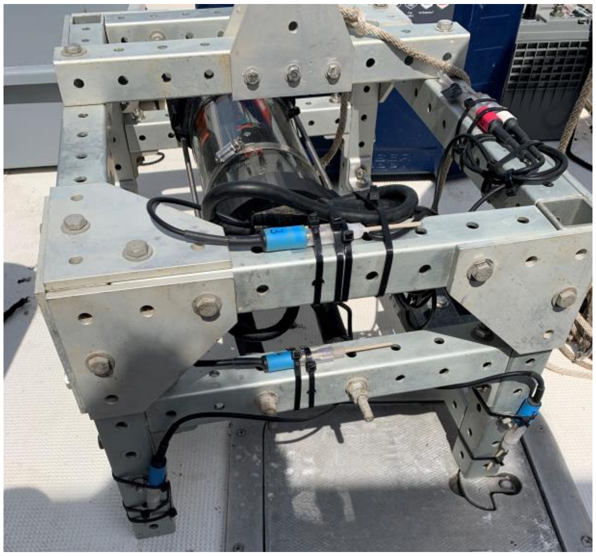

Figure 3C-3: The "mini-lander" being deployed with the ISEA-X and the electrodes individually attached to the lander frame.

In May, the 5-day test of four electrodes operating in a beaker of Lake Okeechobee water after making the major correction to the system programming revealed data of extremely high quality (Figures 3C-4&5). The data demonstrates that dissolved O_2 concentrations were relatively constant over a period of five days, with slight differences mirrored between electrodes and probably caused by laboratory temperature variability. However, one electrode (Elec 3) did experience a drastic current decline after ~24 hours – it is not known what caused this. Fortunately, these types of problems are obvious when analyzing data so can be removed or corrected for. Overall, however, the system was considered optimized at this point of the task timeline.

The system was deployed on 5/27/21, this time with a new electrode array (Figure 3C-6) but the electrode data was only high quality for a few days and only at two of the four electrodes (Figure 3C-7). It was not determined why this was the case, but it is possible that the issues lie with either poor electrodes, a greater distance between the working, reference, and counter electrodes than in a beaker or in sediment cores (see test below), or some other in situ factor to be determined. The deployment did reveal for the first time the intensity of iron solubilization as evidenced by dissolved Fe(II) and organic-Fe(III), as well as other species thought to be associated with the microbial reduction of dissolved iron. The detection of these analytes forms the rationale behind this overall task- it is plausible that more dissolved phosphate is released and accumulates in pore waters at depths at which these processes are occurring. We also detected a sulfur-containing species, likely attributable to either hydrogen sulfide or to some organic-S redox active analyte such as thiols thought to be involved in the overall reduction of iron oxides by iron-reducing microbes. Indeed, the **Task 3A** sediment core electrochemically profiled from April, 2021 also demonstrated the presence of this hydrogen sulfide, suggesting that this is a period of intense respiration (caused by the onset of warmer temperatures) of organic material accumulated over the previous winter.

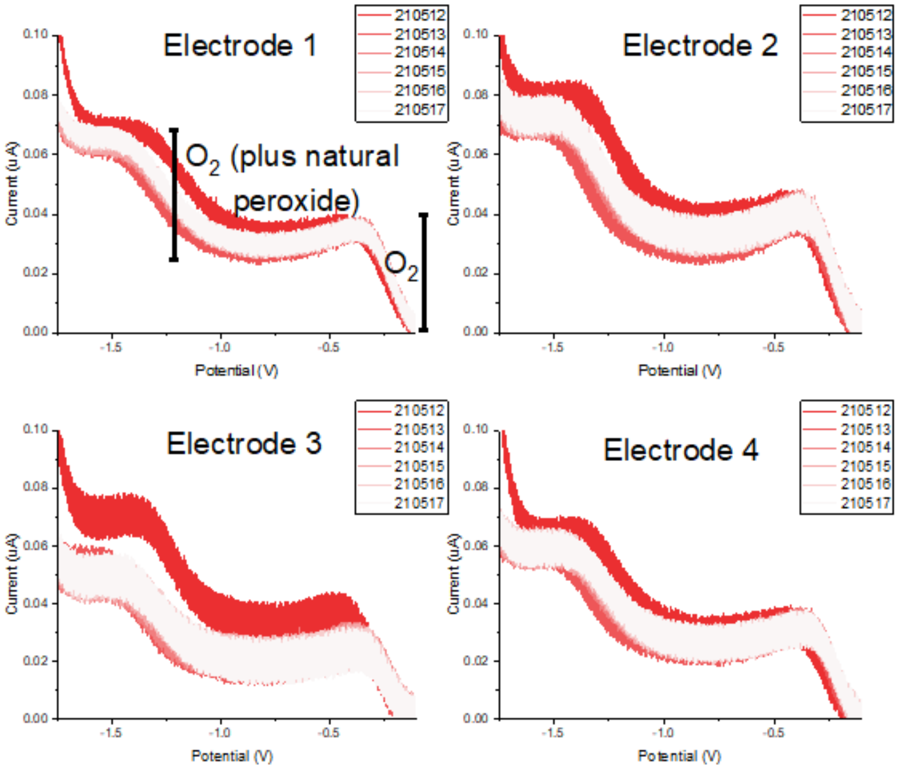

Figure 3C-4. Time series scans from four electrodes from the week-long laboratory experiment with oxygenated lake water.

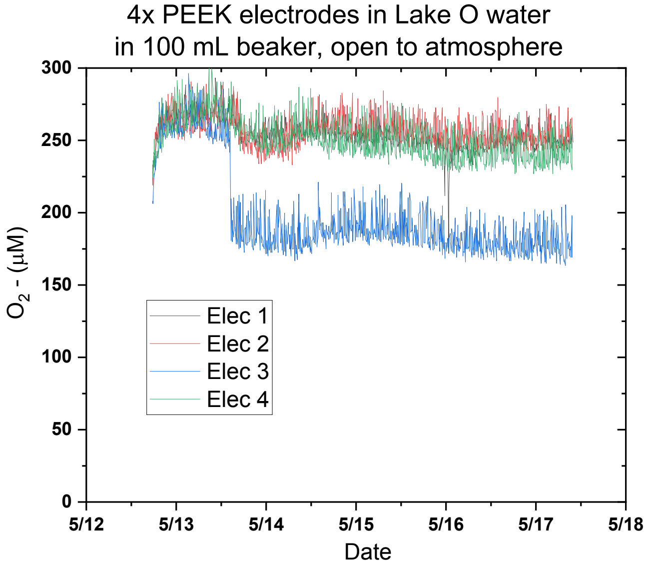

Figure 3C-5. Time series data from the scans in Figure 3C-4. Electrode scans are highly reproducible, and the peak heights can be converted to concentration and plotted as a function of time.

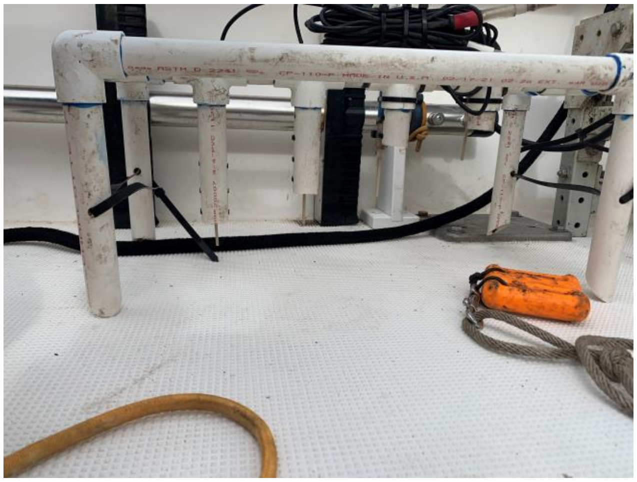

Figure 3C-6: The new electrode array deployed to ensure the electrode insertion does not affect other electrodes. Notice the electrodes are individually mounted on the 4x vertical extension lengths in the center of the array.

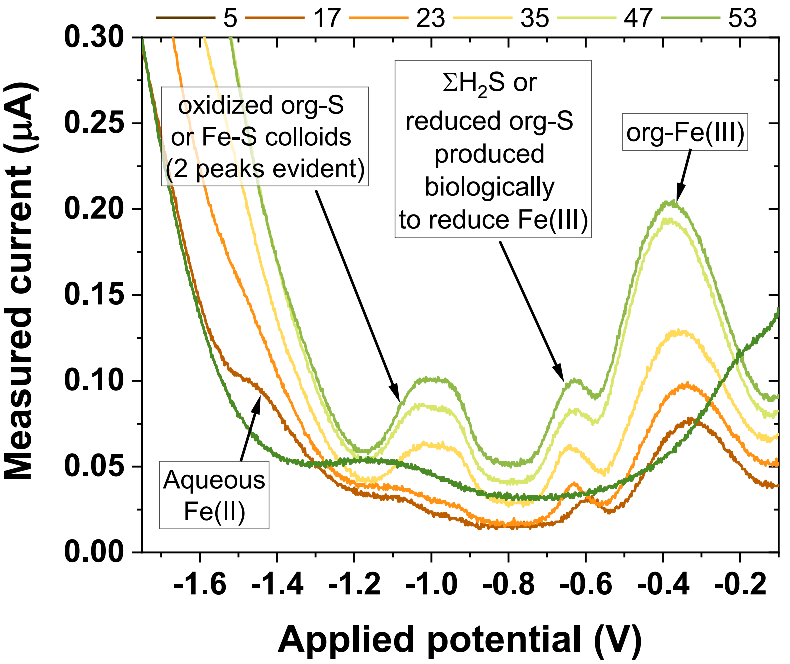

Figure 3C-7. Time series data from the 5 cm depth electrode from the 5/27/21 deployment, with the individual hour of the measurement represented via different colors.

The instrument flooded during the next deployment on 6/17/21, so instead subsequent tests were conducted using the spare smaller ISEA-X in a laboratory sediment core collected from site L001 (Figure 3C-8). This smaller ISEA-X is normally affixed to the larger **Task 3B** benthic lander for use in monitoring the benthic incubation chambers over time. For this experiment, the four rod-shaped electrodes were tightly bundled to form a single 4-electrode probe approximately 5 mm in diameter, and this combined electrode probe was inserted approximately 5 cm below the sediment surface, with scans collected over a period of five days (Figures 3C-9&10). All four electrodes generated high quality data during the entire period, with evidence of all four of the voltammetrically-measured analytes observed in the 5/27/21 deployment (Figure 3C-7). This suggests that these iron solubilization-linked analytes are pervasive throughout the sediments over the spring and summer, also supported by the **Task 3A** electrochemical profile data. The time series data from the lab test demonstrates several important findings: 1) The presence of these microbial iron-reduction linked analytes; 2) their gradual production over time (i.e. not stark sudden increases), suggesting that there is indeed true production or consumption over time; 3) high inter-electrode variability of the relative peak heights during the time series, suggesting a high degree of fine-scale heterogeneity; and 4) similarly, a lack of consistent patterns in the relative production of the four individual analytes between the four electrodes, i.e. different regimes in which the microorganisms in different sediment areas are producing the various intermediates involved in the solubilization and respiration of iron oxides.

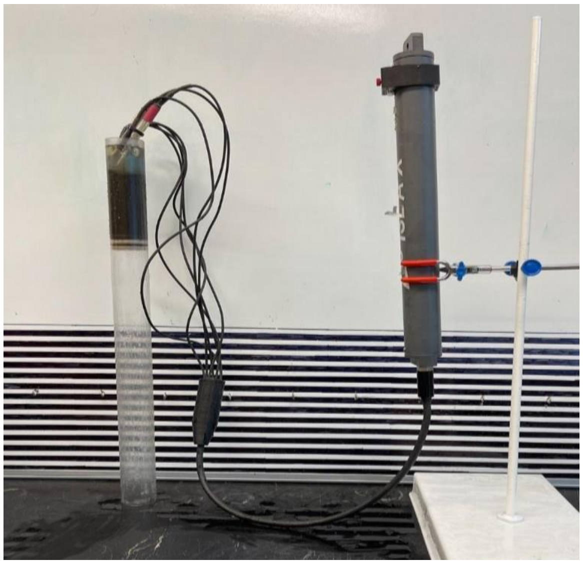

Figure 3C-8. Experimental setup for testing the reproducibility of the 4-electrode system in natural sediments.

CONCLUSIONS & FUTURE WORK

Overall Task comments and future potential of the technique: We did not meet our initial goals of deploying the sensor seasonally, which itself was a first step in demonstrating the capabilities of this system to be deployed in continuous operational mode. However, the technique does demonstrate promise for monitoring both dissolved O_2 in bottom waters, as well as the dominant respiratory processes in the underlying sediments. The data we did manage to collect nicely matched the respiration regimes observed seasonally via discrete measurements as part of **Task 3A**. With less than a year of testing for this innovative, research-oriented task, we believe progress was significant and does not discount the future potential of this sensor system in monitoring lake sediment processes. Per FDEP's request, we did eliminate, because of cost, the inclusion of a real time monitoring system; therefore, we could not monitor the electrode data as it was generated and were therefore unable to act on retrieving the sensors shortly after realizing that there were problems with the data. We continue to refine the techniques and only through building up a seasonal bank of measurements will we see the true potential for these activities. We are excited to continue to deploy the system alongside **Task 9** activities through the spring and early summer of 2021.

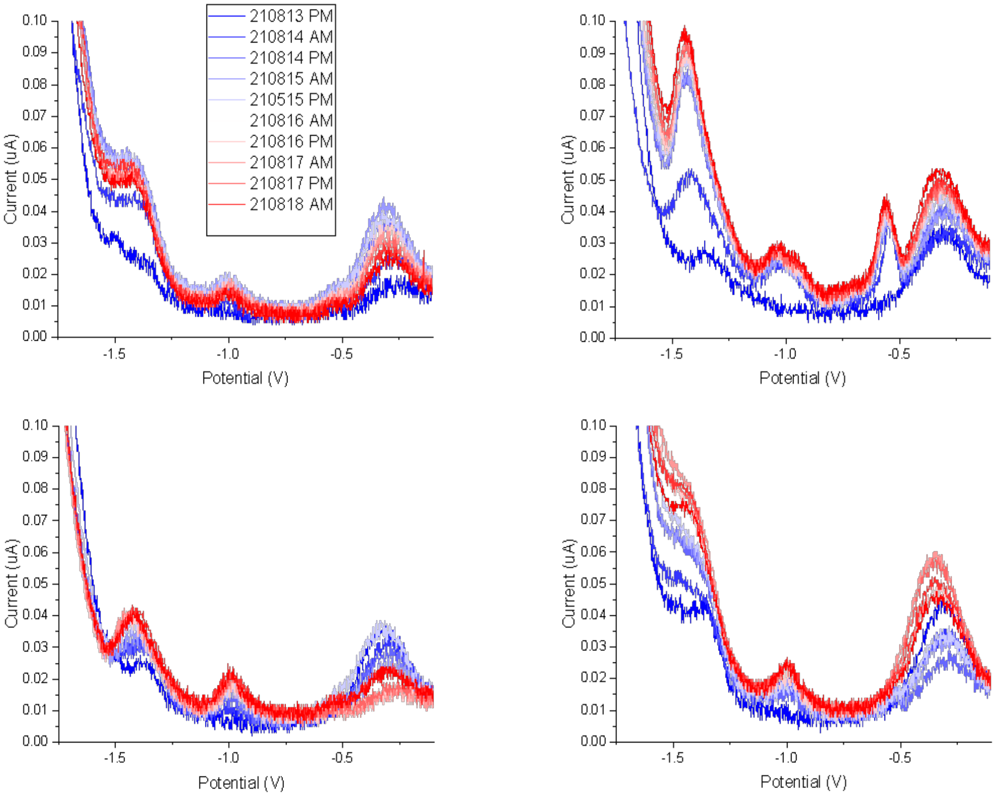

Figure 3C-9. Individual electrode scans from a 5-day laboratory experiment with four electrodes at a static position approximately 5 cm below the sediment-water interface. All four electrodes detected presumably the same four analytes that are commonly observed in sediments hosting dissimilatory iron reduction.

<u>Scientific insights:</u> Beyond dissolved O_2, the four analytes tentatively identified have been associated with the activity of dissimilatory iron-reducing microbes (Taillefert et al. 2006). The activity of these microbes is arguably one of the largest controls on pore water nutrients based on correlations between pore water phosphate and the generation of dissolved Fe(II) (**Task 3A**). Dissolved Fe(II) serves as evidence of iron oxide reduction, which subsequently results in the release of adsorbed phosphate. Indeed, we observed excellent correlations between dissolved Fe(II) and dissolved phosphate (**Task 3A**). Because phosphate cannot be monitored in sediment pore waters at present with any commercially available technologies, the dissolved Fe(II) that we demonstrate can be measured electrochemically both in situ and in laboratory sediment cores thus serves to some extent as a mechanistic proxy for the pore water phosphate inventories. **Task 3B** findings, on the other hand, demonstrated that fluxes of this phosphate are not diffusion dominated except under rare instances of hypoxia (in this case, induced by long in situ benthic incubations). Therefore, if we can subsequently monitor both pore water phosphate (via electrochemical Fe(II) proxy) and resuspension in situ, we can potentially infer the extent of phosphate resuspension fluxes from pore waters. We are employing a new technique to monitor resuspension as part of Amendment #3 (**Task 11**). Together, these techniques may prove to be a powerful coupling for obtaining a better understanding of the timing of nutrient fluxes and thus potential corresponding mitigative actions. On the other hand, we suspect from **Task 3A** results that iron redox processes are also responsible for oxidizing and removing ammonium from the pore waters as the warm season progresses. It is possible that the voltammetrically-measurable analytes may also be used to trace the intensity of these processes as well.

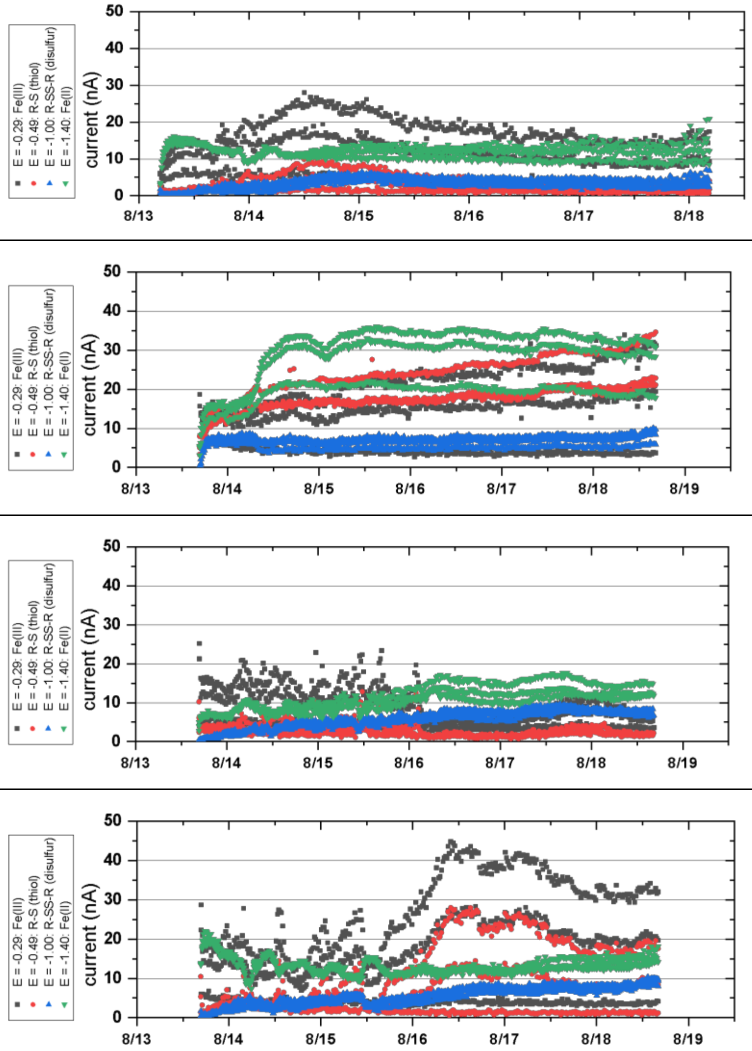

Figure 3C-10: Time series processed peak heights from the scans from the laboratory experiment from Figure 3C-9, for electrodes 1 thru 4 (top to bottom). The four colors correspond to the individual analytes detected at each of the applied potentials. It appears that there is three time series per individual analyte (potential) per electrode; these are each associated with the triplicate scans conducted at each time point. These can be averaged, but their presentation in this raw format is important to reveal how these individual analytes behave upon replicate scans. The measured current typically decreases between replicate scans, suggesting that the first two scans may demonstrate accumulation at the electrode surface. This can be either beneficial as it expands the limit of detection, but may also affect reproducibility, suggesting the first scans should be discarded until stabilized.

The suite of chemical analytes detected as part of this task do provide strong evidence of microbial iron reduction as the dominant respiratory process. Comparison of electrochemical data collected during pure culture laboratory incubations demonstrates a similar suite of metabolic intermediates (Figure 3C-11) are generated as in the Lake Okeechobee sediments (Taillefert et al. 2006). In one proposed mechanism for the anaerobic microbial respiration of iron oxides, the microbe releases an organic molecule that serves to solubilize the solid phase iron oxides prior to their reduction, in turn generating a more soluble and easily reducible organic-Fe(III) intermediate. In an alternative proposed metabolic pathway for microbial iron reduction, the organism generates reduced sulfur electron “shuttles” that are biologically secreted to abiotically reduce the iron (Figure 3C-12; Eitel et al. 2017). These analytes are oxidized in the process and spontaneously combine to form a disulfur-bridged molecule:

$$2Fe(OH)_3 + 2RSH + 4H^+ \leftrightarrow RSSR + 2Fe^{2+} + 6H_2O \qquad \text{Eq. 3C-1}$$

These low molecular weight molecules are tentative assignments to the voltammetric peaks observed at -0.6 and -1.0 V observed to accumulate in both pure cultures of iron reducing microbes and in Lake Okeechobee sediments, although this is based on circumstantial evidence (redox potential and genetic evidence). Regardless of the actual process, we suspect that any one of these molecules may be used as a potential indicator that dissimilatory iron reduction is intensifying or decreasing. The relative concentrations of the individual analytes, or their time series concentrations, may also be indicative of the trend in microbial iron reduction, e.g. if it is increasing or decreasing in intensity. Overall, we are excited about this dataset and plan continued deployments in an effort to continue establishing the use of in situ voltammetry as a powerful and unique tool in the arsenal to monitor nutrient dynamics in sediments.

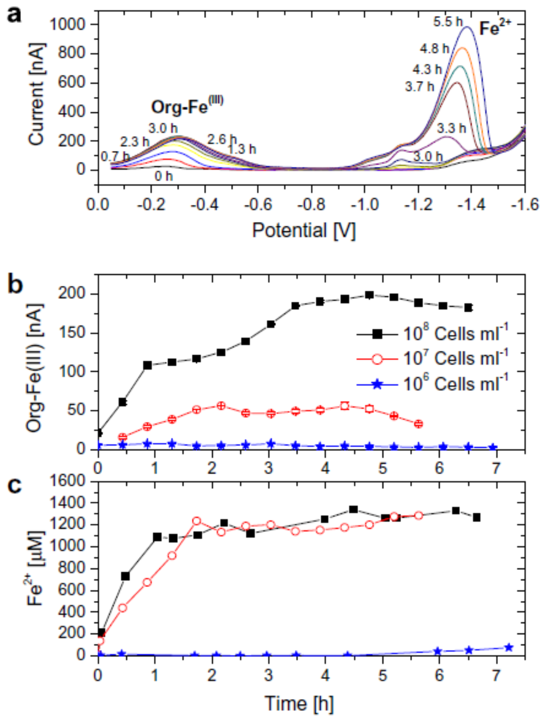

Fig. 1. Reduction kinetics of 2 mM Fe(III) citrate by 10^6, 10^7, and 10^8 cells ml^{-1} of *S. putrefaciens* strain 200R in Westlake medium. (a) Selected cathodic square wave voltammograms showing the production of soluble organic-Fe(III) complexes (ca. −0.3 V) and Fe^{2+} (at −1.35 V) as a function of time. (b) Change in current intensity of the organic-Fe(III) complexes as a function of time in each incubation; (c) change in Fe^{2+} concentration as a function of time in each incubation.

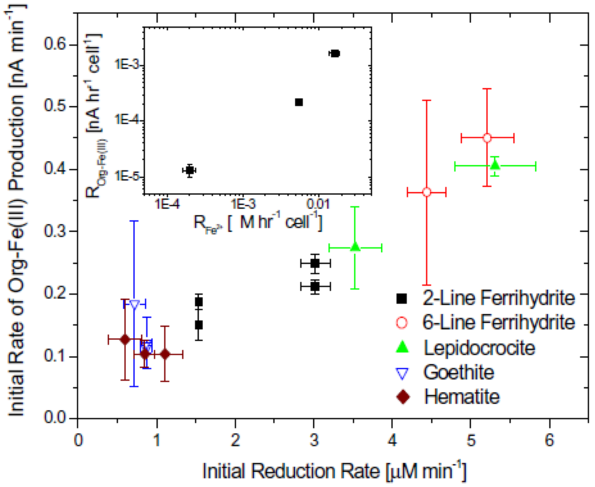

Fig. 4. Correlation between initial production rates of soluble organic-Fe(III) and Fe(III) reduction rates for incubations conducted with *S. putrefaciens* strain 200R and different forms of Fe(III) oxides (hematite, goethite, lepidocrocite, 6L-ferrihydrite, 2L-ferrihydrite). Inset shows correlation between initial production rates of soluble organic-Fe(III) and Fe(III) reduction rates normalized to the initial cell concentrations in the Fe(III) citrate incubations (Fig. 1).

Figure 3C-11: Left: Incubations with *Shewanella putrefaciens*, a model iron(III) reducing microorganism, demonstrate the production of a similar suite of voltametric redox analytes as those measured in Lake Okeechobee (compare to Figure 3C-9; note that the Applied Potential x-axis is horizontally inverted). With solid phase iron minerals such as those dominant in Lake Okeechobee sediments (2-line ferrihydrite as evidenced by high yields of ascorbic acid extractable iron in Task 3A), organic-Fe(III) current intensity production over time is correlated to the overall iron reduction rate (i.e. Fe(II) formation rate), suggesting that both voltammetrically-measurable species serve as evidence of these microbial activities (reprinted from Taillefert et al. 2007)

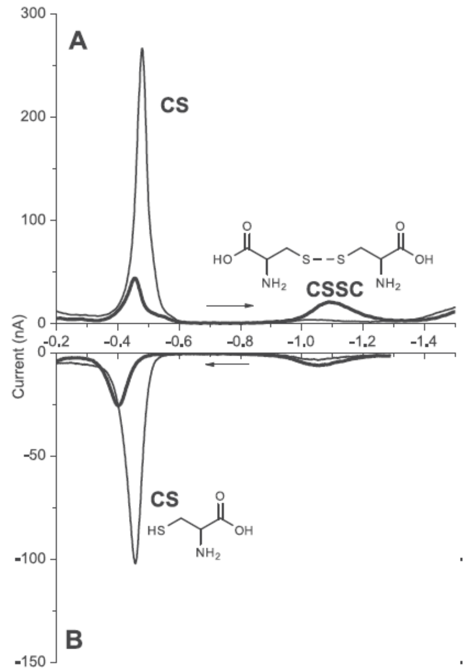

Figure 3C-12: Voltammetric scans of organic reduced (-0.45 V) and oxidized (-1.1 V) sulfur species demonstrate a similar fingerprint as those analytes observed in Lake Okeechobee sediment pore waters (reprinted from Eitel et al. 2017).

TASK 3D: SEDIMENT HAB CYST MEASUREMENTS (TASK LEAD: MCFARLAND)

INTRODUCTION

In many freshwater lakes *Microcystis* has a seasonal resting stage within surface sediments (Tsujimura et al. 2000, Kitchens et al. 2018). This resting stage allows cells to remain dormant during periods when environmental conditions are not suitable for growth. When environmental conditions are more favorable, cells and colonies can emerge from sediments and return to the water column where cell division and growth can resume. In other locations, the resting population is thought to be important seed stock for subsequent blooms (Brunberg and Blomqvist 2003). The timing and magnitude of seasonal blooms may be strongly influenced by the concentration of resting cells within sediments. Large resting populations can lead to higher cell concentrations in early spring and allow *M. aeruginosa* to outcompete other phytoplankton by quickly consuming available nutrients before other species. It is not known if *M. aeruginosa* populations in Lake Okeechobee exhibit this life history strategy. To determine if *M. aeruginosa* in Lake Okeechobee have a benthic resting stage, we looked for resting colonies within surface sediment samples using epifluorescence microscopy.

METHODS

Using samples collected in Task 3A, *M. aeruginosa* colony resting stages in surface sediments were quantified using epifluorescence microscopy. Samples were kept refrigerated at 4 ˚C for up to 48 hours before analysis. Various sample dilutions were tested to optimize the technique prior to analysis of lake sediment samples. Diluent (deionized water) was added to samples until viscosity was low enough to allow transfer by pipet. One mL of diluted sediment samples were then transferred to a Sedgwick-Rafter chamber and viewed on a Nikon Eclipse Ni compound microscope at 100X magnification using epifluorescence illumination. Chlorophyll was excited with blue light (480 nm) and fluorescence was visualized at wavelengths greater than 530 nm. Resting colonies of *M. aeruginosa* were manually identified by cell size and colony morphology. The entire chamber was scanned, and colonies were enumerated. Concentrations (colonies/mL) were then determined by correcting for the amount of diluent added to each sample.

ACTIVITIES SCHEDULED vs. COMPLETED

Analysis of samples from 7 sampling events were planned between May and October 2021 for analyses of cells from the Tiers 1-3 sites (L001, L005, and L006) for a total of 35 samples, but due to an agreed change in scope we did not continue to collect sediment cores from L005 and L006 beyond March 2021. Instead, we ultimately analyzed samples from 10 sampling events (34 total samples) as core samples became available (Table 3D-1).

RESULTS AND DISCUSSION

Resting colonies of *M. aeruginosa* were only found in two sediment samples collected at L001 on 7/28/21 and 8/25/21. Corrected concentrations were 4 and 10 colonies per mL of sediment, respectively (Table 3D-1). Colonies were easily identified using fluorescence microscopy (Figure 3D-1), so we have a high degree of confidence that their presence was consistently lacking. Numerous other algal cells were also observed in sediments but could not be identified.

Table 3D-1: Sample dates and sites analyzed to determine M. aeruginosa colony concentrations in surface sediments.

Date	Site	Colonies/mL	Date	Site	Colonies/mL
2/26/2021	L001	0	7/28/2021	L001	4
2/26/2021	L005	0	7/28/2021	LZ40	0
2/26/2021	LZ40	0	7/28/2021	L004	0
2/26/2021	L004	0	7/28/2021	Pahokee	0
3/25/2021	L001	0	8/10/2021	L001	0
3/25/2021	L006	0	8/10/2021	LZ40	0
3/25/2021	L004	0	8/10/2021	L004	0
4/29/2021	L001	0	8/25/2021	L001	10
4/29/2021	LZ40	0	8/25/2021	LZ40	0
4/29/2021	L004	0	8/25/2021	L004	0
5/27/2021	L001	0	9/15/2021	L001	0
5/27/2021	LZ40	0	9/15/2021	LZ40	0
5/27/2021	L004	0	9/15/2021	L004	0
6/17/2021	L001	0	9/15/2021	Pahokee inner	0
6/17/2021	LZ40	0	9/15/2021	Pahokee outer	0
6/17/2021	L004	0	9/29/2021	LZ40	0
7/13/2021	L001	0	9/29/2021	LZ40	0

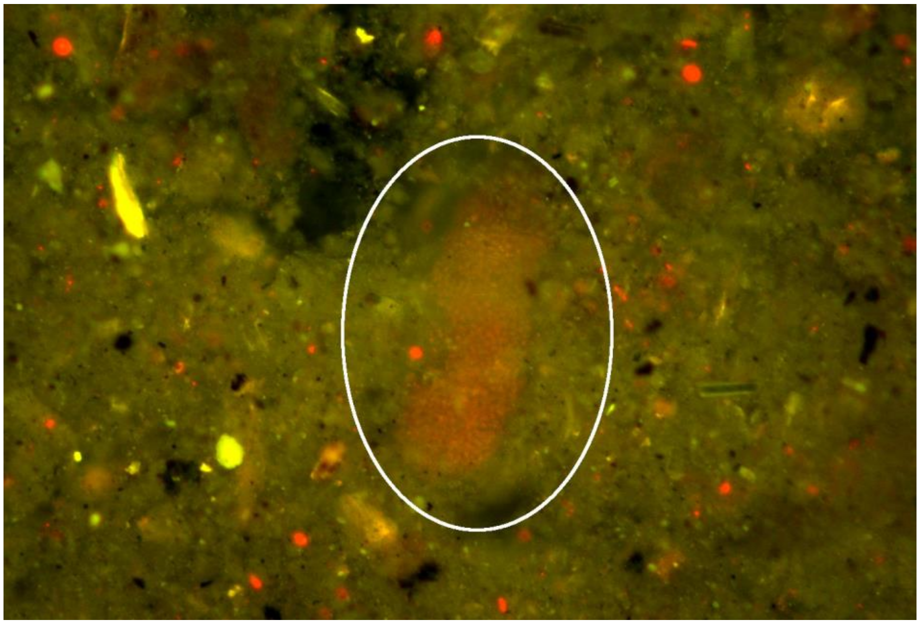

Figure 3D-1: An epifluorescence microscope image of an M. aeruginosa colony (circled).

CONCLUSIONS & FUTURE WORK

Surprisingly few colonies of *M. aeruginosa* were found in surface sediments despite high concentrations in overlying surface waters. Although it is common to find resting colonies in sediments of other lakes (Brunberg and Blomqvist 2003), it appears this is not the case for Lake Okeechobee. Annual recurring blooms, therefore, are most likely seeded from populations already present in the water column and not from sediments. It is possible that *M. aeruginosa* does not require an over-wintering life history stage in this system since temperatures are consistently relatively warm; instead, cells anecdotally do persist in low concentrations in the water column year-round (McFarland, unpublished). Since the lake is relatively shallow, sediments may also be too frequently disturbed by wind events to allow for accumulation of colonies in sediment surface layers. Furthermore, conditions within surface sediments may produce an environment that is unsuitable for colony survival and preservation. Task 3E additionally demonstrates that sediment toxin concentrations are low. Lake Okeechobee sediments are likely a relatively harsh environment with respect to the persistence of cells. Overall, these results suggest that additional efforts should not necessarily focus on quantifying sediment stages of *M. aeruginosa*, and potentially limit the possibility that nutrient uptake/transformations within sediments are driven by sediment nutrient acquisition by cysts. These results also scope the Task 1E modeling effort going forward, by setting a low priority for including sediment-specific *M. aeruginosa* behavior.

TASK 3E: SEDIMENT MICROCYSTIN TOXIN MEASUREMENT (TASK LEADS: BECKLER/MCFARLAND)

INTRODUCTION

There is no standard operating protocol for measuring microcystins (MCs) in sediments established for Lake Okeechobee, FL, and to our knowledge, the sediment microcystin concentrations have yet to be established. A previous study found that 0.1M sodium pyrophosphate + 0.1M Ethylenediaminetetraacetic acid (EDTA) was the most effective at extracting microcystins from lake sediments (Chen et al. 2006), although methanol or ethanol are other possibilities. During the methods development for this task, sodium pyrophosphate + EDTA and methanol were tested. However, these solvents may have additional interference effects on quantification via ELISA (in fact the kits directly state that the solvents are a problem). However, ELISA is a potential a lower cost alternative to requiring all microcystin extracted samples undergo mass spectrometric analyses. Further, the ELISA kits have a small detection window, 0.1 – 5ppb, potentially requiring several dilutions and thus complicating workflow.

This study aimed to 1) develop and microcystin extraction protocol and evaluate the extraction efficiency of these solvents, and 2) to quantify sediment microcystin from several lake sites seasonally throughout Lake Okeechobee. For the development, sediments were allowed to equilibrate in microcystin-containing solution for several days, and the amount subsequently extracted was compared to the amount initially lost from the soak water to determine recoveries. Both had similar recoveries of microcystin, but methanol had a slightly more consistent percent yield and was therefore chosen as the extractant. While the extraction efficiency was demonstrated to be reasonable (> ~70%), the decision was made to routinely employ mass spectrometry analyses for actual samples. Results ultimately showed that while sediment microcystin toxins can reach significant concentrations and were most elevated during highest bloom periods, Lake Okeechobee sediments do not appear to be a significant long term reservoir for microcystins.

METHODS

Extraction development procedure: Sediments from site LZ40 collected in Dec. 2021 (frozen for several weeks prior to the experiment) were dried for 48 hours at 60ºC and subsequently pulverized. Two beakers containing 12 g of the dried sediments were each amended with 60 mL of microcystin-spiked deionized water and pure deionized water. The mixtures were agitated to suspend the sediments, placed in a fume hood for 68 hours, and resuspended a total of four times to promote uptake of the microcystin by the solid phase sediments. After the incubation period, the water was decanted and collected from each beaker. New deionized water (50 mL) was added to the wet sediments, the mixtures were resuspended, centrifuged, and the water was collected again in different vials. This allows the removal of any unadsorbed microcystins. The collected rinse-water will eventually be analyzed for microcystin concentrations to determine the total adsorbed microcystin by difference. The microcystin-equilibrated sediments were again dried for 18 hours at 60ºC and subsequently pulverized.

Two extraction solutions were prepared: 50% Methanol, and 0.05 M Na pyrophosphate + 0.5 M EDTA. Two grams of the dried microcystin-equilibrated sediments were added to five scintillation vials, and 10 mL of solvent was added to each of the five vials (2x 50% Methanol, 2x pyrophosphate/EDTA, and 1x deionized water control). The vials were shaken and allowed to rest for 24 hours. After extraction the extractant (and original rinses) were diluted by both 50 and 100x and filtered thru GFF filters and analyzed as per the ELISA kit manufacturers instructions. After adjusting resulting concentrations for the two dilutions, the two dilutions allow evaluation as to whether the solvent is affecting the ELISA protocol by creating enhanced or depressed signals.

Routine sample analyses: Duplicate sediment samples (1-3 grams wet weight) were collected from each of the surface-most layer of the sediment cores (0 – 1 cm) and added to a scintillation vial. The vials underwent three freeze-thaw cycles to lyse cells, were subsequently oven dried at at 60ºC for 48+ hours (necessary drying time depends on sediment grain size), pulverized in an aluminum foil packet, and added back to tared and weighed scintillation vials for extraction. 10 mL of the 50% Methanol solution was added to each vial and allowed to extract for 24 hours, with at least four agitation/resuspension events during this time period. Post extraction, the vials were filtered thru GFF fiters and filtrates stored at -20ºC until measurement via ELISA or LC-MS. A dilution of 100x was typically used, or several dilutions can be attempted simultaneously to ensure results are in the ELISA detection window. The data is reported by first determining the total µg of microcystin in each 10 mL extract by multiplying the extractants dilution-adjusted measured concentration (ug/L) by the liters of extractant (i.e. 0.01 L), then dividing this total toxin amount (µg) by the dry weight of the sediments.

ACTIVITIES SCHEDULED vs. COMPLETED

Analysis of samples from 3 sites L001, L005, and L006 were planned for a total of four sampling events. This was based on the original "tiered" site sampling, but due to the early realization that L006 was not an ideal site it was scrapped. Instead, we analyzed the samples ad-hoc based on sample availability at the time, e.g. based on successful core obtainment. We did meet the required number of samples (12, in duplicate). After early realization that the ELISA assay was returning many non-detects relative to LC-MS (Greenwater Labs), samples all underwent LC-MS analyses instead (Table 3E-1).

Table 3E-1: Dates and sites and qualitative microcystin toxin results that were analyzed. ELIS= ELISA assay, LCMS = LC-MS results, ND = not detected, L = 0.001 - 0.010 µg/gram sediment dry weight, M = 0.01 – 0.1 µg/gdw, H = > 0.1 ug/gdw. The L/M/H scale designation is relative to this particular Lake Okeechobee study; overall, all concentrations in the lake were relatively low compared to previous sediment microcystin toxin studies. Site locations correspond to the map in Figure 1A-1 and Table 1A-1, with the PHKM site being inside the Pahokee Marina.

Date	L001 ELIS	L001 LCMS	LZ40 ELIS	LZ40 LCMS	L004 ELIS	L004 LCMS	L005 ELIS	L005 LCMS	PHKM ELIS	PHKM LCMS
2/26/21	ND	L	ND		ND	L	ND	ND		
5/27/21	ND	L	ND		ND	ND				
7/28/21		H		ND		ND				ND
9/15/21		M		ND		ND				ND

RESULTS & DISCUSSION

Extraction development procedure: The extracted solutions were visibly different, suggesting that sample color of the pyrophosphate/EDTA solution could potentially stain the antibodies adhered to the bottom of the 96-well plate during the ELISA assay (while unlikely, this is one potential drawback of this extractant; Figure 3E-1). The 50% methanol solution did not have any observable matrix effects on the ELISA results (i.e. direct measurement of the undiluted extractant solution with no toxin present). Undiluted sodium pyrophosphate + EDTA, on the other hand, did register a quantifiable effect on the plate, yielding a microcystin concentration of 2.6ppb when there was no microcystin present (data not shown). The kit manufacturer tested methanol on the kits and confirmed that there was no matrix effects when diluted <20%, but did not test sodium pyrophosphate or EDTA, so it is not known if diluting the sodium pyrophosphate would remove this matrix effect.

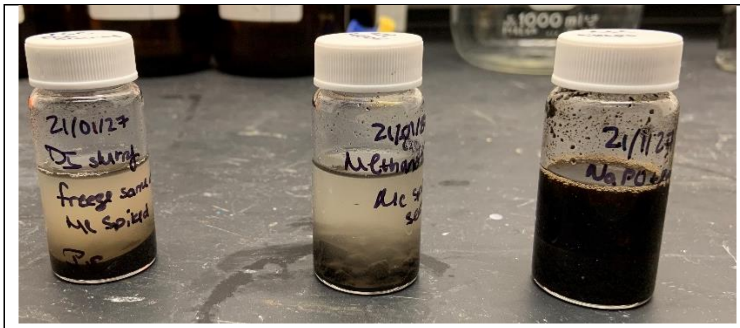

Figure 3E-1: Deionized water mixture (left), Methanol (center), and sodium pyrophosphate+EDTA (right) were used to extract microcystins from toxin-amended sediments. After multiple mixing events over the course of 20 hours, the sediments were allowed to settle for the last 4 hours of extraction. The methanol was the clearest after settling (but still somewhat cloudy), and the sodium pyrophosphate+EDTA remained a very dark color.

Methanol additionally generated a slightly higher percent recovery (72.1 ± 3.3%) than sodium pyrophosphate + EDTA (59.1 ± 14.4%) with toxin-amended samples (Figure 3E-2), and after accounting for variable dilution (i.e. 50 vs 100x), did not show significant differences between extracted duplicate samples nor variable dilution. Therefore the methanol solution was selected as the sample extractant going forward. Deionized water extracted only 11.0% of the microcystins from the sediments (not performed in duplicate to conserve ELISA kit wells), suggesting that most of the microcystins amended to the sediments were indeed mineral associated and required an extractant to release and quantify.

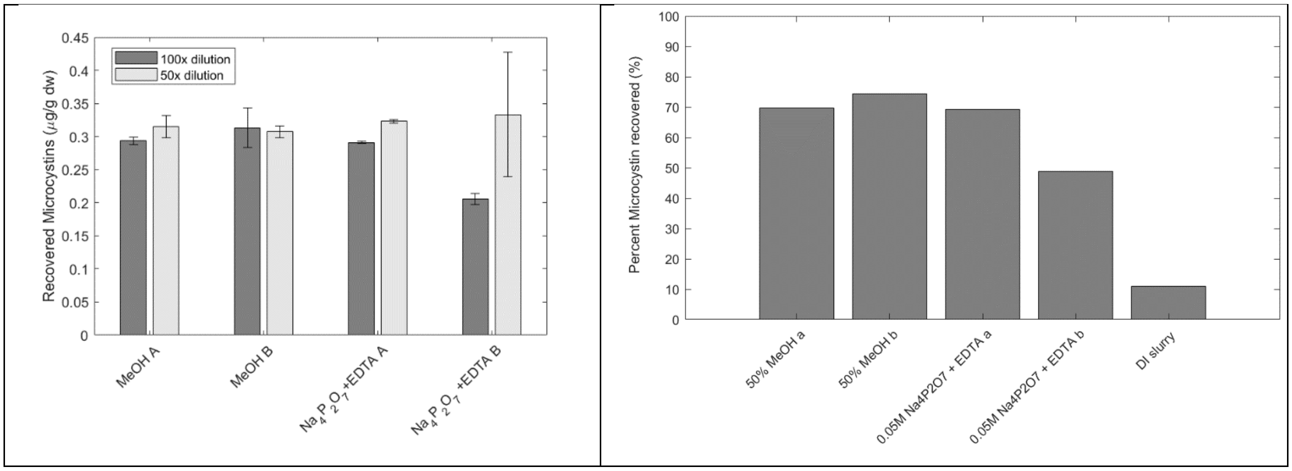

Figure 3E-2: Results from the two extractants plus a deionized water control with respect to releasing and quantifying microcystin-amended test sediments. Left: direct concentrations yielded from duplicate extractions per solvent. Error bars on the columns represent duplicate ELISA measurements per each 50/100x dilution of each extraction. Right: Percent yield of the microcystins extracted per solvent (performed in duplicate) relative to the original amount inferred to be associated with the sediments, which is calculated by difference with respect to the known microcystin toxin concentration added and accounting for that not associated with the sediments that was detected in the rinse solutions.

Sample analyses: The 50% methanol solution extractions of Lake Okeechobee sediment samples revealed relatively low to intermediate concentrations when compared to other studies (Figure 3E-3). The maximum measured toxin concentration was 0.3988 ± 0.0604 µg/gdw sediment, which is intermediate to measurements in previous studies. There have been several studies that have attempted to measure MCs in sediments of other freshwater bodies with varying degrees of success (Chen et al. 2006; Babica et al. 2006; Zasteppa et al. 2017). Average MC concentrations in natural sediments from Baptiste Lake, Canada and Lake Taihu, China, fell within the range of 0.7µg/g dry weight to 3µg/ g dry weight (Chen et al. 2006; Zasteppa et al. 2017), while concentrations in the Brno Reservoir (Czech Republic) were between 0.003 to 0.380 µg/g dry weight (Babica et a. 2006).

Table 3E-2: Quantitative results from LC-MS analyses of extracted sediment samples with sediment toxin concentrations in units of µg/g sediment dry weight. Parentheses represent the standard deviation of duplicate extractions. Compared to Table 3E-1, the ELISA results were all non-detects so this data is omitted from this table.

Date	L001 LCMS	LZ40 LCMS	L004 LCMS	L005 LCMS	PHKM LCMS
2/26/2021	0.0046 (0.0033)		0.0048 (0.0021)	ND	
5/27/2021	0.0086 (0.0004)		ND		
7/28/2021	0.3988 (0.0604)	ND	ND		0.0071 (0.0024)
9/15/2021	0.0119 (0.0083)	ND	ND		ND

The sediment toxins were detected in the greatest concentrations during active blooms, with minimal preservation – or burial in deeper layers – evident close to the end of the wintertime quiescent period (i.e. Feb. 2021). At L001, the sediment toxin concentrations progresively increased over the course of the bloom season, with a peak in mid-summer, and an apparent decline already by Sep. 2021. Interestingly, very little toxin was detected at the two highly turbid sites LZ40 and L004. These results ultimately demonstrate that microcystin toxins have a short lifetime in Lake Okeechobee, and are consistent with findings from other tasks. Viable cells in sediments were typically observed inconsistently and in low concentrations (Task 3D), and apparent sediment-to-water column microcystin toxin fluxes were also insignificant when *M. aeruginosa* blooms were not present at the time of deployment (Task 3B).

We hypothesize that warm temperatures, frequent oxygenation, and elevated iron hydroxide concentrations (Task 3A) catalyze the degradation of these toxins in this lake. In batch and flow-thru sediment column incubations, 84-100% of microcystin toxins were removed from sediments in 3-4 weeks due to biodegradation, while degradation rates were substantially lower in autoclaved abiotic controls (Grutzmacher et al. 2009). Degradation was also elevated under aerobic relative to anaerobic conditions, although the exact nature of the anaerobic conditions was not determined (i.e. denitrifying, iron reducing, etc.). In slurry incubations under variable redox conditions, microcystin was removed by over an order of magnitude after 7 weeks under microaerobic conditions; however, under denitrifying conditions, degradation after a single day results in a 5-fold toxin decrease (Holst et al. 2003). Toxin biodegradation in toxin-amended batch cultures with sediment inocula (from a cyanobacterial-rich lake) proceeded rapidly under warm temperatures (20 – 30ºC) and aerobic conditions (near complete removal in 4-5 days), but was similarly stimulated by nitrate additions (Chen et al. 2010). Ammonium additions did not further stimulate degradation. Finally, abiotic degradation of microcystin can proceed via Fenton catalysis, i.e. the oxidation of reduced Fe^{2+} generating oxygen radical species that non-selectively degrade organic contaminants (Liang et al. 2021).

In our results, despite blooms being intense at L004 and LZ40, only low sediment toxin concentrations were detected. These sites are frequently disturbed and resuspended, resulting in surface sediment oxygenation (i.e. aerobic conditions) and oxidation of the sediment iron (i.e. presumed Fenton catalysis) (Task 3A). Sediment nitrate concentrations are routinely below detection at all sites (L001, L004, and LZ40), although the surface-most sediment layer sometimes contained nitrate concentrations in line with or slightly elevated with respect to the overlying water column. This points to intense denitrification of any nitrate entrained in this surface layer, whether from water column mixing or nitrification of ammonium generated in sediments. We suspect that iron hydroxide-driven nitrification/denitrification is intense (Task 3A). Regardless of the nature of the process, the denitrification capacity of the sediments appears to be high. Overall, Lake Okeechobee sediment characteristics are likely high conducive to sediment microcystin toxin degradation.

CONCLUSIONS & FUTURE WORK

While this was a pilot scale study to generate baseline information about the sediment microcystin toxin concentrations, results convincingly support the finding that sediment toxins have a low persistence in lake sediments. Along with results from other tasks, the potential for sediment-derived toxins to affect the overall water column toxin inventory is likely low under static, diffusive dominated conditions, and in resuspension conditions is likely only significant during periods of active blooms. However, the overall implication is that sediment conditions are important for sustaining the degradation capacity and should therefore be considered explicitly when considering the fate of these compounds. Based on a combination of our own results and literature knowledge, more oxygenated sediments appear to accelerate degradation, while more chemically reducing conditions may result in a longer persistence. In a follow up study, depth-resolved toxin analyses would be preferrable to further constrain that the toxins are truly degraded and not simply buried. Based on the findings from this work, the modeling efforts of Task 1E will set a low priority for the parameterization of sediment toxins.

TASK 4: AUTONOMOUS SURFACE VEHICLE MONITORING (TASK LEADS: RUIZ-XOMCHUK/DUNCAN/BECKLER)

INTRODUCTION

Conventional methods for monitoring HABs are constrained in their ability to capture all relevant spatial and temporal extents of population dynamics (Urquhart et al., 2017). Smaller temporal and spatial patterns are largely undercaptured not only for Lake Okeechobee but even for regions with a greater intensity of monitoring, although these patterns are recognized to be critical for understanding HAB formation (Wells et al., 2015). HABs can follow not only seasonal trends, but also respond to short term weather events and anthropogenic impacts (Michalak et al., 2013). In terms of temporal trends, while the community is aware of a HAB season in lake Okeechobee, anecdotal (unmeasured or scarcely measured) in situ observations and sometimes remote sensing images show that these blooms can form, grow, move, and senesce in a matter of a few days. It is also known that these blooms might develop over different regions in the lake in different seasons, whereas long term annual averages have also revealed major shifts in bloom distributions (**Task 5**). Some of these temporal dynamics can be captured by fixed-location continuous monitoring systems (e.g., **Task 6**), but those are obviously restricted to point locations and HAB behavior is particularly challenging to infer in the event of horizontal transport. Current satellites, on the other hand, are limited to daily image captures at best, and only when cloud coverage allows good visibility. Further, product derivation is challenging due to atmospheric interferences, and in Lake Okeechobee, the highly turbid environment as well (discussed in **Task 5**).

Monitoring by a mobile platform offers an alternative solution, that can cover a broad spatial range at a high temporal resolution (Beckler et al., 2019). The dual propulsion Nav2 ASV sailboat “Vela” (Navocean Inc.) was in turn used to monitor HAB and environmental conditions in the north/western region of Lake Okeechobee, selected for its ease of access (from the Okeetantee Marina) and its historical frequency of hosting HAB activity. Vela is 2 m long, ~45 kg, and navigates at a slow steady speed (1-2 knots), making it inherently safe to deploy and a minimal navigation hazard. Vela is capable of autonomous waypoint-guided navigation under a broad range of weather conditions and is powered primarily by renewable energy, with batteries only for powering sensors (Beckler et al., 2019). Vela patrolled around the clock (except for maintenance periods or for occasional repair) while equipped with optical (Chl-a, phycocyanin, FDOM, and backscatter), environmental (water temperature/conductivity, DO), and meteorological sensors, as well as an ADCP for generating vertically-resolved water currents (10 bins of depth resolution). Vela was configured to transmit near real time conditions via a satellite or cellular signal every 15 minutes (a set of scientific and navigation data), but also stored for post-retrieval a higher resolution dataset with more than 2 million multivariable data points. This dataset has already revealed unexpected patterns that would not be acquirable via any other techniques, and continuing data processing and interpretation will reveal many more discoveries.

METHODS

A high-endurance Autonomous Surface Vehicle (ASV) was used to provide sustained in situ environmental, biogeochemical, and physical measurements on Lake Okeechobee 24 hrs/day through one full year (Figure 4-1). The ASV was controlled remotely by a shore-based operator capable of adjusting waypoints and survey patterns and was equipped with sensors for HAB detection and environmental characterization. Near-surface (immediately below the boat at ~0.15 m depth) geolocated measurements were obtained tentatively every 30 seconds including: fluorometric (Chl-a, CDOM, phycocyanin), optical backscatter (red, green, blue), and dissolved O_2, conductivity, temperature, and meteorological

measurements (wind speed and direction, air temperature, barometric pressure). Further, ADCP 3D current measurements were taken at 0.6 m depth interval (bins) throughout the water column to full lake depth. Near-real-time data samples were compressed and transmitted every 15 minutes or more via satellite and cellular communications to the HALO web portal. The ASV also recorded a complete data set to onboard memory accessed post mission for comprehensive detailed analysis and archiving.
The ASV was planned to repeatedly survey a polygonal area in NW Lake Okeechobee, encompassing multiple routinely monitored SFWMD sites (L001, NES135, NCENTER, KBARSE, POLESOUT, POLESOUT1, POLESOUT2, POLESOUT3, L008, L005). In addition, the survey area encompassed HALO Tier 1 and Tier 2 sites at L005 and L001, the latter being the location of fixed-location intensive water quality and SeaPRISM remote sensing reflectance monitoring installations (**Tasks 6&5**, respectively) and the site of numerous other comprehensive observations (e.g. **Task 2** autonomous HAB sensors and **Task 3** benthic lander deployments). This facilitated measurement cross-comparison and multi-channel sensor validation. This region is considered to be a priority region with respect to the tendency for early-stage bloom formation and intensification. On-the-fly adjustments were periodically implemented to redirect Vela to emerging areas of interest to perform raster pattern surveys at spatial and temporal scales necessary to analyze these emerging or established HAB hotspots. Monthly water samples were collected from the location of the ASV (usually near the L001 site when logistically feasible), just beneath the ASV where the sensors are located, to validate the in-water sensors for chl-a (subsequently laboratory measured) and CTD/DO/fluorometer (in the field with a sonde), as well as cell counts in the laboratory. This geographical restriction allows cross- comparison between the fixed-location continuous measurements (**Task 6**) with sensors on the mobile ASV platform. Finally, several ad-hoc water samples were collected as the ASV surveyed bloom area to validate the exact chl-a and phytoplankton community composition that corresponded to the ASV sensor measurements.

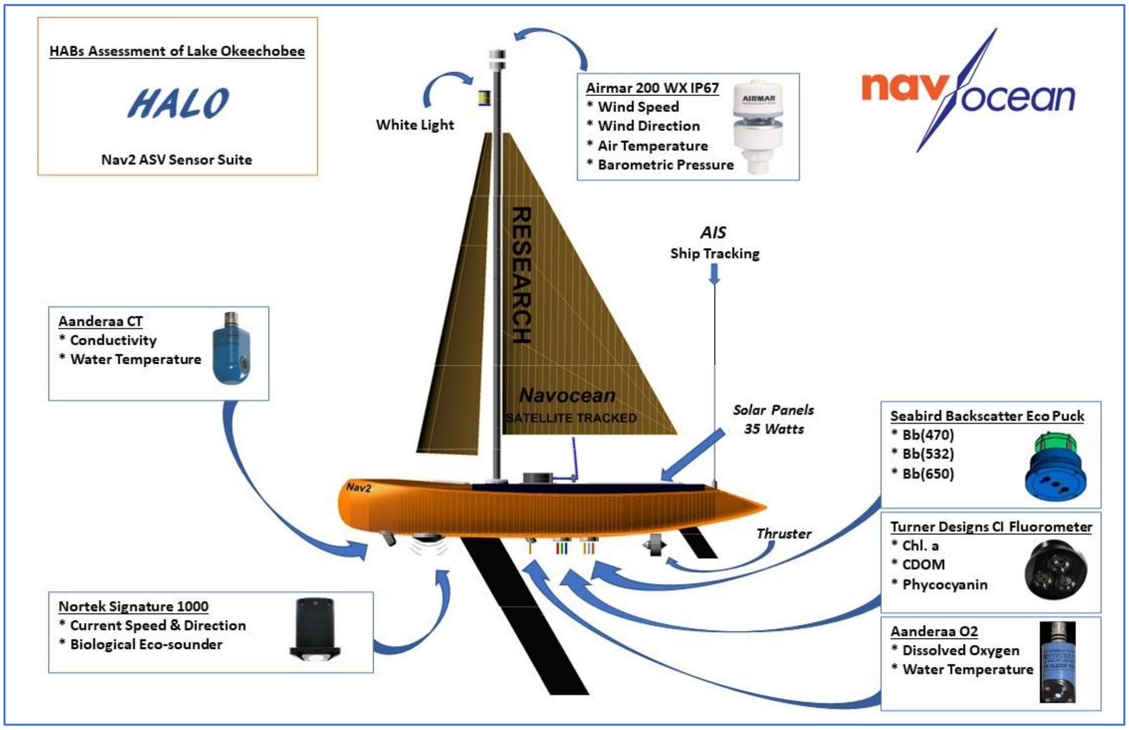

Figure 4-1: Nav2 Sail and Solar ASV showing the full sensor suite integration plan for HALO.

ACTIVITIES SCHEDULED vs. COMPLETED

Overall, this task was completed highly successfully with little deviation from scheduled activities. All sensors were integrated and calibrated, routine validation was conducted as planned, and the ASV deployment reached ~80% uptime and 79 circuits of the HALO loop during the period of performance (calendar year 2021).

Sensor Systems Integration: The C/T (Aanderaa), ADCP (Nortek), BB3 backscatter (Wetlabs), dissolved O_2 (Aanderaa) and Fluorometric sensors (Turner Cyclops Integrator) were all integrated into Vela successfully (Figure 4-2). This step included custom housing design and machining and integration of a Campbell Scientific CR6 data logger with customized cables and connectors. The meteorological sensor (Airmar) was previously integrated as it is standard on all Nav2 ASVs. Assembly also included software algorithm development and engineering to power and duty cycle the sensors, log the raw sensor data, and process the incoming data stream for sending over the Nav2 ASV onboard near-real-time communications systems (cellular and satellite). Industrial quality SD memory cards were purchased for the ASV onboard data logger. The science water quality and ADCP sensors were set for one measurement per second with 5 seconds on and 25 seconds off for the C/T, backscatter, O_2 and fluorometric sensors. The ADCP was designed to retrieve East/North/Up (ENU) vectors from 10 different water levels (bins) for the full archival data set. The 10 bins are spaced every 0.6 meters for a total of 6 meters depth which exceeds the maximum lake depth (~5 meters), allowing for full water column data collection. 3 bins (1, 4, 7) were transmitted in near-real-time. To ensure high accuracy synchronization of the GPS derived speed and direction over ground with the ADCP measurements (required for post processing), a dedicated GPS was integrated for the ADCP. Calibration of the meteorological sensor, ADCP, and onboard PRH sensors was completed by Navocean. This step involved following the manufacturers procedure for calibrating the Airmar and ADCP internal compasses, and a flat-water test of the floating ASV to determine the pitch and roll offsets. The CTD, DO, and fluorometer were calibrated at HBOI using conductivity standards, air-saturated deionized water, and chl-a/phycocyanin/quinine sulfate standards.

Figure 4-2: Sensors integrated to the ASV hull, left to right: C/T, ADCP, O2, CI, and BB3.

Data pipeline setup: The data format for real-time and archival purposes was determined via extensive discussion among project partners. In addition, Navocean created a customized real-time data portal on their server to facilitate both the application of calibration coefficients and the obtaining of calibrated data for real time display on the HALO Portal. Via the Navocean portal, it is possible to set date/time ranges for specific calibration windows, thus allowing dynamic adjustment to retrieve properly calibrated data after each sensor cleaning and recalibration using solid-state optical “standards”. For this rapid field validation and monitoring of sensor drift over time, equipment was purchased and assembled or designed and fabricated for each of the water quality sensors subject to potential drift. For the backscatter sensor and fluorometer, custom “Satinice” semi-transparent plexiglass sheets and custom holders were assembled to hold the Satinice lens a precise distance from the sensor face while blocking ambient light. Baseline validation measurements were taken and recorded for future comparison. Telemetry sent near-real-time data was archived in the Navocean server and downloaded for FAU archive on the FAU High Performance Computing cluster. During service events throughout the year, full variable and sensor files were recovered and uploaded, including surface sensors, meteorological, navigation and ADCP data. The list of service file groups stored up to date is discussed in **Task 2C**.

Mission preparation: A roughly triangular pattern of 4 primary waypoints was determined (Figure 4-3). The waypoint survey pattern takes the Nav2 ASV around a loop (the “HALO loop”) encompassing much of the N/W of the lake and targeting HALO and SWFWD water sampling and data collection locations, while avoiding the shoals in the northwestern leg between waypoints 3 and 4. A Local Notice to Mariners (LNM) was submitted to the Region 7 Coast Guard district providing information about the Nav2 ASV mission operations on Lake Okeechobee. FWC law enforcement was also notified of our Nav2 ASV mission plans for HALO and Nav2 photos and specifications were sent to FWC for their information.

1	27.135712°, -80.791565° (20 m)	Distance 9.1 km	79°	173°
2	26.982309°, -80.715439° (20 m)	Distance 27.5 km	66°	160°
3	26.963442°, -80.948608° (20 m)	Distance 31.8 km	116°	210°
4	27.082443°, -80.801140° (20 m)	Distance 15.0 km	85°	180°
5	START OVER AT #1			

Figure 4-3: The primary Nav2 ASV survey region.

Mission Operations: The Nav2 ASV “Vela” was launched one day early on Dec 31st, 2020, from near the Taylor Creek locks at the north end of the lake and began surveying the “HALO Loop” (Figure 4-4). The full loop required typically 2 to 3 days for completion depending on the wind. After completing 2 to 3 loops, Vela was directed to the Taylor Creek locks (roughly every one to two weeks), and then towed through the locks and through the canal to Navocean's project operations location on the canal at SE 24th street (Okeechobee, FL) for servicing, including: sensor validation, cleaning, battery charge and maintenance as needed. Vela was then launched asap, typically within 24 hrs. Mission operations were maintained throughout the year through January 1st 2022. Table 4-2 shows summary highlights of all operations.

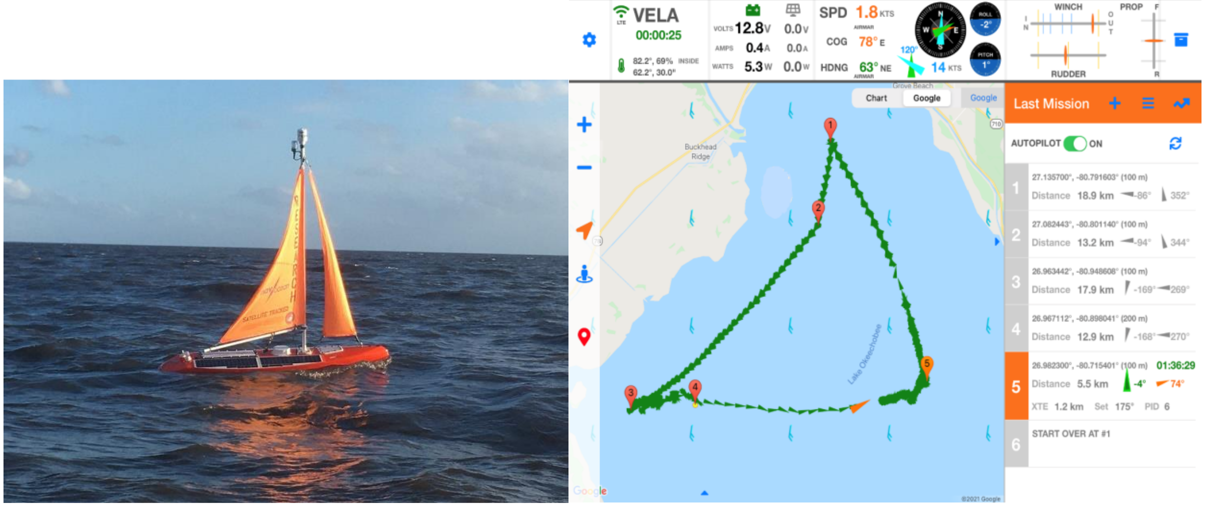

Last Mission

AUTOPILOT ON

1 27.135700°, -80.791603° (100 m) Distance 18.9 km -86° 352°

2 27.082443°, -80.801140° (100 m) Distance 13.2 km -94° 344°

3 26.963442°, -80.948608° (100 m) Distance 17.9 km -169° 269°

4 26.967112°, -80.898041° (200 m) Distance 12.9 km -168° 270°

5 26.982300°, -80.715401° (100 m) 01:36:29 Distance 5.5 km -4° 74° XTE 1.2 km Set 175° PID 6

6 START OVER AT #1

Figure 4-4: Left: Vela launched Dec 31st, 2020, sailing towards the "North Tower" point of the Standard HALO Loop. All sensor data is streaming. Right: Mission Ops screenshots show Vela completing a HALO loop (right).

Table 4-1: Operational statistics of the 2021 Vela ASV Lake Okeechobee surveys.

Total operational days	287
Total down time	78 days
Total "Standard HALO Loops" completed	79
Total distance traveled	more than 10,000 km
Total Measurements taken	> 2 million QC measurements per sensor

During the course of the full year, the piloting of the HALO Loop was the primary objective (Figure 4-4), which was completed a total of 79 times. Some additional small-scale "hotspot" surveys were included as follows: 1) An algae hot-spot region in the north of the lake near Taylor Creek was discovered with elevated sensor readings confirmed visually and by water sampling. As such a survey pattern called the "Taylor Creek Grid" was established in March and was surveyed opportunistically throughout the rest of the year, e.g. at times when Vela was returning to or launched from Taylor Creek before/after servicing (Figure 4-5 top); 2) Vela was directed to sail from Taylor Creek on 2 side missions: one to Pahokee during an intense *M. aeruginosa* bloom, and another to the south end of the lake and the Clewiston area to validate feasibility of operating in other areas of the lake and to survey a suspected *M. aeruginosa* bloom in the area (Figure 4-5); 3) On several occasions Vela was directed to re-visit and survey in more detail areas where sensor measurements indicated hotspots of potential algal bloom growth based on near-real time data posted to the GCOOS HALO web portal (e.g. Figure 4-5, bottom).

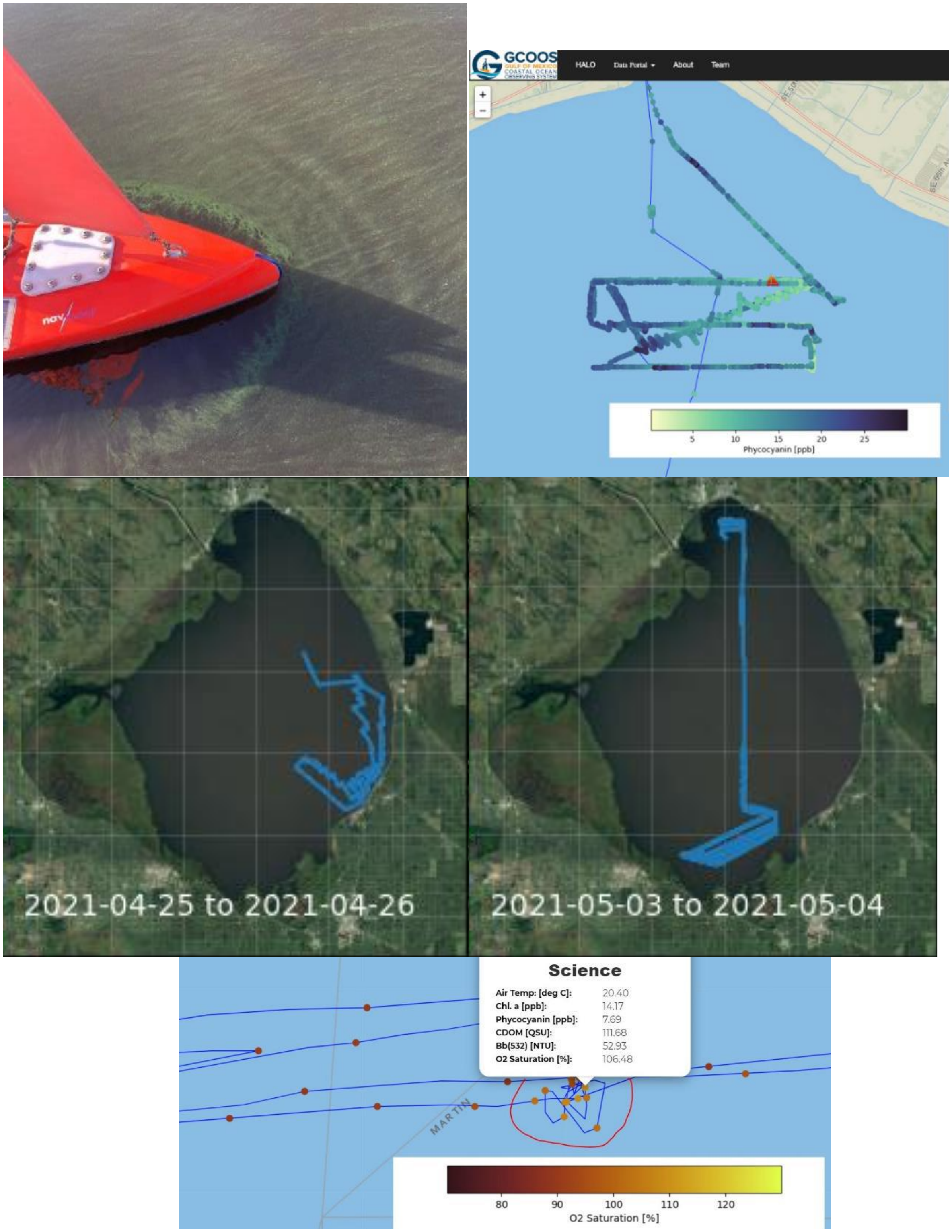

Science

Air Temp: [deg C]: 20.40
Chl. a [ppb]: 14.17
Phycocyanin [ppb]: 7.69
CDOM [QSU]: 111.68
Bb(532) [NTU]: 52.93
O2 Saturation [%]: 106.48

Figure 4-5: Top-left: Vela sailing through the bloom near Taylor Creek; Top-right: GCOOS portal screen captures showing Vela measurements at the Taylor Creek Grid, added to the survey pattern in March; Center-left: Navigation path of the Pahokee side mission; Center-right: Navigation path of the Clewiston side mission; Bottom: Elevated dissolved O_2 hotspot investigated in more detail.

In Feb. and Mar. 2021, anomalous sensor measurements led Navocean staff to investigate for visual signs of algal bloom development at the north end of the lake near Taylor Creek while launching/landing Vela. Visible algal scums on the surface of the lake as well as blooms mixed into the near surface water column were discovered and found to be intensifying as the seasonal change progressed, allowing additional team mobilization for surveys. This additional local "man on the ground" capability should not be underemphasized as an added bonus of this work. In addition, the Navocean staff frequently discussed the project with local residents and stakeholders, raising additional awareness of the project and the on-water operations – considered critical to avoiding any vandalism of the vessel. In comparison, the benthic lander (**Task 3B**) was sabotaged during a deployment despite only being in the water for a cumulative period of a week or two.

Routine validation: Water samples and sensor validation data were collected by FAU and Navocean staff (Figure 4-6), and lab analysis was later performed on the water samples (Table 4-2). Vela was directed to the North Tower (L001) to meet with the HBOI field staff on those days, and water samples were collected from immediately below the ASV sensors. The samples were collected near the SeaPRISM mounted on the L001 (North tower) and near Taylor Creek and Pahokee during those additional surveys.

Table 4-2: Dates of sensor validation water sample collection throughout the year:

Site	Date	Time	Lat	Lon
L001 North Tower	2/19/21			
L001 North Tower	3/25/21			
Taylor Creek 210421_1	4/21/21	12:30	27.18111	-80.7971
Taylor Creek 210421_2	4/21/21	12:35	27.18111	-80.7971
Taylor Creek 210421_3	4/21/21	12:55	27.18902	-80.8034
Taylor Creek 210421_4	4/21/21	13:00	27.18902	-80.8034
Taylor Creek 210421_5	4/21/21	13:20	27.17725	-80.8052
Taylor Creek 210421_6	4/21/21	13:25	27.17725	-80.8052
Pahokee 210426_1	4/26/21	10:45	26.86752	-80.6412
Pahokee 210426_2	4/26/21	10:50	26.86752	-80.6412
Pahokee 210426_3	4/26/21	11:05	26.86985	-80.6405
Pahokee 210426_4	4/26/21	11:05	26.86985	-80.6405
Pahokee 210426_5	4/26/21	11:20	26.87027	-80.6405
Pahokee 210426_6	4/26/21	11:20	26.87027	-80.6405
L001 North Tower	4/29/21	8:40	27.13914	-80.7807
L001 North Tower	6/17/21	9:30	27.13914	-80.7807
L001 North Tower	6/29/21	9:21	27.13946	-80.789
L001 North Tower	7/13/21	8:35	27.13905	-80.79081
L001 North Tower	8/10/21	8:47	27.13896	-80.78885
L001 North Tower	9/14/21	9:36	26.998517	-80.90378

The Satinice validation system was applied to the fluorometer and backscatter sensors every 1 to 2 weeks throughout the year. Notably, the instrument optical and housing surfaces remained remarkably free from biofouling growth in January through March and growth was only moderate during the warmer summer months. It is possible that the high turbidity of the lake water is likely inhibiting sunlight from reaching below the waterline of the ASV thus slowing biofouling organism growth. Satinice validation data sets were uploaded to FAU for scientific analysis and archiving, and adjustments to calibration coefficients are reflected on the data displayed on the HALO portal.

Figure 4-6: Vela at the north tower for validation water sample collection.

Discussion of problems encountered and solutions: The ADCP measurements must be precisely time stamped with the ASV speed and course over ground in order for the ASV movement over ground to be removed properly from the current speed measurements. The first two weeks of ADCP data were found to have a time stamp problem which invalidated the measurements recorded from that time period, 1/1/21 to 1/15/21. The problem was discovered to be in the data logger code and was repaired. ADCP measurements recorded in the primary data archive from 1/15/21 through task completion are correct. A second problem in the ADCP time stamp, causing slow but steady drift, was discovered but only pertaining to the near-real-time transmitted data where the synchronizing of the time stamp is unrelated to the primary data log. This problem was repaired in the data logger code. In June, The dissolved O_2 sensor failed to send in the near-real-time data set for posting to the GCOOS HALO portal. A repair was attempted multiple times but failed for the duration of the mission. However, all O_2 data was properly recorded to the archival data log and posted to the KOKO system.

RESULTS & DISCUSSION RELATED TO METHOD DEVELOPMENT

Data recovery and quality control: Vela operations improved over time. While initial deployments lasted only a few days, and sensors required adjustments to reduce noise on turbid waters, rapid improvement is observable in the data recoveries and mission tracks (Figure 4-7). Being a sail-driven vessel and due to changing wind patterns, the ASV tracks are inherent "zigzags" due to the boat tacking. However, as boat autonomous navigation algorithms improved over time, the tacks began to increasingly resemble straight lines from a lake-wide overhead perspective. Collected datasets are later discussed in further detail for the environmental and the ADCP sensors.

Table 4-2 summarizes environmental data collected from a total of 22 logger recoveries (herein called missions with Id's from 0 to 21) from the first deployment on December 30, 2020, until December 14, 2021. Atmospheric and ADCP data is not included as this vector data (current and wind velocities) are discussed separately. Figure 4-7 shows the corresponding paths covered per mission. In the table are shown start and end times of the data logger mission, the number of raw entries (line records stored independent of sensor functioning), line data entries stored, and number of data points for every variable after first level quality control. First level quality control included the use of a range limit (allowable min and max), and removal of spikes (unaccounted noise). More than 2 million 1st level QC data points were collected for each sensor, and individual timeseries for each variable per mission are shown in figures in the Annex. Original data frequency logs correspond to 1 second, but this frequency is reduced in segments after QC control and filtering.

After 1st level QC, some irregularities remained in the data (see individual mission time series in the annex). It was identified that irregularities corresponded to times of deployment and recovery when Vela sensors were functioning but not in the water. These irregularities were not only found during the start and end of the data log, but occasionally temporary recovery/deployment events were carried within the mission (e.g., see mission 5 timeseries in annex) making automatic cleanup difficult. For automatization, to remove this data, a geofence was applied to discard values registered North of 27.19° Latitude, which is the region where sailboat deployment/collection could have taken place. After geofencing, the complete environmental data set is discussed later.

Validation of environmental set: Field validation provided reasonable results. Figure 4-8 shows the continuous time series (over 15 min frequency near real-time data) transmitted by Vela vs. the field sensors (see methods) for water surface parameters and grab sample for chlorophyl a, collected on the times indicated in Table 4-1. Given the large number of validation data sources (both laboratory and field), full sensor validation and comparison will be an ongoing effort to ultimately be included in a related publication.

Table 4-2: Summary of data collected on logger recoveries from Vela missions. Numbers indicate counts, and the counts shown for the Backscatter, CI, CT, and DO sensors correspond to data after 1st level quality control. Columns indicate start and end of mission log recording, and data counts.

N	Start	End	Raw	Data	BB [470nM]	BB [532nM]	BB [650nM]	Chla	Phyco	CDOM	Cond.	Temp	DO	DO%	Temp (DO)
1	2020-12-31T13:32:15-05:00	2021-01-02T21:09:12-05:00	96490	2228	1313	1313	1312	1315	1315	1310	1309	1315	1315	1315	1315
2	2021-01-04T08:40:30-05:00	2021-01-08T13:41:58-05:00	179063	4092	2363	2377	2365	2400	2402	2362	2285	2424	2341	2424	2424
3	2021-01-09T09:47:03-05:00	2021-01-14T09:25:15-05:00	215179	5013	2901	2903	2916	2963	2949	2908	2835	2968	2965	2968	2968
4	2021-01-15T08:25:31-05:00	2021-01-17T02:43:06-05:00	151508	25260	14621	14582	14591	14925	15007	14682	14051	15156	15017	15153	15129
5	2021-01-21T09:35:01-05:00	2021-01-27T19:00:00-05:00	811516	135293	77702	79234	79965	79831	79498	77395	74408	81175	74222	81158	81140
6	2021-02-02T10:11:02-05:00	2021-02-07T12:21:01-05:00	437662	72009	42046	41823	41782	42268	42277	42080	40667	43205	37068	43191	42989
7	2021-02-11T10:00:31-05:00	2021-02-18T14:31:34-05:00	597457	99540	59301	59275	59244	59376	59088	59254	57616	59724	55730	59284	59680
8	2021-02-19T07:27:01-05:00	2021-02-23T19:02:13-05:00	294245	48357	28554	28597	28424	28659	28488	28409	25727	29012	28722	28926	28965
9	2021-02-26T18:19:20-05:00	2021-03-06T10:56:12-05:00	1275165	209780	123582	123441	123856	124651	123551	123365	116412	125865	122004	124302	125311
10	2021-03-15T12:11:05-04:00	2021-03-23T20:00:00-04:00	728993	121235	71156	70992	70702	72146	70328	70820	66078	72741	70582	72493	72104
11	2021-03-25T06:54:01-04:00	2021-04-02T20:00:00-04:00	1303181	215923	126661	126146	125628	127702	125542	126293	116871	129552	123711	128155	128173
12	2021-04-16T08:15:50-04:00	2021-04-24T20:00:00-04:00	1157437	192870	114981	114350	114134	114925	111357	110302	103532	115722	111267	113768	115334
13	2021-05-01T07:50:02-04:00	2021-05-19T10:26:10-04:00	1390994	231065	136776	132711	131588	136503	119571	136713	126866	138641	127766	134096	138082
14	2021-05-28T07:25:26-04:00	2021-06-12T19:43:45-04:00	1335649	223095	130396	129607	129372	131859	126362	132059	119475	133857	129285	132313	133136
15	2021-06-13T12:08:17-04:00	2021-07-15T15:41:56-04:00	2512817	418941	244847	238694	234460	248032	212359	248424	231443	251363	237704	243419	250905
16	2021-07-19T09:55:24-04:00	2021-08-04T01:00:10-04:00	1274319	212855	127289	126799	127279	127662	112722	127357	122538	127713	122741	124543	127621
17	2021-08-08T08:26:03-04:00	2021-08-10T19:24:47-04:00	211544	35143	19971	19836	20155	4822	5008	4614	17941	21085	19868	20949	21047
18	2021-08-11T20:37:56-04:00	2021-08-19T20:00:00-04:00	2155409	359546	206406	204137	205922	212136	206653	209351	204615	215725	211170	214132	215226
19	2021-09-09T19:00:39-04:00	2021-10-09T10:28:10-04:00	2263907	377938	201890	203538	220420	225111	217382	225560	218305	226760	216948	222284	226648
20	2021-10-18T20:00:06-04:00	2021-10-18T20:00:00-04:00	1604067	267841	158049	154355	157498	159212	154562	159121	154096	160701	157593	160661	160676
21	2021-11-12T07:55:32-05:00	2021-11-21T19:00:00-05:00	1498400	250257	143368	143581	144579	143596	147185	141940	144368	150152	148423	150071	149936
22	2021-12-05T08:00:50-05:00	2021-12-14T19:00:00-05:00	825073	137753	80448	80340	80338	80963	79939	80890	78650	82649	69213	80671	82322
				TOTAL	**2114621**	**2098631**	**2116530**	**2141057**	**2043545**	**2125209**	**2040088**	**2187505**	**2085655**	**2156276**	**2181131**

Figure 4-7: Paths covered under each mission. M0 and M1 are excluded for conciseness. Mission 10, 11 and 12 included excursions outside the regular path to monitor HAB events (Figure 4-6).

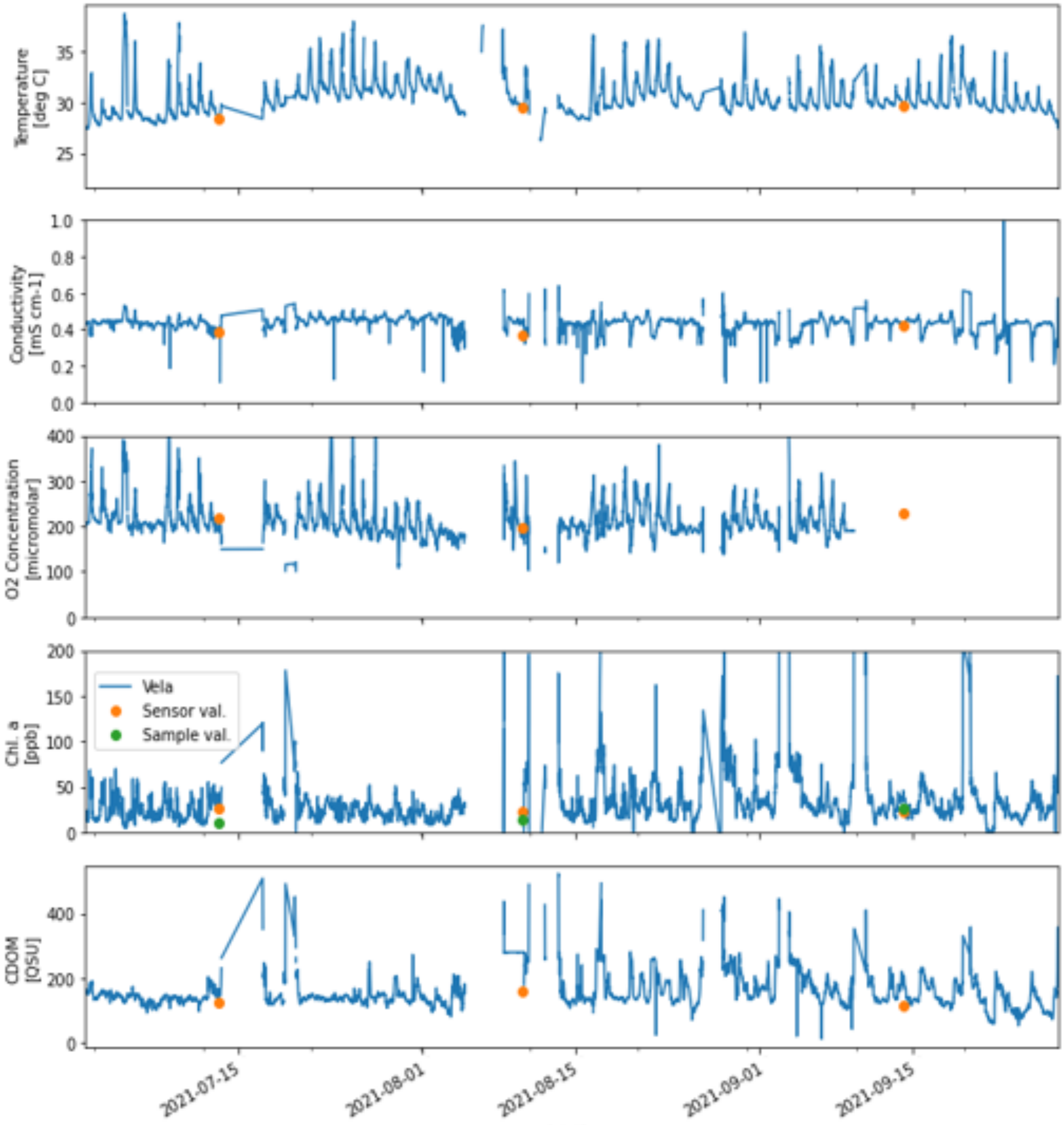

Figure 4-8: Sailboat sensor values compared to field fluorometer (orange) and laboratory sample analysis (green).

ADCP data processing and troubleshooting: An ADCP (Nortek Signature1000) was mounted in Vela's hull just forward of the keel for a clear downward view to provide an overview of the 3-D instantaneous velocity distributions within the water column. The Signature1000 is equipped with the vendor AHRS option for automatic vessel motion correction of the ENU current velocities. The ADCP was then calibrated by standard vendor procedure. In addition, a time synchronized dedicated GPS was added to the data set for high accuracy removal of vessel speed over ground. Raw ADCP data was extracted from the instrument using Vendor software and downloaded on a periodic basis along with the GPS data for processing. The data was binned in 10 depth bins of 46 cm each, with the first bin ranging from 0.1-0.56 m in depth. Over the course of the project, extensive effort was extended to fix several bugs associated with the ADCP data processing to ensure accurate outputs.

A MATLAB routine was developed to work with the full resolution ADCP data. This code: (i) reads in full-resolution ADCP data; (ii) integrates co-located GPS data; (iii) includes a sub-routine to subtract vessel motion to obtain true water column velocities based on the GPS measurements; (iv) filters out bad data based on geofencing and magnitude thresholds; and (v) generates plots of velocity data at different depths superimposed on a satellite image of Lake Okeechobee showing Vela's trajectory.

The ADCP data from a HALO Loop from 5/24/21 to 5/27/21 is shown in Figure 4-9. The velocity vectors are computed from the individual horizontal velocities (East and North in ENU coordinates). Data from the top four (shallowest) depths, corresponding to bin center depths of 0.33 m, 0.79 m, 1.25 m and 1.71 m, respectively, are shown, demonstrating the ability of the ADCP to provide valuable ancillary data on physical parameters during Vela's deployments. Figure 4-10 shows some unusual features in the surface velocities during the East-West transect of Vela when tacking against a persistent headwind resulting in a zigzag path. This motion does not appear to be completely subtracted from the final surface current output. The problem was identified as an offset between the ADCP and GPS directional data, due to the lack of correction for the magnetic declination angle. Based on the findings, this issue was fixed in the MATLAB subroutine and applied to all Vela data. It should be noted that depending on the local depth, there is some contamination in the bottom bins (e.g., bin 7 and higher) during some of the runs. This is to be expected as there is no way to account for the variable depth; such data can be visually identified easily due to their extreme values and are not considered for the purposes of this analysis.

Additionally, a second Matlab routine was developed to compare the ADCP data with wind speed data obtained from Vela's weather logs. Here, the wind speed data underwent a similar processing method to subtract the vessel motion. Once this was achieved, the horizontal velocity components (zonal and meridional) from the surface bin of the ADCP (centered at 0.33 m below the surface) was compared with the wind speed. While keeping in mind that the wind and water velocities are not exactly going to be the same or completely in sync, this approach at least provides a decent reference point. One such comparison is shown in Figure 4-11 from 9/7/21-9/9/21. Broadly speaking, the trends are quite consistent, lending further confidence in our processing methodology.

The vertical U velocities presented some problematic aspects. Upward velocities (currents) are typically very small and an order of magnitude or more lesser than the horizontal velocities. Furthermore, unless there are some atypical events (like strong upwelling), these currents may be (and likely would be) smaller than the noise floor of the ADCP and would therefore be undetectable. This is seen in most of the data (~ 99%). In some cases, however, e.g., strong wind conditions, there is a possibility that these values may be significant. Even in this scenario, it is not straight-forward to separate out the 'up' velocity from the noise (vessel motion, etc.). Secondly, visualization of such data in a meaningful manner would require significant work. With the relatively high effort and 'low rewards' associated with this analysis, this was out of the current scope and can be considered as part of any future analysis of this data.

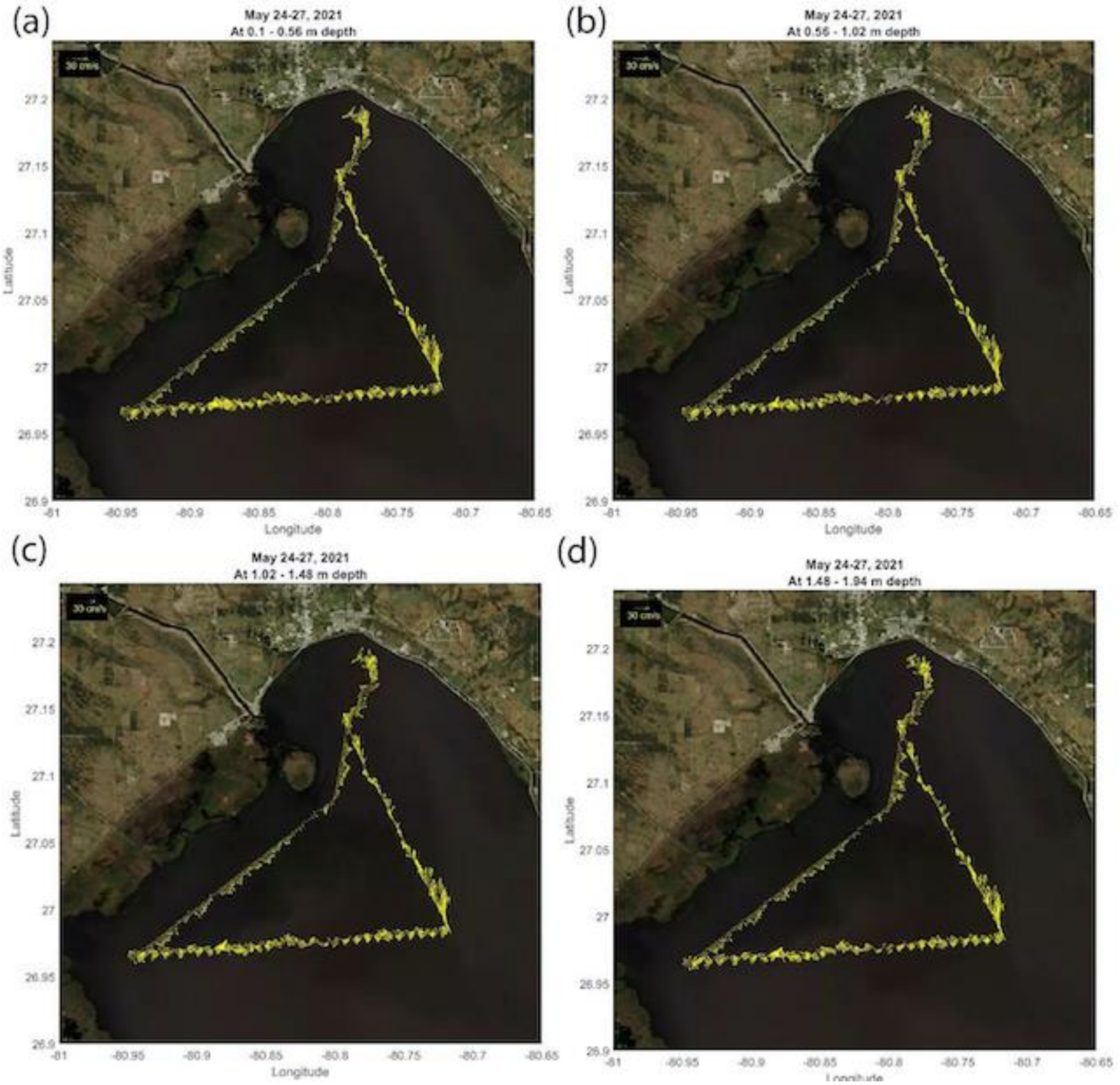

Figure 4-9: ADCP data from the sailboat path from 5/24/21-5/27/21 at the surface-most four depth bins; (a) 0.1-0.56 m; (b) 0.56-1.02 m; (c) 1.02-1.48 m; and (d) 1.48-1.94 m.

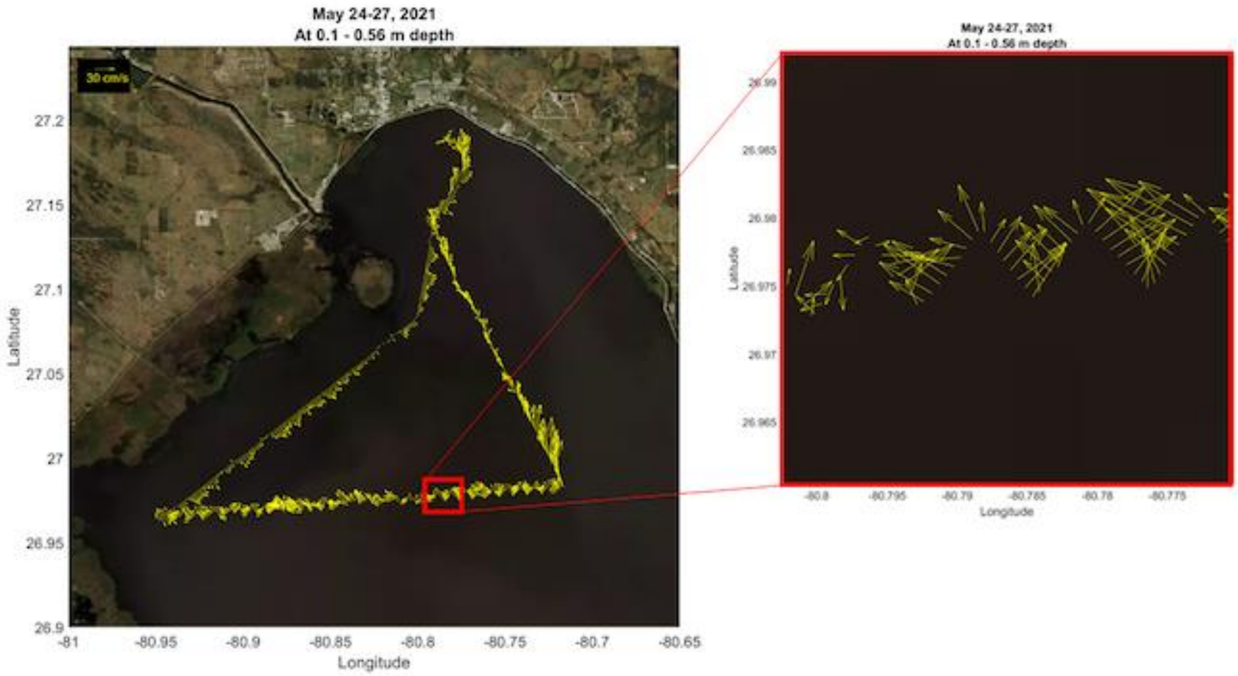

Figure 4-10: Zoomed ADCP data from Figure 4-9 showing only the top depth bin (0.1-0.56 m). Inset shows errors in the repeated 'zig zag' pattern in the data caused by magnetic declination not accounted for, the correction was then made in the MATLAB subroutine.

Figure 4-11: ADCP and wind data comparisons. Both instruments were mounted on the same ASV.

RESULTS & DISCUSSION RELATED TO OBSERVATIONS

ADCP velocities: Sample ADCP data from several different Vela deployments for the following dates are discussed below: (i) 8/12/21 – 9/9/21; (ii) 9/9/21 – 10/9/21; (iii) 10/15/21 – 11/10/21; (iv) 11/12/21 – 12/4/21; and (v) 12/17/21 – 1/1/22. In each case, the velocity distributions at the top four surface bins (centered at 0.33 m, 0.79 m, 1.25 m and 1.71 m) are presented. Figure 4-12 to 4-14 show the velocity vectors over the entire course of three ASV deployments. No unexpected trends are apparent in any of these cases, with the velocity vectors within the expected ranges. In Figure 4-15 the highlighted regions in the ADCP data show unexpectedly high values in all the bins. In Figure 4-16 the highlighted regions show unexpectedly high values in bins greater than 1 m depth; this feature is not seen in the top two near surface bins. Closer examination of the data didn't reveal any issues with processing artefacts; it is unclear what caused these events. A likely explanation for the otherwise unaccounted for ADCP data variations is the infrequent but documented occurrence of large floating aquatic vegetation debris catching on the keel enough to interfere with the ADCP beams (Figure 4-17). Reeds of grasses up to 3 meters in length have been found afloat on the lake surface following high wind events. Vela's keel is designed to shed weeds, but these very long reeds can, infrequently, wrap on the keel for a period of hours in quantities large enough to interfere with sailing and ADCP performance.

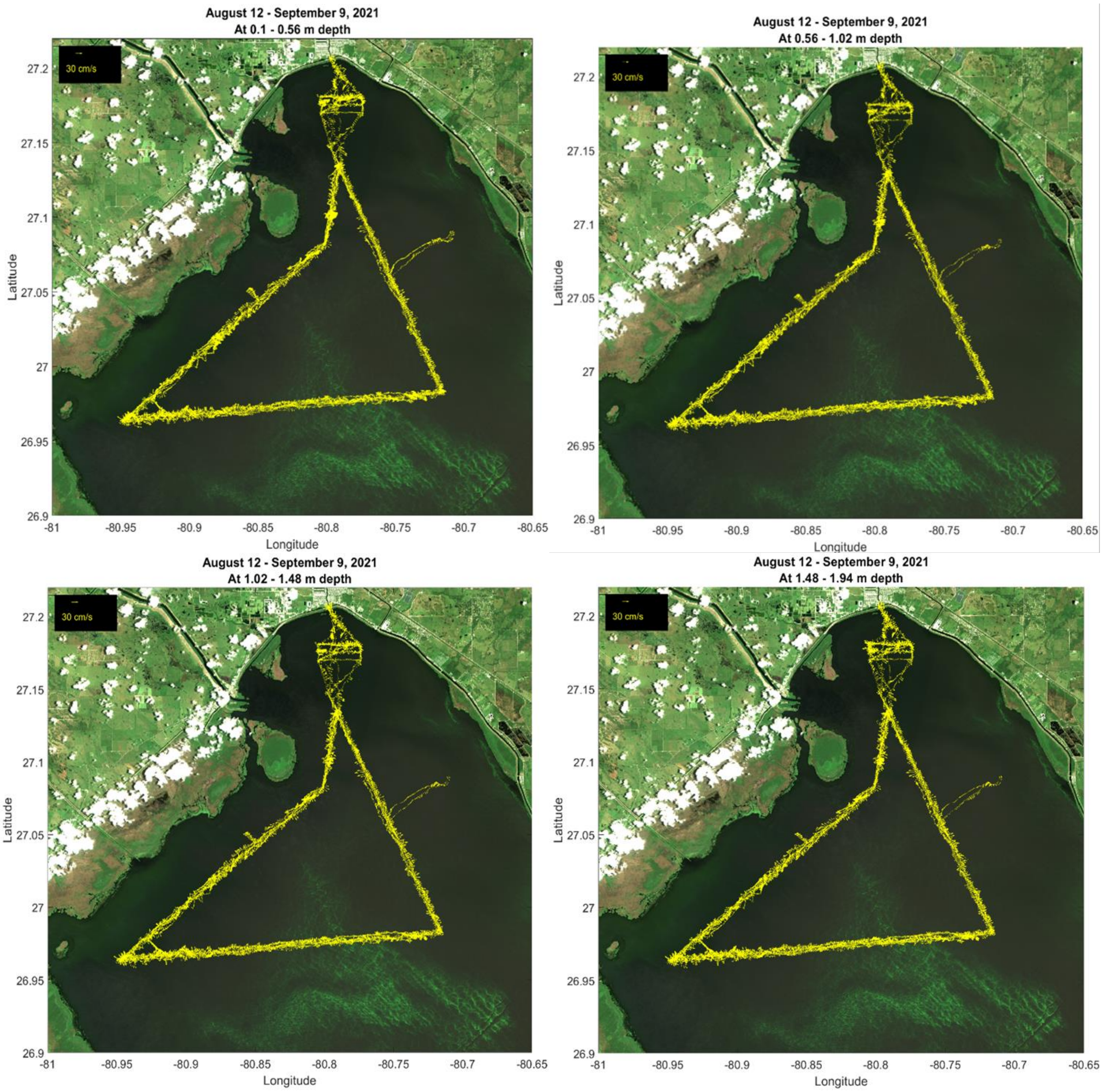

Figure 4-12: ADCP data from the sailboat path from Aug 12 – Sep 9, 2021 at the top 4 different depth bins; (a) 0.1-0.56 m; (b) 0.56-1.02 m; (c) 1.02-1.48 m; and (d) 1.48-1.94 m.

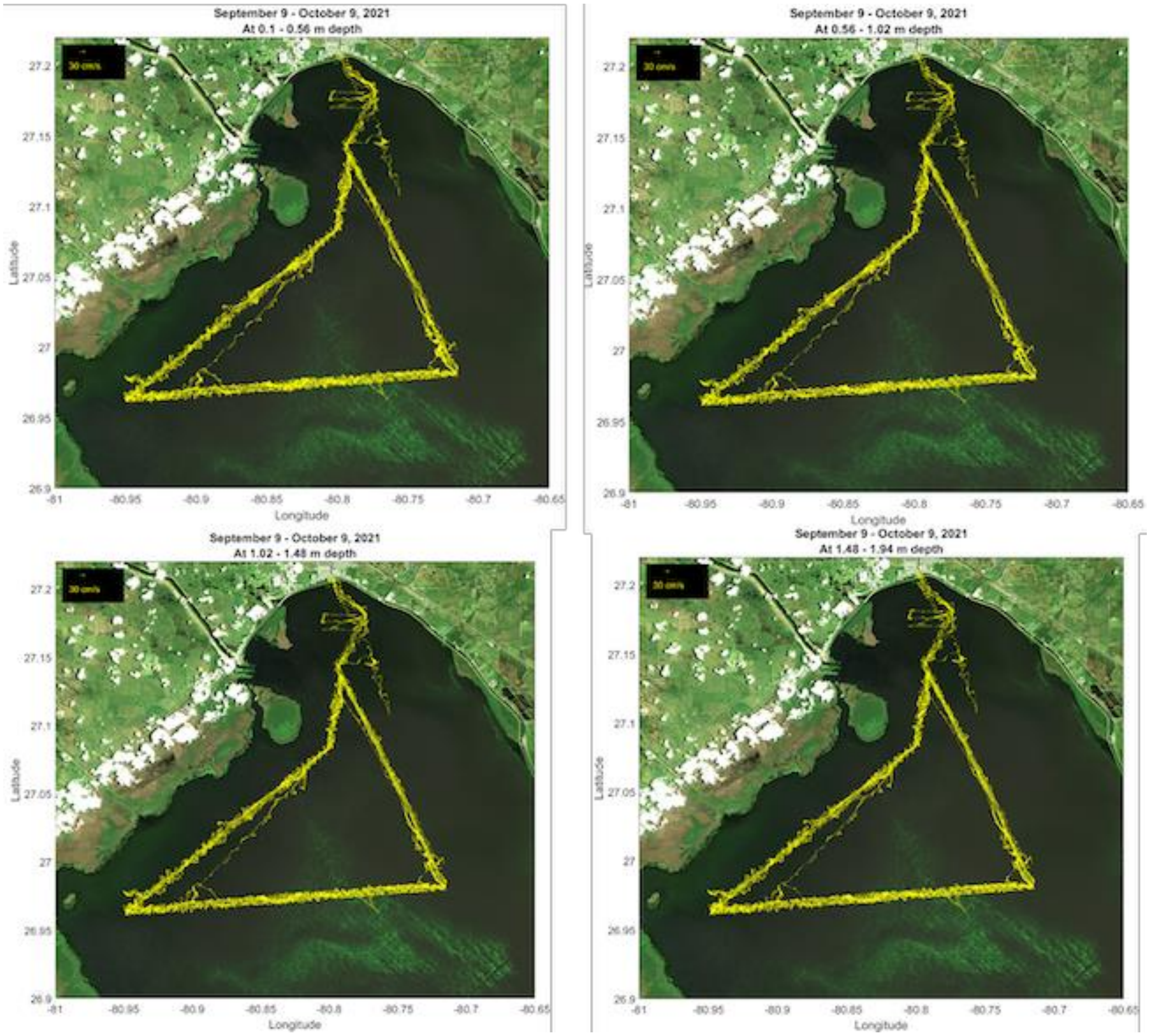

Figure 4-13: ADCP data from the sailboat path from Sep 9 – Oct 9, 2021 at the top 4 different depth bins; (a) 0.1-0.56 m; (b) 0.56-1.02 m; (c) 1.02-1.48 m; and (d) 1.48-1.94 m.

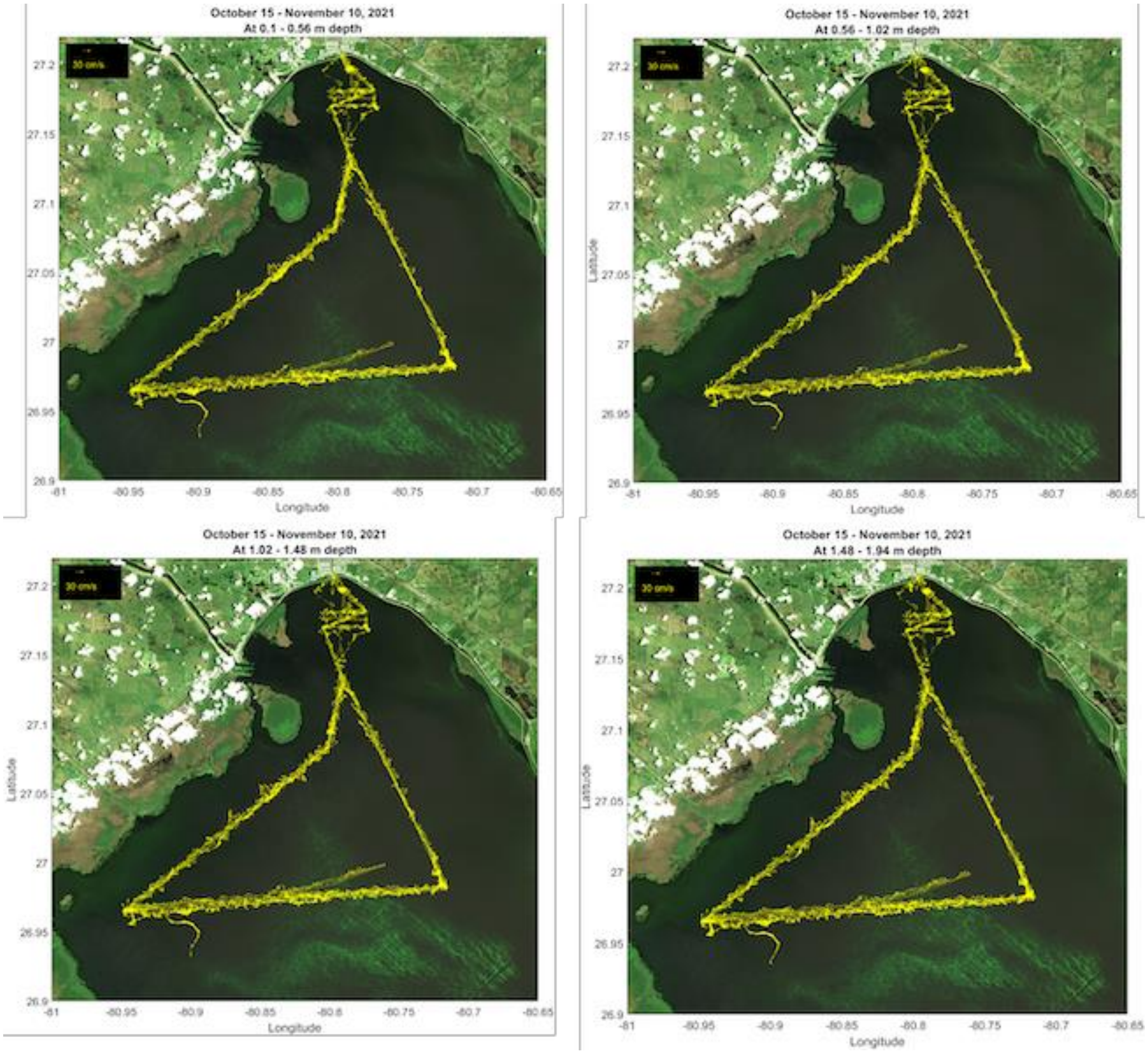

Figure 4-14: ADCP data from the sailboat path from Oct 15 – Nov 10, 2021 at the top 4 different depth bins; (a) 0.1-0.56 m; (b) 0.56-1.02 m; (c) 1.02-1.48 m; and (d) 1.48-1.94 m.

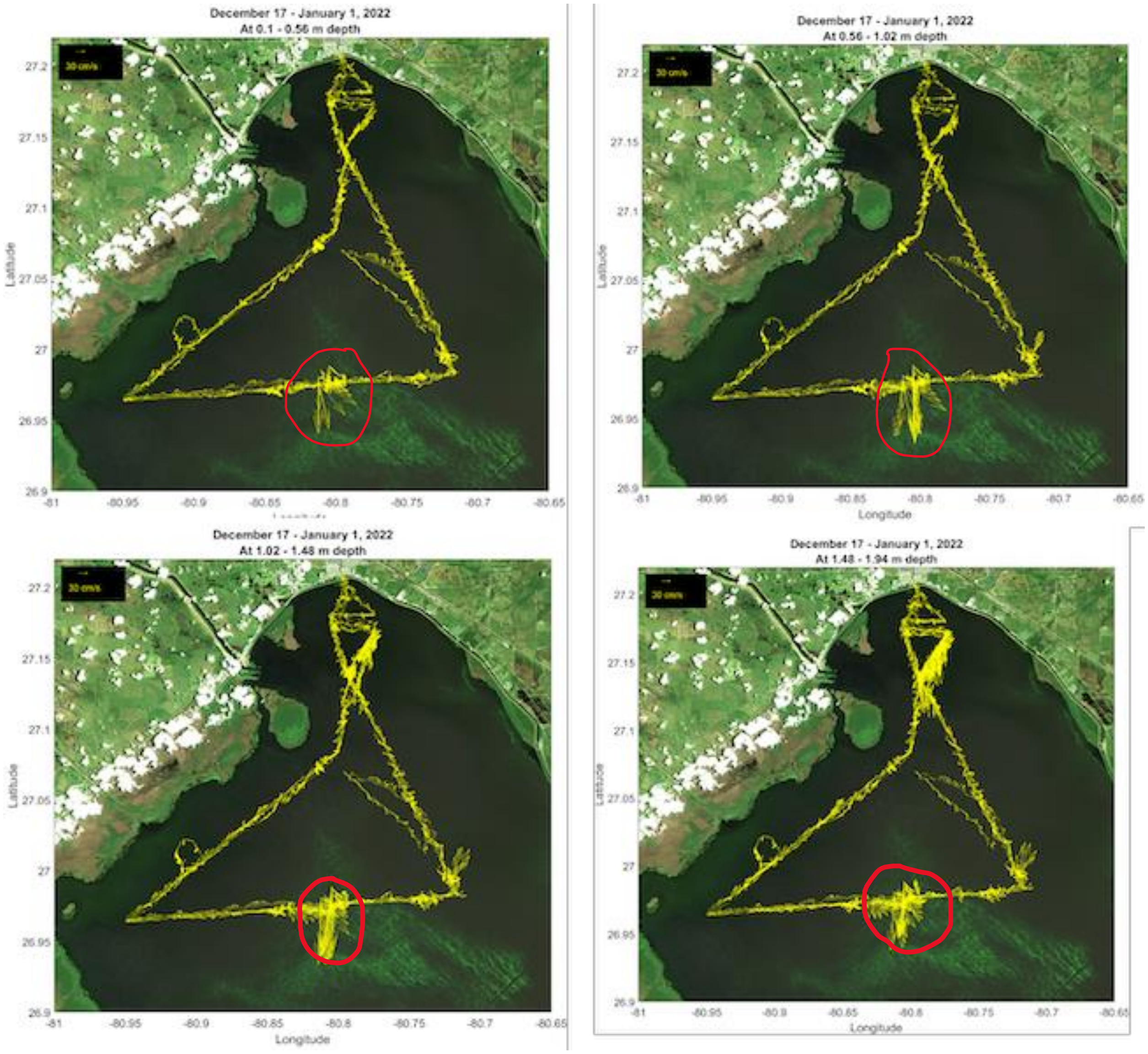

Figure 4-15: ADCP data from the sailboat path from Dec 5 – 17, 2021 at the top at the top 4 different depth bins; (a) 0.1-0.56 m; (b) 0.56-1.02 m; (c) 1.02-1.48 m; and (d) 1.48-1.94 m.

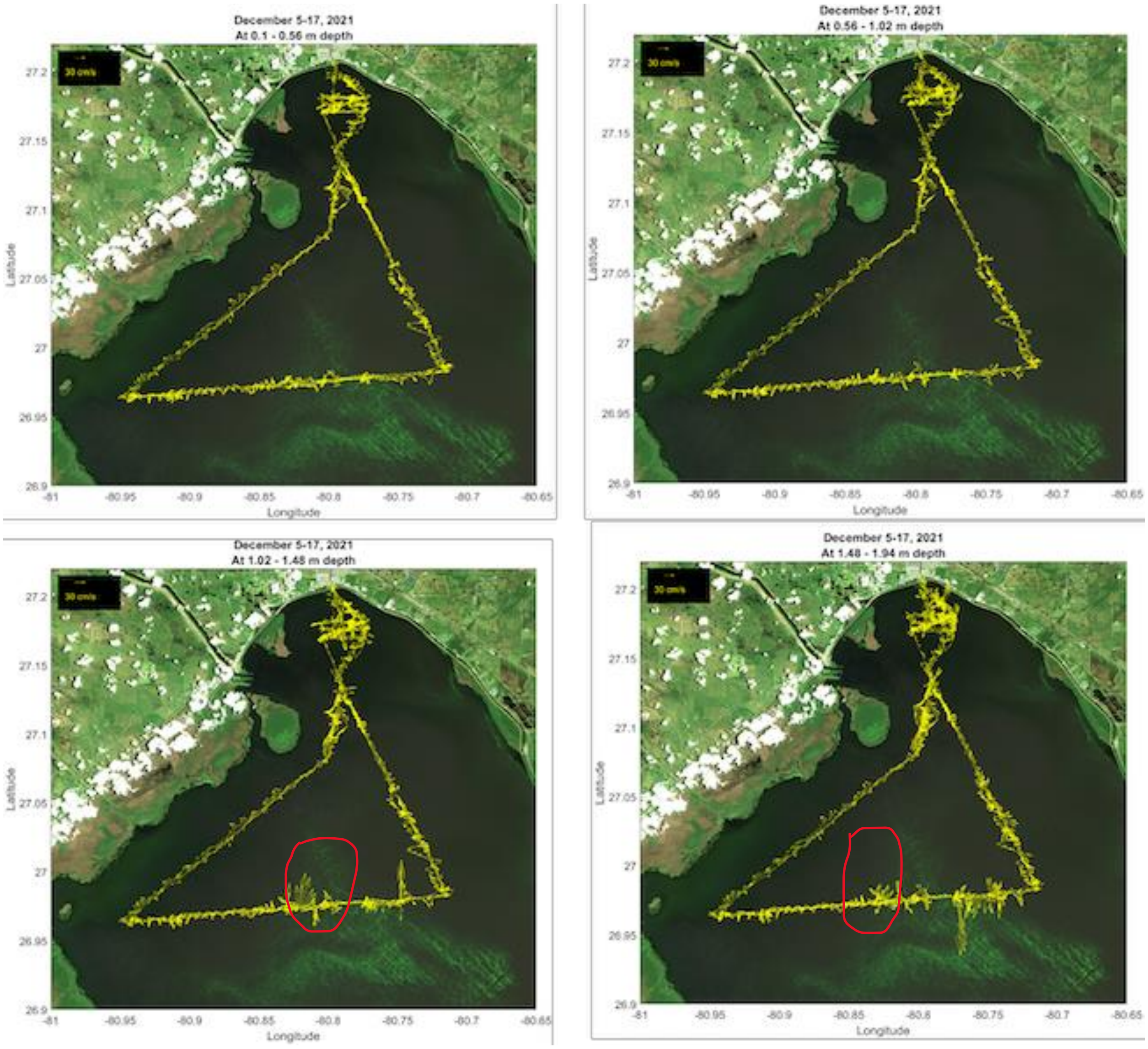

Figure 4-16: ADCP data from the sailboat path from Dec 17, 2021 – Jan 01, 2022 at the top 4 different depth bins; (a) 0.1-0.56 m; (b) 0.56-1.02 m; (c) 1.02-1.48 m; and (d) 1.48-1.94 m.

Figure 4-17: Long floating reeds affecting ADCP beams.

General environmental trends: While seasonality is evident in the typical environmental variables (conductivity, surface temperature, oxygen concentration), we also detected high variability at high frequency (e.g.: daily, sub-daily, and sub-hourly) (Figure 4-18). The high frequency variability responds to small scale features in the lake and, for fluorometric variables (backscatter, chlorophyll, phycocyanin and FDOM) can represent the presence of patches and scums of algae. It is important to recognize that this variability can cross several orders of magnitude and is otherwise lost during point observation monitoring.

As lake-wide seasonal trends, conductivity and temperature peaked in summer months. FDOM had an inverse relationship with conductivity (with increased variability during fall), and dissolved O_2 concentrations inversely followed temperature as expected. However large diurnal variability in the dissolved O_2 concentration surpassed that of temperature and could also be related to peaks in variability of phycocyanin.

Vela detected the presence of algal blooms (i.e. Chlorophyll) as early as February, which also corresponded to a local peak in blue green algae as seen in the Phycocyanin record (ancillary data collection confirmed this was likely *Dolichospermum* sp., formerly known as *Anaebaena* sp.). Aside from short HAB episodic events in February and March (see individual mission timeseries for better resolution) two maxima can be roughly identified: in summer, starting to increase in late April, peaking in July and August, and declining in September; and in fall, from late September to mid-November. These trends tend to match the *M. aeruginosa* patterns observed from other tasks, e.g. in Figure 3A-16. Following broad trends, a lag between phycocyanin and FDOM peaks is observable. High FDOM (and high variability) is more likely to be observed following decreasing trends in Phycocyanin. In contrast, this high variability in phycocyanin is associated with low turbidity (backscatter) the first half of the year. High frequency variability is difficult to observe in the full time series dataset, but specific missions illustrate serve to highlight this variability. In general, a strong diurnal signal was captured in the environmental parameters (temperature, conductivity, and dissolved oxygen) but this is not always true (e.g., missions 1-7, no signal, vs 17-21, strong signal in the Annex). We attribute the removal of the diurnal signal to strong wind mixing at the surface.

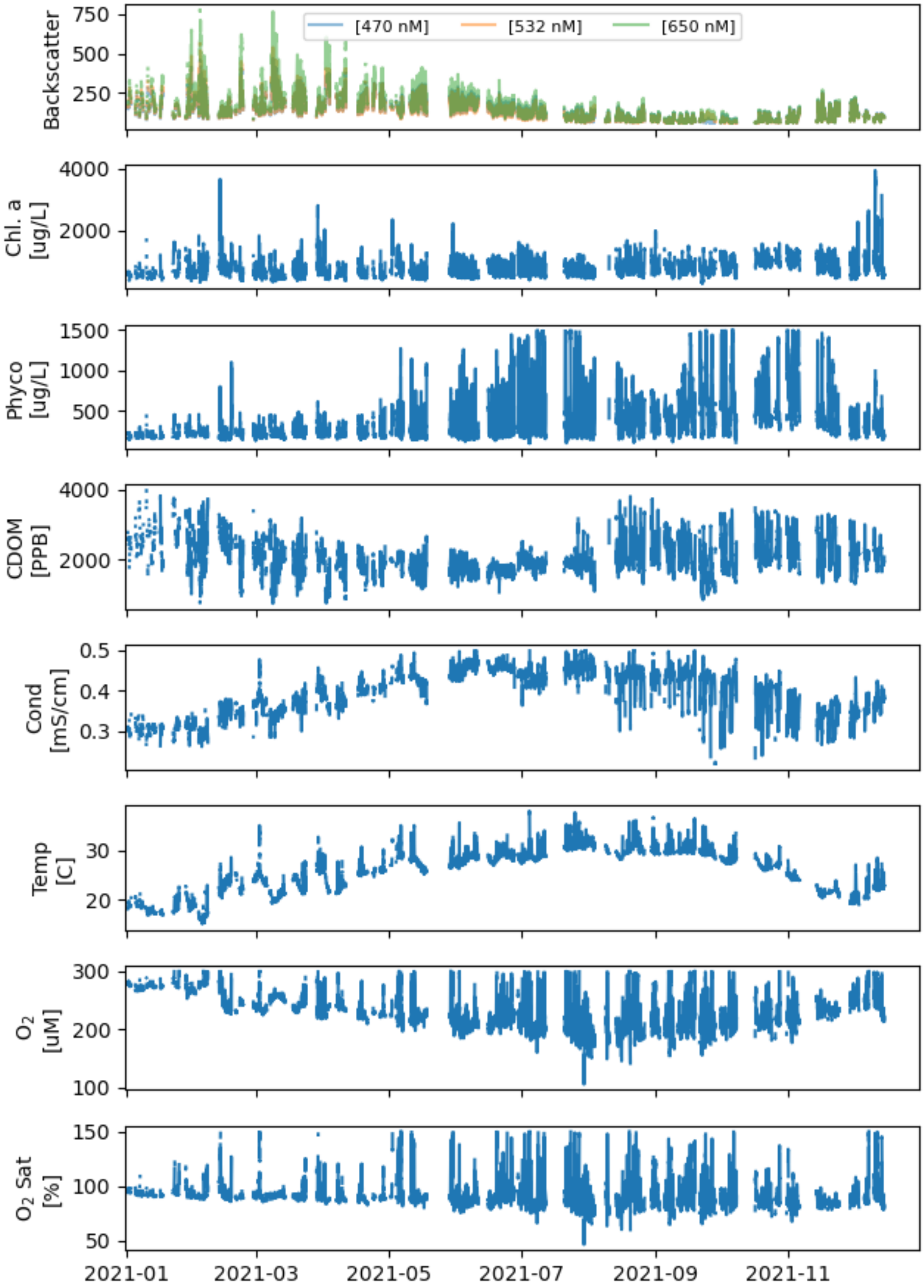

Figure 4-18: Time series of environmental and fluorometric variables collected during all missions in 2021, after 1st level QC and geofencing. A 5min mean filter was applied for regularity.

Further work on analyzing independent missions is ongoing, but it is important to make a note on the role of wind, and why separating datasets for analysis is crucial. While we have attributed scarcity of data early in the year to difficulties and progress in establishing continuous operations of the sailboat, it is important to notice the presence of stronger and chaotic winds during the first missions (e.g., February to March, see Figure 4-19), making navigation more challenging. Worth noting is the effect on the ASV steering and navigation accuracy caused by hydrodynamic drag from the full HALO sensor suite. This problem was addressed through software code and sail trim adjustments made throughout the year. The more continuous and better stream of data since July (Figure 4-18 and figures in the next section), was possible with our continuous improvement of navigation, but also to calmer conditions in the lake. Thus, correlation responses among variables might be different under windy and calm conditions (e.g., presence or lack of diurnal signals), or even lost entirely if considering the bulk of the dataset. More on this topic is discussed in the point-to-point comparison section below.

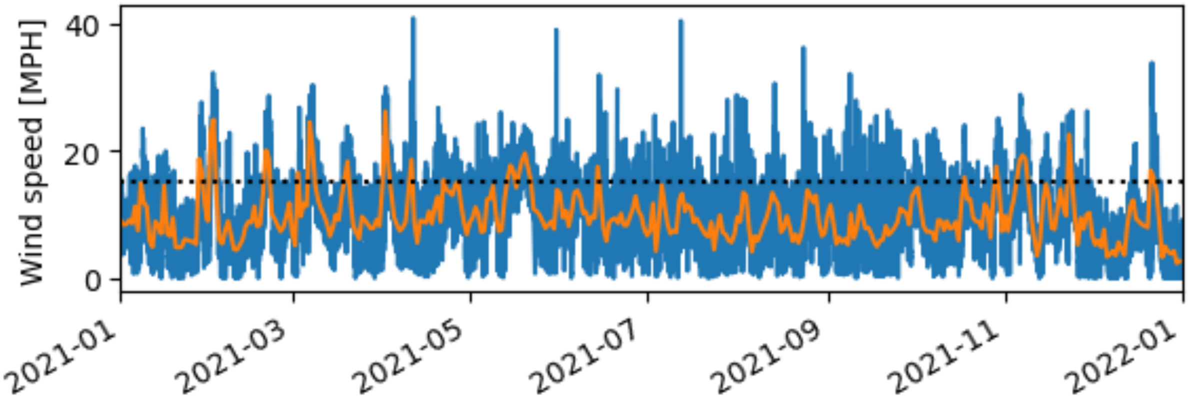

Figure 4-19: Wind speed measured at DBHydro station LZ40 during 2021. Instantaneous record in blue and daily average in orange. A dashed line is shown to mark an arbitrary threshold of 15MPH to indicate strong sustained wind periods in the daily average.

Spatiotemporal structure: To separate spatial and temporal trends, we constructed the spatiotemporal plane for three different transects: the right leg of the triangular path, the bottom leg, and the left leg as shown in Figure 4-20, for all fluorescence variables. We constructed narrow geofences enclosing the transects to capture data in the path, and project the data to line transects (in the middle of the geofence). This projection allows the identification of the development and movement of algal blooms along a transect. Figures 4-21 to 4-24 show the spatiotemporal distribution of Chlorophyl, Phycocyanin, Backscatter and FDOM respectively during the entire year, projected over the transects as defined. Increased chlorophyl patches were detected as early as 2/12/21 – 2/13/21 and later in May (Figure 4-21). As described above, data resolution is lower in these early months, and when data is present the signal is noisy. It should be noted that there will always remain gaps (white space) in these projection plots due to the periods of time in which the ASV was conducting one of the other two transect legs. As of the beginning of June, the dynamics of chlorophyll patches start to show. These patches show up near more coastal waters (northern edge of R near L001 and western edge of B, near L008), and seem to last for weeks but do not geographically displace along the transects. However, on the western transect (L), an apparent motion is observed in the northwest direction along the coast (from L008 towards KBARSE, see slope of increased Chl-a concentrations). High concentrations are widespread along transects in the later months, with the highest peaks recorded appearing in the right and bottom transects.

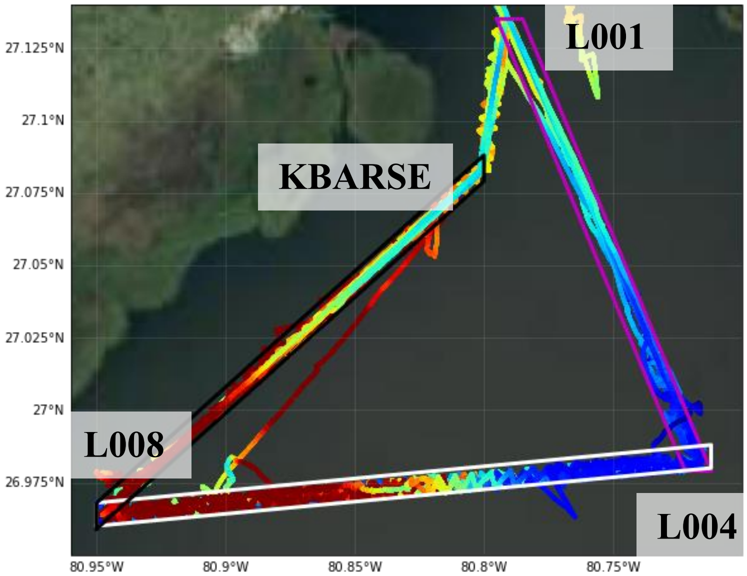

Figure 4-20: Geofences to define regions that enclose the right (R, magenta), bottom (B, white) and left (L, black) transects, to generate spatiotemporal planes. Lines in jet colormap indicate a selected variable measured along the path for reference. Data falling outside the geofences was discarded for the following analysis.

Phycocyanin dynamics better illustrate bloom transport in the lake (Figure 4-22), mostly because peaks in chlorophyl can span rapidly over several orders of magnitude, while peaks in phycocyanin are more moderate in magnitude (Figure 4-18). In the left transect (L), the northeast along-coast displacement of a small bloom is confirmed in June, a large bloom appears relatively stationary during July, and two successive large blooms appear to be displaced in the inverse direction (southeast) of the transect in October and November.

Motion is also observed in the right transect from L001 towards the interior of the lake from the end of June and lasting till August. Lower concentration blooms hint to motion in the same direction during fall (October-November). For the bottom transect, small episodic peaks appear in the summer months (seen as spots in Figure 4-22). A medium bloom appears roughly in the middle of the transect in late July early August, and slowly moves eastward until September. A large concentration bloom appears on the coastward edge (L008) in the second half of September and remains high until mid-November. Some displacement of lower concentration mases toward the interior are seen during this period, but the bloom does not reach the eastern edge of the transect (L004).

Blooms tended to occur at widespread relative low turbidity conditions (as seen in the backscatter signal (Figure 4-23), and immediately followed by a higher CDOM signal (Figure 4-24). The existence of a small perceivable lag between CDOM and chlorophyl (CDOM increasing following a bloom appearance) should be confirmed with continuous stationary measurements (e.g., combined analysis with Task 6), as this signal is difficult to separate in the convoluted spatiotemporal dimension.

Backscatter products (470 nM, 532 nM, 650 nM) showed relatively similar patterns and the first band (470) is shown in Figure 4-23. More in depth optical analysis should be performed on this dataset, but general trends show higher turbidity during strong wind events, not only near coast (e.g., L001, L008 or the entire left transect), but also in the interior of the lake (e.g., the entire bottom transect), indicating resuspension processes of sediment load are occurring widespread.

In contrast to turbidity (Figure 4-23), CDOM (Figure 4-24) was consistently higher in coastal locations (e.g., left transect, and near L001 and L008). We suspect that some of this is due to the suppression of the fluorescence signal at higher turbidities; thus we are considering a fluorometric correction algorithm to provide turbidity-independent data.

To better understand relationships among these variables, and detect higher frequency signals, we will analyze specific missions and perform point-to-point comparisons. Some general trends on point-to-point comparisons are highlighted in the next section.

Point-to-point data comparison: To illustrate the complexity of the full dataset (>2 million datapoints), scatterplots of Chlorophyll vs other fluorometric and environmental variables are presented (Figure 4-25). Observed patterns among fluorescence variables include: a negative nonlinear relationship with turbidity (through backscatter), two distinguishable trends on the chlorophyll a vs phycocyanin relationship, indicating the existence of more than one population causing blooms widespread in the lake (i.e. *M. aeruginosa* vs. *Dolichospermum* sp.), and a positive but noisy relationship with CDOM. Correlations with environmental variables seem weak, but our hypothesis is that trends are obscured by multiple superimposed processes at different spatial and temporal scales, requiring investigation of individual episodes as mentioned above.

CONCLUSIONS & FUTURE WORK

Lake Okeechobee (1732 km2 area) is sufficiently large to allow the development of complex dynamic features in its water column environmental composition and thus biogeochemical responses, including algal blooms. For example, wind velocity is responsible for the main surface current regime in Lake Okeechobee, and it can affect microscale circulation features (<1 km, <1 day). Modeling studies have shown that strong wind events can produce the complete mixing of the entire water column, while thermal stratification is present during calm weather periods (Jin et al., 2002), both processes affecting the distribution of nutrients, and thus biological responses, in the lake. On the other hand, small circulation features in the lake (some captured by our ADCP measurements) can create convergent fast-moving fronts and these motions are responsible of the redistribution of suspended particles, which can include harmful algal blooms. On the other hand, wind driven waves are responsible for sediment (and thus sediment nutrient load) resuspension, while wind induced currents transport those sediments (Jin & Ji, 2004; Jin & Sun, 2007). This complex environment thus makes space for complex responses in HAB dynamics that cannot be captured by traditional monitoring programs.

Fixed station monitoring programs give useful information on HAB and water quality evolution at large time scales (years to decades) and can be used to emit alerts when high concentrations of toxic algae are present in a station. However, this monitoring, even when using a considerable number of stations, will still not provide the ability to measure higher frequency responses, or the spread of a bloom event, or to identify localized features not covered by the station network. The installation of fixed continuous monitoring systems (e.g., **Task 6** and new SFWMD DBHydro installations) can resolve the finer temporal responses, but those are representative of a point station of the lake. Satellite images (**Task 5**) on the other hand, can help identify lake wide distribution patterns of color properties, which are indicative of algal blooms, turbidity or CDOM, but the small-scale temporal variability is lost, and the measurement depend on coverage and disentangling the interference of a highly turbid environment. To supplement these approaches from an observational point, Vela operations have provided very useful information on fluorometric and environmental properties. The sailboat has covered over 10,000 km of the lake cycling a 72 km path including additional detailed targeted investigations of bloom events and side missions, and for a total of 6,888 hours of operation, providing more than 2 million datapoints for every sensor used.

Sensor packets included backscatter (three different bands), fluorometer (chlorophyll, phycocyanin and CDOM), CT (conductivity and water temperature) and dissolved oxygen.

In addition to the environmental dataset, we have successfully acquired a complementary dataset of water column velocities from the ADCP, and atmospheric array which has not been discussed in this report. Future work on integrating the velocity field with to other collocated sensors could help understand better the motions of water characteristics and algal blooms. There is also a massive integration effort still underway, incorporating data from other tasks, focusing on identifying algal species-specific patterns based on spatial gradients of various parameters. Because the ASV inherently travels between different areas with different bloom assemblages, it may be possible to use the gradual transition in parameter values between these disparate phytoplankton species-dominated areas to identify species using only common fluorometric/environmental sensors according to combined multiparameter criteria. For example, *M. aeruginosa* may exhibit higher phycocyanin to chl-a ranges, and a low backscatter, but may also produce an extremely elevated O_2 and high pH during the day. We are currently exploring these fingerprint approaches, as they can be useful not only onboard the ASV but also from other fixed-location and even discrete sonde-based approaches.

Going forward, the strategy of future ASV deployments should be dependent on the desired output. For example, full lake coverage with several ASVs, while costly, could reveal full lake time series images of phyocyanin and other parameter. The temporal resolution Figure 4-21 to 4-24 appears acceptable to resolving most bloom patterns; with two or three ASVs operating at the same low, safe reliable speed, this could be achieved. Alternatively, a single ASV monitoring the "L" transect in Figure 4-20 (repeatedly traveling back and forth from the two vertices) would be ideal from the perspective of understanding bloom transport dynamics in this important initiation region.

Some highlights include:

- This was the first ever attempt in Lake Okeechobee to measure CDOM and phycocyanin directly in the water at wide scale.
- The enormous number of data points collected allow to differentiate daily and sub-daily frequencies, as well as to cover seasonal trends, and responses to specific events.
- We could identify some combined spatiotemporal trends, and further analysis supplemented with satellite images could give insight into spatial spread of bloom formation, development, and decline.
- The data collected during all mission are a big data challenge that can elucidate unexpected results. The data set is complex given the interweaved spatiotemporal dimensions, but modern statistical analysis tools and use of supercomputing power provide multiple approaches.
- We have successfully demonstrated the value of the ADCP data to the ASV (sailboat) platform. As part of this ambitious effort, deployment and data acquisition issues were identified and resolved during the first half of the reporting period. The ADCP data will be critical for **Task 1E** for circulation/transport modeling, but also for sediment resuspension modeling (**Task 3&11**)
- Code routines (in Python and MATLAB) where developed for reading and postprocessing environmental and ADCP data to ensure quality was maintained; for environmental variables, to filter unexpected values, generate time series, and spatiotemporal planes; and for ADCP measurements, to subtract vessel motion accurately from a moving platform and generate images over different depth intervals over the entire path of the sailboat. Separate routines were also developed to use weather data (wind speed) from Vela. All this code libraries will make interacting an analyzing Vela data more straightforward in the future. The same routines can be used in future deployments of the ASV at Lake Okeechobee and elsewhere.

- Future applications could potentially include using the ADCP data for comparisons with other co-located measurements in Lake Okeechobee, thus helping integrate physical aspects to the overall biology, chemistry, and geology of the lake.

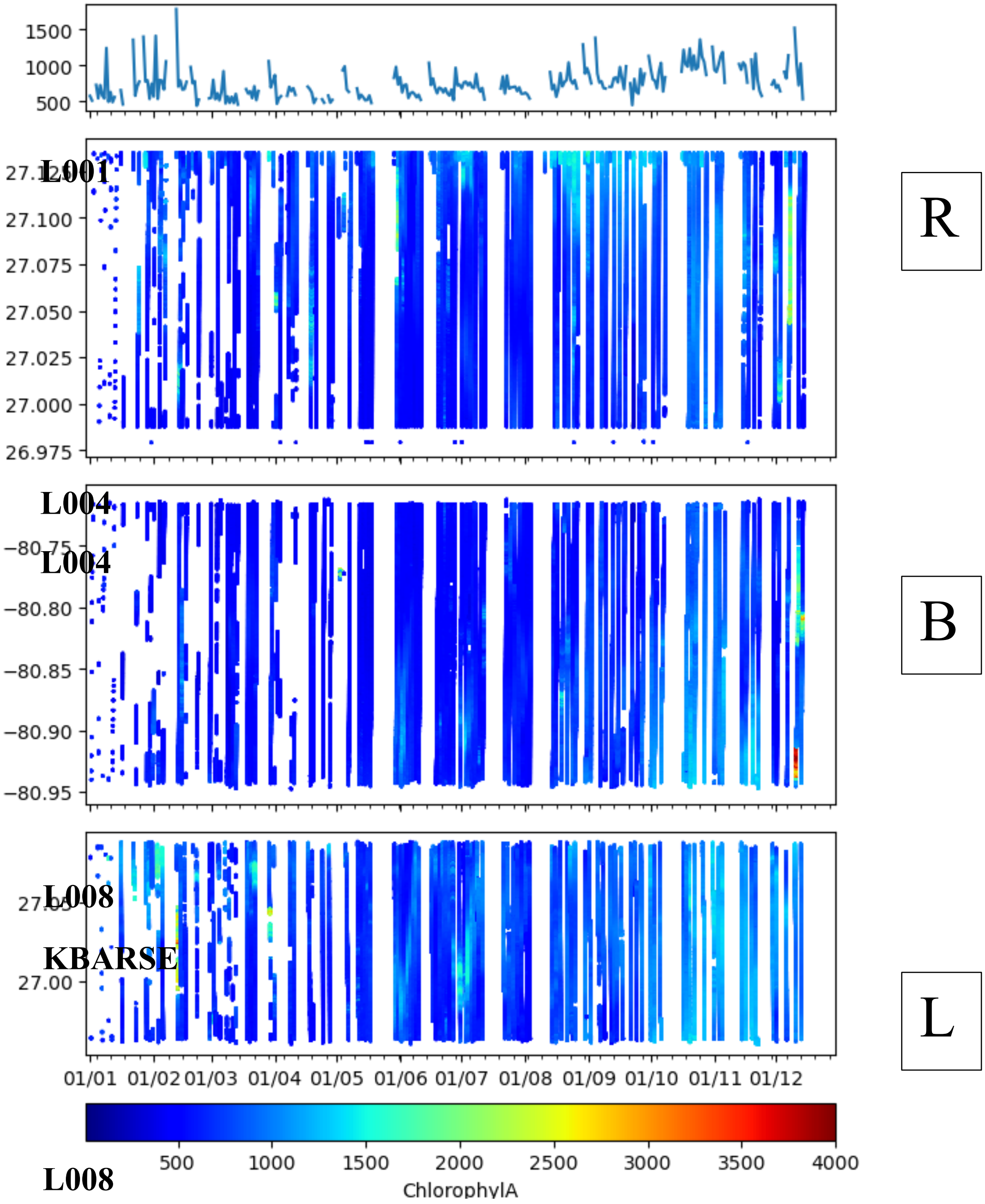

Figure 4-21: Chlorophyl [ug/L] timeseries in time (daily averaged, top), and time and space dimensions for the right (R, between L001- L004), bottom (B, L004-L008) and left (L, L008-KBARSE) transects as shown in Figure 4-11. The edges of the quasi-triangular path dividing the transects are roughly DBhydro stations L001, L004, L008, KBARSE. The section between KBARSE and closing cycle in L001 is not shown.

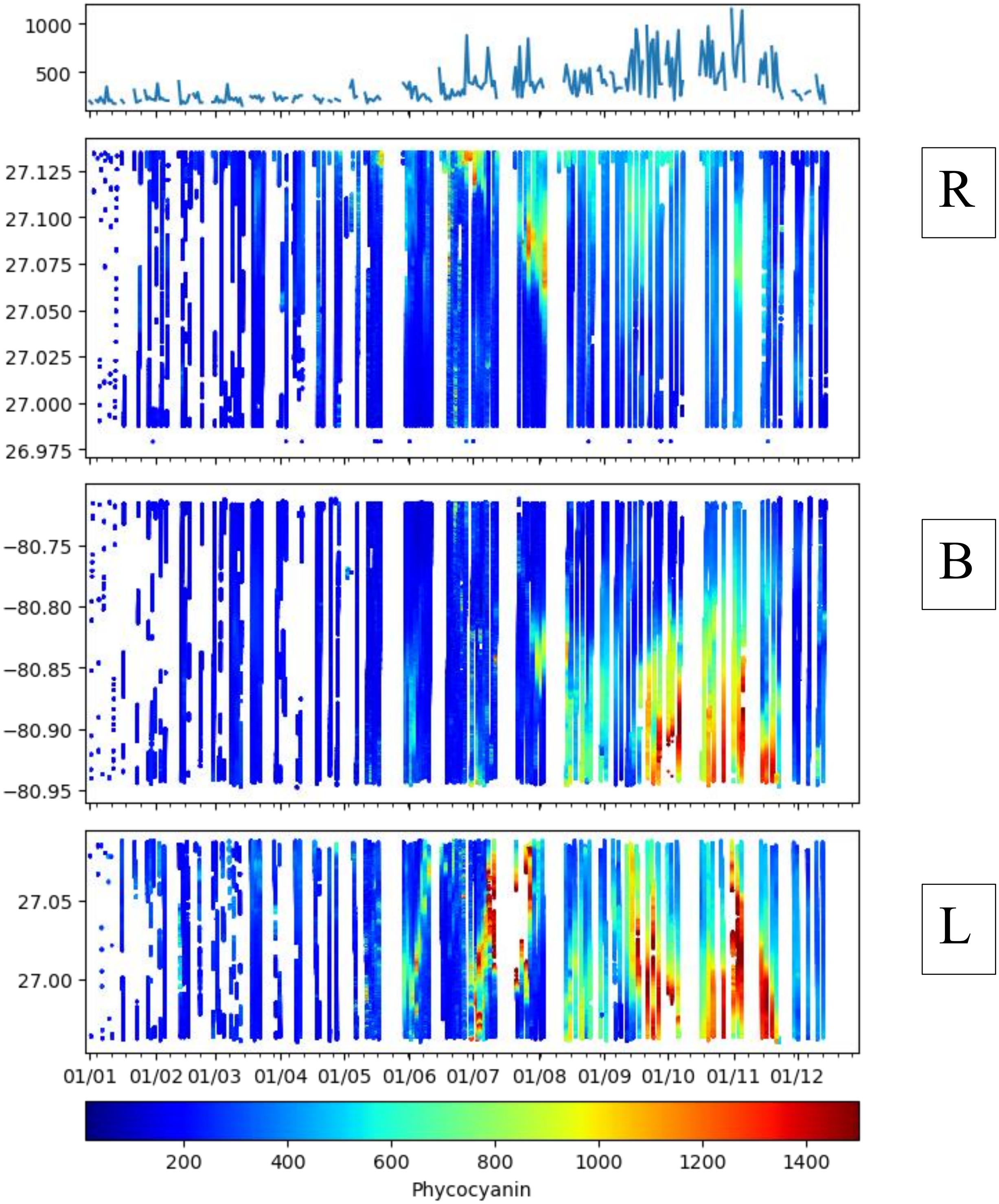

Figure 4-22: Phycocyanin [ug/L] timeseries in one dimension (daily averaged, top), and time and space dimensions for the right (R), bottom (B) and left (L) transects as shown in Figure 4-11.

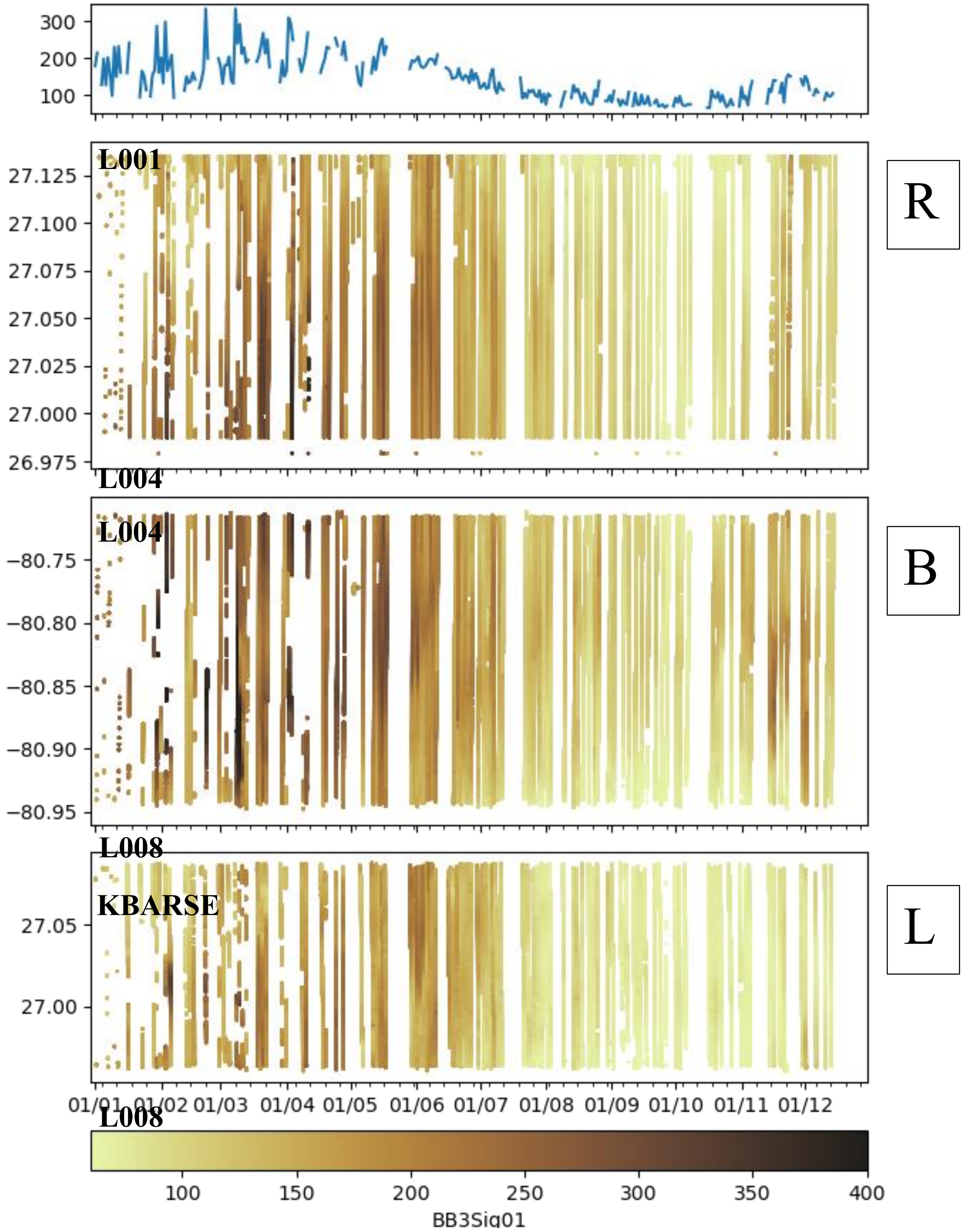

Figure 4-23: Backscatter [470 nM] in one dimension (daily averaged, top), and time and space dimensions for the right (R), bottom (B) and left (L) transects as shown in Figure 4-11.

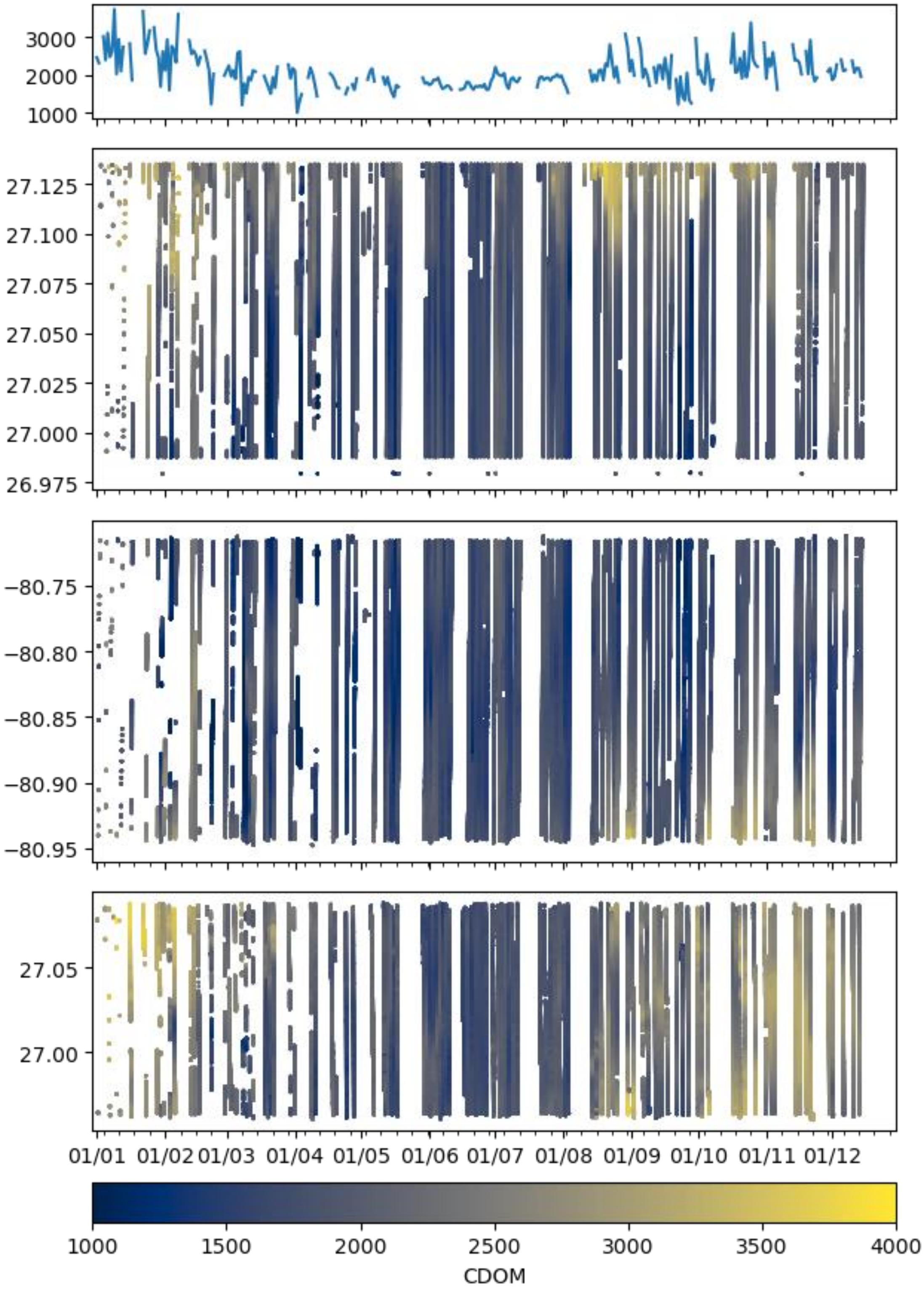

Figure 4-24: CDOM [PPB] timeseries in one dimension (daily averaged, top), and time and space dimensions for the right (R), bottom (B) and left (L) transects as shown in Figure 4-11.

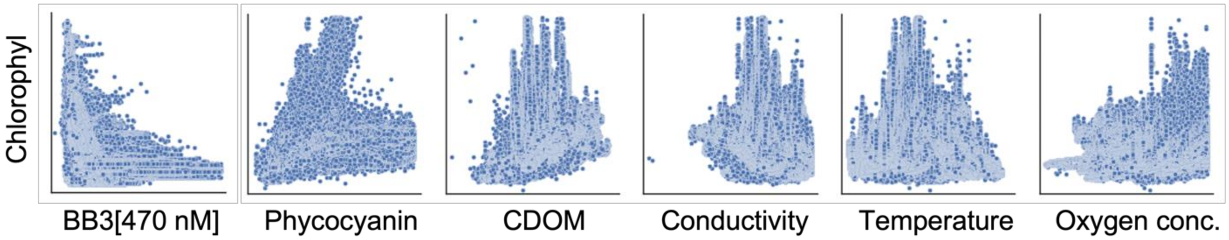

Figure 4-25: Scatter plots of entire unfiltered quality-controlled dataset showing relationship between chlorophyl and other fluorometric and environmental variables.

The following pages contain the Task 4 Annex (Time series for individual missions)

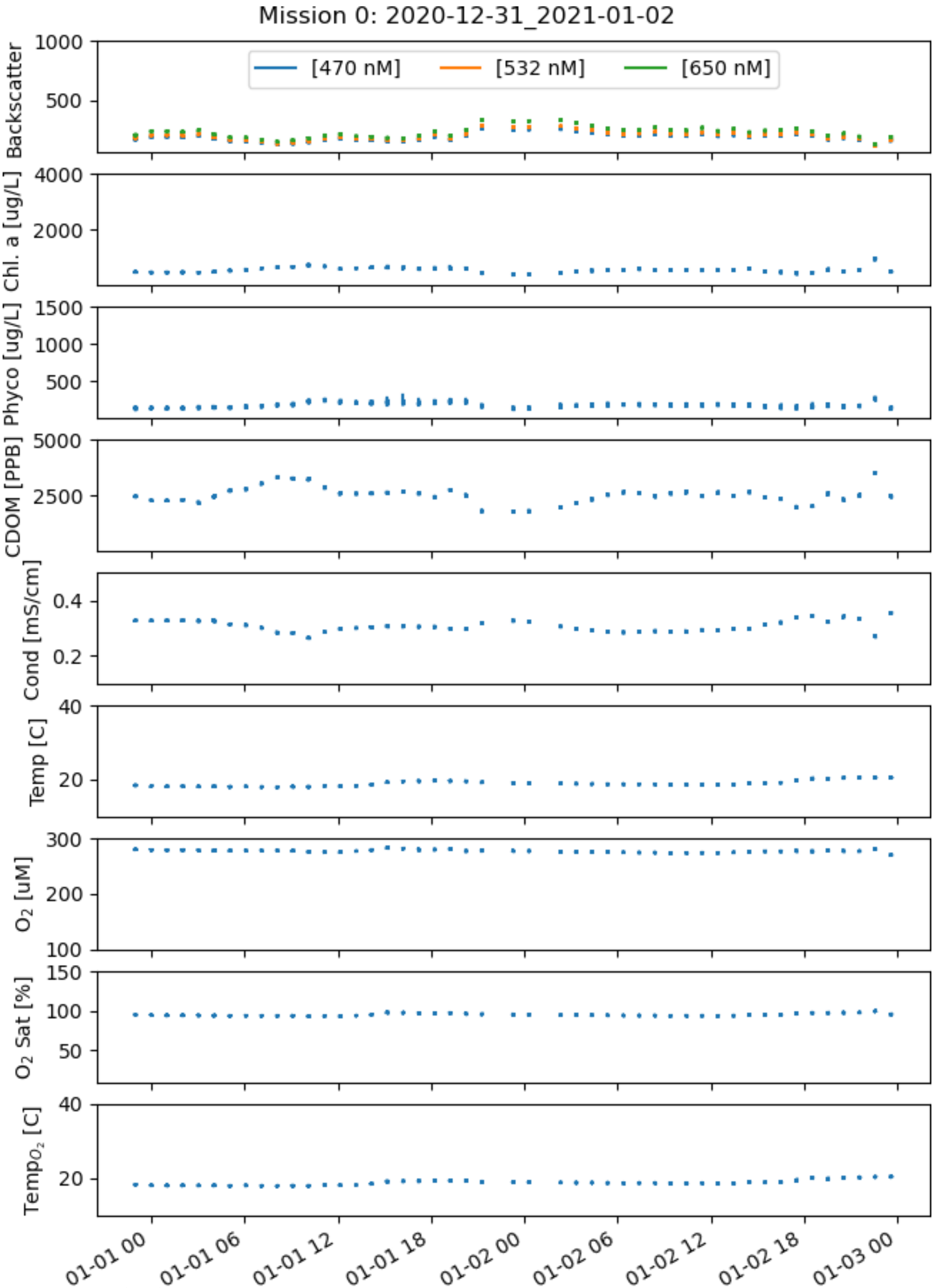
Mission 0: 2020-12-31_2021-01-02
[470 nM]
[532 nM]
[650 nM]
Backscatter
1000
500
Chl. a [ug/L]
4000
2000
Phyco [ug/L]
1500
1000
500
CDOM [PPB]
5000
2500
Cond [mS/cm]
0.4
0.2
Temp [C]
40
20
O_2 [uM]
300
200
100
O_2 Sat [%]
150
100
50
$Temp_{O_2}$ [C]
40
20
01-01 00
01-01 06
01-01 12
01-01 18
01-02 00
01-02 06
01-02 12
01-02 18
01-03 00

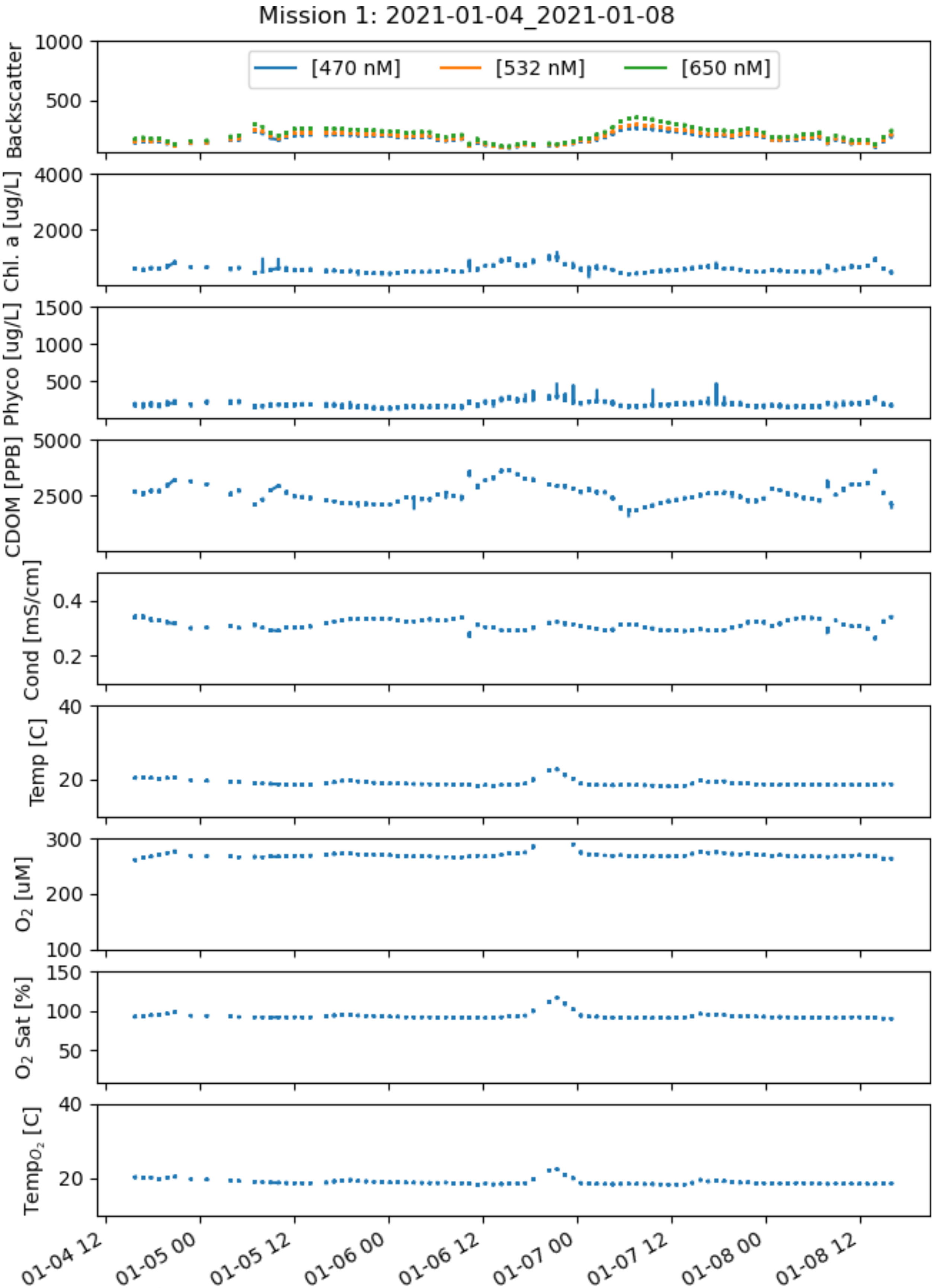
Mission 1: 2021-01-04_2021-01-08
[470 nM]
[532 nM]
[650 nM]
Backscatter
1000
500
Chl. a [ug/L]
4000
2000
Phyco [ug/L]
1500
1000
500
CDOM [PPB]
5000
2500
Cond [mS/cm]
0.4
0.2
Temp [C]
40
20
O$_2$ [uM]
300
200
100
O$_2$ Sat [%]
150
100
50
Temp$_{O_2}$ [C]
40
20
01-04 12
01-05 00
01-05 12
01-06 00
01-06 12
01-07 00
01-07 12
01-08 00
01-08 12

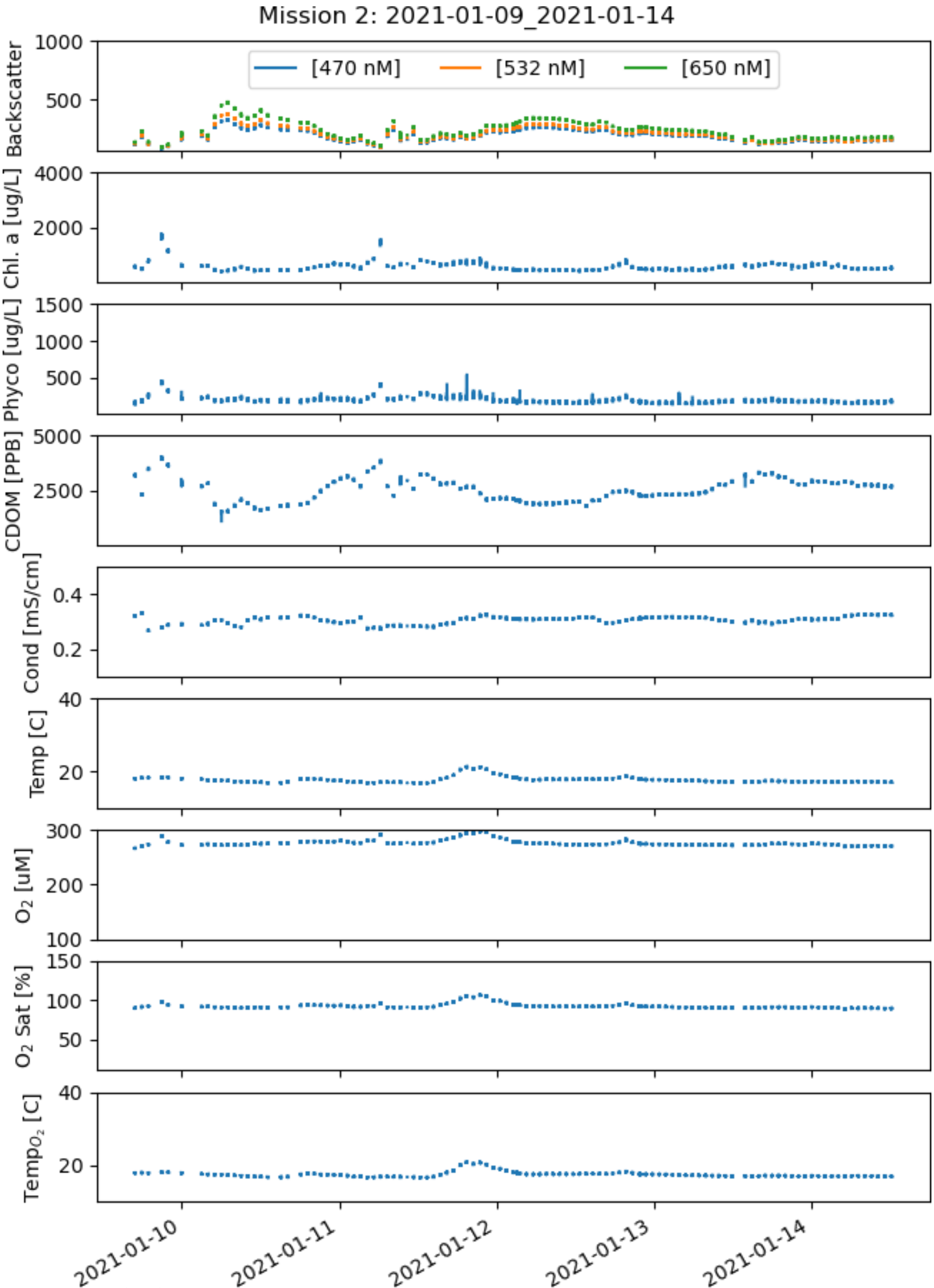
Mission 2: 2021-01-09_2021-01-14
Backscatter
1000
500
[470 nM]
[532 nM]
[650 nM]
Chl. a [ug/L]
4000
2000
Phyco [ug/L]
1500
1000
500
CDOM [PPB]
5000
2500
Cond [mS/cm]
0.4
0.2
Temp [C]
40
20
O$_2$ [uM]
300
200
100
O$_2$ Sat [%]
150
100
50
Temp$_{O_2}$ [C]
40
20
2021-01-10
2021-01-11
2021-01-12
2021-01-13
2021-01-14

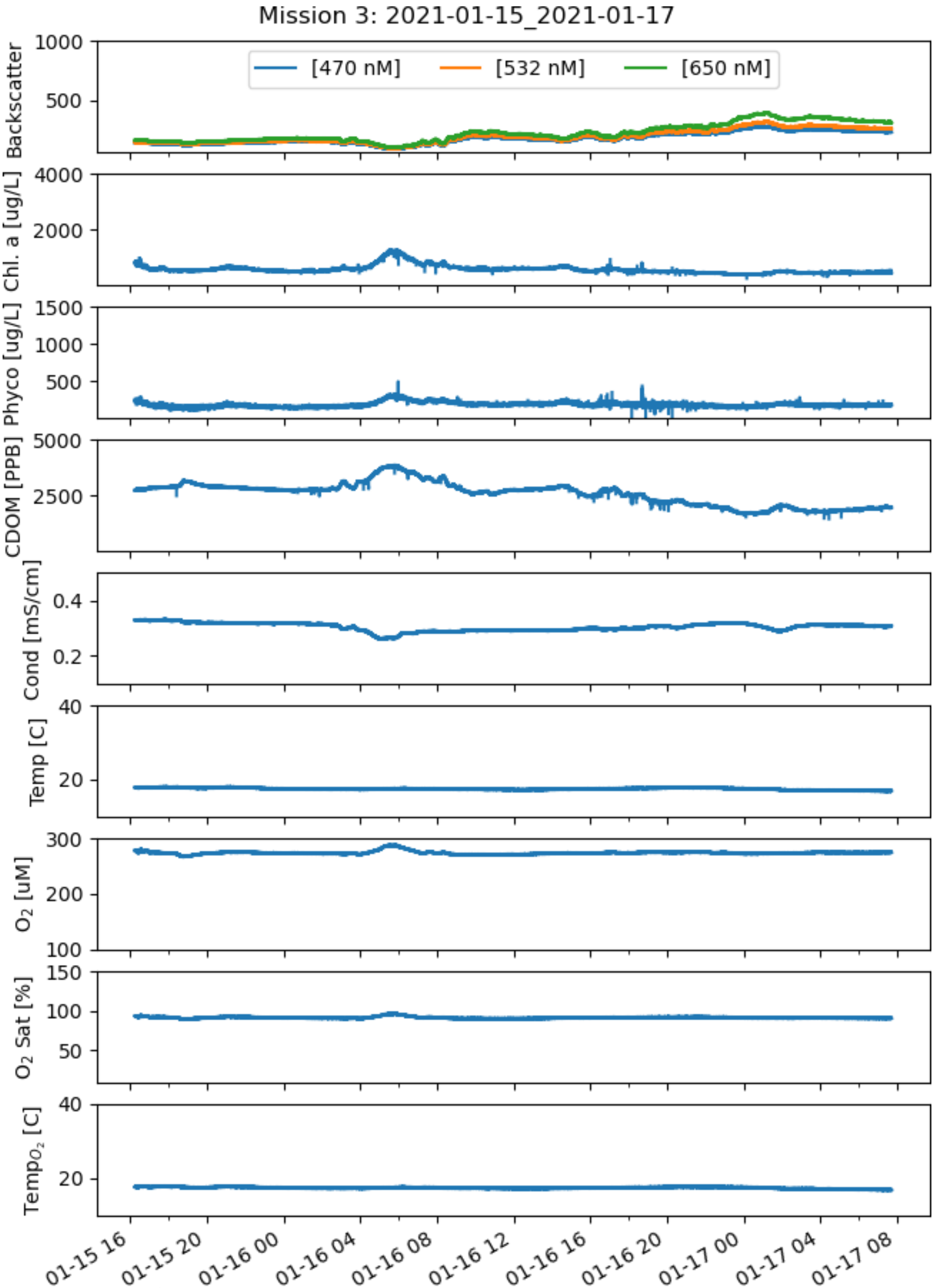
Mission 3: 2021-01-15_2021-01-17
[470 nM]
[532 nM]
[650 nM]
Backscatter
1000
500
Chl. a [ug/L]
4000
2000
Phyco [ug/L]
1500
1000
500
CDOM [PPB]
5000
2500
Cond [mS/cm]
0.4
0.2
Temp [C]
40
20
O₂ [uM]
300
200
100
O₂ Sat [%]
150
100
50
Temp O₂ [C]
40
20
01-15 16
01-15 20
01-16 00
01-16 04
01-16 08
01-16 12
01-16 16
01-16 20
01-17 00
01-17 04
01-17 08

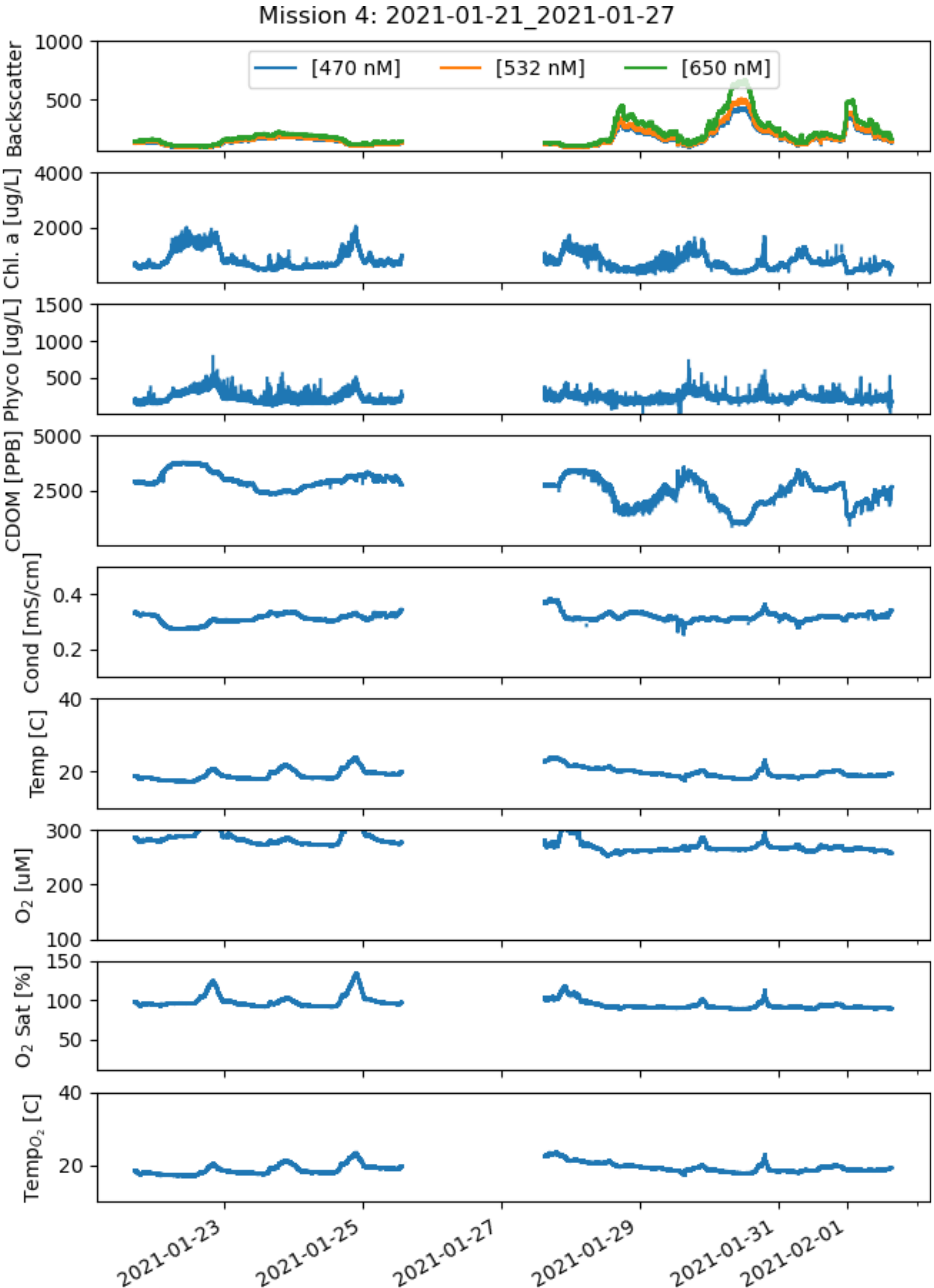

Mission 4: 2021-01-21_2021-01-27
[470 nM]
[532 nM]
[650 nM]
Backscatter
1000
500
Chl. a [ug/L]
4000
2000
Phyco [ug/L]
1500
1000
500
CDOM [PPB]
5000
2500
Cond [mS/cm]
0.4
0.2
Temp [C]
40
20
O2 [uM]
300
200
100
O2 Sat [%]
150
100
50
Temp$_{O_2}$ [C]
40
20
2021-01-23
2021-01-25
2021-01-27
2021-01-29
2021-01-31
2021-02-01

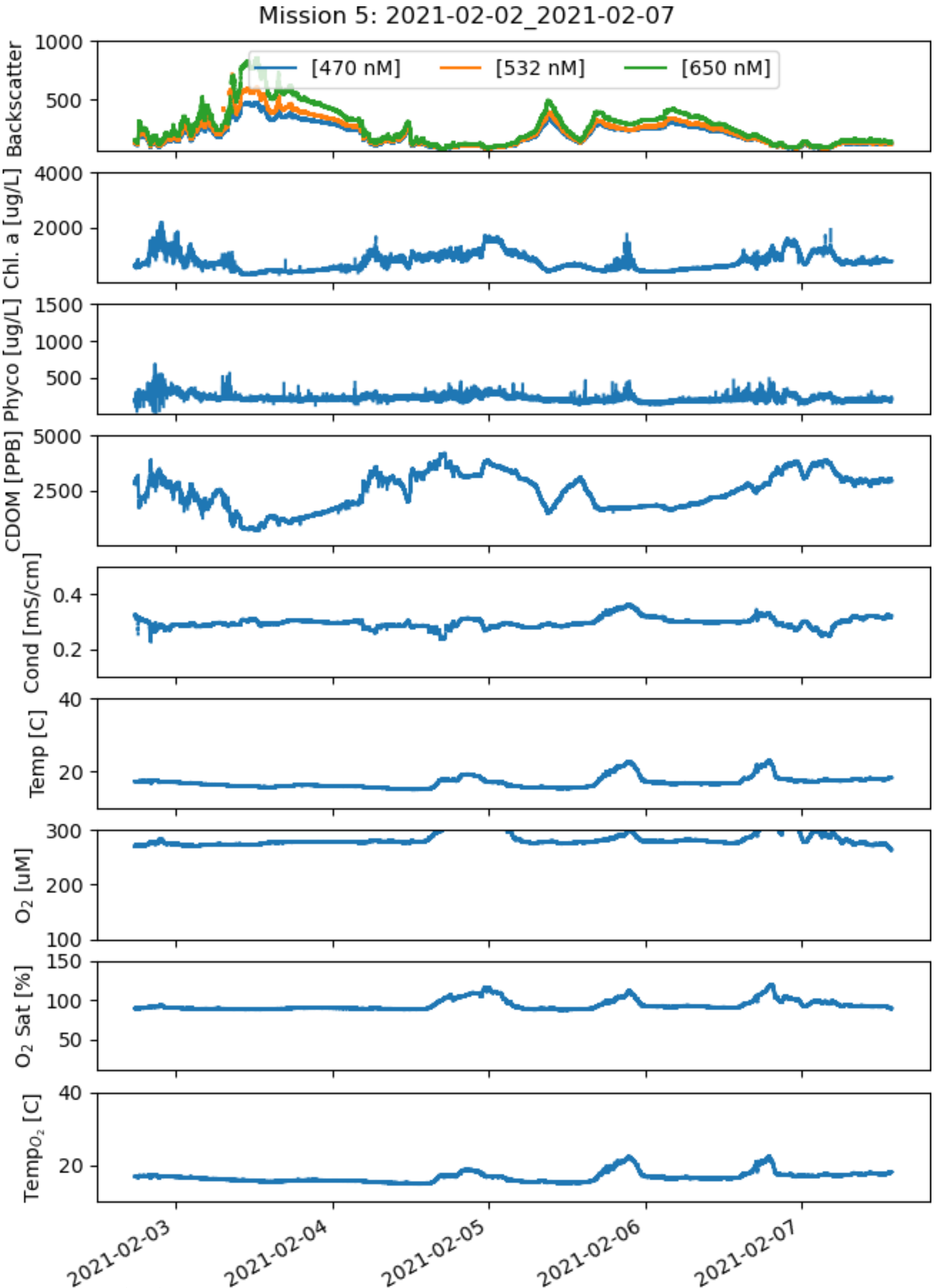
Mission 5: 2021-02-02_2021-02-07
Backscatter
[470 nM]
[532 nM]
[650 nM]
1000
500
Chl. a [ug/L]
4000
2000
Phyco [ug/L]
1500
1000
500
CDOM [PPB]
5000
2500
Cond [mS/cm]
0.4
0.2
Temp [C]
40
20
O_2 [uM]
300
200
100
O_2 Sat [%]
150
100
50
$Temp_{O_2}$ [C]
40
20
2021-02-03
2021-02-04
2021-02-05
2021-02-06
2021-02-07

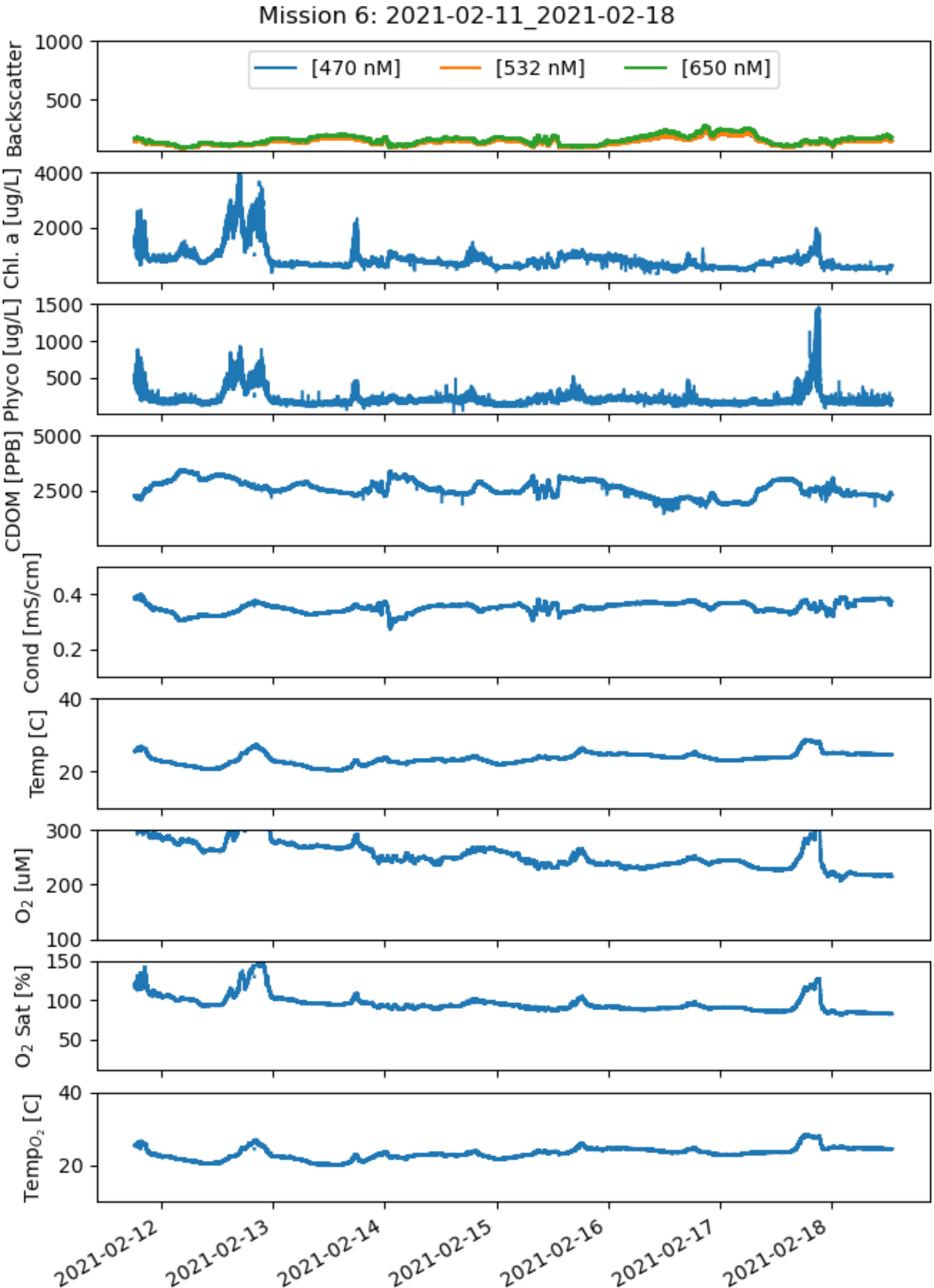
Mission 6: 2021-02-11_2021-02-18
Backscatter
1000
500
[470 nM]
[532 nM]
[650 nM]
Chl. a [ug/L]
4000
2000
Phyco [ug/L]
1500
1000
500
CDOM [PPB]
5000
2500
Cond [mS/cm]
0.4
0.2
Temp [C]
40
20
O_2 [uM]
300
200
100
O_2 Sat [%]
150
100
50
$Temp_{O_2}$ [C]
40
20
2021-02-12
2021-02-13
2021-02-14
2021-02-15
2021-02-16
2021-02-17
2021-02-18

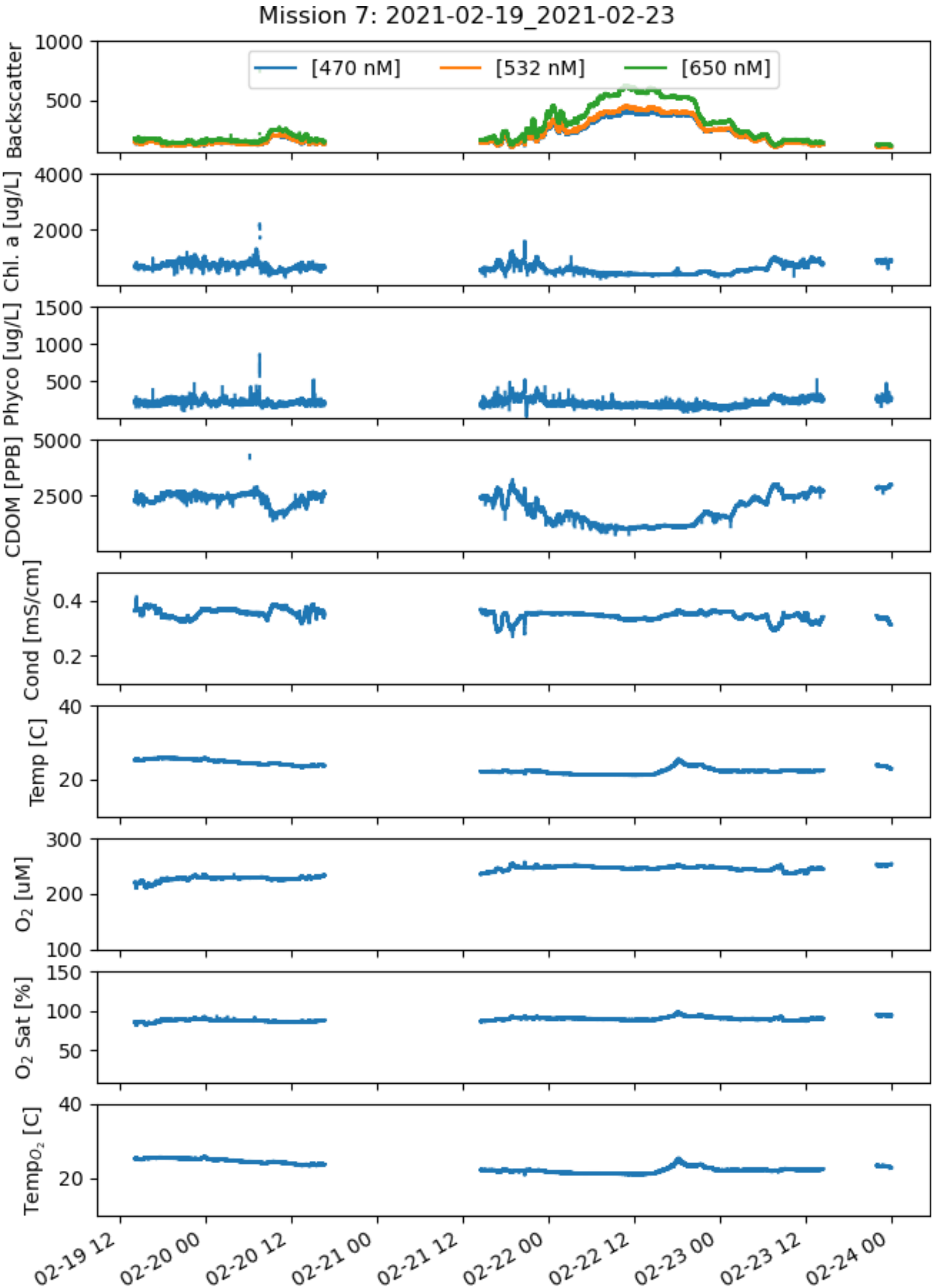
Mission 7: 2021-02-19_2021-02-23
Backscatter
[470 nM]
[532 nM]
[650 nM]
1000
500
Chl. a [ug/L]
4000
2000
Phyco [ug/L]
1500
1000
500
CDOM [PPB]
5000
2500
Cond [mS/cm]
0.4
0.2
Temp [C]
40
20
O_2 [uM]
300
200
100
O_2 Sat [%]
150
100
50
$Temp_{O_2}$ [C]
40
20
02-19 12
02-20 00
02-20 12
02-21 00
02-21 12
02-22 00
02-22 12
02-23 00
02-23 12
02-24 00

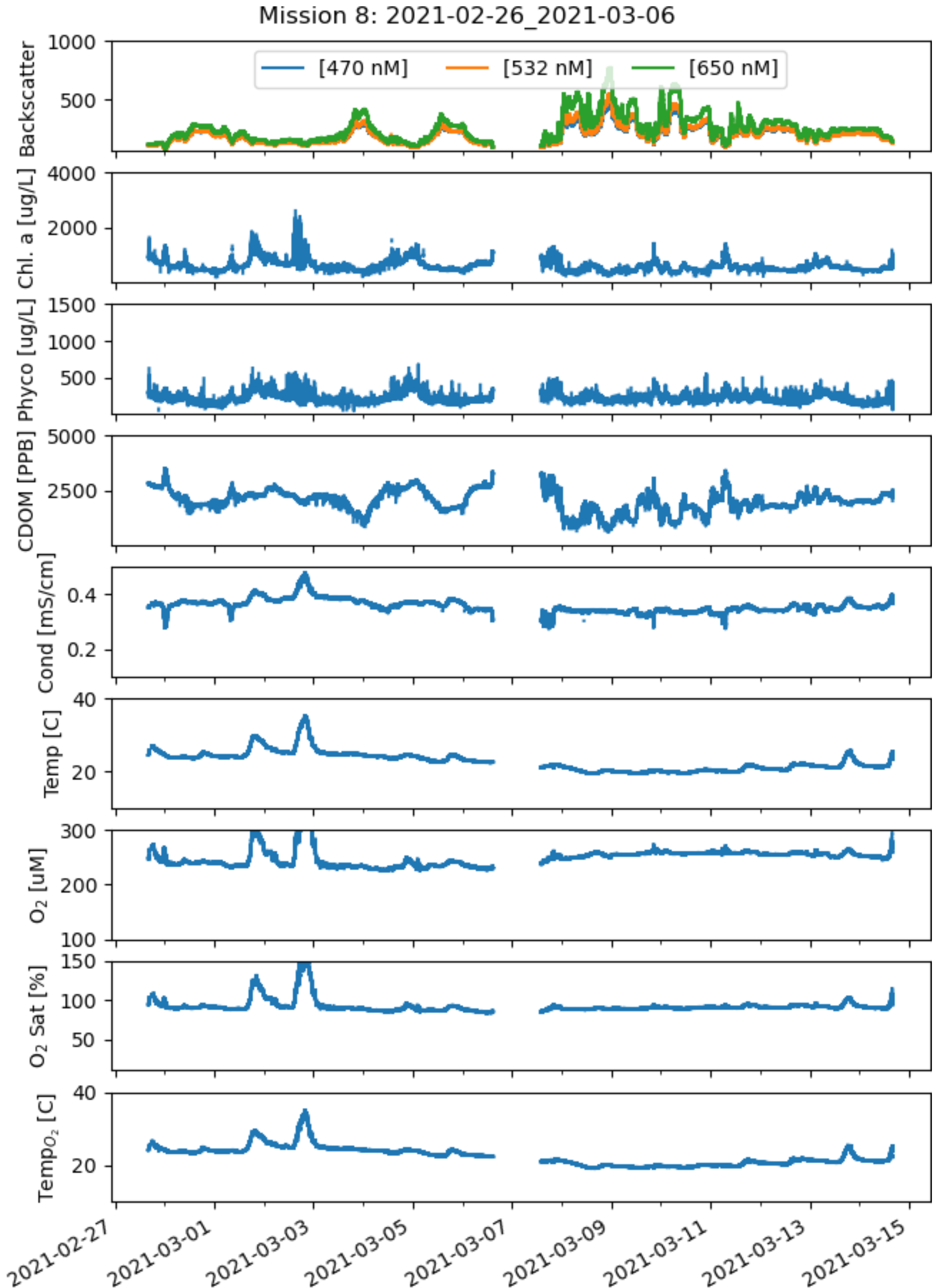
Mission 8: 2021-02-26_2021-03-06
Backscatter
1000
500
[470 nM]
[532 nM]
[650 nM]
Chl. a [ug/L]
4000
2000
Phyco [ug/L]
1500
1000
500
CDOM [PPB]
5000
2500
Cond [mS/cm]
0.4
0.2
Temp [C]
40
20
O$_2$ [uM]
300
200
100
O$_2$ Sat [%]
150
100
50
Temp$_{O_2}$ [C]
40
20
2021-02-27
2021-03-01
2021-03-03
2021-03-05
2021-03-07
2021-03-09
2021-03-11
2021-03-13
2021-03-15

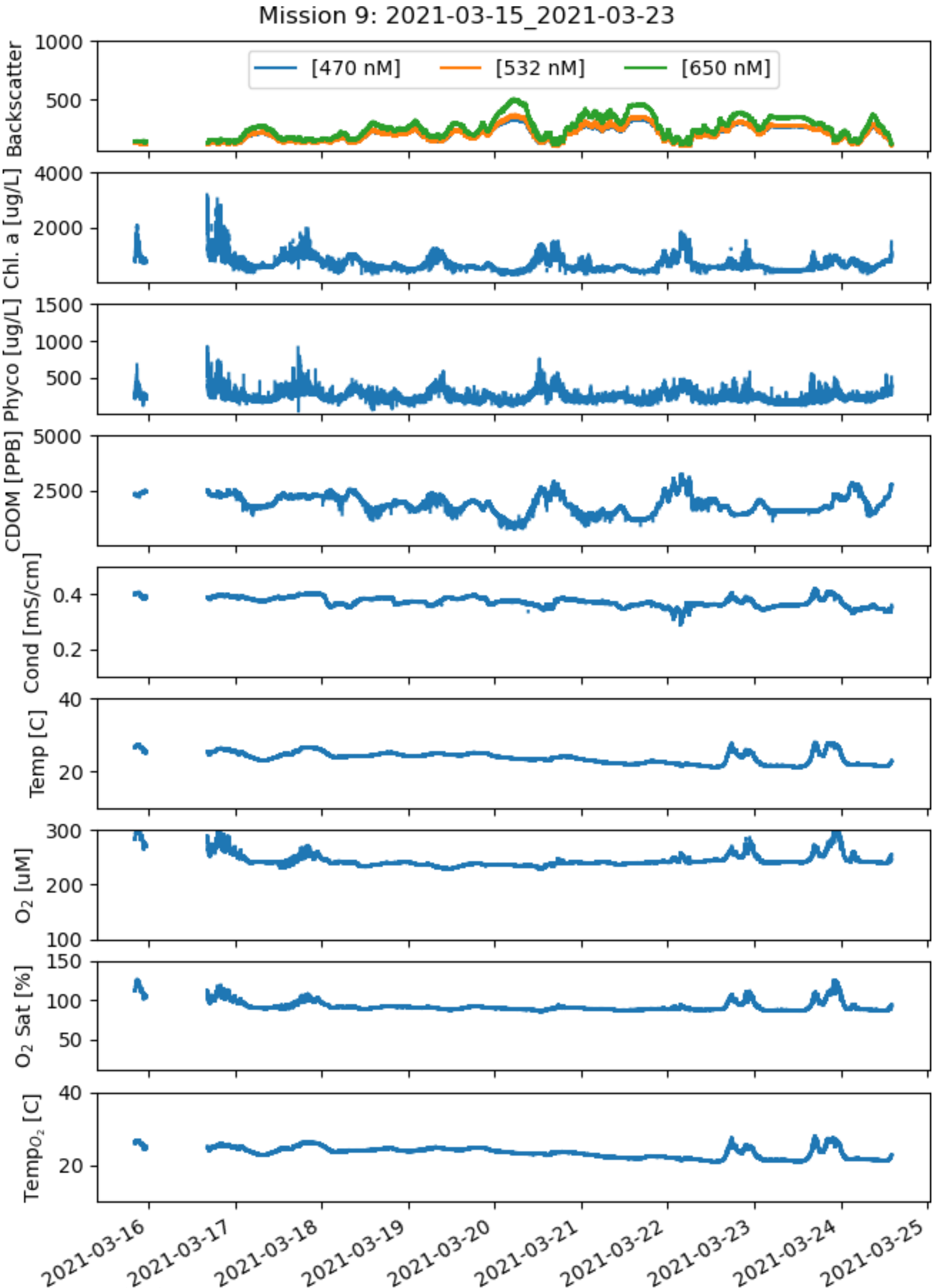
Mission 9: 2021-03-15_2021-03-23
[470 nM]
[532 nM]
[650 nM]
Backscatter
1000
500
Chl. a [ug/L]
4000
2000
Phyco [ug/L]
1500
1000
500
CDOM [PPB]
5000
2500
Cond [mS/cm]
0.4
0.2
Temp [C]
40
20
O_2 [uM]
300
200
100
O_2 Sat [%]
150
100
50
$Temp_{O_2}$ [C]
40
20
2021-03-16
2021-03-17
2021-03-18
2021-03-19
2021-03-20
2021-03-21
2021-03-22
2021-03-23
2021-03-24
2021-03-25

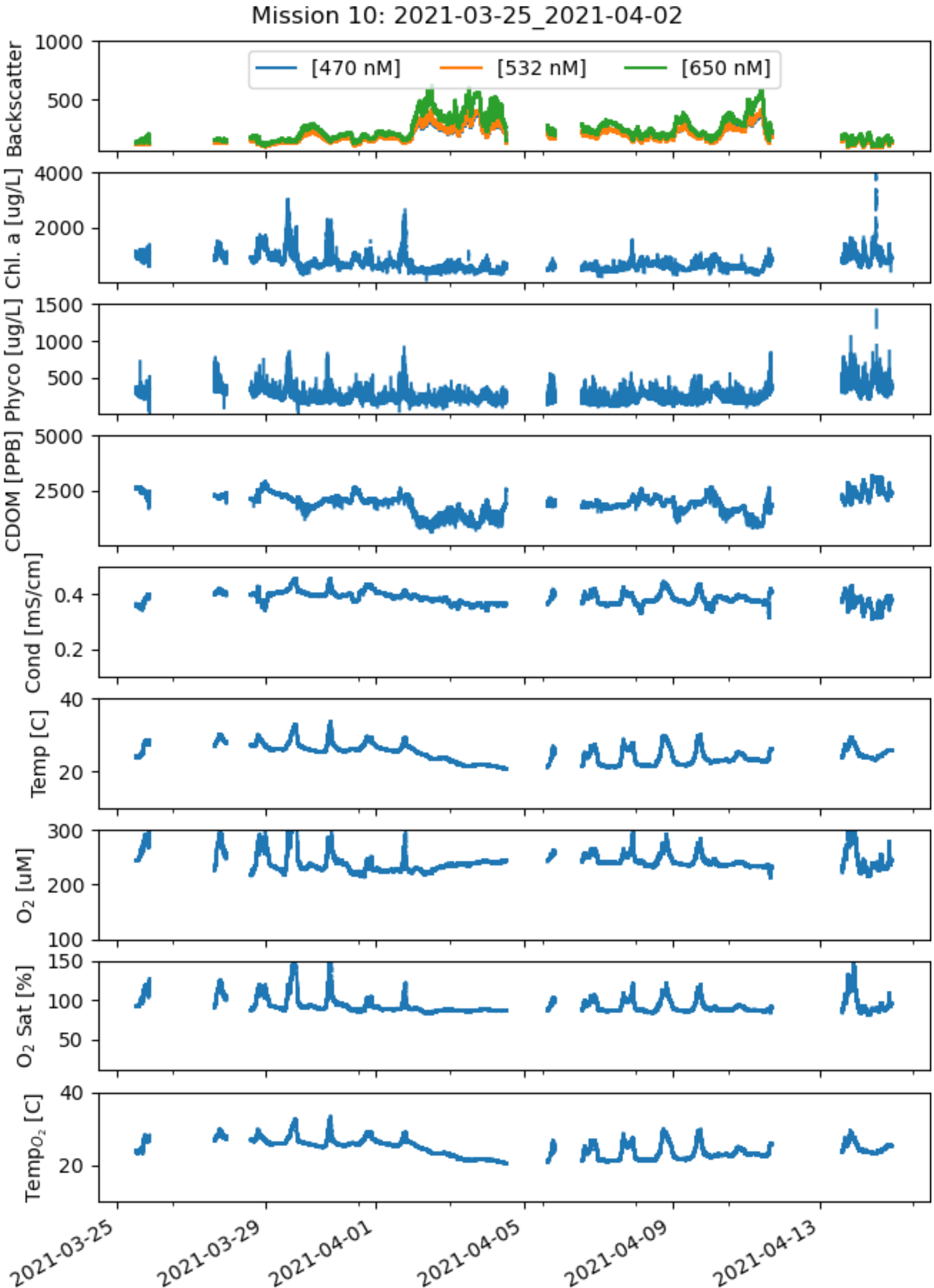
Mission 10: 2021-03-25_2021-04-02
Backscatter
1000
500
[470 nM]
[532 nM]
[650 nM]
Chl. a [ug/L]
4000
2000
Phyco [ug/L]
1500
1000
500
CDOM [PPB]
5000
2500
Cond [mS/cm]
0.4
0.2
Temp [C]
40
20
O_2 [uM]
300
200
100
O_2 Sat [%]
150
100
50
$Temp_{O_2}$ [C]
40
20
2021-03-25
2021-03-29
2021-04-01
2021-04-05
2021-04-09
2021-04-13

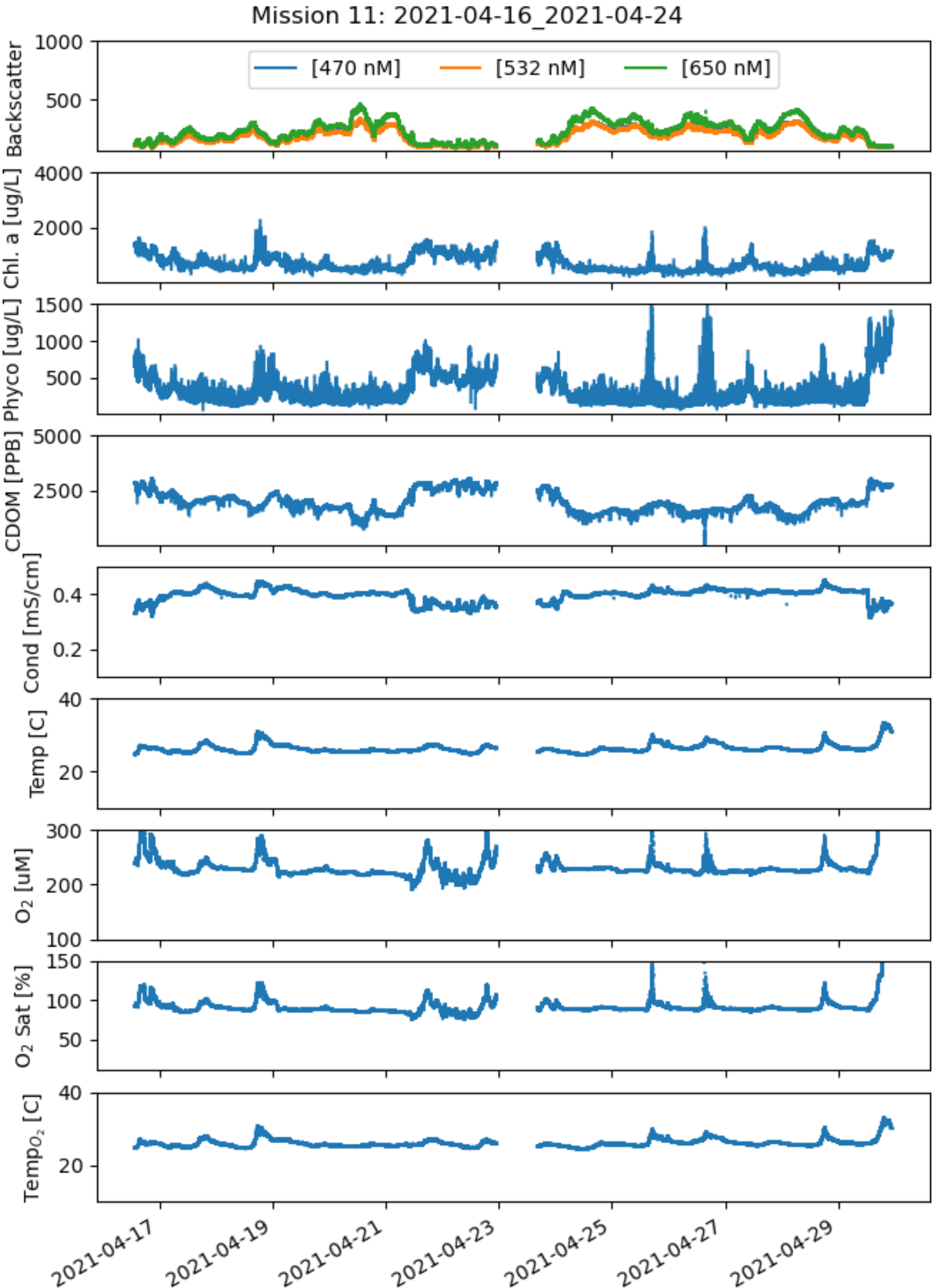
Mission 11: 2021-04-16_2021-04-24
Backscatter
[470 nM]
[532 nM]
[650 nM]
1000
500
Chl. a [ug/L]
4000
2000
Phyco [ug/L]
1500
1000
500
CDOM [PPB]
5000
2500
Cond [mS/cm]
0.4
0.2
Temp [C]
40
20
O_2 [uM]
300
200
100
O_2 Sat [%]
150
100
50
$Temp_{O_2}$ [C]
40
20
2021-04-17
2021-04-19
2021-04-21
2021-04-23
2021-04-25
2021-04-27
2021-04-29

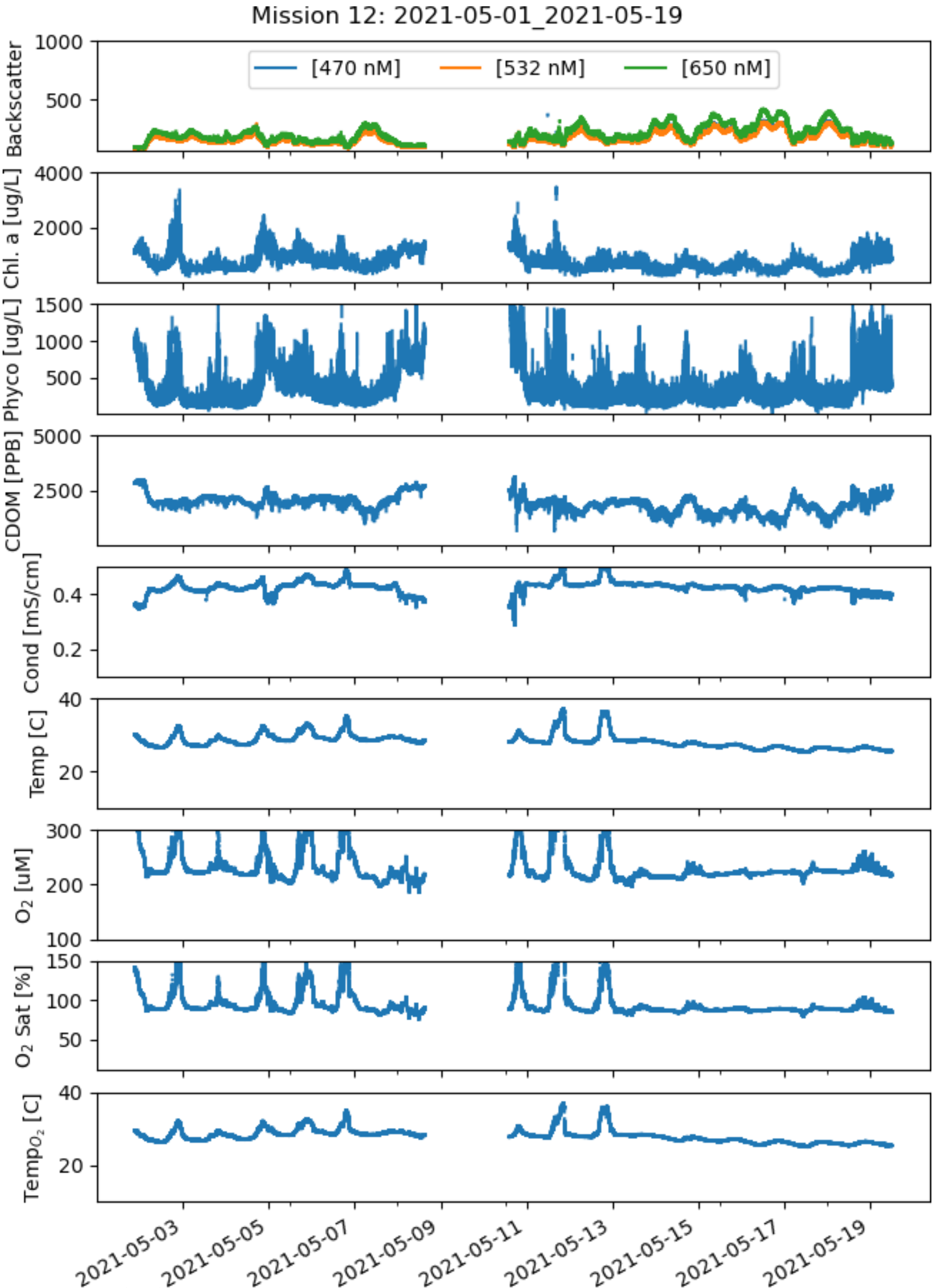
Mission 12: 2021-05-01_2021-05-19
Backscatter
1000
500
[470 nM]
[532 nM]
[650 nM]
Chl. a [ug/L]
4000
2000
Phyco [ug/L]
1500
1000
500
CDOM [PPB]
5000
2500
Cond [mS/cm]
0.4
0.2
Temp [C]
40
20
O$_2$ [uM]
300
200
100
O$_2$ Sat [%]
150
100
50
Temp$_{O_2}$ [C]
40
20
2021-05-03
2021-05-05
2021-05-07
2021-05-09
2021-05-11
2021-05-13
2021-05-15
2021-05-17
2021-05-19

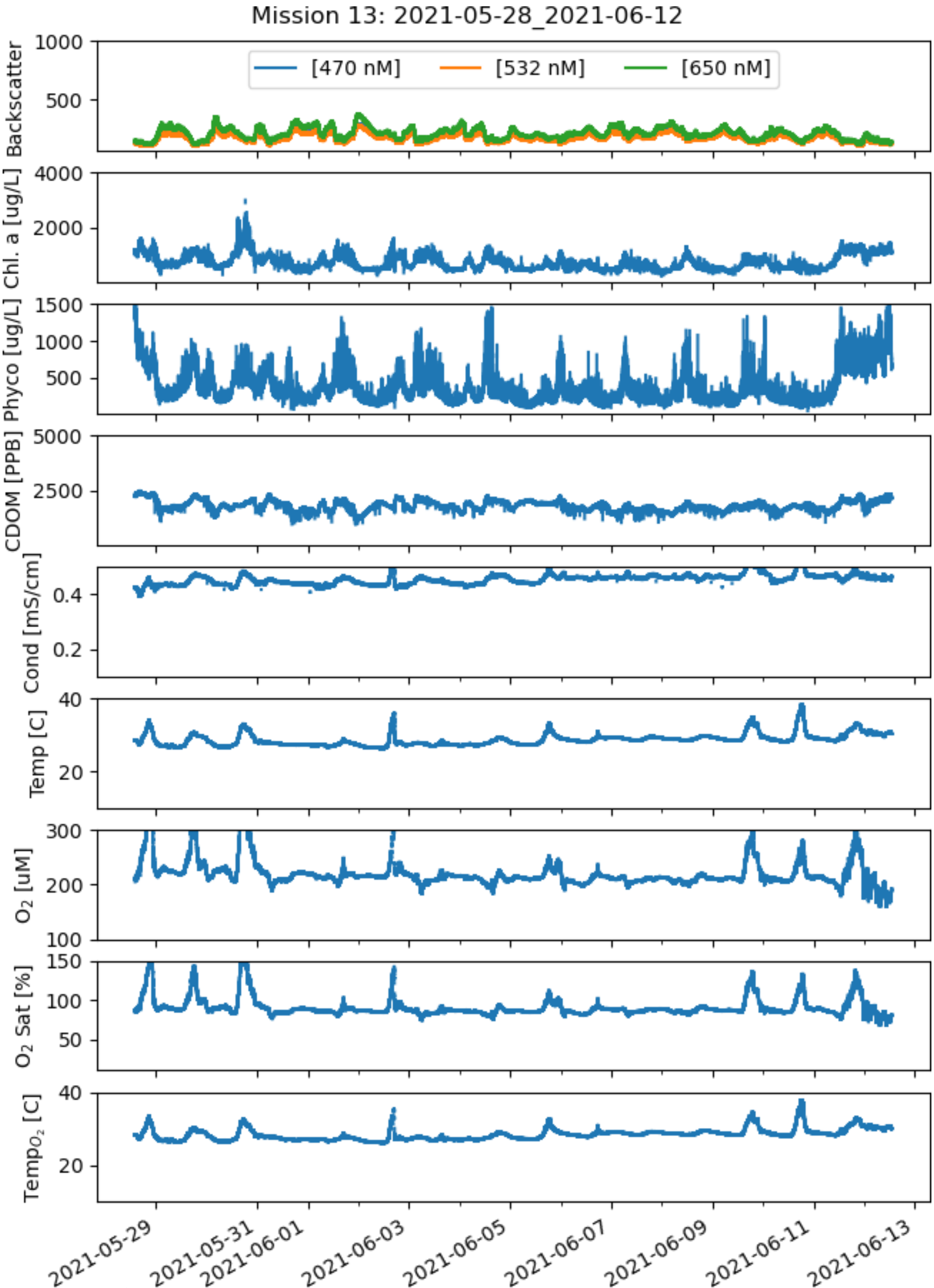
Mission 13: 2021-05-28_2021-06-12
[470 nM]
[532 nM]
[650 nM]
Backscatter
1000
500
Chl. a [ug/L]
4000
2000
Phyco [ug/L]
1500
1000
500
CDOM [PPB]
5000
2500
Cond [mS/cm]
0.4
0.2
Temp [C]
40
20
O$_2$ [uM]
300
200
100
O$_2$ Sat [%]
150
100
50
Temp$_{O_2}$ [C]
40
20
2021-05-29
2021-05-31
2021-06-01
2021-06-03
2021-06-05
2021-06-07
2021-06-09
2021-06-11
2021-06-13

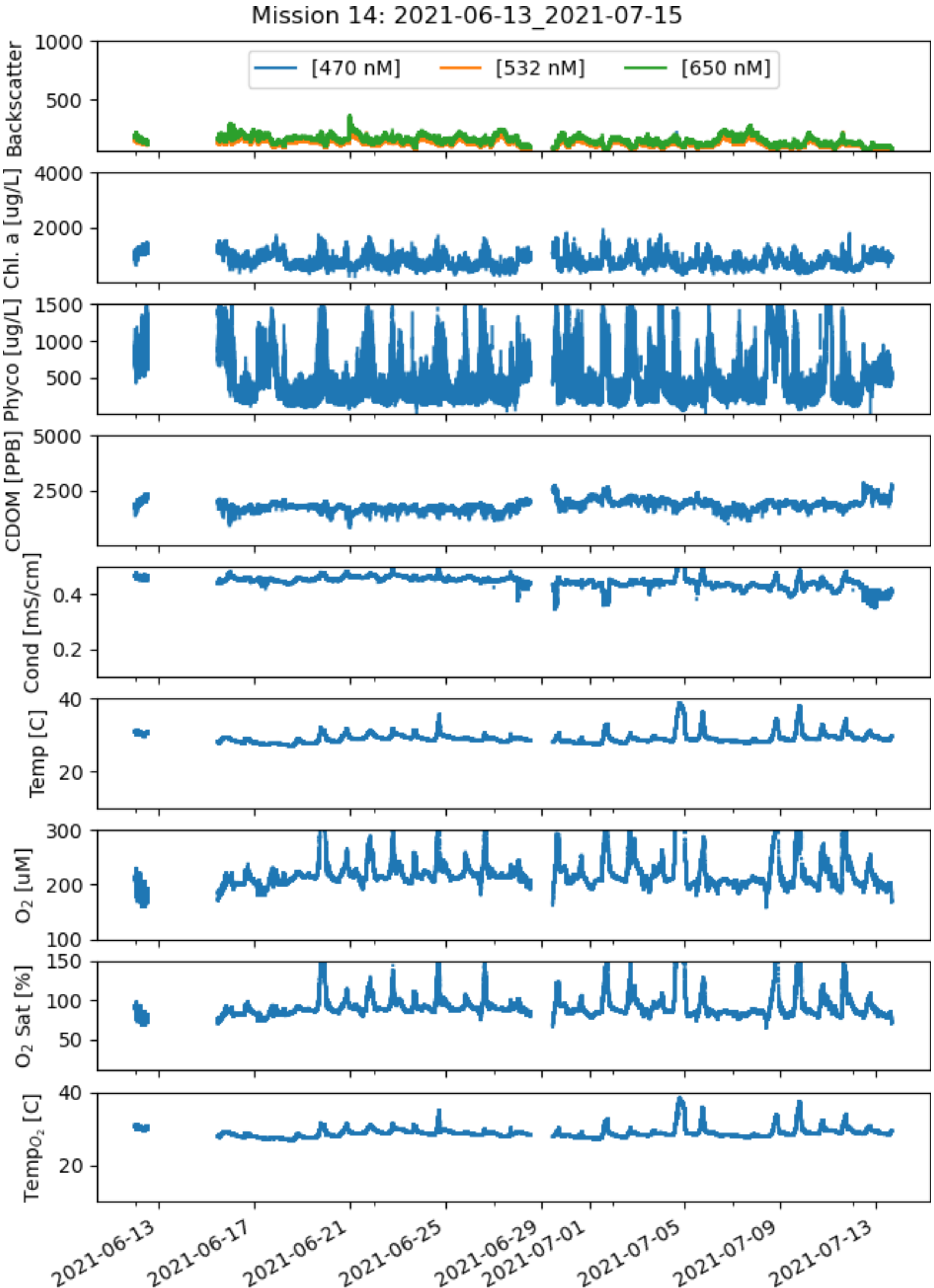
Mission 14: 2021-06-13_2021-07-15
[470 nM]
[532 nM]
[650 nM]
Backscatter
1000
500
Chl. a [ug/L]
4000
2000
Phyco [ug/L]
1500
1000
500
CDOM [PPB]
5000
2500
Cond [mS/cm]
0.4
0.2
Temp [C]
40
20
O_2 [uM]
300
200
100
O_2 Sat [%]
150
100
50
$Temp_{O_2}$ [C]
40
20
2021-06-13
2021-06-17
2021-06-21
2021-06-25
2021-06-29
2021-07-01
2021-07-05
2021-07-09
2021-07-13

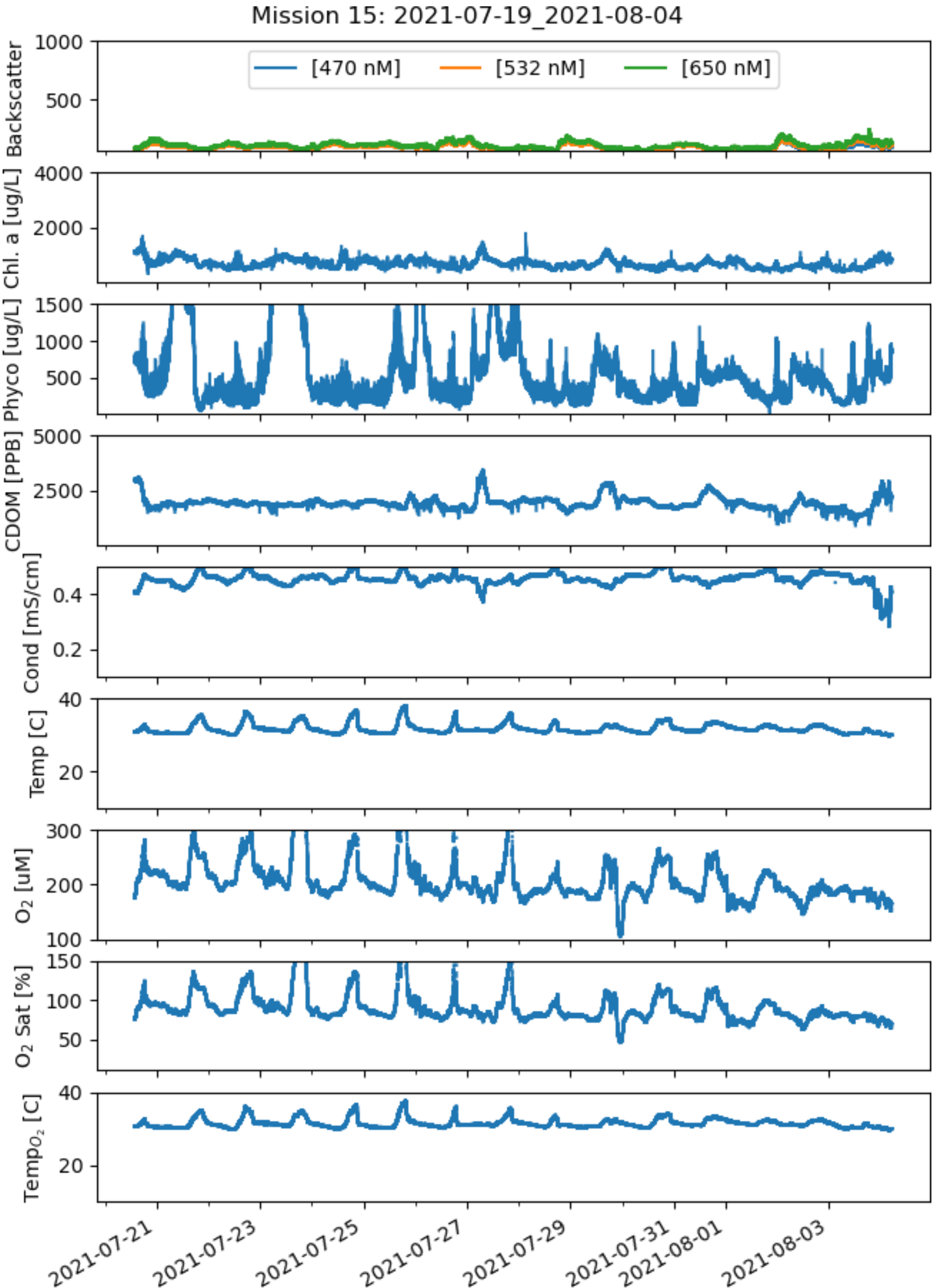
Mission 15: 2021-07-19_2021-08-04
[470 nM]
[532 nM]
[650 nM]
Backscatter
1000
500
Chl. a [ug/L]
4000
2000
Phyco [ug/L]
1500
1000
500
CDOM [PPB]
5000
2500
Cond [mS/cm]
0.4
0.2
Temp [C]
40
20
O_2 [uM]
300
200
100
O_2 Sat [%]
150
100
50
Temp$_{O_2}$ [C]
40
20
2021-07-21
2021-07-23
2021-07-25
2021-07-27
2021-07-29
2021-07-31
2021-08-01
2021-08-03

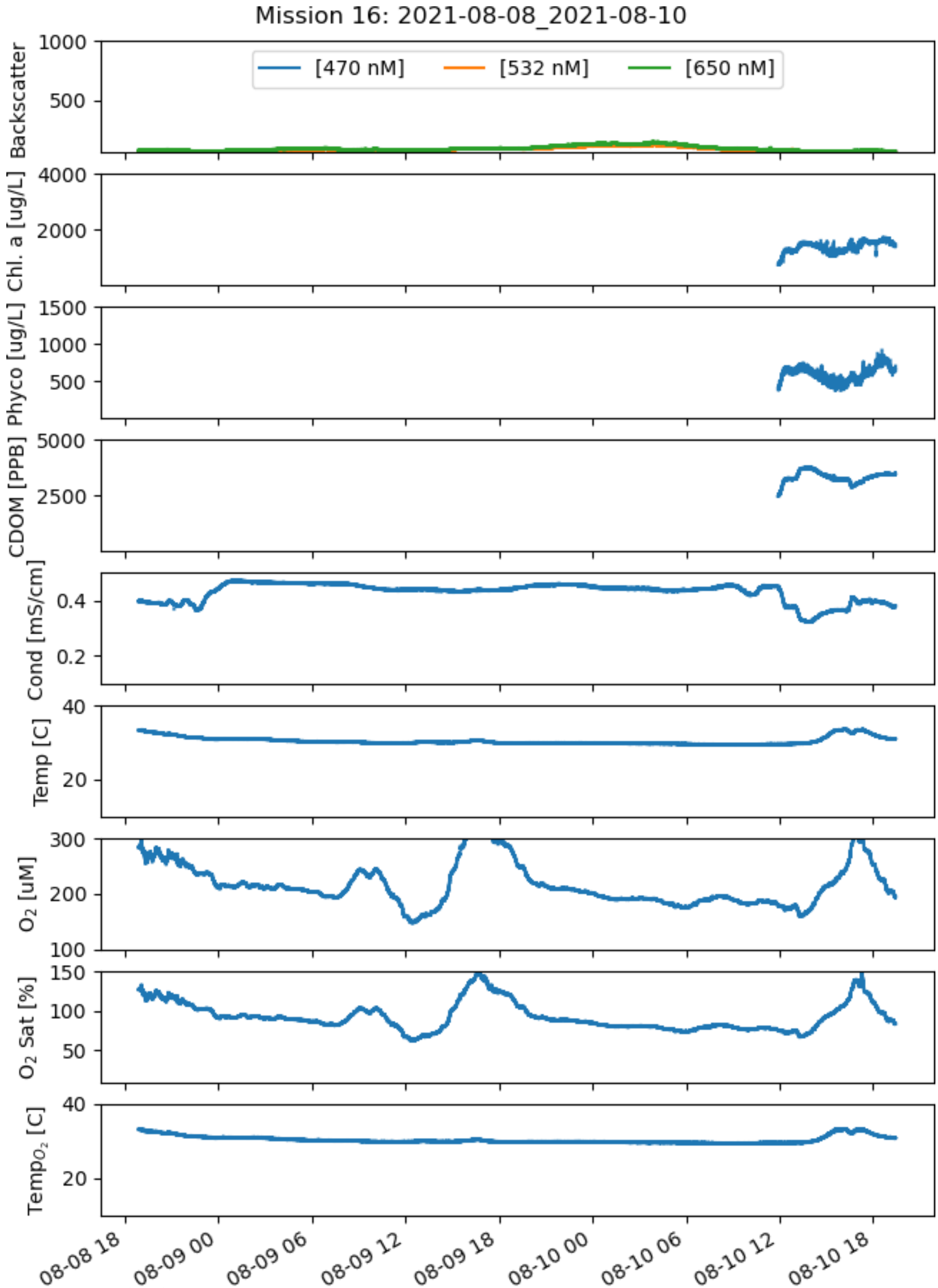
Mission 16: 2021-08-08_2021-08-10
Backscatter
1000
500
[470 nM]
[532 nM]
[650 nM]
Chl. a [ug/L]
4000
2000
Phyco [ug/L]
1500
1000
500
CDOM [PPB]
5000
2500
Cond [mS/cm]
0.4
0.2
Temp [C]
40
20
O₂ [uM]
300
200
100
O₂ Sat [%]
150
100
50
Temp O₂ [C]
40
20
08-08 18
08-09 00
08-09 06
08-09 12
08-09 18
08-10 00
08-10 06
08-10 12
08-10 18

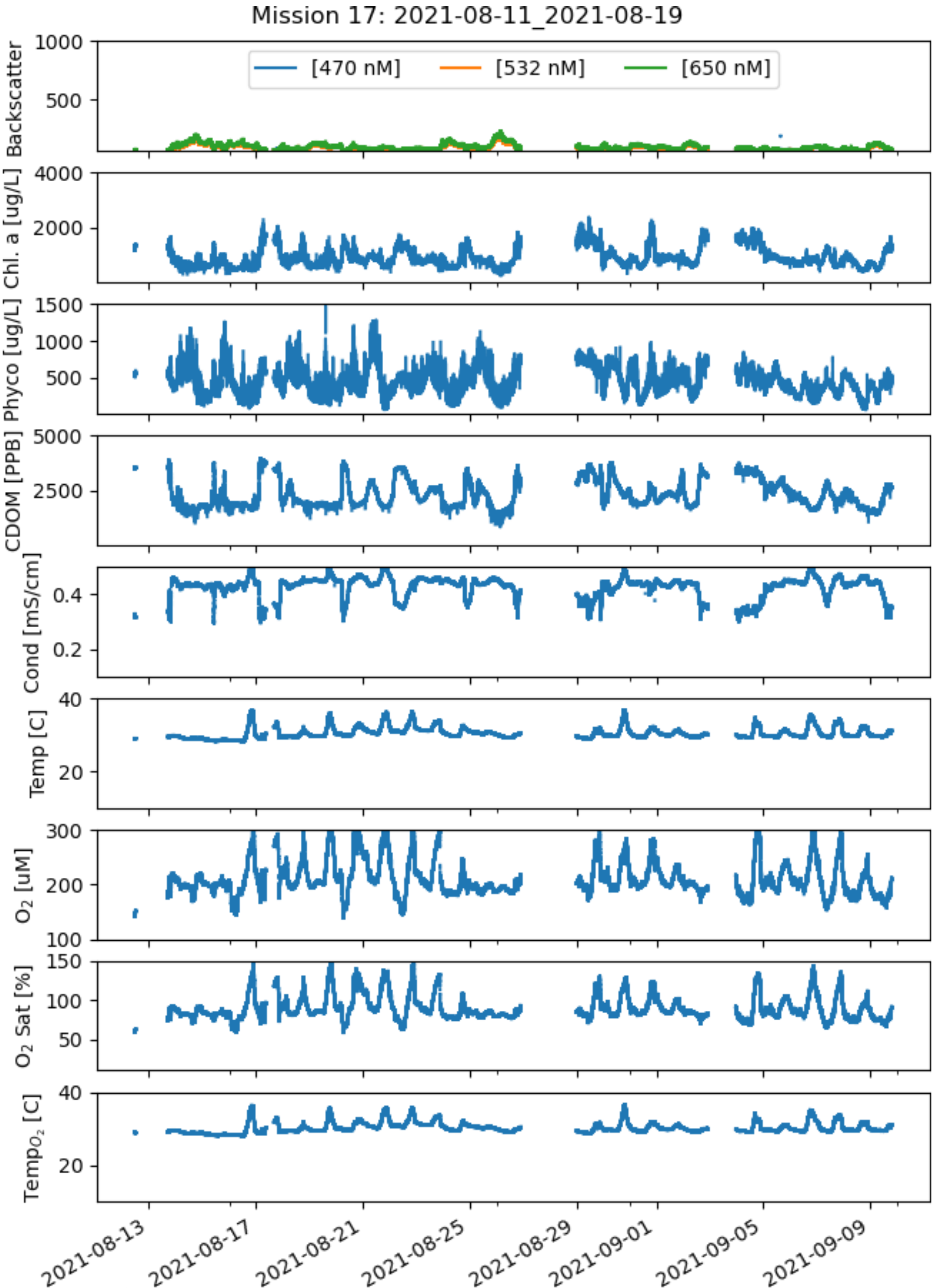
Mission 17: 2021-08-11_2021-08-19
[470 nM]
[532 nM]
[650 nM]
Backscatter
1000
500
Chl. a [ug/L]
4000
2000
Phyco [ug/L]
1500
1000
500
CDOM [PPB]
5000
2500
Cond [mS/cm]
0.4
0.2
Temp [C]
40
20
O$_2$ [uM]
300
200
100
O$_2$ Sat [%]
150
100
50
Temp$_{O_2}$ [C]
40
20
2021-08-13
2021-08-17
2021-08-21
2021-08-25
2021-08-29
2021-09-01
2021-09-05
2021-09-09

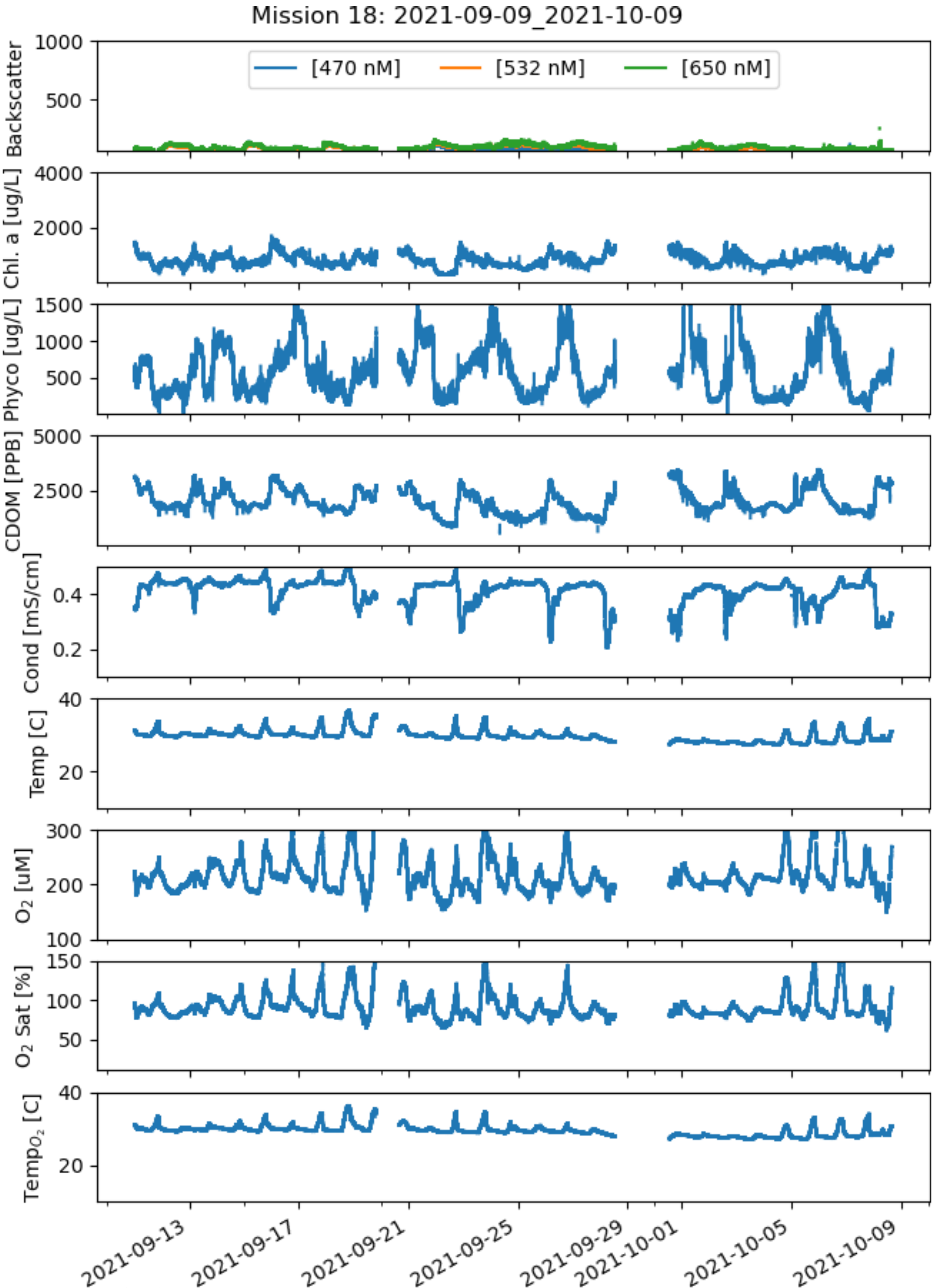
Mission 18: 2021-09-09_2021-10-09
Backscatter
[470 nM]
[532 nM]
[650 nM]
1000
500
Chl. a [ug/L]
4000
2000
Phyco [ug/L]
1500
1000
500
CDOM [PPB]
5000
2500
Cond [mS/cm]
0.4
0.2
Temp [C]
40
20
O_2 [uM]
300
200
100
O_2 Sat [%]
150
100
50
Temp_{O_2} [C]
40
20
2021-09-13
2021-09-17
2021-09-21
2021-09-25
2021-09-29
2021-10-01
2021-10-05
2021-10-09

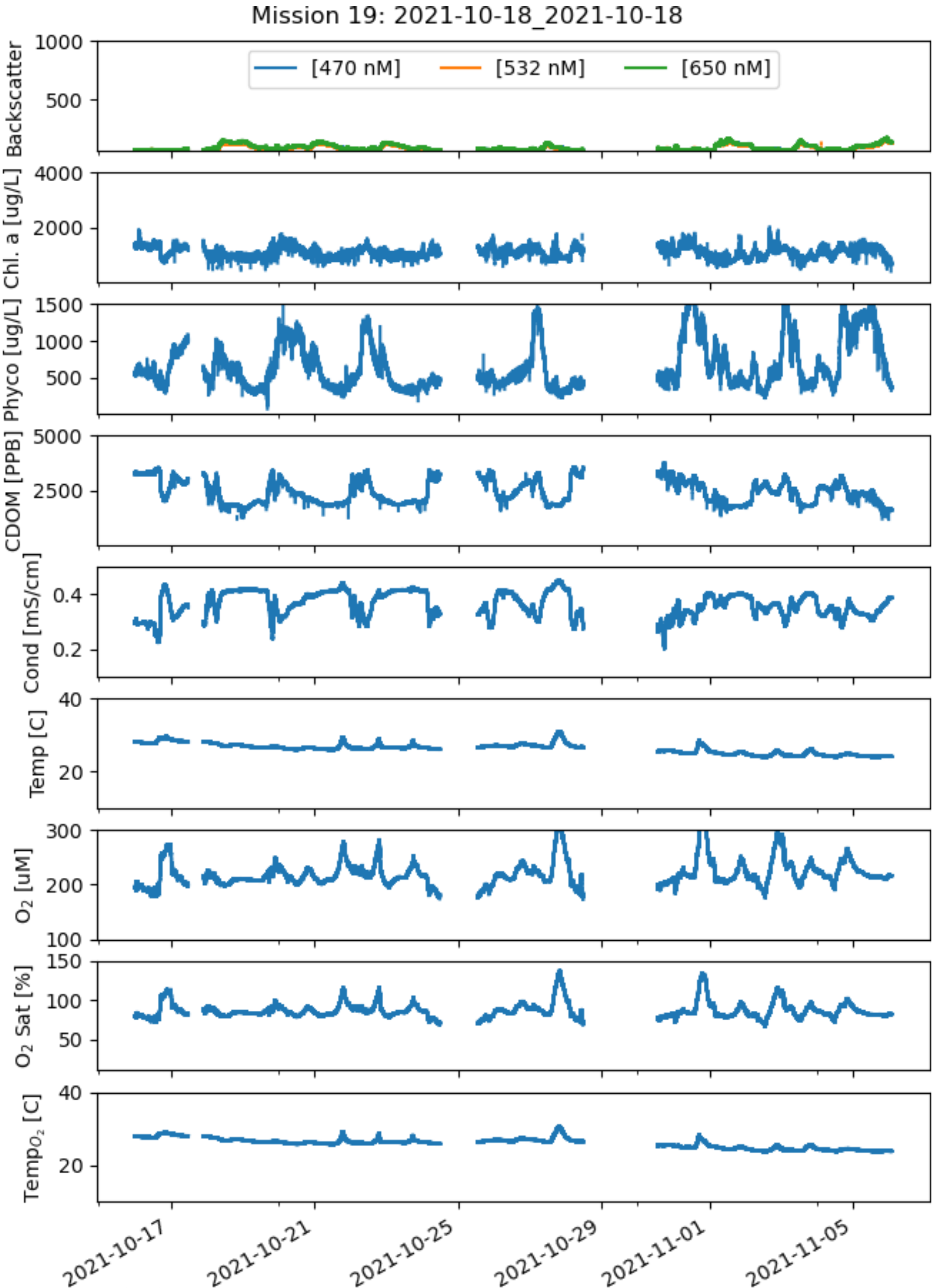
Mission 19: 2021-10-18_2021-10-18
Backscatter
[470 nM]
[532 nM]
[650 nM]
1000
500
Chl. a [ug/L]
4000
2000
Phyco [ug/L]
1500
1000
500
CDOM [PPB]
5000
2500
Cond [mS/cm]
0.4
0.2
Temp [C]
40
20
O_2 [uM]
300
200
100
O_2 Sat [%]
150
100
50
$Temp_{O_2}$ [C]
40
20
2021-10-17
2021-10-21
2021-10-25
2021-10-29
2021-11-01
2021-11-05

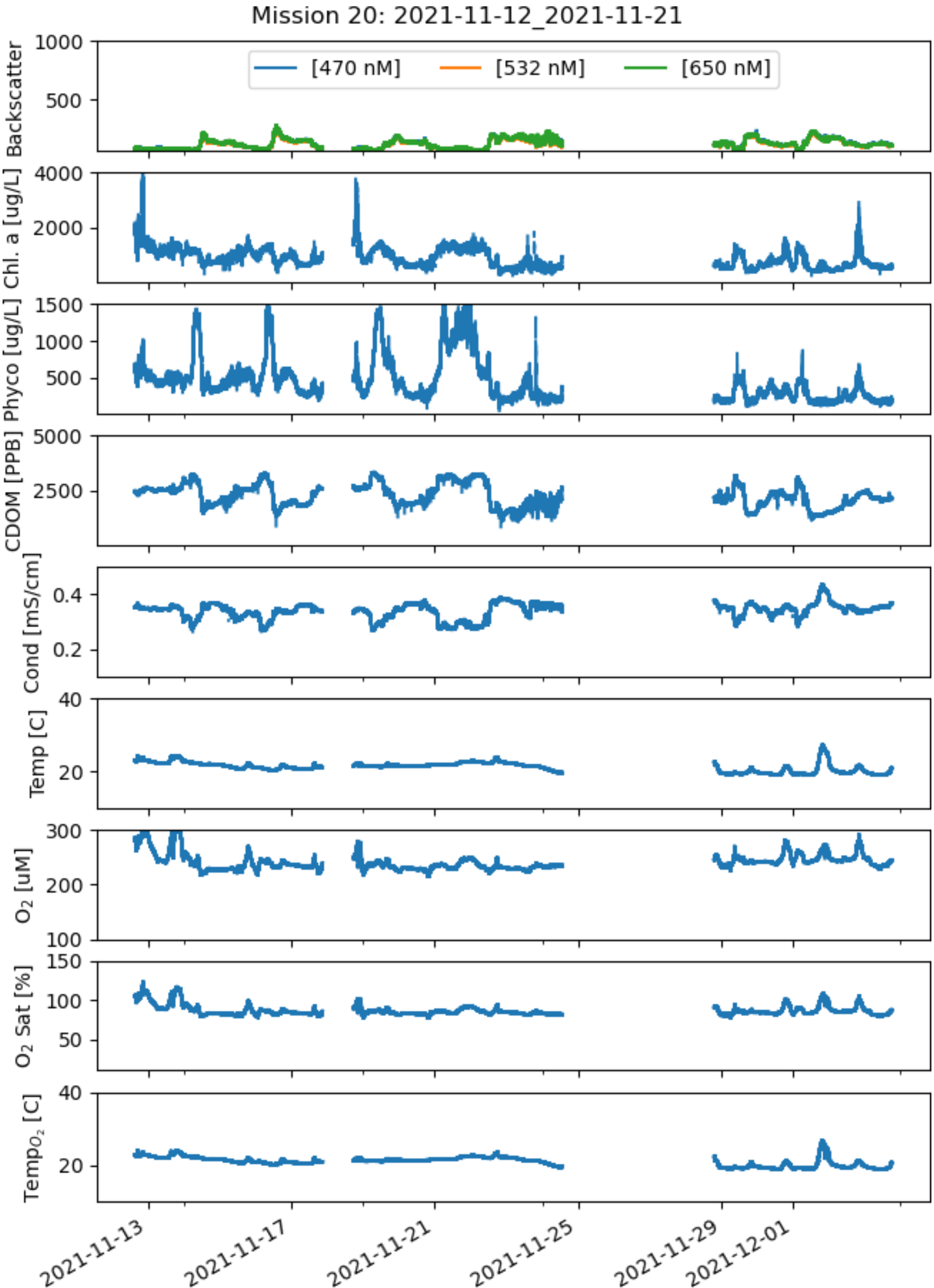
Mission 20: 2021-11-12_2021-11-21
[470 nM]
[532 nM]
[650 nM]
Backscatter
1000
500
Chl. a [ug/L]
4000
2000
Phyco [ug/L]
1500
1000
500
CDOM [PPB]
5000
2500
Cond [mS/cm]
0.4
0.2
Temp [C]
40
20
O_2 [uM]
300
200
100
O_2 Sat [%]
150
100
50
$Temp_{O_2}$ [C]
40
20
2021-11-13
2021-11-17
2021-11-21
2021-11-25
2021-11-29
2021-12-01

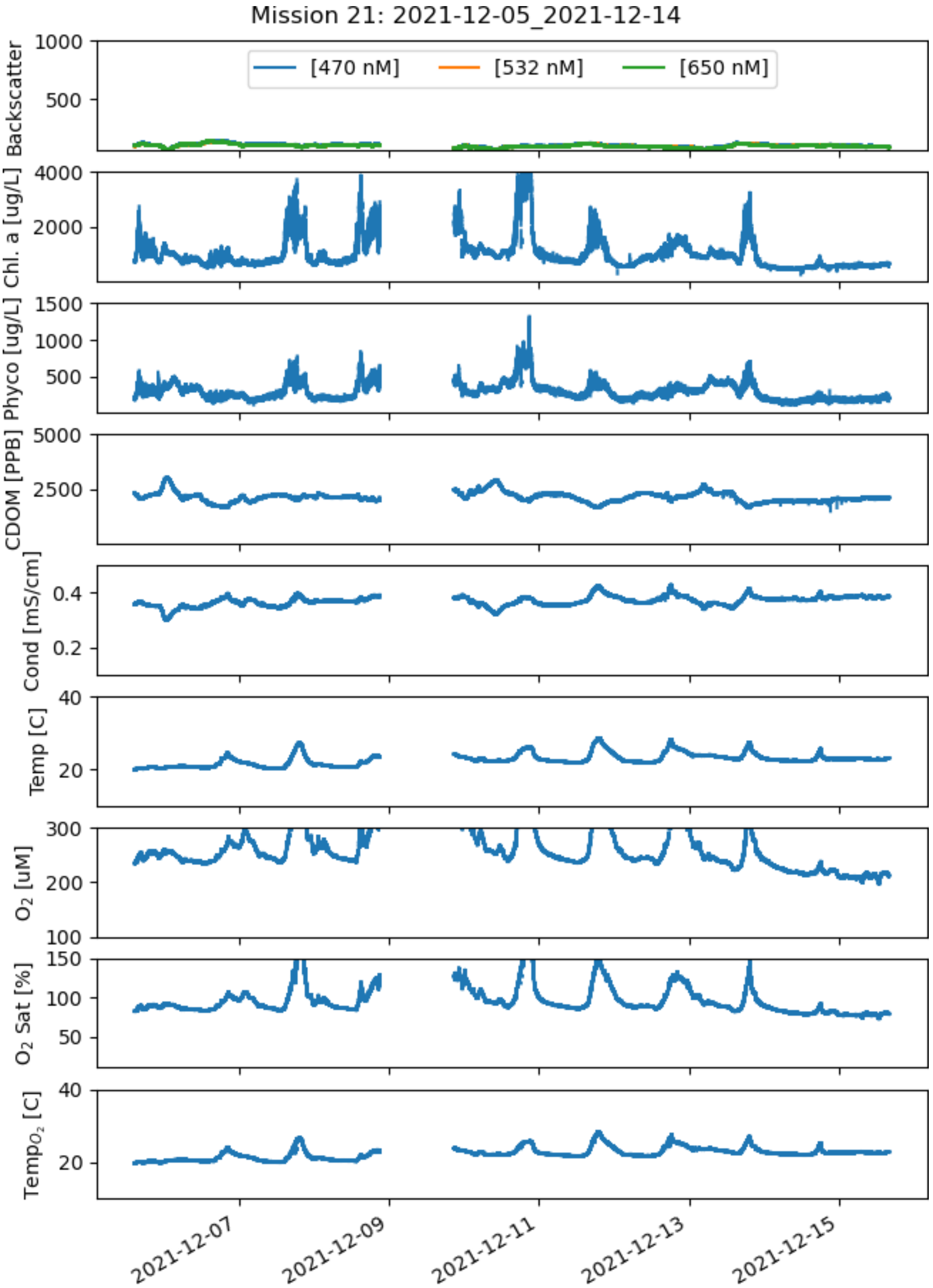
Mission 21: 2021-12-05_2021-12-14
[470 nM]
[532 nM]
[650 nM]
Backscatter
1000
500
Chl. a [ug/L]
4000
2000
Phyco [ug/L]
1500
1000
500
CDOM [PPB]
5000
2500
Cond [mS/cm]
0.4
0.2
Temp [C]
40
20
O_2 [uM]
300
200
100
O_2 Sat [%]
150
100
50
Temp$_{O_2}$ [C]
40
20
2021-12-07
2021-12-09
2021-12-11
2021-12-13
2021-12-15

TASK 5A: SEAPRISM DEPLOYMENT AND OPERATION (TASK LEAD: MOORE)

INTRODUCTION

The main objectives of **Task 5A** were 1) to maintain a SeaPRISM instrument on Tower Platform L001 for a) real-time observation of surface optical properties and b) generation of matchup validation data sets for satellite analysis. The SeaPRISM is an automated radiometer that is connected virtually to NASA's AERONET-OC network. This node (Lake Okeechobee) is one of three sites located in freshwaters in North America. The SeaPRISM measures the spectral light field reflected off the water at 12 wavelengths every 30 minutes during the day, as well as routine atmospheric measurements. The data are transmitted to NASA every hour, where they are processed and quality controlled, and then made available on a dedicated web page.

METHODS

The device is calibrated at NASA each year, and the quality control (QC) procedures at NASA assure high quality data. These QC and processing steps are detailed in Zibordi et al. 2009, and the reader is referred to that document for further information. We note that all SeaPRISMs are standardized and undergo the same QC and processing sequences at NASA by the AERONET-OC protocol (see Zibordi et al. 2009). There are 3 levels of stringency, and we report on the level 1.0 data (first quality), except where otherwise noted. The derivation of the individual remote sensing data products (e.g. Cyanobacterial Index) is more easily conceptualized as part of the satellite remote sensing workflow and is thus further described in the **Task 5B** Methods section.

ACTIVITIES SCHEDULED vs. COMPLETED

The overall objectives of this task were met to completion. Between 1/19/21 and 1/6/22, 3522 observations were generated by the SeaPRISM, and all data were processed and made publicly available by NASA on their AERONET website. The unit was installed on the L001 platform (Figure 5A-1) on 1/19/21 due to a delay in calibration at the NASA facility. It operated normally through the entire project period, except in March for several days when a tangled cable prevented normal robot movement. This was rectified by a site visit, but this was our only issue in the year of operation. The unit was removed on 1/6/22 and returned to NASA for post-calibration.

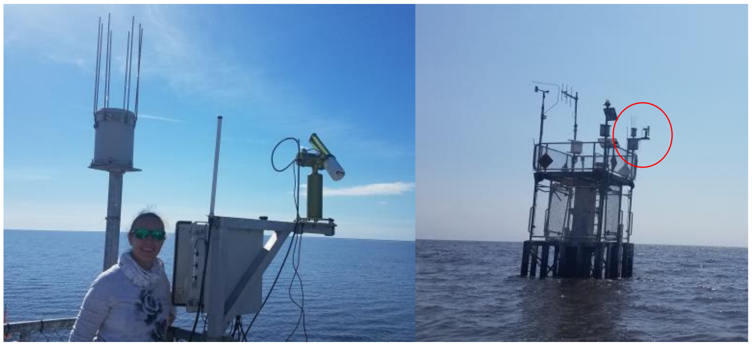

Figure 5A-1: Left: Dr. Liisa Rohtla installing the SeaPRISM on 1/ 19/21 at L001. Right: SeaPRISM installed on L001 as seen from approach (red circle).

NASA reported instrument failures in early March. HALO personnel Moore, Rhotla and McFarland responded and attended the unit. Upon inspection, a control cable was entangled in the preventive bird spikes (Figure 5A-2). The wet sensor was also covered in guano. The unit was cleaned, and cables fixed to avoid repeating the problem. There were no other problems with the unit for the remainder of the deployment.

Figure 5A-2: SeaPRISM maintenance site visit on 3/18/21. Bird spikes and cables visible, along with guano covering the vertical piece of the robotic mount.

RESULTS & DISCUSSION

The collected mean spectra at L001 were compared to the spectra collected the previous year when the sensor was installed at LZ40 (Figure 5A-3). The remote sensing reflectance (Rrs) shape was consistent, but the magnitude was lower at L001. This is probably the result of higher levels of CDOM in the surface waters at L001 (as it is closer to the Kissimmee River inflow).

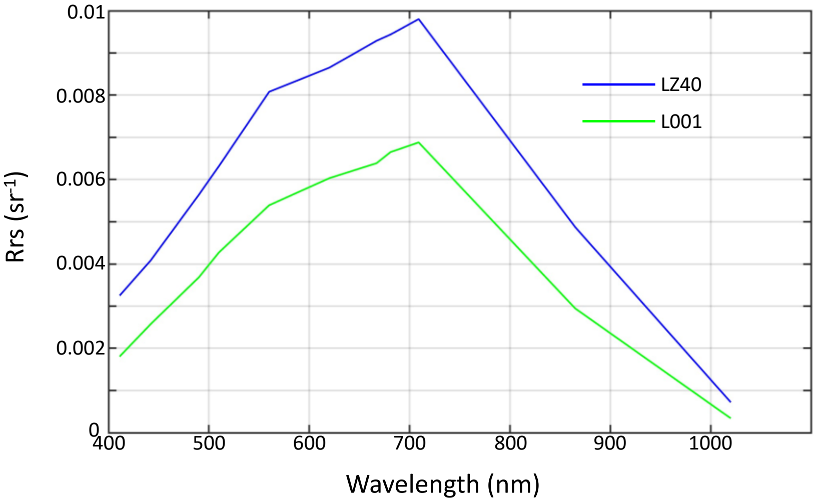

Figure 5A-3: Mean spectra of Rrs from SeaPRISM at L001 (green line) compared to previous location at LZ40 (blue line). The shape is similar, but lower in magnitude at L001.

The data collected by the SeaPRISM is a time series reflecting surface optical properties. When aligned with other environmental data collected by the adjacent buoy system, the combined data provide deeper insight into the processes in the lake as they affect the surface (Figure 5A-4). Highlighting a small window between 6/1/21, and 8/1/21, surface patterns of different variables are inter-related through processes of resuspension, settling, and cyanobacteria surfacing.

The **Task 6** (LOBO) turbidity time series and the Rrs at 709 nm from the SeaPRISM showed coherent patterns over the two-month period in general. High turbidity was associated with higher Rrs 709 and was wavelength-sensitive with respect to particles in the water. The chlorophyll and phycocyanin **Task 6** signals showed opposite patterns: they were lower when turbidity was higher. This is likely a consequence of the impacts of wind induced turbulence on the distribution of particles in the water column. During low winds, sediments will settle, and cyanobacteria cells will begin to ascend to the surface (decreasing turbidity, higher chlorophyll at surface). During higher winds, sediments will become re-suspended and cyanobacteria cells will be mixed throughout the water column (increasing turbidity, lowering chlorophyll at surface).

There were occasions when Rrs 709 was extremely elevated and correlated with high chlorophyll and low turbidity. These were likely situations when cyanobacteria were floating at or near the surface in concentrated forms during low wind periods and beginning to form surface scums. Some of these high values also could be caused as artifacts in the SeaPRISM processing, which were removed during QC screening by SeaPRISM processing at NASA, as some of these points were removed at quality level 1.5 and higher (Figure 5A-5). This is interesting and requires further analysis.

The spectral data were transformed into the Cyanobacterial Index (CI) product, compatible with the satellite CI product, for validation (see **Task 5B** report), and for generating a turbidity relationship with the matchup data with **Task 6**.

Lastly, the data from the SeaPRISM was used to validate the remote sensing data with matchups with satellite overpasses (next section, **Task 5B**). This was useful in guiding atmospheric correction schemes and validating remote sensing products.

CONCLUSIONS & FUTURE WORK

The SeaPRISM unit, an automated radiometer part of the NASA AERONET-OC network, provided a large data set of optical measurements in Lake Okeechobee. The SeaPRISM collected over 3,400 spectral observations of water surface reflectance, which is an order of magnitude higher compared to Lake Erie with the identical SeaPRISM unit. This is partly a reflection of the longer operating window (year-round in Lake Okeechobee compared to 6 months in Lake Erie due to ice cover), but also the greater number of cloud-free windows over southern Florida. The greater exposure to light (and warm temperatures) is an important environmental aspect that is necessary for cyanobacteria bloom ecology.

The SeaPRISM unit operated nominally for much of the deployment period, requiring only one maintenance visit. These data sets are valued by the international ocean color community for the service they provide for satellite matchup analyses. The data collected during this project will be useful for years to come for satellite atmospheric correction scheme research, and provide a unique data set on water quality that enhances the information from other data sources (e.g. **Task 6**).

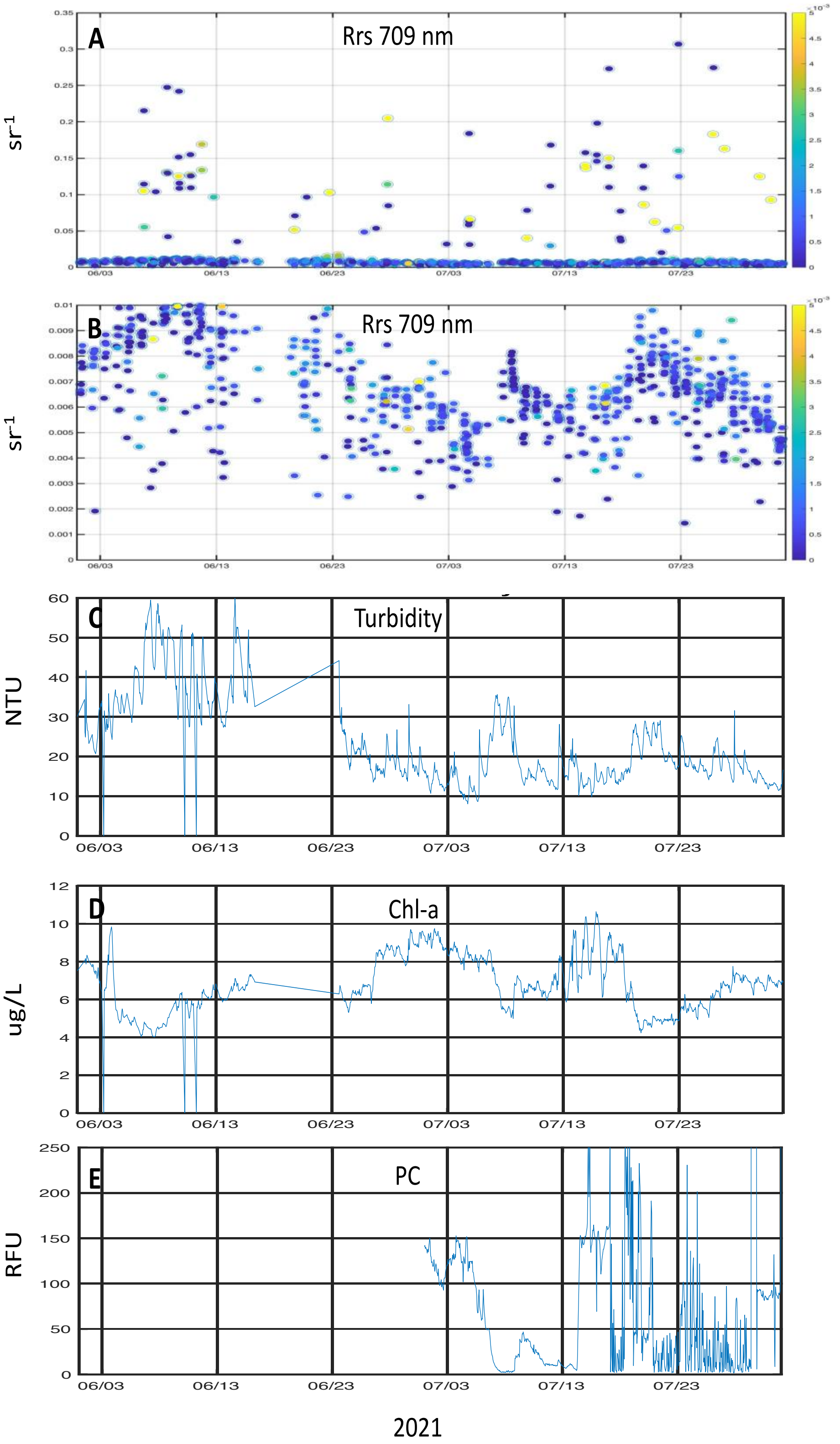

Figure 5A-4: Time series of measurements at L001 from 6/1/21 through 8/1/21. A) SeaPRISM Rrs 709 (color-coded by CI); B) same as A with y-axis re-scaled; C) Task 6 turbidity; D) Task 6 Chl-a; E) Task 6 phycocyanin fluorescence.

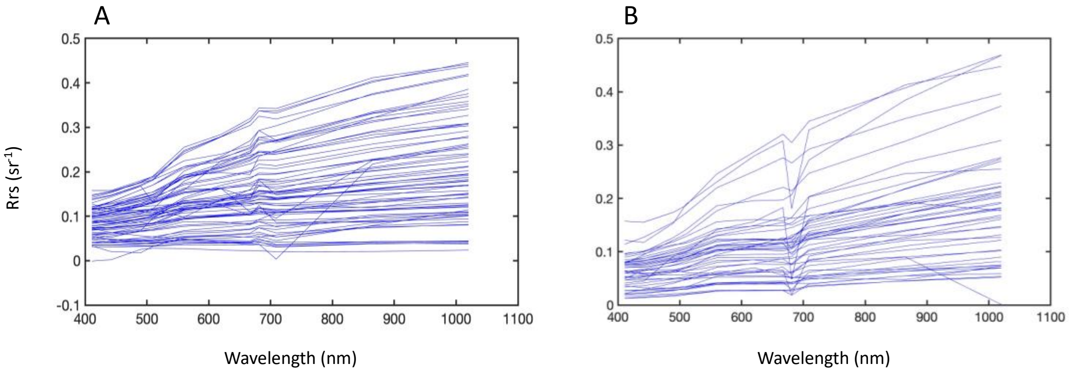

Figure 5A-5: A) Full reflectance spectra of outlier points from Figure 5A-4A for negative CI values (no cyanobacteria). B) Full reflectance spectra of outlier points from Figure 5A-4A for positive CI values (potential cyanobacteria). These spectra are very high, especially in the near infrared and may either be special cases (e.g., floating algal mats) or contaminated measurements.

TASK 5B: REMOTE SENSING PRODUCTS (TASK LEAD: MOORE)

INTRODUCTION

The main objective of this task was to generate mapped satellite products related to water quality and cyanobacteria blooms for Lake Okeechobee over the duration of the project, and to operationalize the transmission of these to the data portal. The data products included determining the best performing algorithms for turbidity, cyanobacteria index or CI, and Chl-a concentration for remote sensing imagery. The satellite products that were used were imagery from the Ocean Land Color Imagery (OLCI) sensor on board the twin satellite pair Senintel-3A/B operated by the European Space Agency (ESA). Satellite data processing was automated for this purpose using NASA's SeaDAS image processing package, and custom algorithms were applied to the atmospheric-corrected imagery for generation of water quality products. These were then automatically uploaded to the HALO database for display on the HALO data portal. Goals included 1) Satellite data acquisition, 2) Satellite image processing, 3) Product generation and uploading, 4) Satellite validation with SeaPRISM data, 5) Algorithm validation with field data and satellite data, 6) Uncertainty characterization of generated algorithms and associated products.

ACTIVITIES SCHEDULED vs. COMPLETED

Task objectives were met in entirety. Between 1/1/21 and 12/31/21, there were 365 Sentinel-3 satellite images downloaded from the European Space Agency's online data portal Copernicus. Of those, 169 were of sufficiently usable quality for quantitative use. These were processed with NASA's SeaDAS software system and uploaded to the main HALO data portal daily. Project products included the cyanobacteria index (CI) and turbidity. Additional non-scheduled progress was made regarding climatological histories of HABs on Lake Okeechobee.

METHODS

Level-1A data for Sentinel-3/OLCI images were downloaded within 12 hours of acquisition, processed and uploaded to the HALO portal. Acquired images were then processed through 2 atmospheric correction schemes through NASA's SeaDAS package, producing 2 ocean color products for every image – turbidity and the CI. The Cyanobacteria Index (CI) is an optical product based on a line height form using three bands in the red/NIR region (Wynne et al 2008), specifically the reflectance at 665 nm, 681 nm and 709 nm. The CI captures an optical feature that is related to particles in suspension near the surface of the water with a combination of spectral absorbing and scattering properties (Moore et al 2017). The CI is defined as:

$$CI = - [(rho681 - rho667) - (rho709 - rho667)*[681 - 667] / [709 - 665]]$$

where rhoXXX is the partial reflectance at that wavelength. A positive CI indicates presence of cyanobacteria, which we used as a flag in data plots. [Note: the negative sign for CI asserts a positive value when there is trough detected at 681 nm.]

The CI product uses wavelengths in the red and near infrared (NIR) spectrum (Figure 5B-1) and is insensitive to aerosol loads in the atmosphere. To derive this product, images were produced from partially atmospheric correction where only the molecular scattering is removed leaving aerosols. These partially corrected images, which resulted in spectral reflectance products, were then subsequently used in the CI algorithm developed by Wynn et al. 2008. These image products were saved into a NetCDF file. For turbidity, the full atmospheric correction is required. We used a variation of the NASA standard scheme called the Management Unit of the North Sea Mathematical Models (herein MUMM) algorithm. This scheme was developed to account for near infrared (NIR) backscattering using a different water model and assumes a constant shape in the NIR and was derived from waters where particles are dominated by inorganic types (Ruddick et a. 2000; Ruddick et al. 2006).

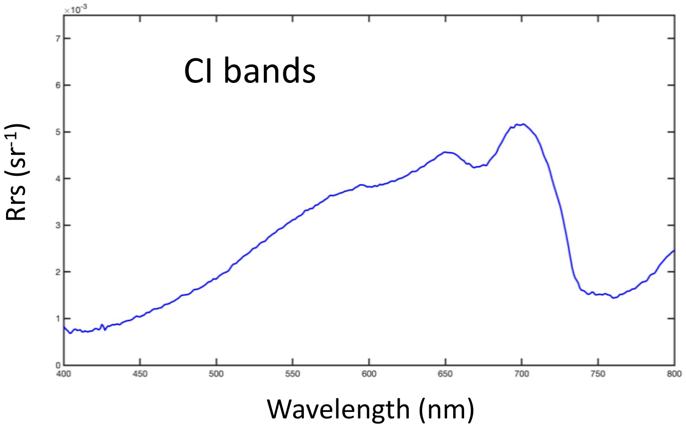

Figure 5B-1: A reflectance spectrum measured in Lake Okeechobee, with the spectral bands used in the cyanobacteria index highlighted.

The MUMM-AC was developed with two main assumptions: 1) the aerosol properties are homogeneous over the area under consideration, and 2) the NIR reflectance ratio at two wavelengths were invariant and could be approximated by a universal constant. The MUMM in NASA SeaDAS (v7.5.3) was used for the image processing, and generated spectral remote sensing (Rrs) products. Two other schemes were also used – the NASA standard scheme (SeaDAS-STD), which also includes a NIR component for turbid waters (Bailey et al, 2010), and the POLYMER scheme (Steinmetz et al, 2010), which is a polynomial-based scheme originally designed for the MERIS sensor (the precursor to Sentinel-3/OLCI).

Measurements from the SeaPRISM were co-located with processed satellite imagery using the protocol outlined in Bailey et al. (2006). For all comparisons, the SeaPRISM L2.0 data were used to ensure a higher degree of confidence in the quality of the ground data. Briefly, all pixels within a 500 meter radius (equivalent to roughly a 3x3 box) were extracted and the median was applied to all valid data. For SeaDAS-STD and MUMM, level-2 flags for atmospheric correction failure, stray light, glint, high light, high satellite zenith angle, high solar angle and clouds masks were applied as a screen. For POLYMER, similar flags were used. The mean, median and standard deviation of valid-remaining pixels were determined. Thresholds for the coefficient of variation (ratio of standard deviation to the mean < 0.15) and minimum number of valid pixels (50%) were also applied to each band. These were matched to the nearest SeaPRISM measurement within a one-hour window (maximum time difference). We note that negative data that passed the flag criteria retained, and that criteria were assessed on a band-by-band basis. Failure at one wavelength did not exclude other matchup pairs for wavelengths from the same pixel. As flags affect all bands in a pixel, different matchup numbers across the bands were attributed to failure of the coefficient of variation test.

Field data collected during this project from **Task 2** and historical data from DBHYDRO were used to develop and evaluate algorithms for turbidity, chl-a, and cell counts.

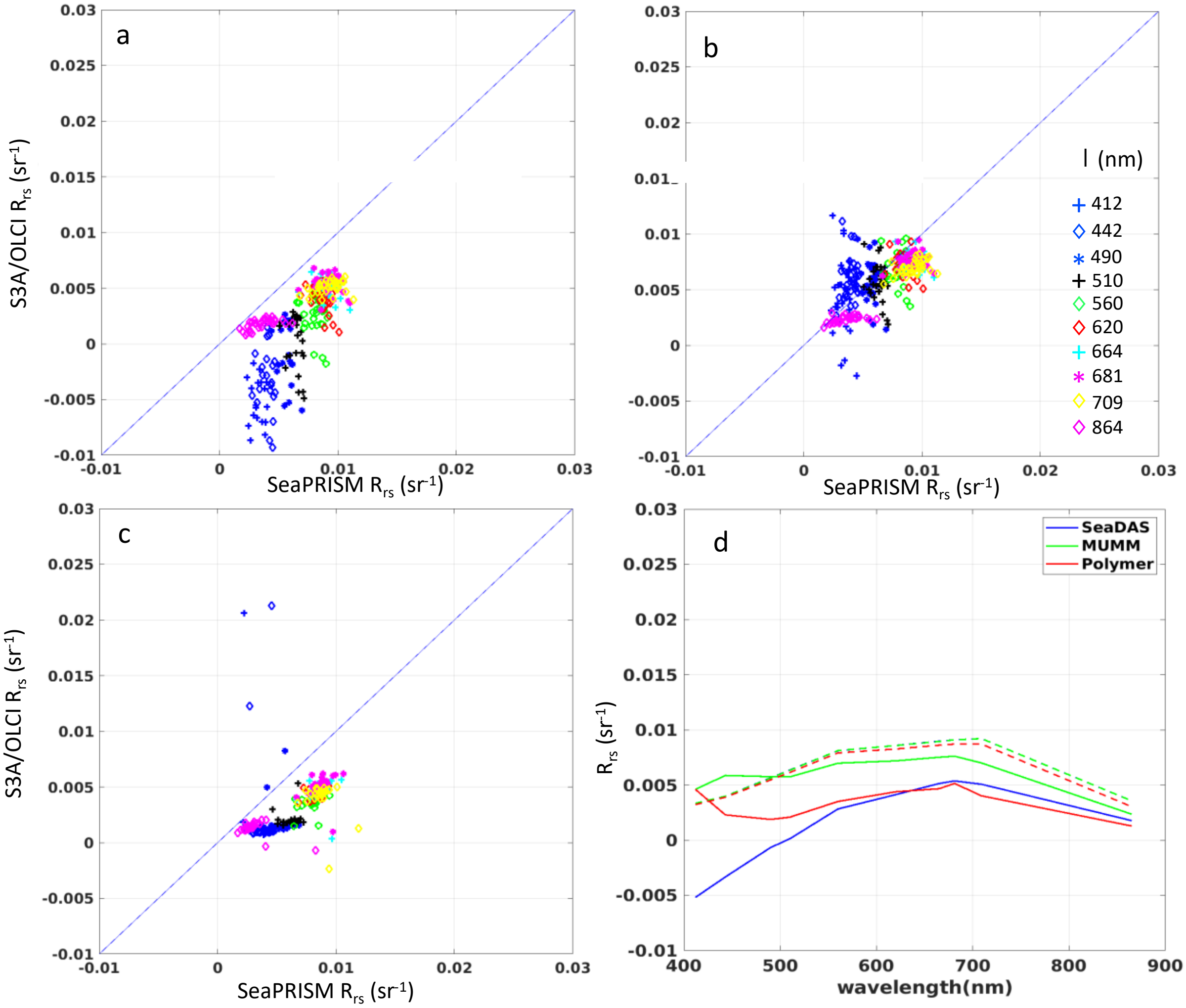

Figure 5B-2: Matchup Rrs spectra for Lake Okeechobee between the SeaPRISM and S3A/OLCI processed with different schemes: a) SeaDAS-STD scheme; b) MUMM scheme; c) POLYMER scheme; d) mean Rrs. Colored dashed lines are SeaPRISM means associated with each AC scheme/matchup. Note: all satellite and SeaPRISM data shown without any f/Q corrections applied.

RESULTS & DISCUSSION

The optical complexity of Lake Okeechobee required a test evaluation for atmospheric correction schemes, which are known to perform poorly over turbid environments (Bailey et al, 2010). Lake Okeechobee is an extreme case of a turbid system, and very much an end-member in terms of turbid environments. This poses challenges for both atmospheric correction and in-water algorithms. An important decision for processing images is the atmospheric correction scheme. This decision would rest on matchup analysis between the SeaPRISM measurements and the collocated satellite prediction for Rrs (the remote sensing reflectance which is the prime output product of atmospheric correction and the prime measurement of the SeaPRISM). The matchup analysis between Sentinel-3 data and the SeaPRISM indicated that the MUMM scheme was optimal over others with the least amount of bias and lowest uncertainties (Figure 5B-2). While all three schemes showed a negative bias, MUMM showed the least.

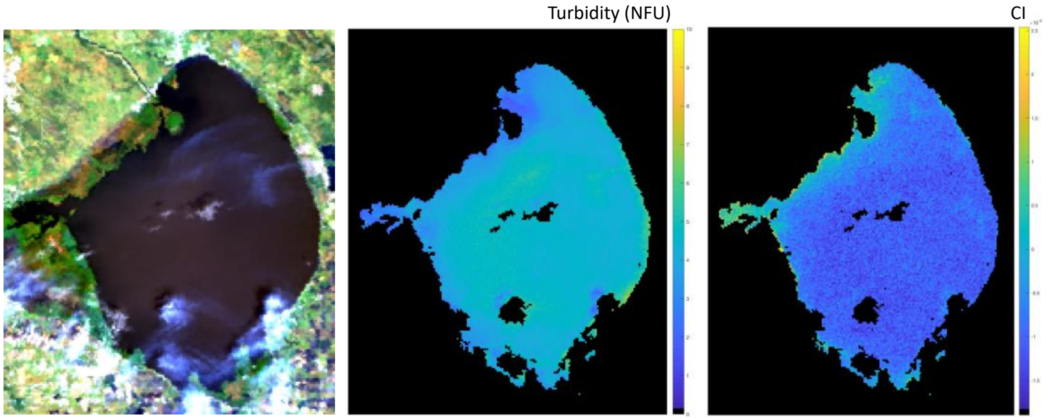

Figure 5B-3: A single satellite image scene from 2/26/21 as captured by Sentinel-3B, and processed through the HALO processing chain. Left: True-color RBG; Middle: Turbidity; Right: the CI. We note that CI was negative for much of the scene, indicating no cyanobacteria were visible in the surface waters.

With the MUMM scheme selected, a turbidity product was generated from a single-band algorithm for turbid waters with Rrs as input, and the CI product was generated for the same image but with the partial atmospheric correction using rho (reflectance) as input (Figure 5B-3). These images were uploaded to the HALO data portal in real-time. Evaluation of the quality of the image data was later assessed with field data matchups – both historical from DBHYDRO and from HALO collected optical data sets which also included fixed-location turbidity measurements from **Task 6**.

The matchup between the SeaPRISM measured Rrs 667 and the surface turbidity from the adjacent buoy showed a good relationship but was much different than expected from the published turbidity relationship from Dogliotti et al 2015. A non-linear curve was fit to these data for a Lake Okeechobee-specific algorithm (Figure 5B-4, left). This algorithm was tested against independent matchup points between Sentinel-3. Overall, the relationship was not as coherent between satellite and in situ turbidity measurements, with a 131% MAPE (Table 5B-1). The differences are likely attributed to atmospheric correction errors with the satellite data. Errors from correcting to Rrs will propagate into derived products. There is also a matchup/co-location error source. Satellite pixels are much larger than point collections and will incur natural errors from the heterogeneity of the environment. Regardless, there is error in the turbidity product, and we have characterized this from the matchup data set. Even with this error, this is likely the most robust optical property derived from ocean color satellite data.

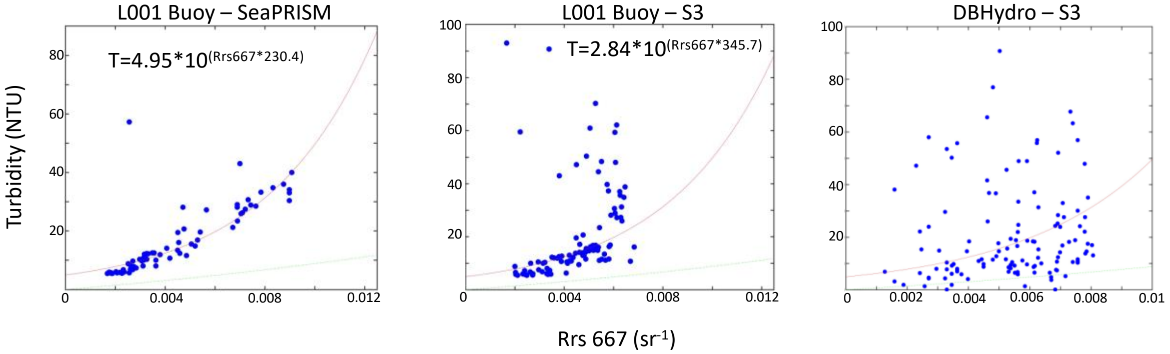

Figure 5B-4: Left: Buoy turbidity plotted against Rrs 667 (from the SeaPRISM; middle: buoy turbidity versus Sentinel-3 Rrs 667; Right: DBHYDRO turbidity versus Rrs 667 Sentinel-3 matchups. The red line is a custom turbidity fit from left plot; the green line is the published Dogliotti et al 2015 function.

The CI product is probably the best indicator of cyanobacteria presence from satellite, however. This product is operational in NOAA HAB bulletins. We have used the exact same method to generate CI as NOAA, with one small difference. The NOAA product is published in terms of cyanobacteria cell counts, but these are generally lacking for Lake Okeechobee. The HALO project collected cell counts, and we evaluated the CI against these data in our satellite product suite.

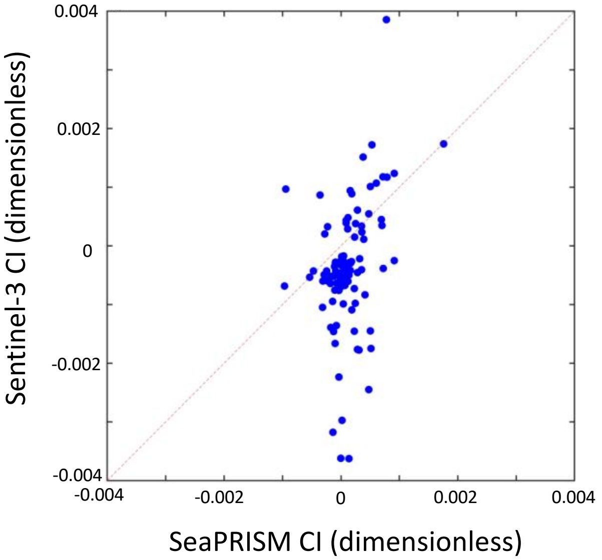

Figure 5B-5: The Cyanobacteria Index (CI) as generated from Sentinel-3 versus the CI derived from the SeaPRISM. The red line is the 1:1 line.

There is interest in the quality of the satellite CI product itself. This is a product that can be generated from SeaPRISM measurements (**Task 5A**), so matchup analysis is possible. A matchup data set between the SeaPRISM and Sentinel-3 for CI was generated for the HALO operating time period (Figure 5B-5). In general, there was a positive relationship between the pairs above the zero-zero coordinate, but a positive bias is evident for the Sentinel-3 CI. As a general indicator (recall that positive CI is an indication of cyanobacteria presence), the CI product appears to be working well in the sense of presence/absence. Further quantitative use encounters increased uncertainties, with the MAPE at over 100% between the pairs (Table 5B-1). The importance of this depends on the use. For simple presence/absence detection analysis, it bodes well. We generated monthly climatologies of the frequency of CI presence for the entire Sentinel-3 archive (dating to 2016) and the MERIS archive (operational from 2004 through 2012) over Lake Okeechobee (Figure 5B-6), in which patterns of frequent occurrences can be observed and compared over time.

The patterns between the two climatologies display both similarities and differences, with bloom frequency highest near the edges of the lake, particularly in the northern shores. The frequency appears to be higher from the Sentinel-3 observations, which would indicate an increase in bloom activity over the last 20 years. The timing of the blooms also appears different, with earlier onset more recently, and the spatial patterns are slightly variabile, with increased bloom excursions in the center of the lake more recently. These patterns are nonetheless interesting and require further study and corroboration with other data to confirm these trends. Although this was not part of the HALO **Task 5B** objective, it was a by-product of the image analysis.

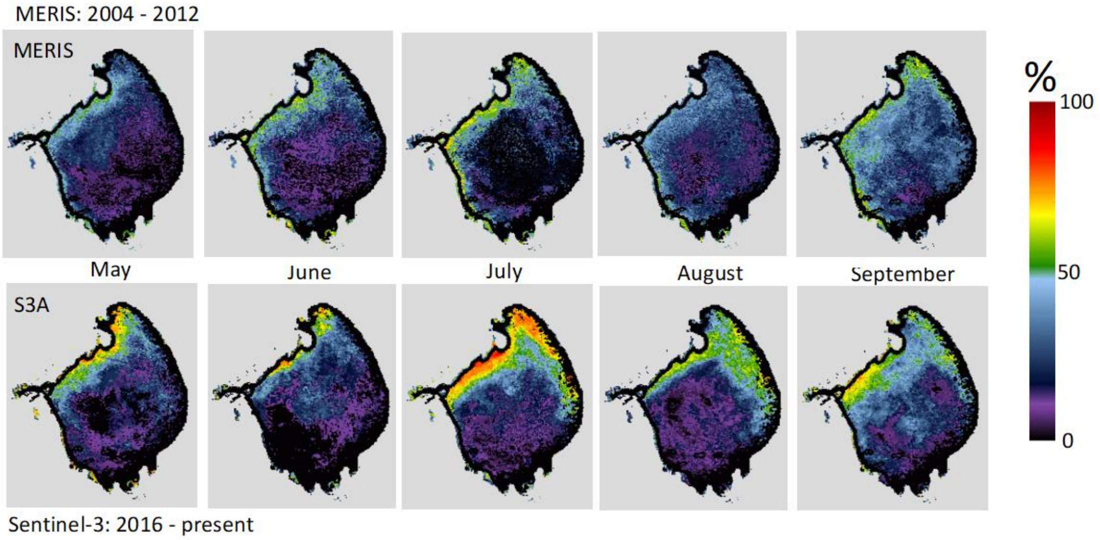

Figure 5B-6: Top row: monthly frequency climatologies of positive CI instances for MERIS between 2004 and 2012; Bottom row: monthly frequency climatologies of positive CI instances for Sentinel-3 between 2016 and 2021. Colors indicate the frequency of observed positive CI as an indicator of bloom presence.

The quantitative relation between CI and cyanobacteria cell counts was explored. The NOAA HAB products are reported in terms of cell counts using a transfer function for CI. In general, CI is proportional to cyanobacteria concentration in surface waters. Using the **Task 2** data, we were able to relate CI from the field data to co-measured cyanobacteria cell counts from flow cytometry (Figure 5B-7). There is a positive and linear relationship between the cell counts and CI, but the NOAA relationship which was derived from data in different waters (Lake Erie) does not apply to Lake Okeechobee. A new functional relationship was developed from the HALO data, and it shows a much higher level of cyanobacteria for a given CI level. This makes intuitive sense: the optical transparency is much lower in Lake Okeechobee compared to almost any other lake, and for cyanobacteria to be visible or have an impact on the light field, the populations must be much closer to the surface and in greater numbers. When compared directly to satellite CI matchups, the Lake Okeechobee trend is higher than the predicted NOAA trend, but lower than the field measurements would indicate. This is higher than current predictions however, and should be further investigated with additional field data. A complete understanding of the optical environment of Lake Okeechobee is still lacking. The HALO data set represents a step forward in this direction, but further study of the optics of the lake is needed to understand why these relationships are different. Nonetheless, these cell count to CI relations are provisional but are likely more accurate than the current NOAA function.

Due to the problems with both atmospheric correction and standard algorithms designed for clear waters, a chlorophyll product was shown to not be robust for Lake Okeechobee. We have a provisional chlorophyll algorithm related to the CI product (Figure 5B-8). While there is a general positive correlation between Chl and CI, the relationship is poor for the HALO data (collected in 2021). This is also evident in the Sentinel-3 CI matchups with the DBHYDRO Chl-a (matched from 2016 to 2021). In light of these relationships, we recommend not applying a Chl-a algorithm widespread to satellite data for Lake Okeechobee. The amount of noise in the relationships is due to the natural optical complexity of the lake, in which the optical signal is dominated by organics and sediments, and the inherent noise in the satellite data itself also owing to the optical complexity of the lake. We recommend that only turbidity and CI are robust enough to be used quantitatively, and even then, there remains a large amount of uncertainty.

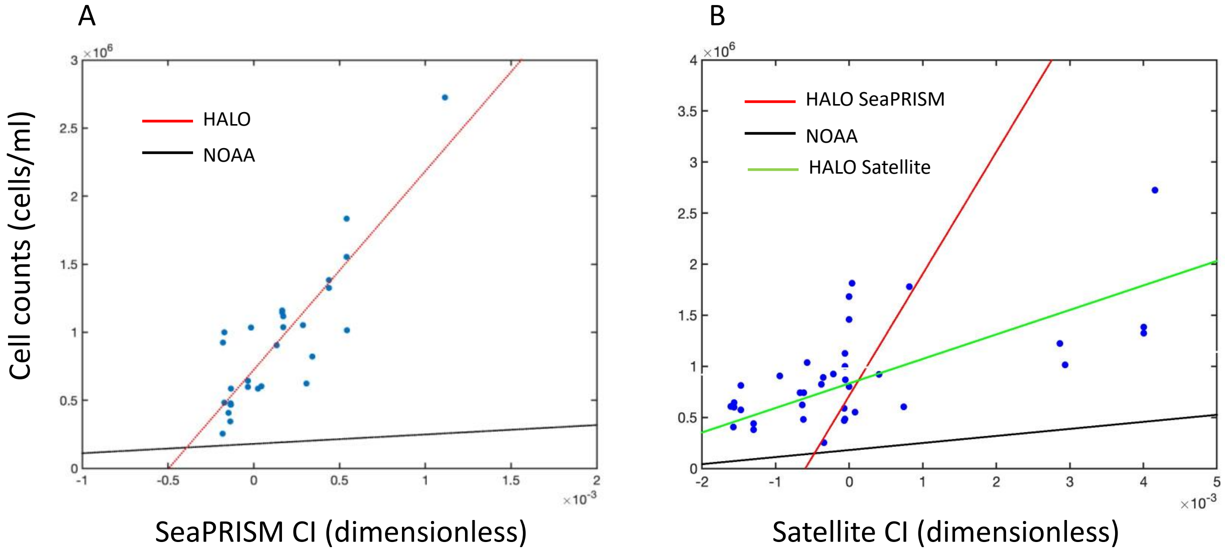

Figure 5B-7: A) Cyanobacteria cell counts from flow cytometry versus CI derived from SeaPRISM Cyanobacteria cell counts from flow cytometry versus CI derived from Sentinel-3 image matchup data. The black line is the NOAA standard curve c; the red line is the SeaPRISM HALO fit; the green line is the Sentinel-3 HALO fit.

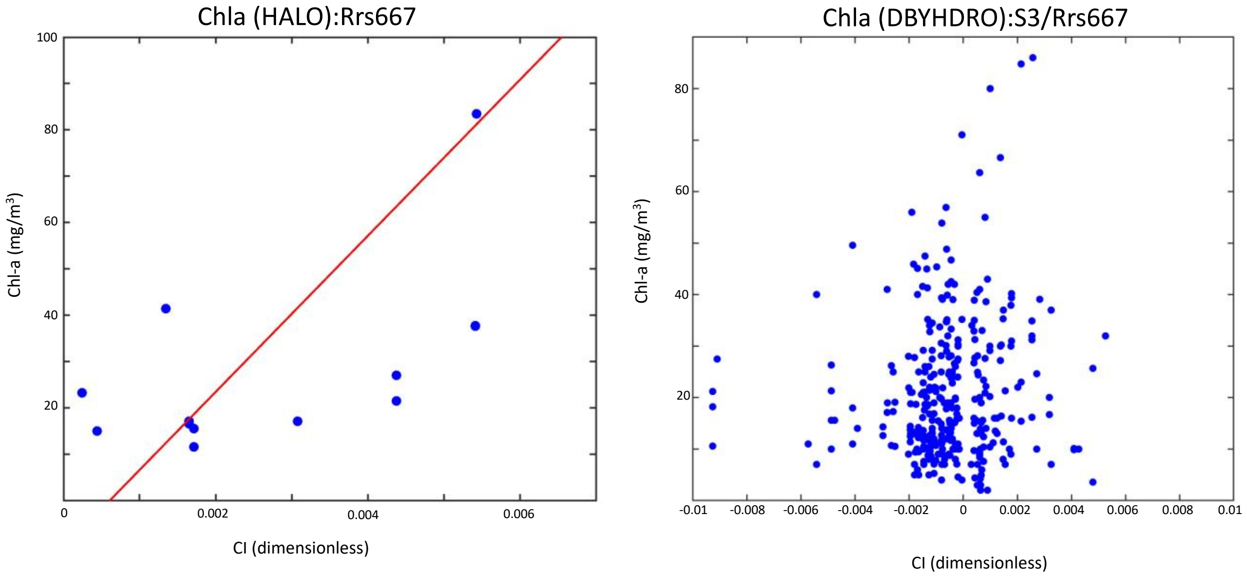

Figure 5B-8: Left: Chlorophyll-a concentration versus the Cyanobacteria Index derived from the Task 2 in situ data set; the red line is a polynomial linear fit; Right: Chl-a from DBHYDRO matched with Sentinel-3 CI products.

CONCLUSIONS & FUTURE WORK

The main elements of Task 5B were met, which was primarily the generation of satellite products used to support other tasks in HALO and to deliver a time-series of mapped products for Lake Okeechobee that were accessible through the HALO data portal. Lake Okeechobee is considered an extremely turbid lake from an optical point of view which poses many challenges for creating meaningful data products from satellite imagery. The challenges involve both atmospheric correction and bio-optical algorithms. The analysis of atmospheric correction schemes showed that even the best scheme (the MUMM method) generated noisy images when full atmospheric correction was applied. This impacted turbidity and standard chlorophyll products. We recommend against using turbidity and/or chlorophyll satellite products as downstream inputs in quantitative analyses, or at least the user should be aware of these serious issues related to image quality. Much more work is needed to improve both the atmospheric correction, and the in-water optical relations which are two inter-related issues. We emphasize, however, that the data sets we collected – both in situ water grabs and the SeaPRISM data – should be useful for future studies in this regard. Many satellite matchup points were generated between the SeaPRISM and satellite overpasses, which did not exist previously. The in situ optical data also are a new data set for Lake Okeechobee, and should be important for remote sensing/optical studies going forward which will likely to continue at some point in the future by researchers as remote sensing technologies improve. There is also much to be done in regards to comparisons of the ASV (**Task 4**) data to this **Task 5** data.

The two most robust water quality products we evaluated were turbidity and the native CI. Tuning algorithms to Lake Okeechobee improved on the transformation of spectral light to turbidity and cell counts (through CI), but considerable noise remains and the products have generally high uncertainties. This is a function of the optical complexity of the lake. Owing to type of algorithm applied for the surface cyanobacteria detection, partial atmospheric correction could be applied for the CI product, avoiding some limitations associated with full atmospheric correction. However, only cyanobacteria immediately at the surface could be detected with any degree of accuracy with this method. Nonetheless, the patterns in the images were useful for observing the spatial scale of events, and were very useful in detecting surface cyanobacteria populations. While these are more qualitative, the expression of CI indicating surface cyanobacteria in and of itself has quantitative information. The climatology maps of CI are important for long-term trend analyses, and here we have documented the surface cyanobacteria patterns over the last 20 years. These will serve as baseline comparative maps for assessing mitigation strategies in the future.

Table 5B-1: Uncertainties for optical parameters in Lake Okeechobee.

Parameter	MAPE %	RMS	Bias
Turbidity	131.1	24.0 (NTU)	-0.07 (NTU)
CI (positive only)	142.6	0.00028	0.00049

TASK 6: FIXED LOCATION WATER QUALITY MONITORING (TASK LEAD: HANISAK)

INTRODUCTION

FAU Harbor Branch launched the Indian River Lagoon Observatory (IRLO) in 2011 and has operated the associated Indian River Lagoon Observatory of Environmental Sensors (IRLON) since 2013. IRLON is an estuarine observation network of biogeochemical and meteorological sensors that provide real-time, high-accuracy and high-resolution water quality/weather data through a dedicated interactive website. IRLON initially built the water quality analytical capabilities with Land/Ocean Biogeochemical Observatory (LOBO) technology, first developed in 2003 by scientists and engineers at the Monterey Bay Aquarium Research Institute with support from the National Science Foundation. Modifications to the IRLON technology, including novel data loggers, telemetry capabilities, and sensors. were completed in 2020. These new sensor arrays are called IRLON Biogeochemical Instrument Packages (BIPs). This innovative technology was incorporated in this project to provide fixed-location intensive water quality monitoring at two depths (= two stations) at the Tier 1 Northern site in Lake Okeechobee [instrument tower L001, operated by the South Florida Water Management District (SFWMD)]. This location was identified as a critical site for the initiation of cyanobacterial blooms in the lake. After installation, the IRLON BIPs at these two stations continuously measured the following parameters on an hourly basis during the period of deployment (7/1/21 – 1/31/22): temperature; conductivity; depth; dissolved oxygen; pH; Chl-a; phycocyanin; turbidity; CDOM; nitrate, (NO_3^{-1}); and orthophosphate (PO_4^{-3}).

METHODS

IRLON staff maintained the BIPs and checked the incoming data daily to ensure that the data were being reliably transmitted or if the units needed servicing. Based on the previous experience of the IRLON team with this technology, each unit was visited by boat every three to four weeks, or more frequently, if there was, for instance, a loss of incoming data or a data drift issue. Each BIP was retrieved by boat and the sensors serviced, which included cleaning and refilling reagents, and calibration checks. The IRLON team also visited the BIPs every 4-6 weeks (depending on season/biofouling) to verify sensor readings for temperature and conductivity with a sonde with a CTD instrument that had been lab calibrated and verified prior to each maintenance event. A YSI ProDSS sonde was lowered concurrently with a Sea-Bird SeaCAT 19*plus*V2 CTD to coincide with *in situ* measurements of temperature, salinity, and pH by the Sea-Bird WQMx or SeaFET. The YSI sonde was calibrated and verified following FDEP SOP FT 1200 and the Sea-Bird CTD was factory calibrated on an annual basis. At that same time, the IRLON team collected validation grab samples for nitrate (NO_3^-), orthophosphate (PO_4^{-3}), and chl-a that can be used to quality assurance/quality control (QA/QC) sensor data and document drift. Discrete samples were taken with a 10-L Niskin bottle at instrument depth following DEP SOPs for collection and preservation. Triplicate samples were taken and sent to Florida International University (FIU) CAChE, a FLDOH and NELAC certified lab, for analysis of nutrients and chl-a (corrected) data. All sensor data used for comparison are considered provisional and have not undergone data processing to correct for sensor drift. All work was done in compliance with the Quality Assurance Project Plan (QAPP) approved by FDEP for this project.

ACTIVITIES SCHEDULED vs. COMPLETED

All proposed activities were fully completed, as follows. During the first quarter of the project, a reconnaissance to the two originally proposed sites in coordination with the SFWMD field team that services the two instrument towers involved; we confirmed existing information and took additional details needed for the design of our deployments. The sensors were ordered from the respective manufacturers for all monitoring sensors (temperature, conductivity, depth, dissolved oxygen, pH, chlorophyll *a*, phycocyanin, turbidity, CDOM, phosphate, nitrate, and backscatter). The QAPP for this task was drafted and edited as per the initial FDEP review. During the second quarter of the project, four of the sensors were received: chl-a, phycocyanin, phosphate, and nitrate. FDEP was notified of the serious delay of the SeaFET sensor after the vendor (Seabird) advised us of interruptions of the temporary suspension of production and shipment of SeaFET instruments due to quality control issues from one of their suppliers (Honeywell). During the third quarter of the project, all additional sensors were received except the SeaFET from the respective manufacturers: temperature, conductivity, depth, dissolved oxygen, pH, chl-a, phycocyanin, turbidity, CDOM, and backscatter. During the fourth quarter of the project, the SeaFET sensors were finally received.

Before deployment, the BIPs were wrapped with copper tape to reduce biofouling. The units were placed at a test site at HBOI to check that the instrument package, platform, and all sensors were functioning correctly and sending data. After the testing period, IRLON staff transported and installed the BIPs in the field. The IRLON team attached the BIPs to Tower L001 in Lake Okeechobee using an HBOI-designed pulley I-beam system for raising and lowering the BIPs into the water from the GRANTEE's small boat. We had previously reconned the SFWMD instrument tower L001 (Figure 6-1) for the deployment of our two sets of instruments: one near bottom (~1 m above the sediment; LO-L1B), and one near surface (~0.5 below the surface, LO-L1S). We returned on 4/26/21 to confirm measurements and made additional measurements to finalize the design (Figures 6-2, 6-3). Following the fabrication of the two I-beams that secure the instruments to the tower, on 5/12/21, we initiated the installation of the fixed-location intensive water quality monitoring, with the installation of the I-beams on the instrument tower (Figure 6-4). Following testing of all sensors and telemetry at our test site at FAU Harbor Branch and some bad-weather delays, the second part of the installation was performed on 6/1/21 (Figure 6-5). Per usual protocol, following sensor deployment, public dissemination of the data was delayed until all issues could be resolved. In this case, we had to resolve a number of issues, most of them in regards to telemetry and working with the backscatter sensor, which is new for the IRLON system. All issues were resolved, except for real-time transmission of the pH (SeaFETs); those data are being recorded on site and currently are not real-time; these data were downloaded until telemetry was resolved. As of 6/30/21, all troubleshooting of the instruments was completed and real-time data (except SeaFETs per above) were available starting 7/1/21. During the fifth quarter, the SeaFETs were received. The originally projected dates for collection were the six months from 4/15/21 to 10/15/21. With the delays previously mentioned in receipt of instruments and the time to resolve telemetry and other deployment issues, the instrumentation was instead operated continuously for the 7 months from 7/1/21 to 1/31/22. This period encompassed the peak season for both cyanobacterial blooms and tropical storms.

During the fifth through the seventh quarter, publicly accessible data from the IRLON BIPs were available from 7/1/21 to 1/31/22. The continuous operations were successful in providing valuable, publicly available water quality data, which were first transmitted to the IRLON data portal (www.irlon.org), with a map-link to the IRLON dashboard visible on the Lake Okeechobee map on the GCOOS web portal(http://halo.gcoos.org/). Sensors were maintained and routinely validated at each station following the approved QAPP. Our two stations were visited by boat every three to four weeks, or more frequently as needed, e.g. a loss of incoming data or suspected malfunction. During these visits, each IRLON BIP was retrieved by boat and the sensors serviced (Tables 6-1 and 6.2)

Figure 6-1: Pre-installation view (north side) of instrument tower L001.

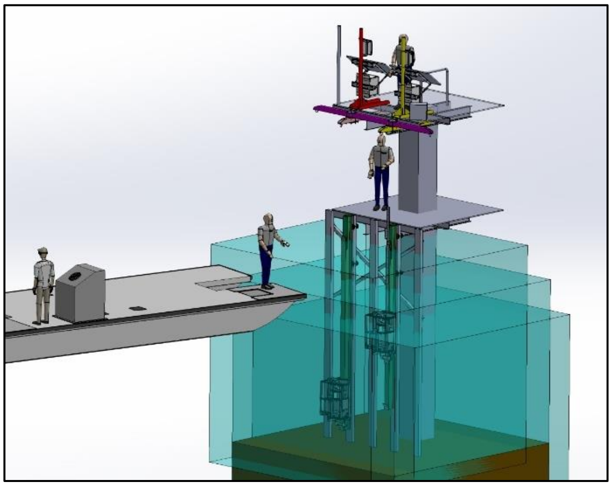

Figure 6-2: Engineering schematic of fixed-location intensive water quality monitoring installation showing the deployment of the biochemical instrument packages (BIPs) on instrument tower L001. Station LO-L1B is the near-bottom BIP (left); station LO-L1S is the near-surface BIP (right).

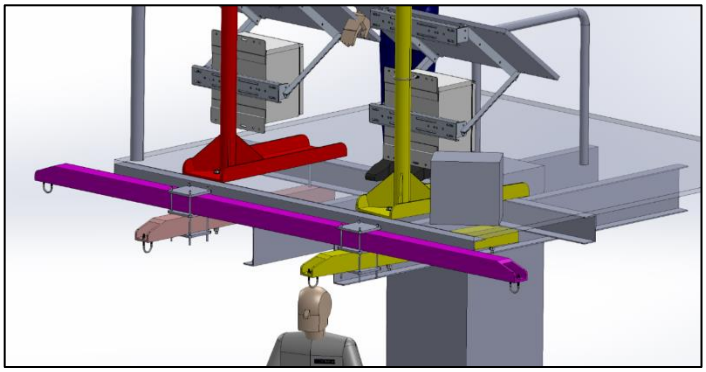

Figure 6-3: Engineering schematic of the secondary lift point (pink beam) which was installed to facilitate deployment and recovery of fixed-location intensive water quality monitoring instrumentation on instrument tower L001.

Figure 6-4: Installation of the I-beams and other support structure on instrument tower L001, 5/12/21, including (clockwise from top left): aerial view of HBOI small boat secured to the tower, lift point, HALO field team finalizing I-beam installation, and completed I-beam installation.

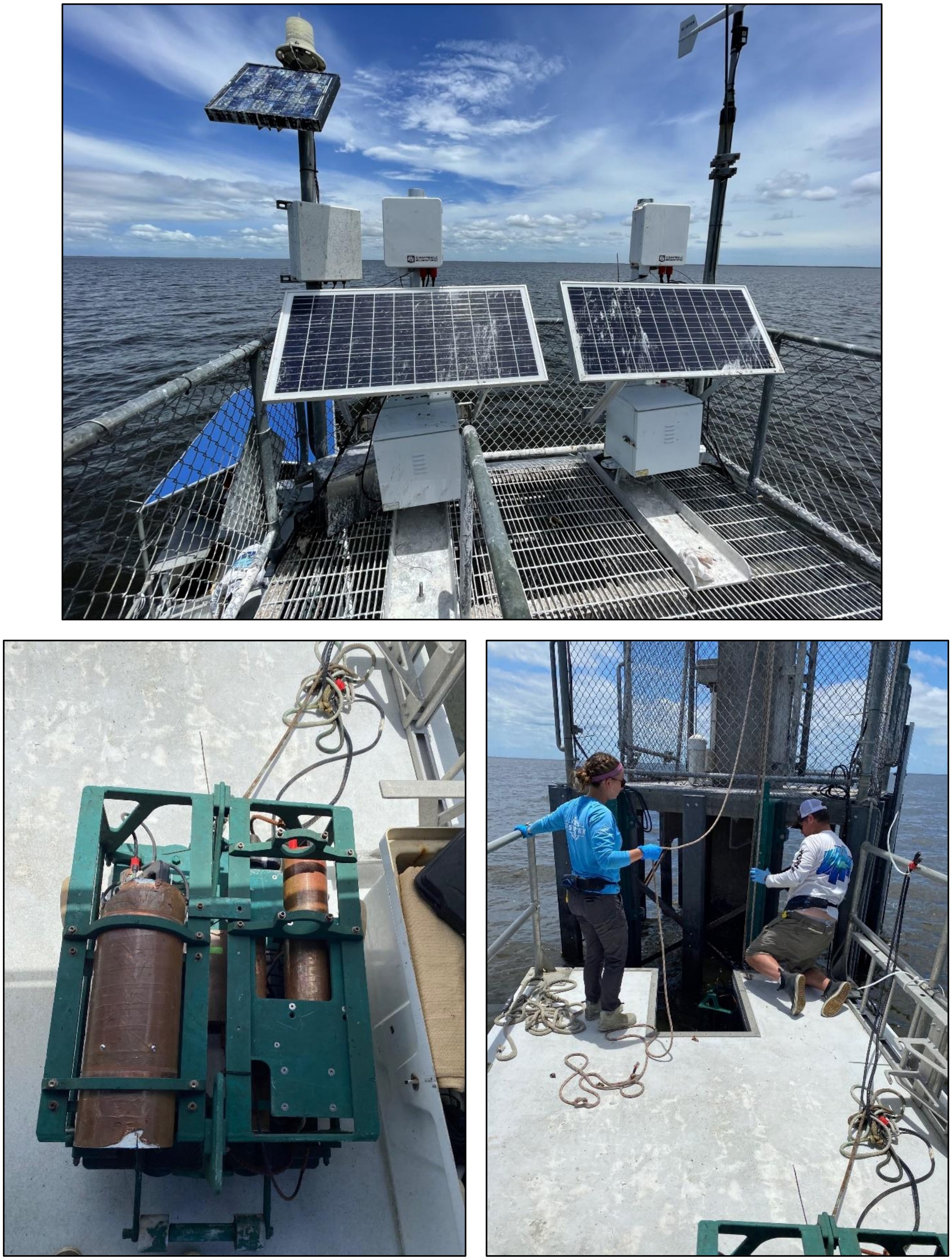

Figure 6-5: Post-installation images of fixed-location intensive water quality monitoring installation: the installed solar panels (top), one of the BIPs (lower left), and BIP deployment.

RESULTS & DISCUSSION

Date Completeness: To effectively evaluate the dynamic interplay of freshwater inputs and tidal flushing, a relatively complete time series of water quality data must be collected. An important performance metric established in the SAP was data completeness. EPA defines completeness as a measure of the amount of valid data needed to be obtained from a measurement system to meet study objectives (EPA QA/G-8, Guidance on Environmental Data Verification and Data Validation). Every effort is made to minimize data loss by keeping well-maintained instrumentation, bringing backup equipment on each station visit, and monitoring data remotely to correct problems as soon as possible. Data Completeness is defined as the collection of 90% of usable data as described in our SAP. The 90% value takes into consideration unexpected data loss resulting from malfunctioning instrumentation and extreme weather events. An assessment of data completeness for the two stations is provided in Tables 6-3 and 6-4. Data Completeness values for most parameters were higher than the targeted 90%. Looking at the stations individually:

- LO-L1S (Table 6-3) – Data completeness was exceptional for all parameters except for Cycle-PO4 and SeaFET, with data loss ranging from 1.90 to 3.47%. Data loss was 53.82% and 11.01% for Cycle-PO4 and SeaFET respectively; the Cycle-PO4 data completeness was due to the failure of the Cycle-PO4 mid-deployment. The SeaFET data completeness was also due to the failure of the instrument mid-deployment on one occasion (see Table 6-1). The SeaFET was non-responsive when retrieved following the mid-deployment failure and was repaired in the lab and re-deployed. Backup Cycle-PO4 and SeaFET sensors were not available.
- LO-L1B (Table 6-4) – Data completeness was exceptional for all parameters except for Cycle-PO4 and SeaFET, with data loss ranging from 0.77 – 1.18%. Data loss for Cycle-PO4 and SeaFET was 27.95% and 23.22% respectively; the Cycle-PO4 data completeness was due to the failure of the Cycle-PO4 mid-deployment. Backup Cycle-PO4 instrumentation was not available until a single Cycle-PO4 was borrowed from PI Beckler and deployed in October 2021. SeaFET data completeness was due to the failure of internal batteries, once in August 2021 and once in September 2021 that required the SeaFET to be returned to the lab. Batteries were replaced and the SeaFET was re-deployed as soon as possible. Backup SeaFET sensors were not available.

Comparison of IRLON Sensors to sonde and laboratory analyzed samples: The discrete sampling activities to document QA/QC sensor data and sensor drift are summarized in Table 6-5. Side-by-side comparison of ECO, YSI Pro DSS and Sea-Bird 19plusV2 CTD during discrete sampling activities are provided in Table 6-6. For all stations across all sampling dates SBE37 temperature ranged from -0.45 to -0.35 ºC and -0.01 to 0.02 ºC of the YSI sonde and Sea-Bird CTD respectively. Provisional SBE37 specific conductance ranged from -1.01 to 11.76 µS/cm and -3.27 to 7.85 µS/cm of the YSI sonde and Sea-Bird CTD across all sampling sites and dates. Provisional SeaFET pH was generally higher than concurrent YSI sonde and Sea-Bird CTD readings (Table 6-7). The overall difference between provisional SeaFET pH and YSI sonde and Sea-Bird CTD ranged from -0.48 to 0.26 and -0.27 to 0.47 respectively across all sampling sites and dates Additionally, it is important to note that SeaFET pH data are reported on the total scale versus data for both the YSI sonde and 19*plus*V2 CTD, which are reported on the NBS scale. Further refinement may also be necessary in the pH calculation to account for the freshwater application. Comparisons between provisional ECO BBFL2-W and FIU laboratory analyzed chl-a are summarized in Table 6-8. Overall comparisons between the ECO BBFL2-W and discrete samples for the majority of sites and sampling dates are poor, especially at higher chl-a concentrations. Further consideration is needed to evaluate inherent differences between *in vivo* fluorescence by *in situ* sensors like the ECO BBFL2-W to laboratory-extracted chlorophyll.

Provisional Cycle-PO4 data varied with laboratory-analyzed phosphate (Table 6.9) due in part to the difference in filter pore size between the Cycle-PO4 and discrete samples (~7.5 µm and 0.7 µm respectively) as well as periodic pump issues yielding suspect data. Additionally, laboratory measurements are subject to less consistent reaction times. It is additionally possible that the reagent differences between the laboratory and in situ colorimetric techniques (which are proprietary as per the manufacturer) could lead to these disparities. For example, a difference in acid strength could provide enhanced dissolution of iron oxide minerals and thus release of additional adsorbed phosphate. Additional data processing is necessary for comparison (Table 6-10) of the SUNA sensor (to laboratory-analyzed nitrate and nitrite (NOx). The SUNAv2, being a direct optical measurement, has a known positive bias in waters with high CDOM. In the future, a site-specific relationship between SUNAv2 and laboratory analyzed samples will be developed and used for correction of provisional SUNAv2 data. As noted previously, we were limited by the lack of back-up instrumentation when we had sensor issues that can not be addressed on site, and especially when the instruments needed to be returned to the vendor for factory repairs.

<u>Example time series data</u>: An multi-task time series is presented in Figure 6-7 with provisional data from site L001 surface depth to demonstrate the power of the combined measurements. The figure shows turbidity as measured by the IRLON BIP from this task as well as measured by SFWMD sondes at the same location. Also shown is surface water SRP measured at high temporal frequency as part of this task, with HALO and SFWMD water column SRP measured from discrete sampling for reference. Finally, **Task 5** SeaPRISM *M. aeruginosa* surface scum measurements are presented. The data demonstrates at least two major novel findings: 1) turbidity and water column SRP are tightly coupled at certain time period, suggesting the direct input of sediment pore water SRP into the water column. However, it is quickly exhausted either by phytoplankton uptake or scavenging by resuspended minerals. A major take home point is that conventional biweekly sampling literally misses an entire water column SRP accumulation/depletion cycling that was captured by the weekly measurements. This finding highlights the critical importance of maintaining in situ high frequency measurements; 2) The *M. aeruginosa* bloom undergoes a rapid, mostly permanent decline after this turbidity and nutrient depletion event. This figure is a critical part of our interpretation of the 2021 HAB season behavior and is referenced in **Task 3** sediment data, in which evidence is provided for the iron-driven termination of sediment diffusive fluxes of SRP.

Table 6-1: Completed activities at LO-L1S (Lake Okeechobee – L1 Surface) in support of continuous monitoring from 7/1/21 through 1/31/22.

Date	Site Visit Type	Troubleshooting resolution (if applicable)
07/14/2021	Regular maintenance & Cycle-PO4 reagent change	SeaFETv2 deployed in autonomous mode
07/19/2021	Troubleshooting erroneous C3 data	Copper antifouling plate was misaligned over sensors and it was fixed
08/11/2021	Regular maintenance	SeaFETv2 deployed in autonomous mode
08/31/2021	Regular maintenance & Cycle-PO4 reagent change	SeaFETv2 deployed in autonomous mode
09/03/2021	Troubleshooting erroneous ECO data	Diagnosed faulty biowiper motor on ECO. Retrieved for further troubleshooting and deployed backup ECO.
09/13/2021	Regular maintenance	SeaFETv2 deployed in autonomous mode
10/07/2021	Regular maintenance & Cycle-PO4 reagent change	N/A
10/11/2021	Troubleshooting erroneous Cycle-PO4 data	Cycle-PO4 retrieved for further troubleshooting; no backup Cycle-PO4 available;
10/26/2021	Regular maintenance	Cycle-PO4 not currently deployed due to malfunction; no backup Cycle-PO4 available;
11/22/2021	Regular maintenance	Cycle-PO4 not currently deployed due to malfunction; no backup Cycle-PO4 available;
12/08/2021	Regular maintenance	Cycle-PO4 not currently deployed due to malfunction; no backup Cycle-PO4 available;
01/10/2022	Regular maintenance	Cycle-PO4 not currently deployed due to malfunction; no backup Cycle-PO4 available;

Table 6-2: Completed activities at LO-L1B (Lake Okeechobee – L1 Benthic) in support of continuous monitoring from 7/1/21 through 1/31/22.

Date	Site Visit Type	Troubleshooting Resolution (if applicable)
07/14/2021	Regular maintenance & Cycle-PO4 reagent change	SeaFETv2 deployed in autonomous mode
07/19/2021	Troubleshooting erroneous C3 data	Diagnosed misalignment of the C3 copper faceplate. The faceplate moved during the deployment and covered the fluorometer optics. Faceplate was aligned correctly, secured and proper data transmission resumed
08/11/2021	Regular maintenance	SeaFETv2 was non-responsive upon retrieval of BIP. SeaFETv2 was retrieved for further troubleshooting in the lab.
08/31/2021	Regular maintenance & Cycle-PO4 reagent change	SeaFETv2 re-deployed in autonomous mode following in-lab repair
09/13/2021	Regular maintenance	SeaFETv2 was non-responsive upon retrieval of BIP. SeaFETv2 was retrieved for further troubleshooting in the lab.
10/07/2021	Regular maintenance	Cycle-PO4 not currently deployed due to malfunction; no backup Cycle-PO4 available;
10/26/2021	Regular maintenance	Cycle-PO4 deployed;
11/22/2021	Regular maintenance & Cycle-PO4 reagent change	N/A
12/08/2021	Regular maintenance	N/A
01/10/2022	Regular maintenance & Cycle-PO4 reagent change	N/A

Table 6-3: Data Completeness for all parameters at LO-L1S accessible on IRLON data portal (http://www.irlon.org/), 7/1/21 through 1/31/22.

Instrument	Parameter	Number of Observations	Number of Missing Observations	Total Possible Observations	Percentage Missing
C3	Chlorophyll (blue) fluorescence [RFU]	4981	179	5160	3.47
C3	Phycocyanin fluorescence [RFU]	4981	179	5160	3.47
C3	CDOM fluorescence [RFU]	4981	179	5160	3.47
Cycle	phosphate concentration [uM]	2383	2777	5160	53.82
ECO	CDOM [ppb QSDE]	5062	98	5160	1.90
ECO	Chlorophyll [µg/L]	5062	98	5160	1.90
ECO	Turbidity [NTU]	5062	98	5160	1.90
ECOBB3	Turbidity (470nm) [NTU]	5062	98	5160	1.90
ECOBB3	Turbidity (532nm) [NTU]	5062	98	5160	1.90
ECOBB3	Turbidity (650nm) [NTU]	5062	98	5160	1.90
SBE37	depth [m]	5062	98	5160	1.90
SBE37	dissolved oxygen [mg/L]	5062	98	5160	1.90
SBE37	pressure [dbar]	5062	98	5160	1.90
SBE37	specific conductance [µS/cm]	5062	98	5160	1.90
SBE37	water temperature [C]	5062	98	5160	1.90
SeaFET	pH	5062	98	5160	11.01
SUNA	nitrate [uM]	4592	568	5160	2.56

Table 6-4: Data Completeness for all parameters at LO-L1B accessible on IRLON data portal (http://www.irlon.org/), 7/1/21 through 1/31/22.

Instrument	Parameter	Number of Observations	Number of Missing Observations	Total Possible Observations	Percentage Missing
C3	Chlorophyll (blue) fluorescence [RFU]	4995	165	5160	3.20
C3	Phycocyanin fluorescence [RFU]	4995	165	5160	3.20
C3	CDOM fluorescence [RFU]	4995	165	5160	3.20
Cycle	phosphate concentration [uM]	3718	1442	5160	27.95
ECO	CDOM [ppb QSDE]	5049	111	5160	2.15
ECO	Chlorophyll [µg/L]	5049	111	5160	2.15
ECO	Turbidity [NTU]	5049	111	5160	2.15
SBE37	depth [m]	5049	111	5160	2.15
SBE37	dissolved oxygen [mg/L]	5049	111	5160	2.15
SBE37	pressure [dbar]	5049	111	5160	2.15
SBE37	specific conductance [µS/cm]	5049	111	5160	2.15
SBE37	water temperature [C]	5049	111	5160	2.15
SeaFET	pH	3962	1198	5160	23.22
SUNA	nitrate [uM]	4986	174	5160	3.37

Table 6-5: Discrete sampling activities to QA/QC sensor data and document sensor drift from 7/1/21 through 1/31/22.

Sampling Date	Site ID	Temperature & Specific Conductivity	pH	Nutrients	Chlorophyll *a* (corrected)
07/19/2021	LO-L1S	X	X	X	X
07/19/2021	LO-L1B	X	X	X	X
08/17/2021	LO-L1S	X	X	X	X
08/17/2021	LO-L1B	X	X	X	X
09/13/2021	LO-L1S	X	X	X	X
09/13/2021	LO-L1B	X	X	X	X
10/11/2021	LO-L1S	X	X	X	X
10/11/2021	LO-L1B	X	X	X	X
11/08/2021	LO-L1S	X	X	X	X
11/08/2021	LO-L1B	X	X	X	X
12/13/2021	LO-L1S	X	X	X	X
12/13/2021	LO-L1B	X	X	X	X
01/26/2022	LO-L1S	X	X	X	X
01/26/2022	LO-L1B	X	X	X	X

Table 6-6: Side-by-side comparison of ECO, YSI Pro DSS and Sea-Bird 19*plus*V2 CTD during discrete sampling activities from 7/1/21 through 1/31/22.

Sampling Date	Site ID	Temperature, C			Specific Conductivity, µS/cm		
		SBE37	YSI	CTD	SBE37	YSI	CTD
7/19/2021	LO-L1S	29.50	29.10	29.50	393.11	392.10	389.84
7/19/2021	LO-L1B	29.48	29.10	29.48	391.49	392.37	390.24
8/17/2021	LO-L1S	28.55	28.20	28.57	285.21	291.60	307.39
8/17/2021	LO-L1B	28.52	28.10	28.52	287.63	290.12	309.50
9/13/2021	LO-L1S	29.54	29.10	29.53	303.06	334.86	305.68
9/13/2021	LO-L1B	29.54	29.10	29.54	304.25	332.80	303.70
10/11/2021	LO-L1S	27.39	27.00	27.40	305.67	309.98	308.62
10/11/2021	LO-L1B	27.39	27.00	27.38	308.99	309.96	308.80
11/08/2021	LO-L1S	20.94	20.50	20.94	350.22	356.50	355.23
11/08/2021	LO-L1B	20.93	20.50	20.92	354.21	356.64	355.38
12/13/2021	LO-L1S	21.95	21.50	21.96	386.12	390.97	390.79
12/13/2021	LO-L1B	21.95	21.56	21.96	389.86	391.04	390.78
01/26/2022	LO-L1S	15.98	15.60	15.99	391.74	403.50	399.59
01/26/2022	LO-L1S	15.99	15.60	15.98	396.15	403.73	399.73

Table 6-7: Side-by-side comparison of SeaFET, YSI Pro DSS and Sea-Bird 19*plus*V2 CTD during discrete sampling activities from 7/1/21 through 1/31/22

Sampling Date	Site ID	pH		
		SeaFET	YSI	CTD
07/19/2021	LO-L1S	7.92	8.18	8.39
07/19/2021	LO-L1B	8.63	8.16	8.37
08/17/2021	LO-L1S	7.92	7.52	7.71
08/17/2021	LO-L1B	NS	7.40	7.63
09/13/2021	LO-L1S	8.30	7.94	8.10
09/13/2021	LO-L1B	8.13	7.88	8.08
10/11/2021	LO-L1S	7.89	7.82	8.04
10/11/2021	LO-L1B	8.03	7.85	8.01
11/08/2021	LO-L1S	8.20	7.91	8.19
11/08/2021	LO-L1B	8.27	7.92	8.18
12/13/2021	LO-L1S	8.11	8.12	8.20
12/13/2021	LO-L1B	8.40	7.93	8.19
01/26/2022	LO-L1S	8.36	8.09	8.26
01/26/2022	LO-L1S	8.46	7.96	8.26

^{NS} SeaFET did not sample

Table 6-8: Comparison of ECO BBFL2W and laboratory-determined chlorophyll *a* (corrected) during discrete sampling activities from 7/1/21 through 1/31/22.

Sampling Date	Site ID	Chlorophyll *a* (corrected), µg/L	
		ECO	FIU CACHE
07/19/2021	LO-L1S	5.13	21.4
			22.5
			16.5
07/19/2021	LO-L1B	4.14	10.2
			12.8
			10.9
08/17/2021	LO-L1S	7.16	32.3
			27.6
			30.1
08/17/2021	LO-L1B	7.56	31.8
			30.8
			31.9
09/13/2021	LO-L1S	5.97	30.9
			27.4
			30.6
09/13/2021	LO-L1B	6.72	29.8
			25.0
			34.4
10/11/2021	LO-L1S	5.41	26.22
			26.05
			27.52
10/11/2021	LO-L1B	5.97	27.51
			29.28
			27.27
11/08/2021	LO-L1S	4.61	20.74
			22.18
			21.86
11/08/2021	LO-L1B	5.19	21.69
			24.04
			23.96
12/13/2021	LO-L1S	3.28	8.60
			8.43
			7.84
12/13/2021	LO-L1B	3.62	8.29
			7.74
			7.90
01/26/2022	LO-L1S	2.94	6.42
			6.62
			6.34
01/26/2022	LO-L1B	3.21	6.86
			7.09
			6.47

^{T} Below MDL

^{I} Below PQL

Table 6-9: Comparison of Cycle-PO4 and laboratory determined PO$_4$ during discrete sampling activities from 7/1/21 through 1/31/22.

Sampling Date	Site ID	PO4, mg P/L	
		Cycle-PO4	FIU CACHE
07/19/2021	LO-L1S	0.035	0.052
			0.053
			0.054
07/19/2021	LO-L1B	0.019	0.056
			0.057
			0.057
08/17/2021	LO-L1S	0.005	0.033^{Q}
			0.032^{Q}
			0.031^{Q}
08/17/2021	LO-L1B	0.006	0.032
			0.032
			0.032
09/13/2021	LO-L1S	0.033	0.023
			0.022
			0.022
09/13/2021	LO-L1B	NS	0.023
			0.023
			0.023
10/11/2021	LO-L1S	0.001	0.029
			0.030
			0.030
10/11/2021	LO-L1B	NS	0.030
			0.030
			0.030
11/08/2021	LO-L1S	NS	0.029
			0.030
			0.030
11/08/2021	LO-L1B	0.005	0.030
			0.031
			0.031
12/13/2021	LO-L1S	NS	0.046
			0.047
			0.048
12/13/2021	LO-L1B	0.011	0.048
			0.047
			0.048
01/26/2022	LO-L1S	NS	0.068
			0.069
			0.069
01/26/2022	LO-L1B	0.019	0.068
			0.068
			0.068

^{T}Below MDL

^{I} Below PQL

^{NS}Not sampled

^{Q}Analyzed ~50 minutes outside of hold

Table 6-10: Comparison of SUNA and laboratory determined NOx during discrete sampling activities from 7/1/21 through 1/31/22.

Sampling Date	Site ID	NO$_X$, mg N/L	
		SUNA	FIU CACHE
07/19/2021	LO-L1S	0.154	0.038
			0.037
			0.037
07/19/2021	LO-L1B	0.180	0.045
			0.040
			0.040
08/17/2021	LO-L1S	0.176	0.038
			0.036
			0.034
08/17/2021	LO-L1B	0.203	0.034
			0.033
			0.031
09/13/2021	LO-L1S	0.133	0.004[I]
			0.003[I]
			0.004[I]
09/13/2021	LO-L1B	0.170	0.004[I]
			0.003[I]
			0.008[I]
10/11/2021	LO-L1S	0.126	0.006[I]
			0.009[I]
			0.005[I]
10/11/2021	LO-L1B	0.166	0.006[I]
			0.006[I]
			0.007[I]
11/08/2021	LO-L1S	0.173	0.053
			0.051
			0.052
11/08/2021	LO-L1B	0.193	0.053
			0.053
			0.052
12/13/2021	LO-L1S	0.258	0.134
			0.134
			0.134
12/13/2021	LO-L1B	0.303	0.133
			0.133
			0.132
01/26/2022	LO-L1S	0.447	0.280
			0.276
			0.276
01/26/2022	LO-L1B	0.445	0.246
			0.277
			0.275

[T] Below MDL
[I] Below PQL

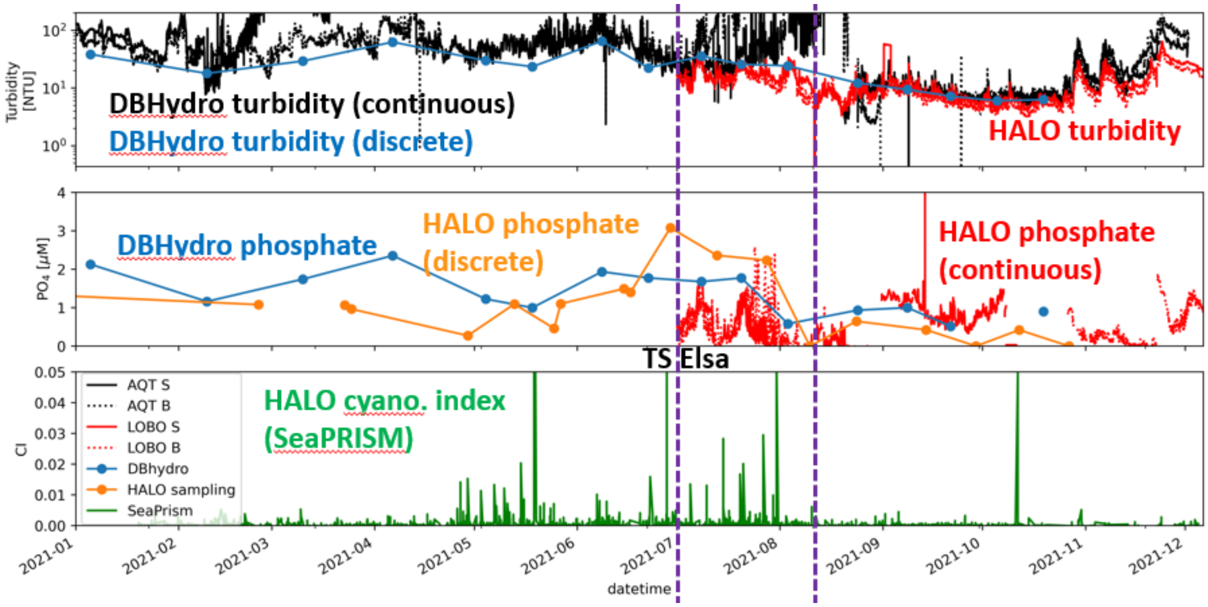

Figure 6-7: Time series of integrated HALO Task measurements demonstrating the specific decline of water column SRP associated with a strong turbidity event in late July 2021, which appeared to have led to the decline of M. aeruginosa surface scums at L001 as evidenced by the SeaPRISM (Task 5A).

CONCLUSIONS & FUTURE WORK

The IRLON BIP technology used in the Fixed Location Water Quality Monitoring in Lake Okeechobee provides research scientists and resource managers reliable, continuous environmental data to better quantify, model and predict the relationships between environmental factors and biological processes, specifically the cyanobacterial blooms that are causing concerns in the lake. The use of continuous environmental data such as those provided by this technology will enhance our ability to understand temporal and spatial variability in the lake's water quality. This high-frequency, continuous observatory data enable better quantification and modeling of relationships between environmental factors and biological processes, such as those reported elsewhere in other task results in this report (e.g. **Tasks 3, 4, & 5**). Should this task be continued in future HALO iterations, it would be highly desirable to purchase additional sensors so that there is a complete back up available, as the very long turnaround by the vendors for factory calibration, repair, and maintenance will otherwise lead to undesirable gaps in the continuous monitoring data. Lastly, the IRLON BIPs have been developed so that other environment or meteorological sensors can be added to the current package to extend/enhance the monitoring capabilities that were deployed in this project. Should this project be continued in the next year, the project team might wish to explore including other sensor capabilities to expand the environmental monitoring of Lake Okeechobee.

TASK 7B: HUMAN EXPOSURE MONITORING: AIR SAMPLING (TASK LEAD: PARSONS)

INTRODUCTION

The large cyanobacteria blooms that have plagued Lake Okeechobee and associated waterways in recent years have created aesthetic and health (human and animal) concerns. In particular, the cyanobacteria *M. aeruginosa* has been the problematic bloomer, creating large mats in the water and producing the cyanotoxin, microcystin – a known hepatotoxin. People have been exposed, sickened and even killed by microcystin (as have domestic and wild animals), leading the World Health Organization to establish exposure guidelines - concentrations >20 µg L^{-1} in recreational waters are considered to be “high risk” for acute health effects. While the water-borne threat of microcystin is well-established, the potential risk associated with air-borne exposure remains under-studied. The purpose of **Task 7B**, therefore, was to collect and analyze air samples during field-based studies to determine if, and to what extent, microcystins become air-borne/aerosolized above and in the vicinity of Lake Okeechobee. The primary sampling instrument used in **Task 7B** was an Andersen-style impactor air sampler, specifically the Tisch TE-20-800 cascade impactor sampler (Figure 7-1), which consists of seven size-fractionated stages that serve as a proxy for the human respiratory system. The two smallest stages (6 and 7) collect particles capable of entering the alveoli (< 1 um in size) and are therefore the most likely proxy for air-borne microcystins for entering the bloodstream.

METHODS

One Tisch air sampler was secured at the helm of the boat used for field sampling as part of **Task 2** for each of four sampling trips (February, March, April and June 2021). The pumps were run continuously during the field sampling (as the boat moved from station to station as part of **Task 2** activities), sampling air for approximately 3.5 to 4 hours (exact times provided in Table 7B-1). Two personal air samplers (Sensodyne BDX II units) were also deployed during June 2021 to test the efficacy of these units in these half-day field studies. At the end of each trip, the samplers were brought back to the laboratory at Florida Gulf Coast University and the filters were immediately transferred to appropriately labeled petri dishes and stored in a -20 ˚C freezer until analysis.

Approximately 25% of each filter was initially analyzed for microcystin content following previously established methods. Each filter was weighed, and a subsample (i.e., “pie wedge”) was cut and weighed to determine the exact proportion of the filter removed. The wedge was extracted in 80% ethanol and analyzed using Enzo ELISA test kits following the procedures outlined in the ENZO Product Manual for the Microcystins-ADDA Elisa (Catalog #: ALX-850-319). These initial analyses determined that the toxin content of each wedge was below the limit of quantification (0.15 ppb), resulting in extraction of the remaining portion of each filter (~75% of original filter) to improve detection and quantification limits. The ¾ filters were extracted and analyzed as above. Filter extracts remaining below 0.15 ppb were recorded as <0.15 ppb, and all filter concentrations of microcystin were converted to air volume equivalents using the following four steps.

First, microcystin concentrations were converted from ppb to ng/filter by multiplying the concentration (ppb) by the extract volume (2 mL) and the dilution factor (0.5), and dividing this value by the percentage of the filter extracted (approximately 75%; actual values provided in Table 7-1)., Then, pump flow rates (liters per minute) were averaged from T_0 and T_{end} and multiplied by the duration of time (minutes) the pumps were on and sampling air to determine the volume of air sampled (L). The average (integrated) microcystin concentration in the ambient air was then calculated by dividing the microcystin content per filter by the volume of air, and then multiplying by 1,000 to covert from L to m^3. Spike-recovery experiments indicated that an average of 52% of the microcystins on the filter could be extracted and quantified using the ELISA method. The concentration value above was therefore multiplied by the inverse of 0.521 (1.92) to estimate final integrated air concentrations reported as ng of microcystins m^{-3} air.

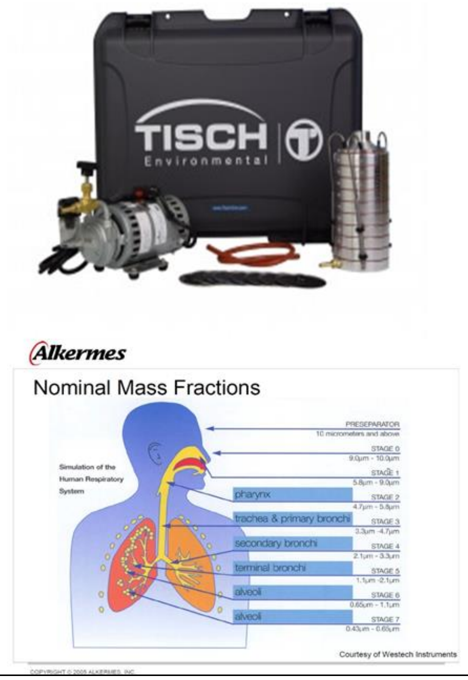

Figure 7C-1: Tisch Cascade Air Impactor used to collect bulk air samples as part of the HALO project (top). The eight stages in the air impactor size fractionate the particles sucked into the unit via a vacuum pump. Each stage represents a section of the human pulmonary system (bottom).

ACTIVITIES SCHEDULED vs. COMPLETED

Two sampling trips were planned (one non-bloom season and one bloom season), but four sampling events were conducted (three non-bloom season; one bloom season) in February, March, April and June, 2021. Air sampling was conducted for approximately 4 hours during each field sampling event (actual values provided in Table 7C-1). All QA/QC criteria established in the FDEP-approved QAPP were satisfied according to Enzo Product Manual criteria. Spike-recovery experiments resulted in recoveries ranging from 45.1 – 60.0% recovery, for an overall average of 52.1%. These values are within the range reported in other studies (45 – 80%; Lawton et al. 1994; Preece et al. 2015), but improvements are being pursued in order to lower limits of detection and quantification for future studies (most relevant for non-bloom conditions).

RESULTS & DISCUSSION

Out of the 37 samples analyzed (in replicate = 74 ELISA tests), only seven samples produced microcystin levels greater than the limit of quantification, defined here as the lowest non-zero standard concentration (0.15 ppb) calculated with respect to air volume equivalents and as indicated by the shaded cells in Table 7B-1. Three of these samples (401b, 408a, and 415b) had replicates that were below LOQ, indicating that replicate variability was influential in the results. As these are very low levels of microcystin, however, the significance of this variability is minimal (i.e., all values were in the vicinity of the LOQ; the overall general result is that microcystin concentrations were very low). As all samples had very low microcystin concentrations, no samples have yet been sent to GreenWater Labs for analysis. The original plan was to have GreenWater validate ELISA results using LC-MS/MS, but the concentrations of microcystins in these samples are too low for LC-MS/MS analysis. Validation will be better served during bloom events when microcystin levels are expected to be higher in the air.

Five out of the seven samples that were above the LOQ were from stages 0 and 1, which collect particles between 5.8 and 9 µm (stage 1) and between 9 and 10 µm (stage 0), equivalent to exposure at the surface of the nose/mouth (stage 0) or in the immediate oral/nasal cavity (stage 1). These samples would be comparable to nasal swab sampling if and when such studies are conducted (while originally planned, these analyses were removed from the scope of work due to loss of personnel). The remaining two samples were from stage 6 of sampler 415 and stage F of sampler 408 (Table 7B-1). Stage 6 collects particles ranging in size from 0.7 to 1.1 µm, representing the alveoli in the human lungs. The detection of microcystins in a stage 6 sample indicates that microcystins are associating with particles capable of reaching deep into the human lung and may be able to enter the bloodstream via the alveoli. The stage F sample is interesting in that this stage is ancillary (i.e., not associated with any size fraction of particles) and collects (some) particles that do not settle on the previous stages (0 through 7). Detection of microcystins was not expected on stage F, and this result may be because the air impactor was utilized on a moving boat (often on a plane; > 20 knots). This "high speed" may have disrupted the air flow over and into the impactor, disrupting the size fractionation process of the units.

Figure 7B-2: Miranda Barrington (research technician from FGCU) collects a bloom sample on Lake Okeechobee (photo courtesy of Mason Thackston, FAU).

Another interesting result that may also indicate interference caused by deploying the impactors on a moving boat is the lack of quantification of microcystin from samples analyzed from the April, 2021 survey. *M. aeruginosa* was blooming at the time (Figure 7B-2), but no samples resulted in concentrations greater than the LOQ. Alternatively, the bloom patches were only encountered for short periods of time

(<10 minutes generally; Barrington, pers. obs.), so an alternative explanation is that an inadequate amount of air was sampled when these patches were encountered.

The personal air samplers did not produce any results that were greater than the LOQ. Note that LOQ values were higher for the personal air samplers (~0.3 versus ~0.03) due to the lower volume of air the BDX II samplers would draw (2 lpm versus 28.3 lpm for the impactors). The LOQ values, however, are reasonable as discussed below.

CONCLUSIONS & FUTURE WORK

The results of this study produced four important findings: 1) microcystins could be detected using a boat platform; 2) airborne microcystin concentrations were low (~ 0.3 ng m^{-3}); 3) the movement of the boat may have disrupted air flow in the impactors (stage F results above); and 4) four-hour deployments appear to be adequate to provide "high resolution" sampling in the field (previous deployments ranged from 2 days to one month). The risk of exposure to airborne microcystins is poorly known. Based on WHO criteria for microcystins in drinking water (1 µg microcystin-LR), Wood and Dietrich (2011) calculated that an equivalent threshold for exposure to airborne toxins would be 4.58 ng m^{-3}. As the LOQ values in this study were ~0.03 and ~0.3 ng m^{-3} (impactors and personal air samplers, respectively), our approach clearly met this benchmark (i.e., our results did not reflect poor detection limits per se but instead reflect low microcystin concentrations measured over the course of this study. Patches of *M. aeruginosa* were observed during this study (e.g. **Task 2B & 4** results), but did not result in the measurement of "high" microcystin concentrations from the air. This observation could results from 1) the bloom was not large enough to elevate airborne microcystin concentrations; 2) the bloom/environmental conditions were not conducive to producing airborne microcystins; or 3) the boat-based approach disrupted air flow to the degree that the air was "under sampled" by the impactors (i.e., laminar flow over the impactor orifice may have over-powered flow into the impactor cavity/stages. The best way to address these possibilities would be to sample using the same approach during a large bloom event (such as 2018), and to conduct laboratory-based studies to examine conditions conducive to producing airborne microcystins (as other researchers are doing). Going forward, the new Amendment #3 **Task 13** work will deploy the aerosol samplers at a fixed-location on the Lake during extended time periods, but while still maintaining short time intervals to examine diurnal and storm/quiescent period-driven factors.

Table 7C-1: Summary of air sampling results conducted over the four sampling periods. The impactor data (SID # 401-428) are provided for stages and their replicates where at least one replicate had a microcystin concentration > than the limit of quantification (LOQ; shaded cells). Impactor minima, maxima and averages are given to provide information on the range of values for all stages impactors. The data for the personal pumps SID # 436 & 437) are shown for comparative purposes (microcystin concentrations were below LOQ).

SID #	Replicate	Sample	Impactor/ Pump #	Sampling Date	% filter extracted	Deployment Time (mins)	Flow Rate (lpm)	Air volume sampled (L)	ng m^{-3}	LOQ ng m^{-3}
401	a	Stage 0	795/FGCU#2	2/25/2021	76%	249	28.41	7074.09	0.027	0.028
401	b	Stage 0	795/FGCU#2	2/25/2021	76%	249	28.41	7074.09	0.036	0.028
408	a	Stage F	795/FGCU#2	2/25/2021	78%	249	28.41	7074.09	0.032	0.027
408	b	Stage F	795/FGCU#2	2/25/2021	78%	249	28.41	7074.09	0.019	0.027
415	a	Stage 6	795/FGCU#2	3/25/2021	75%	225	29.07	6540.75	0.024	0.030
415	b	Stage 6	795/FGCU#2	3/25/2021	75%	225	29.07	6540.75	0.032	0.030
427	a	Stage 0	794/FGCU#1	6/29/2021	100%	222	28.88	6411.36	0.047	0.023
427	b	Stage 0	794/FGCU#1	6/29/2021	100%	222	28.88	6411.36	0.034	0.023
428	b	Stage 1	794/FGCU#1	6/29/2021	100%	222	28.88	6411.36	0.024	0.023
428	a	Stage 1	794/FGCU#1	6/29/2021	100%	222	28.88	6411.36	0.026	0.023
436	a	filter	PP#3	6/29/2021	100%	219	2.01	439.31	0.157	0.341
436	b	filter	PP#3	6/29/2021	100%	219	2.01	439.31	0.135	0.341
437	a	filter	PP#5	6/29/2021	100%	167	2.01	335.67	0.184	0.447
437	b	filter	PP#5	6/29/2021	100%	167	2.01	335.67	0.184	0.447
impactor minimum					73%	222	28.41	6411.36	0.008	0.023
impactor maximum					100%	249	29.58	7074.09	0.047	0.031
impactor stage average					82%	233.3	29.00	6765.38	0.021	0.027

TASK 7C: INTEGRATED WATER COLUMN ALGAL TOXINS (TASK LEAD: MCFARLAND)

INTRODUCTION

Solid Phase Adsorption Toxin Tracking (SPATT) uses a porous hydrophobic resin to passively adsorb toxins produced by harmful algal blooms (Roue et al. 2018). Resin packets are deployed within water bodies for periods of days to weeks. Upon recovery, toxins can then be extracted from the resin and quantified to determine an integrated toxin adsorption rate over the entire deployment period. We employed SPATT technology in Lake Okeechobee to assess variability of microcystin concentrations among sites and over time during the 2021 bloom season. This technique provides both advantages and disadvantages to discrete toxin sampling/analyses (e.g. Task 2B). While there is a greater probability of detecting transient toxins, including lesser-studied/sampled toxins from species other than *M. aeruginosa*, it is not possible to pinpoint the occurrence to a single time point and is more difficult to extrapolate an in-water concentration. However, instead of targeting "blindly" those toxins with an unknown presence, SPATT bags are a more cost-effective approach to evaluating the likelihood of detecting these emerging problem HAB species/toxins, with follow-up studies then focused on targeting these toxins at improved temporal resolution sampling.

METHODS

Bags of SPATT resin were deployed at sites L001, L005, LZ40, and L006 for two week periods from May 13 to October 27, 2021. SPATT bags were attached to SFWMD platforms at these sites and submerged below the water surface on a weighted line. Once SPATT bags were recovered, they were kept in zip lock bags and frozen until toxin extractions took place approximately every two to three sampling events. Extractions were performed by column chromatography according to methods described by Howard et al. (2018). Steps include first pipetting methanol through chromatography columns containing resin from SPATT bags, then collecting samples in scintillation vials and keeping them in the dark at < -4 ºC. The extraction method used 50% MeOH, where three consecutive extractions took place for each bag: one with 10mL of MeOH and two with 20mL of MeOH. After extraction, the resin was left to dry and was weighed to normalize toxin concentrations per gram of resin. Microcystin concentrations were measured with ELISA kits (Microcystins-ADDA SAES, Abraxis LLC, Warminster, PA #520011SAES) according to the manufacturer's instructions.

ACTIVITIES SCHEDULED vs COMPLETED

Two-week deployments at 4 sites were planned to cover the bloom season between May and October, 2021. All bags were deployed in according to this schedule but not all bags were recovered. Of the 44 total deployed bags, 26 were recovered. The remainder were missing upon recovery, presumably having become detached due to wave action or other physical disturbance (being a "soft" device, adhesion is non-trivial issue). Nine SPATT bags were recovered from site L001 while only three were recovered from site L005 (Table 7C-1). All recovered SPATT bags were analyzed to determine microcystin adsorption rates as planned.

RESULTS & DISCUSSION

Microcystin adsorption rates per week varied between 5.28 and 233.6 µg toxin per gram of resin (Table 7C-1, Figure 7C-1). Site LZ40 had the highest measured adsorption rate as well as the highest average adsorption rate over the course of the study. Site L005 had the lowest average adsorption rate but only three SPATT bags were recovered. Variation within sites over time was comparable to variation among sites throughout the lake.

Table 7C-1: Concentrations of micrograms microcystins per gram of resin for each 2-week deployment period, per week, and per day of each deployment.

Deployment date	Sites	Integrated Toxin Concentration	Concentration per week	Concentration per day
13-May	LZ40	229.90	114.95	16.42
13-May	L001	159.37	79.68	11.38
27-May	LZ40	242.99	121.50	17.36
27-May	L001	293.78	146.89	20.98
29-Jun	LZ40	194.67	97.34	13.91
29-Jun	L001	174.41	87.21	12.46
29-Jun	L005	67.53	33.77	4.82
29-Jun	L006	10.55	5.28	0.75
13-Jul	L001	205.36	102.68	14.67
28-Jul	L001	220.13	110.07	15.72
28-Jul	L006	240.83	120.42	17.20
10-Aug	LZ40	181.10	90.55	12.94
10-Aug	L001	282.93	141.46	20.21
10-Aug	L006	194.42	97.21	13.89
24-Aug	LZ40	134.91	67.45	9.64
24-Aug	L001	37.14	18.57	2.65
24-Aug	L005	66.50	33.25	4.75
24-Aug	L006	93.16	46.58	6.65
14-Sep	L001	54.67	27.33	3.90
14-Sep	L005	60.51	30.25	4.32
14-Sep	L006	11.22	5.61	0.80
29-Sep	L001	131.32	65.66	9.38
29-Sep	LZ40	467.18	233.59	33.37
12-Oct	L006	309.33	154.67	22.10
12-Oct	LZ40	13.15	6.57	0.94
27-Oct	LZ40	12.60	6.30	0.90

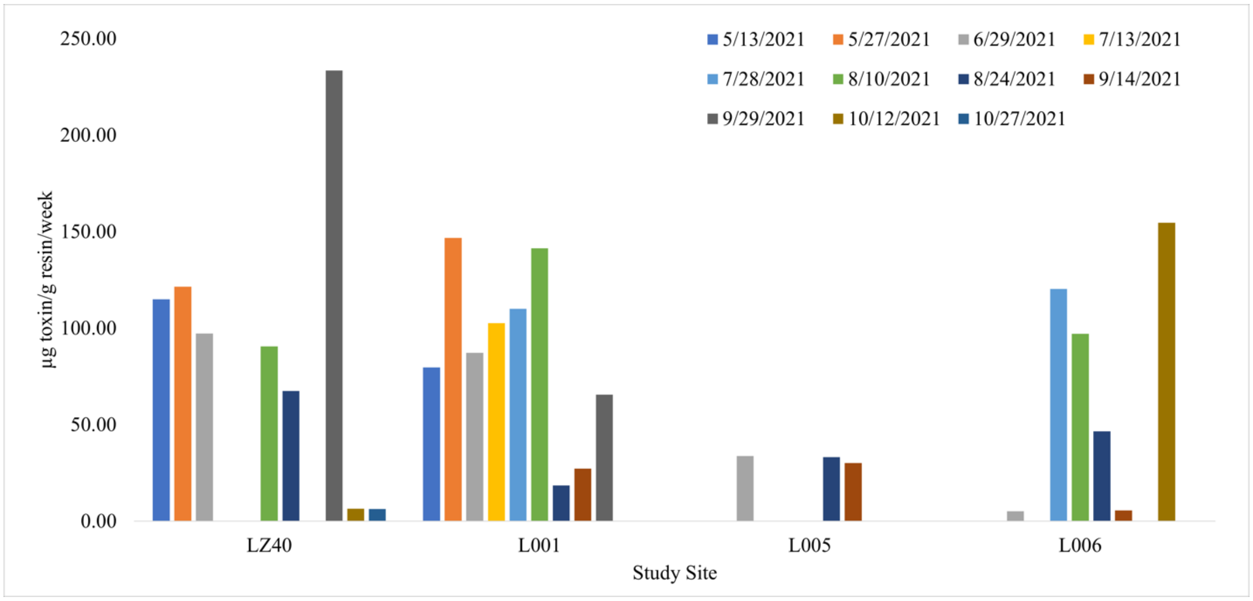

Figure 7C-1: Amounts of microcystins adsorbed to SPATT bags per gram of resin and per week of deployment.

CONCLUSIONS & FUTURE WORK

SPATT technology proved effective at assessing microcystin dynamics in Lake Okeechobee revealing high total loads of this toxin throughout the lake. Although variability among deployments was high, no temporal trends were identifiable at any of the monitored sites within the context of this task only. This is reflective of the patchy nature of *M. aeruginosa* blooms which can be concentrated in a small area and move rapidly from one region to another depending on wind and weather conditions. No consistent spatial trends were identifiable in the data except for at site L005 in the western portion of the lake where toxin adsorption rates appeared to be lower. However, the low SPATT bag recovery rate at this site reduces confidence in this result. This task data is undergoing interpretation into the other task results (e.g. Tasks 2, 4, 5, 6, & 7B), with the most obvious example being the direct comparison of the integrated toxins from this task with discrete in-water toxins measured from **Task 2**. Anecdotally, the L001 integrated toxins appear to match the toxin results (most easily visualized via comparison to Figure 3A-16. Overall, the cost-effective SPATT technology, shown to be effective here, may be even more useful in Lake Okeechobee during the winter, non-bloom season when toxin concentrations are generally below detectable levels. The technique can be more sensitive and detect lower concentrations of toxins than traditional water sample-based analyses.

REFERENCES

Anderson, H. S., Johengen, T. H., Godwin, C. M., Purcell, H., Alsip, P. J., Ruberg, S. A., & Mason, L. A. (2021). Continuous In Situ Nutrient Analyzers Pinpoint the Onset and Rate of Internal P Loading under Anoxia in Lake Erie's Central Basin . *ACS ES&T Water*. https://doi.org/10.1021/acsestwater.0c00138

Arar, E.J., Collins, G.B., 1997. Method 445.0: In vitro determination of chlorophyll *a* and pheophytin a in marine and freshwater algae by fluorescence. United States Environmental Protection Agency, Office of Research and Development. Cincinnati, OH.

Babica, P., Kohoutek, J., Bláha, L., Adamovský, O., & Maršálek, B. (2006). Evaluation of extraction approaches linked to ELISA and HPLC for analyses of microcystin-LR, -RR and -YR in freshwater sediments with different organic material contents. *Analytical and Bioanalytical Chemistry*, *385*(8), 1545–1551. https://doi.org/10.1007/s00216-006-0545-8

Baker JA, Neilan BA, Entsch B, Mckay DB (2001) Identification of cyanobacteria and their toxigenicity in environmental samples by rapid molecular analysis. Environmental Toxicology 16:472 482.

Bailey, S., Franz, B., and Werdell, P. (2010). Estimation of near-infrared water-leaving reflectance for satellite ocean color data processing. *Optics Express*, 18:7521–7527.

Bailey, S. and Werdell, P. (2006). A multi-sensor approach for the on-orbit validation of ocean color satellite data products. *Remote Sensing of Environment*, 102:12–23

Beckler, J. S., Jones, M. E., & Taillefert, M. (2015). The origin, composition, and reactivity of dissolved iron(III) complexes in coastal organic- and iron-rich sediments. *Geochimica et Cosmochimica Acta*, *152*, 72–88. https://doi.org/10.1016/j.gca.2014.12.017

Beckler, J. S., Arutunian, E., Moore, T., Currier, B., Milbrandt, E., & Duncan, S. (2019). Coastal Harmful Algae Bloom Monitoring via a Sustainable, Sail-Powered Mobile Platform. *Frontiers in Marine Science*, *6*, 587. https://doi.org/10.3389/fmars.2019.00587

Bouchard, J.N., Purdie, D.A., 2011. Effect of Elevated Temperature, Darkness, and Hydrogen Peroxide Treatment on Oxidative Stress and Cell Death in the Bloom-Forming Toxic Cyanobacterium Microcystis Aeruginosa1. Journal of Phycology 47, 1316–1325. https://doi.org/10.1111/j.1529-8817.2011.01074.x

Boudreau, B. P. (1997). *Diagenetic models and their implementation.* Springer.

Bower, C. E., & Holm-Hansen, T. (1980). A Salicylate–Hypochlorite Method for Determining Ammonia in Seawater. *Canadian Journal of Fisheries and Aquatic Sciences*, *37*(5), 794–798. https://doi.org/10.1139/f80-106

Burdige, D. J., & Zheng, S. (1998). The biogeochemical cycling of dissolved organic nitrogen in estuarine sediments. *Limnology and Oceanography*, *43*(8), 1796–1813. https://doi.org/10.4319/lo.1998.43.8.1796

Brendel, P. J., & Luther, G. W. (1995). Development of a Gold Amalgam Voltammetric Microelectrode for the Determination of Dissolved Fe, Mn, O2, and S(-II) in Porewaters of Marine and Freshwater Sediments. *Environmental Science and Technology*, *29*(3), 751–761. https://doi.org/10.1021/es00003a024

Brezonik, P. L., & Engstrom, D. R. (1998). Modern and historic accumulation rates of phosphorus in Lake Okeechobee, Florida. *Journal of Paleolimnology*, *20*(1), 31–46. https://doi.org/10.1023/A:1007939714301

Bristow, G., & Taillefert, M. (2008). VOLTINT: A Matlab®-based program for semi-automated processing of geochemical data acquired by voltammetry. *Computers & Geosciences*, *34*(2), 153–162. https://doi.org/10.1016/J.CAGEO.2007.01.005

Brunberg, A.-K., Blomqvist, P., 2003. Recruitment of Microcystis (cyanophyceae) from Lake Sediments: The Importance of Littoral Inocula. Journal of Phycology 39, 58–63. https://doi.org/10.1046/j.1529-8817.2003.02059.x

Buffle, J. (Jacques), & Horvai, G. (2000). *In-situ monitoring of aquatic systems : chemical analysis and speciation*. Wiley. http://old.iupac.org/publications/books/author/buffle.html

Carey CC, Ibelings BW, Hoffmann EP, Hamilton DP, Brookes JD (2012) Eco-physiological adaptations that favour freshwater cyanobacteria in a changing climate. Water Research 46:1394 1407.

Carmichael WW (2001) Health Effects of Toxin-Producing Canobacteria: "The CyanoHABs" Human and Ecological Risk Assessment: An International Journal 7:1393 1407.

Chapman, I.J., Esteban, G.F., Franklin, D.J., 2016. Molecular Probe Optimization to Determine Cell Mortality in a Photosynthetic Organism (Microcystis aeruginosa) Using Flow Cytometry. J Vis Exp. https://doi.org/10.3791/53036

Chen, W., Li, L., Gan, N., & Song, L. (2006). Optimization of an effective extraction procedure for the analysis of microcystins in soils and lake sediments. *Environmental Pollution*, *143*(2), 241–246. https://doi.org/10.1016/J.ENVPOL.2005.11.030

Chen, X., Yang, X., Yang, L., Xiao, B., Wu, X., Wang, J., & Wan, H. (2010). An effective pathway for the removal of microcystin LR via anoxic biodegradation in lake sediments. *Water Research*, *44*(6), 1884–1892. https://doi.org/10.1016/j.watres.2009.11.025

Couceiro, F., Fones, G. R., Thompson, C. E. L., Statham, P. J., Sivyer, D. B., Parker, R., Kelly-Gerreyn, B. A., & Amos, C. L. (2013). Impact of resuspension of cohesive sediments at the Oyster Grounds (North Sea) on nutrient exchange across the sediment–water interface. *Biogeochemistry*, *113*(1–3), 37–52. https://doi.org/10.1007/s10533-012-9710-7

Cox PA, Banack SA, Murch SJ (2003) Biomagnification of cyanobacterial neurotoxins and neurodegenerative disease among the Chamorro people of Guam. PNAS 100:13380 13383.

Cox PA, Banack SA, Murch SJ, Rasmussen U, Tien G, Bidigare RR, Metcalf JS, Morrison LF, Codd GA, Bergman B (2005) Diverse taxa of cyanobacteria produce B-N-methylamino-l-alanine, a neurotoxic amino acid. PNAS 102:5074 5078.

Davis TW, Berry DL, Boyer GL, Gobler CJ (2009) The effects of temperature and nutrients on the growth and dynamics of toxic and non-toxic strains of Microcystis during cyanobacteria blooms. Harmful Algae 8:715 725.

Dawson RM (1998) The toxicology of microcystins. Toxicon 36:953 962.

Dogliotti, A., Ruddick, K., Nechad, B., Doxaran, D., and Knaeps, E. (2015). A single algorithm to retrieve turbidity from remotely-sensed data in all coastal and estuarine waters. *Remote Sensing of Environment*, 156:157–168

Eitel, E. M., & Taillefert, M. (2017). Mechanistic investigation of Fe (III) oxide reduction by low molecular weight organic sulfur species. *Geochimica Et Cosmochimica Acta*, *215*, 173–188.

Fennel, K., Wilkin, J., Levin, J., Moisan, J., O'Reilly, J., & Haidvogel, D. (2006). Nitrogen cycling in the Middle Atlantic Bight: Results from a three-dimensional model and implications for the North Atlantic nitrogen budget. *Global Biogeochemical Cycles*, *20*(3), n/a-n/a. https://doi.org/10.1029/2005GB002456

Fisher, M. M., Reddy, K. R., & James, R. T. (2001). Long-Term Changes in the Sediment Chemistry of a Large Shallow Subtropical Lake. *Lake and Reservoir Management*, *17*(3), 217–232. https://doi.org/10.1080/07438140109354132

Fisher, M. M., Reddy, K. R., & James, R. T. (2005). Internal Nutrient Loads from Sediments in a Shallow, Subtropical Lake. *Lake and Reservoir Management*, *21*(3), 338–349. https://doi.org/10.1080/07438140509354439

Fujimoto N, Sudo R, Sugiura N, Inamori Y (1997) Nutrient-limited growth of Microcystis aeruginosa and Phormidium tenue and competition under various N:P supply ratios and temperatures. Limnology and Oceanography 42:250 256.

Geary, S., Ganf, G., Brookes, J., 1998. The use of FDA and flow cytometry to measure the metabolic activity of the cyanobacteria, Microcystis aeruginosa. Internationale Vereinigung für theoretische und angewandte Limnologie: Verhandlungen 26, 2367–2369.

Gorbunov, M.Y., Shirsin, E., Nikonova, E., Fadeev, V.V., Falkowski, P.G., 2020. A multi-spectral fluorescence induction and relaxation (FIRe) technique for physiological and taxonomic analysis of phytoplankton communities. Marine Ecology Progress Series 644, 1–13. https://doi.org/10.3354/meps13358

Gould, R.W., Arnone, R.A., Sydor, M., 2001. Absorption, Scattering, and, Remote-Sensing Reflectance Relationships in Coastal Waters: Testing a New Inversion Algorithm. Journal of Coastal Research 17, 328–341.

Grützmacher, G., Wessel, G., Klitzke, S., & Chorus, I. (2010). Microcystin elimination during sediment contact. *Environmental Science & Technology*, *44*(2), 657–662.

Holst, T., Jørgensen, N. O. ., Jørgensen, C., & Johansen, A. (2003). Degradation of microcystin in sediments at oxic and anoxic, denitrifying conditions. *Water Research*, *37*(19), 4748–4760. https://doi.org/10.1016/S0043-1354(03)00413-5

Homma T, Komatsu N, Negishi M, Katagami Y, Nakamura K, Park HD (2008) Influence of dissolved inorganic nitrogen and phosphorus concentrations on the horizontal and temporal changes of Microcystis population in lake. In: Proceedings of Taal2007: The 12th World Lake Conference. p 1429

Houghton JT, Ding Y, Griggs DJ, Noguer M, van der Linden PJ, Dai X, Maskell K, Johnson CA (2001) Climate change 2001: the scientific basis. The Press Syndicate of the University of Cambridge.

Howard, M.D.A., Kudela, R., Caron, D., Smith, J., Hayashi, K., 2018. Standard Operating Procedure for Solid Phase Adsorption Toxin Testing (SPATT) Assemblage and Extraction of HAB Toxins. (Report). University of California and University of Southern California. https://doi.org/10.17504/protocols.io.xkpfkvn

Hudnell HK, Dortch Q (2008) A Synopsis of Research Needs Identified at the Interagency, International Symposium on Cyanobacterial Harmful Algal Blooms (ISOC-HAB). In: Cyanobacterial Harmful Algal Blooms: State of the Science and Research Needs. Advances in Experimental Medicine and Biology, Hudnell HK (ed) Springer New York, p 17 43

Integrated Ocean Observing System. (2022). *IOOS Metadata Profile Version 1.2*. Retrieved April 15, 2022, from https://ioos.github.io/ioos-metadata/ioos-metadata-profile-v1-2.html

Jiang, **M.S.,** David Townsend, M. Zhou, D. Borkman, and S. Libby, 2014, Nutrient inputs and the competition between diatoms and Phaeocystis in Massachusetts Bay spring bloom, Journal of Marine Systems. 134, 29–44.

Jin, K.-R., & Ji, Z.-G. (2004). Case Study: Modeling of Sediment Transport and Wind-Wave Impact in Lake Okeechobee. *Journal of Hydraulic Engineering*, *130*(11), 1055–1067. https://doi.org/10.1061/(ASCE)0733-9429(2004)130:11(1055)

Jin, K.-R., Ji, Z.-G., & Hamrick, J. H. (2002). Modeling Winter Circulation in Lake Okeechobee, Florida. *Journal of Waterway, Port, Coastal, and Ocean Engineering*, *128*(3), 114–125. https://doi.org/10.1061/(asce)0733-950x(2002)128:3(114)

Jin, K.-R., & Sun, D. (2007). Sediment Resuspension and Hydrodynamics in Lake Okeechobee during the Late Summer. *Journal of Engineering Mechanics*, *133*(8), 899–910. https://doi.org/10.1061/(ASCE)0733-9399(2007)133:8(899)

Kaebernick M, Neilan BA (2001) Ecological and molecular investigations of cyanotoxin production. FEMS Microbiology Ecology 35:1 9.

Kalnejais, L. H., Martin, W. R., & Bothner, M. H. (2010). The release of dissolved nutrients and metals from coastal sediments due to resuspension. *Marine Chemistry*, *121*(1–4), 224–235. https://doi.org/10.1016/J.MARCHEM.2010.05.002

Kitchens, C.M., Johengen, T.H., Davis, T.W., 2018. Establishing spatial and temporal patterns in Microcystis sediment seed stock viability and their relationship to subsequent bloom development in Western Lake Erie. PLOS ONE 13, e0206821. https://doi.org/10.1371/journal.pone.0206821

Kononets, M., Tengberg, A., Nilsson, M., Ekeroth, N., Hylén, A., Robertson, E. K., Van De Velde, S., Bonaglia, S., Rütting, T., & Blomqvist, S. (2021). In situ incubations with the Gothenburg benthic chamber landers: Applications and quality control. *Journal of Marine Systems*, *214*, 103475.

Kostka, J. E., & Luther, G. W. (1994). Partitioning and speciation of solid phase iron in saltmarsh sediments. *Geochimica et Cosmochimica Acta*, *58*(7), 1701–1710. https://doi.org/10.1016/0016-7037(94)90531-2

Lapointe BE, Herren LW, Bedford BJ (2012) Effects of Hurricanes, Land Use, and Water Management on Nutrient and Microbial Pollution: St. Lucie Estuary, Southeast Florida. Journal of Coastal Research:1345 1361.

Lawton, L.A., Edwards, C. and Codd, G.A., 1994. Extraction and high-performance liquid chromatographic method for the determination of microcystins in raw and treated waters. *Analyst*, *119*(7), pp.1525-1530.

Lehman PW, Marr K, Boyer GL, Acuna S, Teh SJ (2013) Long-term trends and causal factors associated with Microcystis abundance and toxicity in San Francisco Estuary and implications for climate change impacts. Hydrobiologia 718:141 158.

Liang, D., Li, N., An, J., Ma, J., Wu, Y., & Liu, H. (2021). Fenton-based technologies as efficient advanced oxidation processes for microcystin-LR degradation. *Science of The Total Environment*, *753*, 141809. https://doi.org/10.1016/J.SCITOTENV.2020.141809

Liu X, Lu X, Chen Y (2011) The effects of temperature and nutrient ratios on Microcystis blooms in Lake Taihu, China: An 11-year investigation. Harmful Algae 10:337 343.

Luther, G. W., Glazer, B. T., Ma, S., Trouwborst, R. E., Moore, T. S., Metzger, E., Kraiya, C., Waite, T. J., Druschel, G., Sundby, B., Taillefert, M., Nuzzio, D. B., Shank, T. M., Lewis, B. L., & Brendel, P. J. (2008). Use of voltammetric solid-state (micro)electrodes for studying biogeochemical processes: Laboratory measurements to real time measurements with an in situ electrochemical analyzer (ISEA). *Marine Chemistry*, *108*(3–4), 221–235. https://doi.org/10.1016/J.MARCHEM.2007.03.002

Marie, D., Simon, N., Vaulot, D., 2005. Phytoplankton cell counting by flow cytometry, in: Algal Culturing Techniques. Elsevier Academic Press, pp. 253–267.

Meiggs, D., & Taillefert, M. (2011). The effect of riverine discharge on biogeochemical processes in estuarine sediments. *Limnology and Oceanography*, *56*(5), 1797–1810. https://doi.org/10.4319/lo.2011.56.5.1797

Michalak, A. M., Anderson, E. J., Beletsky, D., Boland, S., Bosch, N. S., Bridgeman, T. B., Chaffin, J. D., Cho, K., Confesor, R., Daloğlu, I., DePinto, J. V., Evans, M. A., Fahnenstiel, G. L., He, L., Ho, J. C., Jenkins, L., Johengen, T. H., Kuo, K. C., LaPorte, E., … Zagorski, M. A. (2013). Record-setting algal bloom in Lake Erie caused by agricultural and meteorological trends consistent with expected future conditions. *Proceedings of the National Academy of Sciences*, *110*(16), 6448–6452. https://doi.org/10.1073/pnas.1216006110

Mikula, P., Zezulka, S., Jancula, D., Marsalek, B., 2012. Metabolic activity and membrane integrity changes in Microcystis aeruginosa – new findings on hydrogen peroxide toxicity in cyanobacteria. European Journal of Phycology 47, 195–206. https://doi.org/10.1080/09670262.2012.687144

Miller MA, Kudela RM, Mekebri A, Crane D, Oates SC, Tinker MT, Staedler M, Miller WA, Toy-Choutka S, Dominik C, Hardin D, Langlois G, Murray M, Ward K, Jessup DA (2010) Evidence for a Novel Marine Harmful Algal Bloom: Cyanotoxin (Microcystin) Transfer from Land to Sea Otters. PLOS ONE 5:e12576.

Missimer, T. M., Thomas, S., & Rosen, B. H. (2020). Legacy Phosphorus in Lake Okeechobee (Florida, USA) Sediments: A Review and New Perspective. *Water*, *13*(1), 39. https://doi.org/10.3390/w13010039

Moore, P. A., Reddy, K. R., & Fisher, M. M. (1998). Phosphorus Flux between Sediment and Overlying Water in Lake Okeechobee, Florida: Spatial and Temporal Variations. *Journal of Environmental Quality*, *27*(6), 1428–1439. https://doi.org/10.2134/jeq1998.00472425002700060020x

Moore, T. S., Mouw, C. B., Sullivan, J. M., Twardowski, M. S., Burtner, A. M., Ciochetto, A. B., McFarland, M. N., Nayak, A. R., Paladino, D., Stockley, N. D., Johengen, T. H., Yu, A. W., Ruberg, S., & Weidemann, A. (2017). Bio-optical Properties of Cyanobacteria Blooms in Western Lake Erie. *Frontiers in Marine Science*, *4*, 300. https://doi.org/10.3389/fmars.2017.00300

Nair, V. D., & Graetz, D. A. (2002). Phosphorus Saturation in Spodosols Impacted by Manure. *Journal of Environmental Quality*, *31*(4), 1279–1285. https://doi.org/10.2134/jeq2002.1279

Paerl HW (1988) Nuisance phytoplankton blooms in coastal, estuarine, and inland waters. Limnology and Oceanography 33:823 843.

Paerl HW, Huisman J (2009) Climate change: a catalyst for global expansion of harmful cyanobacterial blooms. Environmental Microbiology Reports 1:27 37.

Peretyazhko, T., & Sposito, G. (2005). Iron(III) reduction and phosphorous solubilization in humid tropical forest soils. *Geochimica et Cosmochimica Acta*, *69*(14), 3643–3652. https://doi.org/10.1016/J.GCA.2005.03.045

Preece, E.P., Moore, B.C., Swanson, M.E. and Hardy, F.J., 2015. Identifying best methods for routine ELISA detection of microcystin in seafood. *Environmental monitoring and assessment*, *187*(2), pp.1-10.

Quinan, M., Vazco, C., & Beckler, J. (2022). Efficient anaerobic sediment processing via a novel sediment core extruder. *MethodsX*, *9*, 101664. https://doi.org/10.1016/J.MEX.2022.101664

Reddy, K. R., Fisher, M. M., Wang, Y., White, J. R., & James, R. T. (2007). Potential effects of sediment dredging on internal phosphorus loading in a shallow, subtropical lake. *Lake and Reservoir Management*, *23*(1), 27–38.

Ross C, Santiago-V zquez L, Paul V (2006) Toxin release in response to oxidative stress and programmed cell death in the cyanobacterium Microcystis aeruginosa. Aquatic Toxicology 78:66 73.

Roué, M., Darius, H.T., Chinain, M., 2018. Solid Phase Adsorption Toxin Tracking (SPATT) Technology for the Monitoring of Aquatic Toxins: A Review. Toxins (Basel) 10. https://doi.org/10.3390/toxins10040167

Rozan, T. F., Taillefert, M., Trouwborst, R. E., Glazer, B. T., Ma, S., Herszage, J., Valdes, L. M., Price, K. S., & Luther III, G. W. (2002). Iron-sulfur-phosphorus cycling in the sediments of a shallow coastal bay: Implications for sediment nutrient release and benthic macroalgal blooms. *Limnology and Oceanography*, *47*(5), 1346–1354. https://doi.org/10.4319/lo.2002.47.5.1346

Ruddick, K., Ovidio, F., and Rijkeboer, M. (2000). Atmospheric correction of SeaWiFS imagery for turbid coastal and inland waters. *Applied Optics*, 39:897912.

Ruddick, K., Cauwer, V. D., and Park, Y. J. (2006). Seaborne measurements of near infrared water-leaving reflectance: the similarity spectrum for turbid waters. *Limnology and Oceanography*, 51:1167-1179

Rozan, T. F., Taillefert, M., Trouwborst, R. E., Glazer, B. T., Ma, S., Herszage, J., Valdes, L. M., Price, K. S., & Luther III, G. W. (2002). Iron-sulfur-phosphorus cycling in the sediments of a shallow coastal bay: Implications for sediment nutrient release and benthic macroalgal blooms. *Limnology and Oceanography*, *47*(5), 1346–1354. https://doi.org/10.4319/lo.2002.47.5.1346

Steinmetz, F., Deschamps, P.-Y., and Ramon, D. (2011). Atmospheric correction in presence of sun glint: application to MERIS. *Optics Express*, 19:9783–9800

Smith, L., Watzin, M. C., & Druschel, G. (2011). Relating sediment phosphorus mobility to seasonal and diel redox fluctuations at the sediment–water interface in a eutrophic freshwater lake. *Limnology and Oceanography*, *56*(6), 2251–2264. https://doi.org/10.4319/lo.2011.56.6.2251

Stookey, L. L. (1970). Ferrozine---a new spectrophotometric reagent for iron. *Analytical Chemistry*, *42*(7), 779–781. https://doi.org/10.1021/ac60289a016

Strickland, J., & Parsons, T. (1972). *A practical handbook of seawater analysis*. Fisheries Research Board of Canada.

Sullivan, J.M., Twardowski, M.S., Zaneveld, J.R.V., Moore, C.C., 2013. Measuring optical backscattering in water, in: Kokhanovsky, A.A. (Ed.), Light Scattering Reviews 7, Springer Praxis Books. Springer Berlin Heidelberg, pp. 189–224.

Taillefert, M., Beckler, J. S., Carey, E., Burns, J. L., Fennessey, C. M., & DiChristina, T. J. (2007). Shewanella putrefaciens produces an Fe (III)-solubilizing organic ligand during anaerobic respiration on insoluble Fe (III) oxides. *Journal of Inorganic Biochemistry*, *101*(11–12), 1760–1767.

Taillefert, M., Bono, A. B., & Luther, G. W. (2000). Reactivity of freshly formed Fe(III) in synthetic solutions and (pore)waters: Voltammetric evidence of an aging process. *Environmental Science and Technology*, *34*(11), 2169–2177. https://doi.org/10.1021/es990120a

Tengberg, A., De Bovee, F., Hall, P., Berelson, W., Chadwick, D., Ciceri, G., Crassous, P., Devol, A., Emerson, S., & Gage, J. (1995). Benthic chamber and profiling landers in oceanography—a review of design, technical solutions and functioning. *Progress in Oceanography*, *35*(3), 253–294.

Tsukada, H., Tsujimura, S., & Nakahara, H. (2006). Effect of nutrient availability on the C, N, and P elemental ratios in the cyanobacterium Microcystis aeruginosa. *Limnology*, *7*(3), 185–192. https://doi.org/10.1007/s10201-006-0188-7

Theberge, S. M., & Luther, G. W. (1997). Determination of the Electrochemical Properties of a Soluble Aqueous FeS Species Present in Sulfidic Solutions. *Aquatic Geochemistry*, *3*(3), 191–211. https://doi.org/10.1023/A:1009648026806

Tsujimura, S., Tsukada, H., Nakahara, H., Nakajima, T., Nishino, M., 2000. Seasonal variations of Microcystis populations in sediments of Lake Biwa, Japan. Hydrobiologia 434, 183–192. https://doi.org/10.1023/A:1004077225916

UCAR Community Programs. (2022). *Network Common Data Form (NetCDF)*. Unidata Sata Services and Tools for Geoscience. Retrieved April 15, 2022, from https://www.unidata.ucar.edu/software/netcdf/

Urquhart, E. A., Schaeffer, B. A., Stumpf, R. P., Loftin, K. A., & Werdell, P. J. (2017). A method for examining temporal changes in cyanobacterial harmful algal bloom spatial extent using satellite remote sensing. *Harmful Algae*, *67*, 144–152. https://doi.org/10.1016/J.HAL.2017.06.001

Viollier, E., Inglett, P. ., Hunter, K., Roychoudhury, A. ., & Van Cappellen, P. (2000). The ferrozine method revisited: Fe(II)/Fe(III) determination in natural waters. *Applied Geochemistry*, *15*(6), 785–790. https://doi.org/10.1016/S0883-2927(99)00097-9

Warner, J.C., W.R. Geyer,and J.A. Lerczak, 2005, Numerical modeling of an estuary: A comprehensive skill assessment, Journal of Geophysical Research C: Oceans, 110(C5), 1-13, 10.1029/2004JC002691.

Wells, M. L., Trainer, V. L., Smayda, T. J., Karlson, B. S. O., Trick, C. G., Kudela, R. M., Ishikawa, A., Bernard, S., Wulff, A., Anderson, D. M., & Cochlan, W. P. (2015). Harmful algal blooms and climate change: Learning from the past and present to forecast the future. *Harmful Algae*, *49*, 68–93. https://doi.org/10.1016/J.HAL.2015.07.009

Wood, S.A. and Dietrich, D.R., 2011. Quantitative assessment of aerosolized cyanobacterial toxins at two New Zealand lakes. *Journal of Environmental Monitoring*, *13*(6), pp.1617-1624.

Wynne, T., Stumpf, R., Tomlinson, M., Warner, R., Tester, P., Dyble, J., and Fahnenstiel, G. (2008). Relating spectral shape to cyanobacterial blooms in the Laurentian Great Lakes. *International Journal of Remote Sensing*, 29:3665–3672

Xiao, X., Han, Z., Chen, Y., Liang, X., Li, H., Qian, Y., 2011. Optimization of FDA–PI method using flow cytometry to measure metabolic activity of the cyanobacteria, Microcystis aeruginosa. Physics and Chemistry of the Earth, Parts A/B/C, Science, Technology and Policy for Water Pollution Control at the Watershed Scale: Current issues and future challenges 36, 424–429. https://doi.org/10.1016/j.pce.2010.03.028.

Xie L, Xie P, Li S, Tang H, Liu H (2003) The low TN:TP ratio, a cause or a result of Microcystis blooms? Water Research 37:2073 2080.

Yao, X., Zhang, Y., Zhang, L., Zhu, G., Qin, B., Zhou, Y., & Xue, J. (2020). Emerging role of dissolved organic nitrogen in supporting algal bloom persistence in Lake Taihu, China: emphasis on internal transformations. *Science of the Total Environment*, *736*, 139497.

Zibordi, G., Holben, B., Slutsker, I., Giles, D., D′Alimonte, D., Melin, F., Berthon, J.-F., Vandemark, D., Feng, H., Schuster, G., Fabbri, B., Kaitala,S., and Seppala, J. (2009). AERONET-OC: A network for the validation of ocean color primary products. *Journal of Atmospheric and OceanicTechnology*, 26:1634–1651